Mohsen Sherif
Vijay P. Singh
Ahmed Sefelnasr
M. Abrar   *Editors*

Water Resources Management and Sustainability

Solutions for Arid Regions

Springer

Water Science and Technology Library

Volume 121

The aim of the *Water Science and Technology Library* is to provide a forum for dissemination of the state-of-the-art of topics of current interest in the area of water science and technology. This is accomplished through publication of reference books and monographs, authored or edited. Occasionally also proceedings volumes are accepted for publication in the series. *Water Science and Technology Library* encompasses a wide range of topics dealing with science as well as socio-economic aspects of water, environment, and ecology. Both the water quantity and quality issues are relevant and are embraced by *Water Science and Technology Library*. The emphasis may be on either the scientific content, or techniques of solution, or both. There is increasing emphasis these days on processes and *Water Science and Technology Library* is committed to promoting this emphasis by publishing books emphasizing scientific discussions of physical, chemical, and/or biological aspects of water resources. Likewise, current or emerging solution techniques receive high priority. Interdisciplinary coverage is encouraged. Case studies contributing to our knowledge of water science and technology are also embraced by the series. Innovative ideas and novel techniques are of particular interest.

Comments or suggestions for future volumes are welcomed.

Vijay P. Singh, Department of Biological and Agricultural Engineering & Zachry Department of Civil and Environment Engineering, Texas A&M University, USA Email: vsingh@tamu.edu

All contributions to an edited volume should undergo standard peer review to ensure high scientific quality, while monographs should also be reviewed by at least two experts in the field.

Manuscripts that have undergone successful review should then be prepared according to the Publisher's guidelines manuscripts: https://www.springer.com/gp/authors-editors/book-authors-editors/book-manuscript-guidelines

Mohsen Sherif · Vijay P. Singh · Ahmed Sefelnasr ·
M. Abrar

Editors

Water Resources Management and Sustainability

Solutions for Arid Regions

Springer

Editors
Mohsen Sherif
National Water and Energy Center
United Arab Emirates University
Al Ain, United Arab Emirates

Ahmed Sefelnasr
National Water and Energy Center
United Arab Emirates University
Al Ain, United Arab Emirates

Vijay P. Singh
Department of Biological and Agricultural
Engineering
Texas A&M University
College Station, TX, USA

M. Abrar
National Water and Energy Center
United Arab Emirates University
Al Ain, United Arab Emirates

Preface

The lack of renewable freshwater in arid and semi-arid regions represents a major challenge to their sustainable development and prosperity. The problem of water scarcity is becoming more pronounced due to the rapid increase in the population, improvement of the living standard, notable expansion in agriculture and industrial activities as well as the impacts of climate changes. The water shortage problem is becoming commonplace, and many countries started to experience long durations of drought. The per capita share of freshwater has declined significantly, and in the meantime, the quality of the available water in stress areas has deteriorated. Nevertheless, water continues to be used unwisely, wasted, and sometimes contaminated. The water shortage problem in arid and semi-arid regions necessitates improved management and efficient utilization of the limited water resources. Focus should also be devoted to non-conventional water resources and water treatment technologies. Low-energy desalination systems, with minimum adverse environmental impacts, need to be developed. In the meantime, treated wastewater need to be fully utilized to elevate the current stress on traditional resources and specifically groundwater.

This issue of the Water Science and Technology Library includes selected papers that have been presented and discussed during the International Conference on Water Resources Management and Sustainability: Solutions for Arid Regions, March 22–24, 2022, Dubai, United Arab Emirates. The conference was organized by the National Water and Energy Center, UAE University in collaboration with the South Australian Goyder Institute for Water Research, and the Department for Environment and Water, Government of South Australia.

The conference attracted a large number of nationally and internationally well-known experts who have been at the forefront of water resources management and sustainability in arid and semi-arid regions. More than 55 countries, covering the five continents, are represented. It is hoped that this conference will contribute, in one way or another, to the water security and sustainability in such regions. The conference was designed to facilitate and encourage new perspectives on how science and innovative technologies can transform water management and sustainability in arid and semi-arid regions around the world. It addressed current challenges and priorities in water management and provided a forum to share knowledge, experiences, research,

and discoveries. The platform was particularly planned to bring together international experts working in the industry, academia, and government and to discuss solutions in the field of water resource management.

The papers contained in this book, *Water Resources Management and Sustainability: Solutions for Arid Regions*, are split up into six parts encompassing major aspects of water resources in arid regions and ordered in a logic technical sequence. Part I deals with hydrological monitoring topics, problems, and principles. Part II deals with rainfall and floods and their related attributes in the arid regions including flood mitigation and risk assessment. Part III addresses the droughts and their analysis and assessment. Part IV discusses the groundwater as an important component in the water budget in the arid regions. Threats, recharges, quality, and management options of this resource were also discussed in this part. Beginning with a perspective on management of this resource, the papers go on to discuss rational decision-making, challenges, use of information technology, integrated management, and modeling for groundwater resources management.

Part V deals with water quality. The papers in this part discuss the modern techniques for water quality assessment and treatment procedures. Part VI discusses the water resources management. This topic has been receiving a fair amount of attention in many arid countries of the world and more specifically in the Gulf region. The papers contained in this part discuss regulations for conservation, reuse, and security. The limited freshwater resources must be developed, managed, and used as efficiently as possible. Decision support systems for water resources planning, management, and water rights analyses and control have been discussed as well in the papers of this part.

The book will be of interest to researchers and practitioners in the field of hydrology, environmental engineering, agricultural engineering, earth sciences, and watershed and range sciences, as well as to those engaged in water resources planning, development, and management in arid and semi-arid areas. Graduate students and those wishing to conduct research in hydrology; environmental science and engineering; and water resources planning, development, and management will find the book to be of value.

Al Ain, United Arab Emirates   Mohsen Sherif
College Station, USA   Vijay P. Singh
Al Ain, United Arab Emirates   Ahmed Sefelnasr
Al Ain, United Arab Emirates   M. Abrar

Acknowledgements

Contents

About the Editors

Prof. Mohsen Sherif, a Ph.D., C.Eng., D.WRE, M.ASCE, Fulbrighter, is currently Professor of Water Resources and the Director of Research and Sponsored Projects at UAE University, United Arab Emirates. He has 35 years of teaching and research experience in groundwater flow and contamination, artificial recharge and management of groundwater systems, hydrology, hydraulics, fluid mechanics, numerical simulation, climate change, and water resources management. He has published more than 150 journal and conference papers and book chapters and completed several large-scale projects. Prof. Sherif received several international and national awards, including two Fulbright Scholarships, in 1993 and 1997, and Sheikh Khalifa Award for Education, Higher Education/Research, First Round, in March 2008. He was also awarded the Designation of Diplomate, Water Resources Engineer, American Academy of Water Resources Engineers. He is currently Associate Editor of the *Journal of Hydrology* and *Journal of Hydrologic Engineering.*

Prof. Vijay P. Singh, Ph.D., D.Sc., D.Eng. (Hon.), Ph.D. (Hon.), D.Sc. (Hon.), P.E., P.H., Hon. D. WRE, Dist. M. ASCE, Dist. Hon. M. IWRA, Dist. F. AGGS, Hon. Member AWRA, is Distinguished Professor, Regents Professor, and the inaugural holder of Caroline and William N. Lehrer Distinguished Chair in Water Engineering in the Department of Agricultural and Biological Engineering and Department of Civil and Environmental Engineering at Texas A&M University. Professor Singh has been recognized for four decades of leadership in research, teaching, and service in the hydrologic and water resources engineering profession. Singh's contribution to the state of the art has been significant in many different specialty areas, including hydrologic science and engineering, hydraulic engineering, water resources engineering, environmental engineering, irrigation science, soil and water conservation engineering, entropy-based modeling, copula-based modeling, and mathematical modeling. He has published 37 books, more than 1475 refereed journal papers, 122 book chapters, and 330 conference proceedings and papers and has edited 85 books. He has been the recipient of 110 national/international awards from professional organizations. He is a recipient of the Arid Land Hydraulic Engineering Award (2002), Ven Te Chow Award (2005), Torrens Award (2009), Norma Medal (2010),

Royce Tipton Award (2019), OPAL Award (2021), and EWRI Lifetime Achievement Award (2015), all given by ASCE; Ray K. Linsley Award for outstanding contributions to surface water hydrology, Wetzen Award, and the Founders Award, all given by AIH; Merriam Improved Irrigation Award, given by USCID; Chow Memorial Award, Crystal Drop Award, and Hon. Dist. Member Award, all given by IWRA; Hancor Award, given by ASABE; among others. He has been awarded three honorary doctorates one by University of Waterloo, Canada; another by the University of Basilicata, Italy; and another by the University of Guelph, Canada. He is a fellow of ASCE, EWRI, AWRA, IE, ISAE, IWRS, IASWC, and IAH; a member of AGU, IAHR, IAHS, and WASER. He is a member of National Academy of Engineering and a member/fellow of 12 other engineering/science academies.

Prof. Ahmed Sefelnasr obtained his Ph.D. in hydrogeology and holds B.Sc. and M.Sc. in Geology and hydrogeology, respectively. With over 25-year experience, he worked in both groundwater science and water resources management. With a Ph.D. in groundwater modeling and water resources management, he has published extensively and notably in the field of groundwater. Prof. Sefelnasr is a full professor of hydrogeology and water resources management at Assiut University, Egypt. He currently works at the National Water and Energy Center, United Arab Emirates University, UAE, as a researcher and expert of projects related to water resources policies and management, transboundary aquifers, water cooperation and water governance, artificial storage and recovery, numerical simulations, coastal aquifer, saltwater intrusion, water security, hydrology, and climate change. Prof. Sefelnasr has extensive international experience in groundwater research, consulting, and advisory work—with a wide variety of academic interests and practical application. He conducted teaching, research, and professional work in different areas and countries, mainly in Egypt, Germany, Japan, UK, and United Arab Emirates. Although Prof. Sefelnasr specialized in groundwater modeling, coupled flow and solute transport processes, groundwater exploration, and water resources management, he currently fosters a keen interest in groundwater resources, including their governance, advocacy strategies, and sustainable management, mainly in arid and semi-arid areas.

Dr. M. Abrar has professional experience in hydro-climatology. His research is focused on ecosystem responses to regional climate change, streamflow variations, fluctuation in precipitation time series, drought monitoring, and other hydrological variables using climate models, hydrological models, and drought indices. He completed several studies on surface runoff modeling, drought monitoring, drought translation, variation in precipitation, and evaluation of different satellite products.

Part I
Hydrological Monitoring

Chapter 1
Wireless Sensor Networks for Hydrological Monitoring, Helpful Tools for Accurate Models

Qasem Abdelal and Abdalrhman Alayan

1.1 Introduction

Arid regions face several hydrologic and hydraulic challenges; they face the challenge of lack of water, and the challenge of flash floods, and in many developing countries, the challenge of inefficient management of the limited water resources. Coupled with these challenges decision-makers face an ever-rising complexity and a noticeable shift in the severity and the nature of the hydrologic and hydraulic conditions of the region rapidly.

Climate change has gained a lot of interest among the public as well as a considerable attention in the scientific community because of the worrying nature of its effects and their implications on communities. (Myhre et al. 2019) reports an increase in the frequency of extreme precipitation events amounting to almost the double per degree of warming. Flash floods have been a significant burden on societies; therefore, efficient flood mitigation measures are highly dependent on accurate identification of the high-risk areas, this can be achieved by having accurate flood inundation maps, which in turn is a function of accurate input data, be it terrain and topography, land use and cover, or precipitation. Environmental monitoring is not a priority in many developing countries. This can be understandable given its need for significant financial and human resources (Hughes 2006), what also adds to the challenge, is the general lack of use of the monitored data in decision making, thereby the reluctance to allocate human and financial resources to such monitoring programs.

Hydrological input data could be utilized in risk detection and alert, this can be done by monitoring for patterns that are highly correlated with certain conditions that would pose danger in urban areas. (Ancona et al. 2014) describes how sensor systems would fit in risk-alert scheduling strategy as they enable monitoring rainfall and

Q. Abdelal (✉) · A. Alayan
Civil and Environmental Engineering Department, German Jordanian University, Amman
Madaba Street, P.O. Box 35247, Amman 11180, Jordan
e-mail: Qasem.abdelal@gju.edu.jo

discharge and converting resulting data using hydrological modeling into information used for event management systems that can give Geo-referenced warnings.

A Flash flood in hydraulic terms represent a very intense precipitation resulting with a very short Lag-Time, where the duration between the rainfall peak and the discharge peak is limited, which leaves little time for a suitable response if not processed through a risk alert detection process.

Conjointly to the changes to the climate, the aspect of human intervention by urban development imposes a further challenge, where development is frequently underdone without proper planning that takes into consideration the hydraulic and hydrological conditions and how these factors would affect the ecology. It is argued that there is a need for accurate, widely spatially distributed data for accurate modeling, which is a very powerful tool for decision-making. Using the classical commercial monitoring systems can be limiting due to financial and administration constraints. This was the motivation for relying on low cost, low energy wireless sensor networks for environmental monitoring. These were developed in house, the electronic components are available in the market, but the development of the whole module, testing and commissioning was done locally. Details on the development of these systems can be found at (Abdelal and Al-Hmoud 2021), and (Abdelal et al. 2019).

The process of hydrological modeling is a vigorous task, not only it depends on various factors but also the models' predictive accuracy relies on the accuracy of the data. Precipitation is a major input in hydrological models, and its precise spatial and temporal presentation is critical. As (Zhao et al. 2022) describes there is no agreed upon consensus on how rainfall variability influences hydrological response.

According to (Zhao et al. 2022), some researchers argue that the spatial variability of rainfall does not cause a considerable difference in runoff generation under specific conditions. It is also reported that the effect of the rainfall variability influenced only the timing characteristics of the runoff not its peak magnitude. (Obled et al. 1994) tested the effect on discharge due to the rainfall spatial variability with different densities of rain gage networks, which concluded that for medium size watershed the spatial variability has a secondary effect on discharge, however noting that large and small-sized watersheds react strongly to spatial variability.

On the other hand, it is concluded in many other research projects that spatial variability has a prominent effect on model outcomes such as peak flow, time to peak and the shape of the hydrograph (Zhao et al. 2022).

In a study assessing the influence of factors including rain gauge density and rain gauge distribution on estimating areal mean rainfall, (Hwang et al. 2020) concluded that the rain gauge density has an effect of the mean absolute percentage discrepancy as more densely gaged catchments would produce more accurate data. This would be even more relevant based on the known sensitivity of spatial distribution in arid regions. An example reported by (Wheater et al. 2007) in Saudi Arabia where extremely spotty rainfall resulted in observed flow in wadis where there was no observed rainfall.

In another study by (Hohmann et al. 2020), it was concluded that it is very hard to quantify a general number of gages needed in order to produce a reliable hydrological runoff model, under heavy rainfall events for small catchments. This is due

to the complex spatiotemporal characteristics especially of short-duration convective events. For long-duration stratiform -type events a density with a mean station distance of around 6 km was sufficient to produce accurate runoff data.

Moreover (Zhao et al. 2022) reported a study concluding that the multi-site generator performance is better than the single-site generator in both mean summer flow and different return period flows based on comparisons of simulations using measured rainfall data. In addition to reporting that more sensitivity for rainfall input and its sampling method was observed in catchments with a smaller size, while (Muleta et al. 2007) reports that the number of rainfall stations impacts SWAT streamflow modling results, as better preformance is corrilated with higher number of rainfall stations. (Arnaud et al. 2011) also stress on the importance and added value of having a good understanding of the catchment characteristics. (Zeng et al. 2018) noted that for lumped hydrological models, the performance increased with a higher number of rain gauges.

Several basic structures for rainfall-runoff modeling are used, ranging from empirical to conceptual or even physical approaches, each methodology can also have a different spatial structure: such as lumped models or semi-distributed models or fully distributed models.

The lumped models deal with the whole catchment area as one unit while the semi distributed relies on a series of lumped and distributed parameters for result generation, lastly distributed models fully account for the spatial variability (Sitterson et al. 2017). Lumped models represent the fast and easy path in rainfall-runoff modeling, as they are good in simulating average conditions, however they can easily be biased and unrealistic due to the loss of the spatial resolution.

A distributed model is more accurate, on the other hand, it is data intensive, which would mean it might be unfeasible to rely on normal precipitation sensors as they may not be able to provide measured data at the needed resolution, temporally and spatially.

The model used for predicting the rainfall runoff patterns for this study is the Hydrologic Engineering Center's Hydrologic Modeling System (HEC-HMS). This software is publicly available, it was developed by the US Army Corps of Engineers for the purpose of simulating several hydrological analysis processes such as unit hydrographs, hydrological routing, infiltration, and a number of other advanced processes.

This study quantifies the variability in the rainfall measurements, establishes the need for high-resolution rain recording by demonstrating the effect on model predictions, and introduces an economical approach for securing the needed data.

1.2 Methods

Some precipitation data used by this study came from official public sources such as the meteorological department, climate directorate, or a private entity such as Arabia Weather (https://www.arabiaweather.com), all have a few rain gages distributed through the region. These are good reliable sources, but their spatial distribution

is not high enough to ensure proper representation of all watersheds in the region, particularly when the analysis is for a small watershed. In addition, their temporal resolution is mostly low.

A network of locally developed rain gages was deployed to collect higher resolution data. The locally developed and distributed network of rain gages are composed of an RK400-4 tipping bucket and a data logger/transmitter apparatus. The tipping bucket is manufactured by Rika, it has a measured rainfall intensity of 4 mm/min at a resolution of 0.2 mm, it can operate between 0 and 60 °C which suitable for the local conditions of the study. The system is composed of multiple parts, a data logger, a data transmitter, numerous sensor inputs, power management components and microcontroller. The microcontroller used was the Arduino Pro Mini Atmega328 5 v-16 MHz, that was used for its ultra-low power consumption and very small footprint, in addition to its relatively good computational capacity. This was mounted to a specifically designed printed circuit board, PCB. The PCB was crucial for ensuring consistent mounting of the different components and reliable production of multiple units. The data logger is composed of a micro-SD card module with a micro SD card, this serves as a backup to store the data in case it transmission fails. The data transmission is performed through a SIM800 GSM module, this module requires a SIM card and transmits the data through a telecommunication network to a specially developed website to display the data and store it for further processing. The sensors connected to the system for this project include a tipping bucket for rainfall measurement and an ultrasonic sensor installed at different locations for flow depth measurement. Water depth readings were then converted to flow rate using manning's equation for uniform flow. Details of the system are available at (Abdelal et al. 2019; Abdelal and Al-Hmoud 2021). Figure 1.1 shows the printed circuit board (PCB) that was specifically designed and fabricated for the current application, it was designed such that several configurations of sensors can be mounted. Figure 1.1 also shows a sample of the PCB with the different modules mounted above it, several other electronic components are added for signal stability.

Figure 1.2 shows two sample installations for a rain gage placed on the roof of a commercial facility, along with the data logger and transmitter. The figure also shows a stream flow ultrasonic gage placed on the ceiling inside a culvert. The culvert is approximately 3 m wide, 1.7 m high and more than 40 m long, thus ensuring uniform flow conditions.

Two locations were used for this study; the first was in Petra, almost 230 km south of Amman, Jordan. The other location was in Madaba, almost 40 km south of Amman. The watershed in Petra has a total area of 59.5 km^2, an average basin slope of 0.22, a length of 9669 m, and a maximum stream length 14,860 m. It is primarily rural with limited urbanization except for the city of Wadi Musa and some small villages. The watershed in Madaba, on the other hand, is much smaller, it has an area of approximately 6.9 km^2, a basin slope of 0.064, a mean flow distance of 5800 m, a mean stream length of 2780 m, and is primarily urban. These two locations represent two different hydrological conditions with an average total annual rainfall in Madaba of 191 mm and in Petra of 362 mm. Both locations are subject to thunderstorms and flashfloods during certain times of the year.
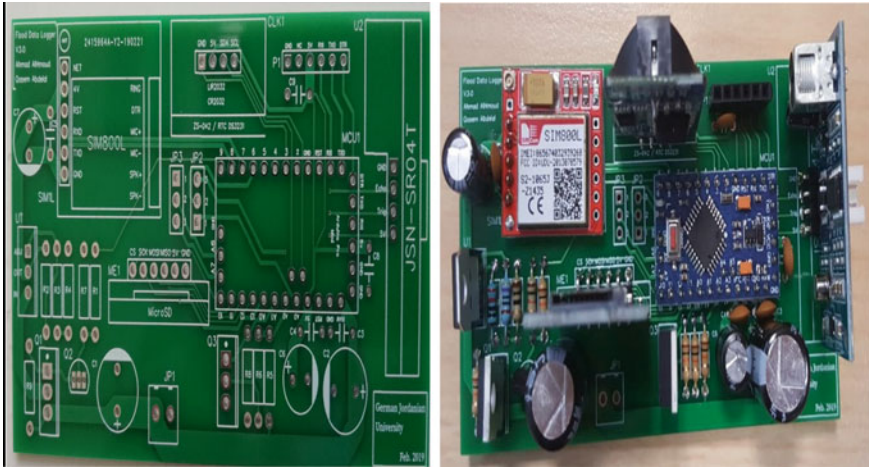
Fig. 1.1 PCB (left) and finished module (right) with and ultrasonic module attachment

Fig. 1.2 Sample installations of the tipping bucket (left) and ultrasonic (right) sensors

Figure 1.3 shows the relative location of the two study sites in Jordan. The study site in Petra is composed of five rain gaging stations that were installed as part of the current study, their recordings were analyzed against the official records, referred to as the official station. In the Madaba watershed, a total of four stations were installed. The choice of the locations of each of the devices was such that they are spatially distributed inside or outside the watershed of interest. The stream gage was placed at the watershed outlet. Figure 1.4 depicts the wadies within the area of focus in Petra and the setup for the HEC-HMS model used for rainfall runoff analysis of the watershed.
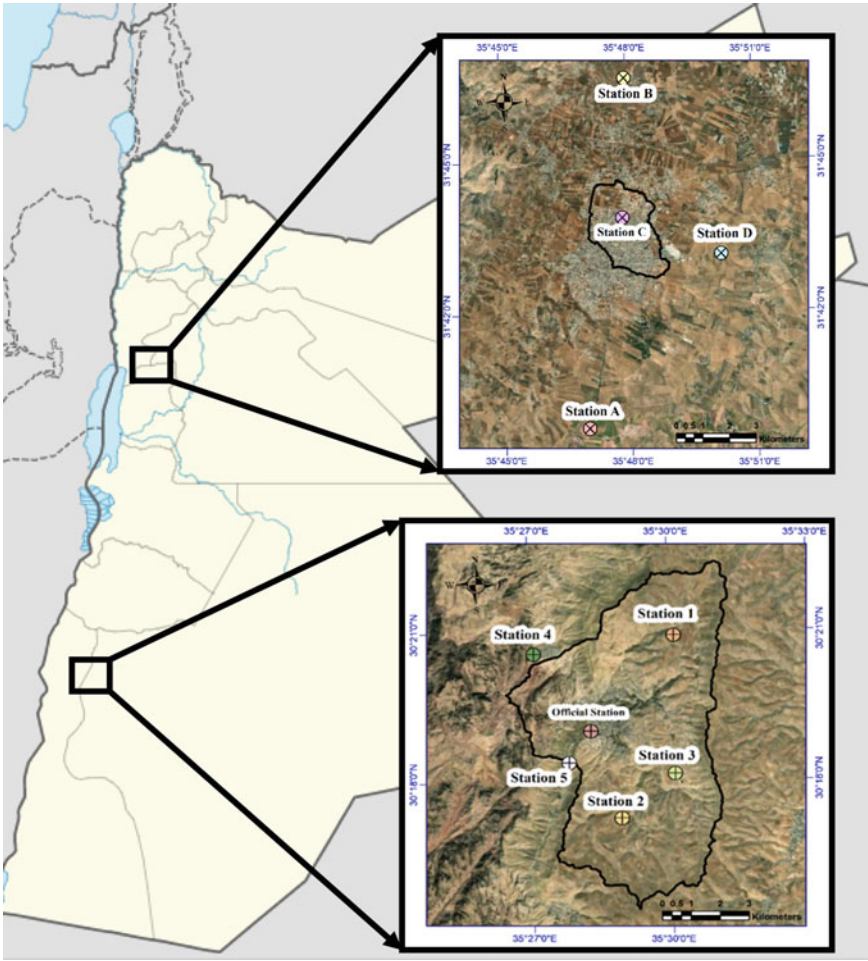
Fig. 1.3 Map of Jordan with the two study area locations, Madaba (top) and Petra (bottom), Google Earth® was used to generate the callouts

The stations in Petra have a much longer record of data (since Oct. 2019), while the ones in Madaba started collecting data the season of 2021 with some older data from some of the stations.

Daily precipitation data is available for the official station in Petra. On the other hand, the five stations we installed report data every minute. A comparative statistical analysis was made between the total daily values of precipitation in the five stations and the daily values of the official stations. The Z test for analysis of the mean is used to study the difference between the two means and the results are presented. While the T-test for analysis of the mean was made to the four stations in Madaba because the number of samples doesn't exceed 30. It is unfortunate that the data available

Fig. 1.4 The developed HEC-HMS model for the Petra watershed

from the official station in Madaba does not extend to the same time duration of the four stations (Stations A, B, C and D).

As the data in Petra has the longest duration, further analysis was done on the five stations (Stations 1–5). The average precipitation over the whole watershed was calculated using both Arithmetic mean and the Thiessen polygon method. Results from both methods are used in the HEC-HMS model of the watershed and a comparison of the runoff predictions is done.

The developed HEC-HMS model includes a watershed of an area of 59.9 km^2. The loss method chosen was the SCS curve number method and the SCS unit hydrograph method was used for transform. The model was set with actual precipitation data from four storms in January, February, and March of 2020. The model was run 12 times using precipitation data from three sources.

1.3   Results and Discussion

An analysis of the rain data in Petra showed that there is a difference between the total daily precipitation in the official rain gage and the average precipitation developed using the arithmetic mean and the Thiessen polygon. Figure 1.5 illustrates that difference, it can be clearly noted that certain events are captured using the distributed rain gages but are not captured using the official station, a clear example of that is the storm of January 9, 2020.

It is noticed that the difference between the total records of the individual stations and that of the official station ranges between 3.0 and 62.0%. It was also noted that the difference between the average precipitation calculated using the Thiessen polygon and the official station is 30.4% and the difference between the average precipitation calculated using the arithmetic mean and the official station is 34.4%. This difference has been statistically verified by conducting the Z test for difference in the mean, and a T test. The results of both tests demonstrate that the difference is significant in all conducted tests. Refer to Tables 1.1 and 1.2.

These results clearly indicate the high variability of the precipitation values even within a circular area less than 5 km. This is related to the very localized nature of the thunderstorms, in which different precipitation values and rates fall on different areas. Figure 1.6 shows the variations in a sample storm (storm 3) and highlights the difference between the precipitation records at each locality.

This difference can cause a big variation in the predicted runoff values. Accurate prediction of these flows is crucially important for decision making process, it is important for safety considerations, for management of floodwater and for emergency and logistical preparations. This is clearly visible in Petra where tourists' and locals' evacuations may need to be arranged based on an early warning system that could
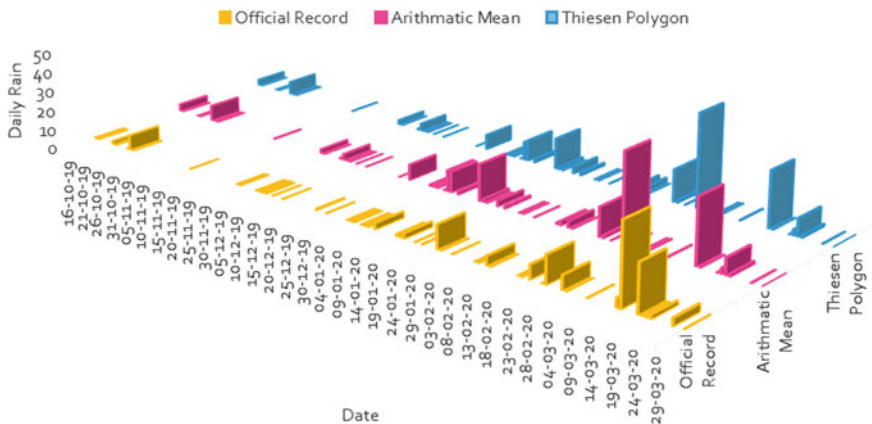
Fig. 1.5 An illustration of the difference in total daily rain for various storms between the official records in Petra, the average calculated using the arithmetic mean and the weighted average calculated using Thiessen polygon

Table 1.1 statistical analysis for mean between the stations in Petra

Comparison between	Z value	Critical Z two tail	Test results
Official record and station 1	− 0.895	1.960	Statistically different mean
Official record and station 2	− 0.987	1.960	Statistically different mean
Official record and station 3	− 0.074	1.960	Statistically different mean
Official record and station 4	− 0.347	1.960	Statistically different mean
Official record and station 5	− 0.361	1.960	Statistically different mean
Official record and Arithmetic mean	− 0.619	1.960	Statistically different mean
Official record and Thiessen polygon	− 0.552	1.960	Statistically different mean

Table 1.2 statistical analysis for mean between the stations in Madaba

Comparison between	T value	Critical T two tail	Test results
Station A and C	− 0.72	2.16	Statistically different mean
Station B and C	− 0.36	2.16	Statistically different mean
Station D and C	− 1.03	2.23	Statistically different mean
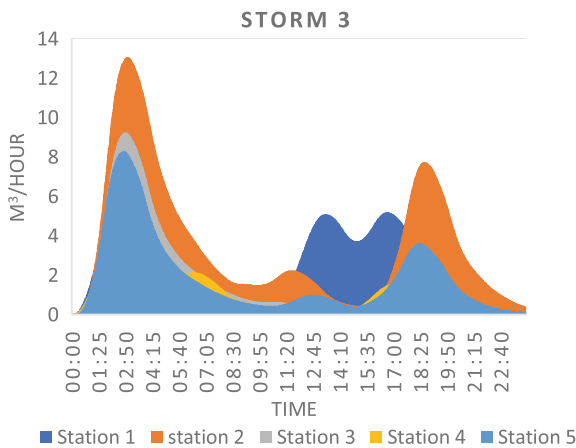
Fig. 1.6 Variable precipitation rates at different stations for storm 3 dated 14/3/2021

be designed to be triggered by the precipitation record. Thus, accurate predictions are necessary for taking the proper action.

To quantify the effect this uncertainty in precipitation has over the runoff predictions, a HEC-HMS model for the Petra watershed was developed. Several model runs where done using different storms and the effect on the predicted runoff is reported as shown in Fig. 1.7.
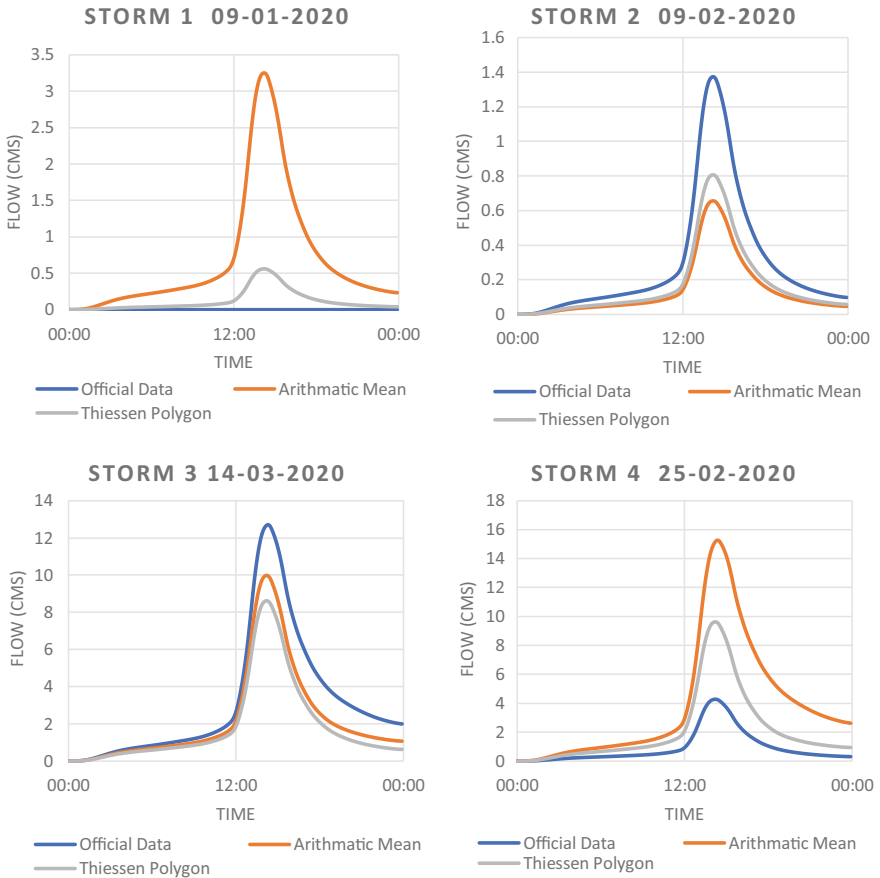
Fig. 1.7 HEC-HMS model results for four sample storms

Model results clearly indicate that the predicted flows are highly dependent on the variation of the precipitation quantities. The storm of 9/1/2020 for example was only detected using the distributed rain gages and not the official gaging station, and therefore, the runoff model didn't predict flow using the official station's data, when on the other hand, it predicted more than 3 CMS when using the data from the arithmetic mean averaging system. This stresses the need for a localized measurement of precipitation in cases where runoff quantification is needed. This suggests that an analysis of the watershed associated with a certain discharge point is necessary, and a sufficient distribution of rain gages is needed to properly predict flows.

1.4 Conclusions

With the relative ease of deploying many more units for hydrological monitoring, in particular rain gages, it is recommended to increase the number of units when performing rainfall-runoff analysis. The units are becoming more affordable and therefore, the benefit of their use outweighs the costs. High-resolution deployment can be particularly needed in early warning system, where warnings need to be issued based on localized real time data. Arid regions usually suffer the most from thunderstorm and flash floods, localized rain gages could help mitigate their effect.

References

Abdelal Q, Al-Hmoud A (2021) Low-cost, low-energy, wireless hydrological monitoring platform: design, deployment, and evaluation. J Sens 1–14. https://doi.org/10.1155/2021/8848955

Abdelal Q, Al-Hmoud A, Abu Jaber N (2019) Low cost monitoring systems for environmental and water resources applications. In: World environmental and water resources congress pittsburg, pp 1–14. https://doi.org/10.1155/2021/8848955

Ancona M, Corradi N, Dellacasa A, Delzanno G, Dugelay J-L, Federici B, Gourbesville P, Guerrini G, Camera AL, Rosso P, Stephens J, Tacchella A, Zolezzi G (2014) On the design of an intelligent sensor network for flash flood monitoring, diagnosis and management in urban areas—position paper. ANT/SEIT

Arabia Weather (2022) Arabia weather. http://stations.arabiaweather.com/

Arnaud P, Lavabre J, Fouchier C, Diss S, Javelle P (2011) Sensitivity of hydrological models to uncertainty in rainfall input. Hydrol Sci J 56(3):397–410. https://doi.org/10.1080/02626667.2011.563742

Hohmann C, Kirchengast GOS, Rieger W, Foelsche U (2020) Runoff sensitivity to spatial rainfall variability: a hydrological modeling study with dense rain gauge observations. Hydrology Earth Syst Sci Discuss 1–28. https://doi.org/10.5194/hess-2020-453

Hughes DA (2006) Comparison of satellite rainfall data with observations from gauging station networks. J Hydrol 327(3):399–410. https://doi.org/10.1016/j.jhydrol.2005.11.041

Hwang SH, Kim KB, Han D (2020) Comparison of methods to estimate areal means of short duration rainfalls in small catchments, using rain gauge and radar data. J Hydrol 588:125084. https://doi.org/10.1016/j.jhydrol.2020.125084

Meteorological Department (2022) Meteorological department, climate directorate. http://jmd.gov.jo/EN

Muleta MK, Nicklow JW, Bekele EG (2007) Sensitivity of a distributed watershed simulation model to spatial scale. J Hydrol Eng 12(2):163–172. https://doi.org/10.1061/(ASCE)1084-0699(2007)12:2(163)

Myhre G, Alterskjær K, Stjern CW, Hodnebrog Ø, Marelle L, Samset BH, Sillmann J, Schaller N, Fischer E, Schulz M, Stohl A (2019) Frequency of extreme precipitation increases extensively with event rareness under global warming. Sci Rep 9(1):16063. https://doi.org/10.1038/s41598-019-52277-4

Obled C, Wendling J, Beven K (1994) The sensitivity of hydrological models to spatial rainfall patterns: an evaluation using observed data. J Hydrol 159(1):305–333. https://doi.org/10.1016/0022-1694(94)90263-1

Sitterson J, Knightes C, Parmar R, Wolfe K, Muche M, Avant B (2017) An overview of rainfall-runoff model types 30

Wheater H, Sorooshian S, Sharma KD (eds) (2007) Hydrological modelling in arid and semi-arid areas. Cambridge University Press, Cambridge Core. https://doi.org/10.1017/CBO9780511535734

Zeng Q, Chen H, Xu C-Y, Jie M-X, Chen J, Guo S-L, Liu J (2018) The effect of rain gauge density and distribution on runoff simulation using a lumped hydrological modelling approach. J Hydrol 563:106–122. https://doi.org/10.1016/j.jhydrol.2018.05.058

Zhao Y, Nearing MA, Guertin DP (2022) Modeling hydrologic responses using multi-site and single-site rainfall generators in a semi-arid watershed. Int Soil Water Conserv Res 10(2):177–187. https://doi.org/10.1016/j.iswcr.2021.09.003

Chapter 2
Automatic Extraction of Surface Water Bodies from High-Resolution Multispectral Remote Sensing Imagery Using GIS and Deep Learning Techniques in Dubai

Lala El Hoummaidi and Abdelkader Larabi

2.1 Introduction

The research community has always been fascinated by the properties of water, and, consequently, several investigations continue to address this ubiquitous fluid responsible for life on this planet. Water bodies, which play an essential role in climate change and the global carbon cycle, are mapped in the spatiotemporal domain to analyze, and assess the extent and rate of their degradation and disappearance (Fletcher et al. 2013).

Mapping natural resources such as water bodies using high-resolution satellite imagery has gained much attention from government entities in the last few years, especially since these water resources are subject to intense exploitation and monitoring them regularly is critical for better sustainable management. Remote sensing and image processing experts across the globe have used a wide range of satellite data with different spatial, spectral, and temporal characteristics to generate thematic maps of land use, land cover, and maps with particular emphasis on water bodies. Simultaneously, various techniques were developed to extract these features from satellite imagery, and each method has its strengths and weaknesses (Wang et al. 2013; Senaras et al. 2014; Yang et al. 2015).

L. E. Hoummaidi (✉) · A. Larabi
Laboratory Analysis and Modeling of Water and Natural Resources (LAMERN), Mohammed V University in Rabat, Mohammadia School of Engineers, P.O. Box 554, Rabat, Morocco
e-mail: lelhoummaidi@scad.gov.ae

L. E. Hoummaidi
Geographic Information Systems Centre (GISC), P.O. Box 67, Dubai Municipality, Dubai, UAE
e-mail: larabi@emi.ac.ma

With the advancement in the spatial resolution of remote-sensing images, many remote-sensing satellites (such as IKONOS, WorldView-2, and RapidEye) can provide high-resolution images (Huang et al. 2017). Most high-resolution remote-sensing images have only four bands (blue, green, red, and near-infrared), lacking the short-wave infrared (SWIR). However, SWIR is necessary to compute the modified normalized difference water index (MNDWI) and the automated water extraction index (AWEI) indices. High-resolution multispectral images can support much more detailed spatial features information, which would significantly improve the accuracy of water body extraction. Many algorithms were designed for collecting water bodies from remote-sensing imagery, including single-band threshold and multi-band threshold methods, water body index, sub-pixel water mapping, and supervised and unsupervised classification. The water body index method has the advantages of fast calculation and high accuracy; therefore, it is the first choice used by government entities. McFeeters put forward the normalized difference water index (NDWI) model based mainly on the normalized difference vegetation index (NDVI). However, this model cannot distinguish between dark shadows and water bodies. Xu worked on a Modified Normalized Difference Water Index (MNDWI) to enhance the open water features. This index uses mid-infrared bands for normalization instead of near-infrared and green bands and has better results for open water bodies extraction (McFeeters 1996). These improvements and variations of water index methods are generally difficult to implement in high-resolution satellite imagery due to the limited spectral resolution. Hence, image classification methods such as supervised classification or machine learning are the favourite option for extracting water bodies from drone and multispectral satellite images. Mainly, machine-learning methods include neural networks, while unsupervised classification methods include k-means clustering and ISODATA clustering methods. These algorithms are commonly used on low spatial resolution remote-sensing images and have undergone less research for urban water body extraction (Shen 2012).

Among current water extraction technologies adopted by Geographic Information Systems Centre (GISC) at Dubai Municipality, a mainstream method uses drones and high-resolution satellite imagery to collect water information quickly and accurately. Previous water-resource surveys have been based on photo interpretation and supervised classification of multispectral satellite imagery. However, small water bodies such as neglected artificial water bodies and small ponds cannot be extracted due to either the limited spatial resolution of these remote-sensing images or the color reflectance of polluted water that cannot be visually interpreted.

Whatever the approach, generally, government organizations are interested in a fast, accurate, and automated method. Towards this objective, GISC specialists adopted hybrid approaches using different algorithms like decision tree classifier, neural network, and other methods (Kang et al. 2016). This study discusses an intuitive approach to extracting water bodies using an end-to-end deep learning workflow designed to extract water features and detect building shadows effectively even in complex circumstances. This novel approach offers promising opportunities to

update water bodies features with high accuracy in meters while saving the cost and time invested in traditional methods such as field visits and photo interpretation (Qi et al. 2012; Dixon and Candade 2008).

2.2 Methods

2.2.1 Study Area

Dubai Emirate is the second largest Emirate in the United Arab Emirates. Positioned in the southeast coast of the Arabian Gulf between 25°16′ North and 55°18′ East, Dubai spreads on a total area of 3900 km^2 and stretches along the Arabian Gulf coast for 72 km. The Emirate of Dubai shares borders with Sharjah in the northeast, the capital Abu Dhabi in the south, and Oman in the southeast. Figure 2.1 illustrates the administrative boundaries of the Dubai Emirate, which occupies 5% of the United Arab Emirates' total area.

Dubai's landscape is a mixture of sandy desert, shallow shores, and coral reefs. The waters of Dubai are the living environment of more than 300 species of fish, and such rich marine life of Dubai has provided its inhabitants with a significant source of income for thousands of years (Böer 1997; Hadji 2019) The flat sandy desert falls to the Hajar Mountains, which run alongside Dubai's border with Oman. The Western Hajar mountains chain has an arid, jagged, and shattered landscape, whose mountains rise to about 1300 m in some places. Dubai has scarce natural river bodies and oases; however, Dubai has a natural bay, Dubai Creek, dug up to make it deep enough for large vessels to pass through. Dubai Emirate also has multiple gorges and waterholes which spot the base of the Hajar mountains. A gigantic sea of dunes covers much of southern Dubai and eventually leads into the desert known as The Empty Quarter (Sherif et al. 2021).

2.2.2 Input Data

This study used two categories of high-spatial-resolution remote sensing images for water extraction: Drone images using DJI Matrice 600 Pro and WorldView2 high-resolution satellite images. The detailed specifications of these images are provided in Table 2.1, considering the complex water network differences in Dubai Emirate between Dubai and Hatta Regions. The selected areas were located in both regions.

The airframe from Dajiang Baiwang Technology (DJI Matrice 600 Pro) accommodates the latest DJI technologies, along with the Lightbridge 2 HD transmission system, A3 Pro flight controller, Battery Management system, and Intelligent Batteries. Several gimbals and Zenmuse cameras are natively compatible and fully integrated with existing GIS Software at Dubai Municipality, making
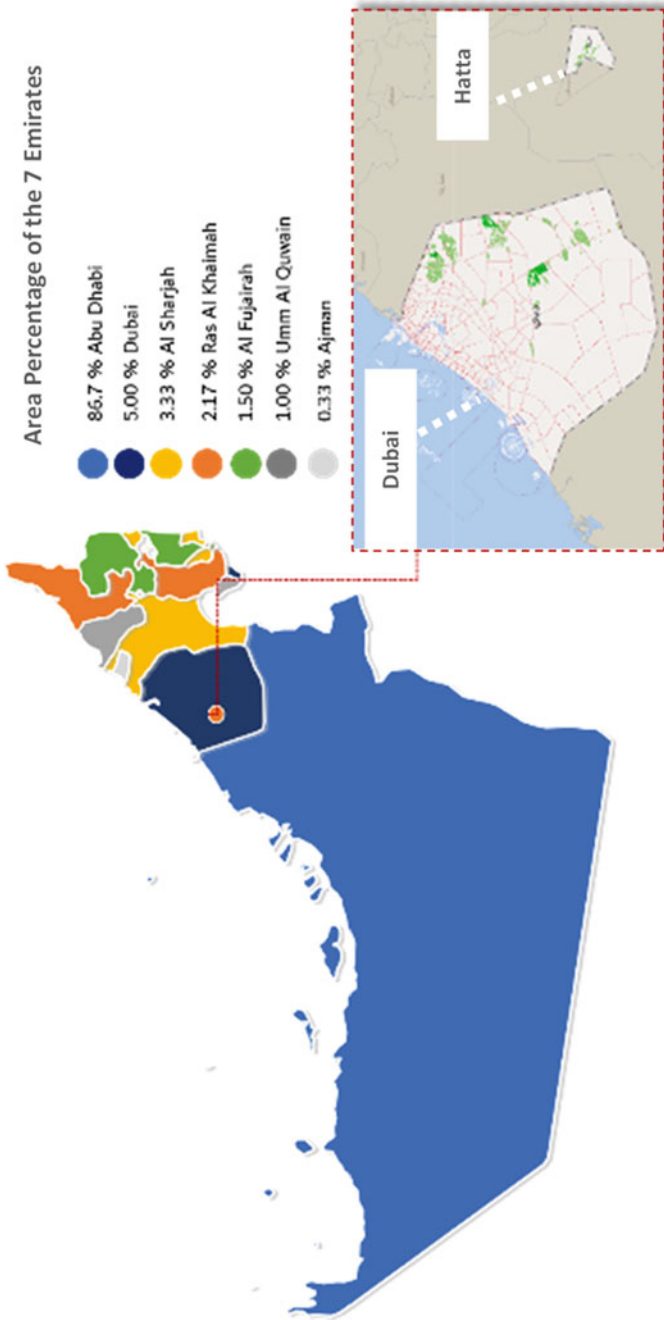
Fig. 2.1 Location map of Dubai Emirate (Dubai and Hatta regions)

Table 2.1 Overview of drone imagery and Worldview2 multispectral Imagery

Parameters	Drone (DJI Matrice 600 Pro)	WorldView2
Number of bands used	4	8
Spectral range	450–780 nm	400–1040 nm
Spatial resolution (m)	0.01	1.8
Dynamic range (bit)	8 bit/pixel	11 bit/pixel

M600 Pro one of the best solutions for field data capturing (Messina et al. 2020). On the other hand, WorldView-2 high-resolution optical products are available as part of the DigitalGlobe Standard Satellite Imagery products from the QuickBird, WorldView-1/-2/-3/-4, and GeoEye-1 satellites.

Figure 2.2 shows examples of the leading products of DJI Matrice 600 Pro used by GISC, the right figure (a) refers to the true Ortho-Photo captured with 10 cm ground resolution, the left figure (b) refers to the Data Surface model generated from the point clouds, and figure (c) shows the normalized difference vegetation index (NDVI) (Gandhi et al. 2015).

Figure 2.3 summarizes the process of capturing aerial data with downward-facing multispectral cameras and LIDAR payloads using DJI Matrice 600 Pro. During such a survey, the ground is photographed several times from different angles, and each image is tagged with coordinates. For an area like Hatta, the field survey takes 4 days to cover the entire area (2 km^2), while the processing time takes 1 day only for the automatic production of the Data Elevation Model (DEM) and the rectified Ortho-Photo of the area.

Figure 2.4 shows the drone images captured for two different sites in Dubai (Al Khayran and Safari Dubai) with a high resolution that reached 10 cm. These images, along with all the other input images across the Emirate, were adjusted for radiometric and geometric correction. Reference water mapping was manually digitized through a visual interpretation process by GISC Data Team using the WorldView2 Imagery (Zhou et al. 2014). Satellite imagery often includes other bands than just the visible spectrum. It might seem standard to use all available bands for training the selected model (PyTorch framework) (Bote-Curiel et al. 2019; Subramanian 2018). However, since there are certain advantages to using the 3 true color bands, therefore, multiple combinations were used for this project to test the results, including RGB and RGNIR combinations.

Figure 2.5 summarizes the deep learning integrated into the ArcGIS platform where third-party deep learning frameworks are integrated, including TensorFlow, PyTorch, CNTK, and Keras, to extract features from single images or imagery collections. The ArcGIS.learn module from the ArcGIS API for Python had been used during this study to train deep learning models by consuming the exported training samples directly (Zhang et al. 2020; Li et al. 2015).
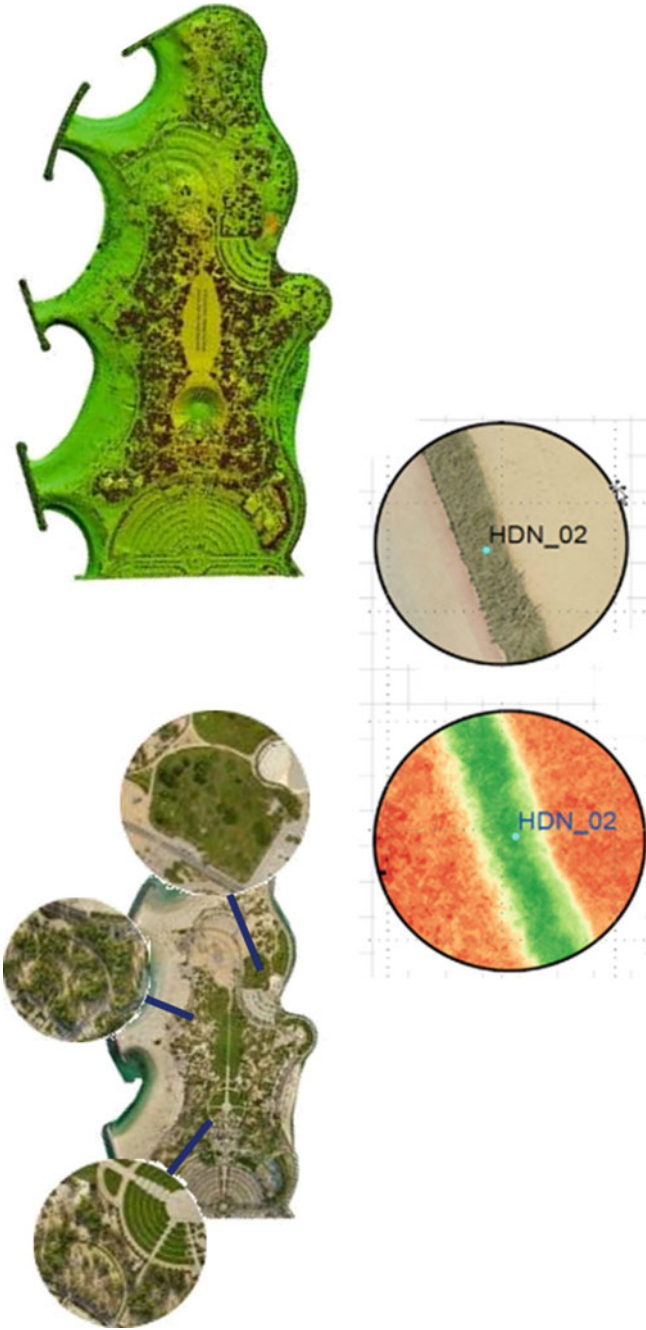
Fig. 2.2 DJI Matrice 600 Pro Products: true Orthophoto, DSM and NDVI
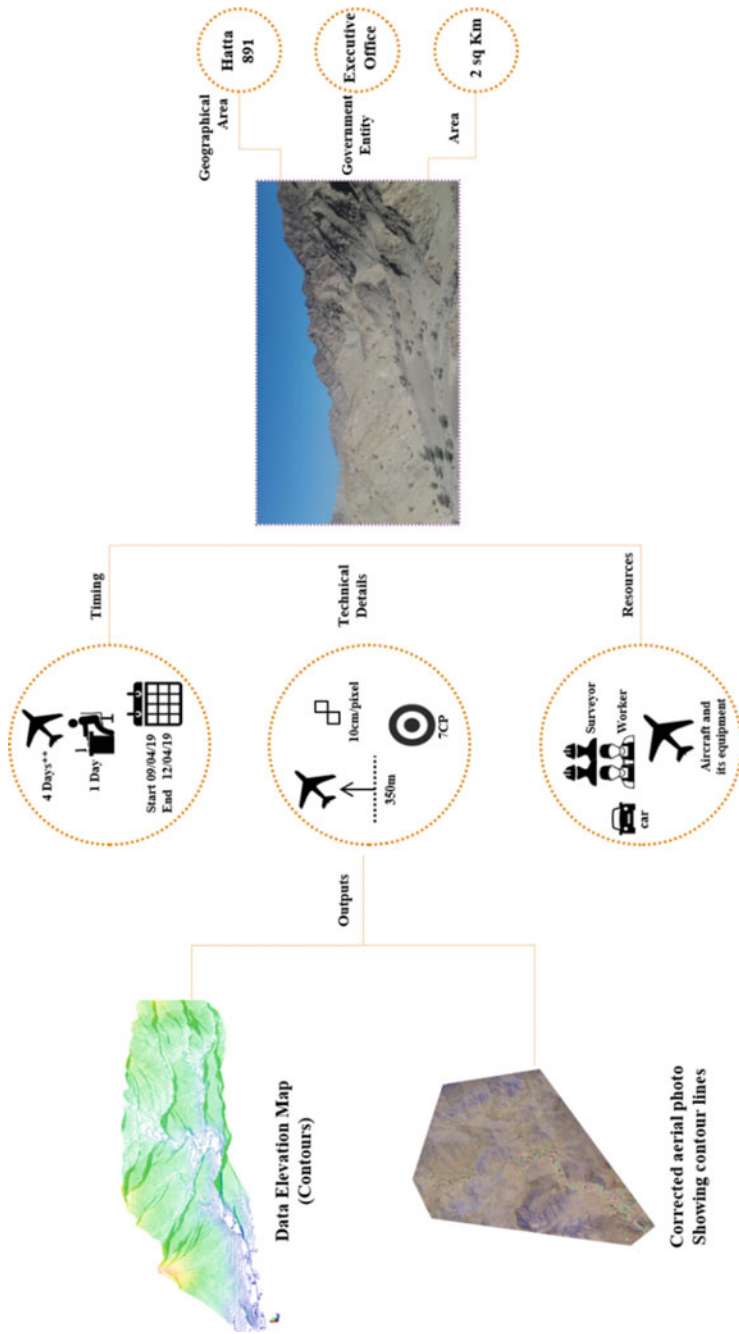
Fig. 2.3 Process of drone mapping field mission—Hatta region

Fig. 2.4 Drone map results 10 cm resolution (**a** Al Khayran community, **b** Safari Dubai)
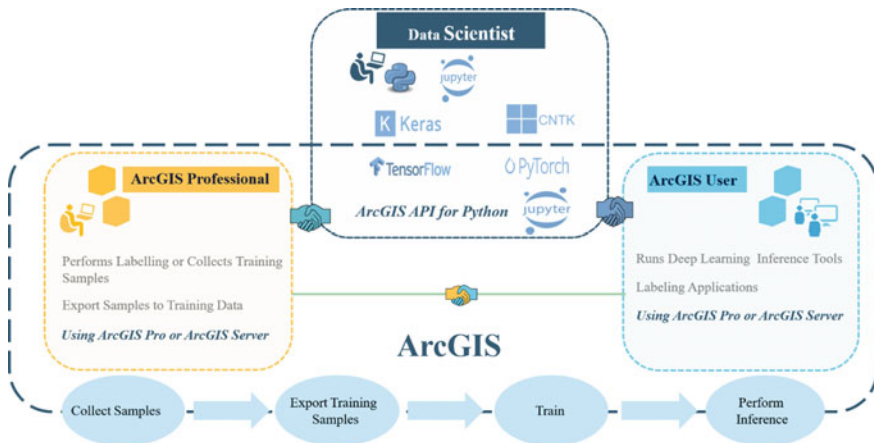
Fig. 2.5 ArcGIS pro deep learning integration workflow

Furthermore, several model types were tested to train the selected deep learning model, including the Single Shot Detector (Object detection) where Pascal Visual Object Classes metadata format was used, U-Net (Pixel classification), Feature classifier (Object classification), RetinaNet, MaskRCNN, FasterRCNN, BDCN Edge Detector (Pixel classification)—The Bi-Directional Cascade Network (BDCN) and HED Edge Detector (Pixel classification)—The Holistically-Nested Edge Detection (HED). In the end, the results of the single-shot detector and HED Edge Detector proved to be both satisfying and very useful for water boundary detection (Tsang
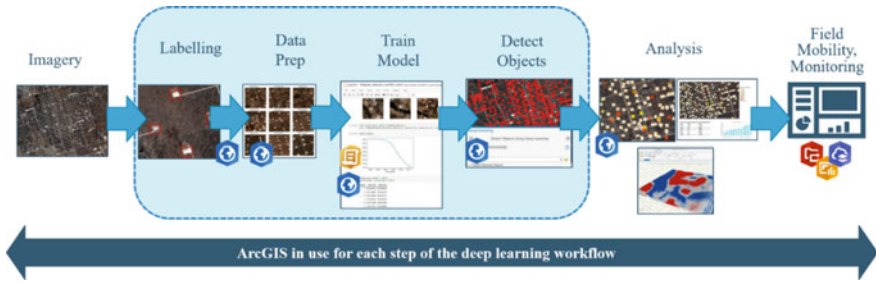
Fig. 2.6 End-to-end from raw imagery to structured information about water body feature layers

2019). First, the model was trained on both types of imagery (WorldView2 and Drone) using RGB and RGNIR bands composites, respectively. This strategy was also used for data and test time augmentation and further improve the model performance. Second, transfer learning was used during this study. Even though satellite images are pretty different from photographs of objects, they tend to have similar features such as edges, textures, shadows, curves, etc. These are the lower-level features that neural networks first learn to detect. A neural network that has been pre-trained using over 1 million images from different types of source imagery knows already how to extract target features; therefore, fine-tuning it is superior to training a new network from scratch using a small number of satellite images (Hu et al. 2015; Chen et al. 2018a, b).

Figure 2.6 demonstrates the workflow adopted for this study. ArcGIS tools were used at different steps to extract water bodies from the input processed imagery, including the labeling, data preparation, model training, object detection, analysis, and then field monitoring.

The next step was to use three bands but not the true band combination (RGB). The chosen bands compositions use the Near-Infrared, Red, and Green bands. Such composition allows the water bodies to stand out due to their reflectance properties. Water generally reflects high in the visible spectrum. However, turbid water has more reflectance than more transparent water. In the Mid-IR and Near IR regions, water increasingly absorbs the light making it darker. This is dependent upon water wavelength and depth. Increasing amounts of dissolved inorganic materials in water bodies tend to shift the peak of visible reflectance toward the red region from the green region.

Figure 2.7 demonstrates examples of using false color compositions captured using worldview2 in Al Khor Wildlife Reserve and Burj Al Arab in Dubai. The green areas in figure (a) are mudflats used by flamingos for breeding and feeding. The channels that cut through the flats are distinguished clearly. In comparison, natural and artificial water bodies in figure (b) are also clearly visible.

Table 2.2 shows the unique bands available in worldview 2, such as coastal blue, yellow, red-edge, and two near-infrared. Based on the tests conducted in GISC, the
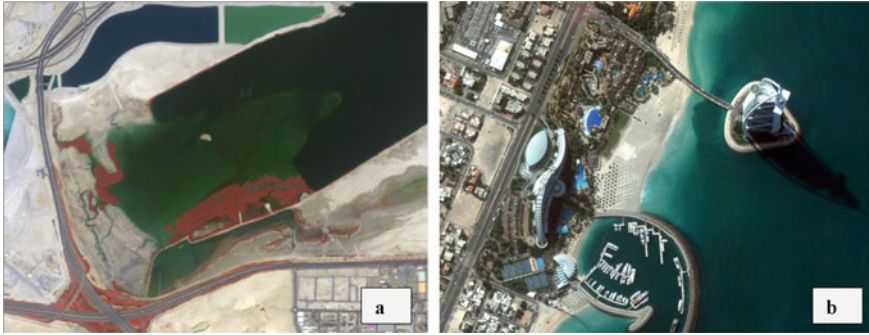
Fig. 2.7 WorldView 2 bands compositions, **a** mud flat composite, red edge|Yellow|coastal in Al Khor Area, **b** red edge|green|coastal in Burj Al Arab

Table 2.2 WorldView2 bands specifications

Spectral band	Center wavelength (nm)	Minimum lower band edge (nm)	Maximum upper band edge (nm)
Pan	625	447	808
MS1 (NIR1)	831	765	901
MS2 (red)	659	630	690
MS3 (green)	546	506	586
MS4 (blue)	478	442	515
MS5 (red edge)	724	699	749
MS6 (yellow)	608	584	632
MS7 (coastal blue)	427	396	458
MS8 (NIR2)	908	856	1043

best composition for water depth is Yellow, Green, and Coastal. Mudflats are more visible in Red Edge, Yellow, and Costal, while Vegetation is best studied in NIR2, Yellow, and Coastal bands composition.

2.2.3 Training Data of the Deep Learning Model

The first task was about searching for Training samples of water bodies available from reliable sources such as ESRI Lab. However, after spending some time exploring openly available labeled datasets for water bodies detection using satellite imagery, it was evident that such data is very limited and should be enhanced. Hereafter, the GISC team labeled around 863 water bodies in urban and rural areas across Dubai Emirate. ArcGIS Pro 2.4 was chosen to label the water bodies' locations where worldview2 and GISC Drone Imagery were the primary data source for labeling.

2.2.4 Load Model Architecture

The models were chosen for this study from "arcgis.learn" are based upon pre-trained Convolutional Neural Networks (CNNs or convnets) trained on millions of images similar to those in the ImageNet dataset. The intuition of a CNN is to use a hierarchy of layers, where the first layers learn to identify simple features like edges and blobs, middle layers combine these primitive features to identify corners and object parts, and the last layers combine the inputs from these in unique ways to grasp what the whole image should be about. In a typical convnet, the final layer is a connected layer that essentially computes a weighted sum of all layers to determine the probability of each object class (whether it's an image of a water body or a building, etc.). Therefore, a convnet trained on a massive corpus of images such as ImageNet is considered as a ready-to-use feature extractor. In practice, we can replace the last layer of these convnets with something different that uses those features for other tasks (e.g., pixel classification and object detection), which is also called transfer learning. The advantage of such transfer learning is that we won't need as much data to train an excellent model, as explained in further paragraphs. The arcgis.learn module is based on fast.ai and PyTorch and enables fine-tuning pre-trained torch vision models on remote sensing imagery. The arcgis.learn models leverages fast.ai's learning rate finder and one-cycle learning, allows for much faster training, and removes the guesswork in picking hyperparameters.

Figure 2.8 describes the Single Shot MultiBox Detector (SSD) as a CNN architected used in this study as a well-recognized object detection algorithm for water bodies detection. An SSD model architecture using Resnet-34 as the base model has already been predefined in ArcGIS API for Python, making it easy to use (Csillik 2017; Ren et al. 2015; Ross et al. 2013).
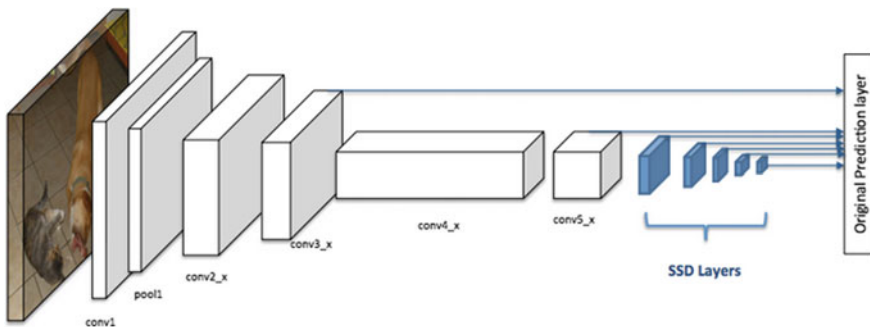
Fig. 2.8 The architecture of a convolutional neural network with an SSD detector

2.2.5 Train the Model Through Learning Rate Tuning and Transfer Learning

Learning rate is one of the main parameters in model training. The learning rate controls how quickly the model is adapted to the problem. Lower learning rates require more training epochs given the smaller changes made to the weights of each update, whereas larger learning rates result in rapid changes and require fewer training epochs. In this study, the range of learning rate was explored to guide selecting the best options for enhancing the results.

According to the learning rate (see Fig. 2.9), the loss drops dramatically starting from 1e-04. Therefore, the learning rate had been set to be within the range from 1e-04 to 1e-03, which means lower rates will be applied to the first few layers and larger rates will be applied the last few layers, and intermediate rates for middle layers, which is the idea of transfer learning.

Inferencing

Once the model was fully trained and provided acceptable results, it had been tested on a larger area than the small image chips used for training and validation. A script was created to export a larger area of the false-color imagery and find all its water bodies. This was done by splitting the larger image further into smaller-sized chips as required by the model. All these chips were passed simultaneously as a batch to the model, and the predictions were gathered, combined, and visualized. Figure 2.10 shows that the losses are still gradually decreasing, but not at a significant level; therefore, the model is ready and saved for inferencing.
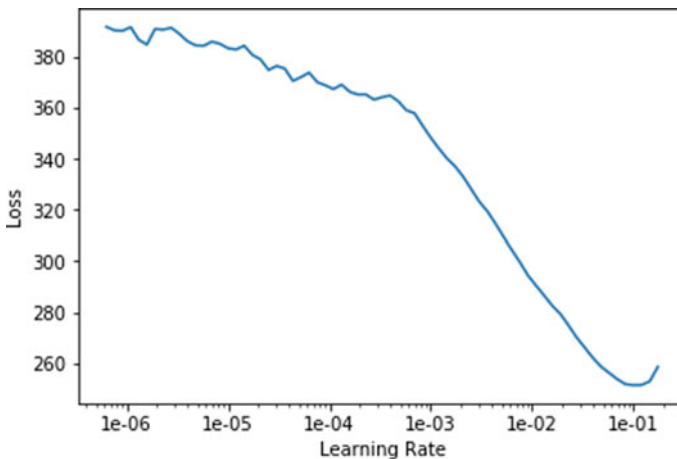
Fig. 2.9 Learning rate versus loss
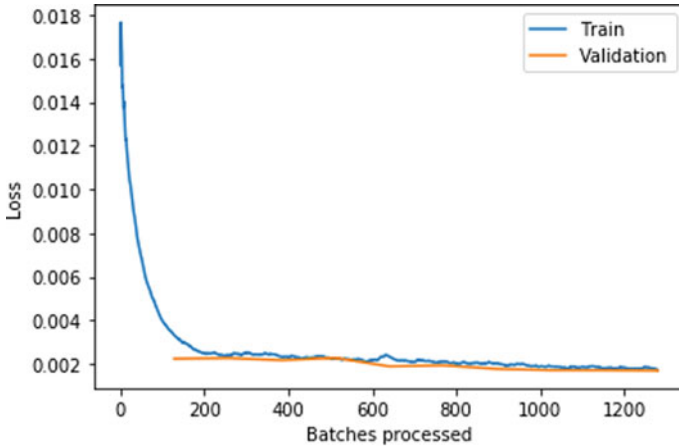
Fig. 2.10 Model validation metrics—train and valid loss

2.2.6 Test Time Augmentation

While observing the visualizations carefully, missing water bodies were noticed throughout the images. Another strange trend was also noticed: missing water bodies used to lie in a line either horizontally or vertically. After further analysis, the missing water bodies were mainly at the edges of the chips. To overcome this issue, as described in Fig. 2.11, test time augmentation had been performed where the model had been shown a couple of slightly altered versions of the same image, which gives better results than using a single image. Firstly, the stride of chipping out the imagery was reduced so that no water body is left at the edge of the chip.

Secondly, predictions were estimated twice. The first time on the actual chip and the second time on a center crop from the original chip. The center crop was selected so that the water bodies that were positioned at the edges of the smaller chips started to
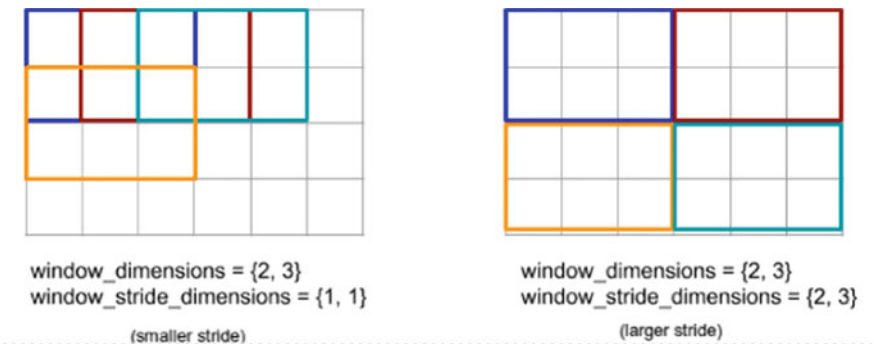
Fig. 2.11 Test time augmentation. *Source* TensorFlow website
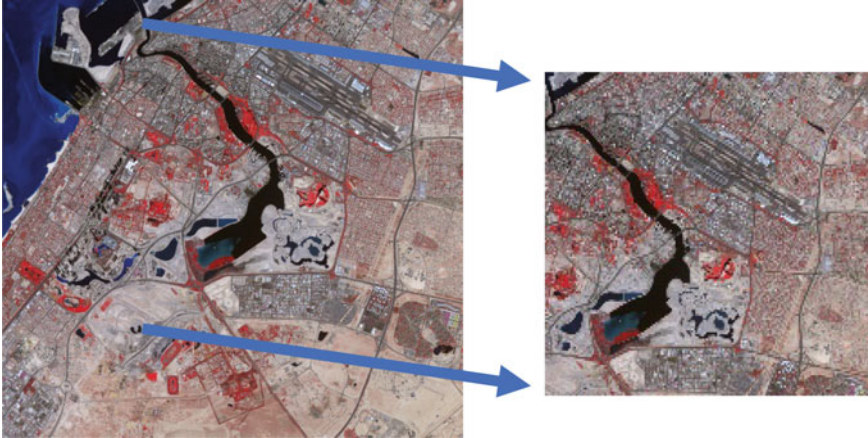
Fig. 2.12 Inner cropping mechanism

appear at the center. This simple strategy allowed the missing features to be detected. Extending this approach to five different center crops enabled to increase the Recall (fraction of correctly detected water bodies over the total amount of actual water bodies) without negatively affecting the precision (fraction of correctly detected water bodies among all detected water bodies). Figure 2.12 demonstrates the inner cropping mechanism performed on the source NDVI image around the Deira area.

2.2.7 Accuracy Assessment

The criteria selected to perform quality assurance and quality control (QA/QC) on the deep learning results are based on the particularity of the layer. Several measures are not considered since those are not applicable for this case, such as timeliness, uniqueness, suitability, etc. The criteria chosen are Positional Accuracy (Horizontal and Vertical) and Completeness. In feature extraction from imagery, where classification might be a problem, having only one classification accuracy might not give the whole figure. Therefore, a confusion matrix or error matrix is used for summarizing the performance of the classification algorithm. Calculating a confusion matrix identifies where the classification model is suitable and what types of errors it is making. It is used to check the performance of the classification model on a set of test datasets for which the valid values are known. Most performance measures such as Precision and Recall are calculated from the confusion matrix (Bhandari 2020; Patro and Patra 2015). Figure 2.13 explains the parameters of the confusion matrix, which is the basis for calculation accuracy metrics relevant to this study.

PREDICTIVE VALUES

	POSITIVE (1)	NEGATIVE (0)
POSITIVE (1)	TP	FN
NEGATIVE (0)	FP	TN

ACTUAL VALUES

Fig. 2.13 Confusion matrix parameters

Where TP refers to True Positive: predicted object as water body and it is. While TN refers to True Negative: predicted that object is not a water body, and it is not. FP refers to False Positive (Type 1 Error): predicted that object is a water body, but it is not (it's a crop field, for example). False Negative (Type 2 Error): predicted that object is not a water body, but it is.

It's not satisfying to rely on a single value of accuracy in such scenarios when the classes are imbalanced. Therefore, Classification Accuracy is calculated using the relation:

$$Accuracy = \frac{TP + TN}{TP + TN + FP + FN} \tag{2.1}$$

The Recall (aka Sensitivity) is defined as the ratio of the total number of correctly detected positive water bodies divide by the total number of positive water bodies. Or, out of all the positive results, how much had been predicted correctly. The Recall should be high to accept the results of the model and is determined by the following relation:

$$Recall = \frac{TP}{TP + FN} \tag{2.2}$$

The Precision (Formula (2.3)) is calculated as the ratio of the total number of correctly detected positive water bodies divided by the total number of predicted positive water bodies. Or, out of all the predictive positive results, how much had been predicted correctly. Precision should also be high.

$$Precision = \frac{TP}{TP + FP} \tag{2.3}$$

2.3   Results and Discussion

The proposed algorithm was implemented using ArcGIS Pro, where the deep learning model was trained with the PyTorch framework using the Train Deep Learning Model tool (Li et al 2015). The server used for this study has a specialized graphics processing unit (GPU) NDIVIA Tesla M40 with 16G of memory and a CUDA compute capability of 6.0. And the output of this process was a feature layer that identified lands belonging to water or non-water.

2.3.1   Confidence Threshold and Accuracy of Water Bodies Dataset

Table 2.3 gives the results of the object detection approach (Chen et al. 2015), trained on the water bodies dataset. It compares the accuracy results against the threshold argument as one of the most important arguments that refers to the confidence threshold, which identifies when it is acceptable to label an object as a water body. This number was tweaked to achieve the desired accuracy and finally was set to 0.5.

When executing convolution of imagery in convolutional neural network modeling, the pixels at the edge of the image are not used properly. The data is shrunk during the analysis, compared to inner pixels. Therefore, the padding parameter is critical to change to detect the water bodies found at the edge of the images. Hence, a padding parameter of 1 means another additional boundary of pixels added to the outside edges of the image, all with a value of 0.

Figure 2.14 demonstrates the padding applied to the input images to reduce the loss of information from the valid edge pixels and shrinking Zeng et al. 2015; Hu et al. 2015).

The final extracted features were bounding boxes or polygons around the objects found or points at the centers of the objects. Once the locations of the detected water bodies were obtained, it was relatively straightforward to use the analysis tools available in Portal for ArcGIS to identify parcels that were not being assessed correctly. In addition, here comes the power and importance of the GIS Analysis tools to support validating the results of the automatic extraction.

Table 2.3 Confidence threshold tweaking results

Confidence threshold	Detected water bodies	QA/QC accuracy (%)
0.5	1668	98.8
0.3	1317	78.7
0.1	985	59.1
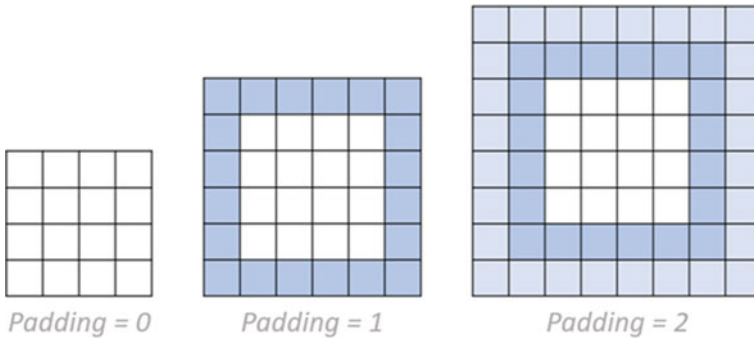
Fig. 2.14 Padding parameters used to enhance the results

Table 2.4 Confusion matrix results—Hatta hills

Accuracy criteria	Value
Sensitivity (recall)	0.8667
Specificity	0.95
Positive predicted value	0.9
Negative predicted value	0.6
Prevalence	0.7
Detection rate	0.8
Detection prevalence	0.9
Balanced accuracy	0.9883

2.3.2 Confusion Matrix

For this study, Table 2.4 summarizes the confusion matrix results generated for Hatta Hills and provides a summary of the predicted results. Where Sensitivity (SN), named also recall (REC) or true positive rate (TPR), reached 0.89, which is quite good for such area. The best Sensitivity is 1.0, whereas the least is 0.0. In contrast, specificity (SP) refers to the number of correct negative predictions, it is also called true negative rate (TNR). As shown in the confusion matrix results, the TNR reached 0.95 in Hatta, which is relatively high.

2.3.3 False Positives

Deep learning is an excellent tool for auto-detection; however, it can still make mistakes at times. For instance, false positives for water bodies were noticed on some major roads and as well as on Hatta hills. Many of the false positives that were of low confidence got filtered out, but some were high confidence false positives resulting from overfitting.
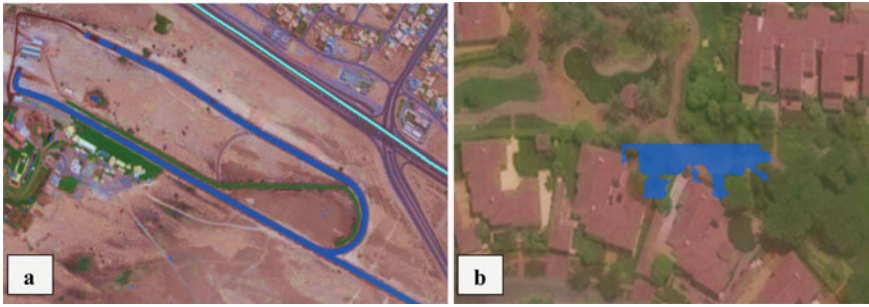
Fig. 2.15 Examples of false positives for water bodies, **a** major roads detected as water bodies in community 559, **b** random hilly area detected as water bodies in Hatta

Figure 2.15 shows two types of false positives recorded by the deep learning model, one of the false detections was in Community 559, where the road reflectance was confused with water bodies. The following detection was found in Hatta Hills and had a meager confidence ratio of 0.1. Both types of false positives were filtered out using geoprocessing tools, then excluded from the water bodies layer for best results Tan et al. (2017).

2.3.4 Cartography Enhancement

The PAEK (Polynomial Approximation with Exponential Kernel) method was used as a GIS tool to smooth the water bodies' polygons based on a 0.5 m smoothing tolerance based on GISC cartography standards. Figure 2.16 shows the smooth lines after removing sharp angles in order to improve the aesthetic appearance of the final water body layer for the best cartographic output.
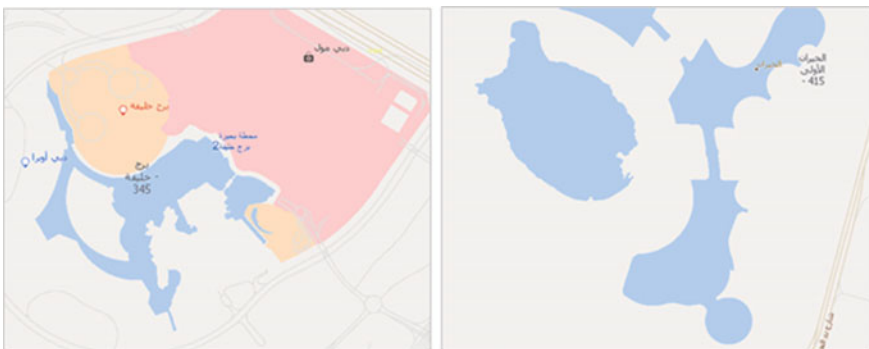
Fig. 2.16 PEAK smoothing algorithm applied to extracted water bodies features

2.3.5 Validate the Extracted Water Body Layer Against Reference Layers

During this work, the model was validated against reference data. Therefore, the extracted features through the deep learning models were compared to manually digitized water bodies using photo-interpretation techniques along with field verification where GISC field experts used mobile apps to record water bodies onsite. In Fig. 2.17 4 rows of images are used at a threshold of 0.3. The threshold is a measure of the probability that a water body exists. The higher is the value, the more is confidence (Yang et al. 2017). And in these 4 locations, the extracted water bodies through deep learning matched the reference layers.

In some areas, the threshold used was 0.5 depending on the input images, however as described in Table2.3, between 0.3 and 0.5, the results were very satisfying for GISC.

Table 2.5 summarizes the total of features extracted through the selected deep learning model and the total features extracted using supervised classification compared to the reference layers for this study (manually digitized features, verified through field site visits during 2019). The UAE climate is known by high temperatures, humidity, and low precipitation levels, which justifies the small number of found features as water bodies across the Dubai Emirate (Szabo 2011).

The Table 2.5 shows that 43% of the supervised classification results match the deep learning ones, whereas the matching between the deep learning outputs and the photo interpretation method reached 97%. The deep learning model produced a few more positives than manual digitization. When verified on the drone imagery, those refer to dirty water that is very hard to classify through photo interpretation.

Fig. 2.17 Rows of images used to check confidence results

Table 2.5 Total number of features result of deep learning compared to reference layers in Dubai city

	Deep learning output	Supervised classification	Manual digitization (photo-interpretation)
Total features	1668	3153	1648
True positives	1635	718	1589
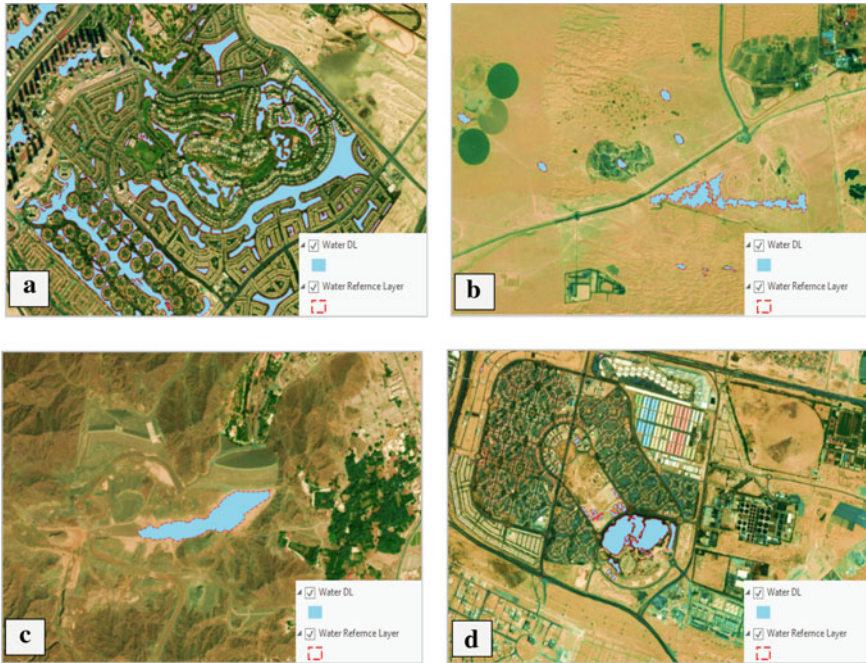
Fig. 2.18 Water bodies detected through deep learning versus reference layers (manual digitization)

2.3.6 Water Bodies Layer Dissemination

After performing generalization and smoothing operations, the number of features recorded by the deep learning model coincides with 98.8% of the reference features (manual digitization) in some areas such as Al Barsha, Al Thanya, and Al Barsha Sofouh, and Al Hebiah, the results were matching 99.9%.

As demonstrated in Fig. 2.18, the boundaries of the water bodies detected using deep learning match perfectly the edges of the reference layers Song et al. (2020). Therefore, the extracted water body using deep learning was approved to be disseminated at Dubai Here Platform as the primary tool used by Dubai Governments and the private sector to access geospatial data.

As shown in Fig. 2.19, the result of this study was used by GISC to create the official basemap of the Dubai Emirate.
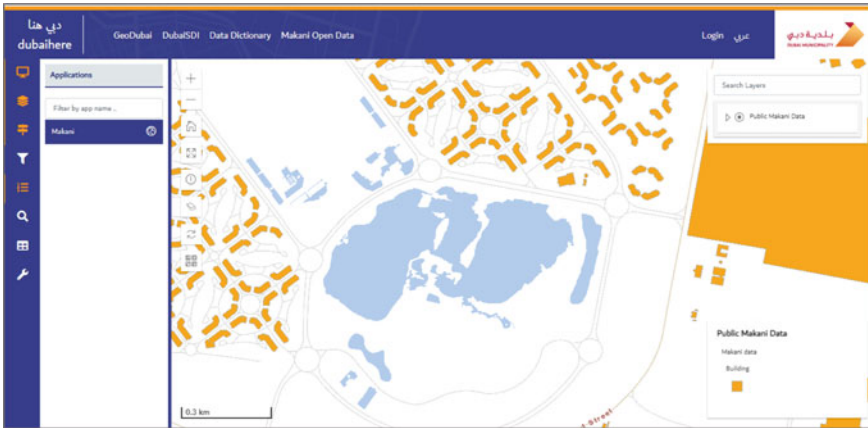
Fig. 2.19 Final output of deep learning results water body disseminated in Dubai here platform

2.4 Conclusions

In this study, a genuine water body extraction method based on PyTorch deep learning framework is elaborated for discriminating water from non-water features using Drone and WorldView2 high-resolution remote-sensing images. The proposed method combines geospatial analysis with deep learning models to extract water bodies and distinguishes between shadow pixels and water pixels.

The proposed method was tested for Dubai and Hatta regions having different water-body types and topography. The results proved that the proposed method performed well with an accuracy of 98.03–99.91%. In addition, QA/QC procedures were automated to support efficiency and ensure robust quality. This study concludes that the proposed deep-learning method can generate decent results with high precision meters, which can automate the manual process of extracting features from imagery and significantly minimizes the manual interaction needed to create data which will certainly reduce the time and heavy amount of expensive human labor involved in editing the records through field visits. Nevertheless, training a deep learning model can be complicated; it needs a lot of data, knowledge of how deep learning works, and extensive computing resources.

References

Bhandari A (2020) Everything you should know about confusion matrix for machine learning. Analytics Vidhya. https://www.analyticsvidhya.com/blog/2020/04/confusion-matrix-machine-learning/

Böer B (1997) An introduction to the climate of the United Arab Emirates. J Arid Environ 35(1):3–16. https://doi.org/10.1006/jare.1996.0162

Bote-Curiel L, Muñoz-Romero S, Gerrero-Curieses A, Rojo-Álvarez JL (2019) Deep learning and big data in healthcare: a double review for critical beginners. Appl Sci 9(11). https://doi.org/10.3390/app9112331

Chen T, Li M, Li Y, Lin M, Wang N, Wang M, ... Zhang Z (2015) Mxnet: a flexible and efficient machine learning library for heterogeneous distributed systems. arXiv preprint arXiv:1512.01274

Chen J, Wang C, Ma Z, Chen J, He D, Ackland S (2018a) Remote sensing scene classification based on convolutional neural networks pre-trained using attention-guided sparse filters. Remote Sens 10(2). https://doi.org/10.3390/rs10020290

Chen Y, Fan R, Yang X, Wang J, Latif A (2018b) Extraction of urban water bodies from high-resolution remote-sensing imagery using deep learning. Water 10(5). https://doi.org/10.3390/w10050585

Csillik O (2017) Fast segmentation and classification of very high resolution remote sensing data using SLIC superpixels. Remote Sens 9(3). https://doi.org/10.3390/rs9030243

Dixon B, Candade N (2008) Multispectral landuse classification using neural networks and support vector machines: One or the other, or both? Int J Remote Sens 29(4):1185–1206. https://doi.org/10.1080/01431160701294661

Fletcher TD, Andrieu H, Hamel P (2013) Understanding, management and modelling of urban hydrology and its consequences for receiving waters: a state of the art. In: 35th year anniversary issue, vol 51, pp 261–279. https://doi.org/10.1016/j.advwatres.2012.09.001

Gandhi GM, Parthiban S, Thummalu N, Christy A (2015) Ndvi: vegetation change detection using remote sensing and Gis–a case study of Vellore District. In: 3rd International conference on recent trends in computing 2015 (ICRTC-2015), vol 57, pp 1199–1210. https://doi.org/10.1016/j.procs.2015.07.415

Hadji K (2019) Reviewing UAE experience in improving the quality of environmental life and sustainable development. Int J Inspiration Resilience Econ 3(1):24–32

Hu F, Xia G-S, Hu J, Zhang L (2015) Transferring deep convolutional neural networks for the scene classification of high-resolution remote sensing imagery. Remote Sens 7(11):14680–14707. https://doi.org/10.3390/rs71114680

Huang S, Miao Y, Yuan F, Gnyp ML, Yao Y, Cao Q, Wang H, Lenz-Wiedemann VIS, Bareth G (2017) Potential of rapideye and worldview-2 satellite data for improving rice nitrogen status monitoring at different growth stages. Remote Sens 9(3):227. https://doi.org/10.3390/rs9030227

Kang L, Zhang S, Ding Y, He X (2016) Extraction and preference ordering of multireservoir water supply rules in dry years. Water 8(1). https://doi.org/10.3390/w8010028

Li L, Chen Y, Xu T, Liu R, Shi K, Huang C (2015) Super-resolution mapping of wetland inundation from remote sensing imagery based on integration of back-propagation neural network and genetic algorithm. Remote Sens Environ 164:142–154. https://doi.org/10.1016/j.rse.2015.04.009

McFeeters SK (1996) The use of the Normalized Difference Water Index (NDWI) in the delineation of open water features. Int J Remote Sens 17(7):1425–1432. https://doi.org/10.1080/01431169608948714

Messina G, Peña JM, Vizzari M, Modica G (2020) A Comparison of UAV and satellites multispectral imagery in monitoring onion crop. An application in the 'Cipolla Rossa di Tropea' (Italy). Remote Sens 12(20). https://doi.org/10.3390/rs12203424

Patro VM, Patra MR (2015) a novel approach to compute confusion matrix for classification of n-class attributes with feature selection. Trans Mach Learn Artif Intell 3(2) Article 2. https://doi.org/10.14738/tmlai.32.1108

Qi Z, Yeh A, Li X, Lin Z (2012) A novel algorithm for land use and land cover classification using RADARSAT-2 polarimetric SAR data. Remote Sens Environ 118:21–39. https://doi.org/10.1016/j.rse.2011.11.001

Ren S, He K, Girshick R, Sun J (2015) Faster r-cnn: towards real-time object detection with region proposal networks. In: Advances in neural information processing systems, pp 91–99

Ross MG, Russ C, Costello M et al (2013) Characterizing and measuring bias in sequence data. Genome Biol 14:R51. https://doi.org/10.1186/gb-2013-14-5-r51

Senaras C, Gedik E, Yardimci Y (2014) A novel dynamic thresholding and categorizing approach to extract water objects from VHR satellite images. IEEE Geosci Remote Sens Symp 2014:4934–4937. https://doi.org/10.1109/IGARSS.2014.6947602

Shen J (2012) A method for object—oriented automatic extraction of lakes in the mountain area from remote sensing image. http://en.cgsjournals.com/article/doi/https://doi.org/10.6046/gtzyyg.2012.03.16?viewType=HTML

Sherif M, Sefelnasr A, Ebraheem AA, Al Mulla M, Alzaabi M, Alghafli K (2021) Spatial and temporal changes of groundwater storage in the quaternary aquifer. Water 13(6). https://doi.org/10.3390/w13060864

Song S, Liu J, Liu Y, Feng G, Han H, Yao Y, Du M (2020) Intelligent object recognition of urban water bodies based on deep learning for multi-source and multi-temporal high spatial resolution remote sensing imagery. Sensors 20(2). https://doi.org/10.3390/s20020397

Subramanian V (2018) Deep learning with PyTorch, a practical approach to building neural network models using PyTorch. Original work published. https://github.com/PacktPublishing/Deep-Learning-with-PyTorch

Szabo S (2011) The water challenge in the UAE

Tan J, Huo Y, Liang Z, Li L (2017) A comparison study on the effect of false positive reduction in deep learning based detection for Juxtapleural lung nodules: CNN versus DNN. In: Proceedings of the symposium on modeling and simulation in medicine

Tsang S-H (2019) One-stage detector, with focal loss and RetinaNet using ResNet+FPN, Surpass the accuracy of two-stage detectors, faster R-CNN. https://towardsdatascience.com/review-retinanet-focal-loss-object-detection-38fba6afabe4

Wang Y, Huang F, Wei Y (2013) Water body extraction from LANDSAT ETM+ image using MNDWI and K-T transformation. In: 2013 21st International conference on geoinformatics 1–5

Yang L, Tian S, Yu L, Ye F, Qian J, Qian Y (2015) Deep learning for extracting water body from Landsat imagery 17

Yang X, Zhao S, Qin X, Zhao N, Liang L (2017) Mapping of urban surface water bodies from sentinel-2 MSI imagery at 10 m resolution via NDWI-based image sharpening. Remote Sens 9(6). https://doi.org/10.3390/rs9060596

Zeng C, Bird S, Luce JJ, Wang J (2015) A Natural-Rule-based-connection (NRBC) method for river network extraction from high-resolution imagery. Remote Sens 7(10):14055–14078. https://doi.org/10.3390/rs71014055

Zhang Q, Wang Z, Wang B, Ohsawa Y, Hayashi T (2020) Feature extraction of laser machining data by using deep multi-task learning. Information 11(8). https://doi.org/10.3390/info11080378

Zhou Y, Luo J, Shen Z, Yang H, Hu X (2014) Multiscale water body extraction in urban environments from satellite images. IEEE J Sel Top Appl Earth Observations Remote Sens 7(10):4301–4312. https://doi.org/10.1109/JSTARS.2014.2360436

Part II
Rainfall and Floods

Chapter 3
Multiple Non-linear Reservoirs to Model Water Balance Components in Sandy Soils

Giorgio Baiamonte, Carmelo Agnese, and Vijay P. Singh

3.1 Introduction

Infiltration is a key component of the hydrologic cycle, separating rainfall and surface runoff (Smith et al. 2002; Brutsaert 2005). Computing infiltration makes it possible to analyze the subsequent hydrological processes as the overland flow generation, the soil moisture patterns, the root water uptake, or the evaporation losses, because of the infiltration interacting with the other components of the hydrologic cycle. The infiltration process is influenced by many factors, as the soil hydrological characteristics, the rainfall intensity, and the soil moisture initial conditions (Melone et al. 2008; Tramblay et al. 2010; Baiamonte and Singh 2016; 2017), and by secondary factors related to the biological activities into the soil (Singh 1996; Assouline 2013). Because of the important role that infiltration plays in hydrology, the infiltration process has been widely studied, and different models have been developed (Brutsaert 2005; Singh 2010; Cui and Zhu, 2018; Vand et al. 2018).

The movement of water into the soil is fully represented by the Richards equation (Richards 1931). Exact solutions of the Richards (RCH) equation are difficult to obtain for reasons related to the strong nonlinear dependency of the parameters on the dependent variables, and to the difficulty in establishing the constitutive water retention curves and the hydraulic conductivity function (Serrano 2004). These relationships are highly nonlinear and are influenced by the hysteresis in the presence of wetting and drying processes occurring in field conditions.

G. Baiamonte (✉) · C. Agnese
Department of Agricultural, Food, and Forest Sciences, University of Palermo, viale delle Scienze, Bldg. 4, Palermo 90128, Italy
e-mail: giorgio.baiamonte@unipa.it

V. P. Singh
Department of Biological and Agricultural Engineering and Zachry Department of Civil Engineering, Texas A&M University, 321 Scoates Hall, College Station, Texas 2117 TAMU, USA
e-mail: vijay.singh@ag.tamu.edu

However, infiltration models based on the Richards equation, have been widely investigated, since they can be applied to any kind of soil, regardless of the simplified hypotheses considered. The root water uptake, according to the root depth and/or the water content was also taken into account (Broadbridge et al. 2017). The latter is an important issue, since, for both forest and agricultural soils, it allows detecting the role of soil's physical ability to store and provide water to plant roots (Cullotta et al. 2016).

To derive exact solutions of the Richards equations under steady-state conditions in a linearized form, a lot of efforts have been made (Raats 1976; Batu 1978; White and Broadbridge 1988) as well as under time-dependent conditions (Broadbridge and White 1988; Sander et al. 1988). Recently, Broadbridge et al. (2017) developed exact solutions of the Richards equation by considering a nonlinear plant-root extraction. Also, Yadav et al. (2009) incorporated root water uptake non-uniform to develop a variably saturated soil moisture flow model for planted soils with properties varying with the depth.

Many studies also focused specifically on the derivation of water content profiles. Al-Hamdan and Cruise (2010) used the principle of maximum entropy (Singh 2010) to estimate soil moisture profiles. For the simulation of soil water content and infiltration rate profiles, subject to either constant or time-variable rainfall intensity, Serrano (2004) developed approximated solutions of the Richards equation. Sugii (2005) proposed a dynamic soil moisture model distribution in unsaturated soils, to solve the Klute's equation (Klute 1972), which substitutes the volumetric water content to the pore water pressure, and derived the governing equation of one-dimensional vertical seepage flow. More recently, for a constant saturation upper boundary condition, Su et al. (2018) introduced a new approximate analytical method based on the principle of least action and the variational principle for simulating the vertical infiltration of water in unsaturated soils. Su et al. (2018) obtained a functional extremum solution to Richards equation by using the Euler–Lagrange equation and the integral mean-value theorem.

Struthers et al. (2006) used a unit gradient multiple wetting front model to describe infiltration and redistribution behavior of individual "square wave" fronts for unponded rainfall infiltration and found the drainage recession behavior to be equivalent to that of a capacitance (bucket) model for certain scenarios, suggesting a possible physical basis for capacitance model parameters with respect to drainage prediction.

When the sorption component and capillary forces are negligible, the infiltration process is simply driven by the gravity and can be modeled by the capacitance sketch, also denoted as tank or bucket model (Manabe 1969; Struthers et al. 2006; Romano et al. 2011). Commonly, these models are applied for hydrological predictions, because are simple and they can describe the basic constrains on the soil hydrological behavior, especially for specific research aims, as irrigation scheduling and transpiration flux estimates. This line of approach makes it possible to dispose of irrigation management strategies aimed to increase the water use efficiency and to quantify crop water requirements (Rallo et al. 2014). Several studies (Milly 1994; Farmer et al. 2003) showed that some components of the soil water budget can be

efficiently described by the capacitance models, providing results that are like those observed in the field or simulated by much more sophisticated models that consider the soil water dynamics and accurate descriptions of plants ecology (Guswa et al. 2002). This probably explains the reasons why the capacitance approaches are still considered (Romano et al. 2011).

It is important to observe that the capacitance approaches are usually limited by their inability to replicate the delay time between input fluxes and output fluxes generation. However, an attempt to replicate the internal travel times has been addressed through the discretization of the soil profile into multiple tanks connected in series (Struthers et al. 2006).

Recently, following a capacitance sketch and a gravity-driven infiltration process, here denoted as GD, Baiamonte (2020a) derived a simplified solution of the Richards equation, by considering the soil as a non-linear storage reservoir. Baiamonte (2020a) showed that the saturated hydraulic conductivity could be related to the small hole diameter made at the bottom of the tank where drainage volumes outflow. Results showed the possibility to relax the main assumption of bucket models, where commonly drainage occur in the deeper layers after the field capacity or soil saturation (in the GD case) is achieved. The plant-root extraction and the soil evaporation components that were not considered in Baiamonte (2020a), could be addressed by using separate procedures (Vrugt et al. 2001; de Willigen et al. 2012; Javaux et al. 2013).

The objective of this paper is to extend the GD simplified solution applied to one reservoir by Baiamonte (2020a) to the case in which multiple tanks are connected in series, thus accounting for the internal travel times of water movement into the soil (Struthers et al. 2006), in order to derive analytical water content profiles for more reliable field conditions. It is noteworthy that the same approach was already tested for tanks filled by only water, in the case of one tank (Baiamonte 2020b), and for multiple tanks connected in series in Baiamonte (2020c), by using the experimental and theoretical data provided by Zhang et al. (2019).

The paper is organized as follows. Following this introduction, Sect. 3.2 introduces the GD assumption, briefly summarizes and reformulates the solution provided by Baiamonte (2020a) and extends it to multiple tanks. Derivation of water content profiles and related hydrologic components are presented in Sect. 3.3. Sections 3.3 show the mass water balance (3.3.2), the effect of the number of reservoirs (3.3.3), a comparison with the solution numerically derived for the Richards equation, where the GD assumption is relaxed (3.3.4), and an application for time varying rainfall intensity (3.3.5). The paper is concluded in Sect. 3.4.

3.2 Methods

3.2.1 Assumption of Gravity-Driven Infiltration (GD)

For one-dimensional infiltration, the Richards equation can be written as (Richards 1931):

$$\frac{\partial \theta}{\partial t} = \frac{\partial \theta}{\partial h}\frac{\partial h}{\partial t} = \frac{\partial}{\partial z}\left[K(h)\left(\frac{\partial h}{\partial z} + 1\right)\right] \tag{3.1}$$

where $t(T)$ is the time, $\theta(L^3 L^{-3})$ is the volumetric water content, $K(h)$ is the soil hydraulic conductivity ($L\ T^{-1}$), which is a function of the soil matric potential $h(L)$, and $z(L)$ is the elevation.

By assuming the matric potential gradient negligible compared with the gravitational potential gradient, thus under gravity-driven infiltration, we can write:

$$\frac{\partial(z + h)}{\partial z} \cong 1 \rightarrow \frac{\partial h}{\partial z} = \frac{\partial h}{\partial \theta}\frac{\partial \theta}{\partial z} \ll 1 \tag{3.2}$$

Equation (3.2) states that compared with $\partial\theta/\partial z$, the slope $\partial h/\partial\theta$ of the retention curve, $h(\theta)$, is low enough and the GD assumption can be adopted. Therefore, considering the matric gradient negligible is simply a retention property unrelated to the saturated hydraulic conductivity (Bagarello et al. 2019). Under the GD assumption, Eq. (3.1) can be written as the simple 1D continuity equation:

$$\frac{d\theta}{dt} \cong \frac{dK(\theta)}{dz} \tag{3.3}$$

The GD assumption is discussed here, by considering the water retention curve, $\theta(h)$, according to Brooks and Corey (1964):

$$\theta(h) = \begin{bmatrix} \theta_s \\ (\theta_s - \theta_{res})\left(\frac{h_b}{h}\right)^\lambda + \theta_{res} \end{bmatrix} \quad \begin{array}{l} \text{for } h_b \leq h \leq 0 \\ \text{for } h < h_b \end{array} \tag{3.4a}$$

where θ_s ($L^3 L^{-3}$) and θ_{res} ($L^3 L^{-3}$) denote the saturated volumetric water and the residual water content, $\lambda(-)$ is a shape parameter characterizing the shape of the water retention curve, and h_b (L) is the bubbling matric head, corresponding to the largest pore radius of the pore-size distribution. The parameter h_b is denoted as the threshold value at which the soil once it is saturated starts draining, the water into the void spaces is replaced by air, and it is also denoted as the air-entry value. For values of $h > h_b$, the soil pores are filled with water, and the soil hydraulic conductivity is considered constant and equal to K_s (Schelle et al. 2010; Nasta et al. 2013).

For fixed soil hydrological characteristics, θ_{res}, θ_s, h_b and saturated hydraulic conductivity, K_s (LT^{-1}), the shape parameter λ, usually defined as pore size distribution index, plays a fundamental role in the water transfer dynamic (Nasta et al. 2013; Xing et al. 2018), and it is related to the pore connectivity index, c, appearing in the hydraulic conductivity function, $K(\Theta)$, which could be expressed according to Brook and Corey (1964):

$$K(\Theta) = K_s \Theta^{1/c} \tag{3.4b}$$

where $\Theta = (\theta - \theta_{res})/\Delta\theta$ is the actual volumetric water content normalized with respect to the effective porosity, $\Delta\theta = \theta_s - \theta_{res}$. The c parameter is related to the m and n parameters of the van Genutchen water retention curve (van Genuchten 1980) by the following relationship (Nasta et al. 2012; Su et al. 2018):

$$\frac{1}{c} = \frac{2}{mn} + 2 + p \tag{3.5a}$$

where p is the tortuosity that sometimes is considered to be merely empirical coefficient affecting the hydraulic conductivity function (Šimůnek et al. 2011). For large values of pressure heads that is $h/h_b \gg 1$, van Genutchen water retention curve converges to the Brooks and Corey expression (Eq. 3.4a) and $m\,n \sim \lambda$, which is commonly assumed for the Brooks and Corey model (Mualem 1976; Guarracino, 2007; Sarabi and Ghahraman 2020). Thus, the c parameter can be expressed as:

$$c = \frac{\lambda}{2 + (2 + p)\lambda} \tag{3.5b}$$

Different p values have been applied to estimate the unsaturated hydraulic conductivity. According to Childs et al. (1950), who presented the first contribution to predict the unsaturated hydraulic conductivity, assuming the soil to be made up of a bundle of capillary tubes of different radii, p was set 0. The assumption $p = 0$ was also made by Kravchenko and Zhang (1997), who treated a soil's pore geometry as a fractal, whereas $p = 1$ was assumed by Burdine (1953); Wylie and Gardner (1958); and Brooks and Corey (1964), and $p = 1.33$ by Millington and Quirk (1961). Tuli et al. (2005) found a wider range of p variability, reporting $0 < p \leq 12.2$ for water in undisturbed soil samples and $0 < p \leq 0.9$, for disturbed soil samples, whereas $0 < p \leq 2.5$ and $0.87 \leq p \leq 7.7$ for air. Higher values for undisturbed soil samples and for air were suggested than for disturbed soil samples, because of the dominant role of soil structure and macropore flow on permeability (Ghanbarian et al. 2017). Tuli et al. (2005) also indicated that p cannot be universally set, since it is a function of fluid characteristics as well as of pore space morphology.

In this work, none of the aforementioned $p > 0$ values were considered. Indeed, similar to the pioneering work of Childs et al. (1950), it is assumed that $p = 0$, meaning that the soil is composed of a set of randomly distributed interconnected pores characterized by different tube radii in a given cross-section, agreeing with the

Poiseuille assumption. We are aware that this simplified assumption is far from the sharp advances on the characterization of the soil hydrological properties. However, the suggested procedure leads to simplified solutions of the water content profiles and their related drainage and runoff volumes, although for those practical conditions where water moves into the soil pores under gravity gradient only, providing an interesting delimitation of the Richards solution domain (Baiamonte 2020a).

One more advantage of this assumption is its applicability in the case in which tortuosity, together with the other soil hydraulic properties, excluding K_s, are unknown for the study-soil or show large variability, because of errors in measurements and spatial heterogeneity exhibited in the field. This consideration agrees with Govindaraju et al. (1992), who concluded that the use of simplified models is justified when field data exhibit high spread, and the parameter estimates cannot be characterized by a tight bound.

Towards the aim to clarify the GD assumption, for different p values ($p = 0$, 1 and 2), Eq. (3.5b) is plotted in Fig. 3.1a, versus the pore size distribution index, λ. The figure shows the great influence of the tortuosity factor on the shape parameter of the hydraulic conductivity function. At increasing λ, c increases more and more, and attains lower values at increasing p. For $p = 0$, assumed here, Fig. 3.1a also plots the minimum and maximum c values (circle dots) corresponding to the λ extremes reported in Brakensiek et al. (1981)'s data and among the hydraulic properties of the European soils (HYPRES) database (Wösten et al. 1999), indicating that a wide c range of variability is also obtained according to the considered λ ranges.

By assuming a GD infiltration, meaning that retention gradients play no role in the water movement, and that the λ index diverges, it can be observed that for the assumed $p = 0$, c approaches 0.5, as it is also shown by Eq. (3.5b). The effect of the GD assumption is also illustrated in terms of hydraulic conductivity function (Fig. 3.1b) and of water retention curve (Fig. 3.1c), where it can be observed that under a "pure" GD infiltration ($c \sim 0.5$), the fundamental hypothesis is that the slope $dh/d\theta$ of the retention curve attains zero (bolded line), contrary to the curves plotted for the different c values, including the $c = 0.25$ value, found by Clapp and Hornberger (1978) for a sandy soil, and $c = 2$ that matches the Torricelli's laws (Baiamonte 2020a). In Fig. 3.1d, the corresponding matric potential gradients are plotted.

The c value equal to 0.5, which is assumed in the present work, makes it possible to find simplified solutions of water content profiles explicit in Θ, to be applied for multiple tanks, in the knowledge that substantially different values may characterize common soils, and that this value could be only ascribed to very sandy soils (Carsel and Parrish 1988; Sadegh Zadeh 2009), being almost close to that obtained by Clapp and Honberger (1978), as shown in Fig. 3.1b.
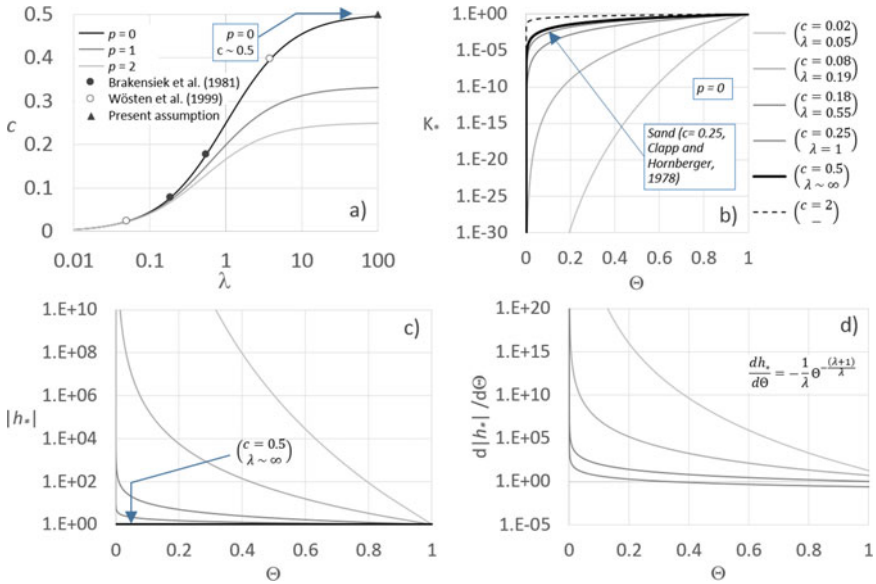
Fig. 3.1 **a** Relationship between the shape parameter, c (Eq. 3.5b), and the λ parameter, by varying the tortuosity, p. Extremes of the λ ranges reported in Brakensiek et al. (1981) and in Wösten et al. (1999), and the asymptotic c value for $\lambda \sim \infty$ and $p = 0$, are indicated. The figure also illustrates the corresponding **b** hydraulic conductivity function, **c** water retention curve, and **d** matric potential gradient, for different c values

3.2.2 One Non-linear Reservoir

Baiamonte (2020a) considered an open cylindrical tank of unit cross sectional area, A, radius R, and for a unit height $Z = 1$ m, as displayed in Fig. 3.2. A small circular hole is made at the bottom of the tank, with a small radius r that could be related to the saturated hydraulic conductivity. Indeed, the radius r was seen as a parameter able to describe the ease with which water can move through soil pore spaces.

A stationary and uniformly distributed normalized rainfall intensity, $\rho = i/K_s$, is applied over the tank. For a homogenous and isotropic soil, the tank water level

Fig. 3.2 Sketch of the tank mimicking the soil water content dynamics (Baiamonte 2020a)
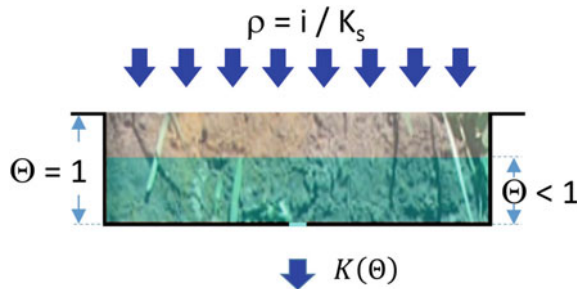
mimics the actual normalized volumetric soil water content, Θ. Thus, for $\Theta = 0$ and $\Theta = 1$ (Fig. 3.2) the soil is completely dry or saturated, respectively. Moreover, the outflow rate represents the water infiltration rate at the bottom of the soil layer, providing, for a free drainage condition, the drainage volumes.

For one-dimensional infiltration, by assuming that the hydraulic conductivity linearly varies with depth, Eq. (3.3) provides:

$$\frac{d\theta}{dt} = \frac{K(\theta)}{Z} \tag{3.6}$$

This, because equating the right-hand terms of Eqs. (3.3) and (3.4), provides a differential equation with solution $K = z$ const, for any value of the constant. Introducing into Eq. (3.6) the normalized inflow, i.e. the rainfall intensity, and the minus sign accounting that K outflows from the reservoir, the differential flow equation, governing the outflow process from the tank, was derived in dimensionless terms (Baiamonte 2020a):

$$\frac{d\Theta}{d\tau} = \rho - \Theta^{1/c} \tag{3.7}$$

where τ denotes the time t (T) normalized with respect to the characteristic time of the infiltration process, t_c (T):

$$t_c = \frac{Z\theta_s}{NK_s} \tag{3.8}$$

where the number of tanks N equals 1 for Fig. 3.2. Equation (3.8) states that t_c also represents to the minimum travel time (under full tank condition) that the water particle, starting from the top of the tank, requires to cross the tank height with constant velocity K_s. In this work, soil profile (and tanks) characteristics are assumed invariant in the space and according to the sketch displayed in Fig. 3.2, a fast mechanism of runoff generation is assumed (Baiamonte and Agnese 2016; Baiamonte 2016), occurring when the rainfall intensity, i, exceeds the saturated hydraulic conductivity, K_s.

For $c = 2$, 2/3 and 2/5, solutions of Eq. (3.7) were already derived for tanks filled by water, in order to provide complex rating curves for sharp crested orifices and for rectangular or triangular weirs under unsteady flow conditions, which were also treated as a non-linear water reservoir (Baiamonte 2020b; 2020c; 2021). Indeed, there are similarities between the two processes (variable water content into the soil and outflow process from a water tank). When the unsteady differential equation (Eq. 3.7) is applied to the water tank, the variation of the water level is the input and the incoming normalized flow rate, ρ, is the discharge to be determined. In the case of soil, the known input is the rainfall intensity and the soil water content, mimicked by the water tank level, has to be determined (Baiamonte 2020a). Moreover, for soils, in Eq. (3.7) exponent c is the conductivity shape parameter of the normalized

water content, commonly used to model soil water fluxes and to assess soil physical characteristics (Cullotta et al. 2016), whereas for tanks filled by only water, c is the exponent of the normalized water level h/Z, which equals 2, for a tank with a hole made at its bottom (Torricelli law), equals 2/3 for rectangular weirs, and equals 5/3 for triangular weirs (Baiamonte 2021).

For $c = 0.5$, which could be assumed for sandy soils (Carsel and Parrish 1988; Sadegh Zadeh 2009), it is interesting to observe that Eq. (3.7) is similar to that derived in a very different context, where the hydrological response of a sloping hillslope, on the assumption of quick runoff generation, was investigated (Agnese et al. 2001; 2007). In particular, Agnese et al. (2001) presented an analytical solution of the non-linear storage model, for different values of the m parameter, which accounts for the overland flow regime ($m = 5/3$, for turbulent flow, $m = 2$, for transitional flow regime, and $m = 3$ for laminar regime). For $m = 2$, the overland flow differential equation is reported:

$$\frac{dq_*}{3\sqrt{k_* r} q_*^{1/2}[1 - q_*(t)]} = dt \tag{3.9}$$

where t [T] is the time; k_* [L$^{-2/3}$ T^{-1}] is a parameter that accounts for roughness, slope and length of the hillslope; and q_* is the discharge per unit area at the bottom of the hillslope normalized with respect to the rainfall excess intensity, r.

The correspondence of the two differential equations (Eq. (3.7) with $c = 0.5$ and Eq. (3.9)) can be shown by imposing the following conditions:

$$t = \tau, \ q_* = \frac{\Theta^2}{\rho}, \ \sqrt{q_*} = \frac{\Theta}{\sqrt{\rho}}, \ dq_* = \frac{2\Theta}{\rho} d\Theta, \ 3\sqrt{k_* r} = 2\sqrt{\rho} \tag{3.10}$$

Accordingly, the solution of the differential overland flow equation reported in Agnese et al. (2001) can be reformulated for the considered case, under the two different conditions $\rho > \Theta_0^2$ and for $\rho < \Theta_0^2$, respectively:

$$\Theta = \sqrt{\rho}\tanh\left[(\tau - \tau_0)\sqrt{\rho} + \text{arctanh}\left(\frac{\Theta_0}{\sqrt{\rho}}\right)\right] \tag{3.11a}$$

$$\Theta = \sqrt{\rho}\coth\left[(\tau - \tau_0)\sqrt{\rho} + \text{arccoth}\left(\frac{\Theta_0}{\sqrt{\rho}}\right)\right] \tag{3.11b}$$

where Θ_0 and τ_0 are the antecedent soil moisture and time conditions, and tanh (.), arctanh (.), coth (.), arcoth (.), are the hyperbolic tangent, the arc of the hyperbolic tangent, the hyperbolic cotangent, and the arc of the hyperbolic arctangent of argument (.), respectively.

For $\rho = 0$, the recession of the water content can be easily derived by solving Eq. (3.7), and accounting to the antecedent moisture condition, yielding:

$$\Theta = \frac{\Theta_0}{1 + \Theta_0(\tau - \tau_0)} \tag{3.12}$$

3.2.3 Multiple Non-linear Reservoirs

For the case of multiple non-linear reservoirs, consider a series of ten open cylindrical tanks ($n = 1, 2, \ldots N$, with $N = 10$) of unit cross sectional area, A, each of depth 0.1 m, for a total unit height $Z = 1$ m, as displayed in Fig. 3.3a. The small circular hole made at the bottom of each tank makes the tanks interconnected. Therefore, the outflow rate of each tank feeds the subsequent tank, and for the last bottom tank, the outflow rate represents the water infiltration rate at the bottom of the soil layer, providing, under a free drainage condition, drainage volumes according to Eq. (3.4b), as in Fig. 3.2. Again, a stationary and uniformly distributed normalized rainfall intensity, $\rho = i/Ks$, is applied over the first tank. As an example, different normalized water contents Θ in Fig. 3.3a, the first three tanks are completely full ($\Theta = 1$), and the last two are completely dry ($\Theta = 0$). Figure 3.3b shows the corresponding water content profile associated with Fig. 3.3a.

Equations (3.11a and 3.11b) can be applied only to the first tank, which is fed by rainfall intensity ρ; whereas for the tank n, ($n = 2, 3, \ldots N$), the normalized input discharge drained by the previous $n-1$ tank needs to be considered (Eq. 3.4b):

$$\rho \equiv K_* = \Theta^{1/c} = \left(\Theta_0^{n-1}\right)^2 \tag{3.13}$$
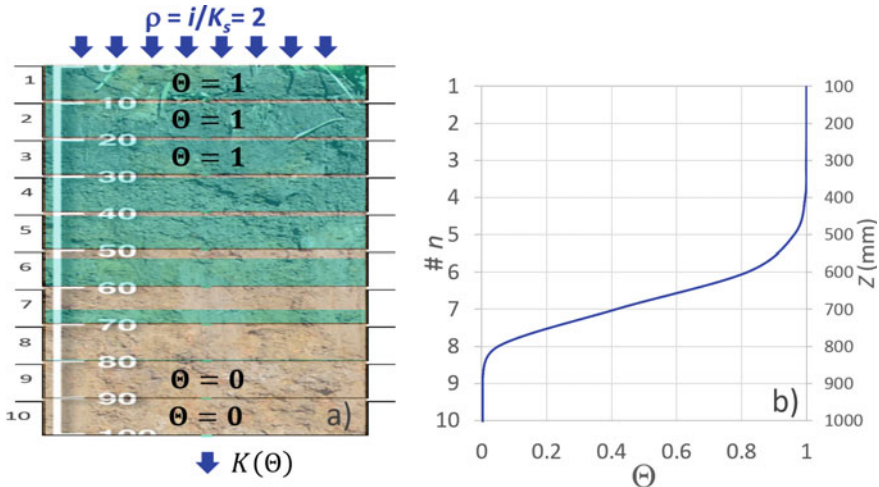
Fig. 3.3 a Soil water content for multiple tanks connected in series and **b** the related water content profile

Therefore, for the tanks below the first one ($n = 2, 3, \ldots, N$), Eqs. (3.11a and 3.11b) have to be rewritten as:

$$\Theta = \Theta_0^{(n-1)} \tanh\left[(\tau - \tau_0)\Theta_0^{(n-1)} + \text{arctanh}\left(\frac{\Theta_0^{(n)}}{\Theta_0^{(n-1)}} \right) \right] for \; \Theta_0^{(n-1)} > \Theta_0^{(n)}$$

$$(3.14a)$$

$$\Theta = \Theta_0^{(n-1)} \coth\left[(\tau - \tau_0)\Theta_0^{(n-1)} + \text{arccoth}\left(\frac{\Theta_0^{(n)}}{\Theta_0^{(n-1)}} \right) \right] for \; \Theta_0^{(n-1)} < \Theta_0^{(n)}$$

$$(3.14b)$$

where the Θ_0 superscript, $n-1$, refers to the antecedent moisture condition of the previous tank.

Similar to Eq. (3.12), when the inflow of the tank n ceases, the emptying process of the tank n can be expressed as:

$$\Theta^{(n)} = \frac{\Theta_0^{(n)}}{1 + \Theta_0^{(n)}(\tau - \tau_0)} \tag{3.15}$$

Contrary to the case of just one reservoir, where the water content profiles are vertical and the drainage process starts simultaneously with rainfall, for multiple reservoirs the internal travel times can be taken into account, providing more reliable conditions. Moreover, it is noteworthy that Eqs. (3.13 and 3.14), which are dimensionless, do not depend on K_s, which is a scale factor of the procedure, whereas the number of tanks N may play an important role that will be analyzed in Sect. 3.3.3.

These results make it possible to use a hydraulic approach affected by the simplified assumptions, but not by uncertainties, to describe the GD infiltration. Moreover, considering that the adopted hydraulic sketch can lead to the drainage and runoff excess volume and intensity, the transportation of the runoff generated could also be modelled by using the aforementioned solutions, where also hyperbolic tangent and the hyperbolic cotangent functions appeared (Agnese et al. 2001), which verified those introduced by Horton (1939), for dry antecedent conditions.

Interestingly, for known characteristic volumetric water contents, only the saturated hydraulic conductivity, K_s, is required to apply the described procedure in dimensional terms, indicating that such procedure could be used as an inverse method to determine K_s, according to an objective function to be minimized, on the basis of monitored soil water content profiles in the field or in the lab, and on covariance (weighting) matrices, which provide information about the measurement accuracy, as well as any possible correlation between measurement errors and/or parameters involved (Clausnitzer et al. 1995; Inoue et al. 1998; Šimůnek et al. 2011).

Thus, this approach could have relevant implications in determining the field saturated hydraulic conductivity, especially for high spatial variability conditions (Leij et al. 2004; Fan et al. 2016), both in the lab and in the field (Baiamonte et al. 2017; 2019).

In the next section, for both constant and time variable rainfall intensity, applications aiming at deriving water content profiles and water balance components, including runoff and drainage volumes, are performed. For constant rainfall intensity, the mass water balance, the effect of the number of reservoirs, and the comparison with Richards equation, are analyzed.

3.3 Results and Discussion

3.3.1 Water Content Profiles for Constant Rainfall Intensity

For a constant rainfall intensity, $i = 10$ mm/h, with indefinite duration, and for a soil hydraulic conductivity at saturation $K_s = 5$ mm/h, so that $\rho = 2$, applications of Eqs. (3.11a and 3.14a) are carried out. Since constant rainfall intensity was assumed, the condition $\Theta_0^{(n-1)} < \Theta_0^{(n)}$ did not occur. It should be remarked that parameters of the water retention curve, λ and h_b, are not involved in this application, and they will be assumed only in Sect. 3.3.4, when applying the Richards equation for a comparison with the GD case.

For $\Theta_0 = 0$, Fig. 3.4a shows the water content profiles derived by the proposed procedure. In particular for the first tank $n = 1$, Eq. (3.11a) was applied, and the outflow discharge was used in Eq. (3.14a) to derive the time-varying water content in the subsequent tank ($n = 2$), and so on for the all the tanks below. The procedure allows determining some characteristic times (as the time to ponding or to soil saturation) that, as it is known, play a fundamental role in synthetically describing the soil hydrological response to a rainfall event (Chu and Mariño 2005; Baiamonte and Singh 2016).
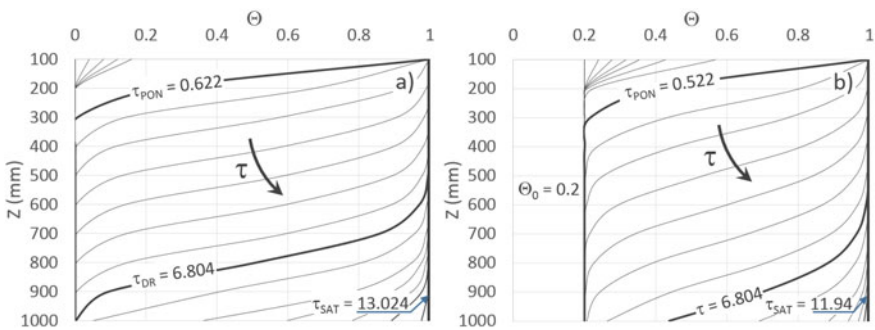
Fig. 3.4 For a constant normalized rainfall intensity $\rho = 2$, water content profiles derived by the present solution (GS), by varying the normalized time, τ, **a** for dry ASMC ($\Theta_0 = 0$), and **b** for ($\Theta_0 = 0.2$). Both panels indicate the normalized time to ponding, τ_{PON}, to drainage, τ_{DR}, and to soil saturation, τ_{SAT}

Figure 3.4a indicates that, for constant normalized rainfall ($\rho = 2 > 1$), a ponding condition occurs at $\tau_{PON} = 0.622$, since the soil becomes saturated. At increasing τ, the wetting front moves down as water infiltrates into the soil. For the considered high soil depth ($Z = 1000$ mm), we need to wait the normalized time $\tau_{DR} = 6.804$ (Fig. 3.4a), for the water to drain from the outlet. For $\tau > \tau_{DR}$, larger and larger portions of soil continue to saturate, when runoff and drainage simultaneously occur, and we need to wait for the time $\tau_{SAT} = 13.024$, for a fully saturated condition of the entire soil profile (Fig. 3.4a).

To investigate the important role of antecedent soil moisture condition (ASMC), another application was performed, by imposing a uniform ASMC with $\Theta_0 = 0.2$. However, the procedure could be applied for any more reliable non-uniform ASMC. Similar to Fig. 3.4a, the corresponding water content profiles obtained by applying Eq. (3.11a and 3.14a) are graphed in Fig. 3.4b. As it would be expected, starting from a wet soil moisture condition ($\Theta_0 = 0.2$), runoff generation started earlier ($\tau_{PON} = 0.522$) than the dry initial condition (Fig. 3.4a), as well as the time to saturation ($\tau_{SAT} = 11.94$), whereas the time to drainage starts with rainfall ($\tau_{DR} = 0$), because of the uniform ASMC assumed (Fig. 3.4b). At the time $\tau = 6.804$, Fig. 3.4b shows that the water content profile is below that corresponding to the start of drainage in Fig. 3.4a, because of the expected ASMC effect.

In conclusion, results show that internal travel times delay the water fluxes, evidencing that assuming an instantaneous water distribution ($N = 1$) may provide high errors in predicting the water balance components, and it is reasonable that differences should be higher and higher at increasing profile depths. This is why the volume domain detected for $N = 1$ (Baiamonte 2020a) and to a lower extent those detected by the present approach could be seen as a boundary of the RCH solutions, over which RCH cannot find solutions.

3.3.2 Mass Water Balance

As previously observed, the proposed procedure makes it possible to determine the water components of the mass water balance, thus allowing the procedure to be checked, although under the simplified hypotheses assumed (GD and $c = 0.5$).

The dimensionless volumes of each component, i.e. the rainfall volume, the stored volume, the drainage volume, and the runoff volume (V_{*IN}, V_{*ST}, V_{*DR}, V_{*RO}, respectively) were calculated as:

$$V_{*IN} = \sum_{\tau=0}^{\tau_r} (\tau - \tau_0)\rho \tag{3.16a}$$

$$V_{*ST} = \begin{bmatrix} \sum_{\tau=0}^{\tau_r} \sum_{n=1}^{N} \Theta_\tau^{(n)} \\ N\Theta_s \end{bmatrix} \begin{array}{l} \text{for } \tau \leq \tau_{SAT} \\ \text{for } \tau > \tau_{SAT} \end{array} \tag{3.16b}$$

$$V_{*DR} = \begin{bmatrix} 0 \\ \sum_{\tau=0}^{\tau_r} \left\{ (\tau - \tau_0) 0.5 \left(\left[\Theta_{\tau_0}^{(N)} \right]^2 + \left[\Theta_{\tau_0}^{(N)} \right]^2 \right) \right\} \end{bmatrix} \begin{array}{l} \text{for } \tau \le \tau_{DR} \\ \text{for } \tau > \tau_{DR} \end{array} \qquad (3.16c)$$

$$V_{*RO} = \begin{bmatrix} 0 \\ \sum_{\tau b=0}^{\tau_r} \left\{ (\tau - \tau_0)(\rho - 1) \right\} \end{bmatrix} \begin{array}{l} \text{for } \tau \le \tau_{PON} \\ \text{for } \tau > \tau_{PON} \end{array} \qquad (3.16d)$$

where as the dimensional volumes as:

$$V_{IN}(\text{mm}) = V_{*IN} K_s t_c \qquad (3.17a)$$

$$V_{ST}(\text{mm}) = V_{*ST} K_s t_c \qquad (3.17b)$$

$$V_{DR}(\text{mm}) = V_{*DR} K_s t_c \qquad (3.17c)$$

$$V_{RO}(\text{mm}) = V_{*RO} K_s t_c \qquad (3.17d)$$

where the star subscript in Eq. (3.16a–d) denotes the dimensionless volume. Equation (3.17a–d) show that the dimensional volumes can be easily determined by the dimensionless ones by multiplying by $K_s t_c$, which represent a characteristic volume of each tank, i.e. the volume that fills a dry closed tank with constant intensity K_s in the characteristic time t_c.

As usual, the mass water balance was checked according to the principle of conservation of mass and considering the soil profile as a closed system, whereby water entering the system (via precipitation), is transferred into either surface runoff, stored into the soil profile or drained by the bottom. Neither crops nor evapotranspiration losses were considered. To verify the procedure, a dimensionless and dimensional check volume, V_{*CK} and V_{CK} [mm], which have to match V_{*IN} and V_{IN} [mm], respectively, can be calculated as:

$$V_{*CK} = V_{*ST} + V_{*DR} + V_{*RO} - V_{*0} \qquad (3.18a)$$

$$V_{CK} = V_{ST} + V_{DR} + V_{RO} - V_0 \qquad (3.18b)$$

where V_{*0} and V_0 denote the soil water volume corresponding to the ASMC that, for the considered uniform case, are equal to $V_{*0} = N \Theta_0$ and $V_0 = V_{*0} K_s t_c$, respectively.

For the case explored in Fig. 3.4b ($\Theta_0 = 0.2$), Fig. 3.5 graphs the cumulative normalized volumes, V_*, and the dimensional volumes, V(mm), referred to the rainfall volume (IN), the storage volume (ST), the drainage volume (DR) and the runoff volume (RO), versus the normalized time, τ, and the dimensional time, t, respectively.
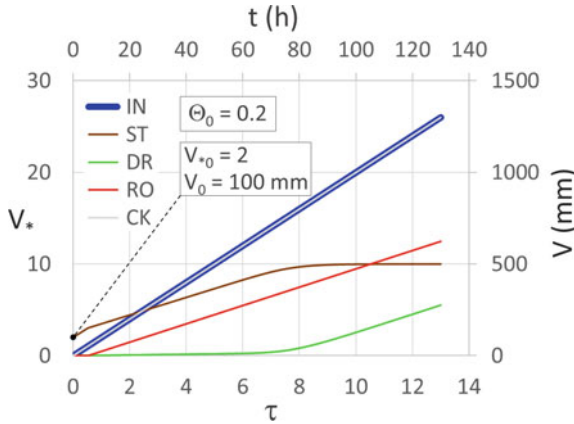
Fig. 3.5 For $\rho = 2$ and $\Theta_0 = 0.2$, normalized volumes, $V*$ (main axes) and dimensional volumes, V (mm) (secondary axes), refer to the rainfall (IN), storage volume (ST), drainage volume (DR) and runoff volume (RO), respectively, versus the time. The check volumes, V_{*CK} and V_{CK} (mm), calculated by Eq. (3.18a and 3.18b), and ASMC are also reported

Of course, dimensionless and dimensional volumes differ by scale factors, i.e. by the characteristic volume $K_s\,t_c$ on the ordinate, and by the characteristic time t_c on the abscissa, thus they can be illustrated in the same graph.

Assuming $N = 10$, $K_s = 5$ mm/h, $\theta_s = 0.5$ cm^3 cm^{-3}, $\theta_0 = 0.1$ cm^3 cm^{-3}, $t_c = 10$ h and $K_s\,t_c = 50$ mm. The volumes V_{*CK} and V_{CK} (CK) calculated by Eq. (3.18a and 3.18b) are also plotted in Fig. 3.5 (main axes and secondary axes, respectively), and made it possible to positively verify the consistence of the mass water balance, overlapping V_{*IN} and V_{IN}, respectively, versus the time.

Equations (3.16a–d and 3.17a–d) highlight that the number of reservoirs N plays an important role, in detecting the hydrologic components of the mass water balance, and this effect is analyzed in the next section.

3.3.3 Effect of Number of Reservoirs

The effect of number of reservoirs, N, on modeling the water balance components, under GD and $c = 0.5$, is an expected issue. For example, moving from $N = 1$ (Baiamonte 2020a) to $N > 1$, the drainage volume, which for $N = 1$ starts with rainfall because of vertical water content profiles, of course for $N > 1$, has to be delayed. In order to explore this effect, for all the considered components, for a fixed very long rainfall duration ($t_d = 120$ h), and by imposing a small enough τ step to obtain a fixed high number of intervals, by varying N in the range $N = 1 - 40$, simulations were performed by calculating the considered volumes (V_{IN}, V_{ST}, V_{DR}, V_{RO}, V_0), and also checking the relative error in the water balance RE:

$$RE = \frac{V_{IN} - V_{CK}}{V_{IN}} \tag{3.19}$$

with V_{CK} calculated by Eq. (3.18b). For a fixed duration of rainfall, t_d, it should be noticed that in dimensional terms, to detect the effect of the number of reservoirs $\# N$, for a fixed number of time steps, n_i, the dependence of the temporal scale t_c (Eq. 3.8) by $\# N$ needs to be considered in order to properly update the time step τ_i:

$$\tau_i = \frac{\tau_d}{n_i} = \frac{t_d}{t_c n_i} = \frac{t_d N K_s}{Z \theta_s n_i} \tag{3.20}$$

where τ_d is the normalized duration of rainfall. Simulations aimed at also analyzing the effect of main input data ρ and Θ_0. Figure 3.6 plots the considered volumes as a function of N, together with RE (secondary axis), for $\rho = 2$ ($i = 5$ mm/h and $K_s = 5$ mm/h), and $\theta_0 = 0.1$ cm^3 cm^{-3} (Fig. 3.6a) and $\theta_0 = 0.2$ cm^3 cm^{-3} (Fig. 3.6b), and for $\rho = 4$ ($i = 20$ mm/h and $K_s = 5$ mm/h), for the same values of θ_0 ($\theta_0 = 0.1$ cm^3 cm^{-3}, Fig. 3.6c, and $\theta_0 = 0.2$ cm^3 cm^{-3}, Fig. 3.6d). For all the considered cases, results show that V_{IN} and V_{CK} overlap, indicating the consistence of the mass water balance. However, RE, which accordingly results to be negligible, shows a very slight increase with increasing N ($< 0.12\%$), starting from RE $\cong 0$ for $\# N = 1$.

As expected, V_{DR} decreases with N, and V_{RO} increases with N, whereas V_{ST} at the equilibrium is not influenced by N. Most importantly, for all the considered cases, for $N > 15$, V_{DR} and V_{RO} do not vary with N, indicating that this threshold value could be
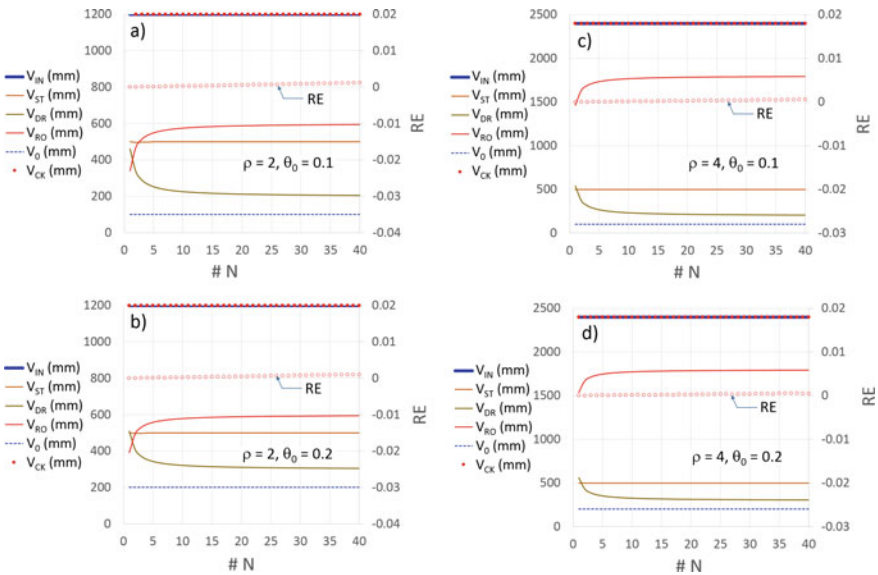
Fig. 3.6 For selected $\rho = 2$ and 4, and $\theta_0 = 0.1$ and 0.2 cm^3 cm^{-3}, variations of the hydrologic components of the mass water balance with the number of the reservoirs $\# N$

considered to obtain reliable components of the water balance. Furthermore, results agree with Agnese et al. (2001) and Baiamonte and Singh (2016), who evidenced that under Hortonian mechanism of runoff generation, for very long duration of rainfall with constant intensity, i, the asymptotic rainfall excess intensity r_∞ approached $i - K_s$, meaning that, for the examined case in which volumes were analyzed, V_{RO} had to approach $(i - K_s) t_d$, i.e. 600 mm for $\rho = 2$, and 1800 mm for $\rho = 4$, as shown in Fig. 3.6.

3.3.4 Comparison Between the GD Solution and the Richards Equation

In this section a comparison between the GD solution, and the much more accurate solution, although numerically demanding, obtained by the Richards equation (RCH), where the infiltration process is driven by both the gravity and the humidity gradients (Eq. 3.1), is performed. HYDRUS-1D (Šimůnek et al. 2011) was applied to obtain the RCH solutions. A different number of parameters is required by the GD and RCH procedures, and within the unsaturated zone, GD and RCH differ in the water redistribution dynamics, because of the influence of the matric potential gradients that in HYDRUS-1D are considered. However, the comparison provided results that are interesting to be described.

In HYDRUS-1D, the Brooks and Corey hydraulic conductivity function, also considered in the GD model (Eq. 3.4b), was set. Furthermore, for a fixed air-entry pressure head, $h_b = -7.25$ cm, which is close to that of a sandy soil (Carsel and Parrish, 1988; Guarracino, 2007), for two λ values ($\lambda = 0.5$ and $\lambda = 1$), the Brooks and Core water retention curve (Eq. 3.4a), of course not considered in GD, was used in HYDRUS-1D. The application was performed for the same $i = 10$ mm/h, $K_s = 5$ mm/h and $\Theta_0 = 0.2$, considered in Sect. 3.3.2.

Although the GD assumption cannot be set in Hydrus-1D, which uses the matric potential corresponding to the water retention curve, a more homogeneous comparison could be performed in terms of hydraulic conductivity function. In order to do that, the tortuosity parameter was modified to impose the same $c = 0.5$ exponent in Eq. (3.5b), and determining the corresponding tortuosity p value as a function of λ, yielding:

$$p = -\frac{2}{\lambda} \tag{3.21}$$

According to the common λ values (Fig. 3.1a), Eq. (3.21) clearly provides negative tortuosity values, which are rarely found in the literature. However, Eq. (3.21) has to be seen as an equivalent value of tortuosity that makes it possible to set the $c = 0.5$ assumption in Hydrus-1D, in order to homogenously analyze the results of comparison between GD and RCH in terms of the adopted hydraulic conductivity function. It needs mentioning that negative values of the tortuosity have been assumed
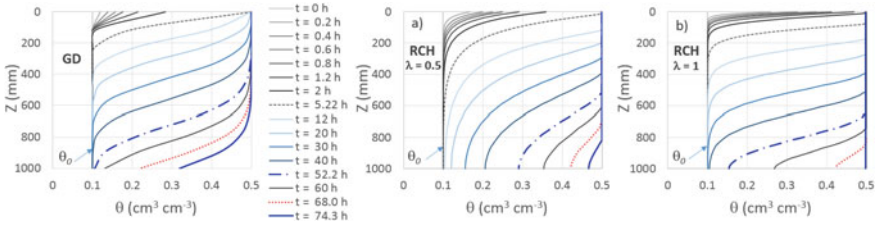
Fig. 3.7 For $i = 10$ mm/h, $K_s = 5$ mm/h, $\Theta_0 = 0.2$, and $h_b = -7.25$, water content profiles **a** derived by the GD model, and by Hydrus-1D, **b** for $\lambda = 0.5$, and **c** for $\lambda = 1$, by imposing the same hydraulic conductivity function as GD

sometimes. Rassam et al. (2003) observed that "optimizing the tortuosity parameter permits one to change the shape of the hydraulic conductivity function independently of the retention function". Since the older version of HYDRUS-1D could not jump over zero, they conducted different runs, one starting with a positive p value and one with a negative p value. Recently, Cai et al. (2018) obtained smaller (even negative) tortuosity parameters for silty soils than for stony soils, implying that the latter exhibited a more strongly hydraulic conductivity decrease with decreasing saturation degree.

It should be also noticed that although suspiciously considered in the present comparison, the importance of tortuosity was fully acknowledged in many studies, governing the infiltration process in porous media (Burdine 1953; Kosugi 1999; Shinomiya et al. 2001; Rezanezhad et al. 2009; Nasta et al. 2012; Bouchemella et al. 2016).

For the aforementioned parameters, Fig. 3.7 shows the water content profiles obtained by the GD model (Fig. 3.7a) and by Hydrus-1D for $\lambda = 0.5$ (Fig. 3.7b) and $\lambda = 1$ (Fig. 3.7c). For the purpose of comparison, Fig. 3.7a, b and c highlight (i) the time to ponding for GD (see Fig. 3.4b, $t_{PON} = 5.22$ h, dashed line,), (ii) the time to drainage for $\theta_0 = 0$ (see Fig. 3.4a, $t_{DR} = 68.04$ h, dot lines), and iii) the time to soil saturation $t_{SAT} = 74.3$ h, corresponding to RCH, for $\lambda = 1$ (Fig. 3.7c).

As can be observed in Fig. 3.7, in the three considered cases, at the bottom of the soil layer (under the free drainage boundary conditions), the drainage starts with rainfall ($t_{DR} = 0$), since a uniform ASMC ($\theta_0 = 0.1 > 0$) was assumed.

The time $t_{PON} = 5.22$ h obtained for GD results lower than that obtained for RCH ($t_{PON} = 8.5$ h for $\lambda = 0.5$, obtained by Hydrus-1D), although from Fig. 3.7b it can be observed that at $t = 5.22$ h soil saturation is achieved. This is because of the influence of the matric potential gradient and of the bubbling pressure considered in RCH, for which ponding is achieved when the matric potential vanishes in the top soil. The value of $t_{SAT} = 130$ h, for the GD (not illustrated), appears much higher than that of RCH, for both λ values, indicating that when the matric potential gradient is considered (RCH), water flows are quicker than in the GD case. Similarly, for any fixed time (for example $t = 68$ h), the water content profiles in RCH are below that in the GD case, because of the additional matric gradient contribution that accelerates the water movement into the soil. For $t = 68$ h, the water content profile is also

below that obtained for GD, because of the effect of ASMC. In conclusion, it should be expected that the water content profiles provided by GD, and the associated volumes, delimit the domain of the Richards equation over which Hydrus-1D cannot find solutions.

3.3.5 Water Content Profiles for Variable Rainfall Intensity

Equation (3.11a and 3.11b) make it possible to extend the applications to time-varying rainfall intensity, when any sequence of rainfall intensities is applied to the soil (at the top tank). For the parameters reported in Table 3.1, four applications (Run #1, #2, #3, and #4), by varying K_s (50 and 5 mm/h), for a fixed $\Theta_0 = 0$ (Run #1, #2), and for a fixed $\Theta_0 = 0.6$ (Run #3, #4), were carried out. The number of tanks, N, was set equal to 15. Table 3.1 also reports the considered duration of rainfall, t_r, the hydrologic components of the mass water balance, corresponding to the high simulation time, t_{sim} [T], which was set to consider the recession of soil moisture after rainfall ceased, and the volume V_{CK} (Eqs. 3.18b) to check the mass water balance, and the runoff coefficient δ. The rainfall distribution and the total rainfall depth (119.58 mm) and its duration ($t_r = 16.92$ h) were set equal for all of the four runs.

Results are graphed in Fig. 3.8. The volumetric water content profiles, at depths of 10, 30, 50, 70 and 90 cm are reported in Fig. 3.8a, c, e, f, together with the time-varying rainfall intensity, $i(t)$ (secondary axis), the related runoff intensity ($i-K_s$), and drainage fluxes (K). The corresponding cumulated rainfall, drainage and runoff volumes are graphed in Fig. 3.8b, d, f, h, where the check volume calculated by Eq. (3.18b) is also indicated.

Some interesting considerations arose by the applications performed. First, results only depended on the input rainfall distribution, and on the hydraulic conductivity at saturation K_s, which is a scale parameter of the suggested procedure, as previously observed. For the all four runs, the water content distributions reasonably delayed more and more with increasing depth, and with a different behavior according to the input parameters. For example, for $K_s = 5$ mm/h (Fig. 3.8c–g), it can be observed that at the top soil, the water content variations were generally quicker than for $K_s = 50$ mm/h (Fig. 3.8a–e). For dry initial conditions ($\theta_0 = 0$), when $K_s = 50$ mm/h, no runoff occurred (Fig. 3.8a, b), whereas for $K_s = 5$ mm/h (Fig. 3.8c), runoff initiated at the third peak of rainfall. The absence of runoff can be also observed for wet initial conditions ($\theta_0 = 0.3$) (Fig. 3.8e, f), because of the high K_s. However, in this case the influence of the wet initial conditions can be seen in terms of drainage volumes that resulted much higher than for $\theta_0 = 0$ (cf. Figure 3.8b). In conclusion, results appear reasonable and agree with what could be expected, verifying the water mass balance in all the considered cases. According to the results shown in Fig. 3.6, slight differences were found by adopting $N = 20$ and 25.

In conclusion, this simple simplified approach could even open doors to estimate as an inverse method the saturated hydraulic conductivity, by monitoring water content profiles in the field or in the lab (Inoue et al. 1998). It needs to remark that

Table 3.1 Times of the rainfall duration, t_d, of the simulation, t_{sim}, characteristic water contents (θ_s and θ_0) and rainfall volume (V_{IN}), drainage volume (V_{DR}), storage volume (V_{ST}), corresponding to the four applications. The check volume (V_{CK}) calculated by Eq. (3.18b) and the runoff coefficient, δ, are also reported

Run #	t_d (h)	t_{sim} (h)	K_s (mm/h)	θ_s (cm^3 cm^{-3})	θ_0 (cm^3 cm^{-3})	V_0 (mm)	V_{IN} (mm)	V_{RO} (mm)	V_{DR} (mm)	V_{ST} (mm)	V_{CK} (mm)	δ
1	16.92	833.25	50	0.5	0	0	119.58	0	117.29	118.02	119.44	0
2		833.25	5		0	0		27.25	70.84	92.12	119.45	0.228
3		167.45	50		0.3	300.00		0.00	409.35	300.00	120.95	0
4		833.25	5		0.3	300.00		34.83	364.93	354.83	121.13	0.291
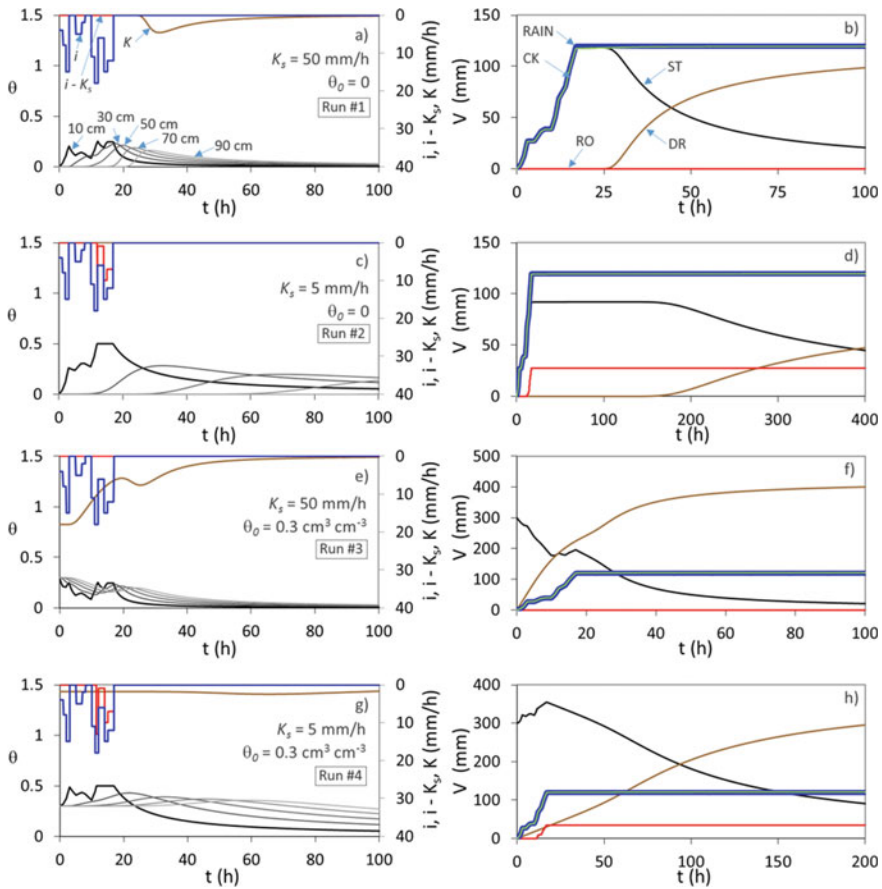
Fig. 3.8 For Runs, #1, #2, #3 and #4 (Table 3.1), for a time-variable rainfall intensity, $i(t)$, indicated in (**a**), (**c**), (**e**), (**g**) (secondary axis), water content profiles (θ), at the depths 10, 30, 50, 70 and 90 cm, versus the time t, and related runoff ($i-K_s$), and drainage (K) fluxes. The corresponding cumulative rainfall, drainage and runoff volumes are reported in (**b**), (**d**), (**f**) and (**h**), where the check volume (V_{CK}) is also indicated

the GD condition is required, which interestingly bounds the solutions that can be obtained when the humidity gradients are also considered (Baiamonte 2020b). The approach followed in this study could be also applied to case in which the gravitational gradient is negligible compared to the matric potential gradient, further delimiting the Richards solutions domain. In fact, it is expected that under the latter condition, new bounds for water content profiles and related water volumes, should emerge. Experimental tests could be advisable for sandy soils, where the adopted GD assumption could be reasonable. However, it needs considering that the same approach was already positively tested for tanks filled by only water, in the case of one tank (Baiamonte 2020b), and for multiple tanks connected in series (Baiamonte 2020c), by

using the experimental and theoretical data provided by Zhang et al. (2019), where the Torricelli law was considered in place of the hydraulic conductivity function of Brooks and Corey.

3.4   Conclusions and Perspectives

The points covered in this paper can be summarized as follows:

1. In the recently introduced simplified solution of the Richards equation under gravity-driven infiltration, the assumption of a capacitance framework applied to only one reservoir was relaxed, in order to derive water content profiles and related drainage and runoff volumes. The internal water content travel times were replicated through the discretization of the soil profile into multiple tanks connected in series.
2. The considered hydraulic approach allows taking into account the whole domain the soil hydraulic conductivity function. Thus, the assumption of the common tank models, where fluxes drain to tank below only after saturation, is relaxed.
3. The approach, applied in dimensionless terms by the Brooks and Corey hydraulic conductivity function, indicates that the saturated hydraulic conductivity is a scale parameter of the simplified procedure, evidencing that the derived water content profiles are only affected by the rainfall patterns.
4. The reliability of the derived solutions is demonstrated by the verification of the mass water balance, according to applications performed under constant rainfall intensity and time-varying rainfall intensity.
5. The suggested solution was compared with the much more accurate Richards equation, where the gravity-driven assumption is relaxed.

Further research on the issues explored in this paper is suggested:

1. Since the proposed procedure is only affected by the saturated hydraulic conductivity, K_s, it could be easy to be used as an inverse method to determine K_s, according to an objective function to be minimized, based on monitored water content profiles in the field or in the lab.
2. Experimental verification would be advisable to investigate the suitability of the GD and $c = 0.5$ assumptions for selected sandy soils.
3. Implementing the procedure for $c < 0.5$ values, which may characterize sandy soils, is also an issue that could be addressed.

References

Agnese C, Baiamonte G, Corrao C (2001) A simple model of hillslope response for overlans flow generation. Hydrological Process-HYDROL PROCESS 15:3225–3238. https://doi.org/10.1002/hyp.182

Agnese C, Baiamonte G, Corrao C (2007) Overland flow generation on hillslopes of complex topography: analytical solutions. Hydrol Process 21:1308–1317. https://doi.org/10.1002/hyp.6354

Al-Hamdan OZ, Cruise JF (2010) Soil moisture profile development from surface observations by principle of maximum entropy. J Hydrol Eng 15(5):327–337. https://doi.org/10.1061/(ASCE)HE.1943-5584.0000196

Assouline S (2013) Infiltration into soils: conceptual approaches and solutions. Water Resour Res 49(4):1755–1772. https://doi.org/10.1002/wrcr.20155

Bagarello V, Baiamonte G, Caia C (2019) Variability of near-surface saturated hydraulic conductivity for the clay soils of a small Sicilian basin. Geoderma 340:133–145. https://doi.org/10.1016/j.geoderma.2019.01.008

Baiamonte G (2016) Simplified model to predict runoff generation time for well-drained and vegetated soils. J Irrig Drain Eng 142(11):04016047. https://doi.org/10.1061/(ASCE)IR.1943-4774.0001072

Baiamonte G (2020a) Analytical solution of the richards equation under gravity-driven infiltration and constant rainfall intensity. J Hydrol Eng 25(7):04020031. https://doi.org/10.1061/(ASCE)HE.1943-5584.0001933

Baiamonte G (2020b) Dimensionless stage-discharge relationship for a non-linear water reservoir: theory and experiments. Hydrology 7(2). https://doi.org/10.3390/hydrology7020023

Baiamonte G (2020c) Discussion of hydraulic model of transition of transient to steady flows in the vadose zone by Yaguo Zhang, Tonglu Li, Wei Shen, and Yu Wang. J Hydrol Eng 25(11):07020022. https://doi.org/10.1061/(ASCE)HE.1943-5584.0002015

Baiamonte G (2021) Complex rating curves for sharp crested orifices and rectangular or triangular weirs under unsteady flow conditions. J Hydrol Eng 26(4):04021005. https://doi.org/10.1061/(ASCE)HE.1943-5584.0002057

Baiamonte G, Agnese C (2016) Quick and slow components of the hydrologic response at the hillslope scale. J Irrig Drain Eng 142(10):04016038. https://doi.org/10.1061/(ASCE)IR.1943-4774.0001053

Baiamonte G, Bagarello V, D'Asaro F, Palmeri V (2017) Factors influencing point measurement of near-surface saturated soil hydraulic conductivity in a small sicilian basin. Land Degrad Dev 28(3):970–982. https://doi.org/10.1002/ldr.2674

Baiamonte G, D'Asaro F, Calvo R (2019) Gravity-driven infiltration and subsidence phenomena in posidonia oceanica residues. J Hydrol Eng 24(6):04019016. https://doi.org/10.1061/(ASCE)HE.1943-5584.0001791

Baiamonte G, Singh VP (2016) Analytical solution of kinematic wave time of concentration for overland flow under green-Ampt infiltration. J Hydrol Eng 21(3):04015072. https://doi.org/10.1061/(ASCE)HE.1943-5584.0001266

Baiamonte G, Singh VP (2017) Modeling the probability distribution of peak discharge for infiltrating hillslopes. Water Resour Res 53(7):6018–6032. https://doi.org/10.1002/2016WR020109

Batu V (1978) Steady infiltration from single and periodic strip sources. Soil Sci Soc Am J 42(4):544–549. https://doi.org/10.2136/sssaj1978.03615995004200040002x

Bouchemella S, Ichola IA, Séridi A (2016) Estimation of the empirical model parameters of unsaturated soils. E3S Web of Conf 9 16007. https://doi.org/10.1051/e3sconf/20160916007

Brakensiek DL, Engleman RL, Rawls WJ (1981) Variation within texture classes of soil water parameters. Trans ASAE [Am Soc Agri Eng]. https://scholar.google.com/scholar_lookup?title=Variation+within+texture+classes+of+soil+water+parameters.&author=Brakensiek+D.L.&publication_year=1981

Broadbridge P, Daly E, Goard J (2017) Exact solutions of the Richards equation with nonlinear plant-root extraction. Water Resour Res 53(11):9679–9691. https://doi.org/10.1002/2017WR021097

Broadbridge P, White I (1988) Constant rate rainfall infiltration: a versatile nonlinear model: 1. Analytic Solution. Water Resour Res 24(1):145–154. https://doi.org/10.1029/WR024i001p00145

Brooks RH, Corey AT (1964) Hydraulic properties of porous media

Brutsaert W (2005) Hydrology: an introduction, Cambridge University Press, Cambridge. https://www.cambridge.org/highereducation/books/hydrology/59A90AFF36F02ECDE7DB2EE21C740612#overview

Burdine NT (1953) Relative permeability calculations from pore size distribution data. J Petrol Technol 5(03):71–78. https://doi.org/10.2118/225-G

Cai G, Vanderborght J, Langensiepen M, Schnepf A, Hüging H, Vereecken H (2018) Root growth, water uptake, and sap flow of winter wheat in response to different soil water conditions. Hydrol Earth Syst Sci 22(4):2449–2470. https://doi.org/10.5194/hess-22-2449-2018

Carsel RF, Parrish RS (1988) Developing joint probability distributions of soil water retention characteristics. Water Resour Res 24(5):755–769. https://doi.org/10.1029/WR024i005p00755

Childs, E. C., Collis-George, N., & Taylor, G. I. (1950). The permeability of porous materials. In: Proceedings of the royal society of London. series a. mathematical and physical sciences 201(1066), 392–405. https://doi.org/10.1098/rspa.1950.0068

Chu X, Mariño MA (2005) Determination of ponding condition and infiltration into layered soils under unsteady rainfall. J Hydrol 313(3–4):195

Clapp RB, Hornberger GM (1978) Empirical equations for some soil hydraulic properties. Water Resour Res 14(4):601–604. https://doi.org/10.1029/WR014i004p00601

Clausnitzer V, Hopmans JW (1995) Non-linear parameter estimation: LM_OPT. General-purpose optimization code based on the Leven- berg-Marquardt algorithm. Land, Air Water Resour. Pap. 100032, Univ. of Calif., Davis

Cui G, Zhu J (2018) Infiltration model based on traveling characteristics of wetting front. Soil Sci Soc Am J 82(1):45–55. https://doi.org/10.2136/sssaj2017.08.0303

Cullotta S, Bagarello V, Baiamonte G, Gugliuzza G, Iovino M, La Mela Veca DS, Maetzke F, Palmeri V, Sferlazza S (2016) Comparing different methods to determine soil physical quality in a mediterranean forest and pasture land. Soil Sci Soc Am J 80(4):1038–1056. https://doi.org/10.2136/sssaj2015.12.0447

Fan L, Lehmann P, Or D (2016) Effects of soil spatial variability at the hillslope and catchment scales on characteristics of rainfall-induced landslides. Water Resour Res 52(3):1781–1799. https://doi.org/10.1002/2015WR017758

Farmer D, Sivapalan M, Jothityangkoon C (2003) Climate, soil, and vegetation controls upon the variability of water balance in temperate and semiarid landscapes: downward approach to water balance analysis. Water Resour Res 39(2). https://doi.org/10.1029/2001WR000328

Ghanbarian B, Ioannidis MA, Hunt AG (2017) Theoretical insight into the empirical tortuosity-connectivity factor in the Burdine-brooks-Corey water relative permeability model. Water Resour Res 53(12):10395–10410. https://doi.org/10.1002/2017WR021753

Govindaraju RS, Or D, Kavvas ML, Rolston DE, Biggar J (1992) Error analyses of simplified unsaturated flow models under large uncertainty in hydraulic properties. Water Resour Res 28(11):2913–2924. https://doi.org/10.1029/92WR01515

Guarracino L (2007) Estimation of saturated hydraulic conductivity Ks from the van Genuchten shape parameter α. Water Resour Res 43(11). https://doi.org/10.1029/2006WR005766

Guswa AJ, Celia MA, Rodriguez-Iturbe I (2002) Models of soil moisture dynamics in ecohydrology: a comparative study: models of soil moisture dynamics in ecohydrology. Water Resour Res 38(9), 5–1–5–15. https://doi.org/10.1029/2001WR000826

Horton RE (1939) The interpretation and application of runoff plat experiments with reference to soil erosion problems. Soil Sci Soc Am J 3(C), 340–349. https://doi.org/10.2136/sssaj1939.036159950003000C0066x

Inoue M, Šimunek J, Hopmans JW, Clausnitzer V (1998) In situ estimation of soil hydraulic functions using a multistep soil-water extraction technique. Water Resour Res 34(5):1035–1050. https://doi.org/10.1029/98WR00295

Javaux M, Couvreur V, Vanderborght J, Vereecken H (2013) Root water uptake: from three-dimensional biophysical processes to macroscopic modeling approaches. Vadose Zone J 12(4). vzj2013.02.0042 https://doi.org/10.2136/vzj2013.02.0042

Simůnek J, Angulo-Jaramillo R, Schaap MG, Vandervaere JP, Genuchten MT van (1998) Using an inverse method to estimate the hydraulic properties of crusted soils from tension-disc infiltrometer data. Geoderma 86, 61–81

Klute A (1972) Determination of the hydraulic conductivity and diffusivity of unsaturaled soils. Soil Science. https://scholar.google.com/scholar_lookup?title=determination+of+the+hydrau lic+conductivity+and+diffusivity+of+unsaturaled+soils&author=Klute%2C+A.&publication_year=1972

Kosugi K (1999) General model for unsaturated hydraulic conductivity for soils with lognormal pore-size distribution. Soil Sci Soc Am J 63(2):270–277. https://doi.org/10.2136/sssaj1999.036 15995006300020003x

Kravchenko A, Zhang R (1997) Estimating soil hydraulic conductivity from soil particle-size distri- bution. In: Proceedings of the international workshop on characterization and measurement of the hydraulic properties of unsaturated porous media, pp 959–966

Leij FJ, Romano N, Palladino M, Schaap MG, Coppola A (2004) Topographical attributes to predict soil hydraulic properties along a hillslope transect. Water Resour Res 40(2). https://doi.org/10. 1029/2002WR001641

Manabe S (1969) Climate and the ocean circulation, I, The atmospheric circulation and the hydrology of the Earth's surface. Mwr 97. https://doi.org/10.1175/1520-0493(1969)09760;0739: catoc62;2.3.co;2

Melone F, Corradini C, Morbidelli R, Saltalippi C, Flammini A (2008) Comparison of theoretical and experimental soil moisture profiles under complex rainfall patterns. J Hydrol Eng 13(12):1170– 1176. https://doi.org/10.1061/(ASCE)1084-0699(2008)13:12(1170)

Millington RJ, Quirk JP (1961) Permeability of porous solids. Trans Faraday Soc 57:1200–1207. https://doi.org/10.1039/TF9615701200

Milly PCD (1994) Climate, soil water storage, and the average annual water balance. Water Resour Res 30(7):2143–2156. https://doi.org/10.1029/94WR00586

Mualem Y (1976) A new model for predicting the hydraulic conductivity of unsaturated porous media. Water Resour Res 12(3):513–522. https://doi.org/10.1029/WR012i003p00513

Nasta P, Lassabatere L, Kandelous MM, Šimůnek J, Angulo-Jaramillo R (2012) Analysis of the role of tortuosity and infiltration constants in the Beerkan method. Soil Sci Soc Am J 76(6):1999–2005. https://doi.org/10.2136/sssaj2012.0117n

Nasta P, Vrugt JA, Romano N (2013) Prediction of the saturated hydraulic conductivity from Brooks and Corey's water retention parameters. Water Resour Res 49(5):2918–2925. https://doi.org/10. 1002/wrcr.20269

Raats P (1976) Analytical solutions of a simplified flow equation. Trans ASAE 683–689

Rallo G, Baiamonte G, Juárez JM, Provenzano G (2014) Improvement of FAO-56 model to estimate transpiration fluxes of drought tolerant crops under soil water deficit: application for olive groves. J Irrig Drain Eng 140(9):A4014001. https://doi.org/10.1061/(ASCE)IR.1943-4774.0000693

Rassam D, Genuchten MT van, Simunek J (2003) Modelling variably saturated low with HYDRUS- 2D. ND Consult

Rezanezhad F, Quinton WL, Price JS, Elrick D, Elliot TR, Heck RJ (2009) Examining the effect of pore size distribution and shape on flow through unsaturated peat using computed tomography. Hydrol Earth Syst Sci 13(10):1993–2002. https://doi.org/10.5194/hess-13-1993-2009

Richards LA (1931) Capillary conduction of liquids through porous mediums. Physics 1(5):318– 333. https://doi.org/10.1063/1.1745010

Romano N, Palladino M, Chirico GB (2011) Parameterization of a bucket model for soil-vegetation- atmosphere modeling under seasonal climatic regimes. Hydrol Earth Syst Sci 15(12):3877–3893. https://doi.org/10.5194/hess-15-3877-2011

Sadegh Zadeh K (2009) Multi-objective optimization in variably saturated fluid flow. J Comput Appl Math 223(2):801–819. https://doi.org/10.1016/j.cam.2008.03.005

Sander GC, Parlange J-Y, Kühnel V, Hogarth WL, Lockington D, O'Kane JPJ (1988) Exact nonlinear solution for constant flux infiltration. J Hydrol 97(3):341–346. https://doi.org/10.1016/0022-169 4(88)90123-0

Sarabai S, Ghahraman B (2020) Tortuosity analysis under the unsaturated flow framework. Eurasian Soil Sci 53:632–642. https://doi.org/10.1134/S1064229320050130

Schelle H, Iden SC, Peters A, Durner W (2010) Analysis of the agreement of soil hydraulic properties obtained from multistep-outflow and evaporation methods. Vadose Zone J 9(4):1080–1091. https://doi.org/10.2136/vzj2010.0050

Serrano SE (2004) Modeling infiltration with approximate solutions to Richard's equation. J Hydrol Eng 9(5):421–432. https://doi.org/10.1061/(ASCE)1084-0699(2004)9:5(421)

Shinomiya Y, Takahashi K, Kobiyama M, Kubota J (2001) Evaluation of the tortuosity parameter for forest soils to predict unsaturated hydraulic conductivity. J for Res 6(3):221–225. https://doi.org/10.1007/BF02767097

Šimůnek J, van Genuchten M, Šejna M (2011) The HYDRUS software package for simulating two- and three-dimensional movement of water, heat, and multiple solutes in variably-saturated media. Technical Manual Version 2.0, p 258

Singh VP (1996) Kinematic wave modeling in water resources: surface-water hydrology|Wiley. Wiley.Com. https://www.wiley.com/en-ae/Kinematic+Wave+Modeling+in+Water+Resources%3A+Surface+Water+Hydrology-p-9780471109457

Singh VP (2010) Entropy theory for derivation of infiltration equations. Water Resour Res 46(3). https://doi.org/10.1029/2009WR008193

Smith RE, Smettem KRJ, Broadbridge P (2002) Infiltration theory for hydrologic applications. Water Resour Monogr Ser. https://www.wiley.com/en-us/Infiltration+Theory+for+Hydrologic+Applications-p-9781118665497

Struthers I, Hinz C, Sivapalan M (2006) A multiple wetting front gravitational infiltration and redistribution model for water balance applications. Water Resour Res 42(6). https://doi.org/10.1029/2005WR004645

Su L, Yang X, Wang Q, Qin X, Zhou B, Shan Y (2018) Functional extremum solution and parameter estimation for one-dimensional vertical infiltration using the brooks-Corey model. Soil Sci Soc Am J 82(6):1319–1332. https://doi.org/10.2136/sssaj2018.01.0016

Sugii T (2005) Modeling of soil moisture profile during infiltration into vadose zone. In: 16th International Conference on Soil Mechanics and Geotechnical Engineering, 5

Tramblay Y, Bouvier C, Martin C, Didon-Lescot J-F, Todorovik D, Domergue J-M (2010) Assessment of initial soil moisture conditions for event-based rainfall–runoff modelling. J Hydrol 387(3):176–187. https://doi.org/10.1016/j.jhydrol.2010.04.006

Tuli A, Hopmans JW, Rolston DE, Moldrup P (2005) Comparison of air and water permeability between disturbed and undisturbed soils. Soil Sci Soc Am J 69(5):1361–1371. https://doi.org/10.2136/sssaj2004.0332

van Genuchten MT (1980) A closed-form equation for predicting the hydraulic conductivity of unsaturated soils. Soil Sci Soc Am J 44(5):892–898. https://doi.org/10.2136/sssaj1980.03615995004400050002x

Vand AS, Sihag P, Singh B, Zand M (2018) Comparative evaluation of infiltration models. KSCE J Civ Eng 22(10):4173–4184. https://doi.org/10.1007/s12205-018-1347-1

Vrugt J, Van Wijk M, Hopmans J, Simunek J, Jirka (2001) One-, two-, and three-dimensional root water uptake functions for transient modeling. Water Resour Res 37, 2457–2470. https://doi.org/10.1029/2000WR000027

White I, Broadbridge P (1988) Constant rate rainfall infiltration: a versatile nonlinear model: 2. Appl Solutions Water Resour Res 24(1):155–162. https://doi.org/10.1029/WR024i001p00155

Willigen P, Dam JC, Javaux M, Heinen M (2012) Root water uptake as simulated by three soil water flow models. Vadose Zone J 11. https://doi.org/10.2136/vzj2012.0018

Wösten JHM, Lilly A, Nemes A, Le Bas C (1999) Development and use of a database of hydraulic properties of European soils. Geoderma 90(3):169–185. https://doi.org/10.1016/S0016-7061(98)00132-3

Wylie MRJ, Gardner GHF (1958) The Generalized Kozeny-Carman Equation: Its Application to Problems of Multiphase Flow in Porous Media. 146:210–227

Xing X, Wang H, Ma X (2018) Brooks–Corey modeling by one-dimensional vertical infiltration method. Water 10(5). https://doi.org/10.3390/w10050593

Yadav B, Mathur S, Siebel M (2009) Soil moisture flow modeling with water uptake by plants (Wheat) under varying soil and moisture conditions. J Irrig Drainage Eng 135. https://doi.org/10.1061/(ASCE)IR.1943-4774.0000068

Zhang Y, Li T, Shen W, Wang Y (2019) Hydraulic model of transition of transient to steady flows in the vadose zone. J Hydrol Eng 24(12):04019052. https://doi.org/10.1061/(ASCE)HE.1943-5584.0001843

Chapter 4
Flood Mapping and Assessment During Typhoon Ulysses (Vamco) in Cagayan, Philippines Using Synthetic Aperture Radar Images

Kezia Shem G. Brusola, Marion Lux Y. Castro, Jerome M. Suarez, Dianna Rose N. David, Christine Jane E. Ramacula, Marifee A. Capdos, Leo Neil T. Viado, Moises A. Dorado, and Vicente G. Ballaran Jr

4.1   Introduction

Geographic Information Systems (GIS) is an essential tool used to read, store, manage, and analyze georeferenced data and attributes. GIS could link spatial and

K. S. G. Brusola · M. L. Y. Castro (✉) · J. M. Suarez · D. R. N. David · C. J. E. Ramacula · M. A. Capdos · L. N. T. Viado · M. A. Dorado · V. G. Ballaran Jr
Institute of Agricultural and Biosystems Engineering (IABE), College of Engineering and Agro-Industrial Technology (CEAT), University of the Philippines Los Baños (UPLB), College, Los Baños 4031, Laguna, Philippines
e-mail: mycastro@up.edu.ph

K. S. G. Brusola
e-mail: kgbrusola@up.edu.ph

J. M. Suarez
e-mail: jmsuarez@up.edu.ph

D. R. N. David
e-mail: dndavid@up.edu.ph

C. J. E. Ramacula
e-mail: ceramacula@up.edu.ph

M. A. Capdos
e-mail: macapdos@up.edu.ph

L. N. T. Viado
e-mail: ltviado@up.edu.ph

M. A. Dorado
e-mail: madorado@up.edu.ph

V. G. Ballaran Jr
e-mail: vdballaran@up.edu.ph

non-spatial data to support better management and decision-making. Quantum GIS (QGIS) is an open-source desktop GIS software application that offers free usage, high compatibility with any operating system, user-friendly interface, easy operation, manageable features, and faster update (Donnelly 2021). One of the most important data sources used in GIS is that provided by remote sensing. Remote sensing (RS) is the science of acquiring information at a distance and no actual contact with the object under observation (Olaya 2018). Millions of satellites revolving around the planet capture images that are helpful in the observation of the changes happening in the land over time. These satellites are useful for researchers and decision makers alike. Some of the applications of RS include mapping of forest fires, prediction of weather, land use mapping, and agricultural monitoring (USGS 2020).

The Philippines is highly vulnerable to disasters due to its physical environment and geographical location, being in the Pacific Ring of Fire. An annual average of 20 typhoons passes through the country, of which five are calamitous (Asian Disaster Reduction Center 2021). The Philippine Atmospheric, Geophysical and Astronomical Services Administration or PAGASA (2020a, b, c) reported that the country is visited by more tropical cyclones than elsewhere on the earth. In 2020, of the 22 tropical cyclones that passed through the Philippine Area of Responsibility (PAR), one of the most destructive was Typhoon Ulysses, internationally known as Typhoon Vamco. Its track is shown in Fig. 4.1. Typhoon Ulysses developed from a low pressure area on November 8 at east of Mindanao to a typhoon on November 11, and totally exited the PAR on November 13. All of its three landfalls occurred within Quezon Province. This typhoon track caused 334 reported incidents in Regions I, II, III, IV-A, IV-B, V, CAR, and NCR, bulk of which (64%) are flooding events. Notably, among the said affected regions, Region II (Cagayan Valley) had the highest worth of damage to infrastructure (PhP 5 billion) and agriculture (PhP 2.1 billion) of the total PhP 13 billion and PhP 7.3 billion, respectively (National Disaster Risk Reduction and Management Council 2021). Then Director Fernando Siringan of the University of the Philippines Marine Science Institute suggested that Cagayan Valley became the drainage area of water from the neighboring mountain ranges, hence the severe flooding in the region. Mayor Cristina Antonio of Alcala, Cagayan added that farming and illegal logging in mountains and slopes cleared the indigenous trees which could have managed the water release and held the soil (Bernardo 2020).

Using Sentinel 1 data, flood occurrence including spatial variation of crops due to their varying growth stages can be observed and analyzed. Beshentsev and Borisova (2019) used GIS in flood monitoring of a river basin in Russia. Measuring subsystems such as geochemical and geophysical instruments, multi-temporal spatial information, space and aerial images, computer evaluation tools and programs, and geoinformation mapping were developed for the GIS flood monitoring system. Moreover, a digital terrain model using the initial data obtained from satellite images was designed for the assessment of flood hazard and damage.

RS data can be used for monitoring agricultural lands and forecasting crop condition and fertility levels. It provides information like the potential effect of weather disturbances to the crops, standing crop area, and yield forecast which according to Raviz et al. (2015) are needed by the government to provide advisory and solution
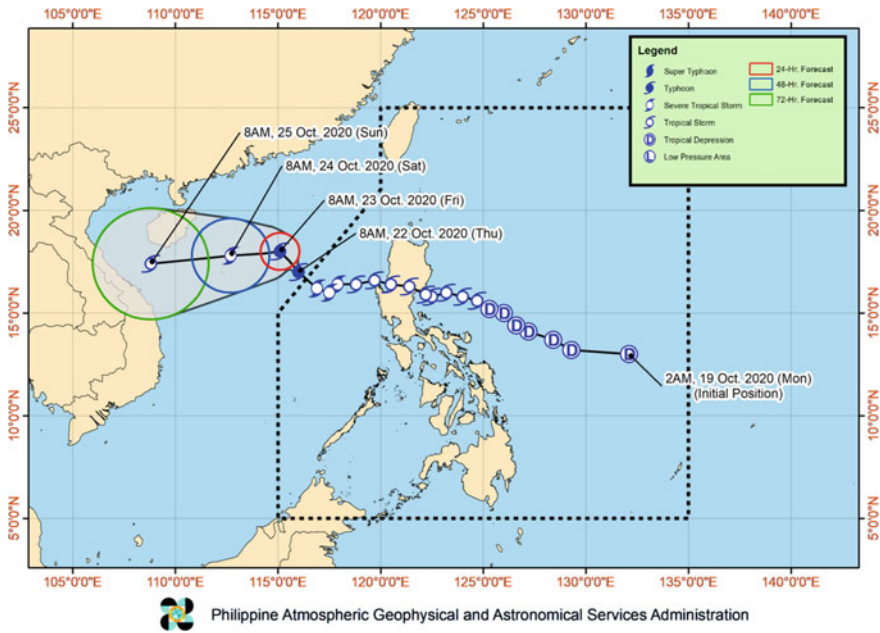
Fig. 4.1 Track of Typhoon Ulysses (PAGASA 2020a, b, c)

for specific problems. Specifically, vegetation indices (VI) give valuable information on the spectral characteristics of the crop. These are derived from optical satellites getting the electromagnetic wave reflectance of the surface (Xue and Su 2017). One of the most common VI is the Normalized Difference Vegetation Index (NDVI). It gives a measure of vegetation density by using visible and near infrared light. NDVI values range from -1 to $+1$, signifying low and healthy vegetation, respectively (Drisya et al. 2018). NDVI varies depending on land use, crop growth stage, the incidence of pest infestation, and the occurrence of threats that may affect vegetation.

Using satellite images, the effect of Typhoon Ulysses (Vamco) was assessed in Cagayan, Philippines. Specifically, the extent of flood inundated areas was determined using the VV and VH bands. The extent of affected agricultural areas was also assessed and quantified.

4.2 Study Area and Methodology

4.2.1 Description of Study Area

Cagayan is in the northeastern part of the Philippines, with some parts near the Sierra Madre and Cordillera Mountain ranges. It has a total land area of 900,270 hectares with 28 towns and one city (Cagayan Government 2021). Cagayan is one of the top
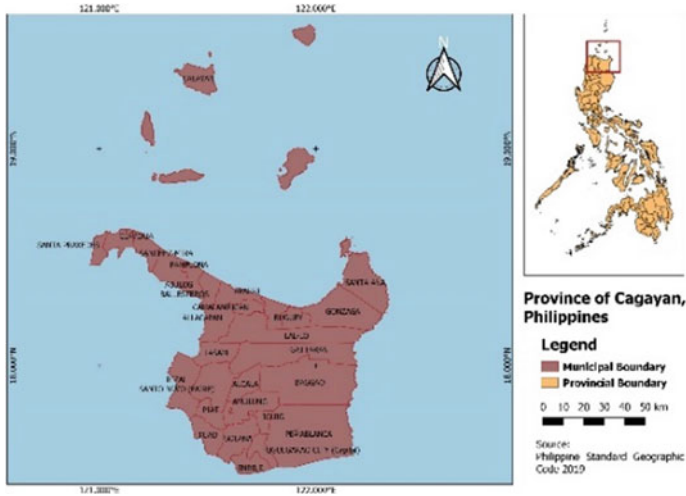
Fig. 4.2 Study area

producing provinces for rice crops. According to Philippine Statistics Authority or PSA (2019), it has about 222,871 ha of rice areas where 176,058 ha, 46,121 ha, and 692 ha are irrigated, rainfed, and upland, respectively. The map of the study area is shown in Fig. 4.2.

4.2.2 Satellite Data

Optical and synthetic aperture radar (SAR) imageries were used in this study. High resolution RS information from the European Space Agency (ESA) obtained from Google Earth Engine was beneficial in deriving accurate and near real-time statistics. Sentinel 1 data with 10 meters resolution and 6 days revisit time, specifically the vertical transmit-vertical receive (VV) and vertical transmit-horizontal receive (VH) polarizations or bands were used to analyze the flood occurrence in the area of interest. On the other hand, Sentinel 2 data was used for the determination and characterization of the vegetation present during the typhoon. It has a spatial and temporal resolution of 10 m and 5 days, respectively due to the mission's two platforms—Sentinel 2A and Sentinel 2B. This satellite has been giving data since March 2017 (ESA 2020a, b).

4.2.3 Flooded Area Determination

Flood inundated area determination was done in Google Earth Engine. Available SAR information from the Earth Engine Data Catalog was already pre-processed. The Sentinel 1 images before and after the typhoon were identified and recognized to be November 1, 2020 and November 13, 2020, respectively. The necessary instrument mode of interferometric wide swath was selected. Two separate processes were done to determine the flooded area—single co-polarization of VV and cross-polarization VH. Finally, a 7-day composite of the images was created for each case. The resulting backscatter was then visualized using the colors white, black, and blue to highlight the water areas in blue. With the combination of the digital elevation model, terrain, and slope data derived from the World Wildlife Fund (WWF) Conservation Science Program HydroSHEDS, the flood extent was determined. The raster file was post-processed in QGIS to quantify the area with water before the typhoon and the affected area flooded by Typhoon Ulysses (Vamco).

4.2.4 Standing Crops Analysis

The rice mask for Alcala, Cagayan was developed through unsupervised classification using the Landsat image collection. The spectral signature was characterized by the algorithm and the rice area was extracted from the resulting clusters.

The flooded agricultural area was determined to be the intersection between the derived rice mask and the flooded area from Sentinel 1. To analyze the standing crops, NDVI data from the Sentinel 2 images were used. Initially, the clearest or least cloudy image before and after the typhoon was determined. For this study, the images from November 13 to November 18 were used. NDVI were computed using Eq. (4.1) where B8 is the near infrared (NIR) band and B4 is the red band.

$$NDVI = B8 - B4 \big/ B8 + B4 \qquad (4.1)$$

With the threshold of NDVI greater than or equal to 0.3, the standing crops can be calculated and computed. Time series analysis was done with Moderate Resolution Imaging Spectroradiometer (MODIS) data to identify the stage of crop growth. The resulting data before and after Typhoon Ulysses (Vamco) were then compared and analyzed.

4.3   Results and Discussion

4.3.1   Quantification of Flooded Area

Sentinel 1 images before (November 1, 2020) and after (November 13, 2020) the occurrence of Typhoon Ulysses (Vamco) are shown in Fig. 4.3. Figure 4.3a shows the Cagayan River along with its tributaries as the only identified water body before the typhoon (November 1, 2020). After the typhoon (November 13, 2020), the river overflowed and affected several towns namely: Aparri, Amulung, Alcala, Solana, Tuguegarao City, and Enrile. The said municipalities were located near the Cagayan River. Meanwhile, using VH band in Fig. 4.3b, the areas with water were clearly highlighted. This proves better applicability of the said band in water detection which was also observed by Conde and Muñoz (2019). There was existing water in the top center of the province before the typhoon which was not initially detected by the VV band. After the typhoon, these municipalities namely Aparri, Camalaniugan, and Buguey were further flooded.

SAR data's high sensitivity to water makes it the finest tool for detecting damp locations. NASA (2021) claims that this is caused by the chemical structure of water, which forms two poles with oxygen being positively charged and hydrogen being negatively charged. As the positively charged poles are drawn to the region creating a wave in a microwave field, the water molecule tends to shift its orientation. Dielectric constant is the ability of an object to store a charge or to act as a capacitor in an electric field (Nurul Hidayah and Mariatti 2021). It is detected low for dry places, high for moist areas, and roughly about 80 for water surfaces. Reflected energy can be scattered back to the radar antenna because water can hold and release a lot of energy.

Table 4.1 shows the estimated flooded areas from both bands for the whole region as well as the estimated affected agricultural area by flooding due to Typhoon Ulysses (Vamco). For both parameters, VH had the larger approximate value which proved that it could detect water better than the VV band.

Figure 4.4 shows the change in backscatter intensity value in decibels of Sentinel 1, before and during flooding of the representative points in the area for VH (Fig. 4.4a) and VV (Fig. 4.4b) bands. The representative points are located in the production areas near the riverbanks. The presence of vegetation in these areas makes the surface rough which increases the magnitude of backscatter intensity. Before flooding, VV polarization shows a more defined range of backscatter values with -5 to -10 dB for vegetated areas compared to VH polarization with a bit wider range of backscatter values from -10 to -20 dB. From this, it can be inferred that VV polarization is better to use in monitoring vegetation. On the other hand, both show a decrease in magnitude of backscatter intensity during flooding due to the change in the surface because of the presence of water. During flooding the surface becomes smooth because of the presence of water in the vegetated areas which decreases the magnitude of backscatter intensity to even more negative values. Backscatter plot in VH polarization shows a more defined range of values from -25 to -30 dB compared to VV polarization
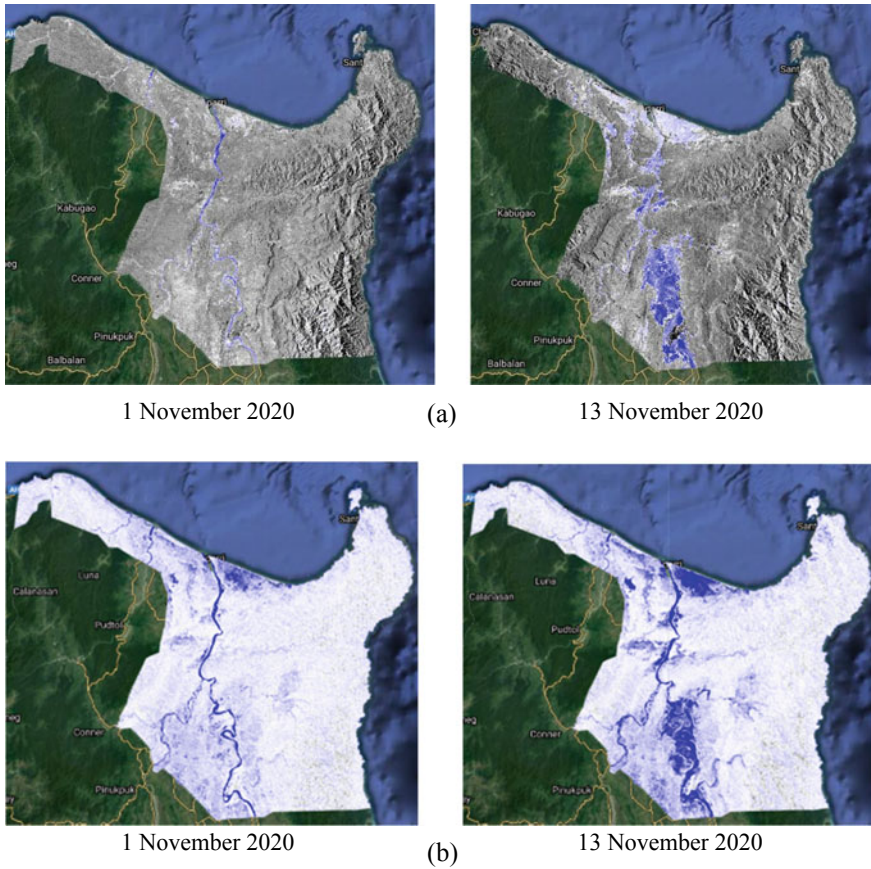
Fig. 4.3 Sentinel 1 images before and after Typhoon Ulysses using VV (**a**) and VH (**b**) polarizations

	Band	Flooded area (ha)	Flooded agricultural area (ha)
Table 4.1 Comparison between the flood extent detected through VV and VH bands	VV	69,501.12	35,606.59
	VH	72,722.30	37,736.70

with -15 to -25 dB. For identification of inundated areas, VH polarization is better to use.

The elevation map of Cagayan is shown in Fig. 4.5. High elevation can be seen in the eastern and central eastern parts of the province due to the presence of the Sierra Madre and Cordillera Mountain ranges, respectively. The Cagayan River, the longest river in the Philippines, is also shown on the map. It can be observed that it is surrounded by flat and low lying areas which are flood prone as the river overflows during the occurrence of heavy rainfall in the area. The same regions were delineated

VH Polarization
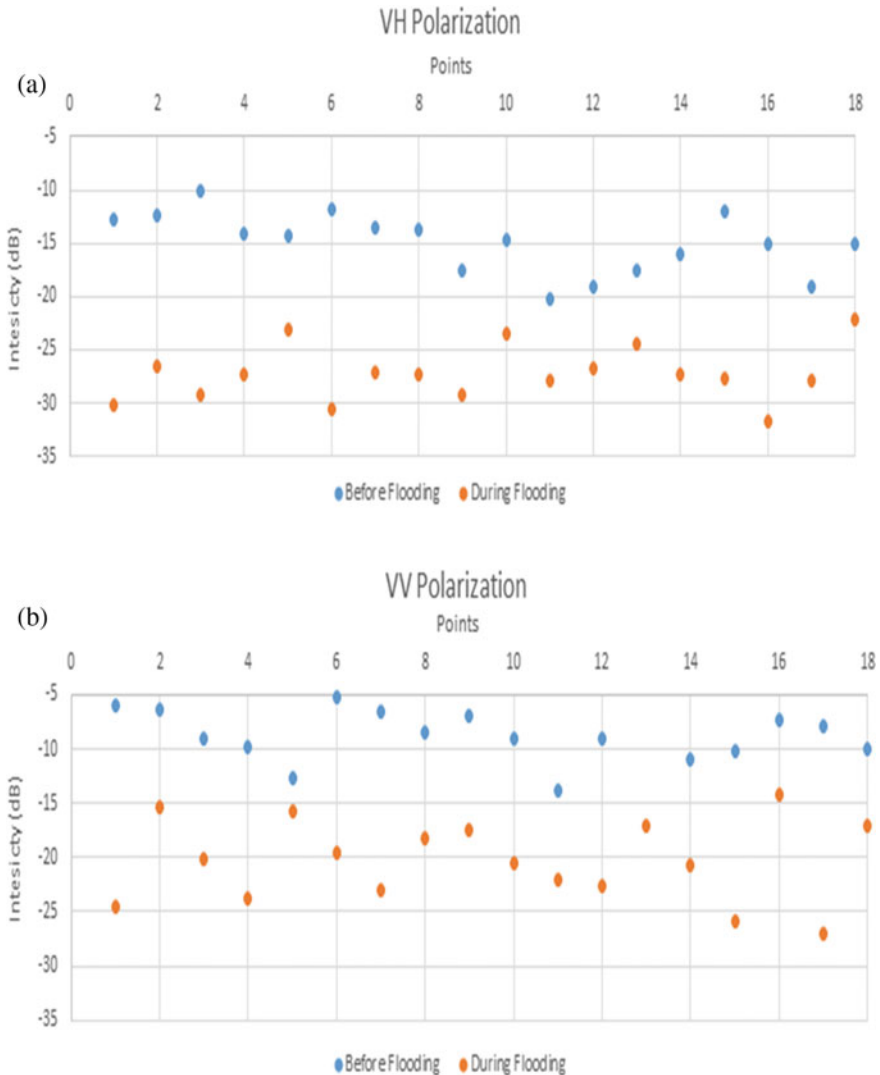
VV Polarization

Fig. 4.4 Backscatter intensity before and during flooding for **a** VH and **b** VV polarization for the representative points

as the flooded areas during Typhoon Ulysses (Vamco). These include the towns of Abulug, Aparri, Buguey, Camalaniugan, Bessang, Alcala, Amulung, Solana, Enrile, and Tuguegarao City.

Maryati (2018) highlighted the usefulness of spatial information in assessing the impacts of natural hazards to agriculture, infrastructure, and economy of a region. Flood prone areas were analyzed based on the topography, land cover, hydrological
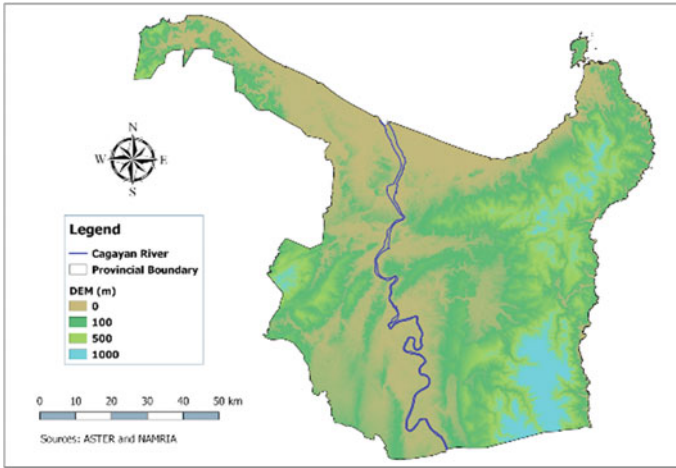
Fig. 4.5 Digital elevation model of Cagayan

condition, and rainfall information. Most of these areas were close to rivers with well-cultivated soils and extensive settlements. These results conform with the determined areas in Cagayan as these were rice-producing areas supplied by the irrigation system coming from the Cagayan River.

With respect to the amount of precipitation received by different provinces in the Philippines, PAGASA (2020a, b, c) released an image showing the classification of Typhoon Ulysses (Vamco) within PAR and the estimated cumulative rainfall as seen in Fig. 4.6. More than half of Cagayan had a cumulative rainfall of greater than 300 mm. Meanwhile, to have a more in-depth view of the situation in Cagayan, Fig. 4.7 demonstrates the amount of rainfall received by the province of Cagayan during Typhoon Ulysses from the Global Precipitation Measurement (GPM) data. The eastern side of the province experienced more rain compared to the western side due to the presence of the Sierra Madre Mountain ranges. Aside from the amount of rainfall, the opening of the flood gates of the nearby Magat Dam contributed to the flooding in the area (Macaraeg 2020). Magat Dam, situated in San Ramon, Isabela, is a part of the Upper Cagayan River Basin and supplies about 15% storage of the Cagayan River Basin (NIA 2021).

4.3.2 Affected Rice Area Analysis

The flooded agricultural areas using VV (Fig. 4.8a) and VH (Fig. 4.8b) polarizations during Typhoon Ulysses (Vamco) are shown. Agricultural areas were presented by the crop mask in yellow. Flooded areas overlaid on the crop mask are delineated in blue. With the intersection of the crop mask and the flood mask, the flooded
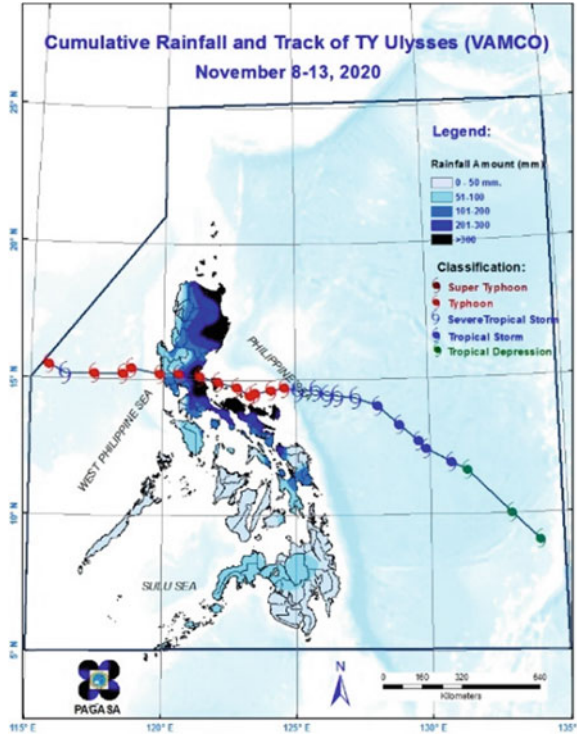
Fig. 4.6 Cumulative rainfall and track of Typhoon Ulysses (Vamco)
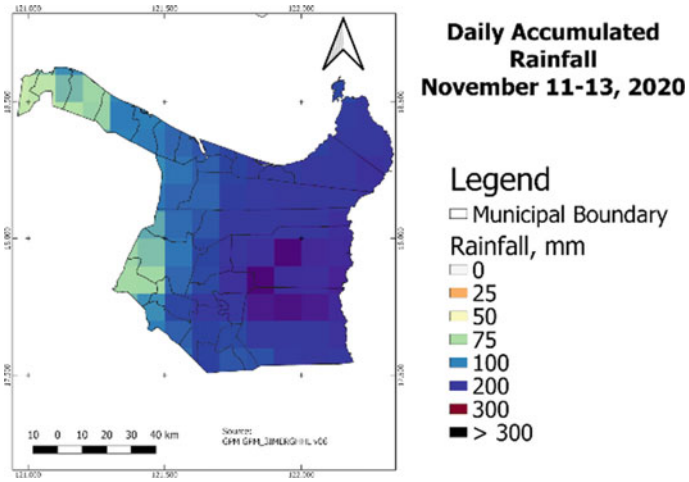
Fig. 4.7 Amount of rainfall received in Cagayan during Typhoon Ulysses (Vamco)
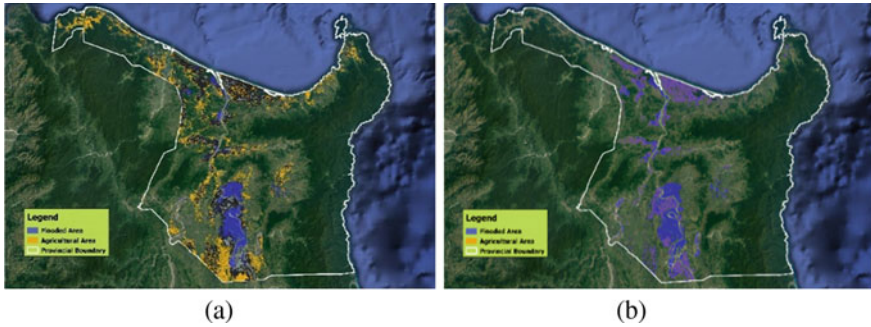
Fig. 4.8 Affected agricultural areas using **a** VV and **b** VH bands due to flooding during Typhoon Ulysses (Vamco)

agricultural areas were estimated at 35,607 hectares, about 36% of the agricultural areas in the province.

Considered as a natural disaster, flooding brings severe damages on human lives and on several aspects of the society. Damages on infrastructure and extent of affected agricultural areas can determine the severity of the flood. In-depth assessment considers several factors to determine the extent of the damage. In agriculture, impact on the vegetation or farmlands are assessed to determine the extent of the damage. Crop losses affect farmers income and food supply in the market. The larger the affected areas, the greater is the effect in the market due to decrease in produce or supply. According to Israel and Briones (2013), natural hazards such as floods have direct and indirect impacts. While flooding can improve soil fertility, it directly reduces farm production, limits planting, and damages farm inputs, facilities and infrastructures, that can lead to more cost incurred in production, decrease in farm productivity, decrease of food supply, and increase in market price of food.

Typhoon Ulysses (Vamco) impacted the agricultural sector for up to PhP12.8 billion comprising losses in production of rice and high-value crops (Miraflor 2020). Southeast Asian Center for Graduate Study and Research in Agriculture (SEARCA) Director Glenn B. Gregorio stated that there had been at least 12% loss in the production of rice in Cagayan Valley due to the flooding (Ochave 2020). With these reports, it can be inferred that the damages and losses due to flooding brought by Typhoon Ulysses (Vamco) in Cagayan Valley were very significant.

Further analysis on the mostly hit municipality of Alcala, Cagayan is shown using Sentinel 1, Sentinel 2 and MODIS data in Figs. 4.9, 4.10 and 4.11, respectively. From Fig. 4.9, the clearest image before the typhoon was taken on October 14 with about 2054.5 hectares standing crops undergoing maturity. During the devastation of Typhoon Ulysses on November 13, the river overflowed, affecting the nearby rice fields, however, these areas were not detected by Sentinel 2 as the NDVI of moist surface is low. The standing crops estimated during this time was about 660.55 ha. Lastly, on November 18 there were about 923.16 ha with standing crops, which was significantly larger than the previous report. This was caused by the receding
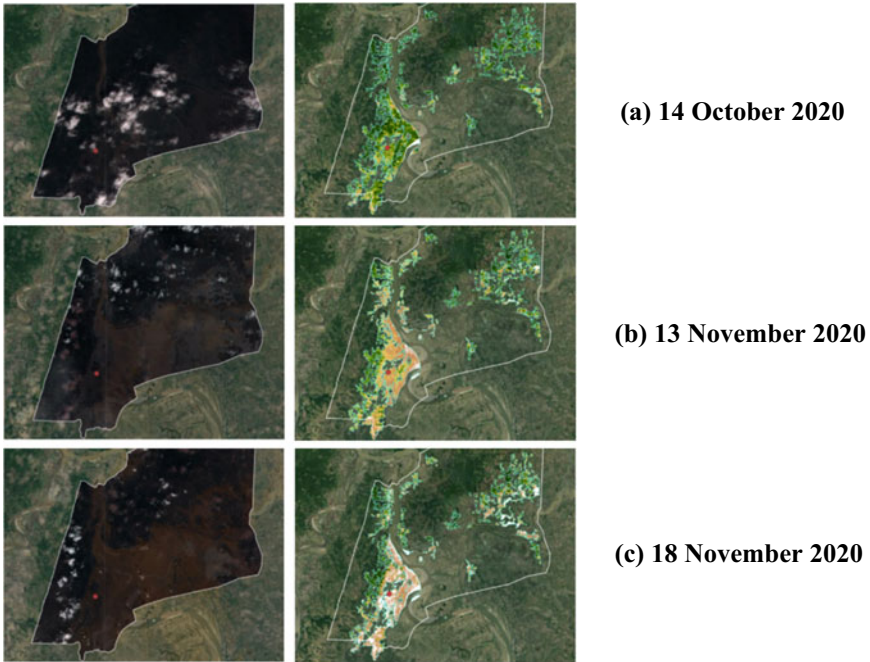
Fig. 4.9 Sentinel 2 data in Alcala, Cagayan visualized in natural color (left) and NDVI (right) before (**a** and **b**) and after (**c**) Typhoon Ulysses (Vamco)

Fig. 4.10 Sentinel 1 data in Alcala, Cagayan **a** before, and **b** after Typhoon Ulysses (Vamco)

flood water, therefore, the vegetation previously detected with water can now be noticeable using NDVI data from Sentinel 2. Figure 4.10 shows a closer look of the water present in Alcala, Cagayan before and after the devastation of Typhoon Ulysses (Vamco). The water extent increased in the areas near the mainstream, affecting the low-lying areas around it. This flood occurrence brought about the damage reported

Fig. 4.11 Historical NDVI chart of rice in Alcala, Cagayan
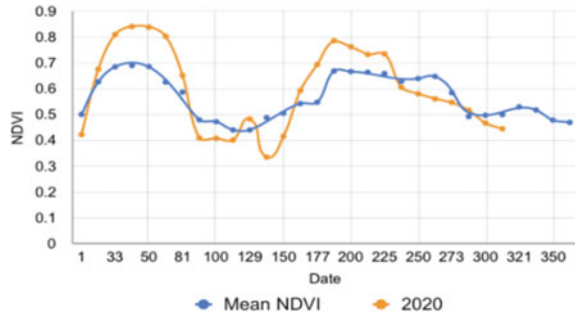
using Sentinel 2. A few days after the typhoon, a decrease in NDVI and vegetation was observed (NASA 2020). This was proven using the time-series analysis using MODIS data presented in Fig. 4.11. During day of year (DOY 319) or November 14, harvesting of the remaining crops started in the area.

4.4 Conclusions

The extent of flooding brought by Typhoon Ulysses (Vamco) in Cagayan, Philippines was estimated using 2 bands (VV and VH) of Sentinel 1 images. There was notable difference in terms of the flooded areas and spatial distribution. More regions were found flooded using the VH band than in the VV band. Using random points in the area, the VV band was found to be better for vegetation assessment as it has a more defined range of backscatter values of −5 to – 10 dB. On one hand, VH band had a range of − 25 to – 30 dB for areas detected with water and can be better used for identification of inundated areas. More than 35,000 ha of rice areas were affected in the town of Alcala. Free RS information provided near real-time data that proved useful for flood and agricultural damage assessment.

References

Asian Disaster Reduction Center (2021) Information on disaster risk reduction of the member countries. https://www.adrc.asia/nationinformation.php?NationCode=608&Lang=en
Bernardo J (2020) What causes severe flooding in Cagayan province?|ABS-CBN News. https://news.abs-cbn.com/spotlight/11/15/20/what-causes-severe-flooding-in-cagayan-province

Beshentsev AN, Borisova TA (2019) Flood monitoring using GIS technologies: a case study of the Selenga River basin. IOP Conference Series: Earth and Environmental Science 381(1):012010. https://doi.org/10.1088/1755-1315/381/1/012010

Cagayan Government (2021) About Cagayan. http://www.cagayan.gov.ph/about-cagayan/#population

Drisya J, Kumar S, Roshni T (2018) Chapter 27—Spatiotemporal variability of soil moisture and drought estimation using a distributed hydrological model (Integrating Disaster Science and Management)

ESA (2020a) Sentinel-1—Missions—Sentinel Online—Sentinel Online. https://sentinel.esa.int/web/sentinel/missions/sentinel-1

ESA (2020b) Sentinel-2—Missions—Sentinel Online—Sentinel Online. https://sentinel.esa.int/web/sentinel/missions/sentinel-2

Israel DC (2013) Impacts of natural disasters on agriculture, food security, and natural resources and environment in the Philippines. 54

Macaraeg P (2020) 3 Issues that need to be addressed in Cagayan flooding. RAPPLER. https://www.rappler.com/newsbreak/iq/issues-need-to-be-addressed-cagayan-flooding/

Maryati S (2018) Mitigation using geospatial approach (A case study in Bone Bolango Regency, Gorontalo Province). In: IOP conference series: earth and environmental science, The 1st UPI International Geography Seminar. https://doi.org/10.1088/1755-1315/145/1/012080

Miraflor MB (2020) Typhoon Ulysses' damage to the agriculture sector at P12.8-B-DA—Manila Bull. https://mb.com.ph/2020/11/26/typhoon-ulysses-damage-to-the-agriculture-sector-at-p12-8-b-da/

NASA (2020) About MODIS. https://modis.gsfc.nasa.gov/about/index.php

NASA (2021) Part 1: Synthetic Aperture Radar (SAR) refresher. ARSET—Agricultural Crop Classification with Synthetic Aperture Radar and Optical Remote Sensing|NASA Applied Sciences. http://appliedsciences.nasa.gov/join-mission/training/english/arset-agricultural-crop-classification-synthetic-aperture-radar-and

NIA (2021) NIA reaffirms that recent flooding in Cagayan Valley is not wholly attributed to Magat Dam. https://www.nia.gov.ph/?q=content/nia-reaffirms-recent-flooding-cagayan-valley-not-wholly-attributed-magat-dam

Ochave RD (2020) Dismal fourth-quarter farm output expected. https://www.bworldonline.com/dismal-fourth-quarter-farm-output-expected/

Olaya V (2018) Introduction to GIS https://volaya.github.io/gis-book/en/gisbook.pdf

PAGASA (2020a) About tropical cyclones. https://www.pagasa.dost.gov.ph/information/about-tropical-cyclone

PAGASA (2020b) Tropical cyclone associated rainfall. https://bagong.pagasa.dost.gov.ph/climate/tropical-cyclone-associated-rainfall

PAGASA (2020c) Tropical cyclone information. https://www.pagasa.dost.gov.ph/climate/tropical-cyclone-information

PSA (2019) 2019 Regional social and economic trends, Philippine Statistics Authority Regional Statistical Services Office II

Raviz J, Raviz J, Mabalay M, Laborte A, Nelson A, Holecz F, Quilang EJ, Barbieri M, de Dios J, Collivignarelli F, Gatti L, Rala A, Garcia C, Mabalot P, Mirandilla J, Doverte M (2015) Mapping rice areas in Mindanao using the first images from Sentinel-1A: the prism project experience

National Disaster Risk Reduction and Management Council (2021) Sitrep No. 29 re Preparedness measures and effects for Typhoon "ULYSSES" (I.N. VAMCO). https://ndrrmc.gov.ph/attachments/article/4138/SitRep_no_29_re_TY_Ulysses_as_of_13JAN2021.pdf

USGS (2020) What is remote sensing and what it is used for? https://www.usgs.gov/faqs/what-remote-sensing-and-what-it-used?qt-news_science_products=0#qt-news_science_products

Xue J, Su B (2017) Significant remote sensing vegetation indices: a review of developments and applications. J Sens 2017:1353691. https://doi.org/10.1155/2017/1353691

Chapter 5
Trends in Annual Maximum Flood Data in New South Wales Australia

S. M. Anwar Hossain, Ataur Rahman, and Taha B. M. J. Ouarda

5.1 Introduction

Flood is one of the worst natural disasters that cause significant economic losses and often deaths of humans. According to Australian Rainfall and Runoff (ARR) (James et al. 2019), there exists growing evidence that in Australia, distribution of flood peaks in every year are not identical, and flood risk is influenced by the long-term climate variability. Australian regional water resources and ecosystems have been severely affected by climate change (Cleugh et al. 2011; CSIRO 2011). In recent time, many devastating floods have happened in Australia (1974, 2011, 2015, 2017, 2021, 2022). In Australia, floods are the number one natural disaster in terms of economic damage, costing over $1 billion per year. The most recent NSW flood in March 2021 was one of the worst floods, costing over $1 billion and noted as a "one in 50-year" flood by the NSW Premier. The Queensland 2010–2011 flood in Australia was also one of the devastating floods in twenty first century, having claimed 33 human lives and caused direct damage costing over $5 billion.

To assess flood risk, it is necessary to estimate the magnitude and frequency of floods. Accurate estimation of design floods is of great scientific interest, as it forms the basis for planning, design and management of water-resources systems. Flood Frequency Analysis (FFA) is generally used for design flood estimation. Current FFA

S. M. Anwar Hossain (✉) · A. Rahman
School of Engineering, Design and Built Environment, Western Sydney University, Sydney, NSW, Australia
e-mail: 18916573@student.westernsydney.edu.au

A. Rahman
e-mail: a.rahman@westernsydney.edu.au

T. B. M. J. Ouarda
Canada Research Chair in Statistical Hydro-Climatology, INRS-ETE, 490 de la Couronne, Québec, QC G1K 9A9, Canada
e-mail: taha.ouarda@ete.inrs.ca

methods, such as Australian Rainfall and Runoff (ARR) 2019, are based on stationary assumptions that the flood data are independent and identically distributed (IID), with no temporal change in flood data statistics.

Due to climate change and anthropogenic activities, the historical AMF data at many locations may not represent future floods. If the AMF data of any region in the world do not satisfy the IID assumption, then the estimation of short-term and long-term flood risk using stationary FFA will be significantly biased and will cause increased flood damage. The impact of possible climate change on flooding is the primary driver for analysing trends in the time series of AMF data. The presence of trends is a sign of non-stationarity in hydrological time series data; therefore, to minimise flood risk, for better water resources management and for more accurate estimation of design floods, it is important to check the temporal trend in AMF data.

Several researchers have found temporal trends in AMF data and in maximum rainfall data (Chu et al. 2019; Hajani and Rahman 2018; Hirsch 2011; Ishak et al. 2013; Kabiri et al. 2014). For example, Gudmundsson et al. (2021) analysed stream-flow time series data (1971–2010) of 7250 gauging stations from different parts of the world for trends and they concluded that there exists clear evidence of recent trends in mean and extreme floods at the global scale due to climate change. In Australia, few studies have been carried out to identify trends in AMF data. For example, Ishak et al. (2013) analysed AMF data from 491 stations (record lengths of 30–97 years) from all over Australia for trends and found significant downward trends in south-west and south-east regions of Australia. Analysis of AMF data from 222 streamflow gauging stations (minimum record length of 30 years) showed long-term monotonic trends and step changes in streamflow in south-eastern Australia (Zhang et al. 2016). Although trend analysis in rainfall and AMF data have been carried out within Australia, no specific study has been carried out to analyse trends in AMF data within NSW using the most up-to-date data with minimum record lengths of 50 years. Hence, this study aims to carry out trend analysis of the most up-to-date AMF data in NSW with record lengths in the range of 50 years–91 years.

5.2 Methods

5.2.1 Selection of AMF Data for Trend Analysis

Selecting available AMF data sets is the first and most important factor to be considered for a trend analysis. Any AMF data series graded as 'poor quality' by the data management authority are assessed and any AMF series with 'low quality' are excluded from our analysis. The selected catchments cover flood plains, mountainous and coastal regions of NSW with catchment area of each stream gauging station ranging from 15 to 894 km^2. As characteristics of larger catchments may change at different parts of the catchment with significantly different spatial and temporal variability, larger catchments more than 1000 km^2 excluded from this study. The

reliability of AMF data series can also be impacted by the presence of gaps in the data series. Therefore, any missing observations in the AMF series are filled-in with sufficient accuracy, using a regression method adopted by Rahman (1997). Initially 176 stream gauging stations are selected where minimum record length of the AMF data in each station is 20 years. Visual and statistical data qualities are checked for all the stations. Finally, 36 stations are selected. The minimum and maximum record length of the AMF data of these stations are 50 years (1971–2020) and 91 years (1930–2020), respectively (Table 5.1).

5.2.2 Trend Analysis

Methods applied for analysing trends include both simple descriptive approach and formal statistical tests. In descriptive statistical approach, the AMF data of each stream gauging station is divided into two equal periods. The mean, standard deviation and skewness of each AMF sub-series are then calculated and compared.

A comprehensive review of the methodologies used for the detection of statistical trends in hydrological time series is presented by Khaliq et al. (2009). Both parametric and non-parametric tests are used for trend detection. Non-parametric tests are robust as compared to parametric ones with respect to nonlinearity, non-normality, outliers, missing values, censored data, and serial dependency, which may present in time-series data (Yue et al. 2002). Mann–Kendall (MK) test (Kendall 1975; Mann, 1945) is the most widely used non-parametric test for identifying trends in AMF data. This is a non-parametric, rank-based, distribution-free method to detect trends when they are significant and to detect the direction of trends, i.e., decreasing or increasing trends. The MK test is used in this study. The advantages of the MK method are that the test statistics are not affected by non-homogeneous time series data. The MK test assumes the null hypothesis H_0 as no trend in time-series with the observations varying randomly with time, and the alternative hypothesis H_1 represents an increasing or decreasing monotonic trend with time. In this study, the MK test is applied at 5 and 10% significance levels.

The MK test statistic (S) can be expressed as:

$$S = \sum_{i=1}^{n-1} \sum_{j=i+1}^{n} sign(X_j - X_i) \tag{5.1}$$

where X is the time-series data, n is the length of data series, and sign is:

$$sign(X_j - X_i) = \begin{cases} +1 & (X_j - X_i) > 0 \\ 0 & if \ (X_j - X_i) = 0 \\ -1 & (X_j - X_i) < 0 \end{cases} \tag{5.2}$$

Table 5.1 Selected AMF data record length and catchment area

Station ID	Record start year	Record end year	Record length (years)	Catchment area (km^2)
201001	1958	2020	63	213
204025	1970	2020	51	135
204036	1953	2020	68	236
204043	1961	2020	60	47
206009	1955	2020	66	261
206014	1955	2020	66	376
206018	1961	2020	60	894
208001	1955	2020	66	20
209003	1969	2020	52	974
210011	1932	2020	89	196
210014	1960	2020	61	395
210017	1941	2020	80	103
210022	1941	2020	80	205
210040	1956	2020	65	676
210044	1957	2020	64	466
210068	1965	2018	54	25
212008	1952	2020	69	199
212011	1962	2020	59	404
215004	1930	2020	91	166
216002	1961	2020	60	857
216004	1971	2020	50	95
218005	1965	2020	56	920
219001	1949	2020	72	15
219003	1944	2020	77	316
219006	1952	2020	69	83
219017	1967	2020	54	152
220003	1967	2020	54	105
220004	1971	2020	50	764
222004	1942	2020	79	621
401009	1950	2020	71	215
410038	1969	2020	52	391
410057	1958	2020	63	673
410061	1948	2020	73	144
410088	1968	2020	53	427
412050	1970	2020	51	740
418014	1971	2020	50	855

The statistic S of this test can be specified by a normal distribution (Kendall 1975; Mann 1945) approximately when $n \geq 10$, and when mean and variance are:

$$\text{Mean; } E(S) = 0 \tag{5.3}$$

$$Var(S) = \frac{n(n-1)(2n+5) - \sum_{i=1}^{q} t_i(t_i - 1)(2t_i + 5)}{18} = \sigma^2 \tag{5.4}$$

where, t_i is the number of data of ith tie group, and q is the number of tie groups. The standardized test statistic (Z) is specified by Eq. (5.5):

$$Z = \begin{cases} \frac{S-1}{\sigma} & for \ S > 0 \\ \frac{S+1}{\sigma} & for \ S < 0 \\ 0 & for \ S = 0 \end{cases} \tag{5.5}$$

At a selected significance level, the null hypothesis (H_0) i.e., no trend is rejected, if absolute value of statistics $|Z| > Z_{\frac{\alpha}{2}}$, where $Z_{\frac{\alpha}{2}}$ is the standard normal variate with exceedance probability $\frac{\alpha}{2}$ (Ishak et al. 2013; Chiew 2005; eWater 2018). The test statistics $Z > 0$ indicate an increasing/positive trend, and vice versa.

5.3   Results and Discussion

Tables 5.2 and 5.3 show the difference between the mean and the standard deviation of equally divided AMF data for station 219001and 216002 respectively. It is seen in the tables that the mean and standard deviation have significantly decreased with time. Most of the selected station's AMF data shows similar decrease of these statistics.

It is seen from Tables 5.2 and 5.3 that the statistical properties of each station have changed significantly between the two periods. It is seen that the mean and standard deviation of the second half of the data is much smaller. This indicates that the stationarity assumption of FFA, "statistical properties of AMF remain constant

Table 5.2 Mean and standard deviation of two periods for station 219001

Station	Sub-data period	Mean	Standard deviation
219001	1949–1984	38.921	36.565
219001	1985–2020	14.258	18.181

Table 5.3 Mean and standard deviation of two periods for Station 216002

Station	Period	Mean	Standard deviation
216002	1961–1990	1271.772	1191.907
216002	1991–2020	743.688	887.387

with time", is grossly violated. Figures 5.1 and 5.2 show that the general trend of AMF at streamflow gauging stations 219001 and 216002 are downward over time. Figures 5.3 and 5.4 show the general trend in AMF data when data period of each station is divided into half. These figures show more sharper downward trend in the second half of data period of each station's AMF data.

Trend analysis is carried out for all the 36 stations at 5 and 10% significance levels. The MK trend test results show that at 5% significant significance level, 9 station's AMF data have statistical trend (Table 5.4), and at 10% significance level, 14 station's AMF data have statistical trend (Table 5.5). The study shows that at 10% significance level, 39% of the selected station's AMF series have significant trends. The study also shows that the average AMF in these 14 stations has decreased by a minimum of 4% to a maximum of 64% with an average decrease of mean by 39%. The study also shows that a general downward trend (without considering significance level) in the AMF data exists in 32 stations of the selected 36 stations (Tables 5.3 and 5.4).
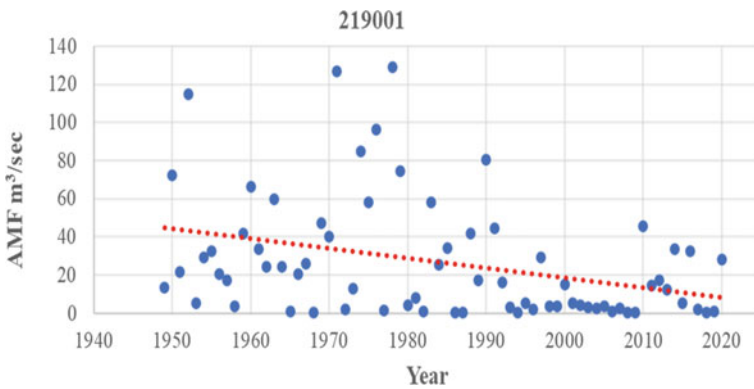
Fig. 5.1 Linear trend in AMF data at station 219001
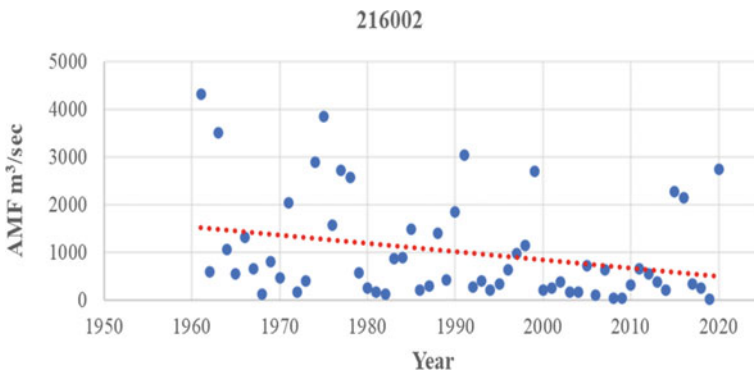
Fig. 5.2 Linear trend in AMF data at station 216002
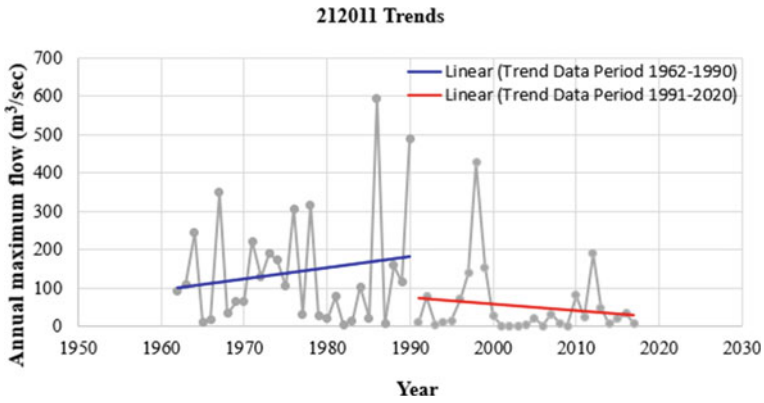
Fig. 5.3 Linear trends in two half of AMF data period at station 212011
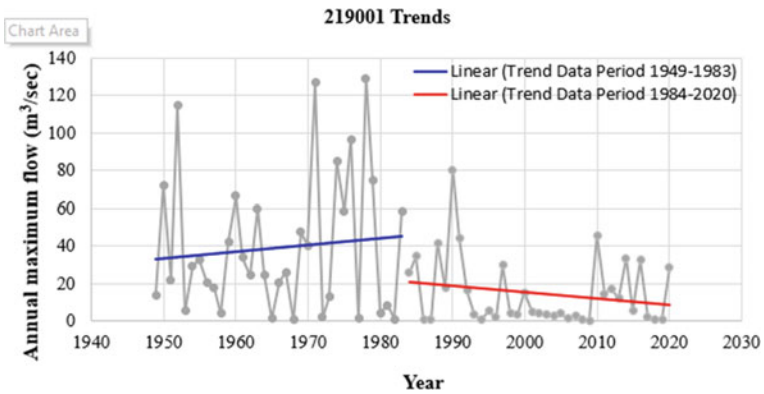
Fig. 5.4 Linear trends in two periods of AMF data at station 219001

Table 5.4 Mann–Kendall test results for the selected 36 stations at 5% significance level

Station ID	Mann–Kendall p-value	Significance level	MK test result	Trend in AMF data	Direction of significant trend (+ve or −ve)
201001	0.286	0.05	0	−ve downward	
204025	0.922	0.05	0	−ve downward	
204036	0.343	0.05	0	−ve downward	
204043	0.009	0.05	1	−ve downward	−ve downward
206009	0.309	0.05	0	−ve downward	
206014	0.002	0.05	1	−ve downward	−ve downward
206018	0.086	0.05	0	−ve downward	
208001	0.014	0.05	1	−ve downward	−ve downward

(continued)

Table 5.4 (continued)

Station ID	Mann–Kendall p-value	Significance level	MK test result	Trend in AMF data	Direction of significant trend (+ve or −ve)
209003	0.492	0.05	0	−ve downward	
210011	0.742	0.05	0	−ve downward	
210014	0.380	0.05	0	−ve downward	
210017	0.755	0.05	0	−ve downward	
210022	0.149	0.05	0	+ve upward	
210040	0.224	0.05	0	+ve upward	
210044	0.441	0.05	0	−ve downward	
210068	0.765	0.05	0	−ve downward	
212008	0.183	0.05	0	−ve downward	
212011	0.001	0.05	1	−ve downward	−ve downward
215004	0.177	0.05	0	−ve downward	
216002	0.014	0.05	1	−ve downward	−ve downward
216004	0.062	0.05	0	−ve downward	
218005	0.216	0.05	0	−ve downward	
219001	0.001	0.05	1	−ve downward	−ve downward
219003	0.073	0.05	0	−ve downward	
219006	0.003	0.05	1	−ve downward	−ve downward
219017	0.425	0.05	0	−ve downward	
220003	0.233	0.05	0	−ve downward	
220004	0.026	0.05	1	−ve downward	−ve downward
222004	0.496	0.05	0	−ve downward	
401009	0.204	0.05	0	−ve downward	
410038	0.007	0.05	1	−ve downward	−ve downward
410057	0.337	0.05	0	+ve upward	
410061	0.088	0.05	0	−ve downward	
410088	0.065	0.05	0	−ve downward	
412050	0.417	0.05	0	+ve upward	
418014	0.228	0.05	0	−ve downward	

Table 5.5 Mann–Kendall test results for the selected 36 stations at 10% significance level

Station ID	Mann–Kendall p-value	Significance level	MK test result	Trend in AMF data	Direction of significant trend (+ve or −ve)
201001	0.286	0.10	0	−ve downward	
204025	0.922	0.10	0	−ve downward	
204036	0.343	0.10	0	−ve downward	

(continued)

Table 5.5   (continued)

Station ID	Mann–Kendall p-value	Significance level	MK test result	Trend in AMF data	Direction of significant trend (+ve or −ve)
204043	0.009	0.10	1	−ve downward	−ve downward
206009	0.309	0.10	0	−ve downward	
206014	0.002	0.10	1	−ve downward	−ve downward
206018	0.086	0.10	1	−ve downward	−ve downward
208001	0.014	0.10	1	−ve downward	−ve downward
209003	0.492	0.10	0	−ve downward	
210011	0.742	0.10	0	−ve downward	
210014	0.380	0.10	0	−ve downward	
210017	0.755	0.10	0	−ve downward	
210022	0.149	0.10	0	+ve upward	
210040	0.224	0.10	0	+ve upward	
210044	0.441	0.10	0	−ve downward	
210068	0.765	0.10	0	−ve downward	
212008	0.183	0.10	0	−ve downward	
212011	0.001	0.10	1	−ve downward	−ve downward
215004	0.177	0.10	0	−ve downward	
216002	0.014	0.10	1	−ve downward	−ve downward
216004	0.062	0.10	1	−ve downward	−ve downward
218005	0.216	0.10	0	−ve downward	
219001	0.001	0.10	1	−ve downward	−ve downward
219003	0.073	0.10	1	−ve downward	−ve downward
219006	0.003	0.10	1	−ve downward	−ve downward
219017	0.425	0.10	0	−ve downward	
220003	0.233	0.10	0	−ve downward	
220004	0.026	0.10	1	−ve downward	−ve downward
222004	0.496	0.10	0	−ve downward	
401009	0.204	0.10	0	−ve downward	
410038	0.007	0.10	1	−ve downward	−ve downward
410057	0.337	0.10	0	+ve upward	
410061	0.088	0.10	1	−ve downward	−ve downward
410088	0.065	0.10	1	−ve downward	−ve downward
412050	0.417	0.10	0	+ve upward	
418014	0.228	0.10	0	−ve downward	

5.4   Conclusions

This study has examined trends in AMF data of 36 stations in New South Wales (NSW), Australia using the latest AMF data with a minimum of 50 years data length. It is evident from the results that there exist decreasing trends in AMF data for most of the stations, which is similar to the findings by Ishak et al. (2013). This result highlights the importance of applying non-stationary FFA in NSW. It should be noted that although a decreasing trend is dominant in the study area, it does not indicate that the large flood will be reducing in future, or their frequency will be decreased. Further research is continued to link the observed trends in AMF data with climate change indices. Also, the trend analysis is being extended to other Australian states.

References

Chiew (2005) CRC for Catchment Hydrology (Trend User Guide). Monash University

Chu H, Wei J, Qiu J, Li Q, Wang G (2019) Identification of the impact of climate change and human activities on rainfall-runoff relationship variation in the three-river headwaters region. Ecol Ind 106:105516. https://doi.org/10.1016/j.ecolind.2019.105516

Cleugh H, Stafford Smith M, Battaglia M, Graham P (eds) (2011) Climate Change: Science and Solutions for Australia

CSIRO (2011) Climate Change: Science and Solutions for Australia. CSIRO. https://www.csiro.au/en/research/environmental-impacts/climate-change/climate-change-science-and-solutions

Kendall (1975) Rank correlation methods. vol 202. London Griffin Publishers

eWater (2018) Ewater Toolkit. University of Canberra. https://ewater.org.au/products/ewater-toolkit/

Gudmundsson L, Boulange J, Do HX, Gosling SN, Grillakis MG, Koutroulis AG, Leonard M, Liu J, Müller Schmied H, Papadimitriou L, Pokhrel Y, Seneviratne SI, Satoh Y, Thiery W, Westra S, Zhang X, Zhao F (2021) Globally observed trends in mean and extreme river flow attributed to climate change. Science 371(6534):1159–1162. https://doi.org/10.1126/science.aba3996

Hajani E, Rahman A (2018) Characterizing changes in rainfall: a case study for New South Wales. Aust Int J Clim 38(3):1452–1462. https://doi.org/10.1002/joc.5258

Hirsch RM (2011) A perspective on nonstationarity and water management1. JAWRA J Am Water Resour AssocI 47(3):436–446. https://doi.org/10.1111/j.1752-1688.2011.00539.x

Ishak EH, Rahman A, Westra S, Sharma A, Kuczera G (2013) Evaluating the non-stationarity of Australian annual maximum flood. J Hydrology 134–145. https://doi.org/10.1016/j.jhydrol.2013.04.021

James B, Mark B, Rory N, William W, Erwin W, Monique R, Isabelle T (2019) Australian Rainfall and Runoff. 235

Kabiri R, Bai VR, Chan A (2014) Assessment of hydrologic impacts of climate change on the runoff trend in Klang Watershed, Malaysia. Environ Earth Sci 73:27–37

Khaliq MN, Ouarda TBMJ, Gachon P, Sushama L, St-Hilaire A (2009) Identification of hydrological trends in the presence of serial and cross correlations: a review of selected methods and their application to annual flow regimes of Canadian rivers. J Hydrol 368(1):117–130. https://doi.org/10.1016/j.jhydrol.2009.01.035

Mann HB (1945) Non parametric test against trend. Econometrica 245–259

Yue S, Pilon P, Phinney B, Cavadias G (2002) The influence of autocorrelation on the ability to detect trend in hydrological series. Hydrol Process 16(9):1807–1829. https://doi.org/10.1002/hyp.1095

Zhang XS, Amirthanathan GE, Bari MA, Laugesen RM, Shin D, Kent DM, MacDonald AM, Turner ME, Tuteja NK (2016) How streamflow has changed across Australia since the 1950s: evidence from the network of hydrologic reference stations. Hydrol Earth Syst Sci 20(9):3947–3965. https://doi.org/10.5194/hess-20-3947-2016

Chapter 6
The Impact of Flash Floods on the Extreme Functioning of Undeveloped Basins: Case of the Srou Catchment (March 2010 Flood) (Oum Er-Rbia Basin, Morocco)

Nadia Lahlou and Mohamed El Ghachi

6.1 Introduction

Hydrological extremes pose à major problem for citizens. If the lack of water leads to the occurrence of low water levels and the degradation of water quality, the rainfall intensity causes floods sometimes with a catastrophic character (Lahlou et al. 2019). Often in the mountains, floods are the great challenge of this population, their occurrence often poses problems for managers, especially in undeveloped basins (Lahlou et al. 2015). To better understand this phenomenon, we study flash floods in a basin heavily influenced by anthropogenic actions. Through this paper we want to show the importance of these phenomena of floods, especially the flash floods recorded in the Srou basin. The main objective is to determine their mechanisms and impacts on the environment. The problem thus revolves around the hydrological functioning of an anthropized watershed.

N. Lahlou (✉)
Department of Geography, Faculty of Letters and Human Sciences, University Mohamed V, Rabat, Morocco
e-mail: nadia.lahlou@usms.ma

Laboratory "Society, Territories, History and Heritage", Rabat, Morocco

M. El Ghachi
Department of Geography, Faculty of Letters and Human Sciences, University Sultan Moulay Sliman, Béni Mellal, Morocco

The study was based on analysis at instantaneous flows, for a long series of observations (1971–2015), hydrometric station, Chacha Namalleh downstream of the basin. We also offer a range of hydrological methods for the identification, extraction and analysis of the March 2010 flash flood.

6.2 Presentation Du Domaine D'etude

IT is located in the great basin of Oum Er-Rbia (second largest basin on the scale of Morocco). The Srou catchment covers an area of 1371.93 km^2. It is equipped with two hydrometric stations, El Heri and Chacha namelleh. The altitudes are between 2195 and 670 m. It is one of the main tributaries of the Oum Erbia wadi that joins it at the Ahmed Elhansali Dam, with a flow direction from north-east to south-west (Lahlou et al. 2017) (Fig. 6.1).

The Wadi Srou watershed is mountainous in character. The geological formations of the region that reigns are limestones, Triassic red clays, as well as shales, The valley of the wadi Srou is covered by impermeable lithological formation.

6.3 Climatic and Hydrological Framework

The climate of the area is semi-arid to subhumid. It is of the Mediterranean type, which is defined by temperate and humid winters and hot and dry summers.

6.3.1 Development of Rainfall Characteristics

The annual variability of precipitation between 1975 and 2015 for the two rainfall stations in the study area shows a decrease in the annual average from the upstream Aval Elhri station (830 m) to the downstream Chacha Nmalh station (685 m) and records them respectively: 603 mm and 493 mm (Fig. 6.2).

If we consider dry years below average and wet years above average, we note that for the 42 years of the chronicle studied (1975–2015), 24 years are dry and 18 years are wet for the station of Aval Elhri, and 22 dry and 20 wet years for the Chacha Nmalh station (Fig. 6.2).

There is variability in annual precipitation at the two stations, and the difference between the maximum (1612 mm) and the minimum (274 mm) at the Downstream Elhri station upstream of the basin, reached 1338 mm and the gap between the maximum and the minimum in the station Chacha Nmallah downstream of the basin of Srou, reached 384 mm, Fig. 6.3.
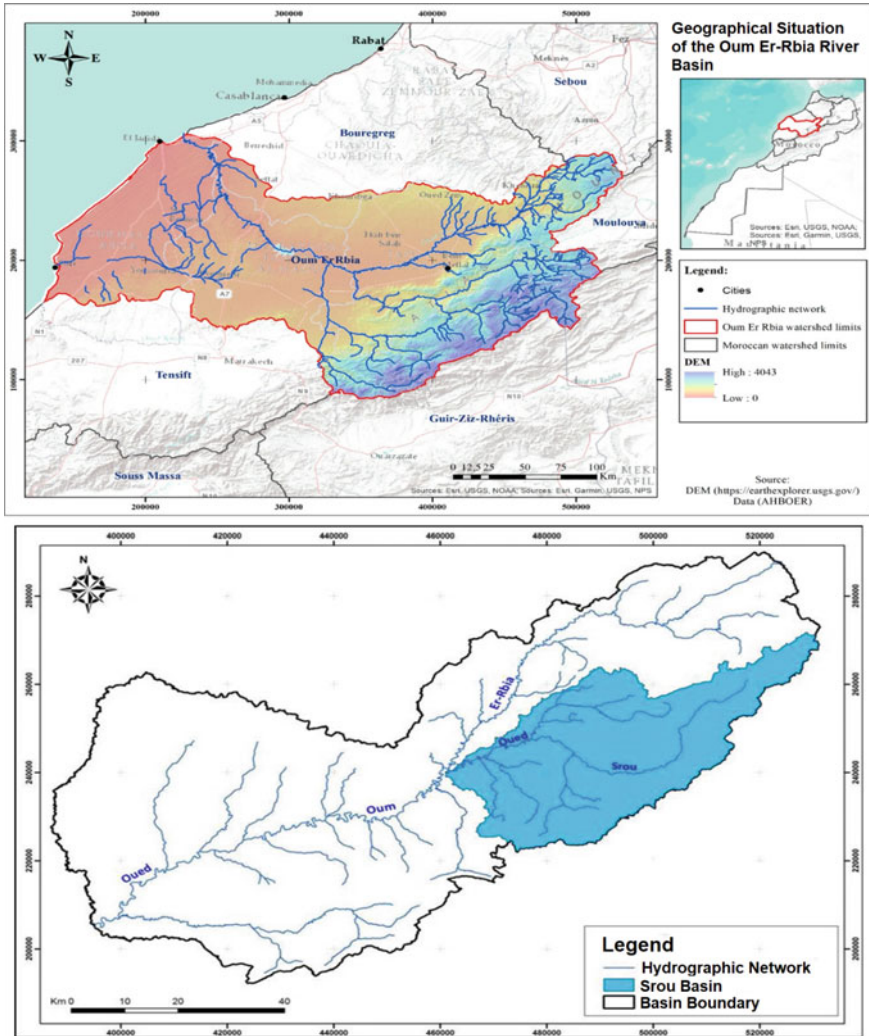
Fig. 6.1 Geographic location of the study area

The analysis of the maximum monthly rainfall for the period 1975–2016, (Fig. 6.3), shows monthly rainfall variability. The rainfall maximums are recorded in winter and spring, the difference between the maximum and the minimum, reaches 468 mm, which clearly shows the rainfall contrast between winter and summer.
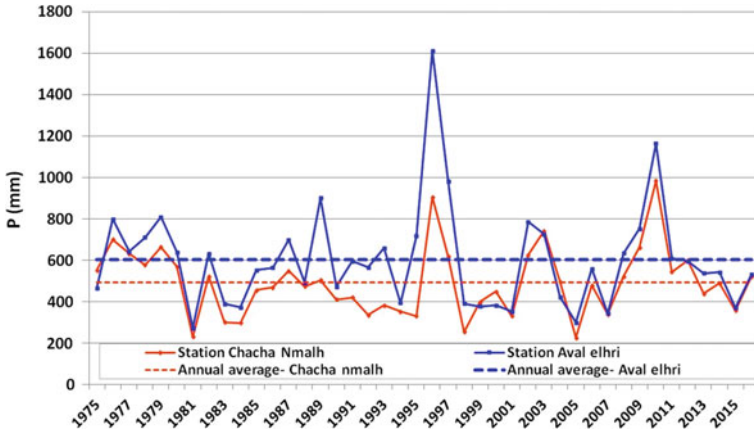
Fig. 6.2 Annual precipitation at Chacha Nmallah and Aval Elhri station compared to the average (1975–2016)
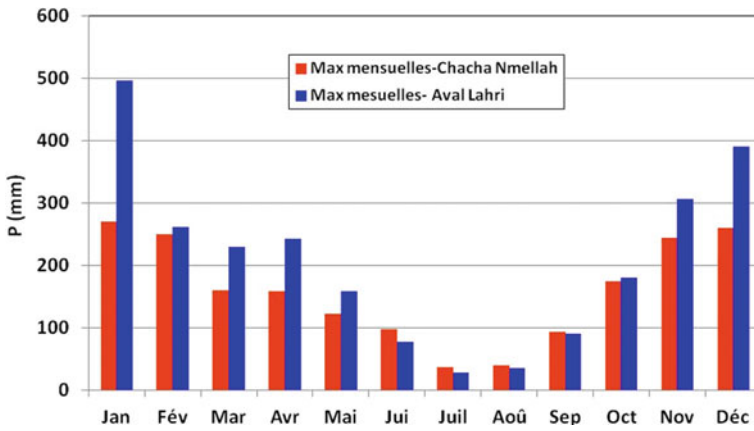
Fig. 6.3 The maximum monthly rainfall of the stations Aval Lahri and Chacha Nmallah (1975–2016)

6.3.2   Monthly Flow Coefficient of Wadi Srou (1975–2016)

The monthly flow coefficient allows us to make a cut to determine the winter and summer period. It is the ratio of the monthly values to the mean of the chronicle (Figs. 6.4 and 6.5).
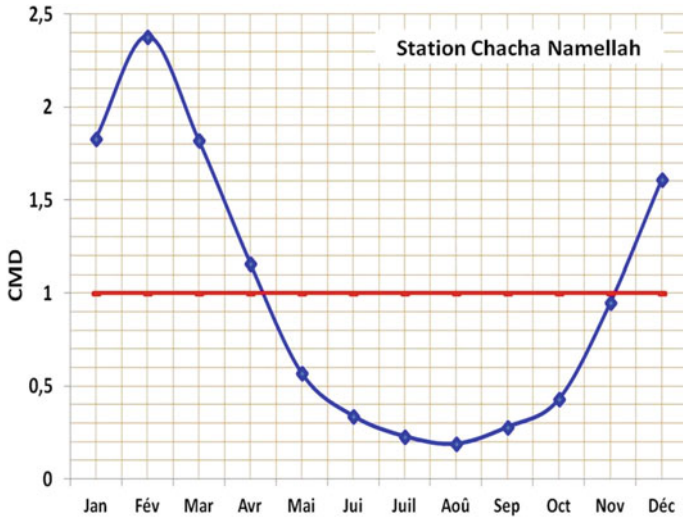
Fig. 6.4 The monthly flow coefficient of Chacha Nmallah station (1975–2016)
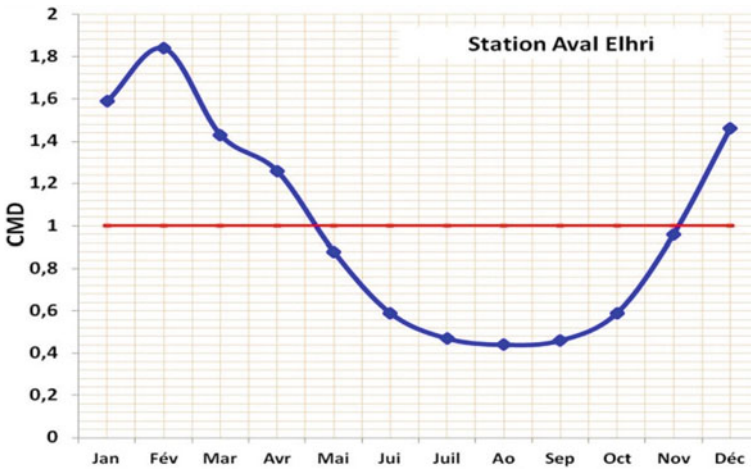
Fig. 6.5 The monthly flow coefficient of Aval Lahri station (1975–2016)

Analysis of Figs. 6.4 and 6.5 shows the existence of two periods in relation to the reference value (0.1) and this in relation to climatological inputs:

- **High water season**: It is the most watered starting in December until April.
- **The low water season**: during the summer period, it begins in May until November.

6.4   Material and Methodology

This method is an essential element for extreme hydrological studies (floods), as it allows a good knowledge of this phenomenon and leads to an overall scientific assessment of the state of the rivers during these hydrological phases. Complemented by the hydrological bases that have been developed in parallel, we want it to be widely applied to understand the behaviour of rivers in critical situations. In order to understand the phenomenon of floods, the statistical analysis of hydrometric data constitutes the main tools of this work on the data of instantaneous flows provided by the Chacha Namellah station downstream (1975–2015).

6.4.1   Extraction of Floods from Instantaneous References

Flash flood extraction is a hydrological approach to identifying flash floods of reference in a basin. It is an approach which aims, therefore, to give an overview of the significant losses to the flow regime in the basin during a phase of the rising waters, to quantify the effects and to assess and represent the resulting hydrological floods (M E G 2007).

In terms of application, several criteria have been adopted for the extraction of the reference flash flood each year.

- Largest Instantaneous Peak Flow in the Year
- Type of flood (fast/slow)
- Flood shape (simple/complex)
- Duration of flood (long/short).

Reference flood classification is a method that results in an indication of the hydrological status of the watershed system by referring to the different flood events. This method is an aid in the identification of the hydrological behavior of a river during the high-water phases.

6.5   Results and Discussion

6.5.1   Extraction of Floods Form Instantaneous References of the Srou Catchment (1975–2015)

In terms of results, there were 42 reference floods for the period (1975–2015) for the Chacha Namalleh station. It is noted that the maximum instantaneous peak flow at Chacha Namalleh can reach 1736.7 m^3/s recorded in March 2010, as for the absolute minimum of these maximums, it can go down to 36 m^3/s in 1981 (Fig. 6.6).
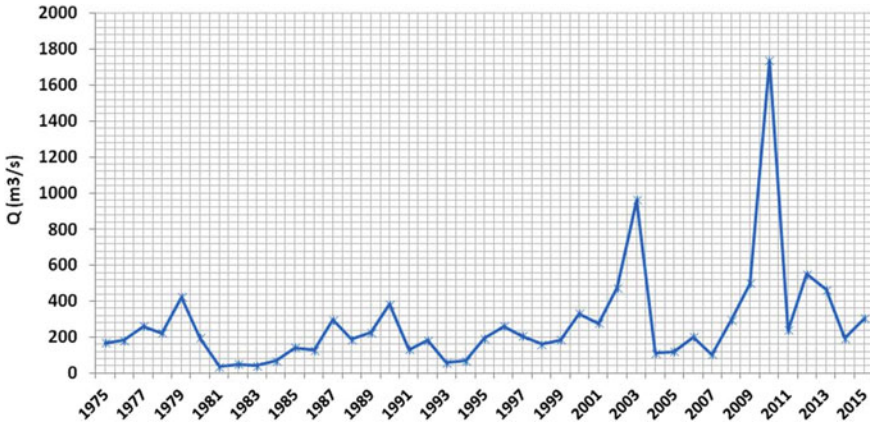
Fig. 6.6 The instant reference cures of the Chacha Namalleh station (1975–2015)

6.5.2   Instantaneous Flood Recorded in 2010

The analysis refers to the 2010 flash floods recorded by the Chacha Namalleh station downstream of the Srou Basin (Fig. 6.7):

The March 2010 spring flood with a peak flow of 1736.7 m^3/s. It is considered the largest instantaneous flood in the statistical series (1975–2015).
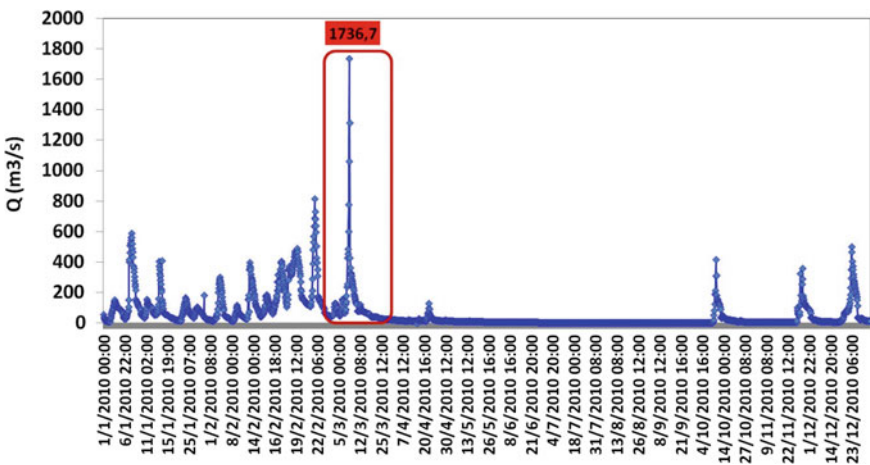
Fig. 6.7 Flood presentation studied from the instant Q of 2010 at the Chacha Namalleh station

6.5.3 2010 Spring Flood Analysis

The Fig. 6.8, represents the instant reference flood of the year 2010 produced at the Chacha Namalleh station, which recorded a large flow in spring and exactly in the month of March.

The flood of March 2010 takes place during the high-water period between 16:00 pm on 06/03/2010 and 12:00 pm on March 15, Fig. 6.8 and Table 6.1.

Downstream from the Srou basin, the Chacha Namalleh station recorded the highest flood at a peak flow rate of 1736.7 m^3/s at 10:00 am, 09/03/10. It is a complex form, composite with 3 peaks. Also characterized by its short duration, 7 days, 82 h uphill and 146 h downhill, Fig. 6.9.

The March 2010 flood follows the 25.3 mm of precipitation of 08/03/2010. It is composite with three peaks that result from a long generalized and continuous but irregular rainy episode, it was followed by days without rain (Fig. 6.9).
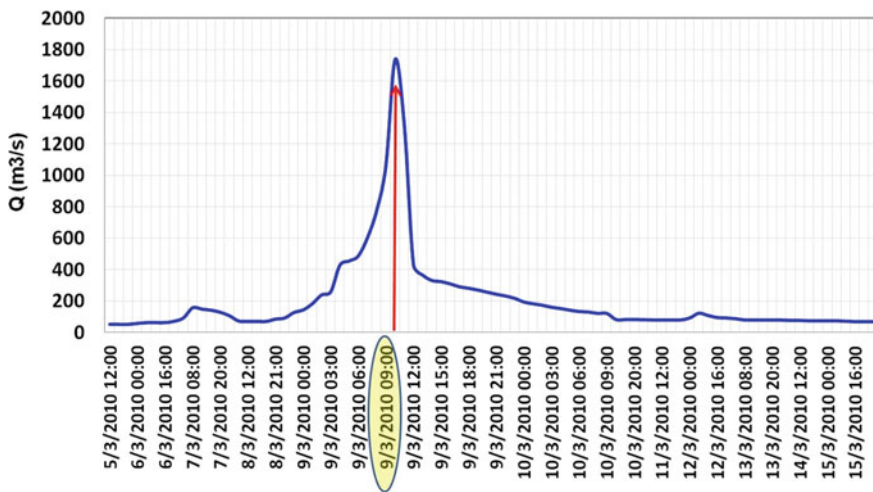
Fig. 6.8 Hydrograph of the March 2010 flood at the Chacha Namalleh station

Table 6.1 Flood characteristics of March 2010 in the Chacha Namalleh station in m^3/s

Year	Station	Q peak (m^3/s)	Date of climb	Duration (H)	Rise time (H)	Descent time (H)	Form
2010	Chacha Namalleh	1736.7	9/3/2010 10:00	228	82	146	Complex
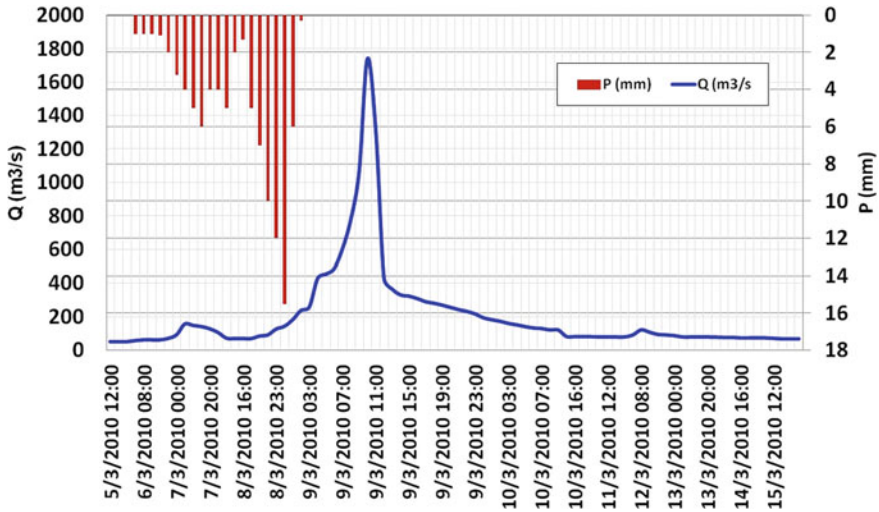
Fig. 6.9 The rain flow relationship

6.5.4 Flood Survey 2010 in Chacha Namalleh and Aval Lahri Station in m³/s

Upstream of the Srou basin, in the main inlet Chbouka, the station Aval Lahri, also recorded a flood in the same phase. The flood to a complex form, composite 2 peaks. Spit out by its duration 20 days, at a peak flow that reaches 294.6 m³/s, Fig. 6.10.
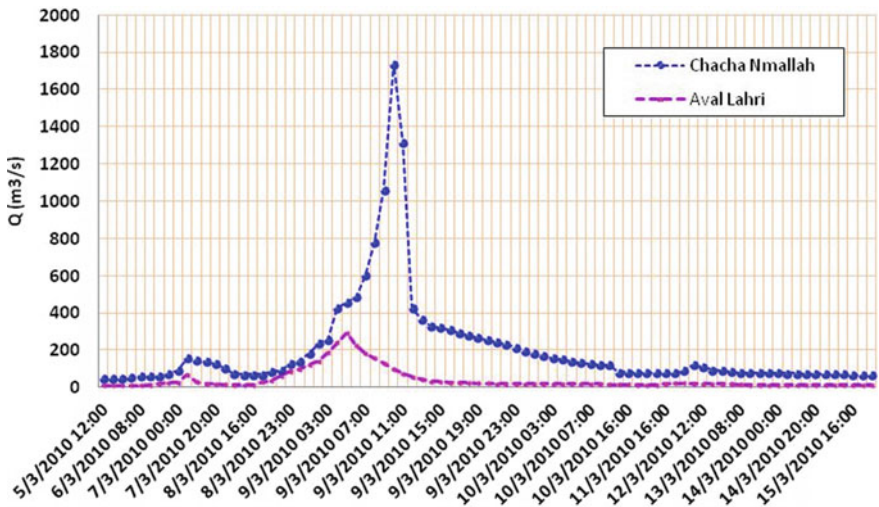
Fig. 6.10 Propagation of the flood studied 2010

Note that the propagation is relatively fast, the displacement of the flood wave is visible, it is necessary to carry out 4 h between the station Aval Lahri upstream and the station Chacha Nmallah downstream. Peak flows from 294.6 m^3/s upstream to 1736.7 m^3/s downstream, with a frequency of 1442.1 m^3/s.

6.6   Conclusions

In the Oued Srou basin, the flash floods are predictable. They follow violent localized rains, which get a sudden and short-lived evolution, and have far-reaching socio-economic impacts.

To sum up, these flash floods can occur at any time of the year with different characteristics. Therefore it is important to understand that the 2010 flood analysis, considered being the most representative instantaneous reference flood in a basin heavily influenced by anthropogenic actions.

To determine the flood processes and its spread from upstream to downstream, to understand their genesis, determine their mechanism and their impact on the environment and man.

References

Lahlou N, El Ghachi M, Yahia EK (2019) Hydrological extremes in ungauged basins: Creation of rating curve and extraction of torrential floods (2016–2018). In: Case of the watershed of Oued Kheniss, vol 8.Oum Er-Rbia Basin, Morocco, p 13

M E G (2007) La seille: Un système fluvial anthropisé (Lorraine, France) Tome 1. Thèse de 3eme cycle. Université Paul Verlaine de METZ, France, p 344

N L, M E G (2015) Le fonctionnement hydrologique dans les bassins montagnards non aménagés dans le Haut Atlas Central: Cas du bassin d'ASSIF GHZZAF (Région Béni Mellal-Khenifra)

N L, M E G (2017) Variabilité pluviométriques et changement climatique dans le bassin supérieur d'Oum Er-Rbia (1934–2010),. (Région Béni Mellal-Khenifra). J Int Sci et Tech de l'Eau et de l'Environnement

Chapter 7
Analysis of Non-stationary Return Levels Using Extreme Daily Rainfall for Surat City, India

Aarti S. Ghate and P. V. Timbadiya

7.1 Introduction

The extreme rainfall intensity-duration-frequency analysis in context to the non-stationary environment is the current need of water related infrastructures around the world. Stationarity is no longer existed because of extensive anthropogenic change of Earth's climate is changing the means and extremes of rainfall, evapotranspiration, and rates of discharge of rivers (IPCC 2007). The assumption of stationarity in the hydrological variables is no longer valid under the effect of changing climate and extreme precipitation return levels are often underestimated under stationarity-based intensity-duration-frequency (IDF) curves (Cheng and AghaKouchak 2015; Su and Chen 2019). As the global temperature rises, the intensity of extreme precipitation increases, resulting in shorter-duration extreme rainfall events. Human-induced climate change and urbanization intensifies the extreme precipitation in every region across the globe (Seneviratne et al. 2021). The climate change invalidated the maximum Intensity-Duration-Frequency (IDF) computation which assumes stationarity in the data (Ren et al. 2019).

In the recent past the non-stationarity in the extreme rainfall events is reported across the world. The non-stationary frequency analysis by introducing the trend in the distribution parameters by using the proper covariates based on regional climate or location is need of the hour. The choice of appropriate covariates for non-stationary analysis helps in evaluating the effect of external factors on hydrological extremes and significantly improves the performance of nonstationary models (Su and Chen 2019).

A. S. Ghate · P. V. Timbadiya (✉)

Department of Civil Engineering, Sardar Vallabhbhai National Institute of Technology Surat, Surat, Gujarat 395007, India
e-mail: pvtimbadiya@ced.svnit.ac.in

The non-stationary extreme rainfall analysis over India using local temperature change, ENSO cycle, and global warming as covariates is performed by Mondal and Mujumdar (2015). The non-stationary extreme rainfall analysis is reported in literature using the covariates from local processes or climate informed global processes, Time, and the effect of covariates on the extreme rainfall return levels are investigated (Sugahara et al. 2009; Agilan and Umamahesh 2017; Su and Chen 2019; Vinnarasi and Dhanya 2021).

The highly urbanised and flood prone Surat city of western coast situated at tail portion of the Tapi River is selected for the present analysis. The city is more vulnerable to floods due to encroachment in floodplains, rapid growth and climate change across the globe. The city has witnessed the several known flood events occurred in the years 1727, 1776, 1782, 1829, 1837, 1872, 1944, 1959, 1968, 1970, 1994, 1998, and 2006 (Timbadiya et al. 2015). Under the changing climate and increasing flood events the computation of non-stationary design return levels for the study area is important.

In light of this, the current study aims to identify the best covariates that have a substantial impact on the computation of non-stationary return levels. The best covariates and the model are identified from the five (atmospheric circulation processes) covariates namely, Local temperature anomaly (LT), Global temperature anomaly (GT), IOD-Dipole mode index (ID), ENSO-Sea surface temperature Index (ES) and, Time used in the study. The following objectives are addressed in the analysis of the present work (a) To evaluate the trend of the extreme daily rainfall (b) To construct the non-stationary GEV models using the covariates selected in the study (c) To compute the stationary and non-stationary return levels using the parameters of the GEV models. In addition, the stationary (non-stationary) extreme rainfall intensity is computed using the empirical equation available in the literature as the rainfall data of finer temporal resolution (less than 1-day) is not available.

7.2 Methods

7.2.1 Study Area and Data Collection

The city of Surat is located in the Gujarat state of western India on the banks of the Tapi River. The city is bounded with latitude and longitude of 21.12° N and 72.84° E in the urban floodplain and witnessed frequent flooding. The area of the city is 462,149 km^2. divided into total 9 municipal zones. The average annual rainfall of the city is 1143 mm (SMC 2022). The Fig. 7.1 shows the location map of the study area.

The daily rainfall records are obtained from the India Meteorological Department (IMD) Pune for the duration of 1951–2018, a total of 68-years. Total five covariates namely, Local temperature anomaly (LT), Global temperature anomaly (GT), IOD-Dipole mode index (ID), ENSO-Sea surface temperature Index (ES) and, Time is
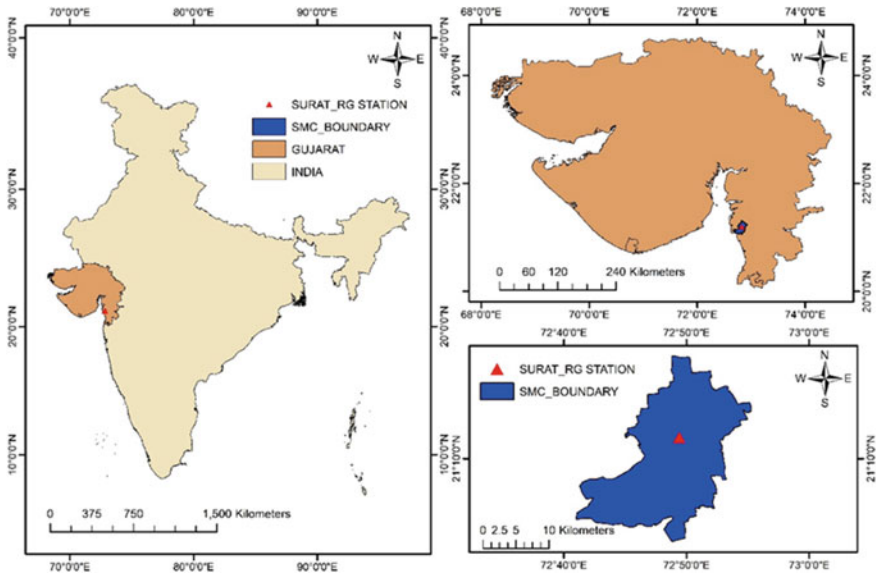
Fig. 7.1 Location map of the study area

used for the computation of non-stationary return levels. The Local temperature anomaly (LT) is calculated from the 0.25° daily gridded temperature data for the duration of 1951–2018. The Global temperature anomaly (GT) is obtained from HadCRUT4 data with respect to 1961–1990 mean as an indicator of the global warming. The data is accessed from https://www.metoffice.gov.uk/hadobs/hadcrut4/. The ENSO cycle is one of the important influencing factors that accounts for 40% of the ISMR's interannual variability (Ashok et al. 2019). The El-Niño Southern Oscillation (ENSO) cycle represented by Sea surface temperature (SST) index is used for Nino 3.4 region. The covariate of ENSO-SST index is represented by ES index in the present study. The data is available at https://www.cpc.ncep.noaa.gov/data/ind ices/sstoi.indices. The positive sign of ID implies the heavy rains and floods over East Africa and drought in Indonesia. The yearly ID averaged from June-November is used as a covariate computed using monthly ID obtained from the HADISST dataset available at https://psl.noaa.gov/gcos_wgsp/Timeseries/Data/dmi.had.long.data.

Time is also considered as one of the covariates in the present analysis. The details of the covariates and selection criteria can be found out in Agilan and Umamahesh (2017), Saji et al. (1999), Sugahara et al. (2009).

7.2.2   Methodology

The observed daily rainfall data for the Surat city raingauge station was analysed calendar year wise. The maximum value from each calendar year is considered while deriving the annual maximum series (AMS). The Generalised Extreme Value (GEV) modelling is adopted to perform the extreme value analysis on the data (Coles 2001). The trend analysis using Modified-Mann Kendall (MMK) test and Innovative trend analysis test (ITA) was performed on the AMS series to check the trend of extremes over the study region (Sen 2012; Hamed and Rao 1998). The non-stationary GEV models are constructed using five covariates namely local temperature anomaly (LT), global temperature anomaly (GT), El-Niño Southern Oscillation cycle -SST index (ES), The Dipole Mode Index-Indian Ocean Dipole (ID) and, Time. The 26 GEV non-stationary models are developed by introducing the covariates in the distribution parameters and its possible combinations. The best model showing significant effect of covariates are shortlisted using likelihood ratio (LR) test. Model-checking is carried out to check the reliability of the distribution fitted using probability plot, quantile plot (Coles 2001). The non-stationary GEV model with significant effect of covariate is selected using minimum AIC value and the extreme return levels are calculated. The extremes under stationary and non-stationary scenario are evaluated for the various return periods. The rainfall intensity for 1-h duration is computed using the empirical equation available for India in the literature (Zope et al. 2016).

7.2.2.1   Stationary GEV Model

The GEV model represented by Eq. 7.1 gives three parameters as location parameter (μ), a scale parameter (σ), and a shape parameter (ξ). The shape parameter, $\xi = 0$, $\xi > 0$, and $\xi < 0$ correspond to Gumbel, Fréchet and Weibull distribution, respectively (Coles 2001).

$$G(z) = \exp\left\{ -\left[1 + \xi\left(\frac{z - \mu}{\sigma} \right) \right]^{-1/\xi} \right\} \tag{7.1}$$

7.2.2.2   Non-stationary GEV Model

The governing equation is same as Eq. 7.1 for Non-stationary GEV model. The location and scale parameters of the GEV are introduced with non-stationarity while the shape parameter is kept constant (Coles 2001).

Combination 1: Stationary shape and scale parameter, non-stationarity in location parameter

$$\mu(t) = \mu_0 + \mu_1(LT) + \mu_2(GT) + \mu_3(ES) + \mu_4(ID) + \mu_5(Time)$$
$$\sigma(t) = \sigma$$
$$\xi(t) = \xi$$

Combination 2: Stationary shape, and non-stationarity in scale parameter, location parameter

$$\mu(t) = \mu_0 + \mu_1(LT) + \mu_2(GT) + \mu_3(ES) + \mu_4(ID) + \mu_5(Time)$$
$$\sigma(t) = e^{(\sigma_0 + \sigma_1 LT + \sigma_2 GT + \sigma_3 ES + \sigma_4 ID + \sigma_5 Time)}$$
$$\xi(t) = \xi$$

7.2.2.3 Goodness-of-Fit Test

The goodness-of-fit is checked using the LR test statistics, AIC, and the model diagnostic plots (QQ plot) and (PP plot) of the best selected models. The LR test is performed on the stationary GEV model $(GEVst)$ and non-stationary GEV model $(GEVnst)$ to check whether the addition of covariates significantly increases the variance explained by the model. The LR test model is defined in Eq. 7.2, where the negative log-likelihood of $(GEVst)$ and $(GEVnst)$ approximately follows the χ^2 distribution with degree of freedom (df) (Coles 2001; Su and Chen 2019). The best $GEVnst$ model over the $GEVst$ model should be adopted for p-value < 0.05 (Coles 2001; Su and Chen 2019).

$$Likelihood\ Ratio(LR)test = 2[(GEVst) - (GEVnst)] \sim \chi^2(df) \qquad (7.2)$$

The AIC is used to choose a model when there are several models to consider (Katz 2013). The smaller the AIC value, the better the model fits the data (Su and Chen 2019), and the covariates of the best GEV model are then chosen as the best covariates. The QQ and PP plots with points close to linearity among empirical and model quantiles and probabilities indicates reasonably good fit of the model (Coles 2001).

7.3 Result and Discussion

7.3.1 Trend Analysis

The nature of extreme rainfall is evaluated by performing the non-parametric trend analysis on the AMS over a study region. The innovative trend analysis (Sen 2012)
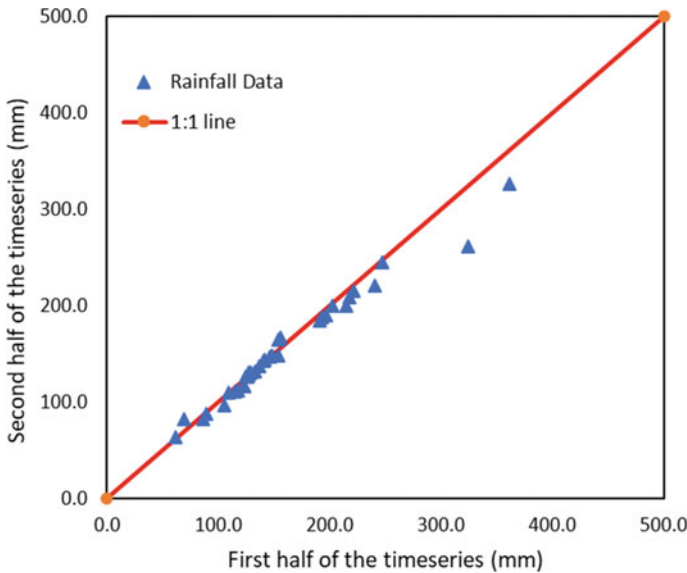
Fig. 7.2 Trend analysis of rainfall at Surat city

(See Fig. 7.2) and MMK test (Hamed and Rao 1998) results reveals the non-monotonic increase in the extreme rainfall events. The MMK trend test statistics represents the nature of trend for all the durations for location under consideration, the values more than $+1.96$ and less than -1.96 represent statistically significant increasing and decreasing trend of rainfall extremes respectively (Hameed and Rao 1988). The MMK test results (0.425) indicate the non-significant increasing trend in extreme rainfall at 5% significance level.

7.3.2 Detection of Non-stationarity in the Time Series

The non-stationarity in the rainfall data series is checked and the shifting of the mean is detected as shown in Fig. 7.3. The total 68-years of the data is subdivided into 22-years of time slice and the change in the stationarity of the time series is evaluated.

7.3.3 The Selection of Best Non-stationary Model

The significance of covariates in the computation of non-stationary return levels is analysed with Likelihood Ratio (LR) test (Su and Chen 2019). The GEV stationary and non-stationary models constructed are tabulated in Table 7.1.
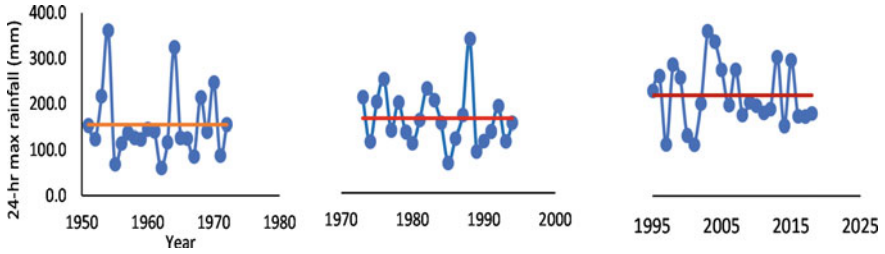
Fig. 7.3 Non-stationarity in the rainfall data

Table 7.1 List of models constructed in the present study

Model ID	Description
GEV 1	$GEV(\mu, \sigma, \xi)$
GEV 2	$GEV((\mu_0 + \mu_1 LT), \sigma, \xi)$
GEV 3	$GEV((\mu_0 + \mu_1 GT), \sigma, \xi)$
GEV 4	$GEV((\mu_0 + \mu_1 ES), \sigma, \xi)$
GEV 5	$GEV((\mu_0 + \mu_1 ID), \sigma, \xi)$
GEV 6	$GEV((\mu_0 + \mu_1 LT + \mu_2 GT), \sigma, \xi)$
GEV 7	$GEV((\mu_0 + \mu_1 LT + \mu_2 ES), \sigma, \xi)$
GEV 8	$GEV((\mu_0 + \mu_1 LT + \mu_2 ID), \sigma, \xi)$
GEV 9	$GEV((\mu_0 + \mu_1 GT + \mu_2 ES), \sigma, \xi)$
GEV 10	$GEV((\mu_0 + \mu_1 GT + \mu_2 ID), \sigma, \xi)$
GEV 11	$GEV((\mu_0 + \mu_1 LT + \mu_2 GT + \mu_3 ES), \sigma, \xi)$
GEV 12	$GEV((\mu_0 + \mu_1 LT + \mu_2 GT + \mu_3 ID), \sigma, \xi)$
GEV 13	$GEV((\mu_0 + \mu_1 LT + \mu_2 GT + \mu_3 ES + \mu_4 ID), \sigma, \xi)$
GEV 14	$GEV\big((\mu_0 + \mu_1 LT), e^{(\sigma_0 + \sigma_1 LT)}, \xi\big)$
GEV 15	$GEV\big((\mu_0 + \mu_1 GT), e^{(\sigma_0 + \sigma_1 GT)}, \xi\big)$
GEV 16	$GEV\big((\mu_0 + \mu_1 ES), e^{(\sigma_0 + \sigma_1 ES)}, \xi\big)$
GEV 17	$GEV\big((\mu_0 + \mu_1 ID), e^{(\sigma_0 + \sigma_1 ID)}, \xi\big)$
GEV 18	$GEV\big((\mu_0 + \mu_1 LT + \mu_2 GT), e^{(\sigma_0 + \sigma_1 LT + \sigma_2 GT)}, \xi\big)$
GEV 19	$GEV\big((\mu_0 + \mu_1 LT + \mu_2 ES), e^{(\sigma_0 + \sigma_1 LT + \sigma_2 ES)}, \xi\big)$
GEV 20	$GEV\big((\mu_0 + \mu_1 LT + \mu_2 ID), e^{(\sigma_0 + \sigma_1 LT + \sigma_2 ID)}, \xi\big)$
GEV 21	$GEV\big((\mu_0 + \mu_1 GT + \mu_2 ES), e^{(\sigma_0 + \sigma_1 GT + \sigma_2 ES)}, \xi\big)$
GEV 22	$GEV\big((\mu_0 + \mu_1 GT + \mu_2 ID), e^{(\sigma_0 + \sigma_1 GT + \sigma_2 ID)}, \xi\big)$
GEV 23	$GEV\big((\mu_0 + \mu_1 LT + \mu_2 GT + \mu_3 ES), e^{(\sigma_0 + \sigma_1 LT + \sigma_1 GT + \sigma_2 ES)}, \xi\big)$
GEV 24	$GEV\big((\mu_0 + \mu_1 LT + \mu_2 GT + \mu_3 ID), e^{(\sigma_0 + \sigma_1 LT + \sigma_1 GT + \sigma_2 ID)}, \xi\big)$
GEV 25	$GEV\big((\mu_0 + \mu_1 LT + \mu_2 GT + \mu_3 ES + \mu_4 ID), e^{(\sigma_0 + \sigma_1 LT + \sigma_2 GT + \sigma_3 ES + \sigma_4 ID)}, \xi\big)$
GEV 26	$GEV((\mu_0 + \mu_1 Time), \sigma, \xi)$
GEV 27	$GEV\big((\mu_0 + \mu_1 Time), e^{(\sigma_0 + \sigma_1 Time)}, \xi\big)$

Table 7.2 The parameters of the shortlisted GEV models

Model	LR test	AIC
GEV 4	0.008	734.30
GEV 7	0.003	735.54
GEV 9	0.004	735.40
GEV 11	0.009	737.17
GEV 13	0.018	738.88
GEV 14	0.007	736.87
GEV 16	0.003	735.26
GEV 18	0.039	740.20
GEV 19	0.002	733.60
GEV 20	0.023	739.41
GEV 21	0.008	736.99
GEV 23	0.009	737.71
GEV 25	0.010	738.74

Out of 26 models constructed the 13 models have shown the covariates are affecting significantly as compared with stationary model. The model with LR test *p*-value less than 0.05 and the lowest Akaike Information Criterion (AIC) is used to select the best non-stationary model (Agilan and Umamahesh 2017) from 13 short listed models based on LR test presented in Table 7.2. The model with lowest AIC is selected for the computation of non-stationary return levels for the present study. The GEV 19 (the non-stationarity in location and scale parameter by introducing local temperature and sea-surface temperature as a covariate) is the best model to represent the non-stationarity in the extreme rainfall over the Surat city.

7.3.4 Model Diagnosis of the Selected GEV Models

The reliability of the distribution fitted is presented in Fig. 7.4 using probability plot (PP plot), quantile plot (QQ plot) (Coles 2001). The GEV-1 model and GEV-19 are checked for its model performance. GEV-19 Fig. 7.4a is showing better performance in capturing the extreme rainfall quantiles as compared to GEV-1 model Fig. 7.4b.

7.4 Stationary and Non-stationary Return Levels

The fitted statistical GEV model parameters are used for the computation of stationary and non-stationary return levels. The one day duration rainfall return levels are presented in Table 7.3 showing the 2-, 5-, 10-, 25-, 50- and, 100-year return period respectively. The return levels are plotted in Fig. 7.5 showing the stationary and
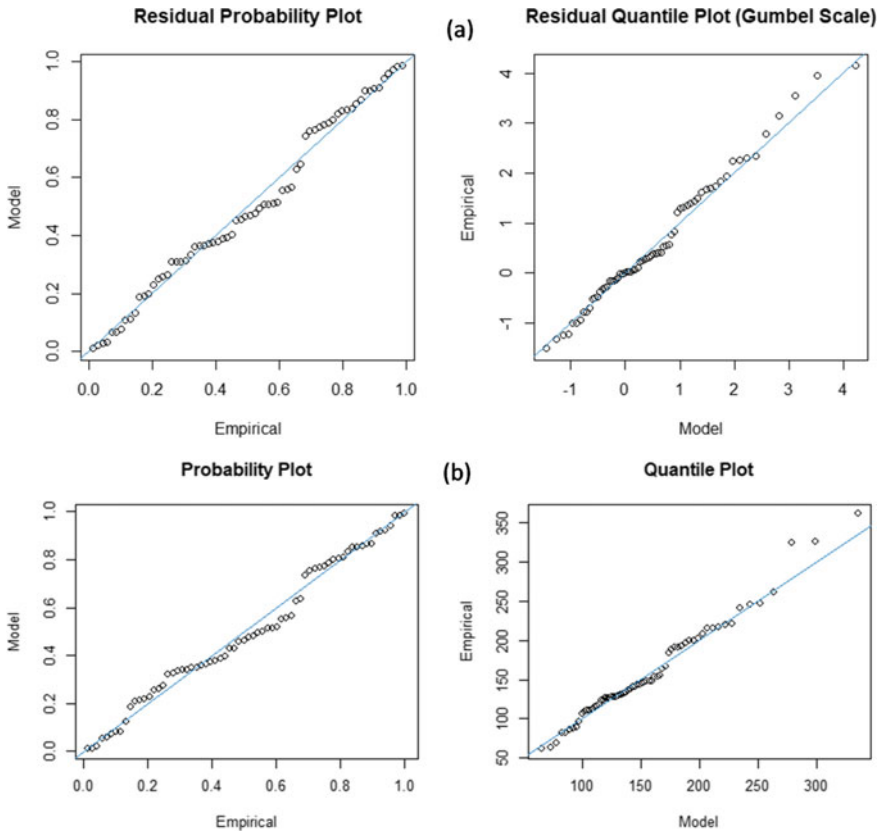
Fig. 7.4 Model diagnosis QQ and PP plot **a** GEV19 and **b** GEV1 model

non-stationary one day return levels for 2–100-year return periods. The Fig. 7.5 shows stationary return levels may not be conservative for the study area under changing climate. Due to the unavailability of the finer resolution data below 1-day the extreme rainfall intensity is worked out using empirical equation given in literature for India. The modified Kothyari and Garde method given by Zope et al. (2016) is used in computation of extreme rainfall intensity stationary (non-stationary). The 1 h duration, 2-, 5-, 10-, 25-, 50-, and 100-year return period the stationary (non-stationary) extreme rainfall is 49 mm/h (52 mm/h), 66 mm/h (71 mm/h), 80 mm/h (87 mm/h), 102 mm/h (113 mm/h), 122 mm/h (136 mm/h), and 145 mm/h (162 mm/h) respectively.

Table 7.3 Stationary and non-stationary return level for one-day duration rainfall

Return period	Stationary	Non-stationary
	One-day return level (mm)	
2-year	146	162
5-year	200	247
10-year	235	305
25-year	283	381
50-year	319	440
100-year	356	500
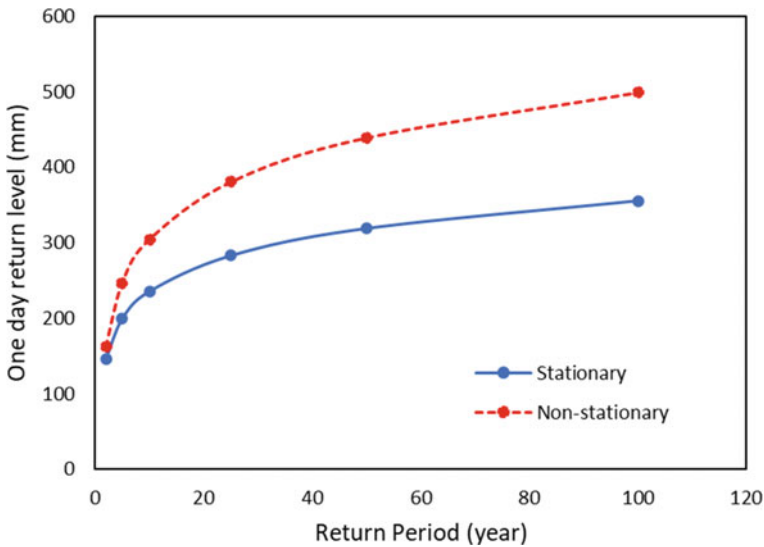
Fig. 7.5 Stationary and non-stationary return level for one day rainfall at Surat city

7.5 Conclusions

Under the non-sgnificant increasing trend of the extreme daily rainfall at the Surat city, the current study was undertaken to evaluate the significant effect of covariates on the extreme rainfall over the region. Total 26 non-stationary GEV models are constructed using Local temperature anomaly (LT), Global temperature anomaly (GT), IOD-Dipole mode index (ID), ENSO-Sea surface temperature Index (ES) and, Time as covariates and 1 stationary GEV model. The 13 GEV models have shown significant effect of covariates over the study area and the model with Local temperature anomaly and ENSO-Sea surface temperature Index is the best model for the computation of non-stationary extreme rainfall. The study revealed the temperature-based covariate is affecting the extreme rainfall over the Surat city in near future. The 2-year, 5-year, 10-year, 25-year, 50-year, and 100-year return period extreme daily

rainfall are 146 mm (162 mm), 200 mm (247 mm), 235 mm (305 mm), 283 mm (381 mm), 319 mm (440 mm), and 356 mm (500 mm) respectively for GEV stationary (Non-stationary LT-ES) model for the Surat city. The current analysis can be useful in design of hydrologic infrastructure of the city under the changing climate.

References

Agilan V, Umamahesh NV (2017) What are the best covariates for developing non-stationary rainfall intensity-duration-frequency relationship? Adv Water Resour 101:11–22. https://doi.org/10.1016/j.advwatres.2016.12.016

Ashok K, Feba F, Tejavath CT (2019) The Indian summer monsoon rainfall and ENSO. Mausam 70(3): 443–452

Cheng L, AghaKouchak A (2014) Nonstationary precipitation intensity-duration-frequency curves for infrastructure design in a changing climate. Sci Rep 4(1):7093. https://doi.org/10.1038/srep07093

Coles S (2001) An introduction to statistical modeling of extreme values. Springer, London. https://doi.org/10.1007/978-1-4471-3675-0

Hamed KH, Ramachandra Rao A (1998) A modified Mann-Kendall trend test for autocorrelated data. J Hydrol 204(1):182–196. https://doi.org/10.1016/S0022-1694(97)00125-X

Intergouvernemental Panel on Climate Change (ed) (2007) Climate change 2007: impacts, adaptation and vulnerability. In: Contribution of working group II to the fourth assessment report of the intergovernmental panel on climate change. Cambridge University Press

Katz RW (2013) Statistical methods for nonstationary extremes. In: Extremes in a changing climate. Springer, Dordrecht, pp 15–37

Mondal A, Mujumdar PP (2015) Modeling non-stationarity in intensity, duration and frequency of extreme rainfall over India. J Hydrol 521:217–231. https://doi.org/10.1016/j.jhydrol.2014.11.071

Ren H, Hou ZJ, Wigmosta M, Liu Y, Leung LR (2019) Impacts of spatial heterogeneity and temporal non-stationarity on intensity-duration-frequency estimates—a case study in a mountainous California-Nevada Watershed. Water 11(6). https://doi.org/10.3390/w11061296

Saji NH, Goswami BN, Vinayachandran PN, Yamagata T (1999) A dipole mode in the tropical Indian Ocean. Nature 401(6751):360–363. https://doi.org/10.1038/43854

Sen Z (2012) Innovative trend analysis methodology. J Hydrol Eng 17(9):1042–1046. https://doi.org/10.1061/(ASCE)HE.1943-5584.0000556

Seneviratne IS, Zhang X, Adnan M, Badi W, Dereczynski C, Di Luca A, Ghosh S, Iskandar I, Kossin J, Lewis S, Otto F, Pinto I, Satoh M, Vicente-Serrano SM, Wehner M, Zhou B (2021) Weather and climate extreme events in a changing climate. In: Climate change 2021 (the physical science basis. Contribution of working group I to the sixth assessment report of the intergovernmental panel on climate change, IPCC, 2021)

SMC (2022) Surat Municipal Corporation. https://www.suratmunicipal.gov.in/TheCity/Weather. Accessed on 15 March, 2022

Su C, Chen X (2019) Covariates for nonstationary modeling of extreme precipitation in the Pearl River Basin, China. Atmos Res 229:224–239. https://doi.org/10.1016/j.atmosres.2019.06.017

Sugahara S, da Rocha RP, Silveira R (2009) Non-stationary frequency analysis of extreme daily rainfall in Sao Paulo, Brazil. Int J Climatol 29(9):1339–1349. https://doi.org/10.1002/joc.1760

Timbadiya PV, Patel PL, Porey P (2015) A 1D–2D coupled hydrodynamic model for river flood prediction in a coastal Urban floodplain. J Hydrol Eng 20:05014017. https://doi.org/10.1061/(ASCE)HE.1943-5584.0001029

Vinnarasi R, Dhanya CT (2022) Time-varying intensity-duration-frequency relationship through climate-informed covariates. J Hydrol 604:127178. https://doi.org/10.1016/j.jhydrol.2021.127178

Zope PE, Eidho IT, Jothiprakash V (2016) Development of rainfall intensity duration frequency curves for Mumbai City, India. J Water Resour Prot 8(7):Article 7. https://doi.org/10.4236/jwarp.2016.87061

Part III
Droughts

Chapter 8
Analysis of Hydrological Drought in the Eastern Part of Slovakia Using Standardized Precipitation Index

Martina Zeleňáková, Tatiana Sol'áková, Pavol Purcz, and Hany F. Abd-Elhamid

8.1 Introduction

Drought indices are indicators that use hydrometeorological parameters to determine the beginning and end of drought as well as quantifying drought into several categories. For each type of drought, it is possible to find appropriate drought index (Tsakiris 2004). The Standardized Precipitation Index (SPI) was developed by (McKeen et al. 1993) for the detection of meteorological drought. SPI index is widely used to monitor meteorological drought and it is highly recommended by World Meteorological Organization for its ability to identify drought characteristics such as duration, severity, intensity, and inter-arrival time.

Meteorological drought begins when a deficiency of precipitation occurs over season or over a longer period. According to McKeen et al. (1993), the deficiency of precipitation accumulates over time scales functionally separates different type of physical drought, namely meteorological, agricultural, and hydrological drought. The short time scales of the index (SPI 1, SPI 3) reflect the precipitation deficit and the soil moisture deficit. A short-term deficiency of precipitation leads to drought in the root zone, which can lead to reduction in the crop yields, the so-called agricultural drought. The long-time scales of the index (SPI 6, SPI 9, SPI 12, or SPI 24) reflect the lack of

M. Zeleňáková (✉) · T. Sol'áková · P. Purcz
Department of Environmental Engineering, Faculty of Civil Engineering, Technical University of Kosice, 040 01 Košice, Slovakia
e-mail: martina.zelenakova@tuke.sk

T. Sol'áková
e-mail: Tatiana.solakova@tuke.sk

H. F. Abd-Elhamid
Department of Water and Water Structures Engineering, Faculty of Engineering, Zagazig University, Zagazig 44519, Egypt

Center for Research and Innovation in Construction, Faculty of Civil Engineering, Technical University of Kosice, 040 01 Košice, Slovakia

Table 8.1 Chosen cumulative distribution function

Probability density function	Cumulative distribution function
Gen. Extreme value	$F_{(x)} = \exp(-(1+kz)^{-\frac{1}{k}})z = \frac{x-\mu}{\sigma}$
Weibull 3P	$F_{(x)} = 1 - \exp(-(\frac{x-\gamma}{\beta})^{\alpha})$
Gamma 3P	$F_{(x)} = \frac{\Gamma_{\frac{(x-\gamma)}{\beta}}(\alpha)}{\Gamma(\alpha)}$
Gen. Gamma	$F_{(x)} = \frac{\Gamma_{(\frac{x}{\beta})^{k}}(\alpha)}{\Gamma(\alpha)}$
Burr	$F_{(x)} = 1 - (1 + (\frac{x}{\beta})^{\alpha})^{-k}$
Lognormal 3P	$F_{(x)} = \Phi\left(\frac{ln(x-\gamma)-\mu}{\sigma}\right)$
Pearson 6	$F_{(x)} = I_{x/(x+\beta)}(\alpha_1, \alpha_2)$
Normal	$F_{(x)} = \Phi\left(\frac{(x-\mu)}{\sigma}\right)$

groundwater, snow cover, flows and storage tanks, the so-called hydrological drought (McKee et al. 1993). The SPI is a useful method for identifying, characterizing, and monitoring the drought phenomenon, which affects excessive number of sectors of human activity as well as can severely affects ecosystems (Mishra and Singh 2010).

SPI is drought indicator that able to identify drought and flood events in a similar probabilistic way, as can be seen in Table 8.1 (Blain 2011). SPI is widely used to establish extreme dryness, or wetness (see e.g., Bothe et al. 2009; Santos et al. 2010; Zhu et al. 2011; Sienz et al. 2012; Nagy et al. 2020). In this study SPI is used to analyze draught at four precipitation stations located in Bodrog catchment that situated in the Eastern part of Slovakia. The meteorological data from the four stations were used to determine the long time scale index (SPI 12 and 24) for hydrological draught analysis in the eastern part of Slovakia.

8.2 Material and Methods

The current case study is located in the eastern part of Slovakia as shown in Fig. 8.1.

The Carpathian Mountains and Pannonian basin are located in the sub-basin of Bodrog. The partial catchment area of Bodrog is more covered with forests, meadow, pastures, and built-up areas. Forests represent 37.4% of this area. The current study considers four stations as shown in Fig. 8.1; Bardejov (49° 18′ 56″ N, 21° 12′ 44″ E), Tisinec (49° 13′ 16″ N, 21° 38′ 13″ E), Kamenica nad Cirochou (48° 59′ 15″ N, 22° 09′ 07″ E), Vysoká nad Uhrom (49° 18′ 20″ N, 21° 34′ 05″ E). The data were collected for the period (1972–2014) from the Slovak Hydrometeorological Institute of Košice.
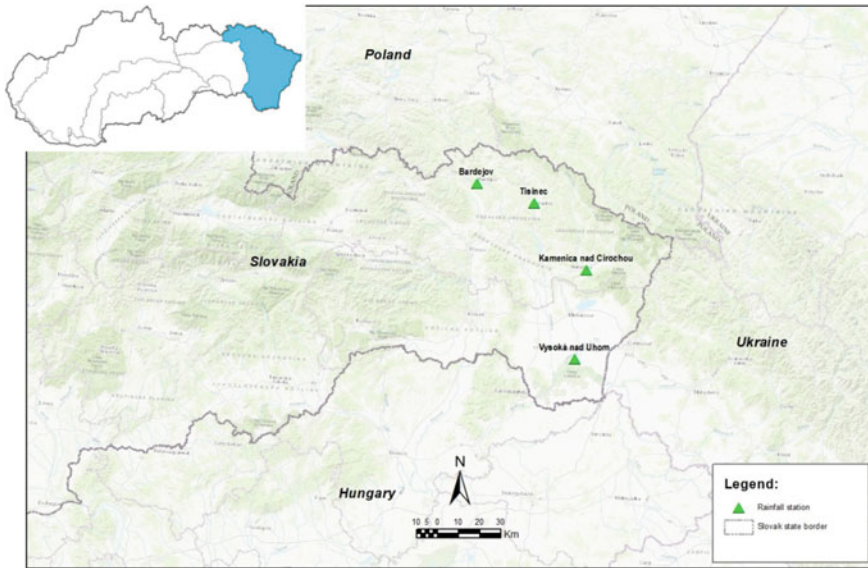
Fig. 8.1 Location map of the study area and the locations of four precipitation stations

The overall calculation procedures consist of five steps as following. First, preparation of statistical files, monthly precipitation in the period were aggregated in 12 and 24-month time scales, then the series of mean values for time interval (d) equals to 12 and 24 months is calculated as following:

$$X(t) = \frac{1}{d} \sum_{\tau=t-d+1}^{t} X(\tau) \tag{8.1}$$

where

X(τ)   is the monthly precipitation for τ month,
d   is 12 and 24,
t   is observed period.

Second, determination a probability density function f(x) capable of describing the long-term precipitation time's series and estimation of its parameters by maximum likelihood method (Kottegoda and Rosso 1997). The selection of the most appropriate theoretical probability density function f(x) from (8) probability density function for each month separately as presented in Table 8.2. Kolmogorov–Smirnov test was used at significant level ($\alpha = 5\%$). The Kolmogorov–Smirnov test which measure the vertical differences between the theoretical F(x) and empirical cumulative distribution function of random variable. The theoretical probability function that has the smallest distances with respect to the empirical probability function was selected. Third, calculation of the cumulative probability functions for each month separately

Table 8.2 Classification of meteorological drought using SPI (Sienz et al. 2012; Blain 2011)

SPI intervals	SPI classes	Probability events (%)
≥ 2	Extreme humidity	2.3
1.5–1.99	High humidity	4.4
1.0–1.49	Mild humidity	9.2
0.99 to −0.99	Almost normal humidity	68.2
− 1.0 to −1.49	Moderate drought	9.2
−1.5 to −1.99	Severe drought	4.4
≤ -2	Extreme drought	2.3

(mathematical background) as presented in Table 8.2. Fourth, mapping transformation of the cumulative probability function F(x) into a standard normal distribution with random variable Z_d, which represents SPI value (McKeen et al. 1993):

$$Z_d = \Phi^{-1}(P_0 + (1 - P_0)F(x)) \tag{8.2}$$

Then: F(x) is a cumulative distribution function, which takes values $(0 \leq F(x) \geq 1)$ (Blain 2011), whereas the P_0 is the probability of occurrence of zero precipitation that can be obtained from the following equation:

$$P_o = \frac{N_0}{(N + 1)} \tag{8.3}$$

where, N_0 is the number of zero precipitations in dataset composted of N observations.

Fifth, checking that SPI values do indeed have a normal distribution by Wu et al. who stated 3 criteria: (i) Shapiro–Wilk statistic: W less than 0.96, (ii) *p*-value less than 0.1, (iii) absolute value of median greater than 0.05. Detection of the beginning of historical extreme drought events during the period (1972–2014) was done by RUN method (Yevjevich 1967) then estimating the average inter-arrival time of drought. As threshold level of drought, we used $(Z_0 = -2)$ to capture the onset of the extreme drought event. Thus if $(Z_d < -2)$ then we are in drought conditions and duration of a drought, (D_d), is the period during which SPI values are continuously less than −2. The severity of a drought (S_d) is the cumulative value of the index in the drought period. The inter-arrival time (T_d) is the time between two successive droughts (Madadgar and Hamid 2013). All the parameters in the Table 8.1 can be found in user manual of EasyFit software (http://www.mathwave.com/easyfit-distribution-fitting.html).

In drought management it is important to classify risk of drought into categories, which have important role to determine its severity. Risk of drought can be classified into five categories as shown in Table 8.2 that presents the classification of meteorological drought according to SPI (Sienz et al. 2012; Blain 2011). We pay attention to extreme drought events in the current study.

8.3 Results and Discussion

The data for 44 years was used for the analysis of hydrological draught in the Bodrog sub-basin with an area of 11,474 km^2. The aim of the work was to analyze the historical events of extreme drought and to identify the average return of long-lasting hydrological drought as well as the susceptibility of this area to drought. The extreme events of long-term hydrological drought were identified by 12 and 24 month SPI. The results of the analysis at the four stations are presented in Table 8.3 and Figs. 8.2, 8.3, 8.4 and 8.5.

At Bardejov station the drought identified by SPI 12, showed that a total of 9 episodes of extreme drought were recorded in 1972, 1974, 1983, 1994, 1995, 2004, 2005, 2007 and 2008 with a total cumulative severity of −31.5 and total duration of 14 months (Fig. 8.2a). The average drought return time at Bardejov station is 4.41 years. However, for SPI 24, a total of 7 episodes of extreme drought were recorded in 1973, 1994, 2003, 2004 and 2008 with a total cumulative severity of −25.27 and total duration of 11 months. The average drought return time at Bardejov station is 5.9 years (Fig. 8.2b). The extreme episodes of drought lasted a short time.

Drought analysis at Tisinec precipitation station showed that a total of 4 episodes of extreme drought were recorded in 1987, 1990, 2004 and 2012 for SPI 12 and a total of 7 episodes of extreme drought were recorded in 1973, 1982, 1992, 1995, 1996 and 2003 for SPI 24. The total cumulative severity is −12.9 and 33.43 for SPI 12 and 24 respectively. The total duration for SPI 12 and 24 was 5 and 14 months

Table 8.3 Drought identification by SPI 12 and 24

Station	Number of drought events		Duration		Cumulative severity		Average Inter-arrival time	
	12	24	12	24	12	24	12	24
Bardejov	9	7	14	11	−31.5	−25.3	53	70.83
Tisinec	4	7	5	14	−12.9	−33.4	110.3	60.33
Kamenicanad Cirochou	6	1	13	9	−29.9	−22.3	100.8	–
Vysokánad Uhrom	6	4	10	12	−21.9	−28.1	50.4	120
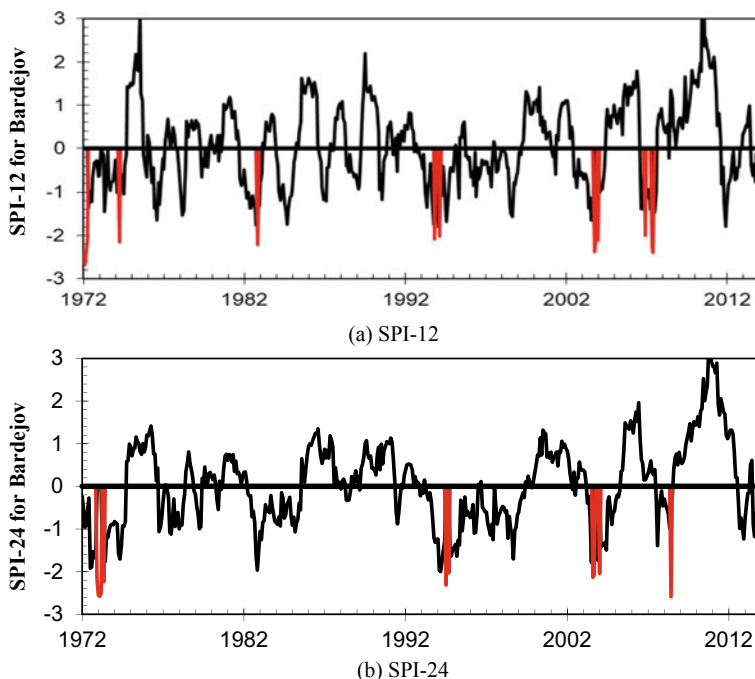
Fig. 8.2 SPI 12 and 24 at station Bardejov for the period (1972–2014)

respectively. The average drought return time for SPI 12 is 8.4 years and SPI 24 is 5 years. The results of SPI 12 and 24 are shown in Fig. 8.3a, b.

Figure 8.4a, b show the results of SPI 12 and 24 at Kamenica and Cirochou. For SPI 12 a total of 6 episodes of extreme drought were recorded in 1972, 1974, 1987 and 2003 with a total cumulative severity of −29.9 and total duration of 13 months (Fig. 8.4a). The average drought return time at Kamenica and Cirochou station is 8.4 years. However, for SPI 24, only one episodes of extreme drought was recorded at the Kamenica and Cirochou precipitation station, in 2003 with a total duration 9 months and cumulative severity of −2.27. It is not possible to determine the inter-arrival time because we had only one episode of extreme drought at this station (Fig. 8.4b).

The results of drought analysis at Vysoka and Uhrom for SPI 12 showed that a total of 6 episodes of extreme drought were recorded at the station, in 1972, 1973, 1993 and 1994 with a total cumulative severity of −21.9 and total duration of 10 months (Fig. 8.5a). The average drought return time at Vysoka nad Uhrom station is 4.2 years. For SPI 24, a total of 4 episodes of extreme drought were recorded at the Vysoka

(a) SPI-12

(b) SPI-24
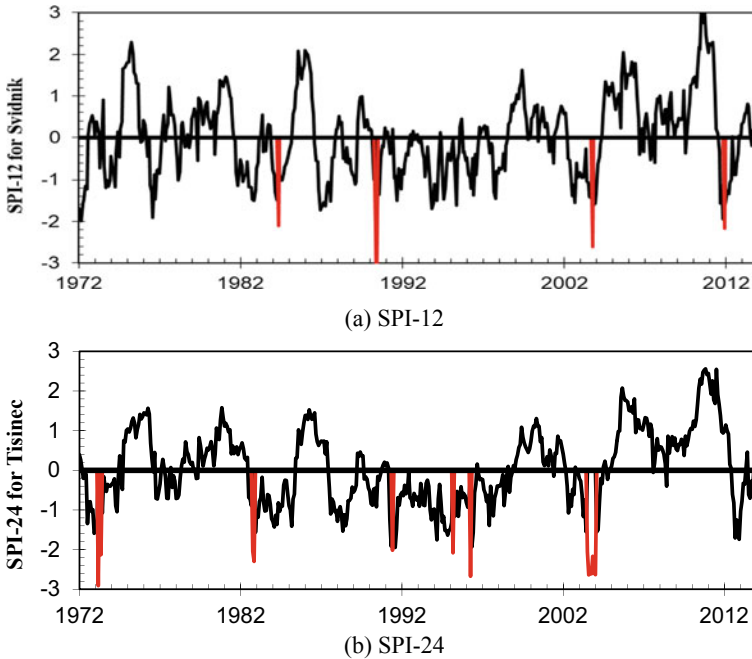
Fig. 8.3 SPI 12 and 24 at station Tisinec for the period (1972–2014)

nad Uhrom precipitation station, in 1973, 1993, 1994, 2003 with a total cumulative severity of −28.06 and total duration of 12 months (Fig. 8.5b). The average drought return time at Vysoka nad Uhrom station is 10 years.

Figures 8.2, 8.3, 8.4 and 8.5 gave the values of SPI for 12 and 24 month timescales for the meteorological data collected from four station IN the Bodrog basin for the period from 1972 to 2014 (44 years). In SPI 12 and 24 histograms, periods in which the SPI 12 and 24 values were less than −2, identified in red. As we can see in Figs. 8.2, 8.3, 8.4 and 8.5 the driest years was 2003 in all the studied stations. Based on 12 month SPI analysis, twenty five extreme hydrological drought events were recorded in the Bodrog basin. The longest period of hydrological drought (14 months) was recorded at the Bardejov station from January to May 1972. The largest cumulative severity was recorded at the Bardejov station (−31.5). However, from 24 month SPI analysis it is possible to see how the extreme hydrological droughts often occurred during the period (1972–2014). The recorded extreme hydrological drought events were eighteen times. At the Kamenica and Cirochou station from June 2003 to February 2004, a drought with longest duration was recorded. The largest cumulative severity was recorded at the Tisinec station (−33.4).

(a) SPI-12

(b) SPI-24
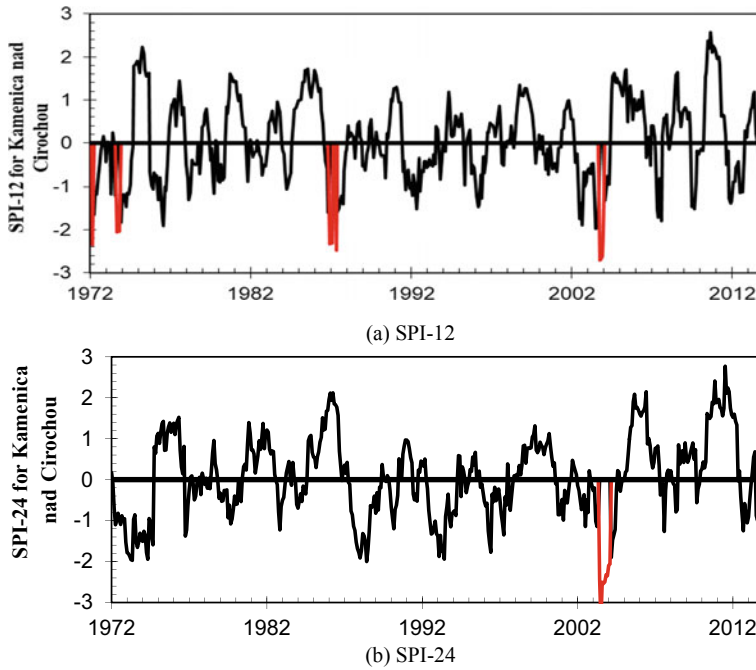
Fig. 8.4 SPI 12 and 24 at station Kamenica and Cirochou for the period (1972–2014)

Based on the results of drought analysis using SPI 12 and 14 for four stations in the the Bodrog basin, we can conclude that the Bodrog river basin faced an extreme long-term hydrological drought. An extreme precipitation deficit in this river Bodrog basin can be expected on average from 5 to 10 years.

(a) SPI-12

(b) SPI-24
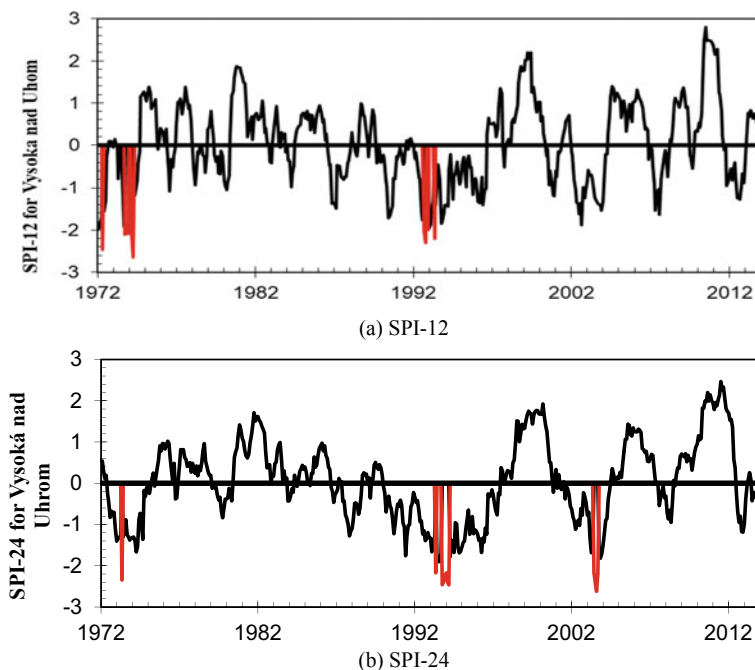
Fig. 8.5 SPI 12 and 24 at station Vysoka and Uhrom for the period (1972–2014)

8.4 Conclusions

Drought is a natural risk which has more negative effects that may increase due to climate changes. Drought analysis using Standardized Precipitation Index (SPI) was implemented for 4 precipitation station situated in Bodrog river basin, as a temperate climate zone. SPI approach was used to assessed extreme historical hydrological drought events during the period (1972–2014). Based on 12 and 24 month SPI analysis, Bodrog river basin had experienced 19 extreme drought events during the period (1972–2014) with a maximum duration 9 months. The results showed that the northern part of Bodrog river basin is expected to have extreme events more intensive and with short duration while in the southern part of the basin, extreme deficiency of precipitation with less frequent. The result of this analysis should be used to create drought vulnerability maps and to predict this risk using average inter-arrival time, thus providing early warning of long-term meteorological drought.

References

Blain G (2011) Revisiting the probabilistic definition of drought: strengths, limitations and an agrometeorological adaptation. Bragantia 71:132–141. https://doi.org/10.1590/S0006-87052012000100019

Bothe O, Fraedrich K, Zhu X (2009) The large-scale circulations and summer drought and wetness on the Tibetan Plateau. Int J Climatol 30:844–855. https://doi.org/10.1002/joc.1946

Kottegoda NT, Rosso R (1997) Statistics probability and reliability for civil environmental engineers. McGraw Hill

Madadgar S, Hamid M (2013) Drought analysis under climate change using Copula. J Hydrol Eng 18:746–759. https://doi.org/10.1061/(ASCE)HE.1943-5584.0000532

McKee TB, Doesken NJ, Kleist J (1993) The relationship of drought frequency and duration to time scales. 6

Mishra AK, Singh VP (2010) A review of drought concepts. J Hydrol 391(1):202–216. https://doi.org/10.1016/j.jhydrol.2010.07.012

Nagy P, Purcz P, Gałaś S, Portela M, Hlavatá H, Simonová D (2020) Trend analysis of drought indices in the eastern Slovakia. IOP Conf Ser Mater Sci Eng 867:012033. https://doi.org/10.1088/1757-899X/867/1/012033

Santos J, Pulido-Calvo I, Portela M (2010) Spatial and temporal variability of droughts in Portugal. Water Resour Res 46. https://doi.org/10.1029/2009WR008071

Sienz F, Bothe O, Fraedrich K (2012) Monitoring and quantifying future climate projections of dryness and wetness extremes: SPI bias. Hydrol Earth Syst Sci 16:2143–2157. https://doi.org/10.5194/hess-16-2143-2012

Tsakiris G (2004) Meteorological drought assessment (project MEDROPLAN)

Yevjevich VM (1967) An objective approach to definitions and investigations of continental hydrologic droughts. Colorado State University, Hydrology Papers, p 23

Zhu X, Bothe O, Fraedrich K (2011) Summer atmospheric bridging between Europe and East Asia: influences on drought and wetness on the Tibetan Plateau. Quatern Int 236(1–2):151–157. https://doi.org/10.1016/j.quaint.2010.06.015

Chapter 9
Low Flow in the Oued El Abid Basin (Morocco): Better Understand It to Better Manage It (Oum Errbia Basin—Morocco)

Khouldia Nafia and Mohamed El Ghachi

9.1 Introduction

The current situation of water resources and their uses in Morocco presents issues that are common to many regions of the arid and semi-arid climate: limited resources already widely exploited to meet growing needs, increased use of so-called unconventional resources, a situation of competition between sectoral uses, an increasing commodification of resources, and restrictive climatic conditions which reinforce tensions around water.

The Oued El Abid watershed (Upstream of the Bin El Ouidane dam) is likely to be at risk of water shortage due to climate change, the climate considerably influences the hydrological cycle. They also increase the risks associated with extreme phenomena such as floods and low water levels, the interest of the latter is currently growing within the scientific community.

The basin of Oued El Abid which is the subject of this study is located between the meridians 5° W and 6° 30′ W, and the parallel 32° N and 33° N with an area of 3001 km² and d he perimeter of 419 km is a sub-basin of the Oum Er Rbia wadi. The watercourse of Oued El Abid is a permanent watercourse, it is born in the jbel Masker (3277 m) and flows from E to W, it is the main tributary of Oued Oum Er Rbia.

The upstream of the El Abid wadi is a mountainous area, with significant water resource potential. Extends in the heart of the limestone high atlas, delimited to the E and S by a line of high ridges above 3600 m. The watershed of Oued El Abid

K. Nafia (✉) · M. El Ghachi
Department of Geography, Faculty of Letters and Human Sciences, Sultan Moulay Slimane University, Beni Mellal, Morocco
e-mail: naf.khouldia03@gmail.com

Laboratory "Dynamics of Landscapes, Risks and Heritage", Beni Mellal, Morocco

upstream of the Bin El Ouidane dam is subject to a mountain Mediterranean type climate, with oceanic influence, rainfall is characterized by an irregular distribution (Figs. 9.1 and 9.2).
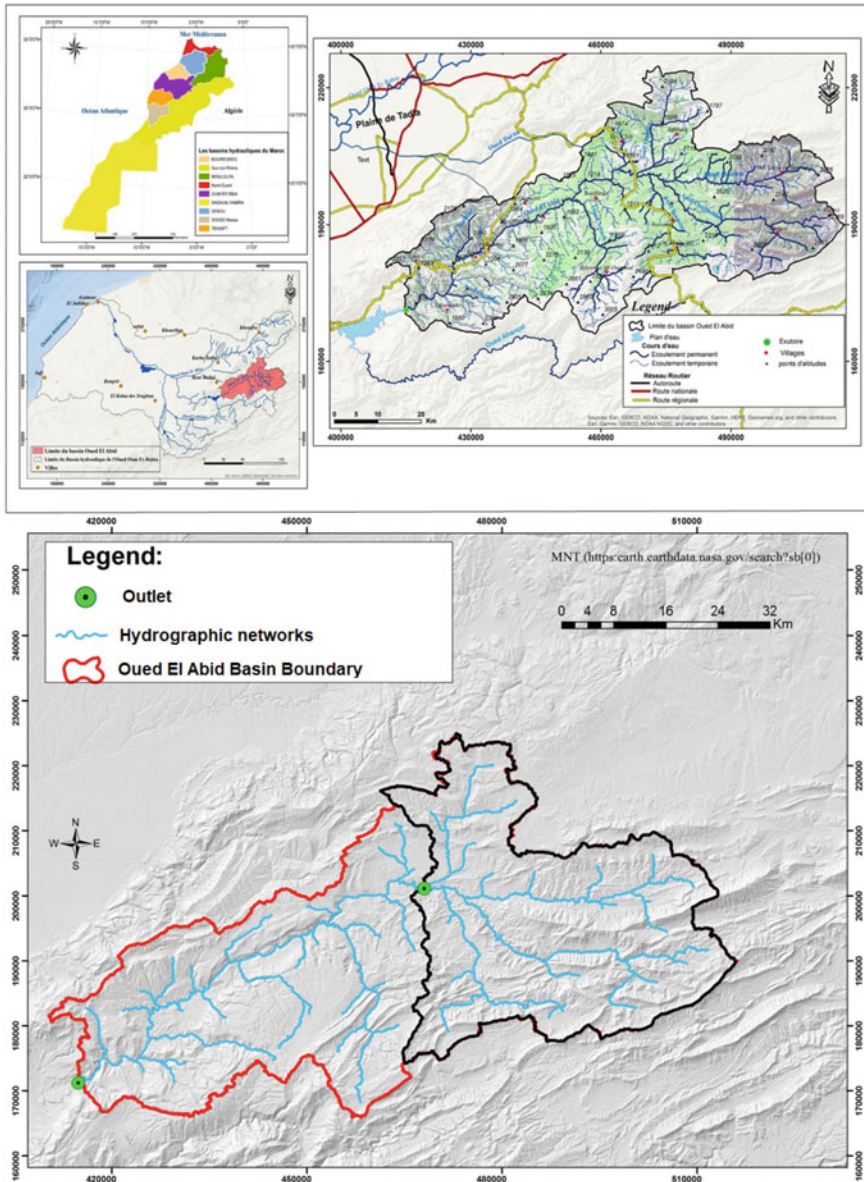
Fig. 9.1 Geographical location of the Oued El Abid watershed Upstream Bin El Ouidane Dam
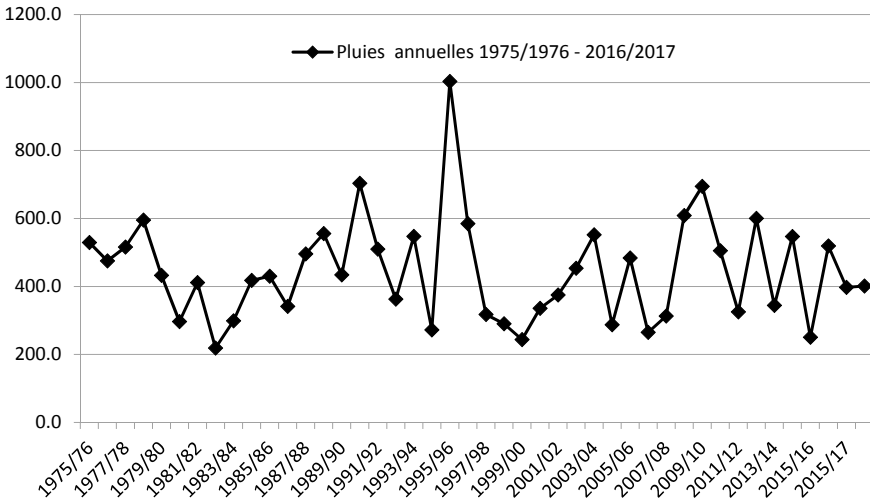
Fig. 9.2 Distribution of annual rainfall in the upper watershed of Oued El Abid recorded by the Tizi N'isly station (1976–2018)

Geologically, it is part of the central calcareous High Atlas where the relief is marked by a series of anticlines and synclines, is marked by the dominance of carbonate rocks composed mainly of Lias, Dogger and Cretaceous limestones. These limestone rocks are found in the catchment area either isolated or alternating with other formations (Dolomites, marls, or sandstones).

From an administrative point of view, the study area belongs to the national territory, Beni Mellal Khnifra region, located in the two provinces Beni Mellal and Azilal. The hydro-climatic functioning is an important element in hydrological research, it intervenes through multiple factors, the most important factors are precipitation and temperature. The climate is also a determining factor in the hydrological cycle, it directs the spatio-temporal distribution of the water resource and influences its hydrogeological potential. Since field of study data is limited to hydrology and rainfall. It will be based on these rainfall data which span a period of more than 40 years (1976–2018). As said before, the analysis of annual rainfall precipitation aims to determine temporal and spatial variations, as well as to extract climate information (Fig. 9.3).

The figure shows the distribution of annual rainfall, there is a decrease in rainfall and all this due to the drought that was in Morocco during this period (1981/1982) after there is an increase in rainfall, and more precisely in 1996 (1000 mm). After the rainfall analysis, we zoomed in on the hydrological functioning of our studied basin. The analysis of the graph shows that the monthly coefficient of CMQ flows (monthly flow/module) for the Tizi Nisli hydrological station was recorded as 2.05 m^3 during the month of March. Then CMQ begins to decrease until it reaches minimum values in the months of July. The average flow remains low between the months of June and October, but from this month, it increases to reach a high flow in January (Figure).
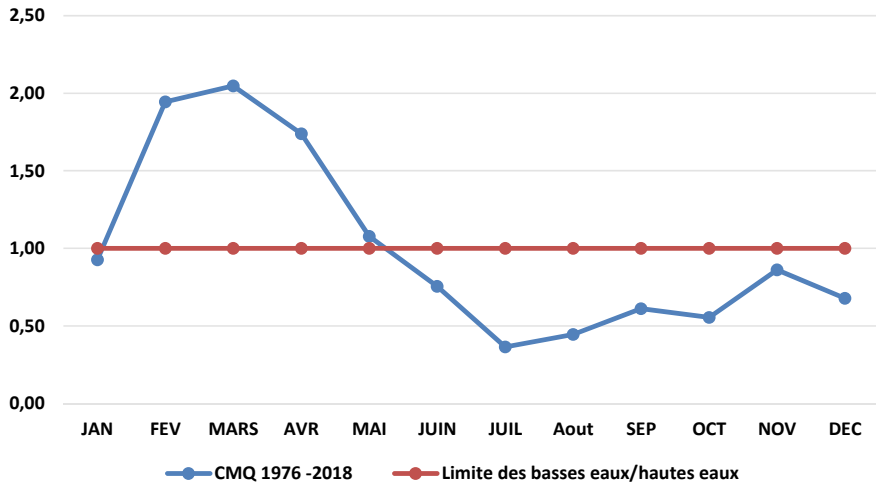
Fig. 9.3 CMP of the station of Tizi Nisli 1976–2018

The flow regime of Oued El Abid (Oued Ouirine station Tizi Nisli) is subdivided into two phases: The high water phase: starts from the month of February until the month of May. It is characterized by more frequent and intense precipitation, resulting in frequent flow peaks) accompanied by turbidity. The low water phase: starts from June to January. It is characterized by a more or less regular decrease between June July and October, which corresponds to the approach of seasonal low water.

9.2 Methods

The study of low water levels on a monthly scale could mask very severe low water situations (Lang 2010). We approach the low water level in daily time steps from the VCNd.

The VCNd made it possible to determine the lowest flows, recorded for a river during "d" consecutive days, from the average daily flows. Low water flows are linked to periods of low water (summer period). The calculation of NCVs could therefore guarantee stabilized flows, in most cases, which is less guaranteed with longer durations or QMNA (Lang 2010). The most severe low water levels are in most cases linked to particularly low winter and spring precipitation (Lang 2010).

So the VCNd are extracted annually according to a fixed duration of d days. Moving averages calculated from average daily flows over d consecutive days result in the calculation of VCNd (Lang 2010).

9.3   Results and Discussion

The values of NCVd were calculated for the Tizi Nisli station upstream of the Oued El Abid watershed.

VCNd are complementary operations to QMNA. NCVd are values extracted annually according to a fixed duration d. Moving averages, calculated from the average daily flows over several consecutive days, lead to the calculation of the VCNd, minimum average flow over d days. Table 9.1 shows the VCNd of the Tizi Nisli station during the 1976–2018 chronicle.

9.3.1   The Appearance of Low Water Levels in the Oued El Abid Basin

Low water levels occur most often in August and then in July, the number is also significant in September. This is normal since it coincides with the summer period which experiences a rainfall deficit and active evaporation, we can have the same conditions in May and June. We also observe that during the 1975–2010 chronicle, all months experienced low water except December and January, however, the appearance of low water once during October, November and February, March and April may be due to precipitation of snow or by the increase in temperature causing strong evaporation (Fig. 9.4).

At the Tizi Nisly station, 33% of VCN10 and VCN5 occur in August and 31% of VCN90 appear in June. While 26% of VCN30 and VCN60 also appear in August and July.

NDVs appeared during the high water phase. This situation is observed in this basin in the months of January and December.

9.3.2   Analysis of the Variability of CNds in the Watershed of Oued El Abid Upstream of the Bin El Ouidane Dam

The VCNd series from the Tizi Nisli station show significant variability at the temporal and spatial scale. The most severe low water levels of the study chronicle were produced in the Oued El Abid basin upstream of the Bin El Ouidane dam in 1988 (Fig. 9.5).

Table 9.1 VCNd (minimum average volume of the year for "d" consecutive days) of the Tizi Nizli station (1976–2018)

Dates	VCN1	VCN 3	VCN 5	VCN 10	VCN 15	VCN 20	VCN 30	VCN 60	VCN 90
1976	1.300	1.337	1.348	1.359	1.365	1.371	1.395	2.114	2.412
1977	1.020	1.037	1.070	1.107	1.140	1.167	1.278	1.365	1.625
1978	1.020	1.020	1.020	1.022	1.038	1.059	1.124	1.283	1.319
1979	1.110	1.110	1.110	1.153	1.190	1.239	1.370	1.482	2.319
1980	0.800	0.810	0.822	0.849	0.866	0.885	0.911	1.194	1.347
1981	0.760	0.760	0.766	0.794	0.792	0.811	0.820	0.860	0.916
1982	0.520	0.520	0.520	0.532	0.585	0.733	0.857	0.934	0.984
1983	0.160	0.160	0.160	0.174	0.183	0.189	0.221	0.263	0.31.5
1984	0.160	0.160	0.160	0.160	0.160	0.160	0.164	0.194	0.242
1985	0.290	0.293	0.310	0.349	0.400	0.400	0.410	0.522	0.719
1986	0.680	0.693	0.712	0.732	0.747	0.771	0.832	1.025	1.175
1987	0.630	0.630	0.630	0.630	0.630	0.632	0.644	0.706	1.048
1988	1.020	1.043	1.062	1.137	1.342	1.529	1.532	1.626	1.711
1989	1.000	1.000	1.000	1.059	1.051	1.086	1.284	1.892	2.387
1990	0.440	0.440	0.440	0.476	0.543	0.664	0.721	0.859	1.263
1991	0.100	0.113	0.122	0.161	0.195	0.334	0.474	0.885	1.069
1992	0.420	0.447	0.518	0.700	0.700	0.709	0.740	0.842	1.01.5
1993	0.470	0.500	0.500	0.534	0.573	0.635	0.681	0.796	0.812
1994	0.470	0.470	0.470	0.480	0.509	0.531	0.580	0.755	1.209
1995	0.010	0.010	0.010	0.058	0.069	0.080	0.083	0.095	1.052
1996	0.010	0.010	0.012	1.001	1.003	1.012	1.022	1.114	1.205
1997	0.360	0.360	0.360	0.375	0.399	0.522	0.543	0.883	1.237
1998	0.260	0.263	0.278	0.289	0.303	0.307	0.366	0.390	0.442
1999	0.290	0.290	0.290	0.290	0.290	0.291	0.299	0.343	0.427
2000	0.400	0.400	0.400	0.400	0.400	0.405	0.409	0.431	0.549
2001	0.300	0.307	0.312	0.320	0.323	0.356	0.778	0.867	0.975
2002	0.530	0.530	0.530	0.530	0.530	0.530	0.534	0.812	0.882
2003	0.370	0.370	0.370	0.370	0.422	0.432	0.433	0.516	0.777
2004	0.750	0.750	0.750	0.750	0.753	0.762	0.789	1.114	1.298
2005	0.400	0.400	0.404	0.412	0.416	0.420	0.423	0.445	0.888
2006	0.450	0.450	0.456	0.471	0.483	0.507	0.542	0.969	0.898
2007	0.630	0.640	0.644	0.657	0.673	0.698	0.774	0.822	0.962
2008	0.670	0.677	0.682	0.686	0.690	0.720	0.745	1.073	1.123
2009	0.520	0.673	0.866	0.934	1.085	1.099	1.113	1.207	2.159
2010	0.370	0.370	0.372	0.380	0.389	0.403	0.763	0.786	1.278

(continued)

Table 9.1 (continued)

Dates	VCN1	VCN 3	VCN 5	VCN 10	VCN 15	VCN 20	VCN 30	VCN 60	VCN 90
2011	0.680	0.707	0.734	0.760	0.781	0.810	0.900	1.019	1.151
2012	0.540	0.550	0.562	0.601	0.647	0.694	0.741	0.913	0.991
2013	0.830	0.880	0.880	0.907	0.996	1.066	1.314	1.617	1.961
2014	0.370	0.380	0.400	0.459	0.488	0.494	0.509	0.732	1.017
2015	1.000	1.000	1.000	1.007	1.025	1.034	1.042	1.131	1.290
2016	0.090	0.150	0.550	0.550	0.550	0.550	0.554	0.702	0.995
2017	0.070	0.070	0.070	0.070	0.086	0.112	0.136	0.248	0.267
2018	0.410	0.417	0.432	0.473	0.488	0.487	0.494	0.673	1.375
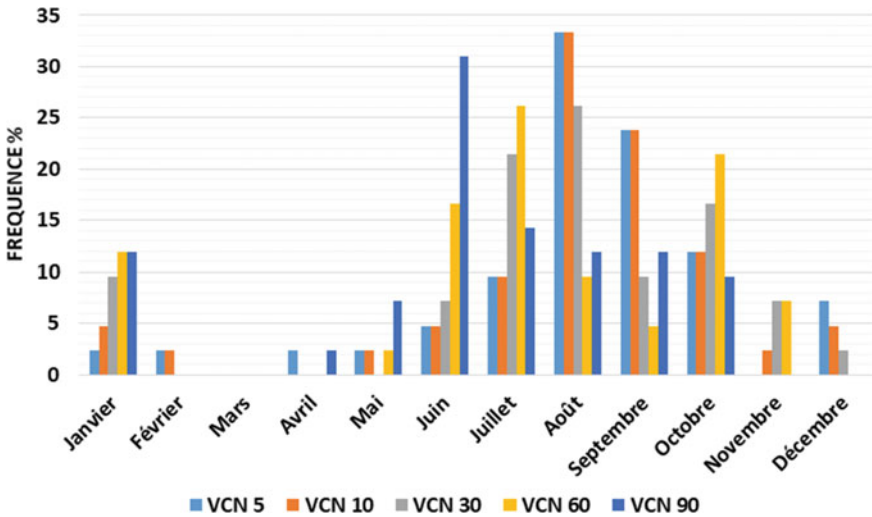
Fig. 9.4 Occurrences of CNDVs from the Tizi Nisli station (1976/2018)

9.3.3 *Frequency Analysis of CNds in the Oued El Abid Watershed*

The frequency analysis of NCVd shows the proposed time that a flow is exceeded or equivalently the average interval in years that the river falls below a given flow.

We tested different laws on the VCNd series of the Tizi Nisli station and we found that these flows fit well with the Normal Root and Gumbul law.
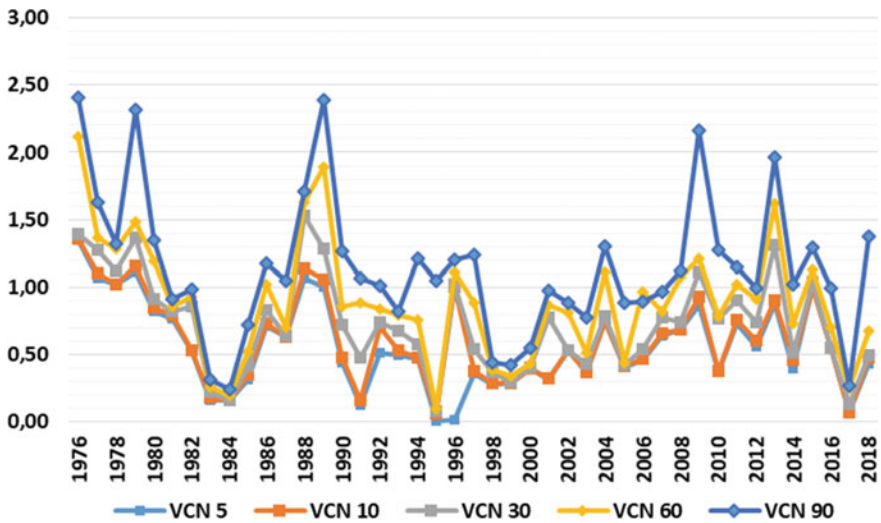
Fig. 9.5 Variation of CNds in the Tizi Nisly station (1976–2018)

The results are shown in the graphs of Fig. 9.6.

The low VCNd values of the study chronicle (1976–2018) were recorded in 1995 during the years 1996, 2017. The high values of VCN5 and VCN10 were observed in 1976, while the high values of VCN30, VCN60 and VCN90 occurred in 2010.

9.3.4 Usefulness of VCNds for Managers

The NCVd makes it possible to identify the low water flows at different time steps in order to limit the influence of precipitation on the flows. In this semi-arid climatic context, the CNDVs do not change over the period languages.

Therefore, the use of long-duration VCNd will be representative of low water situations in Morocco because the flows during the low water phases.
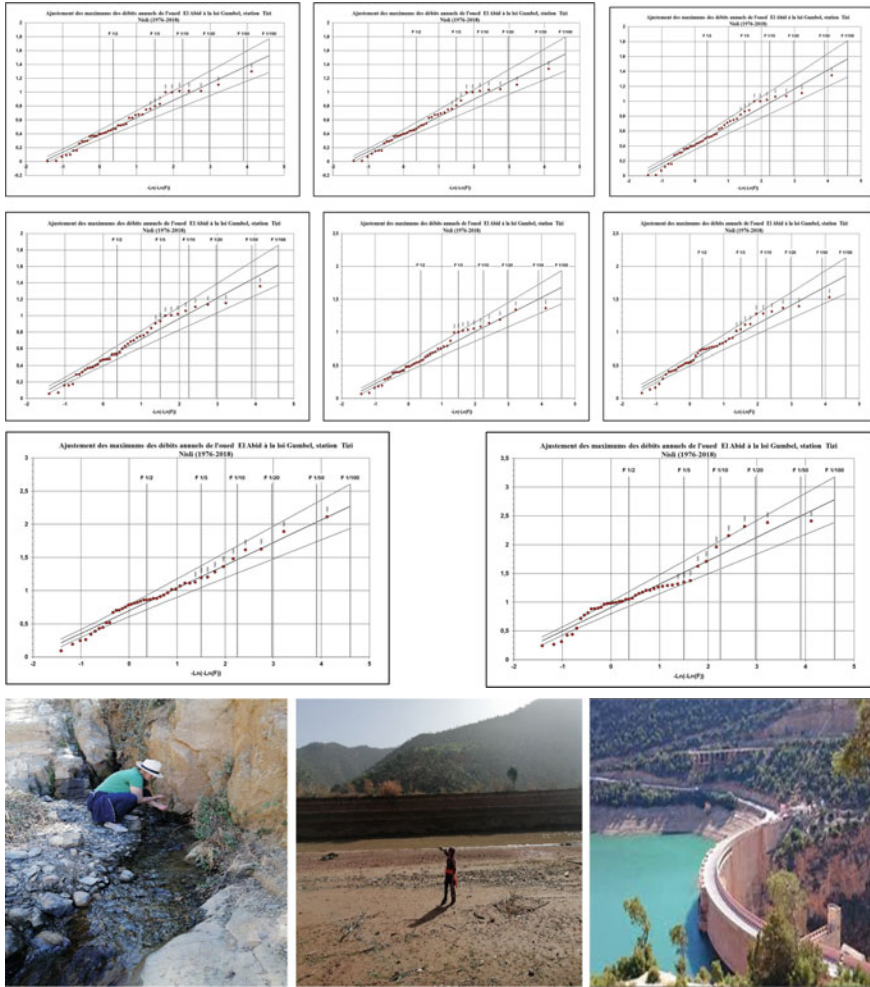
Fig. 9.6 Adjustment of the NCVd of the Tizi Nisli station (1976–2018)

9.4   Conclusion

We understand in the absence of specific legislation for the management of surface water, these considerations on low water levels are only of theoretical interest in Morocco and the underdeveloped country.

Moreover, and given the importance of this phenomenon and its quantification, we can see that the statistics of the Low Flow Indicators (in our case, the VCN indicator was chosen) are fundamental for rational use and management of the resource without long-term imbalance.

Bibliography

Abi-zeid I (1997) La modélisation stochastique des étiages et de leurs durées en vue de l'analyse du risque », Thèse présentée pour l'obtention du grade Philosophiae doctor (phd.) en sciences de l'eau et celui de docteur de l'Engref en statistiques appliquées aux sciences de l'eau, Université du Québec

Elghachi M (2007) Analyse des étiages de 2003 dans un domaine océanique méthodologie et résultats: Le cas de la seille (Lorraine, France). Université Paul Verlaine de Metz, Thèse de doctorat

Gailliez S (2013) Estimation des débits d'étiage pour des sites non jaugés. Application en région wallonne. Thèse de doctorat, Université de Liège—gembloux agro-bio tech

Garcia F (2016) Amélioration d'une modélisation hydrologique régionalisée pour estimer les statistiques d'étiage. 272

Harader E (2015) L'impact du changement climatique sur les événements hydrologiques extrêmes des petits bassins versants méditerranéens: Le cas du bassin versant du Lez. http://www.theses.fr/2015TOU30010/document

Lang C (2010) Étiages et tarissements: Vers quelles modélisations? L'approche conceptuelle et l'analyse statistique en réponse à la diversité spatiale des écoulements en étiage des cours d'eau de l'Est français. 375

Madjid M (2017) Étude des étiages et des débits de base au Nord-Ouest de l'Algérie. » Université de Khmis Miliana

Sirtoum M (1995) Étude hydro-climatologique des bassins du N'fis, du Rhéraya, de l'Ourika et du Zat (Maroc). Thèse de doctorat de l'Université de Metz

Part IV
Groundwater

Chapter 10
Development of Long Short-Term Memory Model for Prediction of Water Table Depth in United Arab Emirates

Pavitra Kumar, Ali Najah Ahmed, Mohsen Sherif, Ahmed Sefelnasr, and Ahmed Elshafie

10.1 Introduction

Ground water is a very crucial source of water supply for humankind (Hanoon et al. 2021). It fulfills one-third of world's water demand (Kombo et al. 2020; Sapitang et al. 2021). Apart from drinking, it is used for lot many purposes, such as, household, agriculture, industries etc. Ground water is being exploited and overused since many years. The demand of groundwater is predicted to rise in upcoming years. However, the recent researches report the decline of ground water level in various part of the world (Kombo et al. 2020), thus requiring awareness for management of groundwater level along with its quality (Afan et al. 2021; Hanoon et al. 2022). The decline of this level is either because of overuse or exploitation of the groundwater or because of the limited groundwater recharge. Overpopulation and intensive use of ground water in agriculture, household and industries have resulted in its overuse (Abuelgasim and Elkamali 2019; Osman et al. 2022). Reduced precipitation and climate change

P. Kumar · A. Elshafie (✉)
Department of Civil Engineering, Faculty of Engineering, Universiti Malaya (UM), 50603 Kuala Lumpur, Malaysia
e-mail: elshafie@um.edu.my

A. N. Ahmed
Institute of Energy Infrastructure (IEI) and Department of Civil Engineering, College of Engineering, Universiti Tenaga Nasional (UNITEN), 43000 Selangor, Malaysia
e-mail: mahfoodh@uniten.edu.my

M. Sherif
Civil and Environmental Engineering Department, College of Engineering, United Arab Emirates University, P.O. Box 15551, Al Ain, United Arab Emirates
e-mail: MSherif@uaeu.ac.ae

A. Sefelnasr
National Water and Energy Center, United Arab Emirates University, P.O. Box 15551, Al Ain, United Arab Emirates
e-mail: ahmed.sefelnasr@uaeu.ac.ae

are considered as the main cause for limited ground water recharge (de Graaf et al. 2017; Haas and Birk 2017; Kombo et al. 2020), thus altering the groundwater balance which results in decline of groundwater level.

United Arab Emirates (UAE) falls within the group of nations with a high evaporation rate due to little precipitation and hot temperatures. Water management is a top priority concern for UAE government (Rizk and Alsharhan 2003). Apart from the groundwater source of water supply, UAE has an alternate source of water supply i.e. desalinated water supply (Al-Ruzouq et al. 2019). Water from the groundwater source is mainly used for agricultural activities and desalinated water is used for non-agricultural activities (UKEssays 2018). Most of the groundwater in entire country is saline, which is mostly used for irrigating date palms due to their salt-tolerance property. Hence, for drinking purpose and other non-agricultural purposes desalinated water is the only option. Artificial recharge of ground water using desalinated water has begun on large scale in some part of the country since 2008. Artificial recharge is an attempt to bring back the declining water table level and also to reduce the dependency on desalinated water, which may not be available in case of any emergency in the country or in case of oil spill in the sea. However, bringing back the declining water level is a tough task for UAE, as most part of the country has seen great decline in water table in recent years (Abuelgasim and Elkamali 2019). According to Sherif et al. (2021), groundwater aquifers have seen a drastic decline in water storage. Quaternary aquifer was recorded to have fresh groundwater of 238 km^3 in 1969 and was again recorded to have just 10 km^3 in 2015. Hence, a great step towards management and restoration of groundwater is urgently needed for UAE. Lot of research work is needed to understand the pattern of the water table level in order to help in its recovery. This paper puts forward an attempt to understand the pattern of water table level and predict the future water table level.

This study's major goal is to look into the possibilities of deep learning modelling in order to create a model that might forecast the groundwater table. In this study, a Long Short-Term Memory (LSTM) model is proposed for predicting the water table depth at six separate wells spread across the UAE one month in advance.

10.2 Materials and Methodology

UAE is situated in the southeastern part of Arabian Peninsula (Fig. 10.1) between the latitude 22 ˚ 50′–26° 4′ N and longitudes 51° 5′–56° 25′ E with total mainland surface area of 83,600 km^2. It has more than 75% of its area covered with desert (Sherif et al. 2014). The temperature of UAE varies from 10 °C in winter season to 48 °C in summer season. UAE is considered as one of the driest places on earth with only less than 200 mm average annual rainfall (Abuelgasim and Elkamali 2019). Such low precipitation throughout the year in entire country is primary reason for limited groundwater recharge in UAE.

For LSTM model development, data from six different water table measuring wells were collected, which are situated at different stations in UAE. Those stations
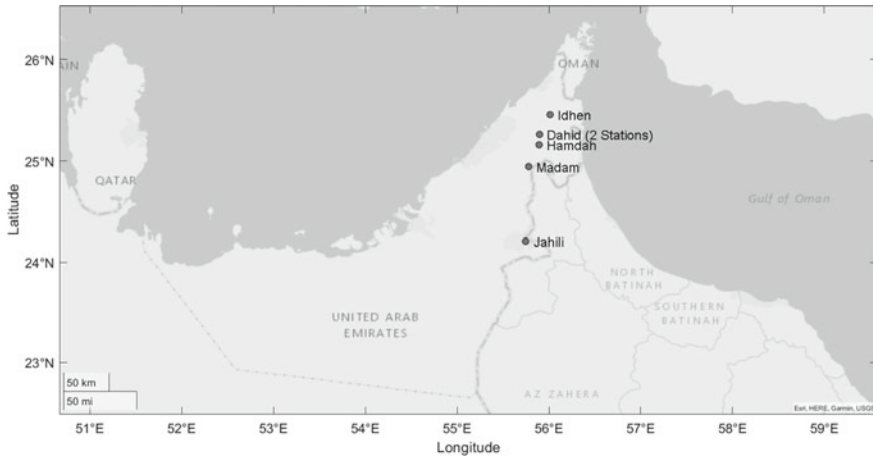
Fig. 10.1 Location of all wells on UAE map

include Madam, 2 wells at Dhaid (Al Naseem, Meliha), Jahili, Idhen, and Hamdah (as presented in Table 10.1 and Fig. 10.1 (plotted on MATLAB)). The water table depth in meters at each well have been collected on monthly basis during the years of operation for each well as presented in Table 10.1. The obtained data was pre-processed to remove the outliers to enable smooth learning of the models. Using these data, six different LSTM models were developed for prediction of water table depth at each selected station. Analyzing the data, the drastic fall of water table was observed in all the six wells. For well1 (station: Madam), water table has declined from 10.85 m in 1977 to 45.68 m in 2011. The decline of water table in other wells can be analyzed from the given opening and closing water table depth data in Table 10.1, where opening data is the depth data at the beginning of the data time period and closing data is the depth data at the end of the data time period. Such drastic decline of the water table depth in such a short time frame in all wells is a very serious concern for the nation.

Table 10.1 Analysis of obtained data

Well	Station Name	Data time period	Opening water table depth (m)	Closing water table depth (m)
Well1	Madam	1977–2011	10.85	45.68
Well2	Dhaid (Al Naseem)	1983–2011	16.74	59.42
Well3	Jahili	1985–2011	31.67	45.26
Well4	Idhen	1979–2007	9.72	58.9
Well5	Hamdah	1983–2011	19.5	30.78
Well6	Dhaid (Meliha)	1983–2011	21.9	27.41

Using the data obtained for all the six wells, six different LSTM models were developed. LSTM model is a special variant of recurrent neural network model. It was designed to overcome the limitation of recurrent neural network, where it faces difficulty in learning long term dependency between the input and target variables (Chung and Shin 2018; Zhang et al. 2017), due to vanishing and exploding gradient problem (Karim et al. 2017; Supreetha et al. 2020). LSTM network contain certain unique gates which is used to learn and memorize the long-term dependence between input and output presented in long sequence of data, which helps in achieving high-precision prediction (Chen 2020). LSTM network is designed to remove or add certain piece of information from the sequence data through these gates (Le et al. 2019; Tian and Pan 2015). Thus, enabling the LSTM network to learn useful piece of information or delete the obsolete piece of information through these gates, thus, improving the learning capability. Figure 10.2 represents the basic structure of LSTM model containing, input (xt), output (ot), input from previous time step (ht − 1, ct − 1) and output to next time stop (ht, ct). These inputs are processed using the Eqs. (10.1–10.6) which uses weight matrices (W, U) and biases b to generate outputs to all output gates.

$$f_t = sigmoid(W_f \times x_t + U_f + h_{t-1} + b_f) \tag{10.1}$$

$$i_t = sigmoid(W_i \times x_t + U_i + h_{t-1} + b_i) \tag{10.2}$$

$$o_t = sigmoid(W_o \times x_t + U_o + h_{t-1} + b_o) \tag{10.3}$$

Fig. 10.2 Basic structure of LSTM
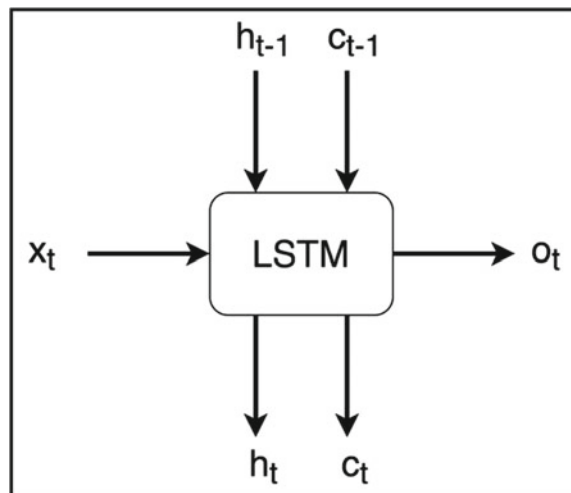
$$c'_t = \tanh(W_c \times x_t + U_c + h_{t-1} + b_c) \qquad (10.4)$$

$$c_t = f_t \cdot c_{t-1} + i_t \cdot c'_t \qquad (10.5)$$

$$h_t = o_t \cdot \tanh(c_t) \qquad (10.6)$$

where: f_t is forget gate; i_t is input gate; o_t is output gate; c_t is cell state; h_t is hidden state.

Observing the unique characteristic of LSTM model, it was chosen for modeling the water table depth at different wells. Data obtained for modeling was only the monthly time series water table depth data. Three time-step lag data was generated using the monthly time series data. The present water table record was utilized as the goal data for the model, while the preceding three time-step water table records were used as the input data. In other words, as shown in Table 10.2, the target water table depth data for a given month is anticipated using the input of the water table depth data from the previous three months. Table 10.2 displays a sample of 10 input and target records for water table depth information from well 1. For all six wells, this process was used to generate input and target data. The LSTM model was then trained using the generated input and target data. Using the Python programming language and TensorFlow libraries, the modelling process was continued.

Table 10.2 Sample of input and target for well 1

Input			Target
Depth (t − 3)	Depth (t − 2)	Depth (t − 1)	Depth (t)
10.81	10.78	10.68	10.85
10.78	10.68	10.85	10.84
10.68	10.85	10.84	10.75
10.85	10.84	10.75	10.73
10.84	10.75	10.73	10.7
10.75	10.73	10.7	10.8
10.73	10.7	10.8	11.08
10.7	10.8	11.08	11.19
10.8	11.08	11.19	11.26
11.08	11.19	11.26	11

Model performance was analyzed using several performance criteria, such as: training and testing R^2, training and testing mean square error (MSE) and maximum percentage error.

R^2 is computed as:

$$r = \frac{n\left(\sum xy\right) - \left(\sum x\right)\left(\sum y\right)}{\sqrt{\left[n\sum x^2 - \left(\sum x\right)^2\right]\left[n\sum y^2 - \left(\sum y\right)^2\right]}} \tag{10.7}$$

MSE us computed as:

$$MSE = \frac{1}{n}\sum_{i=1}^{n}(x - y)^2 \tag{10.8}$$

Maximum percentage error is computed as:

$$Max\,\%Error = \max\left(\frac{|x - y|}{x} * 100\right) \tag{10.9}$$

where: x is target value, y is predicted value, n is number of data samples.

10.3   Results and Discussion

The modeling process resulted in six different LSTM models trained on the generated input and target data for all the six wells. The architecture of the trained model consists of two LSTM layers with a dropout layer after each LSTM layer and a dense layer at the end of sequential layers. Trained models provided good prediction accuracy based on the above-mentioned performance criteria, as presented in Table 10.3. The training R^2 value of all the models is greater than 0.96 and the testing R^2 value of all the models is greater than 0.91. in addition, it is obvious that the proposed LSTM model could achieved a prediction accuracy all wells with acceptable level of accuracy except for Well4. With careful investigation for Table 10.3, it could be depicted that the maximum error ranges between 10 and 28% for all wells except Well4 the maximum error was 96%. It should be noticed here that only one model structure has been applied for all wells, and hence, it is expected the model performance accuracy might be relatively low as in Well4. However, this drawback in the accuracy achieved for Well4 could be improved by adapting the model internal parameters for this particular well to enhance the accuracy.

Table 10.3 Performance analysis of all the six models

Well	Well1	Well2	Well3	Well4	Well5	Well6
Training R^2	0.9881	0.9858	0.9775	0.9679	0.9833	0.9893
Testing R^2	0.9566	0.9905	0.9192	0.9881	0.9557	0.9787
Training MSE	2.2711	1.5339	0.8185	18.4891	0.1596	0.1564
Testing MSE	2.3679	2.0507	0.4358	14.7226	0.1964	0.5542
Testing Max % error	28.47	25.16	11.27	95.96	12.39	10.34

Figure 10.3a–f present the plot of all the performance criteria for wells (1–6), which include the regression plot for testing and training data superimposed in one plot, the percentage error plot with marked maximum percentage error and plot of target and predicted data for both training and testing sets. The plot of target and predicted testing data, presented in Fig. 10.3a–f, represents the prediction capability of the model. It represents that model has learned the pattern of variation of water table depth and is capable of predicting accurately the future water depth data.

With the use of the data from the previous three months' water table depth, separate LSTM models have been trained for each of the six wells to forecast the water table depth one month in advance. In a case when there is a sharp decline in the depth of the water table, these models can aid in the forecast of advanced water table depth at various wells, advancing our understanding and management of the groundwater resource. However, accuracy of all the models could be further enhanced to bring down the maximum percentage error and improve the R^2 values using hybrid modeling. In fact, rather than only using the previous groundwater level as input for the model, further enhancement could be developed by introducing other variables that influence the groundwater level in the model using different scenarios. In addition, the model performance could be improved by integrating it using advanced optimization algorithms that might improve the convergence accuracy and accelerate the time-consuming to achieve the optimal value of the model internal parameters. Furthermore, the model could be examined against other groundwater dataset in different aquifers or different climatic zones.

a

b
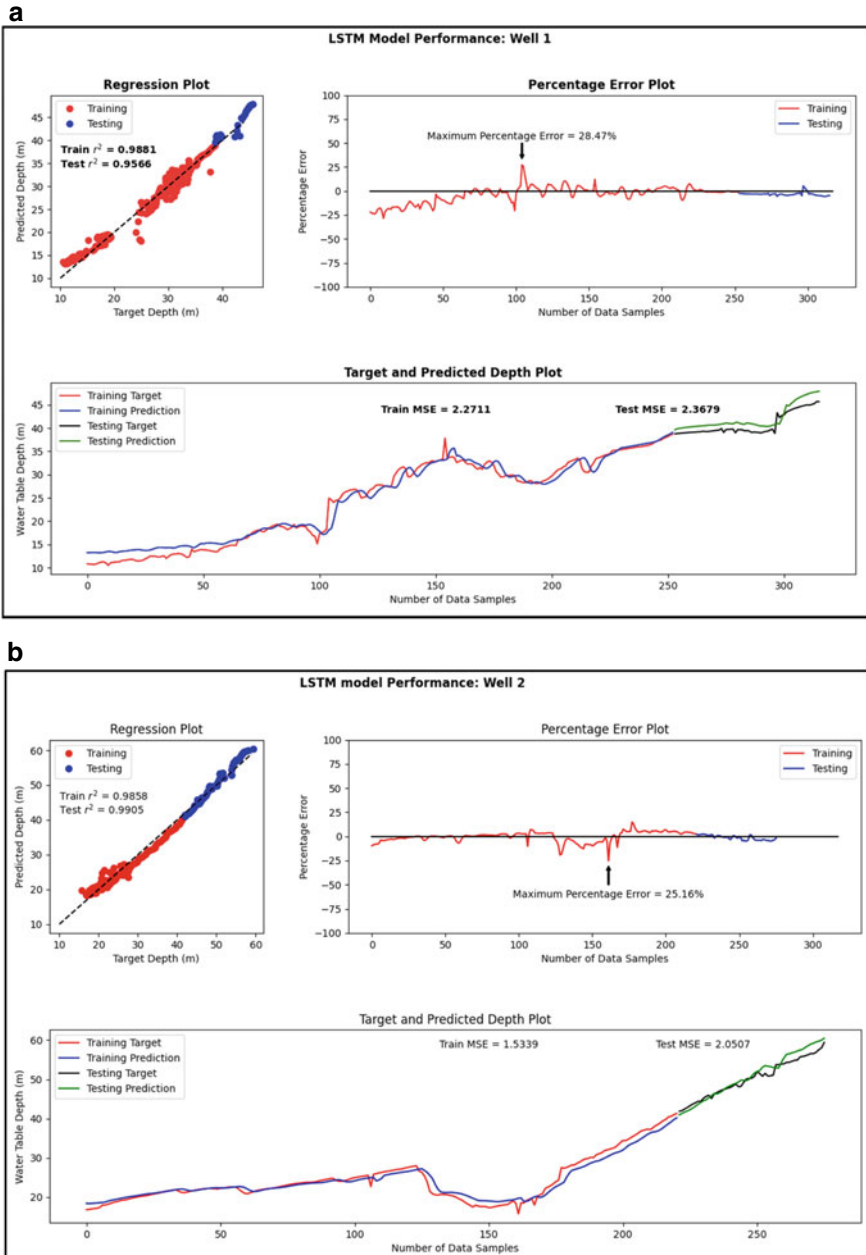
Fig. 10.3 LSTM model performance plot for well 1, **b** LSTM model performance plot for well 2, **c** LSTM model performance plot for well 3, **d** LSTM model performance plot for well 4, **e** LSTM model performance plot for well 5, **f** LSTM model performance plot for well 6
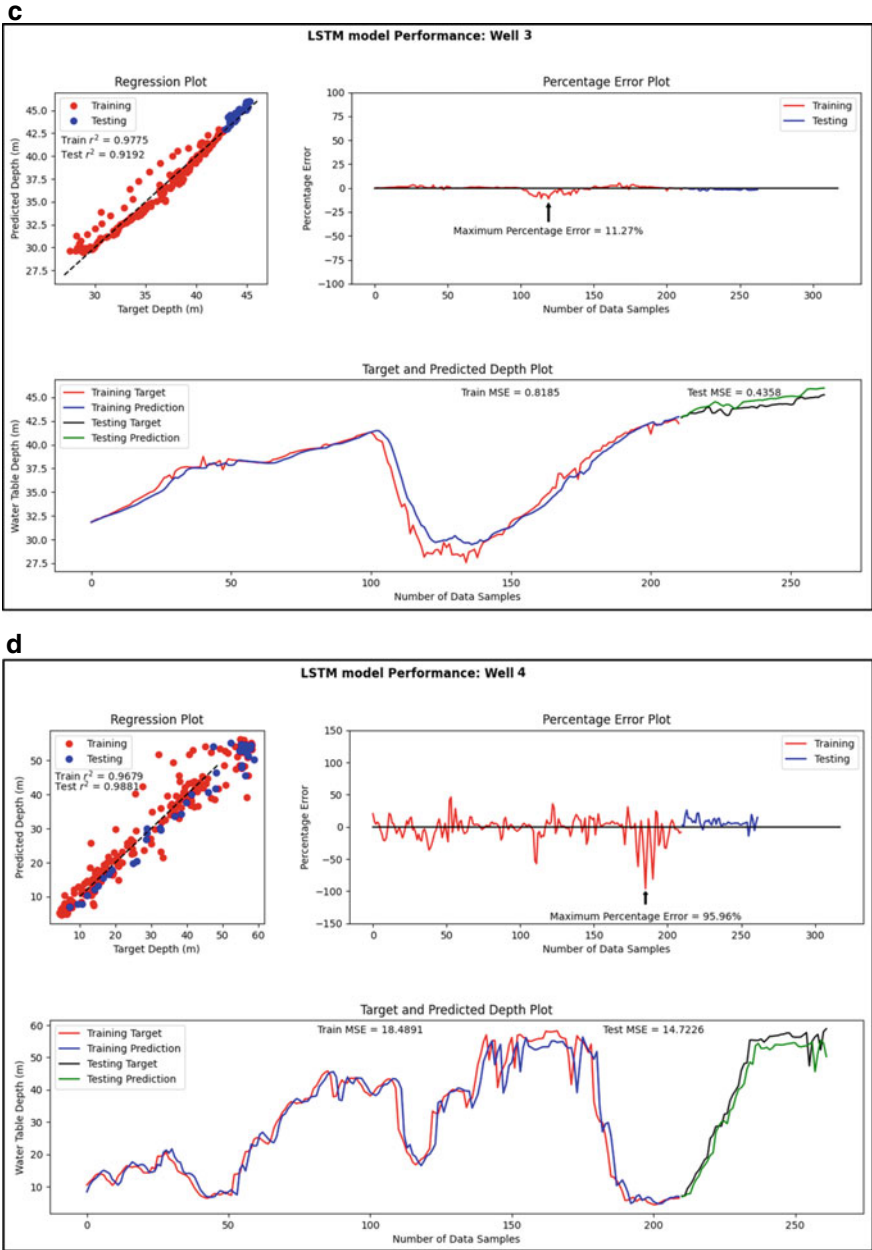
Fig. 10.3 (continued)

e
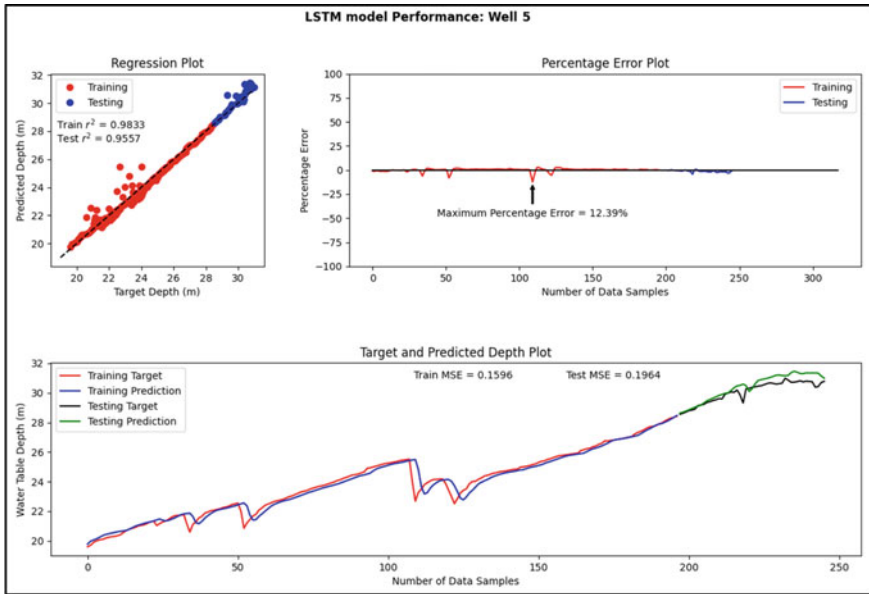
f
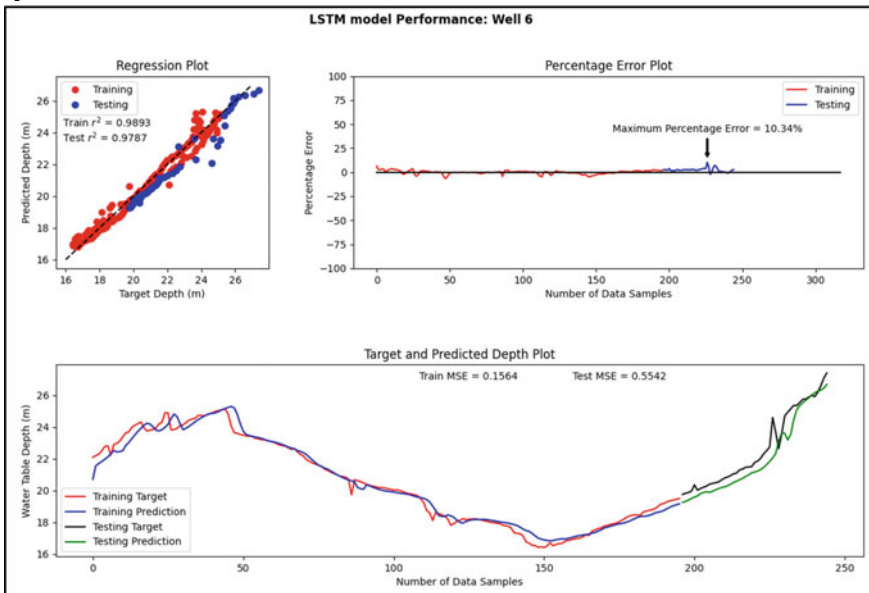
Fig. 10.3 (continued)

10.4 Conclusion

The groundwater table prediction model has been developed using LSTM modeling approach utilizing Python platform as a programming language libraries (Tensor-Flow). The model has been applied using data of six wells at different locations in UAE. These models use data from the past three months' water table depths to predict the water table depth one month in advance. Analysis of the data stated that groundwater has declined drastically between 1977 and 2011. The performance of the models was analyzed through testing and training R^2 values, testing and training MSE values and maximum percentage error. Models trained on this data provide good accuracy in all performance criteria. The coefficient of determination (R^2) achieved during training session were greater than 0.96 for all six models, while during testing session, R^2 values were more than 0.91, which represents consistency in the model performance during training and testing. In addition, these results showed the robustness of the model and its ability for generalization to be applied in different study areas. Predicted one-month in advance water table depth can help in management and restoration of drastically depleting groundwater. However, further modification could be proposed to enhance the accuracy of the results of LSTM models using hybrid models. New direction for modeling structure could be proposed by introducing different input variables that affect the groundwater level and integrate the model with meta-heuristic optimization algorithms to improve the convergence process.

References

Abuelgasim A, Elkamali M (2019) Time series analysis of groundwater levels using geographic information systems in Al Ain region, in the United Arab Emirates

Afan HA, Ibrahem Ahmed Osman A, Essam Y, Ahmed AN, Huang YF, Kisi O, Sherif M, Sefelnasr A, Chau K, El-Shafie A (2021) Modeling the fluctuations of groundwater level by employing ensemble deep learning techniques. Eng Appl Comput Fluid Mech 15(1):1420–1439. https://doi.org/10.1080/19942060.2021.1974093

Al-Ruzouq R, Shanableh A, Merabtene T, Siddique M, Khalil MA, Idris A, Almulla E (2019) Potential groundwater zone mapping based on geo-hydrological considerations and multi-criteria spatial analysis: North UAE. CATENA 173:511–524. https://doi.org/10.1016/j.catena.2018.10.037

Chen K (2020) APSO-LSTM: an improved LSTM neural network model based on APSO algorithm. J Phys Conf Ser 1651(1):012151. https://doi.org/10.1088/1742-6596/1651/1/012151

Chung H, Shin K (2018) Genetic algorithm-optimized long short-term memory network for stock market prediction. Sustainability 10(10). https://doi.org/10.3390/su10103765

de Graaf IEM, van Beek RLPH, Gleeson T, Moosdorf N, Schmitz O, Sutanudjaja EH, Bierkens MFP (2017) A global-scale two-layer transient groundwater model: development and application to groundwater depletion. Adv Water Resour 102:53–67. https://doi.org/10.1016/j.advwatres.2017.01.011

Haas JC, Birk S (2017) Characterizing the spatiotemporal variability of groundwater levels of alluvial aquifers in different settings using drought indices. Hydrol Earth Syst Sci 21(5):2421–2448. https://doi.org/10.5194/hess-21-2421-2017

Hanoon MS et al (2021) Application of artificial intelligence models for modeling water quality in groundwater: comprehensive review, evaluation and future trends. Water Air Soil Pollut 232(10):411. https://doi.org/10.1007/s11270-021-05311-z

Hanoon MS, Ammar AM, Ahmed AN, Razzaq A, Birima AH, Kumar P, Sherif M, Sefelnasr A, El-Shafie A (2022) Application of soft computing in predicting groundwater quality parameters. Front Environ Sci 10. https://doi.org/10.3389/fenvs.2022.828251

Karim F, Majumdar S, Darabi H, Chen S (2017) LSTM fully convolutional networks for time series classification. IEEE Access. https://doi.org/10.1109/ACCESS.2017.2779939

Kombo O, Santhi K, Sheikh Y, Bovim A, Jayavel K (2020) Long-Term groundwater level prediction model based on hybrid KNN-RF technique. Hydrology 7. https://doi.org/10.3390/hydrology7030059

Le X-H, Ho HV, Lee G, Jung S (2019) Application of long short-term memory (LSTM) neural network for flood forecasting. Water 11(7). https://doi.org/10.3390/w11071387

Osman AIA, Ahmed AN, Huang YF, Kumar P, Birima AH, Sherif M, Sefelnasr A, Ebraheemand AA, El-Shafie A (2022) Past, present and perspective methodology for groundwater modeling-based machine learning approaches. Archives Comput Methods Eng 29(6):3843–3859. https://doi.org/10.1007/s11831-022-09715-w

Rizk ZS, Alsharhan AS (2003) Water resources in the United Arab Emirates. In: Alsharhan AS, Wood WW (eds) Developments in water science (vol 50, pp 245–264). Elsevier. https://doi.org/10.1016/S0167-5648(03)80022-9

Sapitang M, Ridwan WM, Ahmed AN, Fai CM, El-Shafie A (2021) Groundwater level as an input to monthly predicting of water level using various machine learning algorithms. Earth Sci Inf 14(3):1269–1283. https://doi.org/10.1007/s12145-021-00654-x

Sherif M, Almulla M, Shetty A, Chowdhury RK (2014) Analysis of rainfall, PMP and drought in the United Arab Emirates. Int J Climatol 34(4):1318–1328. https://doi.org/10.1002/joc.3768

Sherif M, Sefelnasr A, Ebraheem AA, Al Mulla M, Alzaabi M, Alghafli K (2021) Spatial and temporal changes of groundwater storage in the quaternary aquifer, UAE. Water 13(6). https://doi.org/10.3390/w13060864

Supreetha BS, Shenoy N, Nayak P (2020) Lion algorithm-optimized long short-term memory network for groundwater level forecasting in Udupi District, India. Appl Comput Intell Soft Comput 2020:8685724. https://doi.org/10.1155/2020/8685724

Tian Y, Pan L (2015) Predicting short-term traffic flow by long short-term memory recurrent neural network. In: 2015 IEEE international conference on smart city/socialcom/sustaincom (smartcity), pp 153–158

UKEssays (2018) Developing groundwater sources in the UAE. https://www.ukessays.com/essays/biology/developing-groundwater-sources-uae-3714.php?vref=1

Zhang Q, Wang H, Dong J, Zhong G, Sun X (2017) Prediction of sea surface temperature using long short-term memory. IEEE Geosci Remote Sens Lett 14(10):1745–1749. https://doi.org/10.1109/LGRS.2017.2733548

Chapter 11
Assessment and Management of Seawater Intrusion in Gaza Aquifer Due to Over Pumping and Sea Level Rise

Hany F. Abd-Elhamid, Martina Zeleňáková, Akbar A. Javadi, and Khalid Qahman

11.1 Introduction

Coastal regions are increasingly affected by climate change and rising the mean sea levels that increase the erosion, inundation and seawater intrusion (SWI). Climate change is increasing due to natural processes and anthropological activities. Global warming leads to milting polar ice that in turn raises the global mean sea levels. The increase in global mean sea levels has been estimated between 10 and 20 cm during the last century (IPCC 1996). Future sea-level rise is expected to occur at a rate exceeding that of the recent past. In 2100, the rise in mean sea levels is likely to be between 20 and 88 cm (IPCC 2001). Rising sea levels will have numerous effects on coastal regions such as; coastal erosion, submergence of cities, loss of agricultural land, rise in coastal water table and increasing SWI (Abd-Elhamid 2010). Arid regions are likely to be most affected by climate change. These areas suffer from water scarcity and the available water continues to decrease in several countries due

H. F. Abd-Elhamid (✉)
Department of Water and Water Structures Engineering, Faculty of Engineering, Zagazig University, Zagazig 44519, Egypt
e-mail: hany.abdelhamid@tuke.sk; hany_farhat2003@yahoo.com

Department of Environmental Engineering, Faculty of Civil Engineering, Technical University of Kosice, 040 01 Košice, Slovakia

M. Zeleňáková
Institute for Sustainable and Circular Construction, Faculty of Civil Engineering, Technical University of Kosice, 040 01 Košice, Slovakia
e-mail: martina.zelenakova@tuke.sk

A. A. Javadi
Department of Engineering, University of Exeter, Exeter EX4 4QF, UK
e-mail: a.a.javadi@ex.ac.uk

K. Qahman
Environment Quality Authority, Gaza, Palestine

to population growing, excessive abstraction and contamination of groundwater. Appropriate adaptation measures to the expected effect of climate change should be considered. In addition, the over pumping of groundwater that has affected many coastal aquifers should be controlled.

Water scarcity in Gaza Strip is causing a serious and rapidly deteriorating humanitarian crisis. Over pumping has caused depletion of groundwater and increased SWI from the Mediterranean Sea to Gaza aquifer. Gaza aquifer is also exposed to contamination from fertilizers, pesticides and untreated sewage. Pollution has exacerbated by the effect of the conflict on waste-treatment facilities in Gaza Strip that resulted in widespread pollutants in the aquifer. In addition, climate change predictions indicate an imminent catastrophe. When the temperature rises, drought could increase and when the sea level rises SWI could accelerate. Rising sea level poses a major challenge for the people in Gaza, as it might submerge much of Gaza's territory. SWI and aquifer pollution adversely affect the population and environment in Gaza Strip (Qahman 2004).

Previous studies have shown that SWI in Gaza Strip has extended to more than 3 km inland. A number of studies were conducted to simulate SWI in Gaza aquifer (e.g., Yakirevich et al. 1998; Qahman and Zhou 2001; and Qahman and Larabi 2003a, b, 2006). Abd-Elhamid et al. (2015) investigated the effect of rising sea levels and over pumping on SWI in Jabylia in the north of Gaza Strip. The study showed that sea level rise has increased SWI into the aquifer and protection measures are necessary. Abd-Elaty et al. (2020) studied the control of SWI in the aquifer of Gaza through abstraction of saline water, increase of the recharge and applying the two scenarios together. The results showed that increasing recharge of the aquifer could decrease SWI more compared to increasing the abstraction of saline water. Abualtayef et al. (2017) assessed different water resources management plans impact on groundwater levels in Gaza. They applied different management scenarios such as; storm water infiltration, wastewater reuse in agriculture, importing water from Israel and desalination. The study showed that application of these management scenarios could enhance groundwater level in Gaza aquifer. Sarsak (2011) applied SEAWAT to investigate SWI in Gaza aquifer considering climate change. The results revealed that SWI is more sensitive to decrease in recharge compared to increase in pumping rates. The study suggested using new resources such as treated wastewater and desalination to overcome the water shortage in the Strip. Sarsak and Almasri (2013) used SEAWAT code to simulate SWI in Gaza aquifer due to seal level rise and climate change. The results showed that SWI increased by 80 m/year compared to 65 m/year in 2010.

The current study presents the development and application of a coupled transient finite element model to investigate SWI in Gaza aquifer considering over pumping and sea level rise. Different scenarios are applied to manage SWI in Gaza aquifer including; reducing the abstraction, increasing the recharge and combination of reducing abstraction and increasing recharge. The study focuses on Wadi Gaza at the middle of Gaza Strip that is subject to sever SWI and contamination by fertilizers, pesticides and untreated sewage.

11.2 Materials and Methods

This section describes the development of the numerical model (2D-FEST), study area, and the boundary conditions of Gaza aquifer.

11.2.1 Study Area and Boundary Conditions

Gaza Strip is located in the Mediterranean coastal plain between Egypt and Israel (Fig. 11.1). It is in the form of a long and narrow rectangle with length of 45 km and width varing between 5 and 10 km. It mainly slopes toward the sea and groundwater flows to the west toward the Mediterranean Sea, with maximum thickness of saturated zone of 120 m. The total area of Gaza Strip is 365 km^2 and its population is 1.5 million. Gaza aquifer is the only source of freshwater, and supplies more than 95% of the water used in agriculture, household and industry in the Strip. Water is pumped from more than 3000 wells and the total estimated annual production is about 140 million cubic meters (Qahman and Larabi 2006). Three vertical cross sections were selected in the north, middle and south to study SWI in the aquifer at Jabalya, Wadi Gaza and Khan Yunis as shown in Fig. 11.1. Jabalya is located north of Gaza Strip, with 5000 m length and 100 m depth. Wadi Gaza is located in the middle part of Gaza Strip with 2000 m length and 100 m average depth. Khan Yunis is located south of Gaza Strip with 5000 m length and 100 m depth.

Gaza aquifer is considered confined, homogeneous and isotropic in terms of freshwater hydraulic conductivity, molecular diffusion, and longitudinal and transverse dispersivities. The aquifer is exposed to SWI along the sea side boundary and a uniformly distributed lateral flow along the inland side. A 1.0 m constraint head is used on the land side and zero head at the sea side. The hydraulic conductivity is 0.2 m/day and the effective porosity is 0.35. Longitudinal and transverse dispersivities (α_L and α_T) are 50 and 0.1 m respectively. Freshwater density ρ_f and seawater density ρ_s are 1.0 and 1.025 t/m^3 respectively (Qahman 2004). Flow boundary conditions include impermeable boundaries along the top and the bottom of the aquifer. Constant head and concentration are defined to the model along the coast. The aquifer is charged by freshwater with constant flux at the inland side and concentration (TDS) of 35 kg/m^3 is considered on the sea side (Qahman 2004).

11.2.2 Numerical Model

A finite element model was developed to simulate SWI. The partial differential equations of water flow and solute transport are presented in terms of two variables; pore-water pressure (u_w) and solute concentration (c). For detailed information related to
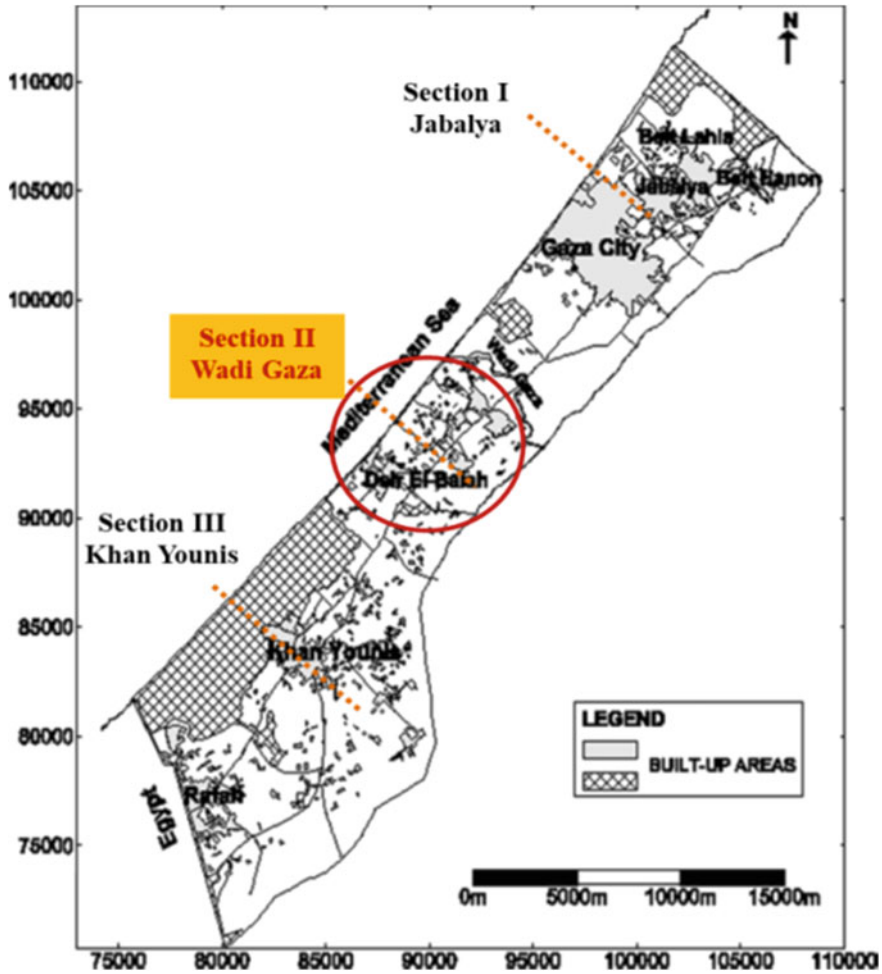
Fig. 11.1 Location map of Gaza aquifer

differential equations and numerical solution of the coupled fluid flow and solute transport (2D-FEST) see (Abd-Elhamid 2010; Abd-Elhamid and Javadi 2011a, b). The differential equations of water flow and solute transport can be described as (Abd-Elhamid 2010):

Water flow equation:

$$
\begin{aligned}
C_{ww}\frac{\partial u_w}{\partial t} + C_{wT}\frac{\partial T}{\partial t} + C_{wa}\frac{\partial u_a}{\partial t} &= \nabla[K_{ww}\nabla u_w] \\
&+ \nabla[K_{wT}\nabla T] + \nabla[K_{wa}\nabla u_a] + \rho_w\nabla(K_w\nabla z)
\end{aligned}
\tag{11.1}
$$

Solute transport equation:

$$\frac{\partial((\theta_w + H\theta_a)c)}{\partial t} = -\left[\left(\frac{\partial}{\partial x}(v_{w_x}c) + \frac{\partial}{\partial y}(v_{w_y}c)\right) + \left(\frac{\partial}{\partial x}(v_{a_x}c) + \frac{\partial}{\partial y}(v_{a_y}c)\right)\right]$$
$$+ \left[\left\{\frac{\partial}{\partial x}\left(D_{w_{xx}}\frac{\partial}{\partial x}(\theta_w c) + D_{w_{xy}}\frac{\partial}{\partial y}(\theta_w c)\right)\right.\right.$$
$$+ \frac{\partial}{\partial y}\left(D_{w_{yy}}\frac{\partial}{\partial y}(\theta_w c) + D_{w_{yx}}\frac{\partial}{\partial x}(\theta_w c)\right)\right\}$$
$$+ H\left\{\frac{\partial}{\partial x}\left(D_{a_{xx}}\frac{\partial}{\partial x}(\theta_a c) + D_{a_{xy}}\frac{\partial c}{\partial y}(\theta_a c)\right)\right.$$
$$\left.\left.+ \frac{\partial}{\partial y}\left(D_{a_{yy}}\frac{\partial}{\partial y}(\theta_a c) + D_{a_{yx}}\frac{\partial}{\partial x}(\theta_a c)\right)\right\}\right]$$
$$- \frac{\partial}{\partial t}(\rho_b K_d c) - (\lambda_w \theta_w + H\lambda_a \theta_a)(1 + \rho_b K_d/\theta_w)c = 0 \quad (11.2)$$

11.3   Results

The developed model (2D-FEST) is used to investigate SWI in Gaza aquifer in the vertical view at three sections. Then Wadi Gaza section is investigated under the condition of over pumping and sea level rise. Then different scenarios are applied to control the SWI at Wadi Gaza.

11.3.1   Current Situation of SWI in Gaza Aquifer

The developed model is used to investigate SWI in the three vertical cross sections in order to predict SWI in different locations in Gaza aquifer. Figure 11.2a–c show the concentration distributions for the three cross sections. The results indicate that the aquifer is subject to severe SWI and the groundwater is not suitable for human consumption. Isoline 1 (1000 ppm) intruded inland 3.75 km along the bottom boundary at Jabalya (Fig. 11.2a). The same isoline intruded inland 1.45 km at Wadi Gaza (Fig. 11.2b) and 2.75 km at Khan Yunis (Fig. 11.2c).

11.3.2   Numerical Model Verification

According to the geophysical survey results obtained by PWA/CAMP (2000), the extent of SWI at Khan Yunis ranged between 1 and 2 km. Qahman and Larabi (2006) used SEAWAT to assess SWI in Gaza aquifer. They estimated that the extent of SWI

(a) SWI at Jabalya

(b) SWI at Wadi Gaza

(c) SWI at Khan Younis
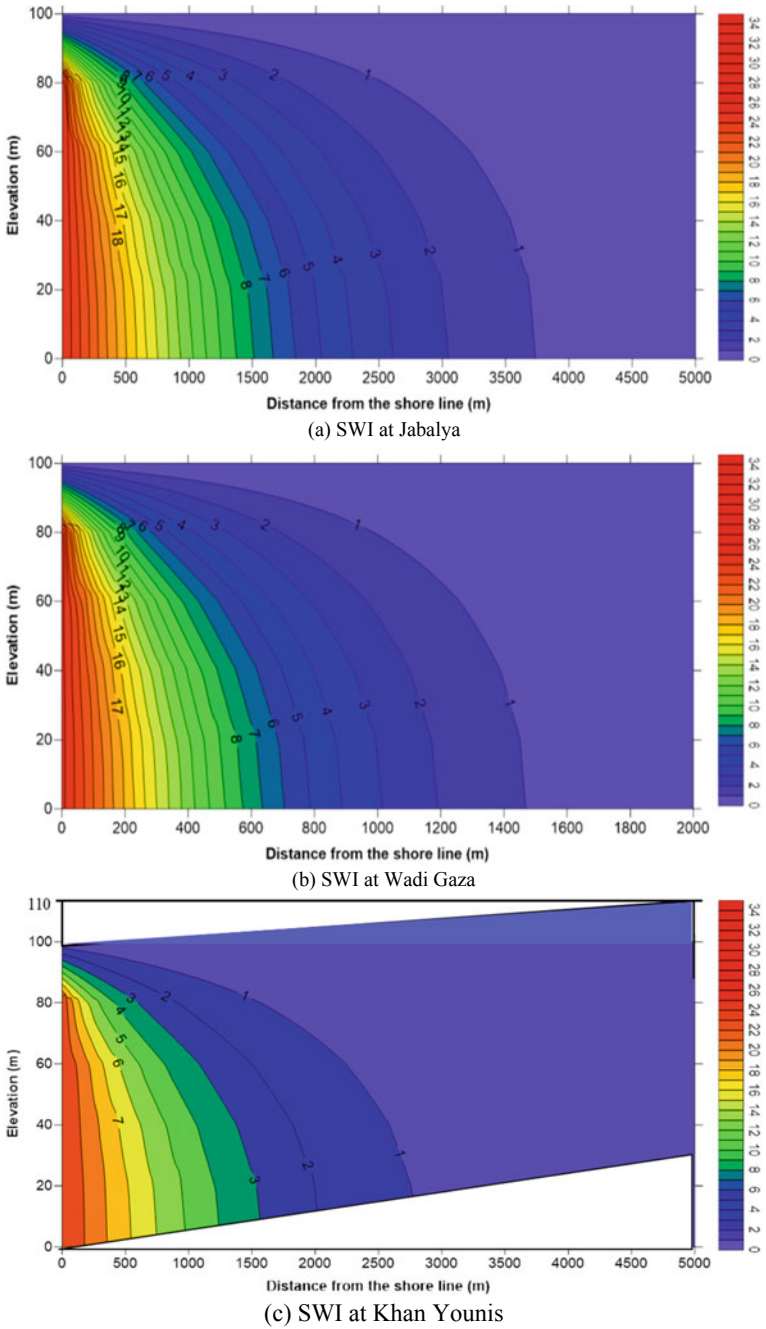
Fig. 11.2 Current situation of SWI in Gaza aquifer

at Khan Yunis (in 2003) ranged between 1 and 2 km for isoline 2 (2000 ppm), which is consistent with the geophysical survey results (see Fig. 11.3a, b). The current model results indicated that SWI at Jabalya was approximately 3 km for isoline 2 (Fig. 11.2a). Also, Qahman and Larabi (2006) estimated the extent of SWI at Khan Yunis to be about 3 km (in 2003) (Fig. 11.3b), which is consistent with the results obtained by the current model (Fig. 11.2c). The results of the (2D-FEST) model are consistent with the results of previous models (e.g. Qahman and Zhou 2001; Qahman and Larabi 2003a, b; Qahman and Larabi 2006) and the geophysical survey results reported by PWA/CAMP (2000). The comparison between the results of (2D-FEST) and (SEAWAT) shows good agreement in concentration distribution in the vertical sections.
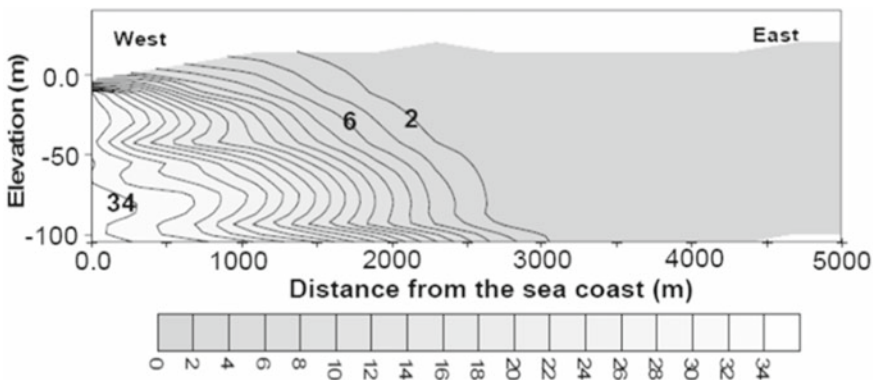
(a) SWI at Jabalya
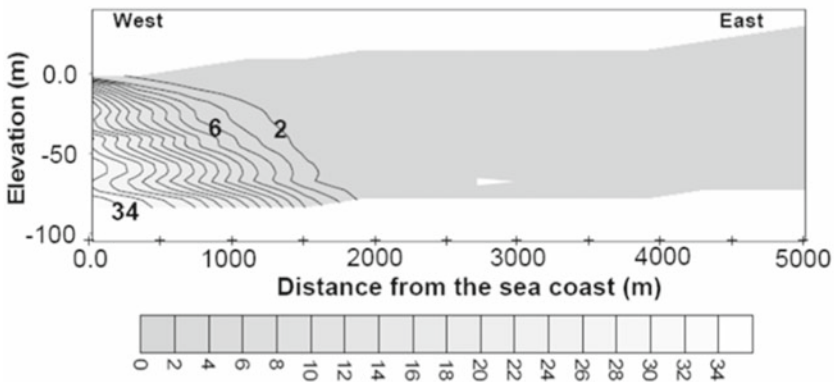
(b) SWI at Khan Yunis

Fig. 11.3   SWI in Gaza aquifer calculated by SEAWAT (Qahman and Larabi 2006)

11.3.3 Seawater Intrusion in Wadi Gaza in Response to Over Pumping and Sea Level Rise

The developed model applied to investigate various scenarios at Wadi Gaza including: over pumping, rising sea level and combination of the two. In the first scenario, to investigate the impact of over pumping, the water level was lowered by 0.5 m on the land side and the sea level was not changed. In the second scenario, sea water level was raised by 1.0 m and the groundwater level on land side was not changed. In the third scenario, the land side water level was dropped by 0.5 m and the sea water level was raised by 1.0 m. Figure 11.4 shows the results of the three scenarios. In the first scenario, when the groundwater level was lowered by 0.5 m, isoline 1 intruded to a distance of 1.65 km. In the second scenario, when the sea water level was increased (1 m), isoline 1 intruded to a distance of 1.7 km. However, in the third scenario, which combines the two previous scenarios, isoline 1 intruded inland to a distance of 1.80 km. The results showed that the aquifer in Wadi Gaza is almost contaminated by saline water and serious actions are necessary to defend the aquifer because groundwater is the main source of water in Gaza strip.

11.3.4 Management of SWI in Wadi Gaza

In order to protect Wadi Gaza from the increase in SWI due to over pumping and SLR, the developed model was used to manage SWI in the aquifer using different scenarios including; decrease the abstraction from the aquifer and use other water sources, increase the aquifer recharge using tertiary treated wastewater and combination of the two. In the first scenario, the pumping rate was reduced by 50%. When this was applied to the model, SWI was retarded 1.55 km toward the sea (Fig. 11.5a). In the second scenario, the aquifer recharge was increased by 50%. This resulted in retardation of SWI to 1.50 km (Fig. 11.5b). However, combination of the two scenarios resulted in further retardation of SWI to 1.35 km (Fig. 11.5c). The results indicate that to adapt with the expected over pumping and sea level rise, the abstraction should be decreased and the recharge should be increased. This would allow mitigating the likely effects of over pumping and sea level rise in the future at Wadi Gaza.

11.4 Discussions

Comparison between different scenarios (7) of SWI in Wadi Gaza is presented in Fig. 11.6. The results show that SWI reached 1.45 km inland in the base case. A 100 cm sea level rise increased SWI to 1.7 km inland. Increasing the abstraction increased the intrusion to 1.65 km inland. However, the combination of the two

(a) SWI in at Wadi Gaza due to over pumping

(b) SWI in at Wadi Gaza due to (SLR=100 cm)

(c) SWI in at Wadi Gaza due to over pumping and SLR = 100 cm
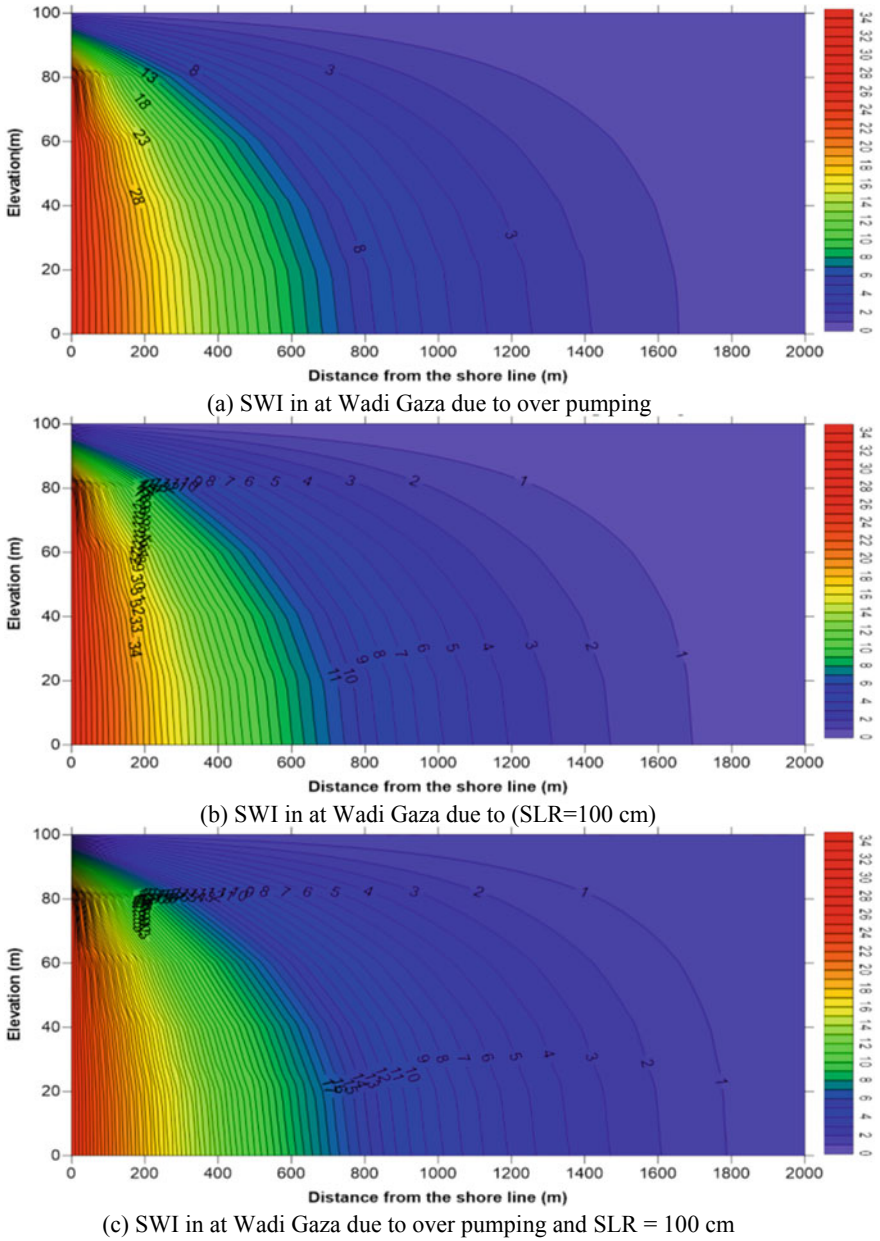
Fig. 11.4 SWI in Gaza aquifer due to over pumping and sea level rise

(a) SWI in Wadi Gaza due to decreasing abstraction (50%)

(b) SWI in Wadi Gaza due to increasing the recharge (50%)

(c) SWI in Wadi Gaza due to combination of decreasing abstraction and increasing recharge
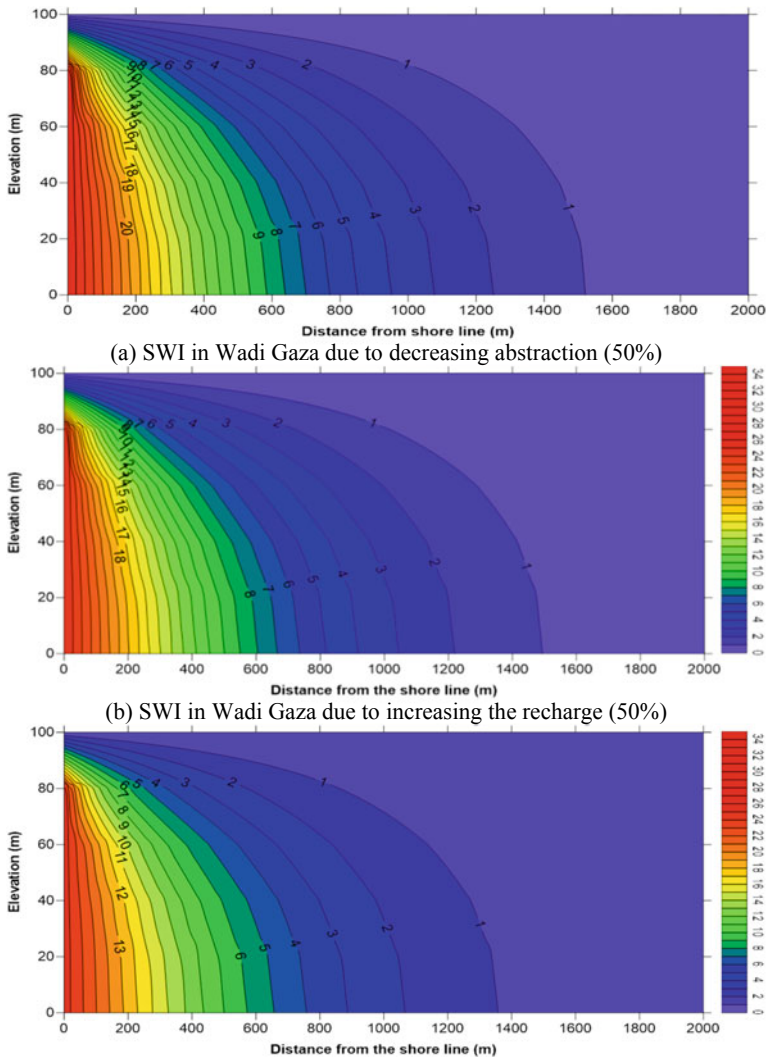
Fig. 11.5 Management scenarios of SWI in Wadi Gaza

scenarios increased the intrusion to 1.8 km inland which is considered the new location of SWI in Wadi Gaza. To prevent such intrusion different scenarios were applied. Decreasing abstraction (50%) retarded the intrusion to 1.55 km; increasing recharge (50%) retarded the intrusion to 1.50 km and combination of the two scenarios retarded the intrusion to 1.35 km.
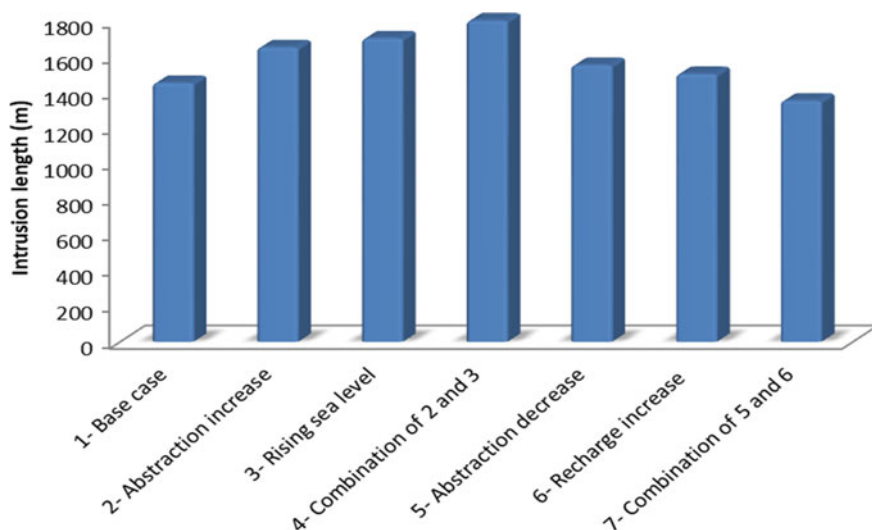
Fig. 11.6 Comparison between different scenarios of SWI in Wadi Gaza

Finally, the results show that over pumping and sea level rise could increase SWI but decreasing abstraction and using other water resources and increasing the recharge using treated wastewater could protect the aquifer from deterioration.

11.5 Conclusions

Climate change and sea level rise could have serious impacts on coastal areas. Sea level is expected to rise between 20 and 88 cm by 2100. This could affect coastal cities and coastal aquifers as it would increase land subsidence and seawater intrusion (SWI). Around the world, several coastal aquifers are being exploited due to over pumping. Gaza aquifer is one of the aquifers that will be affected by over pumping and sea level rise. This study presented the impact of over pumping and sea level rise on Gaza aquifer and suggested some management scenarios. A numerical model was developed and applied to assess SWI in the Gaza aquifer. This study emphases on Wadi Gaza which has been severely affected by SWI. The results revealed that SWI at Wadi Gaza reached to 1.45 km inland for isoline 1 (1000 ppm). over pimping has increased SWI to the aquifer and rising sea levels has also increased the intrusion but combination of the two scenarios has resulted in more intrusion of saline water into the aquifer. Different scenarios have been applied to protect Gaza aquifer from the increase in SWI. These scenarios include reducing the abstraction from the aquifer (50%), decreasing the recharge to the aquifer (50%) and combination of the two. It was shown that decreasing abstraction from the aquifer would result in retardation of SWI toward the sea. Increasing the aquifer recharge would also result in retardation

of the intrusion of seawater. However, combination of the two scenarios would result in more retardation of SWI, which could mitigate the likely influence of sea level rise. These methodologies can be also applied to protect other aquifers around the world from over pumping and sea level rise impacts. However, 3D model such as SEWAT is recommended for future work on Wadi Gaza to include the pollution of the aquifer due to fertilizers, pesticides and untreated sewage combined with SWI.

References

Abd-Elaty I, Abd-Elhamid HF, Qahman K (2020) Coastal aquifer protection from saltwater intrusion using abstraction of brackish water and recharge of treated wastewater: case study of the Gaza aquifer. J Hydrol Eng 25(7):05020012. https://doi.org/10.1061/(ASCE)HE.1943-5584.0001927

Abd-Elhamid HF (2010) A Simulation-optimization model to study the control of seawater intrusion in coastal aquifers. University of Exeter

Abd-Elhamid HF, El-Kilany ME, Javadi AA (2015) A cost-effective method to protect the coastal regions from sea level rise. A case study: northern coasts of Egypt. J Water Clim Change 7(1):114–127. https://doi.org/10.2166/wcc.2015.158

Abd-Elhamid HF, Javadi AA (2011a) Impact of sea level rise and over-pumping on seawater intrusion in coastal aquifers. J Water Clim Change 2(1):19–28. https://doi.org/10.2166/wcc.2011.053

Abd-Elhamid HF, Javadi AA (2011b) A cost-effective method to control seawater intrusion in coastal aquifers. Water Resour Manage 25(11):2755–2780. https://doi.org/10.1007/s11269-011-9837-7

Abualtayef M, Rahman GA, Snounu I, Qahman K, Sirhan H, Seif AK (2017) Evaluation of the effect of water management interventions on water level of Gaza coastal aquifer. Arab J Geosci 10:1–19

IPCC (1996) Climate change the science of climate change: contribution of working group I to the second assessment report of the intergovernmental panel on climate change. Cambridge University Press

PWA/CAMP (2000) Coastal aquifer management program (CAMP) [Final Model Report (task 7)]

Qahman K (2003a) Identification and modelling of seawater intrusion of the Gaza Strip Aquifer, Palestine. In: Proceedings of TIAC03 international conference, Alicante, Spain, vol 1, pp 245–254. https://www.academia.edu/28061298/Identification_and_Modelling_of_Seawater_Intrusion_of_the_Gaza_Strip_Aquifer_Palestine

Qahman K (2003b) Simulation of seawater intrusion using SEAWAT code in Khan Yunis Area of the Gaza Strip aquifer, Palestine. In: Proceedings of JMP2003b international conference, Toulouse. https://www.academia.edu/28061298/Identification_and_Modelling_of_Seawater_Intrusion_of_the_Gaza_Strip_Aquifer_Palestine

Qahman KA (2004) Aspects of hydrogeology, modeling and management of seawater intrusion for Gaza Aquifer Palestine

Qahman KA, Zhou Y (2001) Monitoring of seawater intrusion in the Gaza Strip, Palestine. 23

Qahman K, Larabi A (2006) Evaluation and numerical modeling of seawater intrusion in the Gaza aquifer (Palestine). Hydrogeol J 14:713–728. https://doi.org/10.1007/s10040-005-003-2

Sarsak R, Almasri MN (2013) Seawater intrusion into the coastal aquifer in the Gaza Strip: a computer-modelling study. Lancet 382
Sarsak RFS (2011) Numerical simulation of seawater intrusion in response to climate change impacts in North Gaza Coastal aquifer using SEAWAT. An-Najah National University, Nablus
Yakirevich A, Melloul A, Sorek S, Shaath S, Borisov V (1998) Simulation of seawater intrusion into the Khan Yunis area of the Gaza Strip coastal aquifer. Hydrogeol J 6(4):549–559. https://doi.org/10.1007/s100400050175

Chapter 12
Analysis of a Joint Impact of Climate Change and Anthropogenic Interventions on Groundwater Depletion in Arid and Semi-Arid Areas

Mohammed Nanekely, Furat Al-Faraj, and Miklas Scholz

12.1 Introduction

12.1.1 Aim

The rapid growth of water demand for irrigated agriculture and water supply for domestic, industrial, and commercial uses has noticeably increased the pressure on groundwater resources particularly in arid and semi-arid areas where the dependency on groundwater is between 60 and 100% (Margane 2003). Large-scale pumping of groundwater can pose significant adverse impacts on both the ecosystems and the long-term socio-economic developments. A considerable drop in groundwater levels has been observed and reported in many parts of the world due to excessive use of groundwater, especially for irrigated agriculture (Margane 2003; Nanekely et al. 2017).

M. Nanekely · F. Al-Faraj (✉)
Civil Engineering Research Group, School of Science, Engineering and Environment, The University of Salford, Newton Building, Salford M5 4WT, UK
e-mail: f.al-faraj@bolton.ac.uk

M. Nanekely
e-mail: m.a.a.nanekely@edu.salford.ac.uk

F. Al-Faraj
School of Engineering, The University of Bolton, Bolton BL35AB, UK

M. Scholz
Division of Water Resources Engineering, Department of Building and Environmental Technology, Faculty of Engineering, Lund University, P.O. Box 118, 221 00 Lund, Sweden
e-mail: miklas.scholz@tvrl.lth.se

Department of Civil Engineering Science, School of Civil Engineering and the Built Environment, University of Johannesburg, Kingsway CampusAukland Park 2006, PO Box 524, Johannesburg, South Africa

Accurate measurements of changes in groundwater storage require intense networks of observation wells, continuous monitoring and good knowledge of the aquifer characteristics and groundwater replenishment process (Gale 2005). Alley et al. (2017) reported that there is an urgent need to strengthen current data collection protocols to develop indicators for the sustainable management of groundwater resources and to achieve the United Nations Sustainable Development Goals 2030 Agenda items food security, human health, water, energy generation, resilient cities, and ecosystem conservation (United Nations 2019).

Population growth coupled with related hastened social and economic activities such as expanding agricultural areas are key drivers for increased demand of water world-wide (Wada et al. 2010). Hameed et al. (2015) pointed out that Erbil has undergone remarkable changes to its urban areas, which have increased by 278% between 2004 and 2014. In contrast, the level of groundwater has declined by more than 54%.

The problem of water shortage resulting from excessive abstraction or unwise exploitation of groundwater is further exacerbated by impacts of climate change in many parts of the world suffering from a decrease in precipitation and an increase in temperature and potential evapotranspiration rates (Margane 2003; Nanekely et al. 2017). Groundwater systems are vulnerable to changes in precipitation patterns, particularly in areas where the climate change trend is towards increased temperature and potential evapotranspiration rates as well as reduced precipitation.

Literature sources show that drought episodes and climate change are likely to put challenges to sustainably manage water resources, which require extensive investigations on potential impacts of climate anomalies on water availability and governance (Al-Faraj et al. 2014; Al-Faraj and Al-Dabbagh 2015; Al-Faraj and Scholz 2015, 2014). On the other hand, these anomalies may be buffered by groundwater-fed irrigation supply and are consequently essential to food security. Therefore, irrigation mitigates poverty in low-income countries by reducing harvest failure and increasing production. The exploitation of harvested rainwater and groundwater-fed irrigation have a notable contribution to replenish groundwater by 10.8 and 15.2% of total rainfall and irrigation, respectively, in semi-arid regions (Ebrahimi et al. 2016).

Green et al. (2011) pointed out the importance of assessing and understanding potential impacts of climate anomaly and variability to sustainably manage groundwater aquifers, while taking into consideration increasing stresses on groundwater resources due to population growth, elevated irrigation demands, increased public water supplies, and enhanced ecological needs. However, future groundwater recharge management and mechanisms should be incorporated within general climate models that account for the expected climate alterations (Smerdon 2017).

Lorenzo-Lacruz et al. (2017) mentioned that due to uncertainty associated with precipitation patterns and water availability in many regions under Mediterranean climatic conditions, understanding the spatial–temporal response of groundwater systems to precipitation variability is decisive for the sustainable use and management of groundwater. Nanekely et al. (2017) underlined the need to conduct detailed studies on changes of groundwater storage in water-scarce areas to achieve sustainable utilization of groundwater resources.

Unmanaged extraction of water from aquifers could (a) lead to insufficient water volumes required to sustainably support local socio-economic development; (b) increase energy consumption as higher power is required to pump-out groundwater when the water level is declining; (c) elevated cost and inequity in accessing water; and (d) deteriorate groundwater quality due to over-exploitation of groundwater storage (Gale 2005).

Margane (2003) pointed out the importance of establishing a guideline for delineation of groundwater protection zones in which certain land-use and human activities are either approved or restricted. The guideline associated with enforcement procedures aims to protect water wells from becoming polluted by point sources and diffuse pollution sources. In conjunction with a groundwater regulatory framework associated with well-defined procedures, an intensive monitoring network must be set up to ensure appropriate implementation and follow-up of procedures.

Recent research on groundwater depletion in Erbil city (part of Erbil province) showed that the drops in groundwater levels were between 11 and 88% for the period 2000–2015 (Nanekely et al. 2017). The authors suggested that drops in groundwater levels are mainly attributed to excessive withdrawals of groundwater associated with these two drought periods: 1999–2001 and 2007–2008. This indicated the sensitivity of groundwater storage to both groundwater abstraction and drought periods. However, findings were only based on the examination of 20 observation wells within Erbil city. This called for a more comprehensive study considering a higher number of observation wells covering a larger area of the Erbil province. Moreover, understanding responses of groundwater bodies and changes of groundwater storage with respect to monthly, seasonal, and annual precipitation variability is essential for rational withdrawal and sustainable management of groundwater. Castle et al. (2014) believe that dynamic conditions can be reliable by policymakers to manage water resources in semi-arid areas because of imbalance in consumptions from both surface and groundwater due to a lack of surface water supply.

Gale (2005) pointed out that the rational utilization of groundwater and sustainable management of aquifers can play an important role in (a) poverty and drought mitigation; (b) economic and health risk reductions; (c) irrigated agriculture support; and (d) access to water in an equitable manner. Management of aquifer(s) and rainwater harvesting system(s) maintains the above-mentioned benefits; particularly, if considered and practiced as a fundamental part of integrated water resources management that addresses the imbalance between water demand, supply, and water quality as well as impact of climate change.

12.2   Aim

This study focuses on Erbil province in Iraq, which is comparable to other areas located in arid and semi-arid regions suffering challenges in managing groundwater resources sustainably. This article aims to assess the changes in groundwater levels

responding to seasonal and annual precipitation variability, investigating the long-term decline in groundwater levels, and evaluating the impacts of climate change on groundwater abstraction. The outcomes of this article are an important step in establishing a nation-wide program to achieve sustainable abstraction and rational utilization and management of groundwater resources. This study also supports the achievements of the United Nations Sustainable Development Goals 2, 3, 6, 7, 11 and 15 (United Nations 2019).

12.2.1 Methods

12.2.1.1 Example Case Study Region

Erbil Province, which is located in the northern part of Iraq (Kurdistan region), covers an area of 15,089 km^2 (3.5% of Iraq) and has been chosen as an example case study where (a) groundwater is over-exploited; (b) climate change results in an increase in temperature and potential evapotranspiration rates and reduces precipitation; (c) there is a lack of solid and consistent application of groundwater artificial recharge systems; (d) integrated land-use planning is insufficient; (e) laws and regulations regarding the drilling of wells and enforcement of groundwater development regulations are absent or weak; and (f) there is a shortage of financial provisions needed to implement and/or rehabilitate relevant infrastructure.

Erbil province is located between two rivers, the Greater-Zab River to the north-northwest and the Lesser Zab River to the south-southeast. The study area varies in elevation from 175 m above sea level (masl) south of Makhmur to more than 2500 masl in the north of the province (Fig. 12.1). The average annual rainfall ranges between about 200 and 975 mm. The mean annual temperature of the study area is between 10.5 and 22 ºC. The long-term mean annual potential evapotranspiration is 1614–1995 mm.

The Erbil groundwater basin is dominated by thick Bakhtiari layers covered by recent deposits. While the aquifer characteristics are generally favourable, its recharge is limited by low rainfall and the absence of perennial streams (Erbil Governorate 2018; Stevanovic and Iurkiewicz 2009). In arid and semi-arid regions, rivers and streams typically lose their waters by, for example, recharging ground-water. However, in this case study, both surrounding rivers are acting as water-gaining streams, which is usually more typical for humid regions, where groundwater recharges streams. Thus, the lower reaches of the two Zab rivers (Fig. 12.1) drain the aquifer rather than recharging it. The types of soil across Erbil province vary according to geographical location. Rough mountains as well as broken and stony landforms the upper part of the province (Buday 2006). The middle part comprises two types of brown soil, while gypsi-ferous alluvium, brown soil deep phase and lithosolic soil in sandstone and gypsum shape the lower part of the province, the soil types are shown in (Fig. 12.2) (Hameed 2013).
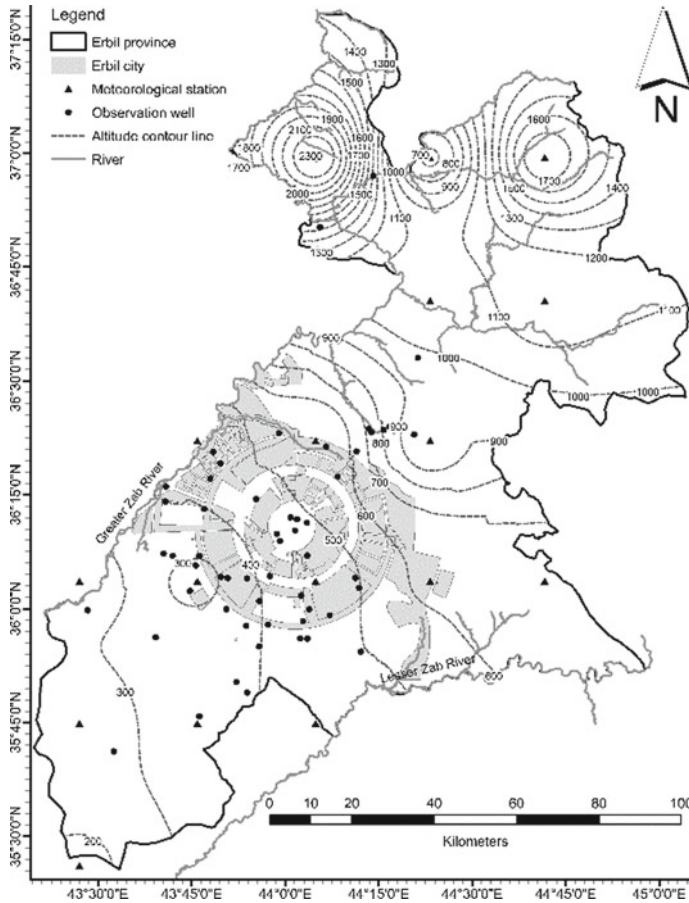
Fig. 12.1 The altitude of the ground surface, MS, and OW

Figures 12.3 and 12.4 are based on data obtained from the General Directorate of Water Resources, Kurdistan Regional Government (KRG)-Iraq (MoAWR-KRG 2016), and Buday (2006), they show the formations of the ground layers represented as intergranular, intergranular fissured, karstic fissured and aquitard as well as aquifer productivity. Two main groups of significant aquifers can be distinguished in the case study area: The karstic and karstic-fissured aquifers of the extended carbonate formations (limestones and varieties) in the central high-folded zones, and the intergranular aquifers of the lowlands, in addition to aquitards between the two types of main aquifers. Well-karstified rock masses can be developed to capture the flood flush waters for later use. Construction of cut-off walls to elevate the discharge level has proved to be an effective method in this regard. Climate change will alter the sustainability conditions of most water resources.
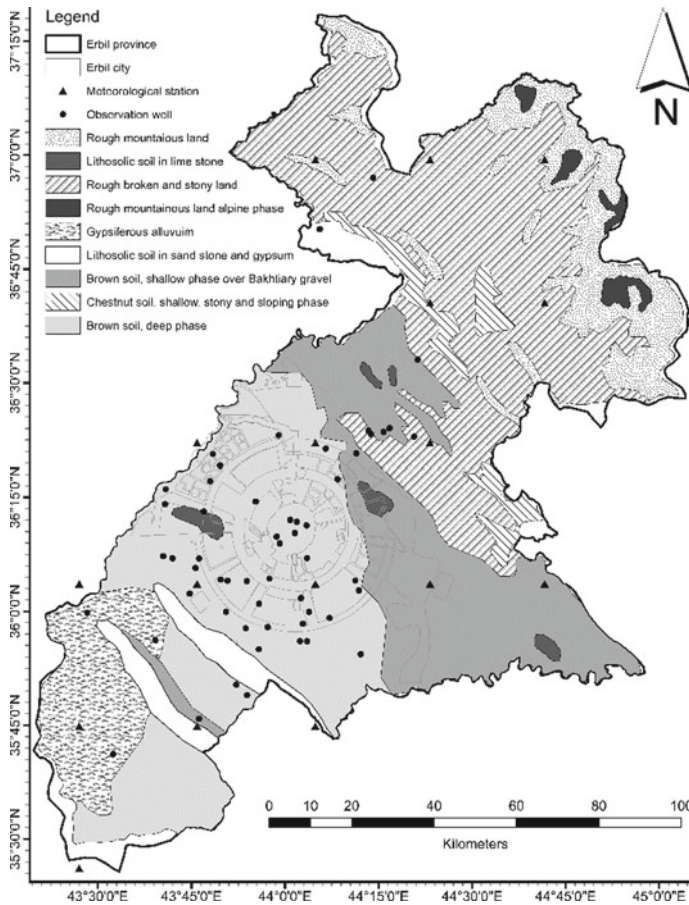
Fig. 12.2 Soil types across Erbil province

Payne and Woessner (2010) pointed out that aquifers of high flow productivity have the potential to be considered a source of water supply for large-scale irrigation projects and municipal water use. Aquifers associated with intermediate flow productivity can also be considered potential suppliers for irrigation and municipal purposes. However, placement of wells may be challenging to ensure a sufficient flow rate. Inter-granular or intergranular fissure formations that have little to offer could be considered suitable sources to single or a small number of households. At any rate, the achievement of a desired minimum flow rate may be difficult (Payne and Woessner 2010).

Figures 12.2, 12.3 and 12.4 provide initial characterization of groundwater and give an indication of the likely variation in groundwater yield and flow type in relation to different geological deposits. The productivity classes shown in Fig. 12.4 provide a potential measure of the expected long-term abstraction rate of groundwater.
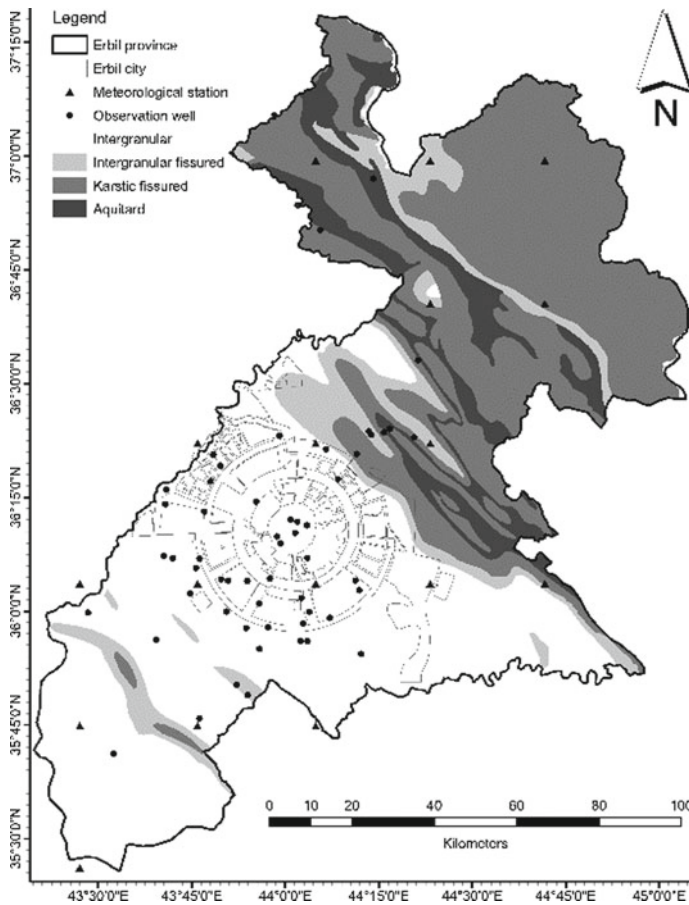
Fig. 12.3 Type of aquifers across Erbil province

12.2.2 Data Collection and Analysis

12.2.2.1 Meteorological Data and Analysis

Meteorological data of seventeen stations (Fig. 12.1, Sect. 5) were analysed for stations ranging from about 175 masl to as high as 2306 masl within and near Erbil Province. Daily meteorological variables such as precipitation (P), minimum temperature (Tmin), maximum temperature (Tmax), mean air temperature (Tmean), radiation, wind speed, and relative humidity between 1980 and 2014 were made available from the National Centres for Environmental Prediction (NCEP 2015) and Climate Forecast System Reanalysis (spatial resolution = $0.5° × 0.5°$).
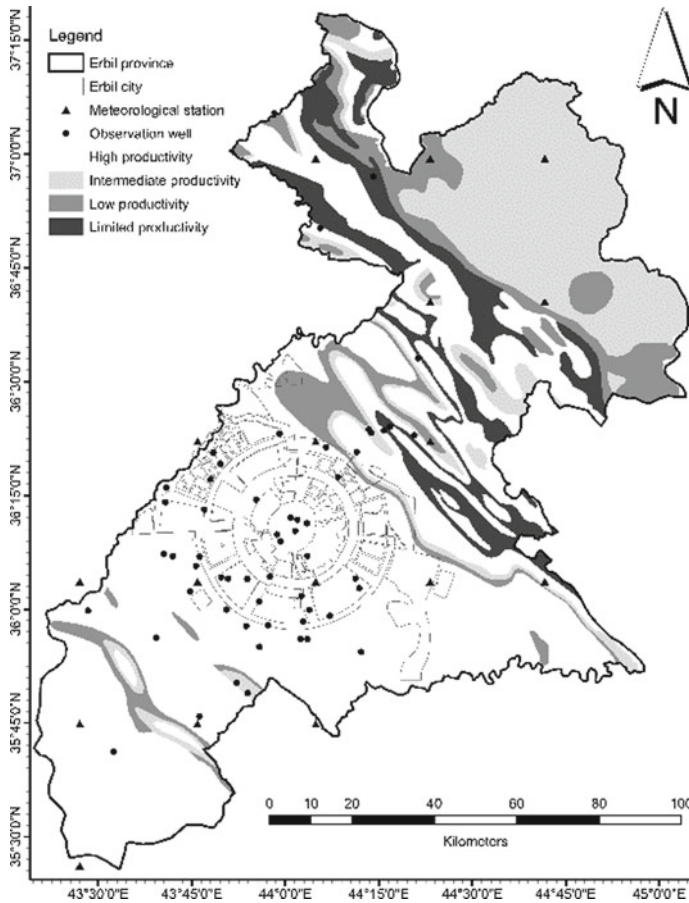
Fig. 12.4 Productivity of aquifers in Erbil province

The Food and Agriculture Organization Penman–Monteith (FAO-PM) method (Allen et al. 1998) was adopted to obtain the potential evapotranspiration (PET). This method has been applied by many researchers and recommended for determining the reference crop evapotranspiration (ETo) (Debnath et al. 2015; Vangelis et al. 2013). The FAO tool version 3.2 (FAO 2012) was utilized to obtain the PET. The Penman–Monteith (FAO-PM) method (Allen et al. 1998) is given in Eq. 12.1, Sect. 7.

$$ET_o = \frac{0.408\Delta(Rn - G) + \gamma\frac{900}{T+273}u_2(e_s - e_a)}{\Delta + \gamma(1 + 0.34u_2)} \tag{12.1}$$

where ET_o is the reference evapotranspiration (mm/day); Rn is the net radiation at the crop surface (MJ/m^2/day); G is the soil heat flux density (MJ/m^2/day); T is the mean daily air temperature at 2 m height (°C); u_2 is the wind speed at 2 m height

(m/s); es is the saturation vapour pressure (kPa); ea is the actual vapour pressure (kPa); (es-ea) is the saturation vapour pressure deficit (kPa); Δ is the slope vapour pressure curve (kPa/°C); and γ is the psychrometric constant (kPa/°C).

12.2.2.2 Groundwater Data and Analysis

Monthly records of groundwater levels between January 2004 and January 2016 observed at 54 observation wells (Fig. 12.1) in Erbil Province were examined to quantify the long-term gradient tendency of the groundwater level over a period of 12 years (2004–2016). The altitudes of these wells are between 258 and 970 masl and the depths of these wells are from 84 to 215 m. The Ministry of Agriculture and Water Resources (MoAWR-KRG 2016), via the general directorate of water resources (both the affiliated directorates of irrigation management and groundwater affairs) made these data available. The groundwater level is a key parameter for evaluating spatial and temporal changes in groundwater environment and storage (Iwasaki et al. 2013). Climate change, as reflected in precipitation and temperature rates, influences the groundwater level fluctuation.

The non-parametric distribution-free Mann-Kendall (M-K) test at 5% significant level was utilized to detect the long-term trend in groundwater level. The SPSS version 25 was used to carry out this analysis.

The M-K test is particularly used to check the alternative hypothesis versus the null hypothesis of no trend of the existence of monotonic decreasing or increasing trend of groundwater time series data. The non-parametric M-K test is fit for those data series where the trend might be supposed to be monotonic (i.e., mathematically, the trend either consistently decreases and never increases or consistently increases and never decreasing), and no seasonal or other cycles are present. Thus, The M-K test is commonly utilized in detecting upward or downward trends associated with the examined parameter (i.e., groundwater level) over time (Seibert and Vis 2012). However, despite the importance of groundwater to Erbil province and other areas where there is over-exploitation of groundwater, there have been insufficient measurements of groundwater fluctuations over time to properly support decision-makers and planners to sustainably manage groundwater resources (Chikodzi 2011; Nanekely et al. 2017).

Table 12.1 shows information partly obtained from MoAWR-KRG (2016) about the total number of wells in Erbil province, the number of legal wells and the purposes for which these wells are being used. ArcGIS v.10.5 was utilized to develop spatial distribution sets of maps that show the temperature, the potential evapotranspiration rates as well as the long-term maximum, minimum and mean annual precipitations. The spatial analysis tool for the ordinary kriging method (Grimes and Pardo-Iguzquiza 2010) was used for the development of isohyetal lines.

Table 12.1 Existing wells in Erbil province (after MoAWR-KRG 2016)

Groundwater wells		Of which are legal	Estimated illegal wells[c]	By well status		By well depth (m)					By purpose			
				In use	Dry/unused	< 50	50– < 100	100– < 150	150– < 200	> 200	Drinking	Irrigation	Livestock watering	Industry
Dataset up to March 2011	Total number	5241	2922	4348	893	170[a]	611[a]	104[a]	1360[a]	677[a]	2229	2787	108	117
	Percentage of total (%)	64.2	35.8	83	17	5.8[b]	21[b]	3.5[b]	46.5[b]	23.2[b]	41.95	51.65	3.6	2.8
Dataset up to December 2016	Total number	8037	4237	6667	1370	195[a]	986[a]	144[a]	2118[a]	794	3679	4056	142	160
	Percentage of total (%)	65.48	34.52	83	17	4.6[b]	23.25[b]	3.4[b]	50[b]	18.75[b]	45.8	50.5	1.7	2
5 Years differences	Of total numbers	2796	1315	2319	477	25	375	40	758	117	1450	1269	34	43
	Percentage (%) of the first dataset	53.34	45	53.3	53.4	14.7	13.4	61.4	55.75	17.3	65	45.5	31.5	36.75
Average yield (l/s)	9.1													

[a]Only legal well depths have been considered due to the unavailability of reliable data regarding drilling of illegal wells.
[b]% with respect to the total number of legal wells.
[c]no further data are available for the purposes of use, depth, and status.

12.2.2.3   Qualitative Survey

Communications with groundwater professionals via visits to both sites and official departments, face-to-face meetings, phone call interviews, workshops and small focus group interviews were carried out over two years (2018 and 2019) to gather useful data and information on laws, regulations, instructions, orders and records of monitoring wells along the study area to assess current and future foreseeable groundwater management policies and arrangements. Multidisciplinary cohorts (hydrologists, hydrogeologists, civil engineers, and water resources engineers) who can offer valuable insight and who represent a wide spectrum of experiences and opinions were involved in this survey. The discussions covered topics such as (a) increased reliance on groundwater; (b) lack of integrated management of groundwater resources; (c) increased number of illegal drilling of wells by individual farmers and households; (d) groundwater quality deterioration; (e) absence or weakness of implementation of the regulatory framework to control illegal drilling of wells and protect groundwater pollution; (f) lack of integrated land use planning; (g) poor protection and maintenance of wells; (h) drying-up of a large number of wells; (i) public awareness of sustainable management of groundwater; (k) absence of reliable statistics on groundwater abstractions; (l) financial provisions; and (m) impacts of climate change.

12.2.2.4   Regulatory Document Review

Groundwater in Iraq is protected through a regulatory framework that includes a set of acts, regulations, and instructions, which address various aspects of groundwater protection and remediation as well as drilling of groundwater wells. Table 12.2 summarizes the Iraqi Federal Government and Iraq-KRG Acts and regulations relevant to groundwater protection and pollution control as well as drilling of groundwater well-related instructions (Instruction 1: Articles 2 to 7 and 10, and the amendment of instruction 1: Articles 6, 7, 10, 11, 14 and 15). A regulatory framework must be established for the protection and preservation of groundwater. It should be designed to prohibit the development of new wells, restrict discharges in critically over-exploited aquifers, and regulate or prohibit groundwater pollution from household sewage, industry, and agriculture.

12.3   Results and Discussion

12.3.1   Characteristics of Climate Parameters

The climate of Erbil province is characterized by Mediterranean climate: warm and dry summers, and cold and wet winters. Precipitation usually takes place from October to May . The dry season typically stretches from June to September. Temper-

Table 12.2 Summary of groundwater resource legislations in Iraq and KRG

The Law No. (8)	Article 2.2	Article 22	Article 23	Article 24
(2008) Environment Protection and Improvement in Iraqi KRG (EPIC-KRG, 2008)	Natural resources conservation, development, and rational uses	This article prohibits discharging or putting any harmful substances, liquid, gaseous, radioactive, or thermal into water resources and all their courses, unless when processed in accordance with applicable standards. This article does not differentiate between public or private water resources. It has generalized all kinds of the water resources and their courses	This article mentions thereof: "regional standards for surface water and groundwater and drinking water should be set systematically"	This article casts the responsibility on the Ministry of Environment of the Kurdistan Regional Government to determine the standard levels of pollution allowed in water used for drinking, irrigation, industry and services, which shall be reviewed from time to time as the circumstances may require

Table 12.2 (continued)

The Law No.	Article 14			Article 24		
(27) Environmental Protection (2009), (IPC, 2009)	Item 1: It is prohibited to dispose any household, industrial, or agricultural liquid wastes into inland water resources, surfaces or underground, or Iraqi maritime areas, unless passed through necessary treatments that must be done that are consistent with specific specifications in national environmental legislation and international conventions	Item 2: It is prohibited to connect household wastewater, industrial wastes other activities to rainwater drainage networks	Item 3: It is prohibited to dispose of solid wastes or animal wastes to water resources bodies	Item 1: The Minister shall appoint an (Environmental Controller) from among the Ministry's employees to implement the provisions of the Act to control the activities affecting the environment subject to its provisions and to organize reports to be submitted to the Ministry to take the necessary action	Item 2: The environmental Controller shall be granted the status of a member of the judicial control who shall be assisted in the performance of his duties by elements of the environmental police, and activities controlled by him/her during and after official working hours	Item 3: The Environmental Controller shall carry out the following legal oath in front of the head of the competent department: (I swear by Great Allah to do my job faithfully and honestly and I pledge to keep the confidentiality of the information that I have seen by virtue of my official work)

Table 12.2 (continued)

The Instructions	Article 2	Article 3	Article 4	Article 5	Article 6	Article 7	Article 10
No. (1) Groundwater Wells Drilling in Kurdistan region, Iraq (MoWR-KRG, 2010)	The distance between neighbour wells identified for karstified formations should be within 450 to 600 m, and for inter-granular formations, they have to be less than 200 m	It is not permissible to drill wells closer than 500 m from springs, groundwater aqueducts, and water resources projects	It is permissible to drill wells for agricultural uses in case that surface water resources cannot be utilised for that purpose	Item 1: Public wells will be drilled for drinking, industrial and agricultural uses, based on a formal request that must be submitted by the recipient to groundwater authorities. Item2: Alternative wells will be drilled in case that a well has dried or collapsed after the exploration undertaken by a professional committee	Identifies the instructions for drilling wells for private sector uses	Identifies the instructions for drilling wells for agricultural purposes	Financial penalties and sanctions Fines rage from $200 to $600 for illegal drilling

The Instructions	Article 6	Article 7	Article 10	Article 11	Article 14	Article 15	
No. (1) Groundwater Wells Drilling in Kurdistan region, Iraq (MoWR-KRG, 2015)	Item 5: No longer should well drilling licences be issued for the purpose of fuel stations, car washing places, commercial buildings, aggregate plants, mineral water factories, etc.… Item 6: It is not permissible engage in groundwater trading by the licensed private wells	Items 1, 2 and 3: Specify the number of wells per agricultural parcels area, this based on the rainfall pattern in that region. Item 5: specifies the irrigation system for agricultural wells to be used, and it is not allowable to change that system. Item 10: Water measure gauges should be installed on agricultural wells. The limited quantity of water must be abstracted based on the planted crops. Item 11: In case of drilling a well in an artesian basin, the upper layers should be detained	The general directorate of water resources has full authority to not issue any licences or invalidate any licenced wells if it observes that the water level in the basin or sub-basin has dropped or the water quality has changed	Item 1: The general directorate of water resources, has full authority to not issue a licence or invalidate any licenced wells, if it can be demonstrated that these wells have negative impacts on public interests. Item 1: Water is not owned by anyone. Therefore, the person who has a license has no permission to use whatever he/she wants to do with the resource	Penalties: Companies that are professional in drilling water wells must be subjected to the instructions which are in force and issued by the general directorate of water resources. Fines will be doubled in case the violation is repeated, and the machines will be retained for a period	It is not permissible for digging any shallow wells, in case that any drilling company implemented that; the machines well be confiscated to the general directorate of water resources	

Table 12.2 (continued)

The Regulation	Article 3	Article 4	Articles 12	Articles 13	Articles 14
No. (2) Water Resources Conservation, (2001), Iraq (IPC, 2001)	The disposal of waste from the shops shall not be allowed to public water bodies, whatever its quality or quantity, except it is permissible by a license from Department of Environmental Protection and Improvement	The disposal of any contaminants, including toxic or radioactive substances, shall not be permitted in public waterbodies, except licensed by the Environmental Protection and Improvement Department or whoever is entitled to it	For the protection and improvement of the environment, the provincial councils in coordination with the local community councils must prepare plans for their districts to protect public water from pollution and improve its quality according to a timetable. These plans are presented to the Environmental Protection and Improvement Council for reviewing	The plans include identifying the water contamination source The requirements to tackle this issue Plans for future projects and proposing required funds Time tables for water contamination treatments	Provincial councils for the protection and improvement of the environment provide periodic follow-up reports to the Protection and Improvement Council Environmental progress in the field of public water conservation

Table 12.2 (continued)

The Law No. (9) issued in 2006 Ministry of Water Resources in the Kurdistan Region–Iraq (MoWR-KRG, 2006)	**Article 2** The Ministry aims to develop strategies, policies and plans for the development and investment in water resources (surface and groundwater) in the region, and prepare technical feasibility studies, and economic projects for water resources. Construction and maintenance of dams and irrigation projects
Regional Development Strategy for Kurdistan Region Report 2012–2016 (MOP-KRG, 2011)	**Chapter 4 clause 4** Calls for ground water exploitation have to be expanded, especially water wells. Statistical results for 2006 indicate that the wells were mostly used for drinking water provision, 20% used in agriculture, and the rest were exploited for industrial, and agricultural extension and research purposes

ature rate rises, and precipitation decreases are characteristic over the period from 1980 to 2014. Two dry periods were observed: 1999–2001 and 2007–2008. The year 2008 was found to be the driest year in terms of precipitation observed at all meteorological stations.

Results revealed that the aggregated precipitation of the wet months (October–May) represents about 99% of the total annual precipitation. Accumulated precipitation of the non-rainy months (June–September) accounts for nearly 1% of the total. The aggregated precipitation of the months November–April represents approximately 88% of the total annual precipitation. The long-term minimum annual precipitation was between 31.5 mm and 370.4 mm. The corresponding temperature ranged from 7.4 °C to 20.4 °C. The long-term annual maximum precipitation ranged from 392.2 mm to 1625.3 mm. The temperatures were between12.1 °C and 24.0 °C. However, the long-term mean annual precipitations were from 201.5 mm to 980.9 mm. The corresponding temperatures were between 9.7 °C and 22.3 °C. The long-term minimum annual potential evapotranspiration rates were found to be between 1098 and 1443 mm with a mean of 1295 mm and a standard deviation of 72.0 mm. The corresponding maximum and mean values ranged from 1986 to 2347 mm with a mean of 2145 mm and a standard deviation of 87 mm, and between 1614 and 1995 mm with a mean of 1795 mm and a standard deviation of 98 mm, respectively. Table 12.3 shows the long-term minimum, maximum and mean annual precipitation and the corresponding temperature and potential evapotranspiration rates for Erbil province.

Figure 12.5 illustrates the variations in annual precipitation and mean annual temperature between 1980 and 2014 at seventeen meteorological stations. Relatively wet periods were observed from 1992 to 1998 and from 2011 to 2014. Significant reductions in precipitation were noticed between 1999 and 2001, and between 2007 and 2008. The minimum annual temperature was observed for 1992 at all stations, while the maximum annual temperature was recorded in 2010 at all stations except for station 2, where the maximum annual temperature was noted in 2014, and at station 4 in 2013. However, higher temperature rates were recorded between 2000 and 2010. An overall precipitation-downward trend and temperature upward tendency were perceived at all stations in Erbil province. This suggests that Erbil province is vulnerable to drought.

Figure 12.6 shows the spatial distribution of the long-term minimum annual precipitation (LTMinAP) across Erbil province. The long-term minimum annual precipitation varies from 420 mm at the most upper part of Erbil province to 40 mm at the lower part of the province. The long-term maximum annual precipitation (LTMaxAP) ranges between 1450 mm at the most upper part of Erbil province and 550 mm at the lowest part of the province (Fig. 12.7). The long-term mean annual precipitation (LTMAP) extends from 200 mm at the lowest part of the province to as much as 975 mm at the most upper part of the province (Fig. 12.8).

The range of the long-term minimum (LTMinAT) and maximum annual (LTMaxAT) temperatures are between 7.5 °C and 20.0 °C (Fig. 12.9) and between 10.0 °C and 24.0 °C (Fig. 12.10), respectively. The long-term mean annual temperature ranged between 10.5 °C and 22.0 °C (Fig. 12.11). However, despite of the

Table 12.3 Long-term minimum, maximum and mean annual precipitation, temperature, and potential evapotranspiration

Meteorology station representing a weather data point (WDP)	Coordinates			Long-term mean annual precipitation (mm)			Long-term mean annual temperature (°C)			Long-term mean annual potential evapotranspiration (mm)		
	Longitude	Latitude	Altitude (masl)	Min	Max	Mean	Min	Max	Mean	Min	Max	Mean
1	44.0625	36.9991	2306	237.5	1372.3	621.6	11.6	15.6	13.8	1430.7	1816.6	1612.7
2	44.375	36.9991	682	241.5	1063.2	615.7	9.4	13.6	11.7	1251.0	1587.7	1434.8
3	44.6875	36.9991	1783	313.9	1378.5	814.2	7.4	12.1	9.7	1097.8	1442.8	1295.0
4	44.375	36.6869	1053	213.2	1150.1	607.9	13	17.6	15.5	1543.8	1948.3	1736.5
5	44.6875	36.6869	1154	370.4	1625.3	980.9	9.4	13.7	11.8	1238.4	1602.7	1440.2
6	43.75	36.3747	401	191.8	1126.9	637.4	18.6	22.4	20.6	1628.9	2072.8	1850.7
7	44.0625	36.3747	507	182.9	1136.6	605.4	17.9	21.7	19.9	1582.7	2192.1	1937.2
8	44.375	36.3747	977	189	1551.9	652.4	16	19.9	18.1	1487.8	2176.9	1905.7
9	43.4375	36.0624	261	100.8	928.8	492.6	18.9	22.6	20.9	1653.0	2017.4	1823.7
10	43.75	36.0624	278	130.1	1070.4	570.2	18.5	22.3	20.6	1619.3	1962.0	1789.1
11	44.0625	36.0624	439	134.9	985.2	575.2	18.2	21.9	20.1	1656.3	2051.0	1851.9
12	44.375	36.0624	605	128	1005.4	533.6	17.8	21.6	19.9	1573.6	2225.3	1965.1
13	44.6875	36.0624	648	145.1	1022	552.9	16	20	18.4	1579.5	2204.4	1936.6
14	43.4375	35.7502	252	44.5	526.5	294.4	19.6	23.2	21.6	1835.7	2200.5	1998.9
15	43.75	35.7502	306	55.4	666.7	360.4	19.2	22.9	21.2	1747.1	2075.1	1898.3
16	44.0625	35.7502	483	63.2	720.5	389.6	19.1	22.8	21.1	1746.8	2080.9	1897.9
17	43.4375	35.438	175	31.5	392.2	201.5	20.4	24	22.3	1986.1	2347.1	2145.1
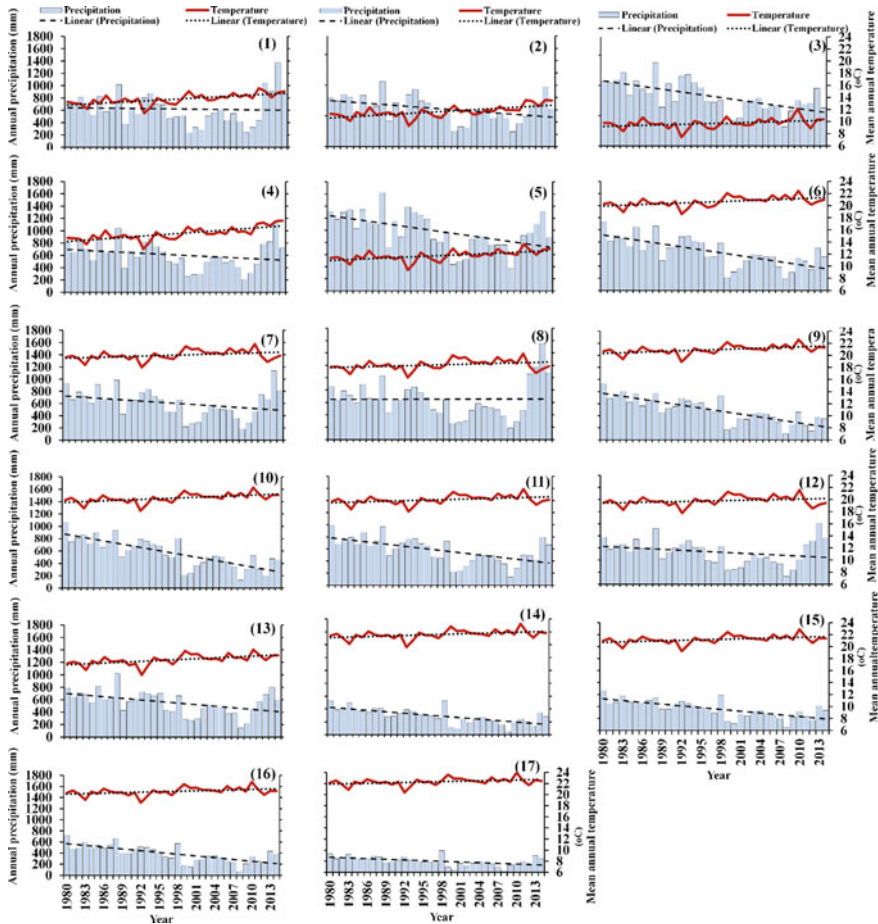
Fig. 12.5 Boxplot of long-term mean total Precipitation and mean annual temperature

climate variability in terms of precipitation and temperature, there is a clear reduction in precipitation and increase in the rate of temperature over the period of 35 years indicating that Erbil province tends to be drier and warmer (Fig. 12.5).

Figure 12.12 shows the monthly variation of PET rates. For the July records, the highest value of evapotranspiration was recorded for all 17 meteorological stations (MS) across the case study area, while the minimum value in the northern mountainous part attributes to December, whereas, in the mid plateau and south steppe parts, January had the lowest record. However, the studied area had the lowest annual record of 2000 mm evapotranspiration. Just after the period 1998–1999; this area had experienced a severe drought, hitting a maximum record of 2347 mm evapotranspiration along the study period (Fig. 12.13).
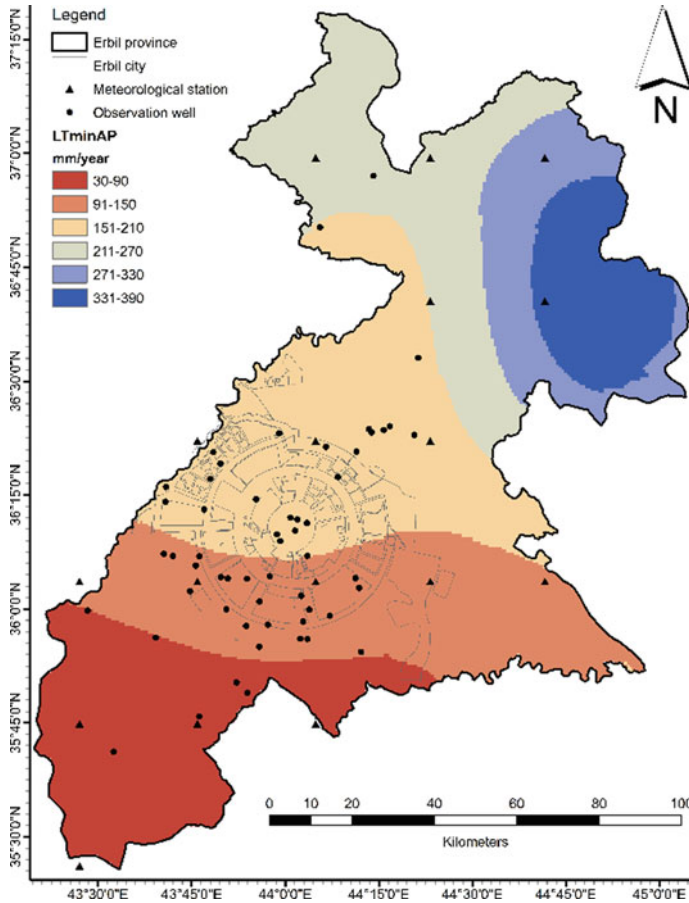
Fig. 12.6 Spatial distribution of the LTMinAP

12.3.2 Climate Condition

AAA Fig. 12.14 portrays the climate variables representing long-term mean monthly precipitation (P) and long-term mean monthly potential evapotranspiration (PET) for the 17 (MS) covering the study area. The Northern and the central parts of the study area that are located within the weather data points 1–13 had surplus amounts of precipitation from November up to the mid of March. These areas represent mountainous and plateaus lands. In comparison, the remaining Southern plain areas that are located within the weather data points 14–17 were subjecting to high temperatures and severe droughts. Water in these areas is particularly needed for multiple use purposes.
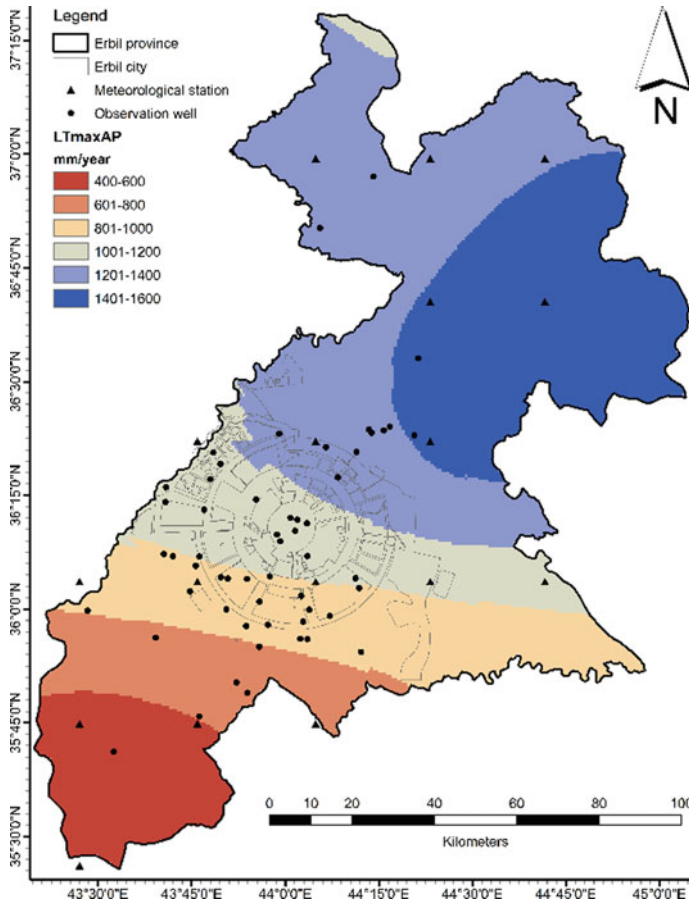
Fig. 12.7 Spatial distribution of the LTmaxAP

12.3.3   Results Related to Groundwater

The qualitative survey reveals that the heavy withdrawals of groundwater for agriculture and drinking water production have caused a notable decline in groundwater levels associated with negative economic and environmental consequences. Short-term or seasonal rainfall and higher temperatures in summer together with a lack of surface water resources has forced individual farmers and households to mainly rely on groundwater resources with extensive drilling programmes, which resulted in a considerable drop in groundwater levels. This corresponds to the results shown in Table 12.3 and Fig. 12.14. Information and data drawn from discussions with the MoAWR-KRG staff and local communities indicated that more drilling activities have increased the cost of pumping as farmers deepen their wells by re-drilling alternative contiguous wells to reach falling water tables. The estimated cost of drilling
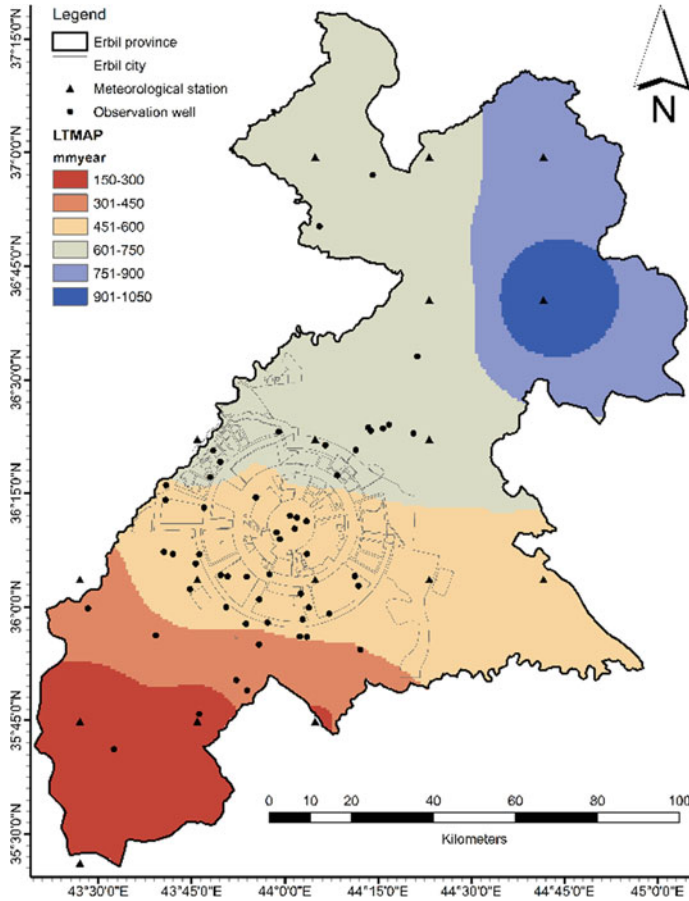
Fig. 12.8 Spatial distribution of the LTMAP

is 40–50$/m depth (casing included) for intergranular formations (unconsolidated deposits) of up to 450 m in depth, 55–60$/m (casing included) for intergranular fissured formations (consolidated deposits) of up to 280 m in depth, and 70–80$/m (casing excluded-open hole) for Karstified formations of up to 180 m in depth (see Fig. 12.3 for corresponding formations). The cost depends mainly on soil type, type of drilling equipment such as rotary or hammer, the type of well casing and the drilling depth. In addition, both the increased cost of pumping and drying up of a notable number of wells has adversely impacted on the socio-economic condition, particularly of the small holder farms. Official correspondences pointed out that the temporal economic growth in Iraq after 2003 has notably increased the number of smallholdings in the countryside and outskirts of towns. People in Erbil and other provinces tend to spend at least the weekend in the countryside, which caused urban sprawl in terms of housing developments, increased farming practices and illegal drilling
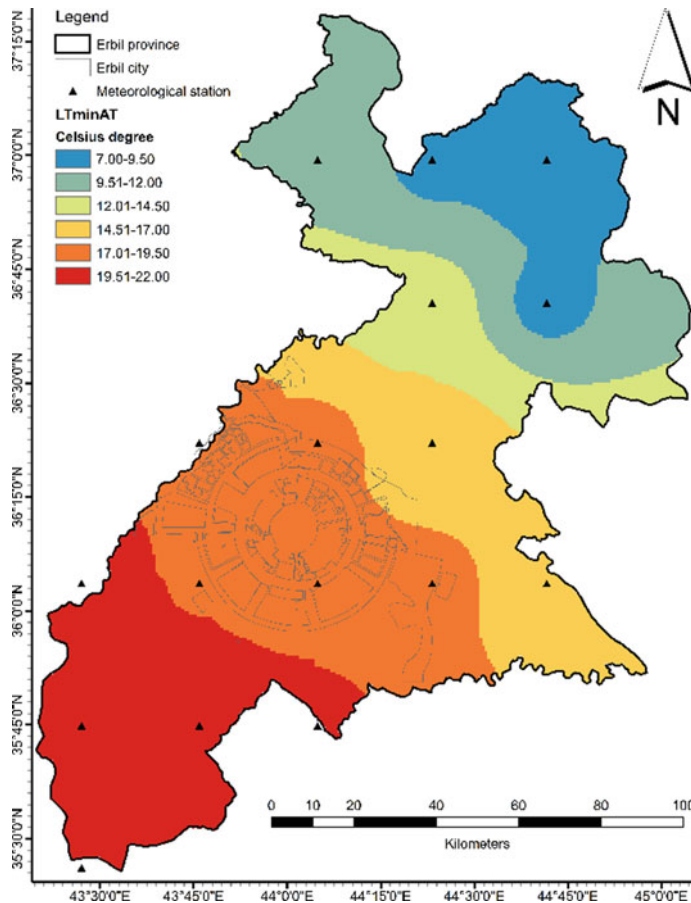
Fig. 12.9 Spatial distribution of the LTminAT

of private wells. Unstable political and security conditions coupled with insufficient financial provisions and the inability of enforcement of civil actions to appropriately implement laws has exacerbated the random development and increased the non-rational abstraction of groundwater.

Voss et al. (2013) have shown that the Northern Middle East aquifers including those in Iraq (semi-arid region) were losing almost 17 mm between 2003 and 2009. This is equivalent to 13 Km^3/year relying on satellite data analysis. However, there are considerable differences between different regions ranging from several centimetres to a few decimetres. The water level in Erbil's basin has fallen several meters in most of the observation wells within a period of 12 years.

The region has been facing frequent dry spells because of climate change (Fig. 12.5 indicates reduced precipitation and increased temperature), which elevated the reliability on groundwater to meet the increased water demands. Inconsistency in
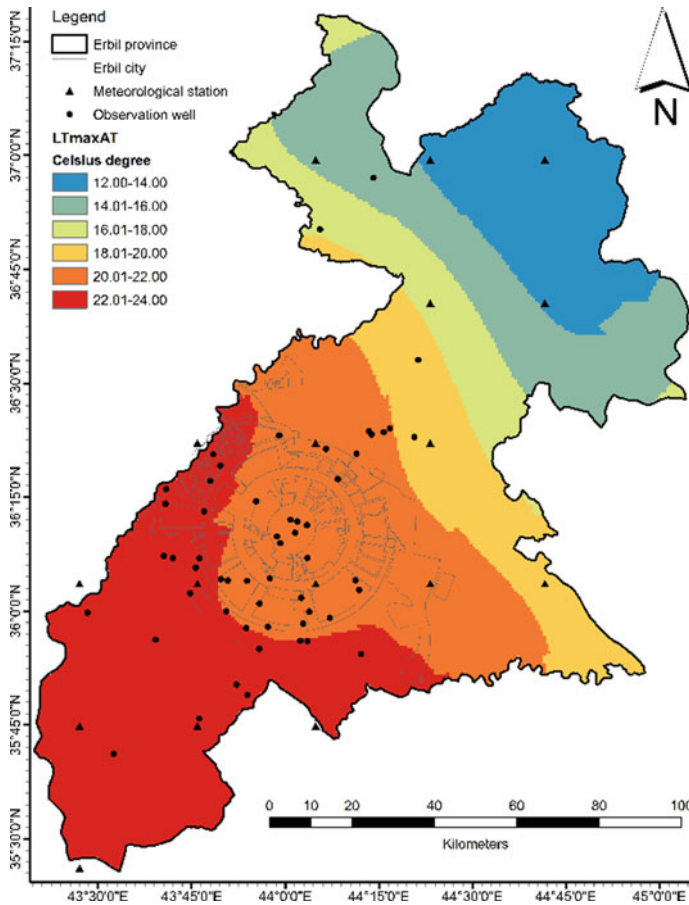
Fig. 12.10 Spatial distribution of the LTmaxAT

managing groundwater aquifers, lack of integrated management of groundwater resources, and the absence of groundwater withdrawal monitoring systems has exacerbated the non-rationality of using groundwater.

Table 12.1 reveals that nearly 53% of the total number of wells in Erbil province are legal. About 35% were illegally drilled by smallholder farms and/or households. This mainly suggests (a) that there is an absence or weakness of law enforcement concerning drilling of wells and groundwater development regulations; (b) notable exhaustion of groundwater resources (the local communities are considerably over-exploiting the groundwater to mainly meet the irrigation and drinking water supply needs); (c) the current existing wells provide 50% of water for irrigated agriculture, 46% for drinking water supply and the remaining 4% are used for industrial and live-stock watering. Furthermore, a considerable number of wells were drilled for almost 200 m and more, which indicates the unavailability of groundwater at shallow levels.
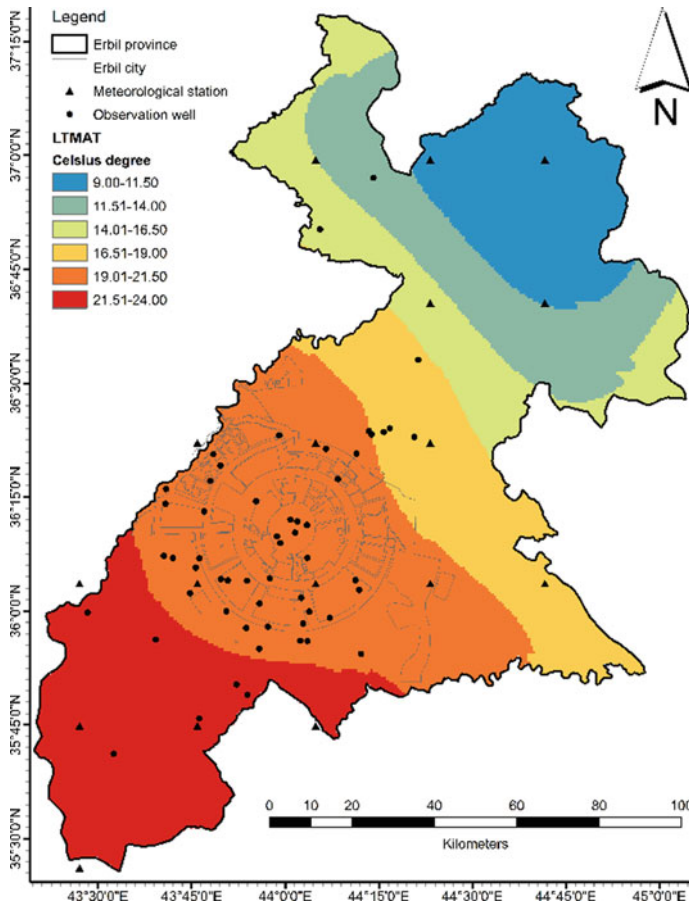
Fig. 12.11 Spatial distribution of the LTMAT

The number of wells increased by 53% within a five-year period. Only 45% of the difference is legally drilled, which can be attributed to a number of reasons that are social prosperity, economic revival and development on one hand, and administrative sagging, poor law enforcement and weakness in instructions and regulations on the other hand. Also, the table shows that almost 60% of recently drilled wells were at 150–200 m depth.

The aquifer permeability is variable both in horizontal and vertical direction. The average yield of the existing wells is 9.1 L/s according to the well database.

Geological formations, total rainfall during the rainy season and abstraction of groundwater are the main factors explaining the observed groundwater trends in Erbil province. Groundwater levels are in a state of decline as proved by the negative trend line equations shown in Fig. 12.5 and Table 12.3.
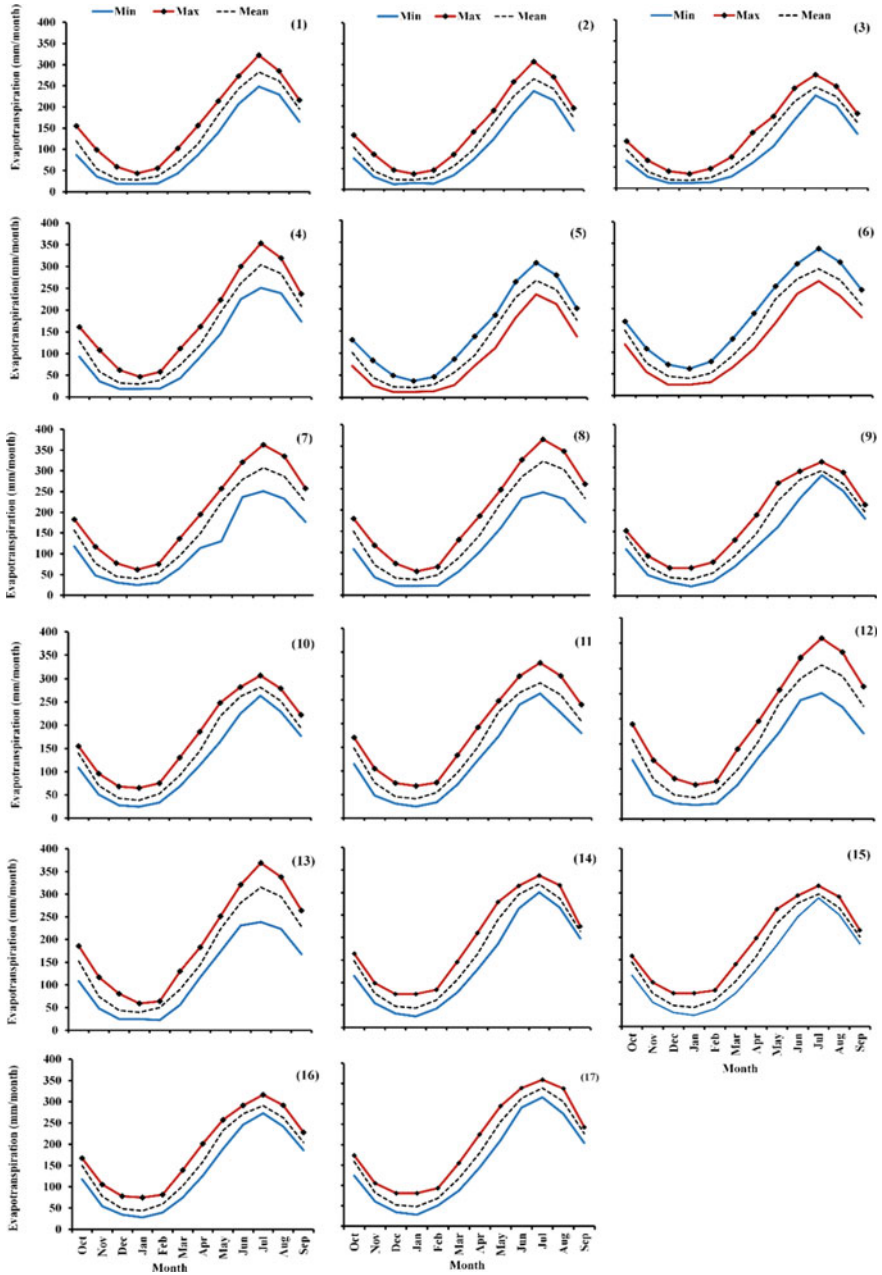
Fig. 12.12 Boxplot of monthly variation of potential evapotranspiration (PET)
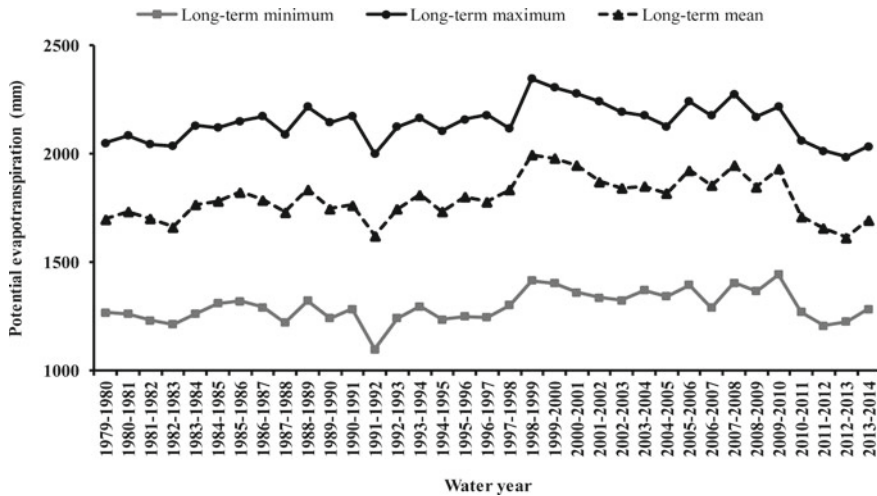
Fig. 12.13 Long-term potential evapotranspiration

Results indicate that nearly 91% of the examined observation wells are associated with declining trends in groundwater levels. About 26% of those of declining trends are associated with low declining trends of slopes less than 0.265 (1st percentile), 50% are linked with strong declining trends of slopes larger than 0.68 (3rd percentile), and the remaining 24% are considered to have moderately declining trends (0.265 $\leq$ slope $\leq$ 0.68). The corresponding drop (m/year) ranges for low, moderate, and strong declining trends are < 0.58 m/year, 0.58 m/year $\leq$ drop $\leq$ 1.73 m/year, and > 1.73 m/year, respectively. This is due to large-scale abstraction of groundwater together with insufficient rainfall for recharge and the absence of a sustainable groundwater replenishment system, which resulted in a substantial loss of storage and reduction in the availability of groundwater as a reliable source for irrigated agriculture and domestic water use.

The remaining 9% of the total wells are associated with stable or slightly rising trends of slopes ranging from 0.005 to 0.32 with a mean of 0.11. This is attributed to the fact that most of those observation wells are situated in Karstified formations, where the corresponding aquifers are subjected to a rapid recharge process. This agrees with Mustafa et al. (2015) concluding that based on a meteoric water line, the recharged precipitation is of Mediterranean origin and infiltrates rapidly. (Fig. 12.15a–c) shows the trends (downward and upward) for groundwater levels of 54 observation wells over a period of 12 years. Table 12.4 shows the results of the M-K analysis; nearly 91% of observation wells experienced a significant declining trend in groundwater levels at a 5% level of significance. About 6% of the examined wells were associated with significant upward trends in groundwater levels and the remaining 3% were linked to insignificant upward trends in levels.
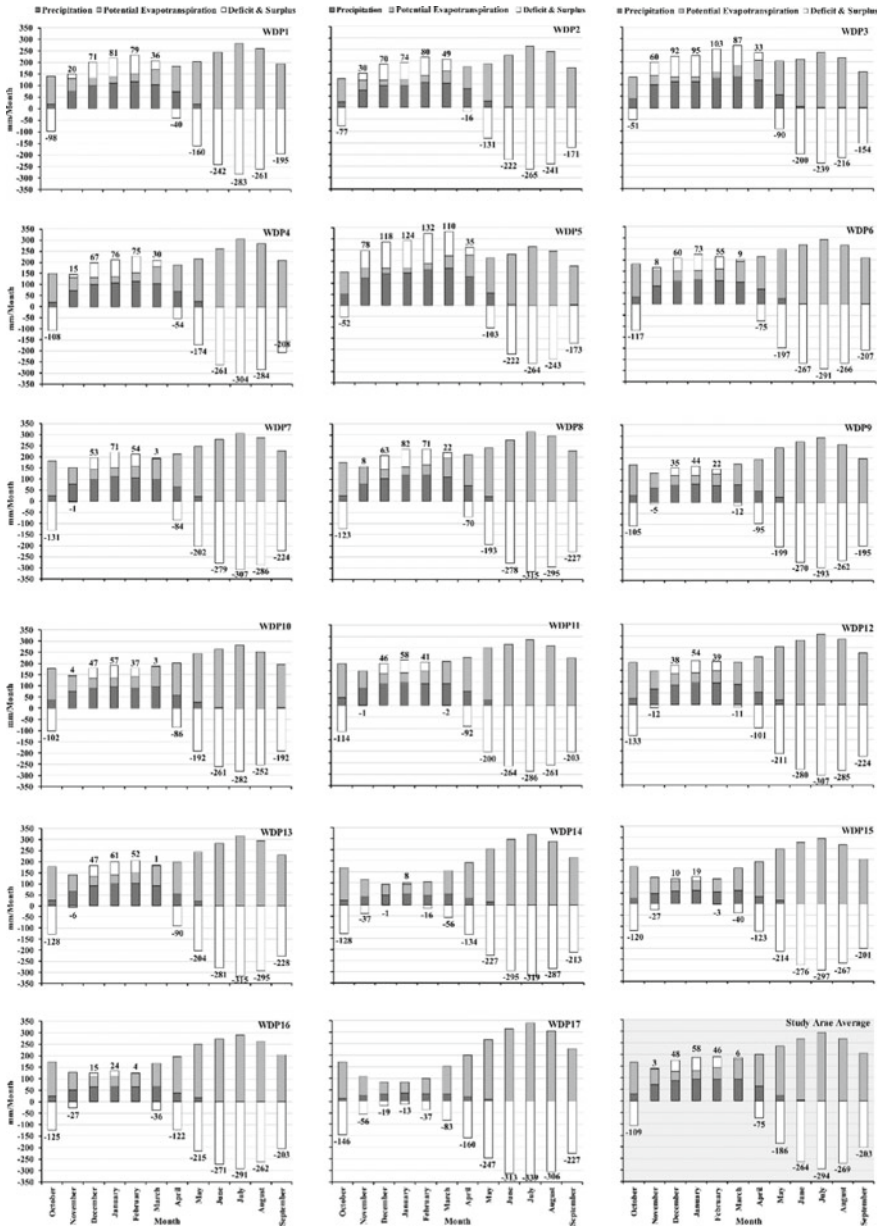
Fig. 12.14 Boxplot of long-term mean monthly precipitation and potential evapotranspiration along 35 years (1980–2015) for 17 MS
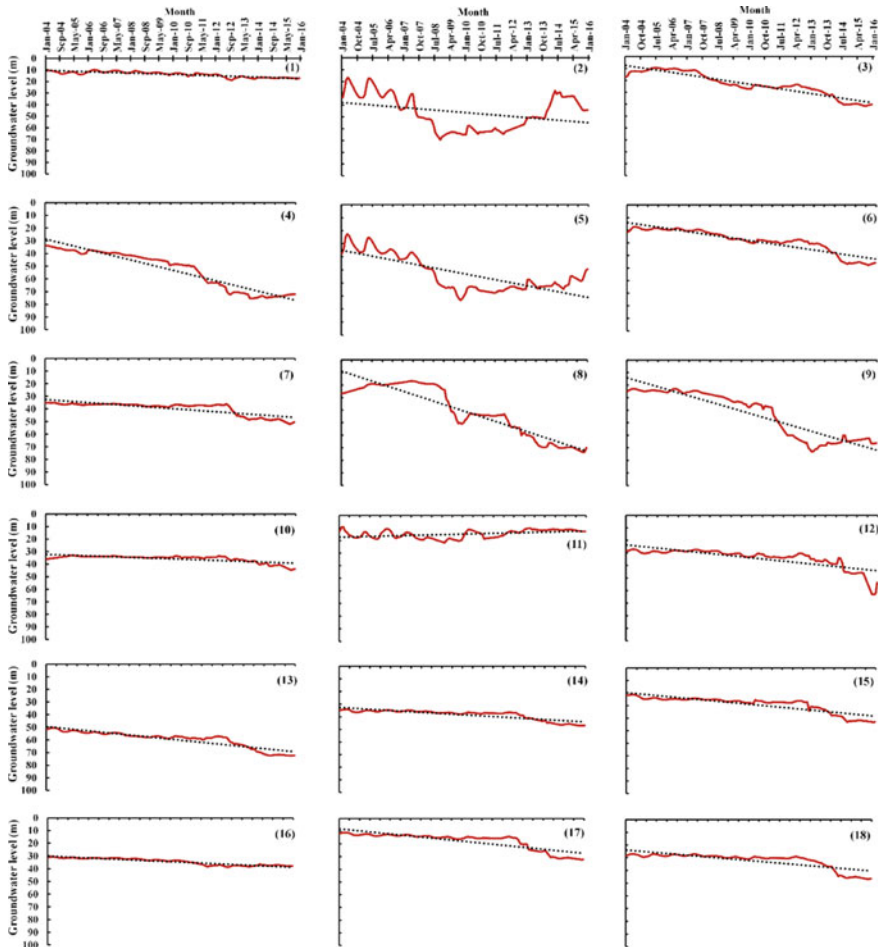
Fig. 12.15 a–c Boxplot of groundwater level for the observation wells for the period January 2004–January 2016
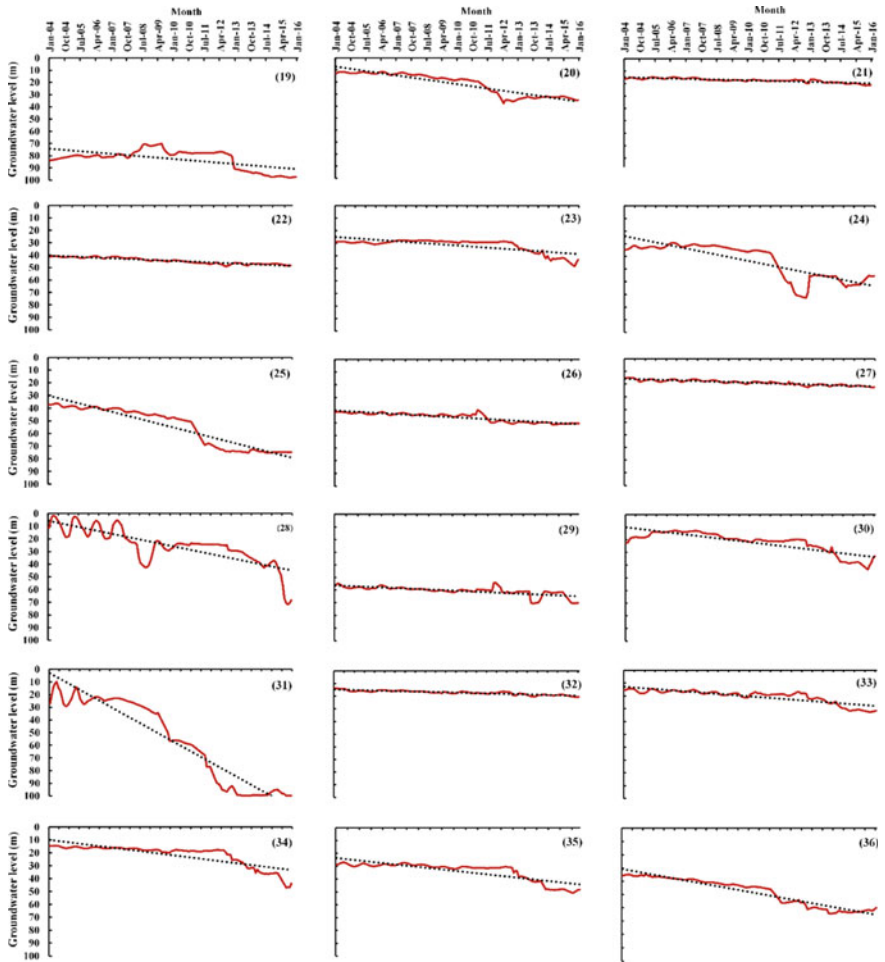
Fig. 12.15 (continued)
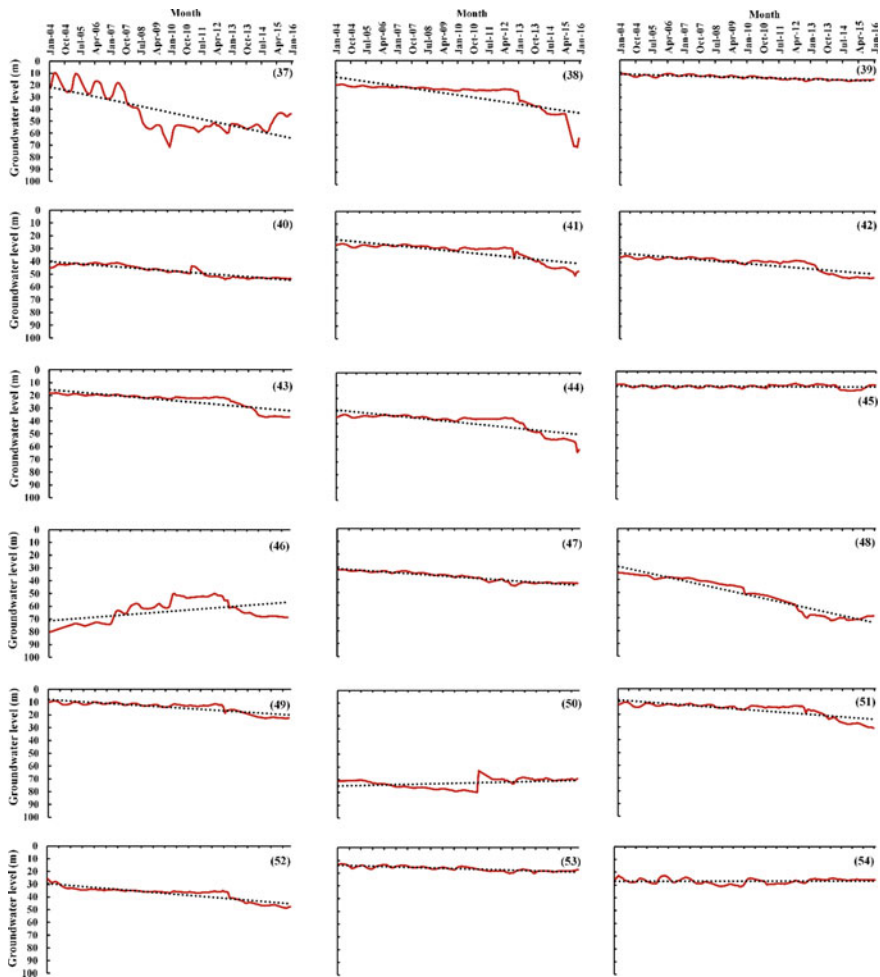
Fig. 12.15 (continued)

12.3.4 Regulatory Framework

A tabulated list of legislation-in-force regarding water and groundwater resources in terms of quantity and quality management in semi-arid Iraq and Kurdistan is presented in Table 12.2. Legislators have shown awareness related to the legal prospect of water resources in the country. This indicates that both governments have a goodwill to develop a competent legal framework for their national water resources. Article 110 of the constitution of 2005 is considered as a benchmark for the Federal Government's solicitude for this framework. Other than the constitution

Table 12.4 Trend results for selected wells

No.	Well name	Correlation coefficient	p-value range (%)
1	Abassia	0.677	< 0.1
2	Armawan-1	0.146	< 1
3	Aziana	0.787	< 0.1
4	Bahar	0.899	< 0.1
5	Banaman-1	0.41	< 0.1
6	Barbian_Gichka	0.846	< 0.1
7	Berabat	0.701	< 0.1
8	Bestanay_Gawra	0.677	< 0.1
9	Betrma-3	0.789	< 0.1
10	Chaghamira	0.568	< 0.1
11	Chama	− 0.282	< 0.1
12	Daldaghan	0.74	< 0.1
13	Darato8	0.858	< 0.1
14	Dorabakra	0.769	< 0.1
15	Dugirdkan	0.818	< 0.1
16	Gainj_Gawra	0.775	< 0.1
17	Gird_Azaban	0.814	< 0.1
18	Gird_Mala-3	0.772	< 0.1
19	Gulan-8	0.19	< 0.1
20	Harir-5	0.784	< 0.1
21	Hujran_Girdachal	0.684	< 0.1
22	Jadida_Zab-3	0.801	< 0.1
23	Kardiz	0.459	< 0.1
24	Kawer_Gosk-1	0.629	< 0.1
25	Kawraban	0.899	< 0.1
26	Khabat-10	0.719	< 0.1
27	Khazna	0.758	< 0.1
28	Kore-3	0.705	< 0.1
29	Kundak	0.668	< 0.1
30	Lajan	0.692	< 0.1
31	Mala_Omer	0.828	< 0.1
32	Malaqara	0.735	< 0.1
33	Mastawa	0.723	< 0.1
34	Minara	0.814	< 0.1
35	Murtika_Shahab	0.739	< 0.1
36	Nawroz-8	0.902	< 0.1

(continued)

Table 12.4 (continued)

No.	Well name	Correlation coefficient	p-value range (%)
37	New_Armawan	0.452	< 0.1
38	Peerdawood	0.851	< 0.1
39	Pemarabir	0.708	< 0.1
40	Qafar-3	0.752	< 0.1
41	Qoritan_Chukul	0.746	< 0.1
42	Qultapa_Yaba	0.755	< 0.1
43	Qurshakhlo	0.811	< 0.1
44	Qushtapa-12	0.696	< 0.1
45	Saadawa	− 0.015	> 5

of 2005, some laws have mainly been directed toward the management, utilization, and preservation of water as national wealth. They established provisions for the discharge of wastes into groundwater (Ahmmad 2012).

Most of the current laws and regulations lack the necessary rational and technical details to ensure proper achievement of the obligations established for managing water resources. Several of them have been drafted in a general style and indicate overlapping provisions, which are still in force, missing an in-depth scientific dimension. Besides, insufficient literature, unreliable texts, and statutory document proceedings on water resources management in Iraq have become a barrier for legal analysts and critics in the field to contribute to the discipline. Furthermore, there is a lack of sufficient funding from the government as well as weak monitoring and follow-up procedures.

12.4   Conclusions

Likewise, Stevanovic and Iurkiewicz (2009), the authors recommend a resilient strategy, which increasingly introduces more restrictive policies in alliance with local traditional systems of water delivery. Therefore, the option of forming water user associations, as applied worldwide, should be tested at the first stage. The survey conducted in this paper points out that a groundwater regulatory framework for sustainable conservation and protection of groundwater resources is lacking.

Mapping of recharge areas and groundwater protection zones is crucial and should be considered as an integral part of long-term integrated watershed management, particularly for sustainable management of groundwater resources. There is a need for identifying the most threatened groundwater zones for decision makers and local authorities to implement their strategies for long-term sustainable use of groundwater.

Several research have checked GRACE-derived groundwater variations with field-data that were obtained from observation wells and boreholes. These ground verification practices have been undertaken in different environments around the world, namely in monsoon climates (India and Bangladesh), in humid tropics (Brazil), and in semi-arid regions (Niger and the High Plains aquifer, Australia, Central United States) with similar climate to Erbil. Research offering a good fit between GRACE-derived groundwater variations and in situ observation well records, with discrepancies between the two datasets ranging from 2.1 to 3.5 cm (Swenson et al. 2008; Syed et al. 2005; Voss et al. 2013). In this regard, the GRACE satellite data can safely be used for semi-arid areas assessing seasonal fluctuations of groundwater.

Current practices of excessive groundwater abstraction for irrigated agriculture and public water supply, pumping of groundwater to store in farm ponds and the competition among smallholder farms and households to illegally drill new and deeper wells have notably dropped the groundwater tables and dried up many wells in the semi-arid Erbil province. The lack of integrated land-use planning and impacts of climate change have exacerbated the pressure on groundwater resources and placed local communities at extreme risk of water shortages as 91% of the observation wells are associated with significant drops in groundwater levels. Therefore, the groundwater reserves of the Erbil basin are increasingly exposed to overexploitation.

The results of the monitoring network indicate that continuous depletion is occurring in the urbanised central part of the Erbil basin. The degree of vulnerability of the local communities to water shortages is expected to increase considering that the current practices of over-abstraction of groundwater cannot be appropriately addressed in the foreseeable future together with the impacts of climate change, decrease in precipitation and increase in temperature and potential evapotranspiration rates. Therefore, undertaking accurate estimations of groundwater recharge and safe yields for semi-arid region basins are important.

Regardless of the impact of climate alterations on groundwater, the groundwater itself has impacts on the climate system conditions in terms of evapotranspiration, downwind precipitations, soil moisture and streamflow, so that it seems like an interchangeable process that one maintains the other. The continuation of current practices (i.e., overexploitation of groundwater and illegal drilling of the new and deeper wells) together with a decrease in precipitation and an increase in temperature and potential evapotranspiration rates would severely cripple the socio-economic development and aggravate the existing vulnerabilities of local communities. This warrants long-term sustainable groundwater management transcending status quos and calls for mitigation measures and adaptation to climate changes.

To enhance the sustainable management of groundwater resources, it is necessary to strengthen the engagement of the local communities, civil organization societies, and the private sector. In addition, governmental institutions require sufficient financial provisions to support the implementation of the existing regulatory framework. The public should be made aware of the adverse consequences of overexploitation of groundwater and the necessity of long-term sustainable management of groundwater resources.

Enforceable management of both surface water and groundwater is required for aquifers shared between different administrative authorities to protect groundwater from depletion and harness surface water to replenish groundwater. Moreover, a technical framework needs to be developed to reduce the consumption and wastage of water resources, and to limit breaching the rights of others when sharing water resources. A water policy that aims to establish a national groundwater database is necessary.

References

Ahmmad YK (2012) Legislations on water resources protection in Iraq. http://www.mpfpr.de/fileadmin/media/Water_Law/Nationales_Recht/Treaties_Iraq/Overview_-_Water_Law_in_Iraq__English.pdf. Accessed 10 Feb 2020

Al-Faraj FAM, Al-Dabbagh BNS (2015) Assessment of collective impact of upstream watershed development and basin-wide successive droughts on downstream flow regime: the Lesser Zab transboundary basin. J Hydrol 530:419–430. https://doi.org/10.1016/j.jhydrol.2015.09.074

Al-Faraj FAM, Scholz M (2015) Impact of upstream anthropogenic river regulation on downstream water availability in transboundary river watersheds. Int J Water Resour Dev 31:28–49. https://doi.org/10.1080/07900627.2014.924395

Al-Faraj FAM, Scholz M (2014) Assessment of temporal hydrologic anomalies coupled with drought impact for a transboundary river flow regime: the Diyala watershed case study. J Hydrol 517:64–73. https://doi.org/10.1016/j.jhydrol.2014.05.021

Al-Faraj FAM, Scholz M, Tigkas D (2014) Sensitivity of surface runoff to drought and climate change: application for shared river basins. Water 6:3033–3048. https://doi.org/10.3390/w6103033

Allen RG, Pereira LS, Raes D, Smith M (1998) Crop evapotranspiration-Guidelines for computing crop water requirements-FAO Irrigation and drainage paper 56. FAO, Rome

Alley W, Furey S, Klingbeil R, Shivakoti BR, Kabede S, Hirata R (2017) The UN-SDGs for 2030: essential indicators for groundwater

Buday T (2006) Geology of Iraq, 1st ed. Dolin, Prague and Moravian Museum, Brno, Prague. https://doi.org/10.1007/s13398-014-0173-7.2

Castle SL, Thomas BF, Reager JT, Rodell M, Swenson SC, Famiglietti JS (2014) Groundwater depletion during drought threatens future water security of the Colorado River Basin. Geophys Res Lett 41:5904–5911. https://doi.org/10.1002/2014GL061055

Chikodzi D (2011) Analysis of monthly and seasonal groundwater fluctuations in Zimbabwe: a remote sensing perspective. J Hydrol Current Res s1:1–5. https://doi.org/10.4172/2157-7587.S1-003

Debnath S, Adamala S, Raghuwanshi NS (2015) Sensitivity analysis of FAO-56 Penman-Monteith method for different agro-ecological regions of India. Environ Process 2:689–704. https://doi.org/10.1007/s40710-015-0107-1

Ebrahimi H, Ghazavi R, Karimi H (2016) Estimation of groundwater recharge from the rainfall and irrigation in an arid environment using inverse modeling approach and RS. Water Resour Manag 30:1939–1951. https://doi.org/10.1007/s11269-016-1261-6

Erbil Governorate (2018) Erbil geography. http://www.hawlergov.org/en/page.php?id=132912
     0973. Accessed 16 Feb 2020

FAO (2012) ETo calculator | land and water | food and agriculture organization of the United Nations
     | land and water | food and agriculture organisation of the United Nations

Gale I (2005) Strategies for managed aquifer recharge (MAR) in semi-arid areas. http://unesdoc.
     unesco.org/images/0014/001438/143819e.pdf. Accessed 11 Jan 2020

Green TR, Taniguchi M, Kooi H, Gurdak JJ, Allen DM, Hiscock KM, Treidel H, Aureli A (2011)
     Beneath the surface of global change: Impacts of climate change on groundwater. J Hydrol
     405:532–560. https://doi.org/10.1016/j.jhydrol.2011.05.002

Grimes DIF, Pardo-Iguzquiza E (2010) Geostatistical analysis of rainfall. Geogr Anal 42:136–160.
     https://doi.org/10.1111/j.1538-4632.2010.00787.x

Hameed HM (2013) Water harvesting in Erbil Governorate, Kurdistan region, Iraq detection of
     suitable sites using geographic information system and remote sensing. Lund University, Lund

Hameed HM, Faqe GR, Qurtas SS, Hashemi H (2015) Impact of Urban growth on groundwater
     levels using remote sensing—case study: Erbil City, Kurdistan Region of Iraq. J Nat Sci Res
     5:72–85

Iwasaki Y, Ozaki M, Nakamura K, Horino H, Kawashima S (2013) Relationship between increment
     of groundwater level at the beginning of irrigation period and paddy filed area in the Tedori River
     Alluvial Fan Area, Japan. Paddy Water Environ 11:551–558. https://doi.org/10.1007/s10333-
     012-0348-9

Lorenzo-Lacruz J, Garcia C, Morán-Tejeda E (2017) Groundwater level responses to precipitation
     variability in Mediterranean insular aquifers. J Hydrol 552:516–531

Margane A (2003) Management, protection and sustainable use of groundwater and soil resources
     in the Arab Region: guideline for the delineation of groundwater protection zones. Damascus

MoAWR-KRG (2016) Internal report, groundwater data for Kurdistan Region. Erbil, Kurdistan
     Region, Iraq

Mustafa O, Merkel B, Weise S (2015) Assessment of hydrogeochemistry and environmental isotopes
     in karst springs of Makook Anticline, Kurdistan Region, Iraq. Hydrology 2:48–68. https://doi.
     org/10.3390/hydrology2020048

Nanekely M, Scholz M, Qarani Aziz S (2017) Towards sustainable management of groundwater: a
     case study of semi- arid area, Iraqi Kurdistan region. Eur Water 57:451–457

NCEP (2015) Global weather data for SWAT. Clim Forecast Syst Reanalysis. https://globalweather.
     tamu.edu. Accessed 4 Feb 2020

Payne SM, Woessner WW (2010) An aquifer classification system and geographical information
     system-based analysis tool for watershed managers in the Western U.S. J Am Water Resour Assoc
     46:1003–1023. https://doi.org/10.1111/j.1752-1688.2010.00472.x

Seibert J, Vis MJP (2012) Teaching hydrological modeling with a user-friendly catchment-runoff-
     model software package. Hydrol Earth Syst Sci 16:3315–3325. https://doi.org/10.5194/hess-16-
     3315-2012

Smerdon BD (2017) A synopsis of climate change effects on groundwater recharge. J Hydrol
     555:125–128. https://doi.org/10.1016/j.jhydrol.2017.09.047

Stevanovic Z, Iurkiewicz A (2009) Groundwater management in northern Iraq. Hydrogeol J 17:367–
     378. https://doi.org/10.1007/s10040-008-0331-0

Swenson S, Famiglietti J, Basara J, Wahr J (2008) Estimating profile soil moisture and groundwater
     variations using GRACE and Oklahoma Mesonet soil moisture data. Water Resour Res 44:1–12.
     https://doi.org/10.1029/2007WR006057

Syed TH, Famiglietti JS, Chen J, Rodell M, Seneviratne SI, Viterbo P, Wilson CR (2005) Total basin
     discharge for the Amazon and Mississippi River basins from GRACE and a land-atmosphere water
     balance. Geophys Res Lett 32:1–5. https://doi.org/10.1029/2005GL024851

United Nations (2019) Transforming our world: the 2030 Agenda for sustainable development.
     United Nations—sustainable development knowledge platform. https://sustainabledevelopment.
     un.org/post2015/transformingourworld. Accessed 3 Feb 2020

Vangelis H, Tigkas D, Tsakiris G (2013) The effect of PET method on reconnaissance drought index (RDI) calculation. J Arid Environ 88:130–140. https://doi.org/10.1016/j.jaridenv.2012.07.020

Voss KA, Famiglietti JS, Lo M, de Linage C, Rodell M, Swenson SC (2013) Groundwater depletion in the Middle East from GRACE with implications for transboundary water management in the Tigris-Euphrates-Western Iran region. Water Resour Res 49:904–914. https://doi.org/10.1002/wrcr.20078

Wada Y, Van Beek LPH, Van Kempen CM, Reckman JWTM, Vasak S, Bierkens MFP (2010) Global depletion of groundwater resources. Geophys Res Lett 37:1–5. https://doi.org/10.1029/2010GL

Chapter 13
Modeling and Prediction of Groundwater Level Fluctuations Using Geoinformatics and Artificial Neural Networks in Al Ain City, UAE

Khalid ElHaj, Salem Issa, Dalal Alshamsi, and Biruk Abera Cherkose

13.1 Introduction

Groundwater is an essential source of water for countries with limited water resources and in particular those having arid climate conditions such as the gulf states. As technology advances, more tools become available to help manage and utilize groundwater resources. GIS and remote sensing were among the noteworthy tools that have been essential in groundwater and environment research (Rango and Shalaby 1998; Sakthivadivel et al. 1999). The techniques have been employed since the early 1990s to draw groundwater potential maps (Krishnamurthy et al. 1996; Saraf and Choudhury 1998) and predict changes in groundwater level (Goossens et al. 1993). Machine Learning (ML) and Artificial Neural Networks (ANN) have been utilized recently to better manage groundwater resources (Coulibaly et al. 2001; Elshorbagy et al. 2010a, b; Kenda et al. 2018; Javadinejad et al. 2020). In this work, we use historic Groundwater Level (GWL) data along with metrological data, including rain, temperature, humidity, and evaporation to predict the changes in groundwater level and factors controlling the changes. The observation data cover the period from January 2004 to December 2012 and the prediction was performed from 2012 to 2019 with comparison to some control observation data of selected years. We apply the Geoinformatics tools (GIS and remote sensing) to interpolate the spatial distribution of the GWL for each year. We have selected an area of interest from a part of Al Ain city, UAE. This area provided relatively good historical groundwater level data, has extensive use of groundwater by agricultural and is highly urbanized (Fig. 13.1).

Application of the ANN and ML techniques for this case study area is aimed at pilot evaluation of the technology and possible expanding of the technology to include the whole Al Ain region and most likely the UAE in the future. Successful ANN and

K. ElHaj (✉) · S. Issa · D. Alshamsi · B. A. Cherkose
Geosciences Department, College of Science, United Arab Emirates University, P.O. Box 15551, Al Ain, UAE
e-mail: 200734761@uaeu.ac.ae

Fig. 13.1 Location of the study area in the UAE (red square) and a portion of Al Ain city and the surrounding agricultural areas used in the modelling. The red dots are the wells used in the study

ML predictions will help decision makers to predict future possible scenarios and suggest or implement remedies in time manner to conserve the groundwater reserves. Another use of ANN technology is to predict the GWL based on other element/factors such as the metrological factors used in this study, this would allow us to fill missing data whenever possible and also have less uncertainty regarding our predictions. This can be seen in any TS prediction model as it would have a direct relationship between the number of predicted steps and the model uncertainty range. And the uncertainty range would be increasing at an exponential rate compared to the time steps. We alleviate this issue by basically hooking the model prediction with available and existing data (metrological in this case), this will limit the model performance for the yet to occur future. However, on the other hand, it will provide a more certain and substantial prediction for any available data and it will help immensely in predicting any missing periods in our dataset. And based on this relationship, the trained model can even be used to predict the past values, based on any available metrological data for the same period.

13.2 Methodology

The actual study is divided into 3 main steps, the first step was the data collection, wrangling, processing, and imputation, the next step was the coding step where we built the ANN and trained it to produce the best possible model for the data. Then we used the produced model for predictions of changes. The final output used the Geoinformatics systems for interpolation and maps.

13.2.1 Data Processing

The project entails datasets covering the period from January 2004 to December 2012. The GWL data required for the study were acquired from the Environment Agency—Abu Dhabi (EAD), while the metrological data were acquired from the National Center of Meteorology (NCM) (Figs. 13.2 and 13.3). Both datasets cover the period from January 2004 to December 2012. However, the metrological data continues until December 2019, which allowed us to predict the GWL for the period 2013–2019. The datasets were divided into training set and validation set. Since the purpose of the project is a Time Series (TS) forecasting, the division of the dataset would be based on time instead of randomly splitting the readings. The training set was composed of the data from January 2004 to December 2012, while the validation set (observation data) covered the period from January 2013 to December 2014. The metrological data covered the whole study period (660 reading for each element, not counting the inference period), the GWL dataset had 70 missing readings out of 660 which was needed to cover the study period.

There are several strategies for data imputation in TS analysis and the simplest ones use the median, the mode or a constant (Howard and Gugger 2020). Other approaches utilize a bit more elaborate methods such as linear regression, quadratic, and polynomial techniques. During this research we experimented with several imputation methods to find the optimal one to use for this case study (Fig. 13.4). Linear regression (McKinney 2018) was initially used to impute the missing reading in the GWL dataset, however, it produced abnormal or unreasonable readings in several instances as can be seen in the example below. Eventually, the best results were obtained using the "pad" method in pandas, which functions by propagating the last valid observation forward until it finds the next valid observation (McKinney 2018).

13.2.2 Artificial Neural Networks

Jupeter Notebook (an interactive top-level programming environment) was used as the main development environment for the entire datasets period. Utilizing Python
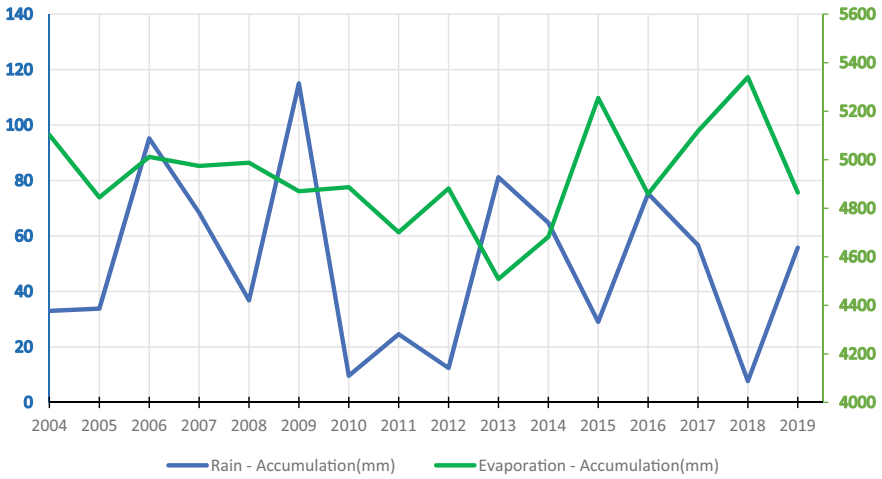
Fig. 13.2 Annual observed metrological data for the rain and evaporation elements covering the complete study period
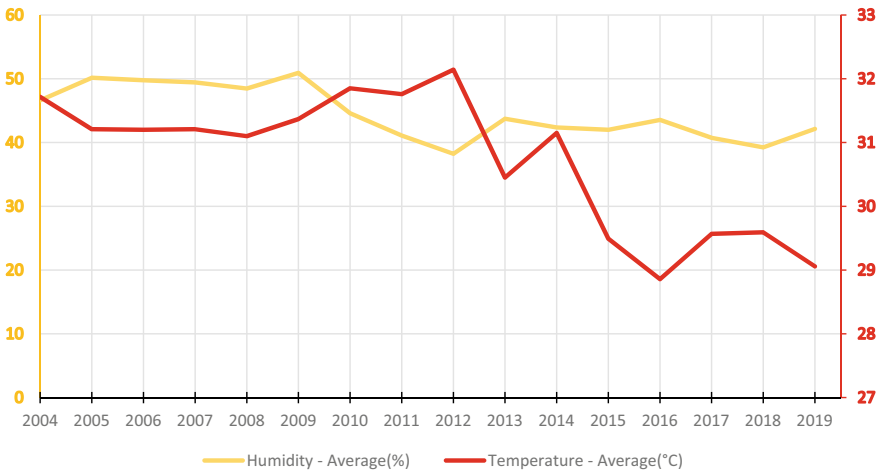
Fig. 13.3 Annual observed metrological data for the temperature and humidity elements covering the complete study period

as the programming language, Pytorch was chosen as the framework to build the ANN, and A high-level API (Fast.AI) was used to implement the ANN and tune the hyperparameters (Fig. 13.5). There were also many Python libraries tested during the project for data wrangling such as Pandas, Scikit-Learn, Numpy, among others. The dataset was fed to the ANN and through a trial and error we were able to optimize the hyperparameter for the Neural Network. The optimum ANN architecture was 5 linear hidden layers with "ReLU" activation functions. The architecture used was
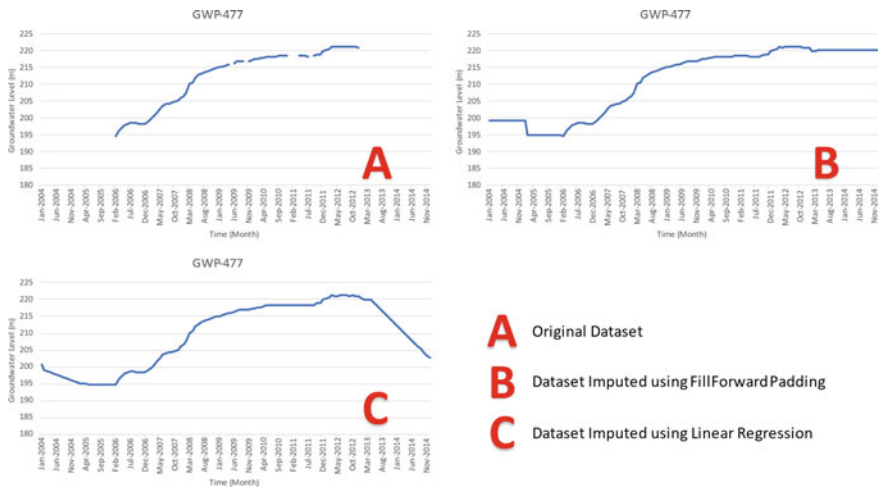
Fig. 13.4 Example of imputation anomalies demonstrated using well "GWP-477"
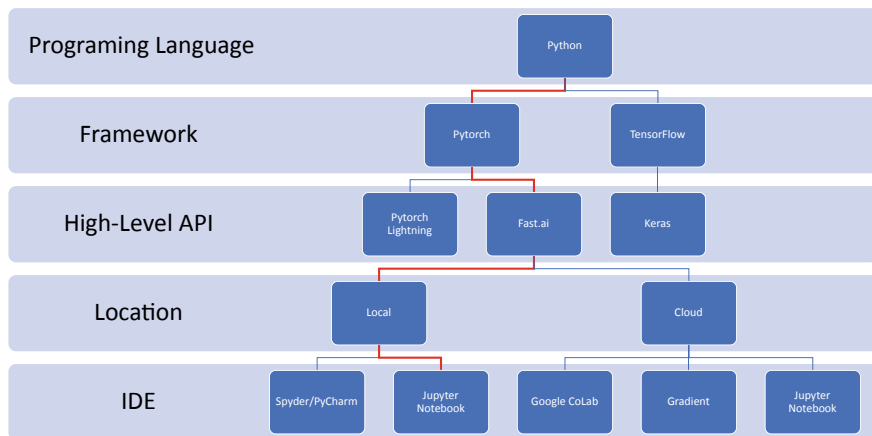
Fig. 13.5 The developmental structure of the artificial neural network used in this research

Feedforward Neural Network and had the following configuration [**700**, **200**, **600**, **100**, **9**]. Aside from the 5 hidden layers, there is one input layer, 3 embedding layers that embed and normalize the values using BatchNorm1d (Ioffe and Szegedy 2015) and one linear output layer that have a single node combined with a sigmoid activation function.

The ANN configuration uses Mean Square Error (MSE) as a loss function, and we flatten the results to couple the values from the other rows into one reading for each batch expecting that the ANN can relate the information in subsequent rows

and not each row independently. As for the optimization function, the Ranger optimization function was chosen due to its impressive performance and high accuracy (Wright 2019; Wright 2022). Ranger is combination of optimizers; it uses Rectified Adam algorithm as a base optimizer. This is mainly due to RAdam ability to create excellent warmup based on the training dataset, which results in minimizing the sensitivity of the user choice regarding the hyperparameters on the testing and training accuracies (Liu et al. 2019). The second algorithm used by Ranger is Gradient Centralization (GC). The goal of using GC algorithm is to have a more efficient and stable training process, this mainly due to the way that GC work, as it centralizes the gradient vectors to have a zero mean thus it operates directly on them, as a result, this allows the optimizer to increase the generalization of the ANN (Yong et al. 2020). Finally, the third algorithm utilized by Ranger is the Lookahead algorithm. The Lookahead algorithm utilizes two optimizers that updates two sets of weights, a "fast weights" and a "slow weights", the slow weight set is updated once the final direction is determined based on the fast weight set. This allows the Lookahead algorithm to avoid many heavy calculations steps and decrease the variance significantly. As a result it produces more consistent results with minimal computation time (Zhang et al. 2019).

13.2.3 Mapping and Visualization

Upon extraction of the data and averaging the values, the findings were exported to ArcGIS for interpolation over the study area. The interpolation used in this study was Ordinary Kriging utilizing Circular semi-variogram model which was proven to the most effective in hydrological modeling and applications (Hengl et al. 2007; Tapoglou et al. 2014; Varouchakis and Hristopulos 2013). Additionally, the Kriging interpolation appeared to represent the hydrogeology of the study area better when compared to IDW. Since the predictions were monthly based and covering a 15-year period, the produced maps would have reached 180 map to represent each month. For the sake of convenience and representation, the monthly maps were averaged into annual data, which resulted in 15 maps. The GWL in the interpolated layers were divided into 9 classes to clearly highlight the fluctuations occurring in the readings. However, since the variations were significantly lower in the later years of the study period, the intervals of the classes were changed to reflect the fluctuations. As such, the observation period is divided into two classifications, the first covers the period from 2004 to 2007, while the second covers the remaining observation period from 2008 to 2012. The second classification is also used to cover the prediction period from 2013 to 2019.

13.3   Results and Discussion

The accuracy metrics used to measure the performance of the ANN were Pearson correlation coefficient (r), Root Mean Squared Error (RMSE) and Coefficient of Determination (R^2). The most optimum model reached during the trial-and-error phase was achieved using an architecture of the following configuration [700, 200, 600, 100, 9]. The resulting accuracies are illustrated along with the training and validation profiles in (Fig. 13.6). The highest accuracies achieved for our metrics were 0.997 for r, while R^2 and RMSE were 0.977 and 10.23, respectively. The results were achieved using a batch size of 15 at the 408th epoch using the Callback function in the (Fast.AI) framework during a 500-epoch run. Taking into consideration the relatively small number of samples, and a Standard Deviation of 19, the model prediction can be rated as good and in line with or better than previous published work in ANN utilization in hydrology (Malik and Bhagwat 2021; Mukherjee and Ramachandran 2018; Paraskevas et al. 2014; Pasandi et al. 2017). The trained model takes 7 inputs [Lat, Long, Time, Rainfall, Temperature, Humidity and Evaporation] to produce one predicted output of water level in a monthly average format. The model was then used to infer the monthly predictions of GWL during the period from 2013 to 2019.

   The monthly GWL averages are shown with annual tick marks to facilitate visual representation (Fig. 13.7). There is rather good approximation in the GWL trends for the period of observation (2004–2012; Fig. 13.8) and prediction (2013–2019; Fig. 13.9) which indicates slight changes in GWL. However, an increase in GWL of more than 20 m is observed in most of the wells during and after 2005 (marked as grey bar in Fig. 13.7 and also shown in Fig. 13.8a). This increase seems to persist in the predicted data (2013–2019) and was also noticeable in the observation data (2005–2017) presented in the Groundwater Atlas of the Abu Dhabi Emirate (Environment

Coefficient of Determination (R^2)	0.977154
Coefficient of Correlation (r^2)	0.997768
Root Mean Square Error (RMSE)	10.237439
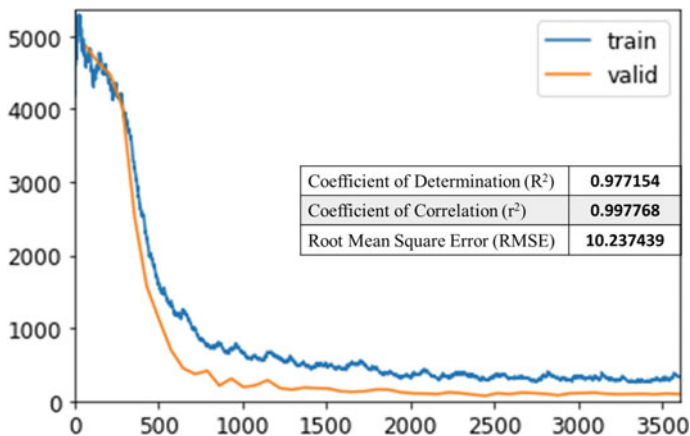
Fig. 13.6   This illustrates the training profile as well as the testing profile, with a box indicating the achieved accuracy in the testing profile
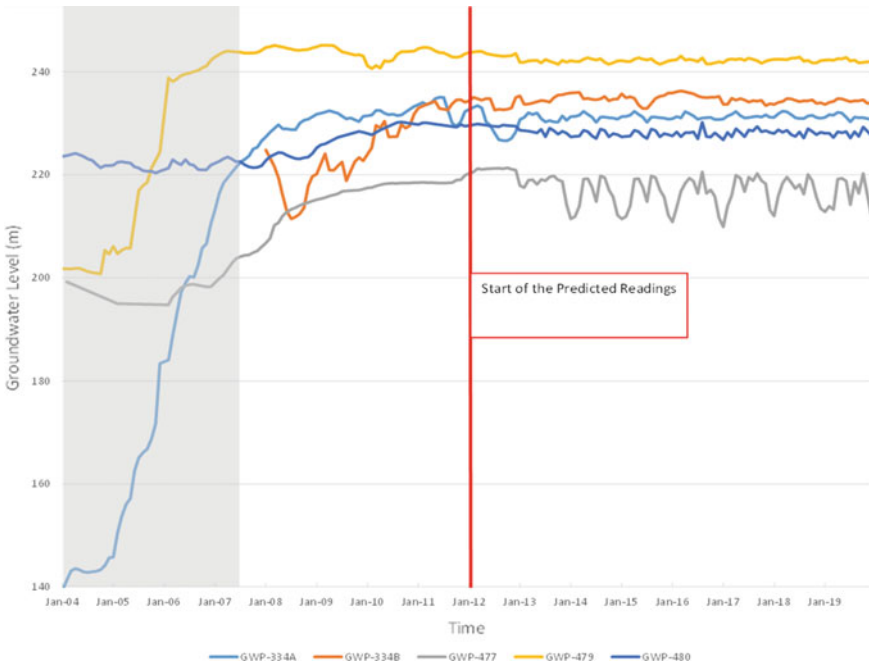
Fig. 13.7 The average annual GWL values. The red vertical line divides the data into observed (2004–2012) and predicted, model, (2013–2019) values. The gray bar indicates the period when changes (mainly increase in GWL) occurred

Agency Abu Dhabi 2018). Among the possible cause of increasing groundwater level in the study area is agricultural landscapes watering and leakage from the water distribution and sewage system. As urbanization advanced the main source of water for public use is the desalination water transported from the coastal cities. The data of rainfall do not show abnormal increase in rainfall after 2005, however, contribution from natural recharge may not be neglected if abstraction has declined in the area due to urbanization effect. Investigations of recharge conditions in the region using radioactive isotopes (Gómez-Alday et al. 2022) suggest that most of the groundwater is modern and has strong imprints of natural recharge. The isotopic data also exposed contribution from anthropogenic sources. Consequently, both sources, natural and anthropogenic, have played a role in the increasing GWL observed in the data of the studied region.
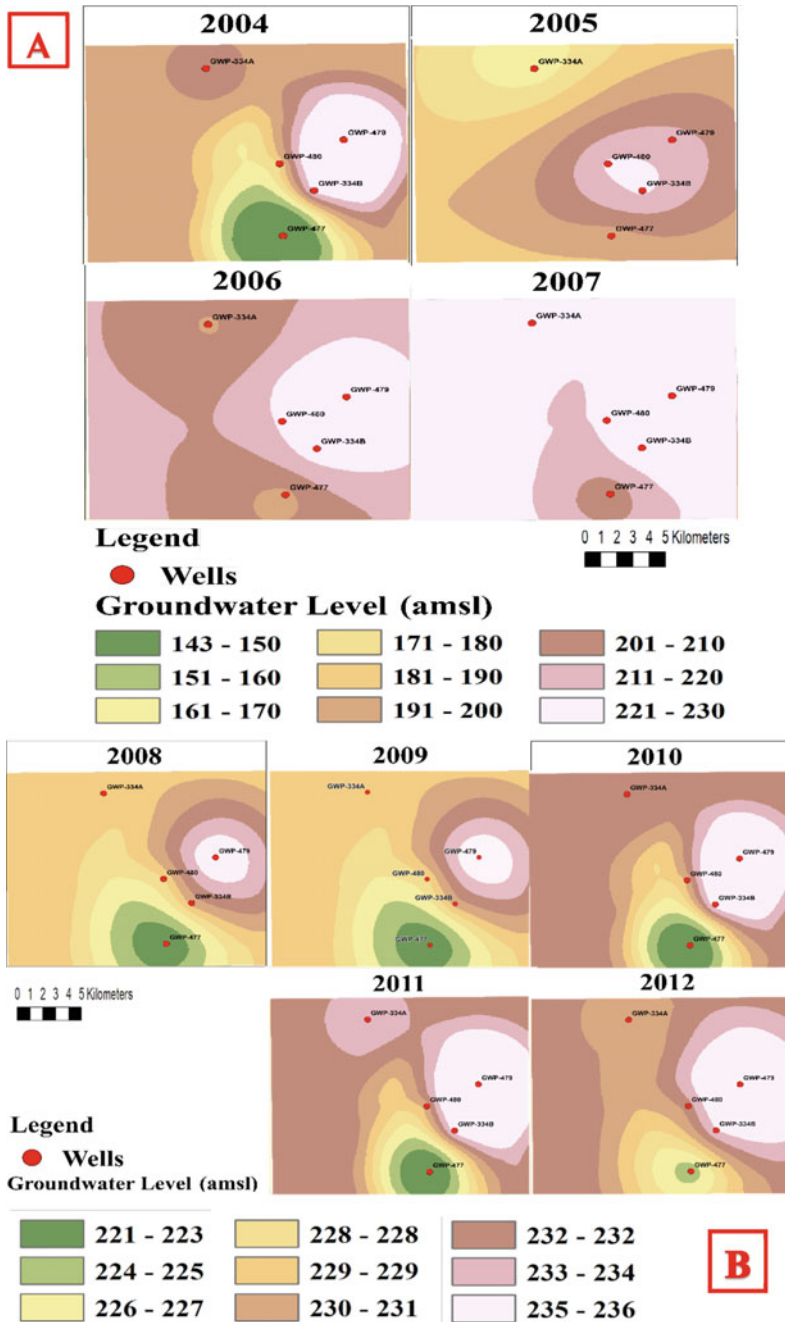
Fig. 13.8 Observed GWL fluctuation during the period **a** 2004–2007, **b** 2008–2012
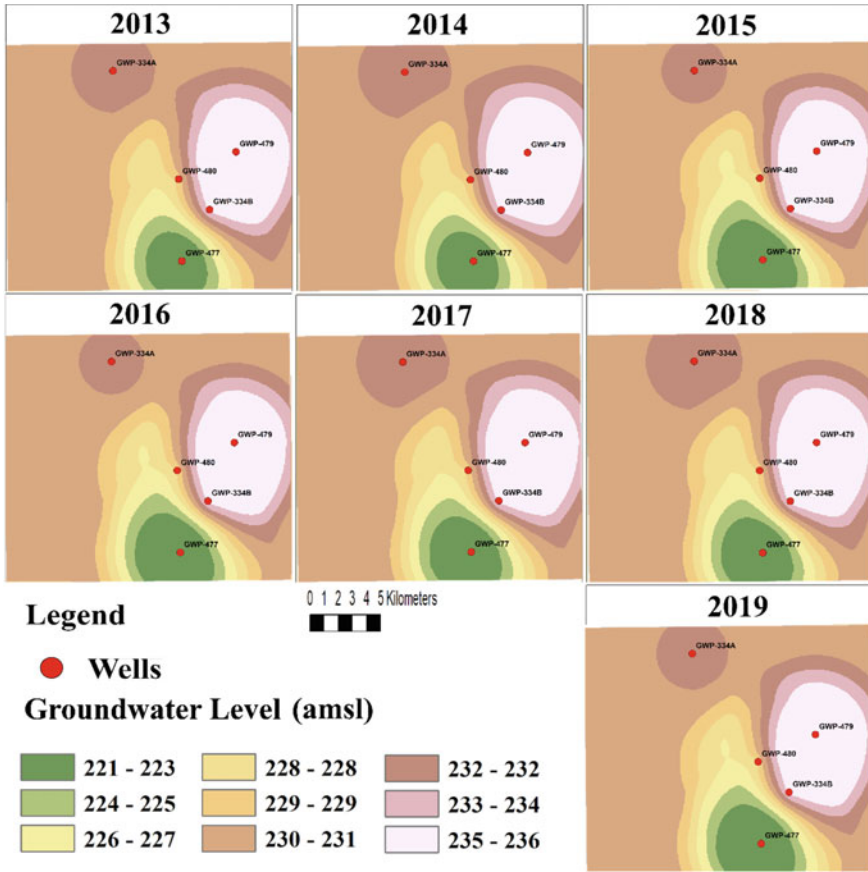
Fig. 13.9 Predicted annual GWL variation with time for the period (2013–2019)

13.4 Conclusions

The pilot study presented here shows that application of state-of-the-art ANN algorithms in a GIS environment to model and predict groundwater level (GWL) fluctuations in the arid region of Al Ain, UAE is promising. Filling the data gaps using linear regression caused unexpected behavior as thus FillForward padding would present the most reasonable and simple gap filling technique for TS analysis and modeling. Utilizing (Fast.AI) helped clear many hurdles in applying the state-of-the-art ML algorithms to our datasets. This includes the application of the ranger optimizer which provided excellent accuracy equaling and, in some instances, surpassing the previous literatures accuracy in predicting the GWL fluctuation. In interpolating between the GWL in the wells, Ordinary Kriging utilizing Circular semi-variogram model produced the most realistic representation of the groundwater surface.

The model predictions indicate comparable trends of the GWL between the observation period (2004–2012) and predicted period (2013–2019). Despite the limited number of observations used here, ML using the ANN algorithm represents a potential approach for future prediction of changes in groundwater levels and other physical and chemical characteristics of groundwater. Accurate and abundant data can improve the prediction and provide essential background information for decision makers regarding management of the groundwater in the region. This approach can be utilized with environmental Isotopes tracing along with metrological data, and it would produce more accurate results. The findings also signify the importance of data management and data imputations for TS analysis, as thus, future research can focus on minimizing the need of significant amounts of data which can be translated into utilizing machine learning to impute a more accurate missing data using regression analysis. And this can be one of the major use cases of this model, as finding the relationship between the metrological data and the GWL fluctuation would allow us to create a model that would be able to simulate the relationship and produce a GWL value based on the given metrological data. Finally, since ML calculations can be considered as Blackbox analyses, a transparent ML, or as it's called (Explainable AI), would be a better fit for hydrology prediction as it would be easier to signify the most important factors affecting the GWL fluctuations, and even eliminate any factors that have minimal or insignificant effects on the GWL fluctuations, thus saving costs on computation time and resources.

References

Coulibaly P, Anctil F, Aravena R, Bobée B (2001) Artificial neural network modeling of water table depth fluctuations. Water Resour Res 37(4):885–896. https://doi.org/10.1029/2000WR900368

Elshorbagy A, Corzo G, Srinivasulu S, Solomatine DP (2010a) Experimental investigation of the predictive capabilities of data driven modeling techniques in hydrology—part 1: concepts and methodology. Hydrol Earth Syst Sci 14(10):1931–1941. https://doi.org/10.5194/hess-14-1931-2010

Elshorbagy A, Corzo G, Srinivasulu S, Solomatine DP (2010b) Experimental investigation of the predictive capabilities of data driven modeling techniques in hydrology—part 2: application. Hydrol Earth Syst Sci 14(10):1943–1961. https://doi.org/10.5194/hess-14-1943-2010

Environment Agency Abu Dhabi (2018) Groundwater atlas of Abu Dhabi Emirate, p 118. https://www.ead.gov.ae/storage/Post/files/276ac7243c429b04c1d781f1ae42d09f.pdf

Goossens RGS, De Dapper M, Ghabour TK, El Badawi M, Gad A-A (1993) Development of a GIS simulation model and the use of remote sensing for monitoring and prediction of soil salinity and waterlogging in the Nile delta (Egypt). 1941:137–150. https://doi.org/10.1117/12.154682

Gómez-Alday JJ, Hussein S, Arman H, Alshamsi D, Murad A, Elhaj K, Aldahan A (2022) A multi-isotopic evaluation of groundwater in a rapidly developing area and implications for water

management in hyper-arid regions. Sci Total Environ 805:150245. https://doi.org/10.1016/j.sci
totenv.2021.150245

Hengl T, Toomanian N, Reuter HI, Malakouti MJ (2007) Methods to interpolate soil categorical
variables from profile observations: lessons from Iran. Pedometrics 2005 140(4):417–427. https://
doi.org/10.1016/j.geoderma.2007.04.022

Howard J, Gugger S (2020) Deep learning for coders with fastAI and PyTorch

Ioffe S, Szegedy C (2015) Batch normalization: accelerating deep network training by reducing
internal covariate shift. arXiv. http://arxiv.org/abs/1502.03167

Javadinejad S, Dara R, Jafary F (2020) Modelling groundwater level fluctuation in an Indian coastal
aquifer. Water SA 46(4 October). https://doi.org/10.17159/wsa/2020.v46.i4.9081

Kenda K, Čerin M, Bogataj M, Senožetnik M, Klemen K, Pergar P, Laspidou C, Mladenić D (2018)
Groundwater modeling with machine learning techniques: Ljubljana polje aquifer. Proceedings
2(11). https://doi.org/10.3390/proceedings2110697

Krishnamurthy J, Venkatesa Kumar N, Jayaraman V, Manivel M (1996) An approach to demarcate
ground water potential zones through remote sensing and a geographical information system. Int
J Remote Sens 17(10):1867–1884. https://doi.org/10.1080/01431169608948744

Liu L, Jiang H, He P, Chen W, Liu X, Gao J, Han J (2019) On the variance of the adaptive learning
rate and beyond

Malik A, Bhagwat A (2021) Modelling groundwater level fluctuations in urban areas using artificial
neural network. Groundw Sustain Dev 12:100484. https://doi.org/10.1016/j.gsd.2020.100484

McKinney W (2018) Python for data analysis, vol 71, no 10, p 541

Mukherjee A, Ramachandran P (2018) Prediction of GWL with the help of GRACE TWS for
unevenly spaced time series data in India: analysis of comparative performances of SVR, ANN
and LRM. J Hydrol 558:647–658. https://doi.org/10.1016/j.jhydrol.2018.02.005

Paraskevas T, Dimitrios R, Andreas B (2014) Use of artificial neural network for spatial rainfall
analysis. J Earth Syst Sci 123(3):457–465. https://doi.org/10.1007/s12040-014-0417-0

Pasandi M, Salmani N, Samani N (2017) Spatial estimation of water-table depth by artificial neural
networks in light of ancillary data. Hydrol Sci J 62(12):2012–2024. https://doi.org/10.1080/026
26667.2017.1349908

Rango A, Shalaby AI (1998) Operational applications of remote sensing in hydrology: success,
prospects and problems. Hydrol Sci J 43(6):947–968. https://doi.org/10.1080/026266698094
92189

Sakthivadivel R, Thiruvengadachari S, Amarasinghe U, Bastiaanssen WGM, Molden D (1999)
Performance evaluation of the Bhakra irrigation system, India, using remote sensing and GIS
techniques

Saraf AK, Choudhury PR (1998) Integrated remote sensing and GIS for groundwater exploration
and identification of artificial recharge sites. Int J Remote Sens 19(10):1825–1841. https://doi.
org/10.1080/014311698215018

Tapoglou E, Karatzas GP, Trichakis IC, Varouchakis EA (2014) A spatio-temporal hybrid neural
network-Kriging model for groundwater level simulation. J Hydrol 519:3193–3203. https://doi.
org/10.1016/j.jhydrol.2014.10.040

Varouchakis EA, Hristopulos DT (2013) Comparison of stochastic and deterministic methods for
mapping groundwater level spatial variability in sparsely monitored basins. Environ Monit Assess
185(1):1–19. https://doi.org/10.1007/s10661-012-2527-y

Wright L (2019) How we beat the fastAI leaderboard score by +19.77%…a. Medium. https://lessw.
medium.com/how-we-beat-the-fastai-leaderboard-score-by-19-77-a-cbb2338fab5c

Wright L (2022) Ranger-deep-learning-optimizer (Python). https://github.com/lessw2020/Ranger-
Deep-Learning-Optimizer (Original work published 2019)

Yong H, Huang J, Hua X, Zhang L (2020) Gradient centralization: a new optimization technique for deep neural networks. In Vedaldi A, Bischof H, Brox T, Frahm J-M (eds) Computer vision—ECCV 2020, vol 12346. Springer International Publishing, pp 635–652. https://doi.org/10.1007/978-3-030-58452-8_37

Zhang M, Lucas J, Ba J, Hinton GE (2019) Lookahead optimizer: K steps forward, 1 step back. Adv Neural Inf Process Syst 32. https://proceedings.neurips.cc/paper/2019/hash/90fd4f88f588ae64038134f1eeaa023f-Abstract.html

Chapter 14
Factors Influencing the Site Selection Criteria for Efficient Aquifer Storage and Recovery (ASR) System in Saline Regions

Shubham Tiwari and Brijesh Kumar Yadav

14.1 Introduction

Groundwater salinity is a concerning challenge to ensuring freshwater availability in arid and semi-arid regions (Krishan et al. 2019). There are 24 million km^2 of groundwater with high salinity at shallow and intermediate depths (Van Weert et al. 2009). West and Central Asian basins have the most area with high groundwater salinity. The conventional managed aquifer recharge techniques are inefficient in ensuring freshwater availability during dry seasons.

Aquifer storage and recovery technique of managed aquifer recharge are performing well in developing countries to store freshwater within saline groundwater and its future recovery. In arid and semi-arid regions, aquifer storage and recovery (ASR) may be successful in saline aquifers when installed at a suitable location and operated appropriately (Yobbi 1996). Therefore, ASR can help to ensure freshwater availability during droughts in saline groundwater regions (Dillon et al. 2019). In the ASR technique, surplus freshwater available on the surface during the rainy season is artificially injected for its future recovery during dry periods. In saline aquifers, the freshwater is stored by flushing the ambient saline groundwater away from the injection well, and it forms a freshwater packet (Kumar and Kimbler 1970; Merritt 1985; Ward et al. 2008). The freshwater packet stays for long storage durations within saline aquifers due to the prolonged rate of mixing between fresh-saline water (Pyne 1995). The recovery efficiency (RE) of the ASR system in saline regions is used to evaluate its performance (Bakker 2010). The performance of an ASR scheme in saline groundwater regions can be improved by selecting a feasible

S. Tiwari (✉) · B. K. Yadav
Department of Hydrology, Indian Institute of Technology Roorkee, P.O. Box 247667, Roorkee, India
e-mail: stiwari@hy.iitr.ac.in

B. K. Yadav
e-mail: brijesh.yadav@hy.iitr.ac.in

site to reduce the mixing rate between stored freshwater and ambient saline ground-water (Johnson et al. 2014; Sathish and Mohamed 2018). Due to the losses from mixing phenomena and the buoyancy stratification process of the stored freshwater, the entire volume of freshwater injected cannot be recovered (Tiwari and Yadav 2021). The mixing losses depend on the ASR site's hydrogeology, ASR well design, and operational management of the ASR project (see Fig. 14.1).

Many studies are available that explain the influence of operational factors on the RE of ASR. By choosing locations with the proper hydrogeological conditions for ASR installations, mixing losses during the storage phase of the ASR scheme can be reduced. However, it is still necessary to comprehend how hydrogeology affects ASR performance in saline aquifers (Pyne 1995). The previous research on ASR performance enhancement in saline groundwater regions has focused on operational factors optimization using different numerical modeling studies. The
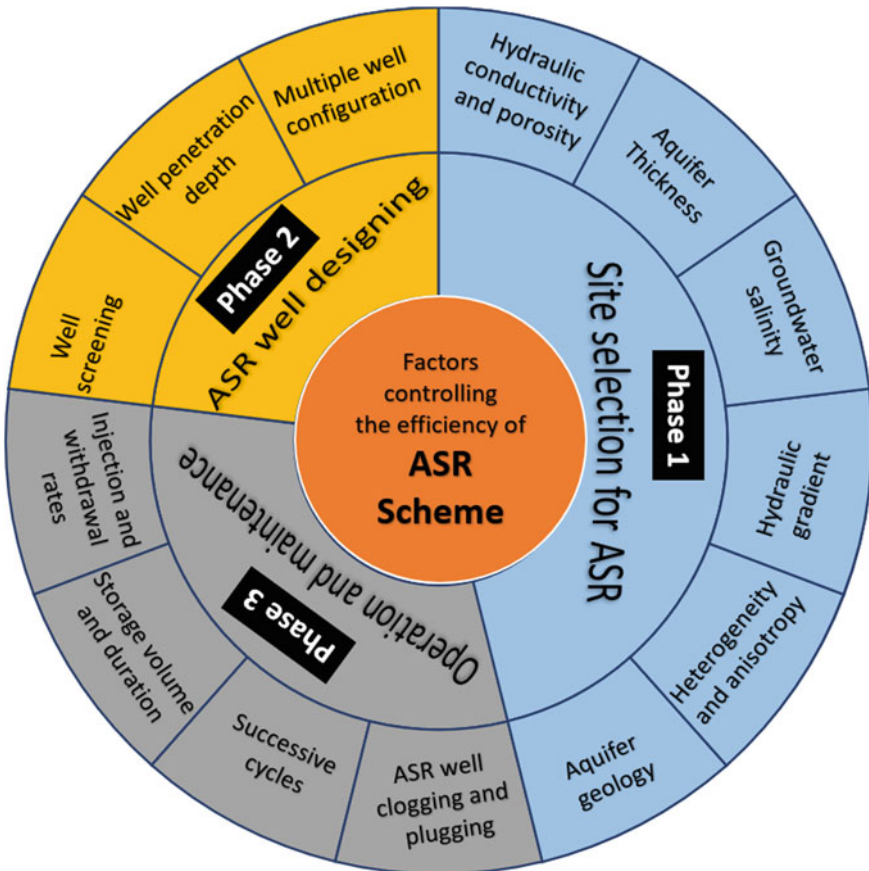
Fig. 14.1 Factors controlling the efficiency of aquifer storage and recovery (ASR) scheme in saline groundwater regions

optimization method for selecting a feasible site for ASR applications in saline aquifers is still missing in the literature. This study aims to identify the effects of aquifer properties (i.e., hydraulic conductivity, effective porosity, hydraulic gradient, longitudinal dispersivity, transverse dispersivity, and groundwater salinity) on the performance of ASR. A new method to optimize the hydrogeological properties before planning an ASR scheme installation may help in ensuring the possibility of ASR scheme success.

14.2 Methods

The main objective of this study is to evaluate the ASR system performance with respect to different influencing aquifer properties in saline groundwater regions. In this study, visual MODFLOW flex is used for density-dependent solute transport modeling using SEAWAT 4 (Langevin et al. 2008), which allows for the simulation of the impacts of free convection. Visual Modflow was used in three-dimensional groundwater flow and contaminant transport simulations, and variations in ASR performance were recorded. The method adopted was to create a general variable-density groundwater flow model for an ASR scheme that can simulate the different processes of stored freshwater within the saline aquifer. This model will replicate the losses in the stored freshwater packet with respect to time. The baseline model for a synthetic aquifer property in a confined aquifer was developed for the ASR system.

This study selected different values for each hydrogeological factor to observe the influence of varying aquifer properties on the ASR performance in saline groundwater regions. Each factor's effect was observed by changing the values of individual hydrogeological characteristics while keeping operational and well-design aspects constant. The synthetic aquifer properties were used in the baseline model, containing ten total layers (Fig. 14.2). The storage zone is 30 m thick and divided into ten layers of equal thickness. The model grid measures 500 m in width and 500 m in length (250 rows by 250 columns). The grid is bounded by constant head and concentration cells. Injection and recovery from the storage zone were simulated through an ASR well located on (X = 250 m and Y = 200 m) as fully penetrating and fully open in the storage zone. This model was solved using the BCF6 property package and Conjugate Gradient Solver (PCG). The Central Finite Difference (CFD) solution method was used for solving the numerical equations, and no influence of viscosity was considered during the process. The simulations were performed to understand the impact of hydraulic conductivity, aquifer porosity, aquifer thickness, hydraulic gradient, longitudinal dispersivity, transverse dispersivity, and density difference between injected freshwater and ambient saline groundwater. The simulation of the ASR model was performed by keeping operational factors constant during all three phases of the ASR scheme, as mentioned in Table 14.1. The recovery efficiency was calculated from the formula mentioned as follows:

$$RE = Vr/Vi * 100\%$$

where Vr is the volume of recovered freshwater, and Vi is the volume of total injected freshwater within the saline aquifer.

Fig. 14.2 Layers and hydrogeological variations considered in this study

Table 14.1 The operational factors used in the baseline model

Injection phase		Storage phase	Recovery phase
Injection rate (m³/day)	Injection volume (m³)	Storage durations (in days)	Active well depth (in m)
4500	405,000	90	906,030

14.3   Results and Discussion

The results obtained from this study are calculated through simulations for different hydrogeological factors on ASR performance for the assumed baseline parameters. These influences of the hydrogeological parameters are presented by increasing the values of these factors.

14.3.1   Aquifer Hydraulic Conductivity and Hydraulic Gradient

The average velocity of groundwater flow depends on the hydraulic conductivity and porosity along with the background hydraulic gradient (Freeze and Cherry 1979). Hence, the higher hydraulic gradient will increase the ambient groundwater velocity. Understanding ambient groundwater flow is vital for planning the artificial replenishment of groundwater aquifers for storage and mixing purposes (Bear and Jacobs 1965). As the groundwater velocities directly depend on the hydraulic gradient, the higher groundwater velocities allow stored freshwater to move faster from the up-gradient toward the down-gradient. This results in the change in the location of stored freshwater and keeping it out of the range of recovery well. Therefore, at the time of recovery, the total stored freshwater is not available in the range of recovery well situated in an up-gradient direction. The results indicate that moderate hydraulic conductivity (= ~ 10 m/day) is a more suitable condition to achieve higher RE, and while increasing or decreasing these values, ASR efficiency reduces (Figs. 14.3 and 14.4). The role of vertical hydraulic conductivity is also crucial for the freshwater storage within saline aquifer. The injected freshwater tends to move in upward direction due to density difference and the freshwater packet moves easily in the porous media with high vertical hydraulic conductivity. When stored freshwater packet comes near the top layer of aquifer, it is very difficult to recover. Therefore, low vertical hydraulic conductivity is recommended to achieve higher RE in saline groundwater regions.
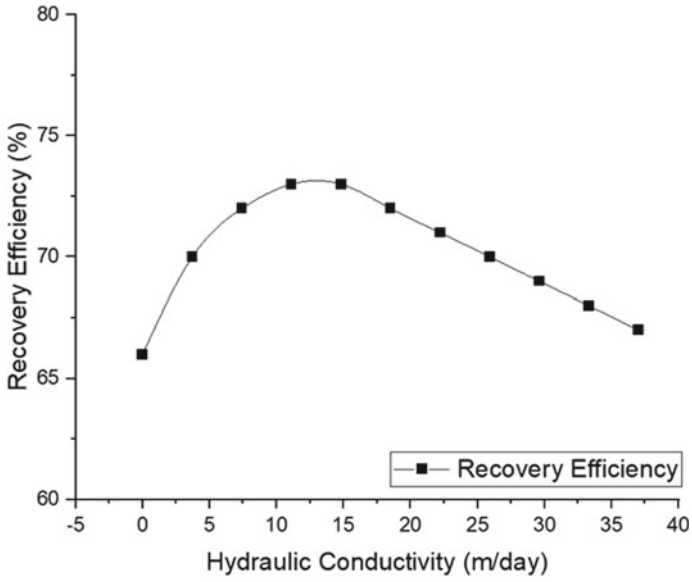
Fig. 14.3 Influence of hydraulic conductivity on recovery efficiency
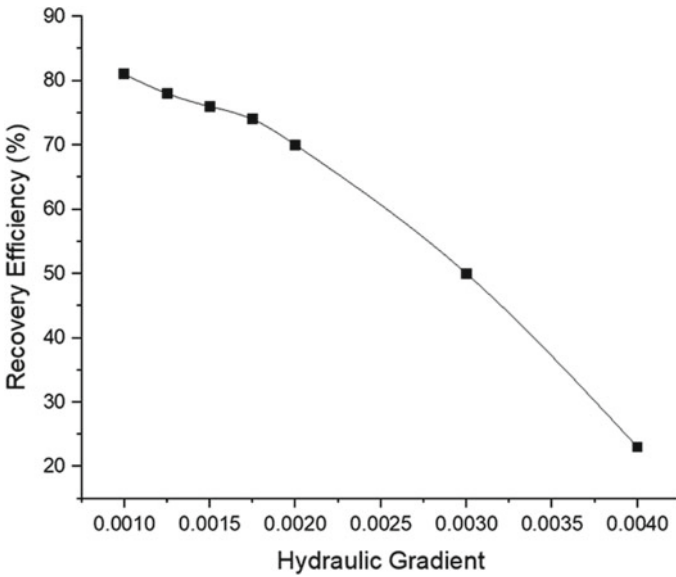
Fig. 14.4 Influence of hydraulic gradient on recovery efficiency
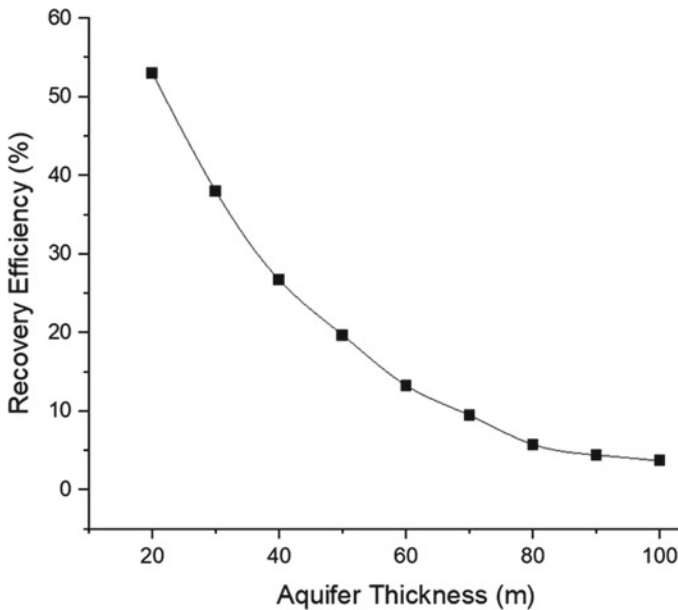
Fig. 14.5 Influence of aquifer thickness on recovery efficiency

14.3.2 Aquifer Thickness

The thickness of the storage zone does affect the recovery efficiency performance. The effect of aquifer thickness on the recovery efficiency depends on different values of longitudinal and transverse dispersivity coefficients, which control the mixing between fresh and saline water (Merritt 1985). Hence, less mixing between stored freshwater and saline water will occur when the vertical extent of the ambient aquifer is less. According to the review of the different case studies and data from other sites' storage zone for the lesser thickness aquifer, the higher the recovery efficiency will be. This study demonstrates that as the aquifer's thickness increased ASR system's performance tended to decrease (Fig. 14.5). Therefore, thin aquifers must be preferred over thick aquifers to achieve higher recovery efficiency while designing ASR projects.

14.3.3 Longitudinal and Transverse Dispersivity

Hydrodynamic dispersion is responsible mainly for the degree of mixing between injected and native water and controls the width of the transition zone (Anderson and Lowry 2004; Reese 2002). Dispersion and mixing at the fresh-saline interface in the saline aquifer produce a diffused region between fresh and saline water, which
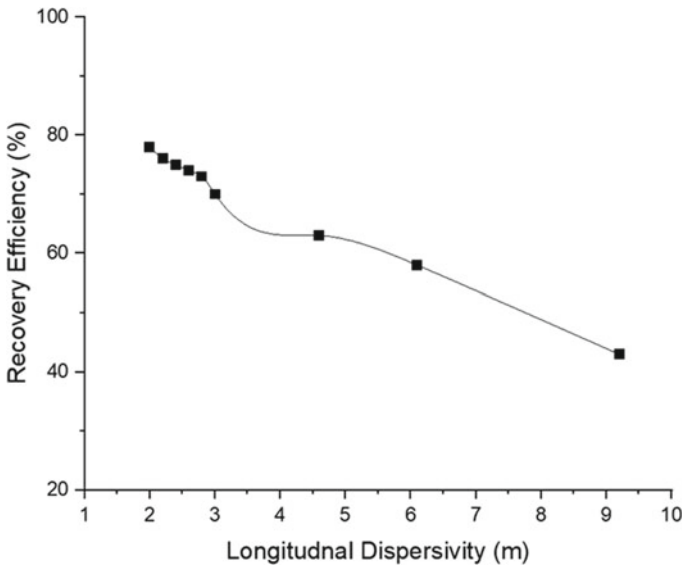
Fig. 14.6 Influence of longitudinal dispersivity on recovery efficiency

is the key thing that affects water recovery (Moulder 1970). The impact on RE is observed for the 5 m increment in the values of longitudinal dispersity for the range of 0–30 m. It is very clear from the results that the longitudinal dispersivity has a significant impact on RE, which is up to −8 to −40% (Fig. 14.6).

However, minor variation in RE is detected due to changes in transverse dispersivity. As the longitudinal dispersivity increases, the mixing increases and decreases the RE of the ASR system. On the other hand, the influence of transverse dispersivity was found to be significantly less on the ASR system performance (Fig. 14.7).

14.3.4 Density Difference

The salinity of the groundwater in which freshwater has to be stored also plays an essential role in the ASR system performance. The higher groundwater salinity means a higher difference in injected freshwater and ambient saline groundwater density. This difference between density controls the mixing phenomena, and increasing the density difference results higher mixing rate and results in low recovery efficiencies. In the case of high ambient salinity and high aquifer's hydraulic conductivity, buoyancy stratification occurs significantly, and the injected freshwater moves upward quickly into the native groundwater (Brown et al. 2005). The influence on RE is observed in the values of density difference between injected and native saline water in the range of 0–45 kg/m3. The total impact of density difference on RE is noteworthy and negative. As the density difference increases, the RE decreases from
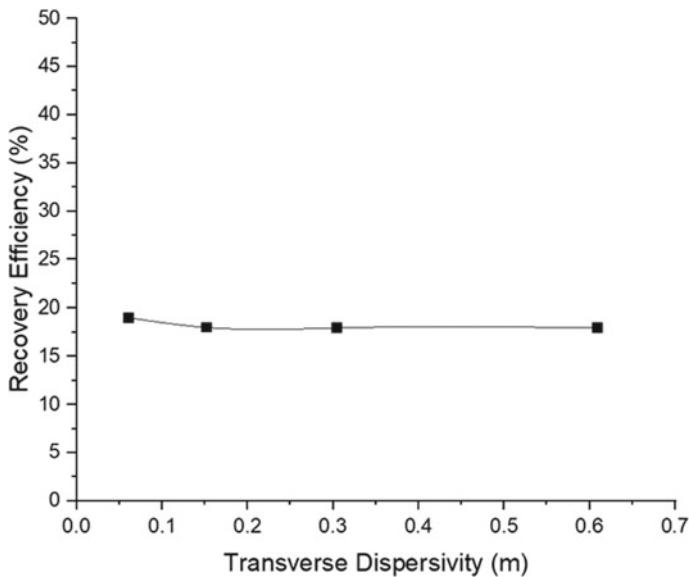
Fig. 14.7 Influence of transverse dispersivity on recovery efficiency

−6 to −63% (Fig. 14.8). Thus, Low salinities in the native formation water are suitable for high recovery efficiencies. The groundwater salinity varies with time, and it is found maximum during dry periods and reduces during the rainy seasons. Therefore, the influence of groundwater salinity level on the ASR performance is significant, and locations with lower salinity levels must be prioritized over highly saline groundwater regions.

These graphs show the impact of each hydrogeological factor on ASR performance in the saline regions individually. This method of determining a suitable site for ASR installation provides the sensitivity of each factor while keeping other factors constant. Hydrogeological data must be collected at various locations while selecting a site for ASR installation in a given region. The variable density model development based on regional hydrogeology provides a location with the best chance of ASR success. A primary survey of the area to collect the hydrogeological data at different sites is required before ASR scheme installation. Geophysical surveys, well test, and water quality analysis provides the basic aquifer properties and groundwater salinity concentration for the different sites of the region. This variable density flow model would help evaluate the ASR recovery for the expected operational management based on these aquifer properties. Therefore, the results of this study would help in understanding the sensitivity of each hydrogeological factor and groundwater salinity level on ASR performance. The proposed model would also assist in evaluating the ASR performance in saline groundwater regions to ensure the success of ASR projects.
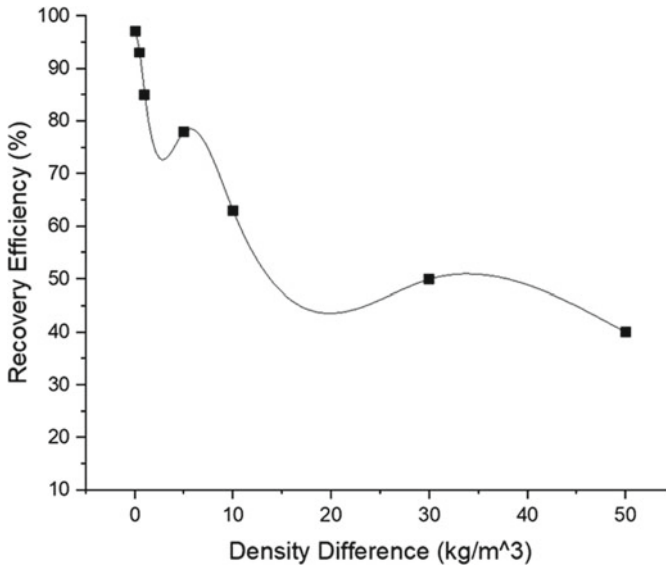
Fig. 14.8 Influence of density difference on recovery efficiency

14.4 Conclusions

This study introduces the role of hydrogeological factors impacting ASR scheme performance and explains how to achieve higher RE by selecting the appropriate site for the ASR system installation. The results from the simulation for the baseline parameters indicate that low hydraulic conductivity combined with a low hydraulic gradient will result in high ASR system performance due to less flow groundwater flow velocity. This study also demonstrates that a thinner aquifer and low longitudinal dispersivity should be selected while installing the ASR scheme to avoid higher mixing losses. It is also observed that low-saline groundwater aquifers are more suitable than higher-salinity aquifers. This study recovered stored freshwater from a fully penetrating ASR well. The fully penetrating well left a large volume of stored freshwater in the aquifer. Therefore, further research and development are needed to find a suitable multiple ASR-well types design to achieve the higher RE from the scheme. This study will help to decide the appropriate site for the ASR project implementation.

References

Anderson MP, Lowry CS (2004) An assessment of aquifer storage recovery for selected representative hydrogeologic settings in Wisconsin, p 15

Bakker M (2010) Radial Dupuit interface flow to assess the aquifer storage and recovery potential of saltwater aquifers. Hydrogeol J 18(1):107–115. https://doi.org/10.1007/s10040-009-0508-1

Bear J, Jacobs M (1965) On the movement of water bodies injected into aquifers. J Hydrol 3(1):37–57. https://doi.org/10.1016/0022-1694(65)90065-X

Brown CJ, Weiss RWJ, Verrastro R, Schubert S, Beach WP (2005) Development of an aquifer, storage and recovery (ASR) site selection suitability index in support of the comprehensive everglades restoration project

Freeze RA, Cherry JA (1979) Groundwater. Prentice-Hall

Johnson C, Tancreto A, Miller J, Linkfield T, Brown C (2014) Preliminary development of an adaptive assessment program for operating aquifer storage and recovery (ASR) sites. https://doi.org/10.13140/2.1.4676.8646

Krishan G, Kumar CP, Yadav BK (2019) Groundwater salinity causes and remediation—a case study from Mewat, Haryana

Kumar A, Kimbler OK (1970) Effect of dispersion, gravitational segregation, and formation stratification on the recovery of freshwater stored in saline aquifers. Water Resour Res 6:1689–1700

Langevin CD, Thorne DT Jr, Dausman AM, Sukop MC, Guo W (2008) SEAWAT version 4: a computer program for simulation of multi-species solute and heat transport (Report No. 6-A22; Techniques and methods). USGS Publications Warehouse. https://doi.org/10.3133/tm6A22

Merritt ML (1985) Subsurface storage of freshwater in South Florida; a digital model analysis of recoverability (Report No. 2261; Water supply paper). USGS Publications Warehouse. https://doi.org/10.3133/wsp2261

Moulder EA (1970) Freshwater bubbles: a possibility for using saline aquifers to store water. Water Resour Res 6(5):1528–1531. https://doi.org/10.1029/WR006i005p01528

Pyne RDG (1995) Groundwater recharge and wells: a guide to aquifer storage and recovery. Lewis Publishers

Reese RS (2002) Inventory and review of aquifer storage and recovery in southern Florida (Report No. 2002–4036; Water-resources investigations report). USGS Publications Warehouse. https://doi.org/10.3133/wri024036

Sathish S, Mohamed MM (2018) Assessment of aquifer storage and recovery (ASR) feasibility at selected sites in the Emirate of Abu Dhabi, UAE. Environ Earth Sci 77(3):112. https://doi.org/10.1007/s12665-018-7251-7

Tiwari S, Yadav BK (2021) Impact of operational factors on aquifer storage and recovery (ASR) scheme in saline regions

Van Weert F, Van der Gun J, Reckman JWTM (2009) Global overview of saline groundwater occurrence and genesis, p 105 (IGRAC Report)

Ward JD, Simmons CT, Dillon PJ (2008) Variable-density modelling of multiple-cycle aquifer storage and recovery (ASR): importance of anisotropy and layered heterogeneity in brackish aquifers. J Hydrol 356(1):93–105. https://doi.org/10.1016/j.jhydrol.2008.04.012

Yobbi DK (1996) Simulation of subsurface storage and recovery of treated effluent injected in a saline aquifer, St. Petersburg, Florida (Report No. 95–4271; Water-resources investigations report). USGS Publications Warehouse. https://doi.org/10.3133/wri954271

Chapter 15
Estimation of Groundwater Resources According to Watershed and Groundwater Divide

José Manuel Murillo, Alberto Padilla, Joaquín Delgado, José Manuel Gómez-Fontalva, Bruno Ballesteros, Jorge Hornedo, and José Luis García-Aróstegui

15.1 Introduction

The hydraulic administration of the Kingdom of Spain has only identified bodies of groundwater (GWB) within the boundaries of each of its river basin districts (Order ARM/2656/2008). This way of proceeding has resulted in no GWB that share two or more river basin districts from a legal and administrative point of view. However, the physical reality of the aquifers does not conform to the above, since there are contiguous GWB, belonging to different hydrographic demarcations, which have common permeable formations with hydrogeological continuity and water connection between them. These special GWB have been designated in this paper with the name of Groundwater Bodies with Hydrogeological Continuity. Its acronym in Spanish is MASCH.

On the other hand, Spanish legislation establishes that the recharge that occurs in a GWB is assimilable to its water resource (Order ARM/2656/2008), so that the resources of a MASCH will be the sum of the recharges of the GWB that constitute it.

This paper estimates and analyzes the evolution of groundwater resources in 4 MASCH, as well as in the GWB that compose them to period 1960 to 2017. The calculations have been carried out applying the RENATA code (IGME-DPA 2012) and have been carried out both from the perspective of the watershed and groundwater divide.

J. M. Murillo (✉) · B. Ballesteros · J. Hornedo · J. L. García-Aróstegui
CN Instituto Geológico y Minero de España del CSIC, c/ Ríos Rosas 23, 28003 Madrid, Spain
e-mail: jm.murillo@igme.es

A. Padilla · J. Delgado · J. M. Gómez-Fontalva
Aljibe Consultores, c/ José Luis Pérez Pujadas 7, 18006 Granada, Spain
e-mail: a.padilla@aljibeconsultores.com

15.2 Methods

15.2.1 Selected MASCH

The four selected MASCH are located in a semi-arid region with low and irregular rainfall (average of 315 mm) and average potential evapotranspiration of 892 mm. They have different hydrogeological characteristics and hydrodynamic properties, although they are located between the hydrographic divide of the Segura and Jucar rivers and very close to each other (Fig. 15.1). The hydrogeological schema of these MASCH is as follows:

Jumilla-Yecla-Castellar MASCH. It consists of limestones and dolomites from the upper Cretaceous. In the natural state, water inflows to the aquifer are produced exclusively by rain infiltration, while outflows take place through 4 springs. The most important is in the Jucar basin. The other three discharge into the Segura basin. In altered regime the entrances are complemented by irrigation returns (Sahuquillo 2016). Discharges currently take place exclusively by abstraction, as all springs dried up before 1960. Since pumping began, a reserve volume of more than 1300 hm^3 has been emptied (Murillo 2021).

Serral-Salinas MASCH. It consists mainly of limestones and dolomites from the Jurassic (Pulido-Velazquez et al. 2015). In a natural state it discharges through a single spring (Fuente de Salinas) and in a diffuse way to a lagoon also fed by the spring. In altered state the outputs take place exclusively by abstraction since the decade of the 60 of the last century, since on that date the spring is dried (Molina et al. 2009). The wetland has a temporary character linked exclusively to surface runoff (Molina et al. 2013). Since the MASCH began to be pumped, a reserves volume of 486 hm^3 has been emptied (Murillo 2021).

Fig. 15.1 MASCHs of Jumilla-Yecla-Castellar, Serral-Salinas, Sierra Oliva and Vega Media and Baja del Segura-Bajo Vinalopó. Location in Spain and in the hydrographic basins of the Jucar and Segura

Sierra Oliva MASCH. Two aquifers that have no water connection between them outcrop in this MASCH. The main aquifer (limestones and dolomites of the Jurassic-Lower Cretaceous) extends over the entire surface of the MASCH. In natural state it drains through a single spring (Paraíso spring). This dried up in 1989 due to the overexploitation to which the aquifer was subjected. This process continues today. On the ceiling of the previous permeable formation is located an impermeable formation of the Albiense and on it several perched aquifers of reduced dimensions. These are made up of limestones and dolomites from the Upper Cretaceous (Cenomanian). Each of them drains through its own spring (Zucana, Tobarrillas and Ramblas de Olula and Agua Verde) (Ballesteros et al. 2020). Most of these springs are captured directly for irrigation. Others have no use. So, at present the operating state of these perched aquifers is natural. Under the action of the disturbed state, there are no irrigation returns in any of the aquifers that are part of this MASCH. Since the MASCH began to be pumped, a reserves volume of 71 hm^3 has been emptied. (Murillo 2021).

Vega Media and Baja del Segura-Bajo Vinalopo MASCH. It is a multilayer aquifer, integrated, according to sectors, by several permeable horizons with different hydraulic loads. Lithologically it is constituted by detrital materials of the Plioquatternary that fill a graben. These materials are in hydraulic connection with others of carbonated nature and Triassic age. In natural state, the recharge is produced mainly by infiltration of precipitation and its discharge according to three components: exits to the surface drainage axes (Segura River and network of drainage channels that are called *azarbes*), discharge to the Mediterranean Sea and groundwater flow to wetlands (El Hondo). In an altered state, infiltration from precipitation is joined by irrigation returns and natural discharges by extractions (Sahuquillo 2016).

15.2.2   Fundamentals RENATA Code

RENATA (Spanish acronym for natural aquifer recharge) is a code that evaluates recharge to aquifers. It combines two methodologies for estimating this variable and a single iterative calculation process. These are: the water balance in the soil and the numerical modeling of groundwater flow in finite differences. The concatenated use of both methodologies improves the coherence between the results offered by the water balance in the soil—which provides the magnitude of the potential recharge—and the fluctuations of the water table—which reflects the effects of the actual recharge—in the aquifer.

The water balance module in the soil operates in a distributed manner. To make this, it divides the permeable surface of the MASCH, on which the water that gives rise to the recharge infiltrates, into three types of sectors: climatic, soil and irrigation. The calibration module uses a finite difference flow model to verify the results provided by the soil water balance module. The flow model used is very simple and incorporates

many simplifications, since its purpose is not to simulate the groundwater flow with a high degree of precision, but to verify the results provided by the water balance module.

15.3 Results and Discussion

15.3.1 RENATA Code Application

The application of the RENATA code includes 4 stages: generation of the calculation mesh and establishment of the simulation period; application of the Soil Water Balance Module (SWBM); application of the Calibration Module (CM) and intersectorization (IS).

15.3.1.1 Spatial and Temporal Discretization

RENATA code requires that a mesh be defined to, on the one hand, frame the surface of the MASCH subject to the calculation process and, on the other, allow the discretization of the different parameters and variables that characterize the MASCH. The number of years simulated has been 57, the passage of time has been daily and the size of the mesh of 1 km × 1 km, except in the MASb Vega Media and Baja del Segura-Bajo Vinalopo which has been 1.5 km × 1.5 km.

15.3.1.2 Soil Water Balance Module (SWBM)

Climate sectors. They have been determined by the method of Thiessen polygons from the corresponding rainfall stations and potential evapotranspiration (PET) series. PET has been calculated by the method of Thornthwaite.

Soil sectors. The soil sectors have been obtained discretizing slope of the land; vegetation cover; type and uses of soil and lithology of permeable outcrops. Effective rainfall (ER) has been calculated using the Thornthwaite soil water balance method modified by Girard and its decomposition into surface runoff (SR) and infiltration (INF) using the Soil Conservation Service method.

Irrigation sectors. Agricultural areas have been identified from the Corine Land Cover land use map published by the European Environment Agency. The monthly distributions of groundwater for irrigation correspond to those foreseen in the hydrological plans of the Spanish Kingdom for the period 2015/2021. RENATA allows you to apply different percentages of return according to the irrigation system used.
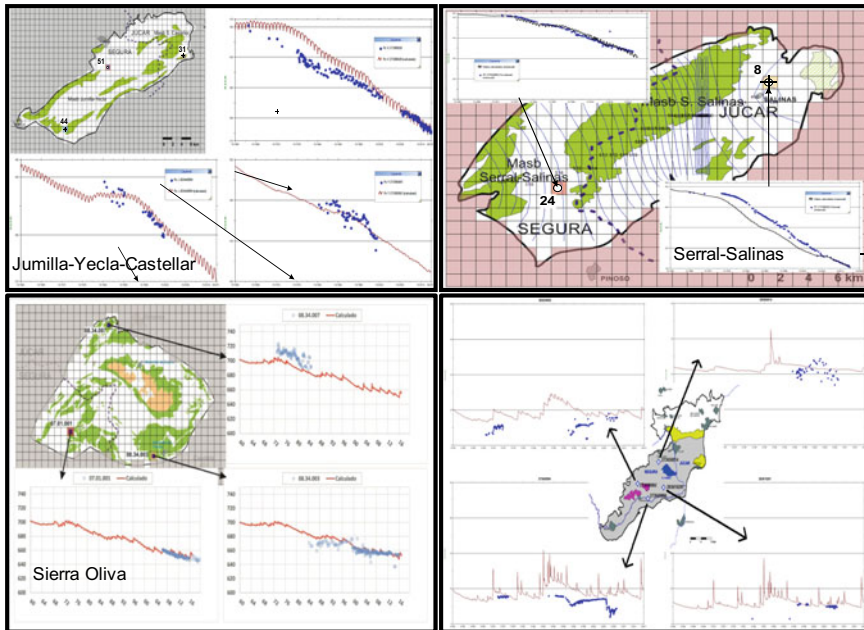
Fig. 15.2 Calibrations. Displaying outputs from computer. Results obtained in the piezometers used to contrast the measured data against those simulated by the model

15.3.1.3   Calibration Module (CM)

The intersectorization of the sectors: climate, soil and irrigation provide a potential recharge discretized spatially and temporally. This constitutes an input data to a flow model in finite differences. Figure 15.2 shows the results obtained in the piezometers used to contrast the measured data against those simulated by the model.

15.3.2   Recharge Distribution According to the Watershed and the Groundwater Divides

Tables 15.1, 15.2, 15.3, 15.4, 15.5 and 15.6 shows the results provided by RENATA for the MASCH of Jumilla-Yecla-Castellar, Serral-Salinas, Sierra Oliva and Vega Media y Baja del Segura-Bajo Vinalopo. Columns (1) and (2) provide resources in absolute and percentage value in each of the GWB that make up the MASCH according to the hydrographic and groundwater divides. The absolute value of the MASCH resources is provided in column (3).

Table 15.1 Groundwater resources according to watershed and groundwater divides in undisturbed study state (Natural) and disturbed state. MASCH Jumilla-Yecla-Castellar. Period 1960/61 to 2016/17

State	Distribution of the resources according to divide	(1) Segura Basin	(2) Jucar Basin	(3) MASCH hm^3/y
Natural	Hydrographical	9.22 hm^3/y (86.8%)	1.40 hm^3/y (13.20%)	10.62
	Groundwater	3.57 hm^3/y (33.5%)	7.05 hm^3/y (66.5%)	
Disturbed	Hydrographical	15.24 hm^3/y (80.51%)	3.69 hm^3/y (19.49%)	18.93
	Piezometric thresholds	2.78 hm^3/y (14.69%)	16.15 hm^3/y (85.31%)	

Table 15.2 Groundwater resources according to watershed and groundwater divides in undisturbed study state (Natural) and disturbed state. MASCH Serral-Salinas. Period 1960/61 to 2016/17

State	Distribution of the resources according to divide	(1) Segura Basin	(2) Jucar Basin	(3) MASCH hm^3/y
Natural	Hydrographical	2.65 hm^3/y (56.0%)	2.07 hm^3/y (44.0%)	4.72
	Groundwater	0.00 hm^3/y (0.0%)	4.72 hm^3/y (100%)	
Disturbed	Hydrographical	2.65 hm^3/y (56.0%)	2.07 hm^3/y (44.0%)	4.72
	Groundwater	Distribution according Table 15.3		

Table 15.3 Temporal distribution of groundwater resources in disturbed regime in the MASCH of Serral-Salinas

Period analyzed	Distribution of the resources according to divide	(1) Segura Basin	(2) Jucar Basin	(3) MASCH (hm^3/y)
1960/61-1966/67	Hydrographical	1.30 hm^3/y (61.61%)	0.81 hm^3/y (38.39%)	2.11
	Groundwater	0.00 hm^3/y (0,00%)	2.11 hm^3/y (100%)	
1966/67–2016/17	Hydrographical	2.84 hm^3/y (55.79%)	2.25 hm^3/y (44.21%)	5.09
	Piezometric thresholds	1.10 hm^3/y (21.61%)	3.99 hm^3/y (78.39%)	

Table 15.4 Groundwater resources according to watershed and groundwater divides in undisturbed study state (Natural) and disturbed state**.** MASCH Sierra Oliva. Period 1960/61 to 2016/17

State	Distribution of the resources according to divide	(1) Segura Basin	(2) Jucar Basin	(3) MASCH (hm^3/y)
Natural	Hydrographical	1.08 hm^3/y (23.0%)	3.60 hm^3/y (77.0%)	4.68
	Groundwater	0.20 hm^3/y (4.0%)	4.48 hm^3/y (96.0%)	
Disturbed	Hydrographical	1.08 hm^3/y (23.0%)	3.60 hm^3/y (77.0%)	4.68
	Groundwater	Distribution according Table 15.5		

In the four MASCHs analyzed in this paper, there are, both in natural and influenced regime, two hydrographic basins that present hydrogeological continuity (Tables 15.1, 15.2 and 15.4). These are: Segura and Jucar. In the case of groundwater basins, since their delimitations do not coincide with that corresponding to the hydrographic ones, the results obtained with RENATA present a greater complexity, since the Segura groundwater basin can occupy part of the Jucar hydrographical basin or vice versa. In addition, while the hydrographic basins remain unchanged for the time scale that is usually used in this type of studies, the hydrogeological ones usually modify their boundaries according to the recharge and extractions that take place at each moment (Fig. 15.3).

Thus, when the regime is natural, in the Jumilla-Yecla-Castellar MASCH there are two groundwater basins: one extends throughout the Jucar hydrographical basin and part of the hydrographical Segura basin, while the other extends over the rest of the hydrographical Segura basin. The same happens in the MASCH Vega Media and Baja del Segura-Bajo Vinalopó. In both MASCH the resources calculated with respect to the hydrographic division of the Segura are greater than those obtained if the calculations are made with respect to the groundwater divide or vice versa (Tables 15.1 and 15.6).

In the MASCH of Serral-Salinas there is only one groundwater basin (Jucar), since all groundwater discharges through a single spring (Salinas spring), which is located in the Jucar river basin, although there are two recharge zones: one in the Jucar hydrographic basin and another in the Segura hydrographic basin (Table 15.2). The same happens in the MASCH Sierra Oliva for the Jurassic-Lower Cretaceous aquifer, since all the water that recharges this aquifer is discharged through a single spring (Paraiso spring) that is located in the Jucar hydrographical basin. From the perspective of this aquifer, which is the more important of the two that have been identified in this MASCH, there is a single groundwater basin that drains to the Jucar hydrographical basin, but two recharge areas that coincide respectively with

Table 15.5 Temporal distribution of groundwater resources in disturbed regime in the MASCH of Sierra Oliva (Upper Cretaceous-Miocene and Jurassic-Lower Cretaceous)

Aquifer	Period analyzed	Distribution of the resources according to divide	(1) Segura Basin	(2) Jucar Basin	(3) MASCH (hm³/y)
Upper Cretaceous-Miocene	October 1960–September 2017	Hydrographical	0.19 (hm^3/y) (12.26%)	1.36 (hm^3/y) (87.74%)	1.55
		Groundwater	0.19 (hm^3/y) (12.26%)	1.36 (hm^3/y) (87.74%)	
Jurassic-Lower Cretaceous	October1960–September 1979	hydrographical	1.02 (hm^3/y) (21.47%)	3.73 (hm^3/y) (78.53%)	4.75
		Groundwater	0.00 (hm^3/y) (0.00%)	4.75 (hm^3/y) (100.0%)	
	October1979–September 2017	Hydrographical	1.11 (hm^3/y) (23.87%)	3.54 (hm^3/y) (76.13%)	4.65
		Piezometric thresholds	0.17 (hm^3/y) (3.66%)	4.48 (hm^3/y) (96.34%)	

Table 15.6 Groundwater resources according to the watershed and the groundwater divides in undisturbed stady state (Natural) and disturbed state**.** MASCH Vega Media y Baja del Segura-Bajo Vinalopó. Period 1960/61 to 2016/17

State	Distribution of the resources according to divide	(1) Segura Basin	(2) Jucar Basin	(3) MASCH (hm^3/y)
Natural	Hydrographical	22.51 (hm^3/y) (57.38%)	16.72 (hm^3/y) (42.62%)	39.23
	Groundwater	12 43 (hm^3/y) (31.68%)	26.80 (hm^3/y) (68.32%)	
Disturbed	Hydrographical	51.77 (hm^3/y) (67.61%)	24.80 (hm^3/y) (32.39%)	76.57
	Groundwater	40 65 (hm^3/y) (53.09%)	35.92 (hm^3/y) (46.91%)	
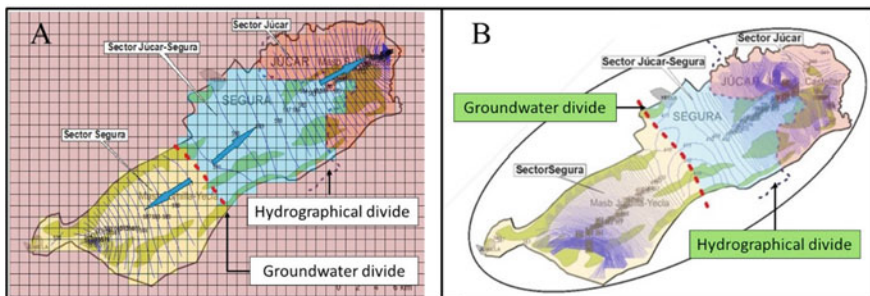
Fig. 15.3 a (Jumilla-Yecla-Castellar MASCH) shows that the Jucar watershed (red color) is smaller than its groundwater basin (red and blue color). On the other hand, the Segura watershed (blue and yellow color) is much larger than its Groundwater basin (yellow color). This fact implies that the resources calculated according to the hydrographical divide should be greater in the Segura than in the Jucar, while if the calculations are made according to the hydrogeological divide, the opposite would happen. **b** Shows that groundwater basins can change in size over time, while watersheds remain unchanged. At equal recharge, the groundwater divide moves in the opposite direction to the groundwater basin where the greatest pumping is carried out. The blue arrows indicate the direction of the groundwater flow.

the Jucar and Segura watershed. With regard to the other aquifer (Upper Cretaceous-Miocene) that has been identified in this MASCH, it is constituted by a series of isolated outcrops that drain each of them through its own spring, either to the Jucar hydrographical basin or to the Segura hydrographical basin, so it is necessary to recognize the existence of two groundwater basins (Table 15.4).

In disturbed state by extractions and irrigated returns, the MASCHs Jumilla-Yecla-Castellar, Serral-Salinas and Sierra Oliva are overexploited (Aguilera and Murillo 2009). The spring that discharges the Jurassic-Lower Cretaceous aquifer of the MASCH, mentioned in last place, has been dry for more than 30 years and the natural drains of the other two MASCH more than 60 years, so the aquifers of

these MASCH have behaved for many years as a watertight reservoir that does not discharge water into the surface hydrographic network. In this sense, it should be noted that while the springs were discharging water it made sense to use the concept of groundwater dividing. However, from the moment they stopped flowing, it is more appropriate to use the term piezometric threshold, as is done in Tables 15.1, 15.3 and 15.5. From that moment on, the notion of recharging as a renewable resource, which is contemplated by Spanish legislation (IPH 2008), is not coherent, since recharging only helps to alleviate or counteract the consumption of reserves.

In Jumilla-Yecla-Castellar MASCH, the presence of any groundwater divide is not identified for the period 1960–2017, since the springs that discharged this MASCH dried up before the start date of the present study, so only the existence of piezometric thresholds is recognized (Table 15.1 and Fig. 15.4). In Serral-Salinas MASCH, the results provided by the RENATA code indicate that the MASCH, which was drained by a single spring, behaves as a watertight deposit from the hydrological year 1966/67, so that from that moment only the presence of piezometric thresholds of greater or lesser magnitude are detected (Table 15.3 and Fig. 15.4). Finally, in Sierra Oliva MASCH, Paraiso spring, which discharges the Jurassic-Lower Cretaceous aquifer, dries up in September 1989, so after that date only the presence of piezometric thresholds are detected (Table 15.5 and Fig. 15.4). With regard to the Upper Cretaceous-Miocene aquifer, the situation in the disturbed regime is similar to that which occurs in the natural regime, since there is no use of groundwater through the pumping (Tables 15.4 and 15.5), so there are two groundwater basins throughout the period analyzed.

The MASCH of Vega Media and Baja del Segura-Bajo Vinalopo discharges water to the surface hydrographic network and to the sea throughout the period analyzed. This fact implies that there are two groundwater basins that behave differently in an undisturbed (natural) and disturbed regime. Thus, in the first case, groundwater resources present a greater amount in the Jucar groundwater basin, while in the influenced regime the opposite occurs. In the first case, the Segura river basin gives groundwater to that of the Jucar, while in the second the opposite occurs. The greater volume of underground resources detected in a disturbed regime is due to the increase in irrigation returns that is associated with a greater use of surface water.
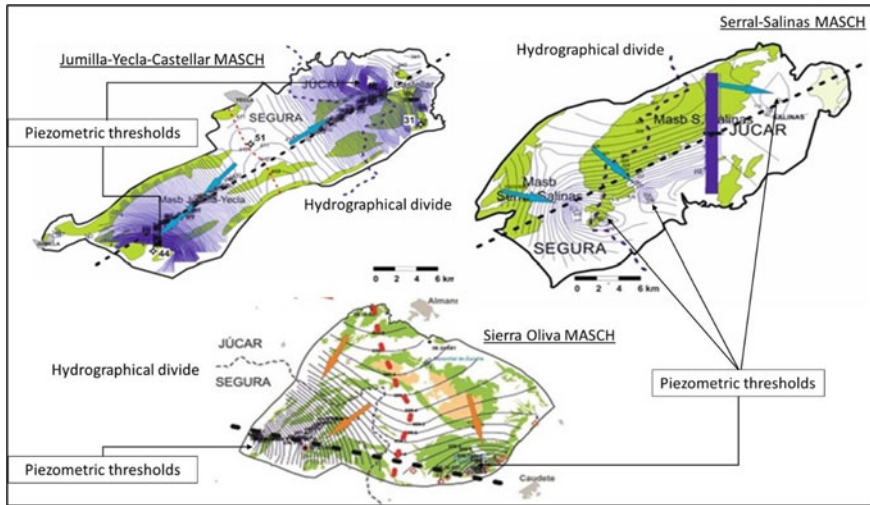
Fig. 15.4 The springs of the MASCH represented in the figure have dried up due to the overexploitation to which they are subjected. When this takes place there is no underground divide, since groundwater does not discharge into the surface hydrographic network, and what is produced are piezometric thresholds. The blue and brown arrows indicate the direction of the underground flow towards the piezometric thresholds caused by the excess pumping

15.4   Conclusions

There are GWB, adjacent between two or more hydrographic demarcations, whose physical reality, with respect to their hydrogeological framework, escapes their administrative limits, so it is necessary to focus their study and management from a scenario that unifies them in a single groundwater entity. In this paper, this entity has been called "a body of groundwater with hydrogeological continuity" and its acronym in Spanish as MASCH. The groundwater resources of a MASCH can be determined under two perspectives: one that develops the calculations from the point of view of the hydrographic divide and another from the perspective of the groundwater divide. Obviously, the overall result provided by both alternatives is the same (column 3 of Tables 15.1, 15.2, 15.3, 15.4, 15.5 and 15.6), although the partial results differ depending on the watershed to which the groundwater runoff discharges, as can be seen in columns (1) and (2) of Tables 15.1, 15.2, 15.3, 15.4, 15.5 and 15.6.

Both in natural and disturbed regime there are for the 4 MASCH analyzed two hydrographic basins, but the same does not happen with hydrogeological ones, since different situations may arise. The scenarios that are presenting in this paper are as follows:

Two hydrogeological basins, whose groundwater divide moves over time from one basin to another because of abstraction and irrigation returns. This is the case of the MASCH of Vega Media and Baja del Segura-Bajo Vinalopó.

Single hydrogeological basin, as the MASCH of Serral-Salinas, which, due to overexploitation modifies, its state giving rise to multiple piezometric thresholds.

Two hydrogeological basins whose groundwater divide moves over time from one basin to another because of abstraction and irrigation returns, but only for a certain time. At the end of that stage, the MASCH modify its state giving rise to multiple piezometric thresholds due to the overexploitation to which it is subjected. This is the case of the MASCH of Jumilla-Yecla-Castellar.

MASCH with several aquifers, where one works in undisturbed (natural) state and another as in the case of the MASCH of Serral-Salinas. To this typology responds the MASCH of Sierra Oliva.

References

Aguilera H, Murillo JM (2009) The effect of possible climate change on natural groundwater recharge based on a simple model: a study of four karstic aquifers in SE Spain. Environ Geol 57(5):963–974. https://doi.org/10.1007/s00254-008-1381-2

Ballesteros B (2020) The hydraulic heritage of the gallery system of Zucaña (Almansa-SE España) and its geological and hydrogeological conditions. BOLETÍN GEOLÓGICO Y MINERO 131(1):7–24. https://doi.org/10.21701/bolgeomin.131.1.001

DPA-IGME, Benítez AP (2012) Renata: Recarga natural a los acuíferos: Manual del usuario. Instituto Geológico y Minero de España. https://books.google.ae/books?id=W0DpoAEACAAJ

Molina J-L, García-Aróstegui JL, José Benavente J (2009) Explotación intensiva de los acuíferos carbonatados del altiplano de Murcia. Geogaceta 46:163–166

Molina J-L, Pulido-velazquez D, García-Aróstegui J, Pulido-Velazquez M (2013) Dynamic Bayesian networks as a decision support tool for assessing climate change impacts on highly stressed groundwater systems. J Hydrol 479:129. https://doi.org/10.1016/j.jhydrol.2012.11.038

Murillo JM (2021) Masas de agua subterránea compartidas entre diferentes ámbitos de aplicación: Singularidad administrativa o entidad hídrica con continuidad hidrogeológica. Aplicación en la divisoria Júcar-Segura. Inundaciones y sequías: Análisis multidisciplinar para mitigar el impacto de los fenómenos climáticos extremos, 2021, pp 997–1022. ISBN: 978-84-1302-138-6. https://dialnet.unirioja.es/servlet/articulo?codigo=8133639

Orden ARM/2656/2008, de 10 de septiembre, por la que se aprueba la instrucción de planificación hidrológica, Pub. L. No. Orden ARM/2656/2008, BOE-A-2008-15340 38472 (2008). https://www.boe.es/eli/es/o/2008/09/10/arm2656

Pulido-Velazquez D, García-Aróstegui JL, Molina J-L, Pulido-Velazquez M (2015) Assessment of future groundwater recharge in semi-arid regions under climate change scenarios (Serral-Salinas aquifer, SE Spain). Could increased rainfall variability increase the recharge rate? Hydrol Process 29(6):828–844. https://doi.org/10.1002/hyp.10191

Sahuquillo A (2016) La explotación intensa de los acuíferos en la cuenca baja del Segura y en la cuenca del Vinalopó. Ingeniería Del Agua 20(1):13–27. https://doi.org/10.4995/ia.2016.4023

Chapter 16
CFD Analysis of a Microchannel Heat Exchanger Based 3-D Printed Solar Receiver

Dinumol Varghese, Ahmed Thaher, Fadi Alnaimat, and Bobby Mathew

16.1 Introduction

As the world population progresses further, major resources such as energy and water have faced severe shortages in their supply. Some occur due to dry weather conditions whereas others occur due to the contamination in the water. According to the World Bank survey in 2017, it was noted that the major area that faced severe shortage of fresh water is the Middle East and North Africa (MENA) region. Thus, there is an urgent requirement of performing desalination to produce freshwater for meeting the daily needs. But most of the desalination plants consume huge amounts of energy that contributes to the increase in global warming—threatening approach for the nearby future. The growing demand of fresh water pushes the need of shifting from non-renewable sources to renewable and eco-friendly sources of energy. Solar energy is abundantly available especially in the MENA region which can be integrated as a source of thermal energy for performing the desalination technique. Desalination processes are normally classified into two types: thermal and membrane desalination whereas each of them are further classified into different categories. Multistage flash desalination (MSF) comes under the thermal category. Almost 21% of the seawater desalination techniques employ MSF due to its better thermal performance on a larger plant. The major disadvantage lies in the consumption of larger quantities of energy. Thus, it is of great importance to integrate solar energy with the MSF system. Concentrated solar photovoltaic (CSP) technologies are one of the most efficient methodologies providing large scale generation of electrical power as well

D. Varghese (✉) · A. Thaher · F. Alnaimat · B. Mathew
National Water and Energy Center, United Arab Emirates University, P.O. Box 15551, Al Ain, UAE
e-mail: dinumol@uaeu.ac.ae

Mechanical Engineering Department, College of Engineering, United Arab Emirates University, P.O. Box 15551, Al Ain, UAE

as maximum solar to electrical efficiency. CSP helps in concentrating solar irradiance onto the solar receivers such as parabolic mirrors, troughs or lenses where this thermal energy is utilized for heating the brine water. Solar air receiver was the first technology to be employed in order to absorb the heat generated from solar energy and combine with the rest of the process. A review (Hasan and Reddy 2015) was conducted on the solar energy driven desalination plant where it emphasized the usage of each methodology integrated with solar energy and the problems associated with it. A performance investigation (Chaouki et al. 2021) was conducted based on the optimization of hybrid Multi-Effect Distillation Adsorption Desalination (MEDAD). The main aim was to implement a low-cost methodology for highly salt concentrated water that employs solar thermal energy. They studied on the effect of the number of stages employed in the Multi-effect Distillation (MED), presence of adsorption desalination (AD) stage and heat recovery through the brine water under hot and humid climatic conditions. The results demonstrated to have better production rates of fresh water, attaining 57.7% lower specific energy consumption on the addition of adsorption desalination stage. The researchers (Qiu et al. 2015) experimented on using pressurized air within a coiled tube having a diameter of 12 mm under a constant heat flux of 300 kW/m^2. The results demonstrated that both the thermal and pressure drop values were improved with the decrease in the inner diameter of the coiled tube. The technology that emerged to provide better heat transfer coefficient was the microchannel gas heater. With the innovative work put forward (Tuckerman and Pease 1983) by the eminent researchers, the use of microchannels has been resulted in various applications.

A microchannel heat exchanger serves to be the most efficient forms of heat exchangers due to its high heat transfer area per unit volume and minimal hydraulic diameters. An experimental investigation (Ahlatli et al. 2016) was conducted to comprehend the heat transfer characteristics of a carbon nano-tube water nanofluid within the microchannel receiver. The results showed to provide a better thermal performance with the use of nanofluids in a microchannel receiver. Several investigations have been performed on the use of different working liquids such as water, ethylene glycol and other nano-fluids. The experimental setup of a microchannel air receiver (Li et al. 2013) was developed and tested having a microchannel width of 2 mm. Various heat fluxes were applied on microchannel air receiver with the mass flow rate up to 0.8 g/s. The results clearly demonstrated that heat transfer coefficient had been significantly enhanced due to the increase in the air flow rate as well as heat flux values. The convective heat transfer mechanism (Zhu and Liao 2006) of a laminar gas flowing inside a microchannel heat exchanger was studied. It was found that the heat transfer coefficient decreased due to the thermal resistance generated by the wall slip effect. Also, the influence of thermal boundary conditions, Knudsen number and channel aspect ratio on the heat transfer performance was also analyzed. The performance of the compact heat exchanger (Li et al. 2013) was studied by varying the heat flux applied on a solar receiver to heat the air flowing through the microchannel. The results determined to obtain a heat transfer coefficient near to 750 W/m^2 K. An experimental investigation (Qiu et al. 2015) based on a microchannel compact heat

exchanger was performed to evaluate the thermal performance of the pressurized air solar receiver employing concentrating solar photovoltaic system.

Different parameters such as pressure, air mass flow rates, solar heat flux as well as temperature elevation. The results found that with the increase in heat flux as well as Reynolds number, the heat transfer coefficient magnitudes increased rapidly Also, the pressure drop of air reduced drastically with the increase in absolute pressure. This is because of the presence of roughness during the manufacturing process of compact heat exchanger. An experimental setup of a microchannel gas heater (Bo et al. 2021) was conducted to evaluate the heat transfer coefficient as well as pressure drop. The results gave certain conclusions: (i) The increase in the air flow rate as well as the heat flux supported in enhancing the heat transfer coefficient (ii) wall temperature profile was analyzed (iii) higher Nusselt number was obtained for an aspect ratio of 1 for the microchannel. Also, the heat transfer enhancement was largely influenced by the wall slip effect and viscous heating phenomenon.

Researchers at Shanghai Jiao Tong University (Zeng et al. 2022) conducted an experimental study to analyze the performance of a microchannel heat exchanger assembly with S-shaped fins. The effect of heat transfer and fluid flow are studied over different Reynolds number resulting in understanding the Nusselt number and friction factor magnitudes. A comprehensive review (Lalagi et al. 2022) on the geometrical designs of microchannel heat exchanger and the use of nanofluids as coolant put forth various numerical and experimental setups to enhance the fluid flow and heat transfer characteristics. The study indicated that the employment of nanofluids in microchannel heat exchangers yields an overall 30–35% increase in heat transfer performance at the expense of increased pressure drop penalty at about 12%. A performance investigation on the microchannel heat exchanger with counterflow arrangement (Hasan et al. 2015) employing nanofluids is conducted. The results revealed that the presence of nanoparticles and low particle concentrations has increased the capability to absorb more heat than that of pure water-cooled microchannel. In addition, it has been found that no extra increase in pressure drop has been initiated.

In this work, a microchannel heat exchanger has been proposed to perform the pre-heating process of brine water during the multi-stage flash distillation (MSFD) desalination process. Figure 16.1 shows the setup of MSFD desalination employing microchannel heat exchanger as solar receiver. Microchannels are narrow internal flow pathways having a hydraulic diameter of less than 1000 μm. The brine water enters the inlet and flows along the microchannel thus absorbing the heat generated by the concentrated solar leading to a rise in the fluid temperature. The brine exiting out of the heat exchanger is collected at the outlet manifold and then passed onto the multi-stage flash distillation desalination process. The thermo-hydraulic performance of the microchannel heat exchanger is characterized by two principal parameters mainly thermal resistance and pumping power. The overall thermal resistance of the microchannel heat exchanger is shown in Eq. (16.1). The overall thermal resistance is divided into three different constituents: convective, calorific and conduction thermal resistance. Equation (16.2) represents the calorific thermal resistance where it is largely dependent on the mass flow rate and specific heat capacity of the working
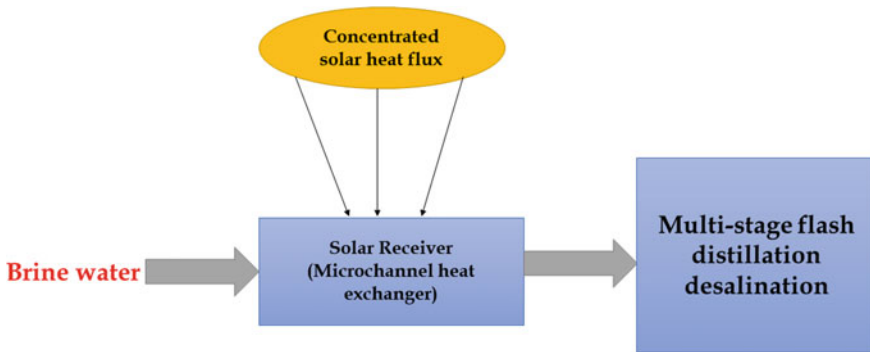
Fig. 16.1 Schematic diagram of multi-stage flash distillation desalination employing microchannel heat exchanger as solar receiver

fluid. The convective thermal resistance is calculated as seen in Eq. (16.3). It is mainly governed by the heat transfer coefficient as well as the area of cross-section between the fluid and solid substrate. The decrease in convective thermal resistance is caused due to the increased heat transfer area and increased heat transfer coefficient, thus increasing the overall size of the microchannel heat exchanger. A lower convective thermal resistance is achieved by improving the heat transfer coefficient without maximizing the heat transfer area. The generation of secondary flows and redevelopment of boundary layer paves the way for enhancing the heat transfer rates. The reduction in the hydraulic diameter leads to increased heat transfer coefficient which led to the employment of microchannel for absorbing maximum amount of thermal energy providing greater efficiency. The conduction thermal resistance is calculated from the calorific, convective and overall thermal resistance as shown in Eq. (16.4). The pumping power required by the fluid to move through the microchannel is expressed in Eq. (16.5). Pumping power is greatly influenced by the pressure drop and volumetric flow rate across the microchannel.

$$R_{th} = \frac{T_{s,\max} - T_{c,in}}{Q} \tag{16.1}$$

$$R_{th,cal} = \frac{1}{c_p \dot{m}_p} = \frac{T_{c,out} - T_{c,in}}{Q} \tag{16.2}$$

$$R_{th,conv} = \frac{1}{A_s \overline{h}} = \frac{LMTD}{Q} \tag{16.3}$$

where $LMTD = \frac{(T_{s.wall,out} - T_{c,out}) - (T_{s.wall,in} - T_{c,in})}{\ln(\frac{T_{s.wall,out} - T_{c,out}}{T_{s.wall,in} - T_{c,in}})}$.

$$R_{th,cond} = R_{th} - R_{th,cal} - R_{th,conv} \tag{16.4}$$

$$PP = \Delta P \dot{Q} \tag{16.5}$$

This study is done for a Reynolds number ranging from 50 to 1500. An analysis on the geometrical and operating parameters is detailed in this paper. The performance of the system is computed with regard to both the thermal resistance and pumping power.

16.2 Mathematical Modelling

This section provides the mathematical modelling to comprehend the working principle and perform the parametric analysis of the proposed microchannel heat exchanger. Laminar flow model has been selected for this study. The computational modelling has been performed with the help of Fluent module of ANSYS Workbench. In order to reduce the computational size and time, only a single repeating heat associated with the heat exchanger has been considered. Figure 16.2 shows the repeating unit of the circular microchannel heat exchanger. The computational model of the microchannel heat exchanger is solved with the help of Navier–stokes equations, continuity equations and energy equations. The continuity equations are shown in Eq. (16.6). Equation (16.7)–(16.9) represents the Navier–stokes equations in x, y and z directions respectively. Equations (16.10) and (16.11) denotes the energy equation of the solid substrate and working fluid respectively.

Continuity Equation

$$\frac{\partial}{\partial x} u_f + \frac{\partial}{\partial y} v_f + \frac{\partial}{\partial z} w_f = 0 \tag{16.6}$$
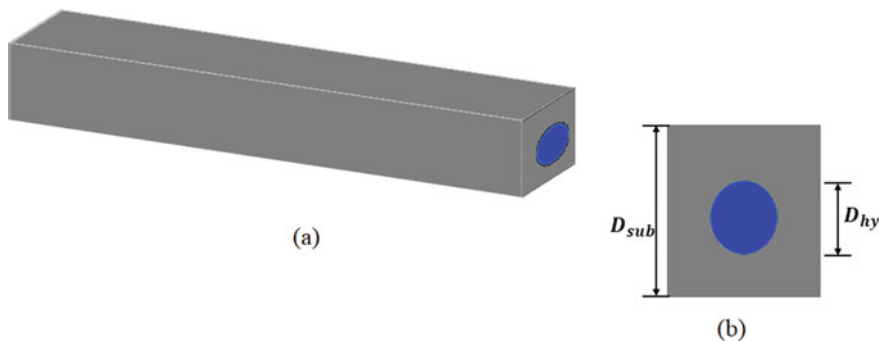
Fig. 16.2 Schematic of the **a** repeating unit of proposed circular microchannel heat exchanger **b** front view of repeating unit

Navier Stokes equation in x-direction

$$u_f \frac{\partial}{\partial x} v_f + v_f \frac{\partial}{\partial y} v_f + w_f \frac{\partial}{\partial z} v_f$$
$$= -\frac{1}{\rho_f} \frac{\partial}{\partial x} P + \frac{\mu_f}{\rho_f} \left(\frac{\partial^2}{\partial x^2} u_f + \frac{\partial^2}{\partial y^2} u_f + \frac{\partial^2}{\partial z^2} u_f \right) \qquad (16.7)$$

Navier Stokes equation in y-direction

$$u_f \frac{\partial}{\partial x} u_f + v_f \frac{\partial}{\partial y} u_f + w_f \frac{\partial}{\partial z} u_f$$
$$= -\frac{1}{\rho_f} \frac{\partial}{\partial y} P + \frac{\mu_f}{\rho_f} \left(\frac{\partial^2}{\partial x^2} v_f + \frac{\partial^2}{\partial y^2} v_f + \frac{\partial^2}{\partial z^2} v_f \right) \qquad (16.8)$$

Navier Stokes equation in z-direction

$$u_f \frac{\partial}{\partial x} w_f + v_f \frac{\partial}{\partial y} w_f + w_f \frac{\partial}{\partial z} w_f$$
$$= -\frac{1}{\rho_f} \frac{\partial}{\partial z} P + \frac{\mu_f}{\rho_f} \left(\frac{\partial^2}{\partial x^2} w_f + \frac{\partial^2}{\partial y^2} w_f + \frac{\partial^2}{\partial z^2} w_f \right) \qquad (16.9)$$

Energy equation of substrate

$$\frac{\partial^2}{\partial x^2} T_s + \frac{\partial^2}{\partial y^2} T_s + \frac{\partial^2}{\partial z^2} T_s = 0 \qquad (16.10)$$

Energy equation of coolant

$$u_f \frac{\partial}{\partial x} T_f + v_f \frac{\partial}{\partial y} T_f + w_f \frac{\partial}{\partial z} T_f$$
$$= \frac{k_f}{\rho_f c_{p,f}} \left(\frac{\partial^2}{\partial x^2} T_f + \frac{\partial^2}{\partial y^2} T_f + \frac{\partial^2}{\partial z^2} T_f \right) \qquad (16.11)$$

The boundary conditions that need to be applied on the computational model involves the use of velocities and temperature. The temperature and fluid velocity at the inlet of the microchannel is represented in Eq. (16.12). The inlet velocity depends on the Reynolds number and the hydraulic diameter of the microchannel. With the increase in Reynolds number, flow rate of the fluid also increases. The gauge pressure at the exit of the microchannel shown in Eq. (16.13) is defined as zero which implies that the fluid is exiting from the microchannel into surrounding condition. The presence of non-slip condition is set as zero which is mathematically represented in Eq. (16.15). The heat source in the multi-stage distillation desalination is replaced

with the solar energy source. The concentrated solar thermal energy striking on the top surface of the microchannel heat exchanger enables the brine water passing through the channel to cause a rise in fluid temperature. The heat flux and temperature interfaced continuously with the substrate is represented in Eqs. (16.16) and (16.17) respectively. The heat flux received on the top surface of the microchannel is given in Eq. (16.18). Since only one repeating unit has been considered for modelling, the side lateral walls are assumed to be the walls of the symmetry which is mathematically expressed in Eq. (16.19). The hydraulic diameter of the circular microchannel is calculated from the radius of the circular one.

$$T_{f,in} = 293K$$
$$u_{f,in} = Re\frac{\mu_f}{D_{hy}\rho_f} \tag{16.12}$$

$$v_{f,in} = 0$$
$$w_{f,in} = 0 \tag{16.13}$$

$$P_{f,out} = 0$$
$$u_{f,wall} = 0 \tag{16.14}$$

$$v_{f,wall} = 0$$
$$w_{f,wall} = 0 \tag{16.15}$$

$$k_f\frac{\partial T_{f,\text{interface}}}{\partial n} = k_s\frac{\partial T_{s,\text{interface}}}{\partial n} \tag{16.16}$$

$$T_{f,interface} = T_{f,interface} \tag{16.17}$$

$$q' = 20,000 \text{ W/m}^2 \tag{16.18}$$

$$\frac{\partial T_s}{\partial n} = 0 \tag{16.19}$$

Several parameters are employed to conduct a parametric study which are listed in Table 16.1. This study deals only with parametric analysis on the performance of the proposed circular microchannel heat exchanger and do not focus on the optimization of the conceptualized work.

Initially, the CAD model of the computational model is created before performing the simulations in ANSYS. A grid dependence test was also carried out to choose the best mesh setting for meshing the computational model. The study employed three different mesh settings where the first one was the coarsest and the third one being the finest. While comparing all the three mesh settings based on the average temperature

Table 16.1 Parametric study configuration

Cases	Designs	L_{ch} (cm)	D_{hy} (mm)	W_{sub}/D_{sub} (mm)	q" (W/m^2)
Case 1	Design 1	5	1	3.5	20,000
	Design 2		2		
	Design 3		3		
Case 2	Design 1	5	0.5	3.5	20,000
	Design 4	10			
	Design 5	15			

Table 16.2 Thermophysical properties of water and aluminium alloy

Properties	Water	Aluminium alloy
Density (ρ)	998.29 kg/m^3	2700 kg/m^3
Specific heat (C_p)	4181 J/Kg K	898 J/Kg K
Thermal conductivity (K_p)	0.6 W/m K	200 W/m K
Viscosity (Pa. s)	0.001002	–

at the outlet of microchannel as well as pressure drop; it was found that the third mesh setting contained a greater number of nodes and had negligible difference in the key parameters from the second mesh setting. Thus, the third mesh setting was chosen for this parametric study. This grid dependency test was only carried for a single design and is assumed to be the best mesh settings for all the designs. After meshing the computational domain, the next step is to assign the appropriate boundary conditions and thermophysical properties of the fluid and substrate. Here, water is used as the working fluid and aluminium alloy is taken as the substrate material. Table 16.2 lists the thermophysical properties employed in this proposed work.

16.3 Results and Discussion

This section explicitly represents the results obtained after performing a parametric study. The effect of geometric and operating parameters such as varying the hydraulic diameter and length of the microchannel are studied. Thermal resistance and pumping power are the two key parameters used to evaluate the performance of the proposed designs.

Figure 16.3 shows the effect of the hydraulic diameter (D_{hy}) of microchannel on the thermal resistance and pumping power. It can be clearly noticed from Fig. 16.3 that the thermal resistance decreases with the increase in hydraulic diameter.

As the hydraulic diameter increases, the convective thermal resistance increases and decreases respectively. This is because with the increase in Reynolds number, the mass flow rate increases thereby resulting in reduction of the calorific thermal resistance. With the increase in the radius of the channel, more fluid is allowed to
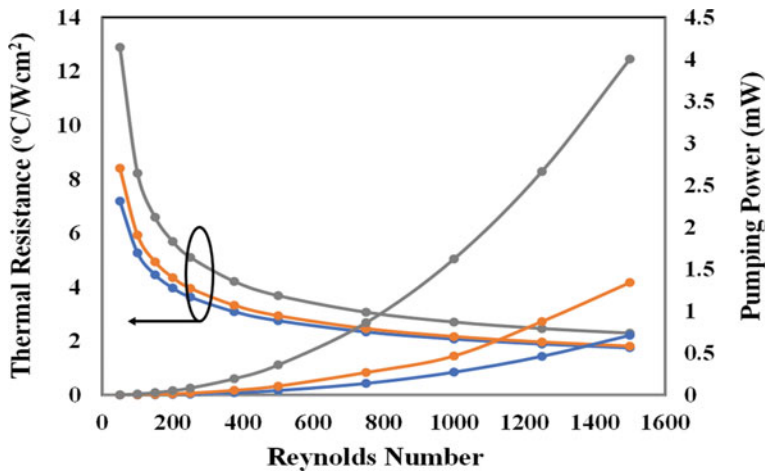
Fig. 16.3 Variation of thermal resistance and pumping power with Reynolds number for varying D_{hy} (— • — : Design 3, — • — : Design 2, — • — : Design 1)

pass through at higher velocity rates which makes the calorific thermal resistance dominant over the convective thermal resistance and calorific thermal. Thus, the overall thermal resistance will be largely influenced by calorific thermal resistance thereby obtaining lowest thermal resistance for the highest magnitude of hydraulic diameter of the circular microchannel. The change in the hydraulic diameter increases the flow disruption and enhances the thinning of boundary layer. This decrease in the boundary layer thickness along with the development of secondary flows result in increased heat transfer coefficient. Figure 16.3 also shows the change in pumping power for Reynolds number for different hydraulic diameter. As the Reynolds number increases, the fluid velocity rises which in turn leads to generate higher pressure drop and increased volumetric flow rate. This increase in pressure drop coupled with the increased volumetric flow rate leads to a higher magnitude of pumping power. At a particular Reynolds number, the pumping power increases with the reduction in the hydraulic diameter. This is because due to the reduction in the hydraulic diameter, the cross-sectional area decreases thus increasing the fluid velocity, amplifying the boundary layer thinning and development of secondary flows resulting in increased pumping power magnitudes. At higher Reynolds number, it can be noticed that due to the enhancement in thinning of the boundary layer and intensified secondary flows, high heat transfer coefficient is generated as shown in Fig. 16.4. It can be observed from Fig. 16.3 that as the hydraulic diameter decreases the heat transfer coefficient increases. This is because as the hydraulic diameter decreases, the cross-sectional area decreases thereby allowing higher heat transfer rates on a smaller area resulting in increased heat transfer coefficient.

Figure 16.5 shows the influence of the length of the microchannel (L_{ch}) on thermal resistance and pumping power. Irrespective of L_{ch}, thermal resistance decreases with the increase in Reynolds number. The increase in Reynolds number is mainly
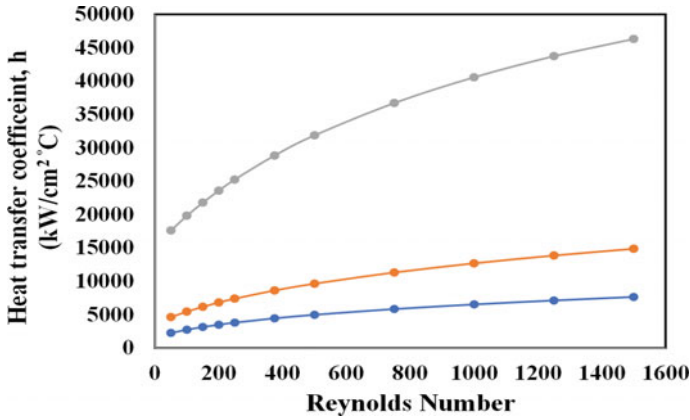
Fig. 16.4 Variation of heat transfer coefficient with Reynolds number for different D_{hy} (— • — : Design 3, — • — : Design 2, — • — : Design 1)
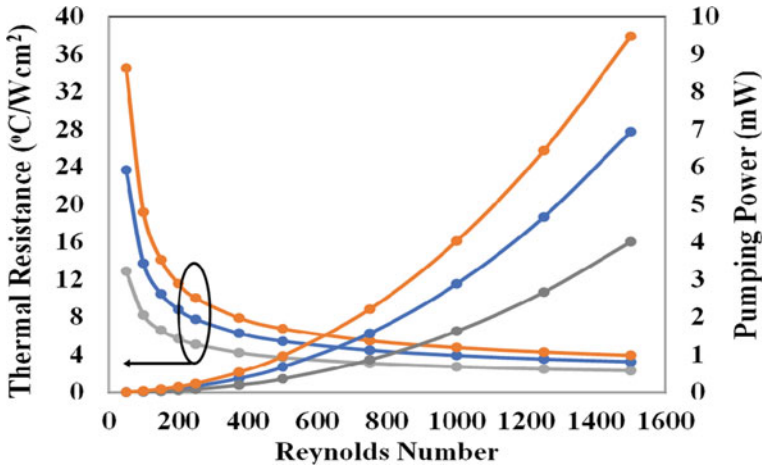
Fig. 16.5 Variation of thermal resistance and pumping power with Reynolds number for varying L_{ch} (— • — : Design 6, — • — : Design 5, — • — : Design 1)

governed by the reduction in the convective thermal resistance and calorific thermal resistance, As the Reynolds number increases, an increase in heat transfer coefficient is observed resulting in the reduction of convective thermal resistance. This increase in heat transfer coefficient occurs due to the reduction in boundary layer thickness and intensification of secondary flows. It can be observed that the thermal resistance decreases with the reduction in L_{ch}. This occurs due to increase heat transfer coefficient associated with the reduction in L_{ch}.
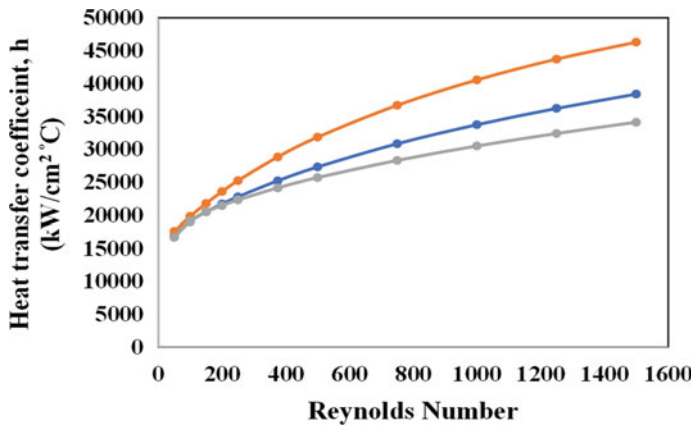
Fig. 16.6 Variation of heat transfer coefficient with Reynolds number for varying L_{ch} (— ● — : Design 6, — ● — : Design 5, — ● — : Design 1)

Figure 16.6 shows the heat transfer coefficient for varying L_{ch}. It can be noticed heat transfer coefficient is maximum for the design Fig. 16.5 shows the influence of the length of the microchannel (L_{ch}) on thermal resistance and pumping power. Irrespective of L_{ch}, thermal resistance decreases with the increase in Reynolds number. The increase in Reynolds number is mainly governed by the reduction in the convective thermal resistance and calorific thermal resistance, As the Reynolds number increases, an increase in heat transfer coefficient is observed resulting in the reduction of convective thermal resistance. This increase in heat transfer coefficient occurs due to the reduction in boundary layer thickness and intensification of secondary flows. It can be observed that the thermal resistance decreases with the reduction in L_{ch}. This occurs due to increase heat transfer coefficient associated with the reduction in L_{ch}.

16.4 Conclusions

This work proposes a methodology of using a less intensive energy source for heating the brine water for use in the multi-flash distillation desalination. For this purpose, a solar receiver based on microchannel heat exchanger is designed. The study is carried out to understand the effect of various geometric and operating parameters associated with the microchannel heat exchanger. It was observed that, the increase in the hydraulic diameter resulted in the reduction of thermal resistance as well as pumping power. The heat transfer coefficient was maximum for the design having lower hydraulic diameter. Also, the decrease in the length of the microchannel led to the reduction in thermal resistance and pumping power. The design associated with lower channel length achieved higher heat transfer coefficient. The future work

suggests the addition of flow disrupting elements, employment of nanofluids and change in microchannel geometry that can enhance the heat transfer performance.

References

Ahlatli S, Mare T, Estellé P, Doner N (2016) Thermal performance of carbon nanotube nanofluids in solar microchannel collectors: an experimental study. Int J Technol 2:78–85. https://doi.org/10.14716/ijtech.v7i2.1575

Bo Y, Sarafraz MM, Arjomandi M (2021) Thermal performance characteristics of a microchannel gas heater for solar heating applications. Energies 14:7625

Hasan S, Reddy KS (2015) A review of solar energy driven desalination technologies. Renew Sustain Energ Rev 41:1080–1118

Chaouki G, Dania K, Ikram D, Ameera Y (2021) Performance analysis and optimization of hybrid multi-effect distillation adsorption desalination system powered with solar thermal energy for high salinity sea water. Energy 215:119212

Lalagi G, Nagaraj PB, Veerabhadrappa Bidari M, Hegde RN (2022) Influence of design of microchannel heat exchangers and use of nanofluids to improve the heat transfer and pressure drop characteristics: a review. Int J Ambient Energy 1–29. https://doi.org/10.1080/01430750.2022.2056918

Li Q, de Tourville NG, Yadroitsev I, Yuan X, Flamant G (2013) Micro-channel pressurized-air solar receiver based on compact heat exchanger concept. Sol Energy 91:186–195

Qiu K, Yan L, Ni M, Wang C, Xiao G, Luo Z, Cen K (2015) Simulation and experimental study of an air tube-cavity solar receiver. Energy Convers Manage 103:847–858. https://doi.org/10.1016/j.enconman.2015.07.013

Tuckerman DB, Pease RFW (1983). Microcapiliary thermal interface technology for VLSI packaging. In: 1983 Symposium on VLSI technology. Digest of technical papers, pp 60–61

Zeng C, Song Y, Zhou X, Zhang F, Jiao M, Liu M, Gu H (2022) Experimental study on heat transfer and pressure drop characteristics in a microchannel heat exchanger assembly with S-shaped fins. Appl Therm Eng 210:118406. https://doi.org/10.1016/j.applthermaleng.2022.118406

Zhu X, Liao Q (2006) Heat transfer for laminar slip flow in a microchannel of arbitrary cross section with complex thermal boundary conditions. Appl Therm Eng 26:1246–1256. https://doi.org/10.1016/j.applthermaleng.2005.10.031

Chapter 17
Mapping Groundwater Potential Zones in UAE Using GIS-Based Hydrogeological Modeling

Abdel Azim Ebraheem, Dalal Alshamsi, Mohsen Sherif, Elke Neuman, Khaled Alghafli, Mohamed Al Mulla, and Ahmed Sefelnasr

17.1 Introduction

Groundwater is the main conventional freshwater resource in UAE (Fig. 17.1). This precious natural resource is nearly the sole source for irrigation water and also provide a small share of potable water for the needs of rural areas. Currently, groundwater extraction for irrigation is more than 95% of the total extraction and groundwater extraction in some areas is 3 to 4 folds of the actual crop water requirements (Fig. 17.2). Though climatic and soil conditions are not ideally suitable for agricultural and horticultural plant cultivation in most parts of the UAE, the area of irrigated land has increased considerably throughout the last two decades. Between 1994 and 2009 the cultivated land surface has approximately doubled (EAIC 2009). Plant cultivation in the UAE comprises of urban landscapes and amenities, as well as land used

A. A. Ebraheem (✉) · D. Alshamsi · M. Sherif · E. Neuman · K. Alghafli · A. Sefelnasr
National Water and Energy Center, United Arab Emirates University, Al Ain, United Arab Emirates
e-mail: abdelazim.aly@uaeu.ac.ae

M. Sherif
Civil and Environmental Engineering Department, College of Engineering, United Arab Emirates University, 15551 Al Ain, United Arab Emirates

D. Alshamsi
Geoscience Department, College of Science, United Arab Emirates University, P.O. Box 15551, Al Ain, United Arab Emirates

E. Neuman
College of Agriculture and Food Technology, College of Engineering, United Arab Emirates University, 15551 Al Ain, United Arab Emirates

K. Alghafli
James Watt School of Engineering, University Glasgow, Glasgow G12 8QQ, UK

M. Al Mulla
Ministry of Energy and Infrastructures, Dubai, United Arab Emirates

for the production of crops. In addition, the UAE maintains a considerable area of man-made forests, which serve plant and wildlife conservational purposes. With an annual average rainfall of only around 120 mm all agricultural plant production and maintenance of forests and parks in the UAE depends on irrigation water supply. Therefore, groundwater availability in the right quantity and quality, contributes to sustainable development of UAE.

The precise amount of groundwater consumed by open field crop production in the UAE is difficult to assess, as most farmers do not use water counters. Estimates vary considerably, depending on the source (Table 17.1). In each estimate there is one or more source of uncertainty. However, the rates of 2480 and 450 MCM/year are the most reasonable estimates for farms and planted forests irrigation respectively. Only 1160 MCM/year of this volume (32%) is replenished by recharge from all different sources (Sherif et al. 2021). Therefore, it is required to enforce the relevant restrictions to change the current practice and supply water in accordance with the needs of the crops. Through this management component, the lifespan of groundwater reserves would be expanded. Successful management of the very limited fresh groundwater reserve in UAE depends largely upon the following:
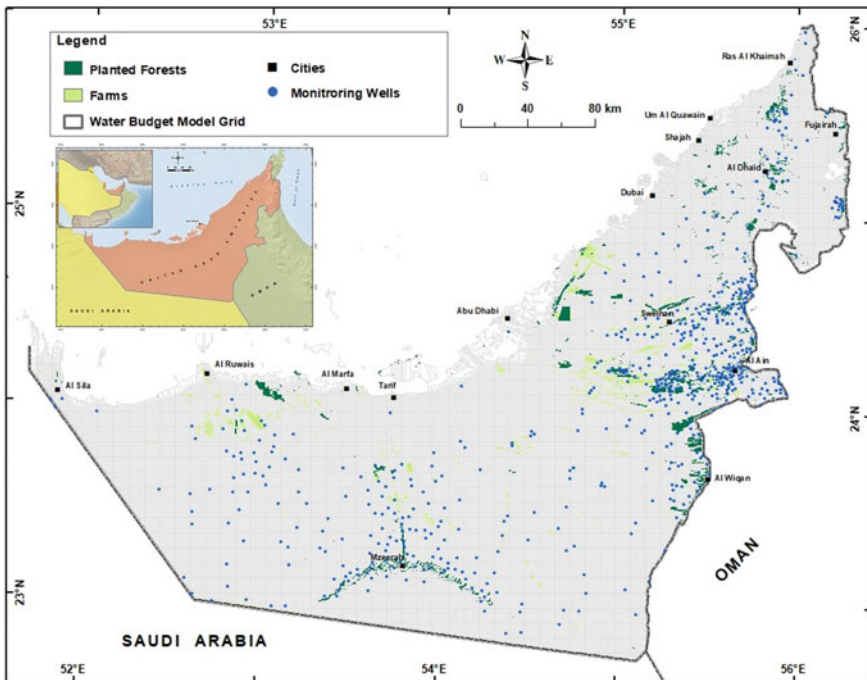
Fig. 17.1 Location map of UAE. The locations of monitoring wells, farms, planted forests, and water budget model grid are also shown (Sherif et al. 2021)
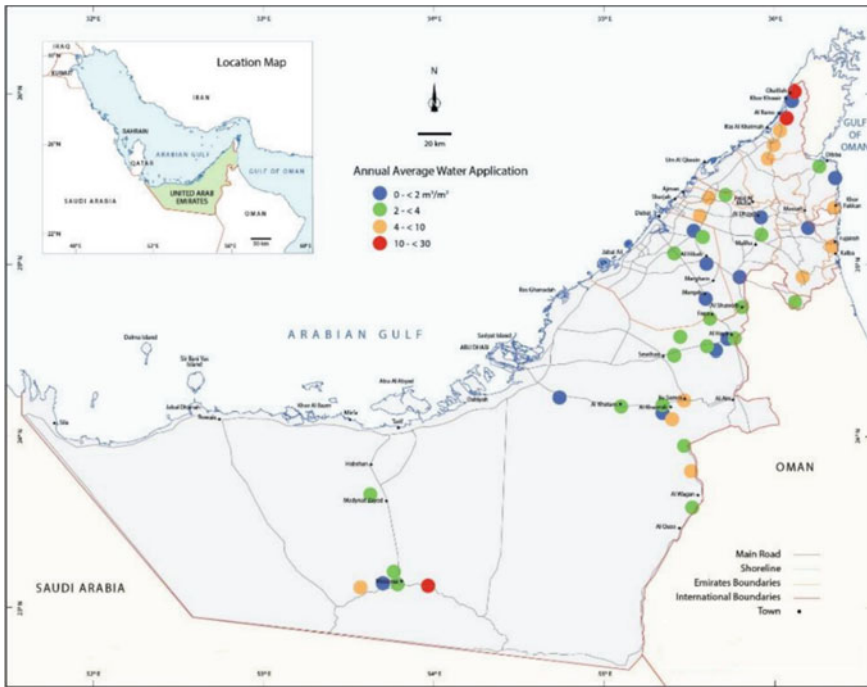
Fig. 17.2 Estimated on-farm annual water application (Hydro Atlas 2015)

Knowledge of the volumes of groundwater reserves (quantity and quality wise) and spatial distribution of the groundwater potential zones (GWPZs).

Estimation of the rates and sources of groundwater recharge

Precise prediction of the impact of stresses on groundwater reserves (quantity and quality wise)

Implementation of a new well permitting system and forcing the installment of meters at the well outlets to measure actual groundwater pumping in all farms.

Delineation of the groundwater potential zones (GWPZs) requires the analysis of several factors relates to the physiographic setting including but not limited to aquifer types and geometry, lineament density, geological structure/lithology, elevation, soil, drainage density, slope, land cover/land use, rainfall, existed water infrastructure, etc. Groundwater investigation and identifying GWPZs in each study area are both greatly facilitated by GIS. It has become simpler to provide the baseline data for designating groundwater potential zones to the extensive usage of remote sensing satellite pictures and ground truth data. Studies have shown that several researchers have used machine learning, simple additive weight (SAW), and analytical hierarchy process (AHP) with GIS to designate groundwater potential zones. The ambiguity of hydrogeological data in several aspects is reduced by the use of remote sensing and GIS technology (Melese and Belay 2022). The main objectives of the current

Table 17.1 Different estimations of groundwater abstraction for irrigation in UAE

The Study	Estimated Irrigation volume for farms and planted forests (MCM)	Remarks
The Pacific Institute (2006)	1564	The estimate was done for farms only
FAO (2009)	3300	Overestimation of the farms area
MOEW (2010)	1970–2070	The estimate was done for farms only
UAE Hydro Atlas (2015) Open field survey method GWBM	3110 (for farms only) The estimated total groundwater abstraction is 2850 MCM per year (1700 coming from groundwater storage mining and 1150 MCM coming from recharge sources). Then the annual groundwater abstraction for irrigation purposes only can be obtained by subtracting the volume of 90 MCM per year for domestic purposes from the total value	
MOEW and ICBA	2370 (for farms and planted forests irrigation)	
Sherif et al. (2021)	2764 (2314 for farms and 450 for planted forests)	

study are (1) to map the potential groundwater zones in the UAE using the analytical hierarchy process (AHP) and GIS techniques, and (2) to provide a digital geodatabase that decision-makers can use to create effective sustainable groundwater management plans to address the UAE's limited natural freshwater resources.

17.2 Hydrogeological Setting

Five aquifers make up the UAE's groundwater systems, and they are mentioned below in order of their physical setting (surface or deep) and location from north to south (Fig. 17.3): (a) Quaternary aquifer, (b) The sand dunes' aquifer, (c) Juweiza aquifer, (d) Carbonates aquifer, and (e) Fractured ophiolite aquifer. The hydraulic connections between the Quaternary and Juweiza aquifers indicate the UAE's primary groundwater system. The aquifer comprises alluvial gravels and sand on both sides of the Northern Oman Mountains (Sherif et al. 2021).

The hydrogeological map shown in Fig. 17.3 indicates that Quaternary aquifer system is the main aquifer system in UAE. The aquifer comprises alluvial gravels and sand on both sides of the northern Oman Mountains in the northern part of the country
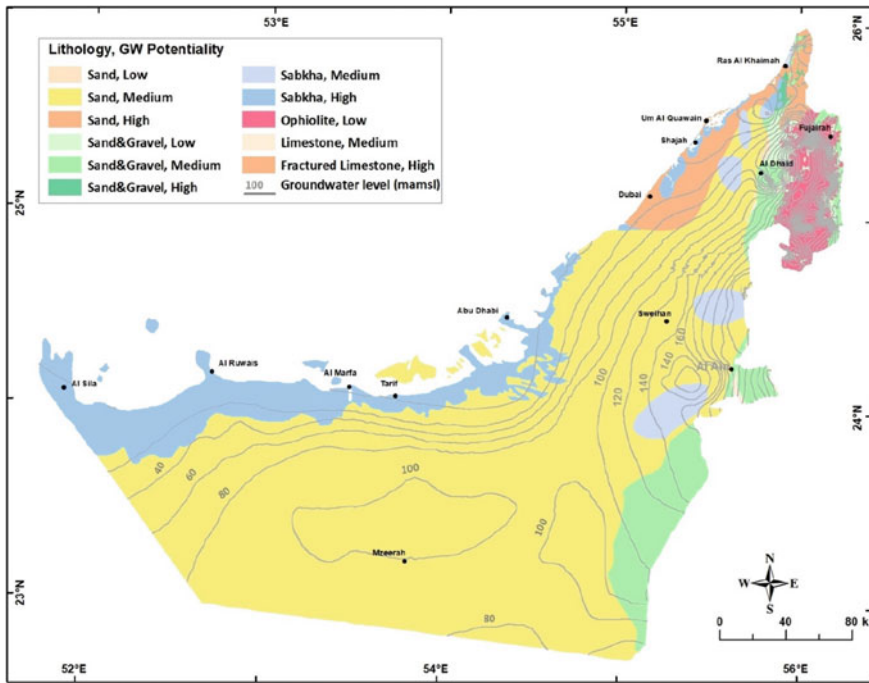
Fig. 17.3 Hydrogeological map of UAE (Sherif et al. 2021)

(Fig. 17.4). This aquifer system contains the largest reservoir of fresh groundwater storage in UAE. Groundwater can be found between 5 and more than 100 m below the surface, according to field measurements. The local terrain, aquifer boundaries and extent, groundwater abstraction, and recharge rate all affect the flow system in this aquifer. This aquifer system has a hydraulic conductivity of 10 to 40 m/day, and the TDS ranges from 500 to 150,000 mg/l in the sabkha zones (e.g., along Al Ain Abu Dhabi main road). The estimated groundwater reserve in the Quaternary aquifers across the UAE is 750,000 MCM (Sherif et al. 2021). Currently, less than 15,000 MCM of this volume is fresh groundwater reserve. Excessive groundwater abstraction from this aquifer system (2854 MCM/year) results in local cone of depressions due to the limited annual replenishment (787 MCM/year).

The carbonates aquifers in the UAE is divided into: (a) northern limestone aquifer (or Wadi Al Bih Aquifer) in Ras Al Khaima Emirate and (b) Jabal Hafit limestone aquifer south of Al Ain City in Abu Dhabi Emirate. The northern limestone aquifer is predominantly composed of fractured limestone and dolomite. Jabal Hafit aquifer is composed of a very thick limestone layer and marl interbedded with gypsum and dolomite and evaporates formations of Lower Eocene to Miocene age. The hydrologic budget of wadi Al Bih basin indicated that the total fresh groundwater reserve and annual recharge are about 14,000 and 9.57 MCM respectively. The total groundwater discharge from this aquifer is about 6 MCM in addition to annual seepage to the sea
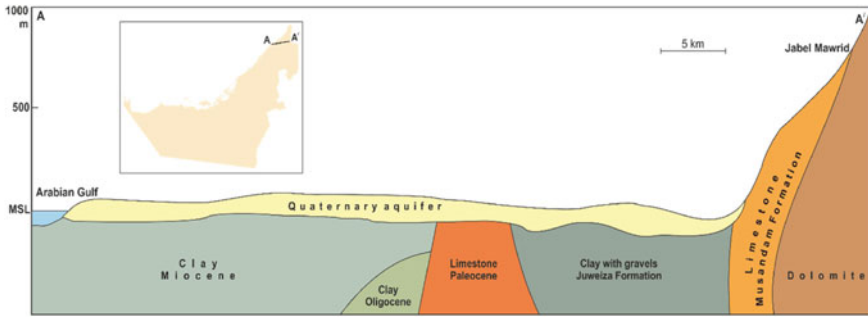
Fig. 17.4 Geological cross-section A-A′ in the east-west direction showing the quaternary aquifer (*Source* Sherif et al. 2021)

of about 1.5 MCM. The estimated groundwater reserve of fresh to saline water categories in the carbonate aquifers across the UAE is 370,000 MCM (Sherif et al. 2021).

17.3 Materials and Methods

To estimate the groundwater reserves in this aquifer, annual groundwater recharge, and average annual groundwater abstraction for irrigation, information held in the water resources geodatabase for the Quaternary Aquifer was employed within the groundwater budget model (GWBM) developed by Sherif et al. (2021) which include two new components which are groundwater recharge and abstraction for irrigation purposes. In the GWB model, the whole area of UAE (excluding islands) was divided into a regular grid of 1 km^2 (7049 cells) as shown in Fig. 17.1. Based on the hydrological, hydrogeological, aquifer surfaces topography under each cell, the above-mentioned volumes were calculated for each cell for years 1969, 2005, 2010, and 2015. Decrease in groundwater storage in the period 2005–2010 was also calculated and divided by 5 at each cell to get the average annual water table decline at each grid cell. By multiplying water table decline at each cell times its surface area times the specific yield, the net groundwater extraction will be obtained at this cell. Then by adding the obtained net groundwater abstraction for all cells, the total net groundwater abstraction was obtained for the whole UAE.

17.4 Results and Discussion

The groundwater salinity map of year 2015 (Fig. 17.5) and a groundwater budget model (GWBM) developed by Sherif et al. (2021) were used to estimate the groundwater reserve of each water quality (fresh brackish/saline) as shown in Table 17.2. The
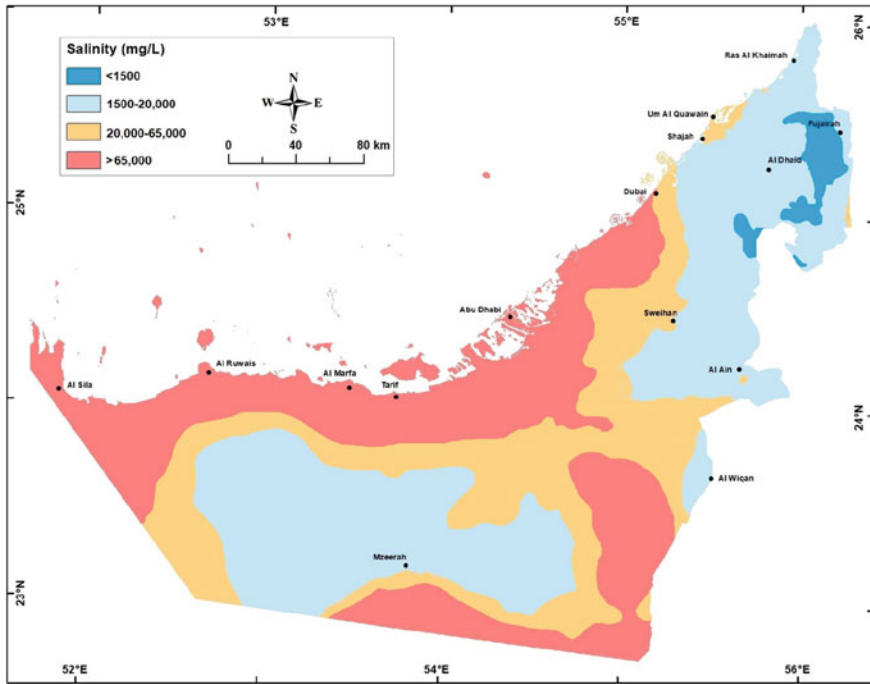
Fig. 17.5 Groundwater salinity (mg/l) in the year 2015 (*Source* Sherif et al. 2021)

Table 17.2 Types of groundwater storage available in the quaternary aquifer as computed from GWBM (cubic kilometers) for year 2015

Water Type	Fresh (km^3)	Brackish (km^3)	Saline (km^3)	Brine (km^3)	Total (km^3)
Salinity	(< 1500)	(> 1500–20,000)	(> 20,000–65,000)	(> 65,000)	–
2020	10	270	380	262	922

Source Sherif et al. (2021)

GWBM was also used to estimate groundwater abstraction for irrigation, remaining lifespan, and replenishment ratio in the year 2020. In the agricultural areas, the replenishment ratio is ranging from 1 to 25% (Fig. 17.6). The main advantage of this model is that it is based on an updated GIS database for the conventional and nonconventional water resources. The recharge from rain and other sources to the Quaternary aquifer was estimated using the potential recharge method with the analytical hierarchy process (AHP) submodules of the same GWBM model (Fig. 17.7). The total recharge to the Quaternary aquifer with and without augmentation is 1197 and 1001 MCM respectively (Table 17.3).
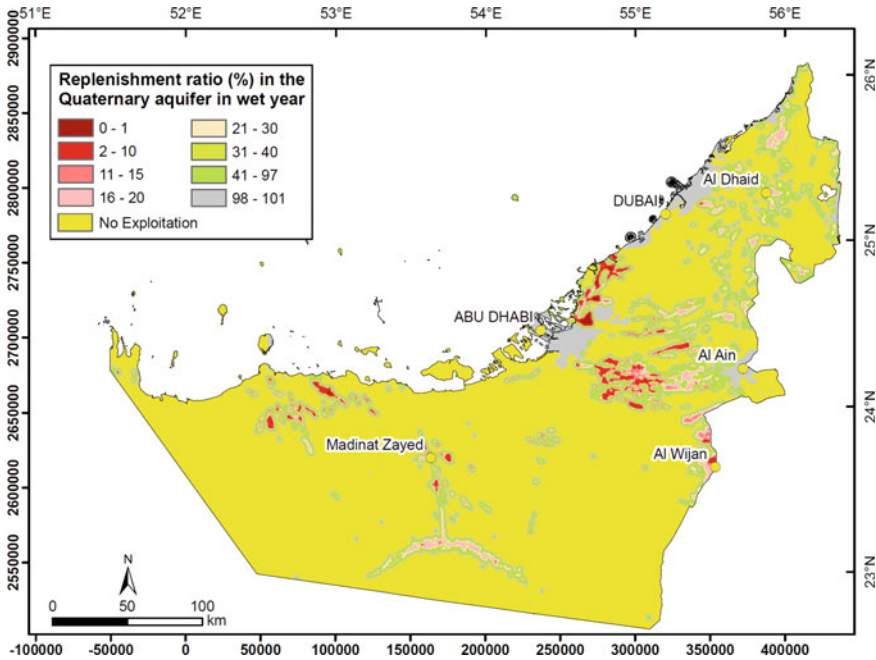
Fig. 17.6 Groundwater replenishment percentage (%) in the quaternary aquifer

The forestry, agricultural, and industries all utilized groundwater. The depletion percentage would be only 0.28% yearly if the annual decline in groundwater storage were compared to the average overall groundwater storage (fresh to saline types, 660 BCM). Since most of the yearly groundwater abstraction came from fresh groundwater storage, it is important to compare it to the current total fresh groundwater resources, which were only around 10 BCM in 2015, since this is a very alarming harbinger signaling the scarcity in agricultural water. It is crucial to remember that the metrics used to evaluate groundwater storage, including the aquifer's effective porosity, were only approximatively known.

The obtained results from the GWBM indicated that the remaining fresh groundwater resources in UAE (including mountainous areas) is less than 15,000 MCM and covering an area of 2160 km^2 (Fig. 17.8). Under the business-as-usual scenario (i.e., same farming and forest areas; Fig. 17.1; and same abstraction rate; Fig. 17.2) and if these resources are used for farming irrigation exclusively, the available fresh groundwater would only last for less than 5 years as technically and environmentally only 70% of available water can be abstracted. Although this is a general conclusion and it is anticipated that the fresh groundwater reserve has significantly increased following the heavy precipitation events in the water years 2019–2020 and 2021–2022, there is a critical need to manage groundwater resources in each location differently.
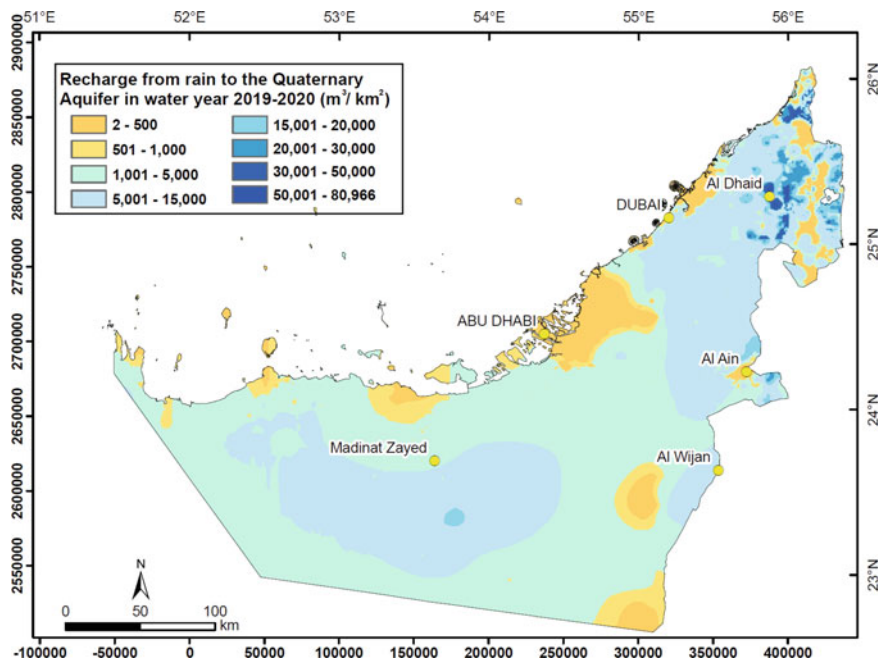
Fig. 17.7 Recharge to the quaternary aquifer in the water year 2019–2020 (m^3/km^2)

Table 17.3 Recharge to the Quaternary aquifer in the water year 2019–2020 (MCM)

Recharge type	Recharge volume (MCM)
Recharge from precipitation for a normal average rainy year with recharge augmentation	160
Recharge from precipitation for a normal average rainy year without recharge augmentation	145
Recharge from precipitation for a wet year with recharge augmentation	356
Recharge from precipitation for a wet year without recharge augmentation	326
Return flow from groundwater-fed irrigation	362
Return flow from desalination, treated wastewater, and network losses	427
Internal flux	52
Total recharge in the normal average rainy year	1001
Total recharge in the wet year	1197
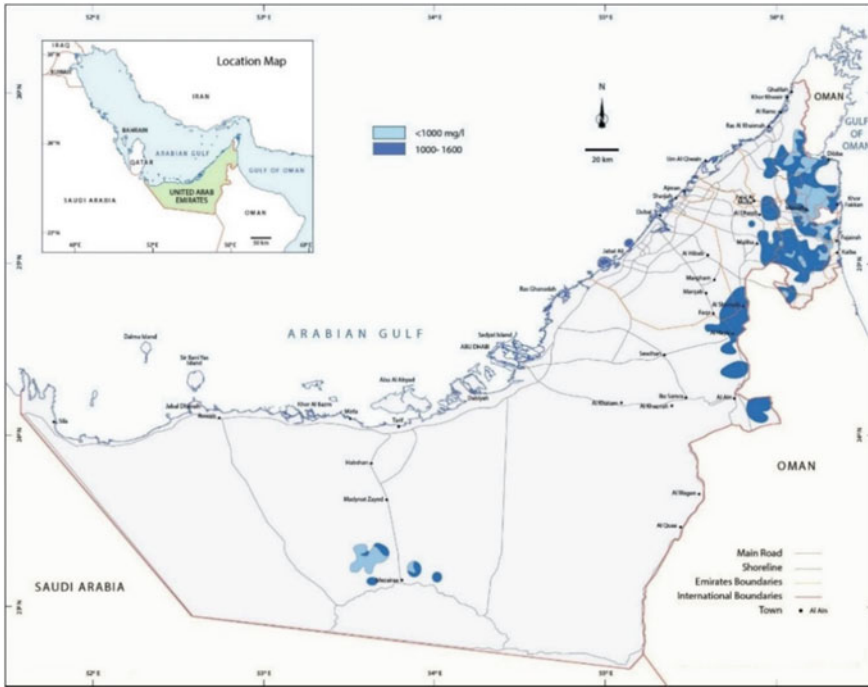
Fig. 17.8 Areal distribution of fresh groundwater resources in 2012

The following six zones can be used to categorize the groundwater conditions in farming areas (only) based on the groundwater budget, TDS in 2015, distance to existing farms (pumping wells), ratio of the present saturated thickness to the maximum saturated thickness, and remaining life duration (Fig. 17.8).

Zone One: TDS in 2015 < 2000 ppm. The area of this zone is 40 km^2 and the total fresh to slightly brackish groundwater reserve is estimated as 581 MCM.
Zone Two: 2000 ppm < TDS in 2015 < 5000 ppm. The area is 50 km^2 and the total low brackish groundwater reserve is 640 MCM.
Zone Three: 5000 ppm < TDS in 2015 < 10,000 ppm. The area is 934 km^2 and the total medium brackish groundwater reserve is 15,600 MCM.
Zone Four: 10,000 ppm < TDS in 2015 < 15,000 ppm. The area is 913 km^2 and the total highly brackish groundwater reserve is 12,400 MCM.
Zone Five: 15,000 ppm < TDS in 2015 < 20,000 ppm. The area is 762 km^2 and the total extremely brackish groundwater reserve is estimated as 8500 MCM.
Zone Six: TDS in 2015 > 20,000 ppm. The area of this zone is 66,256 km^2 and the volume of the slightly saline groundwater reserve is 716,000 MCM.

GWBM results indicated that the net groundwater extraction for farms irrigation is 2325 MCM annually. This value, however, should be adjusted to the unaccounted abstraction (e.g., the abstractions of 450 and 90 MCM per year for planted forests irrigation, and domestic use, respectively) and for recharge from all sources, which is 1150 MCM per year. By doing so, the total adjusted annual groundwater extraction for farms irrigation is coming to 2325 MCM per year of which 1175 is groundwater mining.

The UAE government is considering stringent steps to protect groundwater now that it is aware of the issue. In Abu Dhabi Emirate, for instance, agricultural activities use 72% of the water, although they only provide 1% of the country's GDP. As of right now (2021), Abu Dhabi's Agriculture, Forests, and Parks sector is the emirate's biggest water user. This sector's water consumption is steadily declining, most likely because of the use of demand side management strategies. The demands from the household and industrial sectors are rising, nevertheless. All sectors in which the water demand is on the rise rely on non-conventional water resources. However, if the coverage for irrigation demands started to shift from groundwater to the desalinated water, a sectorial competition for desalinated water may become an economic and environmental challenge. The technical, economical, and environmental feasibility of using desalinated water for farming irrigation on large scale is highly questionable. The change of agricultural pattern and the use of the brackish water and treated wastewater for irrigation seems to be more feasible. The reuse volume of the treated wastewater is currently 547 MCM/year which is 57% of the treated wastewater in year 2020 (Sherif et al. 2021). This indicate that there is an opportunity to use more of the tertiary treated water for farms irrigation and this in accordance with UAE Strategy 2036 (Fig. 17.9).
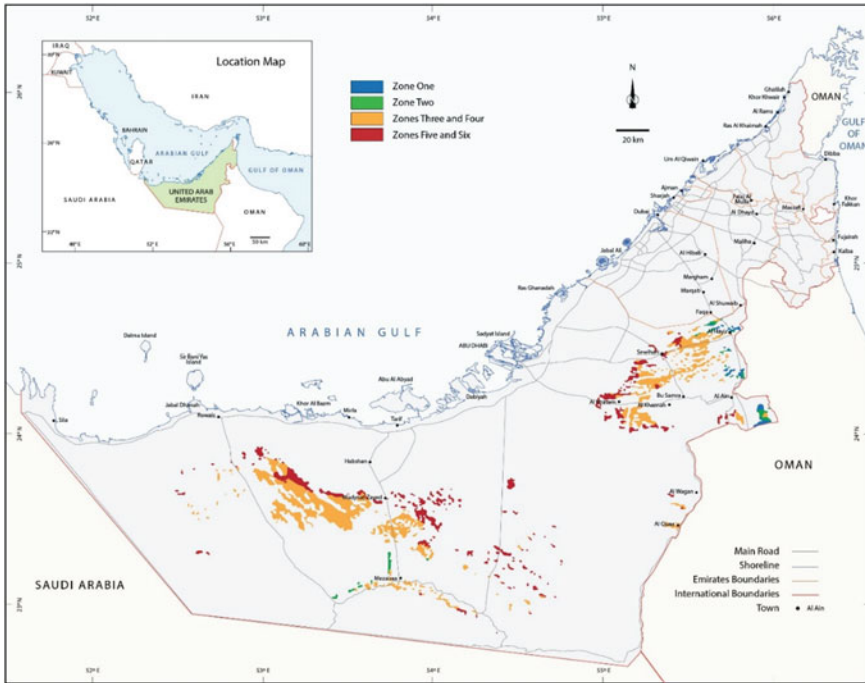
Fig. 17.9 Potential groundwater development zones

17.5 Conclusion

The remaining fresh groundwater resources are extremely scarce and have a relatively short lifespan under the status quo, especially in agricultural areas. For effective groundwater resource management to lengthen its lifespan, the few fresh groundwater potential zones were discovered. New agricultural development shouldn't use the fresh groundwater. According to the results, brackish groundwater is more plentiful than fresh groundwater. This type of water should be treated with the appropriate care as a precious resource for agriculture development with necessary precautions. The technical, economical, and environmental feasibility of using desalinated water for farming irrigation on large scale is highly questionable. The change of agricultural pattern and the use of the brackish water and treated wastewater for irrigation seems to be more feasible.

An essential first step in resource use and management is the evaluation of groundwater potential. The groundwater potential investigations include geology, rainfall, slope, soil, curvature, topographic wetness index, elevation, drainage density, land use land cover, and lineament density in UAE were successfully delineated in the

current study using GIS, and AHP technique. Results from the AHP approach determined the weight of thematic layers in the groundwater potential. The spatial analysis tool in ArcGIS 10.3 was used to overlay all the thematic maps to determine the groundwater potential zones. The obtained results indicated that the groundwater potential zone 1 (TDS less than 2000 mg/L) and zone 2 (TDS is ranging from 2000 to 5000 mg/L) occupied an area of 40 and 50 km^2, respectively. The estimated groundwater reserve in GWPZ1 and GWPOZ2 are 581 and 640 MCM respectively. Groundwater potential zones of medium (5000 < TDS < 10,000 mg/L) and highly brackish water (10,000 < TDS < 15,000 mg/L) cover areas of 934 and 913 km^2 respectively. The total groundwater reserve in zones 3 and 4 is about 28,000 MCM indicating their extreme importance as the only source of irrigation water inland with precautionary desalination. GWPZ 5(15,000 mg/L < TDS < 20,000 mg/L) covers an area of 762 km^2 and the total extremely brackish groundwater reserve is estimated as 8500 MCM. Zone Six (TDS in 2015 > 20,000 mg/L). The area of this zone is 66,256 km^2 and the volume of the slightly saline groundwater reserve is 716,000 MCM. Even though the salinity in zone 6 is more than 20,000, it is still considered as a resource if compared to the highly saline water in sabkha areas (TDS > 100,000 mg/L).

The Abu Dhabi Environment Agency (EAD) began an ambitious project to create the Abu Dhabi Environment Vision 2030 on behalf of the Executive Council in 2010 with the goal of reducing the environmental effects of anticipated socio-economic growth. When conducting business in the Emirate, the Vision offers a broad framework for consideration and environmental preservation. Both UAE Water Conservation Strategy (2010) and Abu Dhabi Environment Vision 2030 will guide government entity planning and coordination, and also inform the private sector, the Abu Dhabi population and international peers about the aspirations of Abu Dhabi and the other Emirates. The following five priority areas are outlined in the Environment Vision 2030, one of which is effective management and conservation of water resources.

Cut residential indoor and outdoor desalinated water use in half: By 2030, indoor and outdoor desalinated water use is predicted to more than triple current levels if nothing is done.

Avoid using groundwater and desalinated water for landscape irrigation: By 2030, the amount of desalinated water consumed for plantations that provide amenities is predicted to increase if nothing is done. The Abu Dhabi Environment Vision 2030 and the UAE Water Conservation Strategy (2010) are expected to replace both groundwater and desalinated water with recycled water.

Increase the longevity of groundwater reserves by twofold. If nothing is done, viable groundwater reserves will run out in conjunction with expected socioeconomic growth. The lifespan of the groundwater reserves is anticipated to be doubled with the implementation of Abu Dhabi Environment Vision 2030.

Policy imperatives for maintaining adequate demand side management for efficient water consumption patterns in all sectors, in general, and the agriculture sector, in particular, are crucial to achieving the UAE 2021 vision, MEW Water Conservation Strategy, and Abu Dhabi Environmental Vision 2030.

References

EAIC (Environmental and Agricultural Information Centre) (2009) Agriculture statistics year book. UAE Government

FAO (2009) Irrigation in the Middle East region in figures—AQUASTAT survey 2008

HydroAtlas (2015) UAE Hydroatlas (Internal Report). National Water Center and Ministry of Energy and Industry

Melese T, Belay T (2022) Groundwater potential zone mapping using analytical hierarchy process and GIS in Muga Watershed, Abay Basin, Ethiopia. Glob Challenges 6(1):2100068. https://doi.org/10.1002/gch2.202100068

MOEW (2010) United Arab Emirates water conservation strategy. Ministry of Environment and Water (formerly)

Pacific Institute (2006) The world's water 2006–2007. Island Press. https://islandpress.org/books/worlds-water-2006-2007

Sherif M, Sefelnasr A, Ebraheem AA, Al Mulla M, Alzaabi M, Alghafli K (2021) Spatial and temporal changes of groundwater storage in the quaternary aquifer, UAE. Water 13(6). https://doi.org/10.3390/w13060864

UAE Water Conservation Strategy (2010) Internal Report, Ministry of Energy and Infrastructure, Dubai, UAE

Chapter 18
Trihalomethane Species Development in Drinking Water

Jasem Alkandari

18.1 Introduction

Drinking water free from toxic chemical compounds and microbial pathogens is considered one of the main goals of a water treatment facility. Chlorination is widely used worldwide to disinfect drinking water from waterborne diseases (Kim et al. 2015a, b). The application of chlorine as a water disinfectant is preferable as it has several advantages over other disinfectants (e. g., chlorine dioxide, chloramines, and ozone). The main advantages of chlorine over other disinfectant agents are its relatively low cost, performance as a strong oxidizing agent, and ability to maintain residual in water distribution systems (Hua et al. 2015). However, there is still one major drawback of using chlorine, which is the formation of toxic disinfection byproduct compounds. Chlorine reacts with natural organic matter and other water inorganic constituents, such as bromide, during the water disinfection process (Alkandari 2015; Singer 1999). Thus, many disinfection byproduct compounds are developed, which include trihalomethanes (THMs) and haloacetic acids. Several studies revealed that exposure to disinfection byproduct compounds through ingestion, inhalation, and dermal absorption could lead to health issues (Richardson et al. 2007). DeAngelo et al. (2007) revealed that cytotoxicity increases with the increase of degree of bromination in disinfection byproduct compounds. The WHO has provided guidelines regarding the concentration levels of the main disinfection byproduct compounds, which often exist in disinfected drinking water, to protect the health of water consumers. The adopted guidelines for the concentration levels of four THM species, which include chloroform ($CHCl_3$), bromodichloromethane ($CHBrCl_2$), dibromochloromethane ($CHBr_2Cl$), and bromoform ($CHBr_3$), in drinking water, are 300 µg/l, 60 µg/l, 100 µg/l,

J. Alkandari (✉)
Water Research Center, Kuwait Institute for Scientific Research, Safat, P.O. Box 24885, 13109 Kuwait, Kuwait
e-mail: jkandari@kisr.edu.kw

and 100 µg/l, respectively (WHO 2017). However, their concentration levels in chlorinated drinking water depend on the existence and concentration of bromide (Ged and Boyer 2014). During the chlorination of bromide-containing waters, the formation of THM species is often shifted towards brominated THM species (e.g., bromoform). The brominated THM species are more toxic than chlorinated ones (Ceretti et al. 2016).

The presence of bromide in drinking water sources is notably seen in arid regions because of utilization of fossil groundwater rich in dissolved minerals. In countries that depend mostly on the thermal desalination of seawater to meet the drinking water demand, drinking water is often produced by blending desalinated water (DW) with groundwater (GW) in a specific ratio to make the water healthy and palatable for consumption. The blending ratio between DW and GW depends mainly on the quality of GW to ascertain that the salinity of the drinking water produced falls within the acceptable levels set by Kuwait Environment Public Authority. Alhumoud et al. (2010) shed light on the effect of using different blending ratios, between DW and GW, on the salinity of the product water during the production of drinking water in Kuwait. The product water of thermal desalination plants is characterized by low salinity (≈ 6.0 mg/l) and is known to be corrosive to metal (Withers 2005). During the production of DW, it is a common practice to find the water of low salinity to be acidified by CO_2 gas and then passed through the process recarbonation unit to increase the alkalinity of the water to a level around 80.0 mg/l, after which, the pH of the product water is raised to approximately 8.0 by the addition of sodium hydroxide. The salinity of the GW utilized in the blending and production of drinking water ranges between 3000 and 8000 µS/cm, which is considered a brackish type of GW. In drinking water production facilities, the DW is blended with small quantities of GW within the range of 1.7–15.0% to produce drinking water with a maximum salinity of 300 mg/l. At the final stage, the chlorination of drinking water is carried out before pumping the water into the water distribution network. In this context, the chlorination process of drinking water became a great concern to the operators of drinking water production facilities, as other factors, e.g., water temperature, water pH, the age of water, organic constituent, and the existence of bromide, could encourage the development of THMs and other disinfection byproduct compounds. In the previous studies, authors have investigated the effect of temperature (Al-Mudhaf et al. 2010), organic constituents (Tubić et al. 2013), residence time (Li and Zhao 2006), chlorine dose (Rodrigues et al. 2007), bromide and pH (Chowdhury et al. 2010), during the water chlorination process, on the development of THMs in water. Agus et al. (2009) have pointed out that chlorination is the widely used disinfectant in the production of drinking from seawater desalination and bromoform is the predominant disinfection byproduct compound formed. Kim et al. (2015a, b) concluded that there is little data on the formation of disinfection byproducts in drinking water produced from desalination methods. This study aimed to assess the potential formation of THM species in synthetic drinking water samples during the blending of GW with DW at different ratios in the laboratory.

18.2   Methods

18.2.1   Sources of Water Samples

The DW and GW samples required for the experiments were collected from the Doha drinking water production facility in Kuwait and transferred immediately to the Water Research Center laboratory of the Kuwait Institute for Scientific Research (KISR). The types (i.e., DW and GW) are used in the production of drinking water in Kuwait.

18.2.2   Experimental Procedure

In the laboratory, simulated distribution system (SDS) tests were carried out on synthetic drinking water to evaluate the formation of four THM species for the extended storage period. The SDS tests were conducted following the method 5710C found in the book Standard Methods for the Examination of Water and Wastewater (Rice et al. 2012). Moreover, synthetic drinking water samples were produced by blending the DW with GW in two different ratios (i.e., GW and DW; ratios of 2.9: 97.1 and 15.0: 85.0). The utilized blending ratios between the GW and DW in this study, are typically used in the Doha drinking water production facility, which represents the minimum and maximum percentages of GW employed in the production of drinking water. The blending of 2.9 ml of the GW with 97.1 ml of DW was carried out using a 1-l measuring cylinder and pipettes to mix the exact volume of the DW and GW. A Teflon magnetic rod and stirrer were used to blend the GW and DW samples together to produce the synthetic water samples. The preparation of the synthetic drinking water in the laboratory was followed by the injection of sodium hypochlorite solution (laboratory reagent, 4% w/v available, Techno PharmaChem, Haryana). The water samples were injected with 30 μl of sodium hypochlorite using a micropipette, mixed for three minutes, and later transferred to 1 L amber bottles. The added volume of sodium hypochlorite resulted in a concentration of residual chlorine equal to 0.7 mg/l in the synthetic drinking samples. A total of 8 L of synthetic water samples in a separate 1 L amber bottle was produced for the test. The produced amount of the synthetic water samples was enough to analyze the four THM species and perform the quality control check. The previous procedure to produce the synthetic drinking water was typically carried out again to produce 8 L of synthetic drinking water samples consisting of 15.0 ml of GW and 85.0 ml of DW. The synthetic drinking water samples were incubated for 240 h to assess a prolonged contact time on the formation of the four THM species under 30 °C temperature. The incubation temperature utilized in this study represented the temperature of drinking water reported during the warm season in Kuwait.

18.2.3   Analytical Methods

The water samples were analyzed for the four THM species at times 24, 48, 72, 120, 144, 168, 192, and 240 h. A gas chromatography series 6890—mass chromatography series 5973 instrument (GC-MS) coupled with a purge and trap instrument (PT) manufactured by the Agilent Company was used to determine the THM species. The instrument was calibrated using a THM calibration mix (200 µg/l THMs in methanol purchased from SUPELCO Analytical, USA). The operating conditions of the GC-MS and PT instruments are listed in Table 18.1.

The analysis of the THM precursors in the sources of drinking water was conducted to determine their levels and concentrations. Bromide was determined using Dionex 300 ion chromatography equipped with an analytical column (IonPac AS9-HC, 2 × 250 mm) and a conductivity detector (Dionex, suppressed conductivity CD25). The dissolved organic compound of the water samples was analyzed using a total organic compound analyzer (ANATOC series II by SGE International). The ultraviolet absorbance at 254 nm of the water samples was measured using a spectrophotometer manufactured by Hach Company (DR/4000U). The electrical conductivity (EC) measurements and pH of the water samples were carried out

Table 18.1   Operating conditions of the THM analyzer

Purge and trap system	
Purge ready temp	35 °C
Transfer line temp	150 °C
Valve temp	150 °C
Purge time	11 min
Trap pressure control	4 psi
Baking time	8 min
Baking temp	250 °C
Desorbing temp	180 °C
Desorbing preheating temp	175 °C
Dry purge time	4 min
Gas chromatograph—mass spectrometer	
Injector	220 °C
Column (DB-624)	30 m × 0.25 mm × 0.25 µm
Temperature programmed	38 °C accelerate to 240 °C
Carrier gas	Helium
MS source temp	230 °C
MS quadrupole temp	150 °C
Electron multiplier	1600 eV
MS scanning range	40–250 amu
Detector temp	280 °C

using Jenway 370 and Orion portable meters, respectively. The residual chlorine of the water samples was analyzed using a spectrophotometer instrument (DR/2000 of Hach Company). Duplicate samples were analyzed to estimate the relative percent difference (RPD) to measure the precision of THM species. However, the results of the RPD for the duplicate samples were below 20%, which fell below the acceptance criteria. Known standard solutions were analyzed to check for accuracy.

18.3   Results and Discussion

Table 18.2 presents the results of water quality parameters of the sources of drinking water: the GW and DW water. The results show that EC measurement reflects water's ion content, and the GW's EC is equal to 4710 μS/cm, representing a brackish type of GW, whereas the EC of the DW is very low, equal to 85.9 μS/cm. The pH of the water samples was 7.72 and 8.21 for the GW and DW, respectively, which were the determining pH levels in the water samples often found in the water distribution system (Alqadi and Kumar 2013). Moreover, the organic content of the samples of drinking water sources was characterized by the dissolved organic compound (DOC) and UV_{254} absorbance of the water samples. The DOC of the water samples was equal to 0.29 and 0.08 for the GW and DW, respectively. This level of organic content is considered low compared with dissolved organics in drinking water sources reported elsewhere (Hu et al. 2016; Tubić et al. 2010). However, the GW sample had a relatively higher dissolved organic content than the DW sample.

Moreover, the absorbance of UV_{254} for the GW sample was higher than that of the DW, as was reflected in the organic content of the analyzed water samples. The bromide concentration of the GW was equal to 0.71 mg/l. Meanwhile, the concentration was below the method detection limit (BMDL) for the DW sample. The results of the water quality parameters showed that the DW was composed of low concentrations of THM precursors (i.e., DOC = 0.08 mg/l, UV_{254} = 0.002 cm^{-1}, and bromide was BMDL). However, the GW comprises a considerable amount of THM precursors (i.e., DOC = 0.29 mg/l, UV_{254} = 0.012 cm^{-1}, and bromide = 0.71 mg/l).

The synthetic drinking water samples prepared from the DW and GW in the laboratory contained relatively different amounts of THM precursors based on the data in Table 18.3. During the blending of the DW with GW, the DW acted as a dilution

Table 18.2   Water quality parameters of the utilized sources of drinking water

Parameter	Unit	GW	DW
EC	μS/cm	4710	85.9
pH	–	7.72	8.21
DOC	mg/l	0.29	0.08
UV_{254} absorbance	cm^{-1}	0.012	0.002
Bromide	mg/l	0.71	BMDL

Table 18.3 Water quality parameters for the prepared synthetic drinking water

Parameter	Unit	GW: DW 2.9:97.1	GW: DW 15:85.0
Electrical conductivity	μS/cm	274	923
pH	–	7.88	7.90
DOC	mg/l	0.08	0.13
UV$_{254}$ absorbance	cm^{-1}	0.0020	0.0039
Bromide	mg/l	BMDL	BMDL

medium for GW because the DW contained low organic and inorganic constituents (in accordance with Table 18.2). Accordingly, the higher the percentages of GW utilized in the blending process during the production of drinking water, the more inputs of THM precursors would be expected in the finished water.

The results of the two SDS tests are presented in Tables 18.4 and 18.5. The tests were conducted for ten days (240 h) on water samples with two different blending ratios of GW and DW. Both tests were performed under 30 °C ambient water temperatures to compare the formation of THM species. The results show the concentrations and development progress of the $CHCl_3$, $CHBrCl_2$, $CHBr_2Cl$, and $CHBr_3$ overtime during the SDS tests.

The results indicate that the development of THM species is preferably directed towards bromine-containing compounds (i.e., $CHBr_3$ and $CHBr_2Cl$), in which the concentrations are in the order of $CHCl_3 < CHBrCl_2 < CHBr_2Cl < CHBr_3$. Furthermore, the results of the tests show that $CHBr_3$ is the dominant compound, followed by $CHBr_2Cl$ and $CHBrCl_2$. The predominance of the brominated THM species is due to the presence of bromide in GW. The lowest concentrations of the THM species were obtained at a time equal to 24 h in both tests, whereas the maximum concentrations were achieved at the end of the tests (i.e., time $=$ 240 h). $CHCl_3$ was detected only in the test conducted on water samples that comprised 2.9% GW after 144 h of starting the test and continued at the same concentration level till the end of the test. However, the $CHCl_3$ was below the detection limit for the test conducted on

Table 18.4 The concentrations of THM compounds for the SDS test conduction on water samples comprising 2.9% GW

Time (h)	CHCl$_3$ (ug/l)	CHBrCl$_2$ (ug/l)	CHBr$_2$Cl (ug/l)	CHBr$_3$ (ug/l)
24	< 0.30	0.46	0.95	8.61
48	< 0.30	0.67	1.47	9.12
72	< 0.30	1.19	2.85	9.77
120	< 0.30	2.10	5.66	12.07
144	0.30	2.06	5.64	12.10
168	0.31	2.36	6.39	12.23
192	0.30	3.09	6.80	13.13
240	0.31	3.19	9.23	13.98

Table 18.5 The concentrations of THM compounds for the test conducted on water samples comprising 15.0% GW

Time (h)	CHCl$_3$ (ug/l)	CHBrCl$_2$ (ug/l)	CHBr$_2$Cl (ug/l)	CHBr$_3$ (ug/l)
24	< 0.30	0.30	1.34	9.87
48	< 0.30	0.31	1.90	12.00
72	< 0.30	0.33	2.42	14.54
120	< 0.30	0.37	2.82	15.81
144	< 0.30	0.37	3.20	17.88
168	< 0.30	0.45	3.91	20.56
192	< 0.30	0.48	4.27	23.59
240	< 0.30	0.47	4.61	24.05

synthetic water samples that comprised 15.0% GW. This was possibly due to the input of extra bromide and organic contents from GW into the synthetic drinking water, which led to the formation of brominated species of THM.

The percentages of each THM species at the end of the tests are presented in Figs. 18.1 and 18.2. The pie charts in Figs. 18.1 and 18.2 show that CHBr$_3$ in both tests is the dominant species, followed by CHBr$_2$Cl, CHBrCl$_2$, and CHCl$_3$. The percentage of CHBr$_3$ in the water samples was 82.58% which comprised 15.0% GW, which was higher than that of the CHBr$_3$ in the water samples that comprised 2.9% GW (i.e., 52.36%) at the end of the tests.
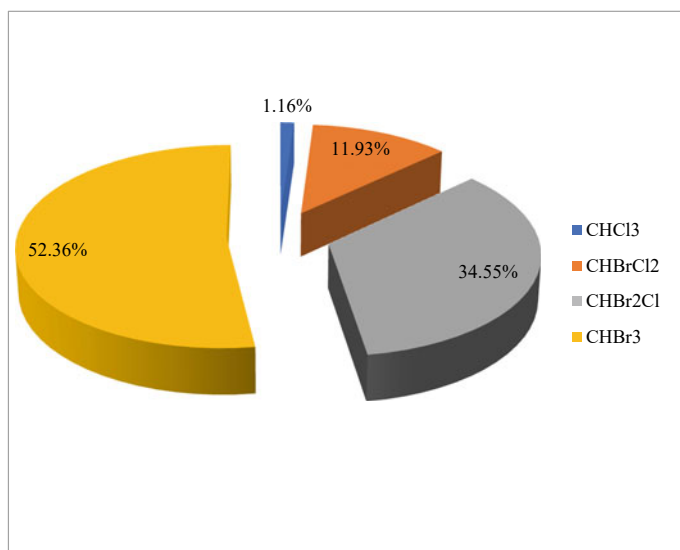
Fig. 18.1 Percentages of THM compounds at the end of the test conducted on the water sample comprising 2.9% GW
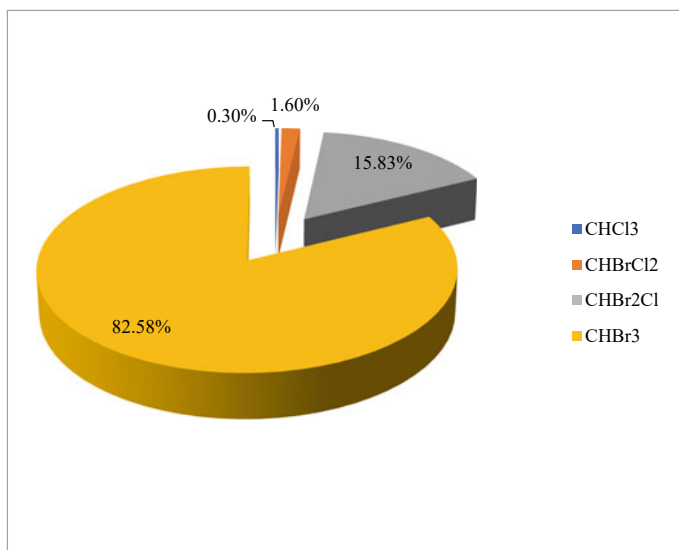
Fig. 18.2 Percentages of THM compounds at the end of the test conducted on the water sample comprising 15.0% GW

18.4 Conclusions

In this study, two SDS tests were carried out on synthetic drinking water samples prepared in the laboratory. The tests were done on the water samples with two different blending ratios for GW and DW (i.e., GW: DW; 2.9:97.1 and 15.0:85.0) under 30 °C ambient temperature to assess the formation of THM species in drinking water. The study revealed that the DW consisted of low THM precursors. Moreover, it is revealed that a considerable amount of THM precursors exist in the GW. The chlorination of synthetic drinking water also resulted in the formation of brominated THM species because of the existence of bromide and organics in GW. $CHBr_3$ in both SDS shows the dominant THM species developed, and the formation of $CHBr_3$ in the synthetic drinking water comprising 15.0% GW was higher than the formation of $CHBr_3$ in the synthetic drinking water samples that comprised 2.9% GW. The blending of GW with DW in the production of drinking water shows that the higher the amount of GW utilized to produce the drinking water, the more bromide, and organics existed in the finished water. This leads to more $CHBr_3$ in the finished water because of the water chlorination process.

References

Agus E, Voutchkov N, Sedlak DL (2009) Disinfection by-products and their potential impact on the quality of water produced by desalination systems: a literature review. Issue 1: Water Resour Manage: New Approaches Technol 237(1):214–237. https://doi.org/10.1016/j.desal.2007.11.059

Alhumoud J, Al-Ruwaih F, Al-Mutairi S (2010) Quality of potable water in Kuwait. Am J Environ Sci 6. https://doi.org/10.3844/ajessp.2010.260.267

Alkandari JM (2015) Laboratory investigation on bromoform formation in potable water of Kuwait, 267

Al-Mudhaf HF, Astel AM, Selim MI, Abu-Shady A-SI (2010) Self-organizing map approach in assessment spatiotemporal variations of trihalomethanes in desalinated drinking water in Kuwait. Desalination 252(1):97–105. https://doi.org/10.1016/j.desal.2009.10.017

Alqadi KA, Kumar L (2013) Are there monthly variations in water quality in the Amman, Zarqa and Balqa Regions, Jordan? Comput Water Energy Environ Eng 02(02):26–35. https://doi.org/10.4236/cweee.2013.22B005

Ceretti E, Moretti M, Zerbini I, Villarini M, Zani C, Monarca S, Feretti D (2016) Occurrence and control of genotoxins in drinking water: a monitoring proposal. J Public Health Res 5(3):769. https://doi.org/10.4081/jphr.2016.769

Chowdhury S, Champagne P, James McLellan P (2010) Investigating effects of bromide ions on trihalomethanes and developing model for predicting bromodichloromethane in drinking water. Water Res 44(7):2349–2359. https://doi.org/10.1016/j.watres.2009.12.042

DeAngelo AB, Jones CP, Moyer MP (2007) Development of normal human colon cell cultures to identify priority unregulated disinfection by-products with a carcinogenic potential. Water Sci Technol: J Int Assoc Water Pollut Res 56(12):51–55. https://doi.org/10.2166/wst.2007.830

Ged EC, Boyer TH (2014) Effect of seawater intrusion on formation of bromine-containing trihalomethanes and haloacetic acids during chlorination. Desalination 345:85–93. https://doi.org/10.1016/j.desal.2014.04.021

Hu H-Y, Du Y, Wu Q-Y, Zhao X, Tang X, Chen Z (2016) Differences in dissolved organic matter between reclaimed water source and drinking water source. Sci Total Environ 551–552:133–142. https://doi.org/10.1016/j.scitotenv.2015.12.111

Hua P, Vasyukova E, Uhl W (2015) A variable reaction rate model for chlorine decay in drinking water due to the reaction with dissolved organic matter. Water Res 75:109–122. https://doi.org/10.1016/j.watres.2015.01.037

Kim D, Amy GL, Karanfil T (2015a) Disinfection by-product formation during seawater desalination: a review. Water Res 81:343–355. https://doi.org/10.1016/j.watres.2015.05.040

Kim H, Kim S, Koo J (2015b) Modelling chlorine decay in a pilot scale water distribution system subjected to transient. In: Computing and control for the water industry (CCWI2015b) sharing the best practice in water management, vol 119, pp 370–378. https://doi.org/10.1016/j.proeng.2015.08.897

Li X, Zhao H (2006) Development of a model for predicting trihalomethanes propagation in water distribution systems. Chemosphere 62(6):1028–1032. https://doi.org/10.1016/j.chemosphere.2005.02.002

Rice EW, Baird RB, Eaton AD, Clesceri LS (eds) (2012) Standard methods for the examination of water and wastewater, 22nd edn. American Public Health Association. https://www.amazon.com/Standard-Methods-Examination-Water-Wastewater/dp/0875530133

Richardson SD, Plewa MJ, Wagner ED, Schoeny R, DeMarini DM (2007) Occurrence, genotoxicity, and carcinogenicity of regulated and emerging disinfection by-products in drinking water: a review and roadmap for research. Sources Potential Hazards Mutagens Complex Environ Matrices—Part II 636(1):178–242. https://doi.org/10.1016/j.mrrev.2007.09.001

Rodrigues PMSM, Esteves da Silva JCG, Antunes MCG (2007) Factorial analysis of the trihalomethanes formation in water disinfection using chlorine. In: Papers presented at the 10th international conference on chemometrics in analytical chemistry, vol 595, no 1, pp 266–274. https://doi.org/10.1016/j.aca.2006.12.031

Singer PC (1999) Humic substances as precursors for potentially harmful disinfection by-products. Water Sci Technol 40(9):25–30. https://doi.org/10.2166/wst.1999.0434

Tubić A, Dalmacija B, Agbaba J, Ivančev-Tumbas I, Klašnja M, Dalmacija M (2010) Tracking disinfection by-products and arsenic removal during various drinking water treatment trains. Water Sci Technol 61(12):3169–3177. https://doi.org/10.2166/wst.2010.926

Tubić A, Agbaba J, Dalmacija B, Molnar J, Maletić S, Watson M, Perović SU (2013) Insight into changes during coagulation in NOM reactivity for trihalomethanes and haloacetic acids formation. J Environ Manage 118:153–160. https://doi.org/10.1016/j.jenvman.2012.11.046

WHO (2017) Guidelines for drinking-water quality, 4th edn. World Health Organization, Geneva. https://www.who.int/publications-detail-redirect/9789241549950

Withers A (2005) Options for recarbonation, remineralisation and disinfection for desalination plants. Membr Drinking Ind Water Prod 179(1):11–24. https://doi.org/10.1016/j.desal.2004.11.051

Chapter 19
Climate Change Impact on Water Resources and Rainwater Harvesting Systems in the Semi-arid Regions of India

Nandimandalam Janardhana Raju, P. Muniratnam, and T. V. Krishna Reddy

19.1 Introduction

Groundwater is dynamic in nature and flows continuously from recharge areas to discharge areas through the porous medium, if it is not harnessed and properly harvested. The rate of groundwater use is rapidly increasing with population growth and climate change conditions throughout the world. Groundwater withdrawals can easily surpass the net recharge where population rely on fresh groundwater for drinking, irrigation, and manufacturing requirements in arid and semi-arid regions. The swift growth in the metropolitan people due to rural–urban movement for better socio-economic benefits has resulted in overexploitation of natural resources and this enforces an additional load on the water deliveries especially metropolitan regions. The main causes for the depletion of groundwater levels in arid and semi-arid regions are erratic rainfall, reduction of recharge areas, shrinking of lakes and ponds in city and rural areas, heavy extraction of groundwater resources and annual increase of groundwater systems. Unpredictable rainfall, population expansion, shrinking of water lakes and ponds because of urban sprawl and heavy-pumping steered to water stress in numerous regions of India. The fast decline of water table has been observed in the Tirupati (> 37 m, granite rocks) and Delhi (> 48 m, quartzite rocks) urban areas due to overexploitation for domestic and agricultural needs (Fig. 19.1a, b). Fast urbanization process in the Tirupati environs led to the total disappearance of about sixteen water bodies (Fig. 19.1c) and implicit termination of surface flood in the ephemeral Swarnamukhi River course (Kim et al. 2001; Raju and Reddy 2006,

N. Janardhana Raju (✉)
School of Environmental Sciences, Jawaharlal Nehru University, New Delhi 110067, India
e-mail: rajunj7@gmail.com

P. Muniratnam
Air Bypass Road, Tirupati, Andhra Pradesh 517502, India

T. V. Krishna Reddy
3-2-3 Vidyanagar, Tirupati, Andhra Pradesh 517502, India
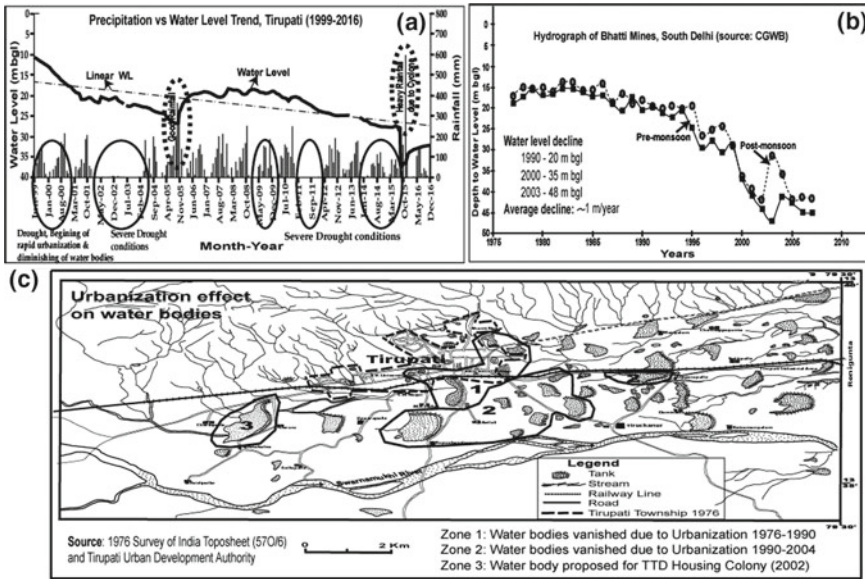
Fig. 19.1 Climate change and urbanization effects. **a**, **b** Water table variation in the urban Tirupati and Delhi, **c** diminishing of water bodies in Tirupati urban environs

2007). The groundwater level rise depends on the principal source of rainfall as well as the surface water storage in water bodies (tanks/ponds) in a particular period. This relation is changing rapidly especially in urban areas due to decrease in number of lakes and ponds due to rapid development and overdraft of groundwater than recharge in many parts of India. Many metropolises/towns had numerous natural collecting water bodies (lakes/ponds) diminished due to greed of a man's activities i.e. rapacious demands of the government and city dwellers.

On one side is prudence about water and other side harnessing rainwater for the consumption of safe drinking water everywhere on the earth. Absence of sufficient sites of storage and impounding of water fairly caused large amount rainfall is lost through surface runoff. In India, excessive surface overflow occurs even in little monsoon years due to flash inundations in a brief spell. The harnessing of excessive surface overflow will be utilized to recharge the exhausted aquifers to improve the groundwater resources (Raju 1998; Raju et al. 2013). To improve domestic and irrigation water resources in water stressed regions throughout the world, presently communities' engineered rainwater harvesting systems to control rainwater (Murad et al. 2007; AbdelKhaleq and Alhaj Ahmed 2007; Ibrahim 2009; Stiefel et al. 2009; Raju et al. 2013; Alataway and El Alfy 2019; Krishna et al. 2020; Khanal et al. 2020; Zabidi et al. 2020). To fight drought on a large scale, construction of small water storage systems (rainwater harvesting) at suitable site is inevitable for the sustainable water resources development and management.

Table 19.1 Rainwater harvesting structures to augment groundwater level

Lithology	Topography	Structures recommended
Hard rock with soil cover	Highly undulating or along hill slopes	Gully plugging, contour trenches and bunds
Bounders with gravel and clay	Piedmont (along the food hills)	Small basins/ponds/pits
Alluvium on hard rock	Plain area or gently undulating region	Check dams, percolation tanks and subsurface dams

It is paradox that Chirapunji in India receives annual precipitation of 11,000 mm impressions water stress about nine months due to absence of surface water storage structures (Agarwal and Narain 1997). Depletion of groundwater table has made water stress around 27 districts of Rajasthan state, Western India (Alok and Batra 2000). Heavy withdrawal of groundwater would badly impact on the groundwater levels which ultimately effects in the salinization and hazard to civil constructions (Choudhury et al. 2000; Nawa and Miyazaki 2009). Groundwater flow in alluvial aquifers have intimate relationship with surface flow and it is an addition of stream course (Mansell and Hussey 2005). Hard rock areas where infiltration is slow and runoff rate is high, the first thing is to harvest and harness surface runoff on particular area using soil conservation systems depending on the topography and drainage patterns (Table 19.1). In this research article an effort is made to deliberate the augmentation of the groundwater recharge in the depleted aquifers by constructing artificial recharge structures (recharge pits/wells and subsurface dams) in urban and rural semi-arid regions of India.

19.2   Methods

Recharge pit and well method implemented to harvest rooftop rainwater by filling porous materials and borewell with slotted pipe. Geological, hydrogeological, geophysical and test auguring methods adopted to select suitable subsurface dam sites to harness the base flow of ephemeral river depending on the physical conditions, geological features and economic viability. Well inventory (well section, nature of aquifer tapped and hydraulic properties) carried out at proposed subsurface dam site. Vertical electrical resistivity sounding method used to ascertain the depth to bed rock and possibilities of fractures. Auger bore holes drilled to corroborate the electrical resistivity soundings.

19.3   Results and Discussion

19.3.1   Rainwater Harvesting

Groundwater development and management is impetus where groundwater over-extraction exceeds the annual replenishment. The rooftop collected water is properly diverted into nearby harvesting structures to recharge groundwater and solve the water scarcity problems in the urban areas. In recent decades, decreasing recharge space especially in urban areas and heavy pumping of groundwater by contemporary abstraction practices, a revival of traditional harvesting systems in several parts of India (Sharma 2002). Alluvial aquifers of small scale provide good source of irrigation water in the summer season to save crops especially in semi-arid regions (Owen and Dahlin 2005; Moyce et al. 2006; Raju et al. 2006, 2013; Mwenge Kahinda et al. 2010; Ward et al. 2010; Mwenge Kahinda and Taigbenu 2011; Rahman et al. 2012). Over-pumping in coastal regions associated with salt-water intrusion creating an inland ward slope of saline water (El Moujabber et al. 2006). A subsurface dam planned to arrest the baseflow in a ephemeral stream by digging trench to bedrock across the ephemeral stream where base flow of occurs (Raju et al. 2006, 2013).

19.3.2   Rooftop and Storm Water Harvesting in Urban Area

19.3.2.1   Recharge Pit and Tube Well: A Case Study in the Vasant Kunj of South Delhi

Rapid urbanization and population explosion due to rural–urban migration are recognized as the major basis of water emergency in the Delhi (Lorenzen et al. 2010). It becomes worst throughout drought periods and sizable number of populations has to be contingent on groundwater along with Jal board water supply in many parts of Delhi environs. Vasant Kunj area of south Delhi (Fig. 19.2a) composed of folded and jointed quartzite of Aravalli-Haridwar ridge. Widespread decline in the groundwater level due to overexploitation and lack of stringent regulations to individual withdrawal of groundwater in southern part of Delhi in which Vasant Kunj is existing. The average rainfall in Delhi is 750 mm. The range of Delhi temperature is 4–46 °C. The recharge of groundwater in urban areas is done by the collection of rainwater from the rooftops and storm water from the streets to a suitable designed site depending on the space availability. Due to the presence of impervious soil (concretization of urban area) surface, usage of recharge pit to stock water in a screen and subsequent improve to groundwater within especially designed revitalize tube well (Fig. 19.2b). Recharging of pits and tube wells are preferred compare to other water spreading structures in the urban areas where space constrains and impervious layer is encountered at shallow depth to augment rainwater recharge to the fast-depleted aquifers. Due to rapid declining of groundwater table in the Aravalli quartzite regions where

percolation of water depends on the secondary porosity conditions, a recharge pit with two tube wells are constructed to collect rooftop and storm runoff to recharge directly to the depleted quartzite aquifers in the Vasant Kunj area, south Delhi (Fig. 19.2c). The size and dimensions of the recharge pit and tube well-constructed close to the newly built mega housing complex in the Vasant Kunj area is around 8 m length, 3 m width and 4 m depth depending upon rooftop/storm water collection and diversion to the proposed structure. Inside the trench a $41/2''$ diameter recharge tube well is drilled by providing slotted pipe casing to allow the silt free filtered rainwater slowly percolate through the slotted tube well directly to the deeper aquifers. The pit was filled at the bottom with 40 mm jelly stone pebble followed by a layer of 20 mm jelly stones which is covered with nylon curtain. Above the nylon curtain coarse and fine sand particles are placed to retain silt and dust particles allowing filtered water through the slotted pipe into the depleted aquifer. An inlet pipe should be fixed into the silt retention chamber (silt and dust particles retained) of the recharge pit in order to collected the rainwater from the roof and excess water from storm water from the streets. The depth of recharge tube well depends upon the depth of occurrence of aquifers being exploited.

19.3.3 Sustainable Environmental Technology to Harvest Rainwater in Rural Area

19.3.3.1 Subsurface Dam: A Case Study in the Swarnamukhi River, Andhra Pradesh, South India

The Swarnamukhi River (Fig. 19.3a) flows in semi-arid drought prone Rayalaseema region of Andhra Pradesh occupied by granite and granitic gneisses rocks and has vital deficiency of drinking and agricultural water resources because of erratic rainfall events and overexploitation of groundwater due to rapid urbanization in Tirupati environs (Fig. 19.3b). The thickness of the river valley and depth to weathered granite rock ranges from 2 to 7 m along the river course. As consequences of drought conditions in this region, subsurface dams across the Swarnamukhi River were constructed to augment the surrounding groundwater levels adjacent to the river course to improve the socio-economic conditions of the local communities through increased agricultural production. The climate is semi-arid in nature and average annual precipitation is around 800 mm in the study area. The range of temperature is 10–48 °C. The overexploitation of groundwater and decreasing surface water resource has kept the pressure further on groundwater resources in the study region. The general decline of water table observed and most of dug wells from weathered and fractured granitic rock part of 20–30 m have gone dry. In order to save the agricultural standing crops mostly depending on groundwater resources, it has become imperative to take up steps to restore the unconfined aquifer by manmade recharge structures to arrest

Fig. 19.2 Construction of recharge pit and tube well to harvest rooftop rainwater in the Vasant Kunj urban housing colony, New Delhi. **a** Location map of the study, **b** schematic recharge pit and well diagram, **c** photos of the recharge pit and tube well construction site (photo: May 2012)

base flow in the natural ephemeral aquifer. As per the estimates of irrigation department of Andhra Pradesh, it is evident that 3077 Mcft of water is available in the Swarnamukhi River basin as base water movement. If part of this water movement is impeded at appropriate places across Swarnamukhi River by constructing subsurface dams, the overall groundwater levels will be increased adjacent the river course which can be utilized for further agricultural practices.
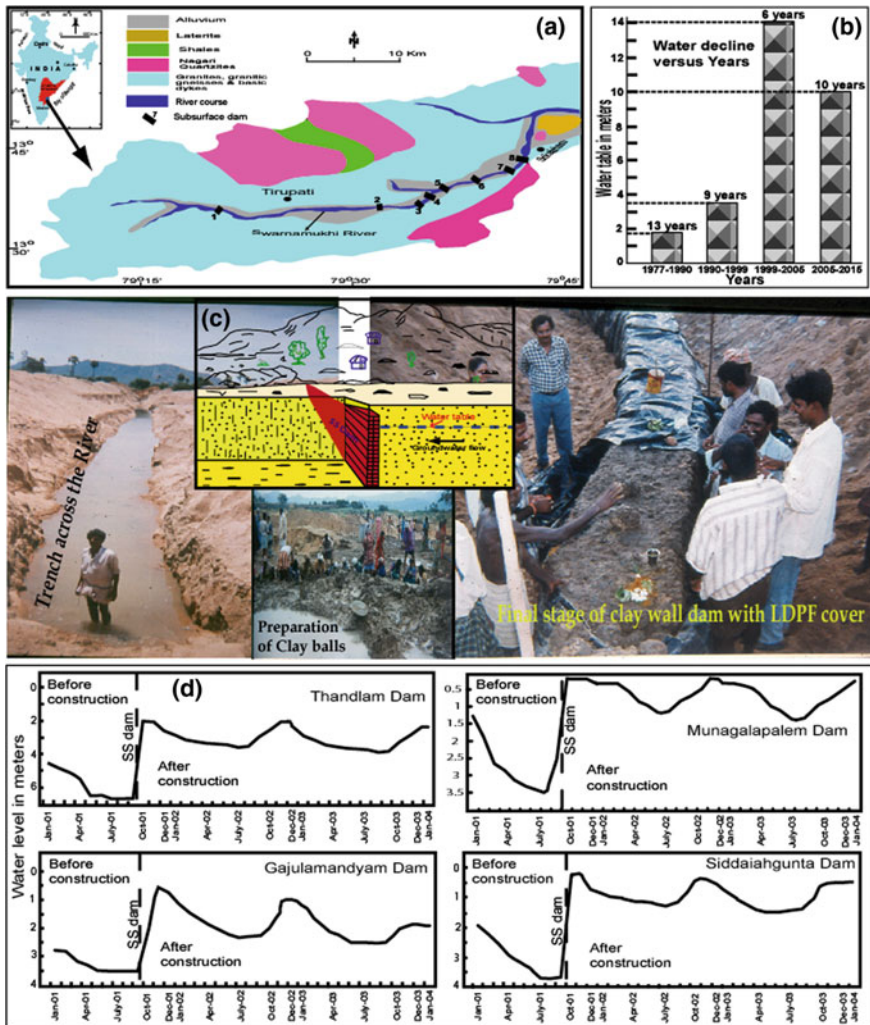
Fig. 19.3 Subsurface dams to collect precipitation across the Swarnamukhi River, Andhra Pradesh, Southern India. **a** Location map of the study, **b** long term water table variations, **c** schematic diagram and photos of construction of SS dams with clay and LDPF sheet (photo: October 2001), **d** hydrographs of piezometers after SS dam construction

A subsurface dam is created across a basin by excavating a channel to bed rock for halting the groundwater course in a permeable alluvial aquifer and the schematic diagram is shown in Fig. 19.3c. The trench filled with the clay about 1 m thick which is set into solid termination linking on sides of riverbank. The subsurface is not projected out and occur 1 m below the riverbed to permit surplus base flows to downstream and riparian privileges of the agrarians are not infringed. The SS dam is entered in the bottom 0.5 m into weathered zone of granitic rock. To retain optimum wetness for longer time 200 μm of black colour low density polyethylene film (LDPE) was covered all sides of dam (Fig. 19.3c). The LDPE film protects the clay wall in contact with sand in summer season from development of cracks thereby no stored water is lost through the dam. Finally, clay filled trench is shielded with quarried material till channel is entirely covered. The impact and imperviousness of construction of the dam has been studied by monitoring water levels (Fig. 19.3d) in the erected piezometers upstream at quarter kilometer away from the dam. The piezometer water level data of dams denotes typical groundwater level upsurge of about 1.5 m subsequently building of few subsurface dams. After construction of dams, agricultural activities are in continuous process in summer period due to increase of artificial recharge conditions which indirectly helps in improvement of groundwater levels in the surrounding wells along the Swarnamukhi River basin.

19.4   Conclusions

The substantial necessity on groundwater warrants the annually growing number of bore wells for domestic and agricultural purposes in the fast growing Tirupati and Delhi urban areas guided to the over-extraction of groundwater resources. Urban development drastically reduces the porous surface zone, therefore swift drop of recharge as well as groundwater levels. To augment groundwater level in the overexploitation regions, it is impetus to device urban and rural manmade recuperate systems (rainwater harvesting) to improve groundwater resources. Due to space constraints and shrinking lakes and ponds in urban zones, roof top collection of rainwater into the recharge pits and tube wells are beneficial to augment the groundwater levels in depleted aquifers. Existing lakes and ponds in the urban areas should be protected and maintained from infringement in the name of urban development. The recharge pits/wells do not require large land area and also dry wells could be converted into recharge wells whereas the benefit of the subsurface dam is to employ large land area for agricultural purposes. Overall increase in agricultural production and substantial enhancement of groundwater availability after construction of the subsurface dams. The advantage of rainwater harvesting structures are eco-friendly, low evaporation, augment groundwater recharge, no submergence of land.

References

AbdelKhaleq RA, Alhaj Ahmed I (2007) Rainwater harvesting in ancient civilizations in Jordan. Water Supply 7(1):85–93. https://doi.org/10.2166/ws.2007.010

Agarwal A, Narain S (1997) Dying wisdom: rise, fall and potential of India's traditional water harvesting systems. Centre for Science and Environment

Alataway A, El Alfy M (2019) Rainwater harvesting and artificial groundwater recharge in arid areas: case study in Wadi Al-Alb, Saudi Arabia. J Water Resour Plan Manag 145(1):05018017. https://doi.org/10.1061/(ASCE)WR.1943-5452.0001009

Alok K, Batra P (2000) Declining groundwater resources and need for its management in Rajasthan. In: Proceedings of the national seminar on groundwater management strategies in arid and semi-arid regions

Choudhury K, Shah D, Ghosh D (2000) Urban geophysical studies on the groundwater environment in parts of Gangetic delta. J Geol Soc India

El Moujabber M, Samra BB, Darwish T, Atallah T (2006) Comparison of different indicators for groundwater contamination by seawater intrusion on the Lebanese coast. Water Resour Manag 20(2):161–180. https://doi.org/10.1007/s11269-006-7376-4

Ibrahim MB (2009) Rainwater harvesting for urban areas: a success story from Gadarif City in Central Sudan. Water Resour Manag 23(13):2727–2736. https://doi.org/10.1007/s11269-009-9405-6

Khanal G, Thapa A, Devkota N, Paudel UR (2020) A review on harvesting and harnessing rainwater: an alternative strategy to cope with drinking water scarcity. Water Supply 20(8):2951–2963. https://doi.org/10.2166/ws.2020.264

Kim Y-Y, Lee K-K, Sung I (2001) Urbanization and the groundwater budget, metropolitan Seoul area, Korea. Hydrogeol J 9:401–412. https://doi.org/10.1007/s100400100139

Krishna RS, Mishra J, Ighalo JO (2020) Rising demand for rain water harvesting system in the world: a case study of Joda Town, India. World Sci News 146:47–59

Lorenzen G, Sprenger C, Taute T, Pekdeger A, Mittal A, Massmann G (2010) Assessment of the potential for bank filtration in a water-stressed megacity (Delhi, India). Environ Earth Sci 61:1419–1434. https://doi.org/10.1007/s12665-010-0458-x

Mansell MG, Hussey SW (2005) An investigation of flows and losses within the alluvial sands of ephemeral rivers in Zimbabwe. J Hydrol 314(1):192–203. https://doi.org/10.1016/j.jhydrol.2005.03.015

Moyce W, Mangeya P, Owen R, Love D (2006) Alluvial aquifers in the Mzingwane catchment: their distribution, properties, current usage and potential expansion. Phys Chem Earth 31:988–994

Murad A, Nuaimi H, Hammadi M (2007) Comprehensive assessment of water resources in the United Arab Emirates (UAE). Water Resour Manag 21(9):1449–1463

Mwenge Kahinda J, Taigbenu AE (2011) Rainwater harvesting in South Africa: challenges and opportunities. Phys Chem Earth 36:968–976. https://doi.org/10.1016/j.pce.2011.08.011

Mwenge Kahinda J, Taigbenu AE, Boroto RJ (2010) Domestic rainwater harvesting as an adaptation measure to climate change in South Africa. Phys Chem Earth 35:742–751. https://doi.org/10.1016/j.pce.2010.07.004

Nawa N, Miyazaki K (2009) The analysis of saltwater intrusion through Komesu underground dam and water quality management for salinity. Paddy Water Environ 7:71–82. https://doi.org/10.1007/s10333-009-0154-1

Owen R, Dahlin T (2005) Alluvial aquifers at geological boundaries: geophysical investigations and groundwater resources. In: Bocanegra E, Hernandez M, Usunoff E (eds) Groundwater and human development. AA Balkema Publishers, Rotterdam, pp 233–246

Rahman A, Keane J, Imteaz MA (2012) Rainwater harvesting in Greater Sydney: water savings, reliability and economic benefits. Resour Conserv Recycl 61:16–21. https://doi.org/10.1016/j.resconrec.2011.12.002

Raju KCB (1998) Importance of recharging depleted aquifers: state of the art of artificial recharge in India. Geol Soc India 51(4):Article 4

Raju N, Reddy T (2006) Urban development and the looming water crisis—a case study, vol 22. http://egsp.lyellcollection.org/content/vol22/issue1/

Raju N, Reddy T (2007) Environmental and urbanization effect on groundwater resources in a pilgrim town of Tirupati, Andhra Pradesh, south India. J Appl Geochem 212–223

Raju N, Reddy T, Munirathnam P (2006) Subsurface dams to harvest rainwater—a case study of the Swarnamukhi River basin, Southern India. Hydrogeol J 14:526–531. https://doi.org/10.1007/s10040-005-0438-5

Raju N, Reddy T, Muniratnam P, Gossel W, Wycisk P (2013) Managed aquifer recharge (MAR) by the construction of subsurface dams in the semi-arid regions: a case study of the Kalangi river basin, Andhra Pradesh. J Geol Soc India 82:657–665. https://doi.org/10.1007/s12594-013-0204-6

Sharma A (2002) Does water harvesting help in water-scarce regions?: a case study of two villages in Alwar, Rajasthan. In: IWMI-TATA water policy research program annual partners' meet, 2002. IWMI working papers (No. H029649; IWMI working papers). International Water Management Institute. https://ideas.repec.org/p/iwt/worppr/h029649.html

Stiefel JM, Melesse AM, McClain ME, Price RM, Anderson EP, Chauhan NK (2009) Effects of rainwater-harvesting-induced artificial recharge on the groundwater of wells in Rajasthan, India. Hydrogeol J. https://doi.org/10.1007/s10040-009-0491-6

Ward S, Memon F, Butler D (2010) Rainwater harvesting: model-based design evaluation. Water Sci Technol J Int Assoc Water Pollut Res 61:85–96. https://doi.org/10.2166/wst.2010.783

Zabidi HA, Goh HW, Chang CK, Chan NW, Zakaria NA (2020) A review of roof and pond rainwater harvesting systems for water security: the design, performance and way forward. Water 12(11). https://doi.org/10.3390/w12113163

Part V
Water Quality

Chapter 20
Soil Erosion Prioritization of Yarmouk River Basin, Jordan Using Multiple Approaches in a GIS Environment

Farah Al-Hantouli, Muheeb Awawdeh, and Mutawakil Obeidat

20.1 Introduction

Soil and water are among the most important renewable natural resources on earth. A primary natural resource, the soil is a key player in natural ecosystems (Singer and Warkentin 1996), and an important habitat for living organisms such as plants, animals, agricultural crops, as well as human beings. However, there are many environmental challenges facing the soil such as erosion. Soil erosion is a natural problem exacerbated by human activities, and if serious sediment management strategies are not put in place, its danger in watersheds may increase. Soil erosion has increased at the global scale and is predicted to increase by an average of 14% across the universe by the end of this century (Yang et al. 2003). Soil erosion is a significant environmental issue and has become a major threat to terrestrial ecosystems, particularly to the sustainable development of agriculture (Sun et al. 2013). If the current rate of soil erosion continues in the future, it will have serious consequences such as (1) the loss of fertile topsoil and hence a decrease in land productivity (Pimentel 2006); (2) decline in environmental quality and biomass productivity (Lal 2004); (3) increase in sedimentation rates of rivers and lakes, leading to more flood-related disasters and water pollution (Rothwell et al. 2005); and (4) change in contents of soil nutrients (e.g., carbon, nitrogen, and phosphorus). Consequently, sustainable management of natural resources is essential to preserve them for the future. Watershed management

F. Al-Hantouli
Faculty of Science, Yarmouk University, Irbid, Jordan

M. Awawdeh
Department of Earth and Environmental Sciences, Laboratory of Applied Geoinformatics, Yarmouk University, Irbid, Jordan
e-mail: awawdeh@yu.edu.jo

M. Obeidat (✉)
Faculty of Science and Arts, Jordan University of Science and Technology, Irbid, Jordan
e-mail: mobeidat@just.edu.jo

implies the proper use of all land and water resources of a watershed for optimum production with minimum hazard to natural resources (Sebastian et al. 1995).

Recognizing the hazardous effects of soil erosion on water quality and agricultural production, different approaches have been developed for prioritizing watersheds and mapping soil erosion prone areas. Various methods have been applied for soil erosion assessment such as the Universal Soil Loss Equation or morphometric analysis method. Many researchers prioritized the watersheds based on morphometric analysis (Ameri et al. 2018; Farhan and Anaba 2016; Shivhare et al. 2018). Also, Land use/land cover has been used by many researchers (Javed et al. 2009; Shivhare et al. 2018) to prioritize watersheds. Morphometric analysis has been used in several fields such as the assessment of natural resources and environmental hazards, and prioritizing watersheds to protect water and soil resources (e.g., Ameri et al. 2018; Bisht et al. 2020; Singh et al. 2008, 2014). Research findings showed that the morphometric analysis provides basic information about hydrogeology erosion-prone areas and characteristics of watersheds in terms of ground and surface water potential.

Morphometry refers to the measurement and mathematical evaluation of the configuration of the earth's surface, and the shape and dimensions of its landforms (Clark 1966). Morphometric parameters describe the form and structure of drainage basins and their drainage networks (Biswas et al. 1999). The physical characteristics of a watershed's vulnerability to various geohazards, such as soil erosion and floods, are identified and understood using morphometric metrics (Bhatt and Ahmed 2014). Different parameters (e.g., lithology, topography, drainage pattern) are important for watershed management (Pisal et al. 2013). Geology, relief, and climate are the key players in running water ecosystem functioning at the basin scale (Frissell et al. 1986). The quantitative analysis of morphometric parameters is a cornerstone in watershed prioritization for soil and water conservation (Kanth 2012). Morphometric descriptors represent relatively simple approaches to describing basin processes and comparing basin characteristics (Mesa 2006). Thus, prioritizing a watershed based on morphometric characterization is crucial for improved water and soil conservation measures (Aher et al. 2014). According to Biswas et al. (1999), watershed prioritization is the ranking of different sub-watersheds of a watershed according to the order in which they must be taken for treatment and soil conservation measures.

Remote sensing and geographic information systems (GIS) are highly efficient and effective in developing, managing, and prioritizing the sub-watersheds for many geohazards such as soil erosion (Chatterjee et al. 2014; Malik et al. 2011; Okumura and Araujo 2014; Pandey et al. 2009; Rudraiah et al. 2008). The availability of free access to high-quality resolution topographic data (digital elevation models) has equipped researchers with effective GIS tools to study drainage basins and to quantify with high accuracy different parameters (basic, linear, shape, and relief) of drainage basins. Additionally, it assists in the prioritization of sub-watersheds for soil erosion or flood susceptibility (Biswas et al. 1999; Farhan and Anaba 2016; Nooka Ratnam et al. 2005; Patel et al. 2012). Awawdeh and Bani Domi (2007) assessed soil erosion of the Yarmouk River Basin using RUSLE in a GIS environment. The results showed that about 4.5% of the basin suffers erosion rates higher than the soil loss tolerance (10 tons/ha/yr) with 0.5 ton/ha/yr mean value of sediment yield. The overall objective

of this study was to prioritize the Yarmouk River Basin in terms of soil erosion. The area of investigation is undergoing a rapid land use/land cover change induced by rapid development, urbanization, and agricultural expansion. Two approaches will be applied to prioritize the study area, namely morphometric analysis and land use/land cover.

20.2 Study Area

The Yarmouk River forms the present northern boundary between Syria and Jordan for 40 km and then continues to form the border between Jordan and Palestine. About 1393 km^2 of the YRB basin total area (7242 km^2) lies within the borders of Jordan (Fig. 20.1), while the remainder is in Syria.

The altitudes of the basin vary from about 186 m below sea level in the northwest (Jordan Valley) to more than 1214 m in the south (Ras Munif) (Fig. 20.2). The climate is arid to semi arid (Awawdeh and Jaradat 2010), with mean annual rainfall ranging from about 133 mm in the east to about 460 mm in the west.
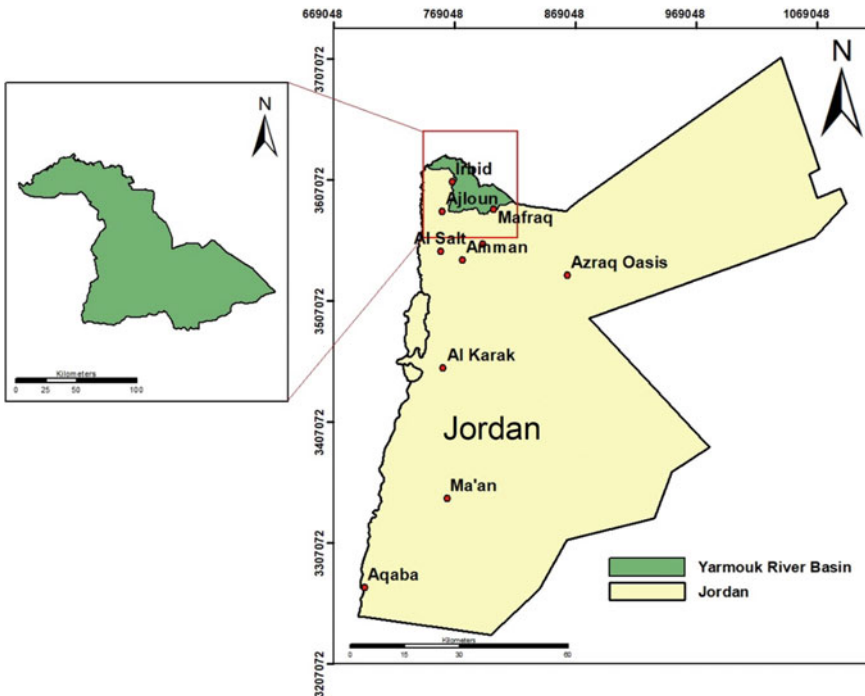
Fig. 20.1 Location map of the study area
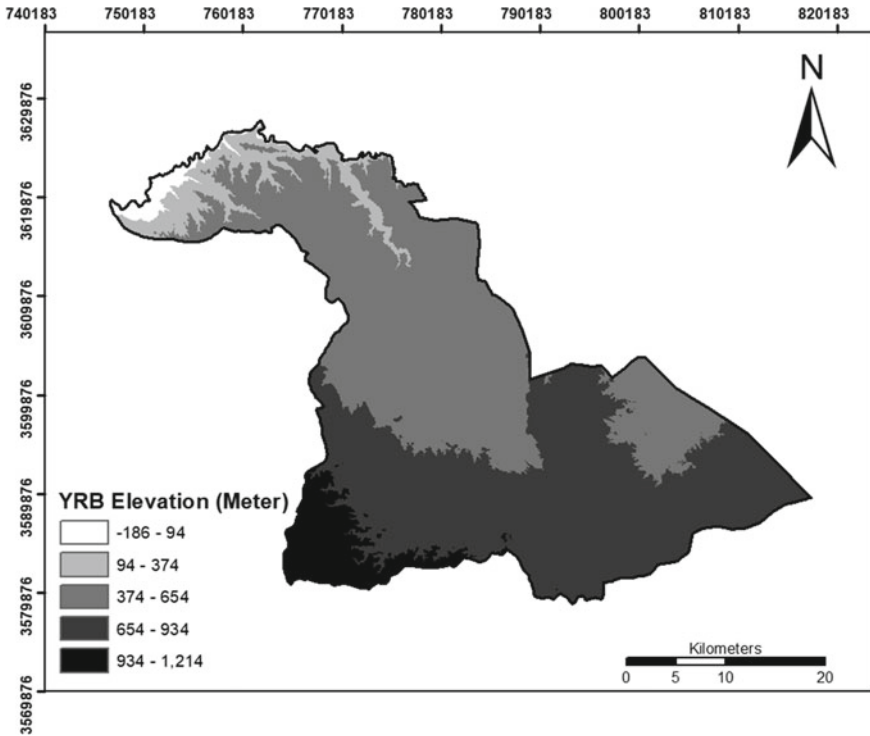
Fig. 20.2 Digital elevation model (DEM) of the study area

The exposed rock formations YRB (Fig. 20.3) include the Ajlun Group, Balqa Group, and Jordan Valley Group of Upper Cretaceous to Tertiary age (Strahler 1952; Makhlouf et al. 1996; Moh'd 2000).

The oldest is the Wadi Es-Sir Limestone (WSL) formation belonging to the Ajlun Group. It consists of massive limestone, dolomite, and dolomitic limestone with chert nodules (Obeidat 1993). The WSL formation is overlain by rocks of the Balqa Group which include the formations: Wadi Umm Ghudran (WG), Amman Silicified Limestone (ASL), Muwaqqar Chalk-Marl (MCM), Umm Rijam Chert-Limestone (URC) and Wadi Shalala (WS). WG formation (the base of the Balqa Group) consists of marl, marly limestone, chalk, and chert. The ASL formation overlying WG consists of limestone, chert, chalk, and phosphorite beds that are exposed in the southern part of the basin. Bituminous marl and clayey marl of the MCM formation exposed in the central part of the basin overlies the ASL formation (Parker 1970; Makhlouf et al. 1996; Moh'd 2000). Alternating beds of limestone, chalk, and chert of the URC formation overlies the MCM formation (Awawdeh and Jaradat 2010). Basaltic flows (BS formation) of the Jordan Valley Group (Oligocene age) cover rocks of the Balqa Group in the eastern part of the basin. Additionally, basalts were found as
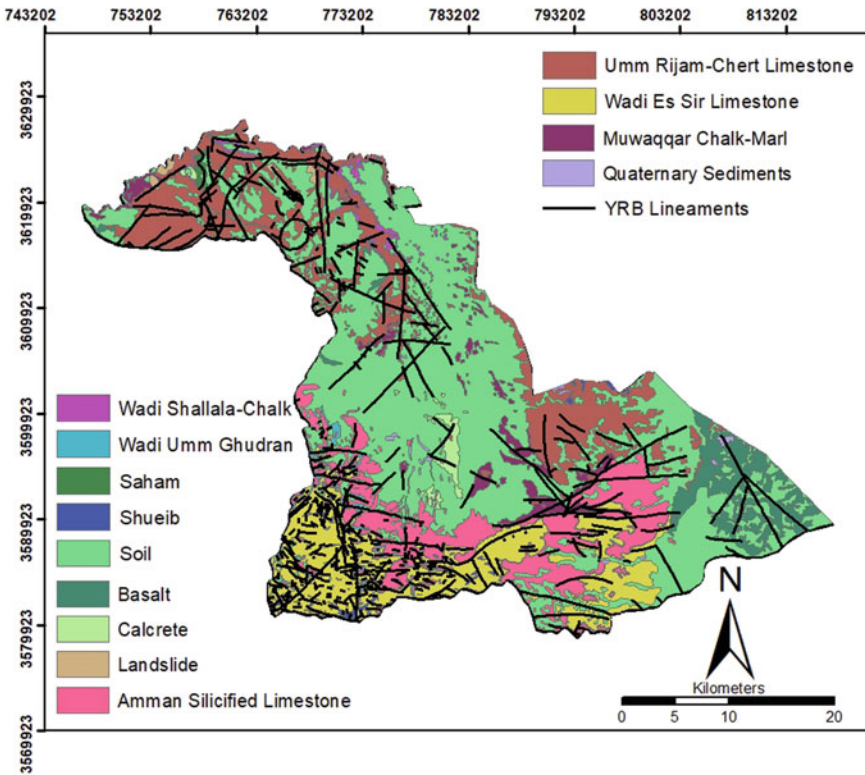
Fig. 20.3 Geological map of YRB

small exposures scattered to the south, north, and northwest of Irbid (Awawdeh and Jaradat 2010).

20.3 Data and Methods

20.3.1 Morphometric Analysis

20.3.1.1 Data Preparation

The following steps were carried out to calculate the morphometric parameters and to prioritize the sub-watersheds:

A digital elevation model from radar imagery (2006–2011), with 12.5 m resolution and UTM coordinate system zone 36 N was downloaded from Alaska Satellite Facility (2017). The DEM was preprocessed to fill in missing data (NoData) by applying the formula:

Filled = arcpy.sa.Con(arcpy.sa.IsNull(in_raster),arcpy.sa.FocalStatistics(in_raster, arcpy.sa.NbrRectangle(5,5),'MEAN'), in_raster).

Based on the stream network and flow direction maps, the watershed was subdivided into sub-watersheds.

The maps of the main sub-watersheds and drainage networks were obtained using a suitable threshold value to evaluate the main and minor streams using the method described by Strahler (1952, 1964). Stream order, number, lengths of streams of each different order, and other basic morphometric parameters were used to classify the watershed into sub-watersheds.

The basic morphometric parameters were calculated using ArcGIS 10.3 software.

Other morphometric parameters were calculated using the standard methods and formulae (Appendix 1).

The Morphometric Ranking Method is based on classifying the morphometric parameters according to their risk potential. The parameters are divided into two groups: group I included morphometric parameters that are considered directly proportional to soil erosion risk, which means that the highest value represents high susceptibility to the risk. By contrast, group II includes morphometric parameters that are considered inversely proportional to soil erosion risk, which means that the highest value represents low susceptibility to the risk. Prioritizing the sub-watersheds by using the morphometric ranking method, based on the compound factor. Preparing the soil erosion susceptibility maps according to the results of the morphometric ranking method.

20.3.1.2 Prioritization by Morphometric Analysis

Morphometric analysis was carried out to assess the susceptibility of YRB to soil erosion with the aid of GIS. The YRB was divided into 44 sub-watersheds based on the digital elevation model using the Hydrology toolbox in ArcGIS 10.3 (Fig. 20.4), and twenty-one morphometric parameters related to the soil erosion were calculated to rank and prioritize the sub-watersheds and evaluate their soil erosion susceptibility (Appendix 1).

The morphometric parameters were classified into four groups: basic, linear, shape, and relief. Basic parameters were derived from the digital elevation model using GIS techniques and included basin area, basin length, basin perimeter, number of streams, lengths of streams for each stream order, and bifurcation ratio. The stream frequency, drainage density, drainage texture, form factor, elongation ratio, and circularity ratio were estimated using mathematical equations (Appendix 1) elaborated by (Strahler 1952). Other important geomorphometric parameters (e.g., relative relief, basin relief, and ruggedness number) were also quantified according to mathematical formulas.

Prioritizing the sub-watersheds for soil erosion can be performed using the Compound Factor (Farhan and Anaba 2016; Shivhare et al. 2018; Ameri et al. 2018). Some of the morphometric parameters are directly related and others are inversely related to soil erosion potentiality (Table 20.1). Linear and relief parameters have
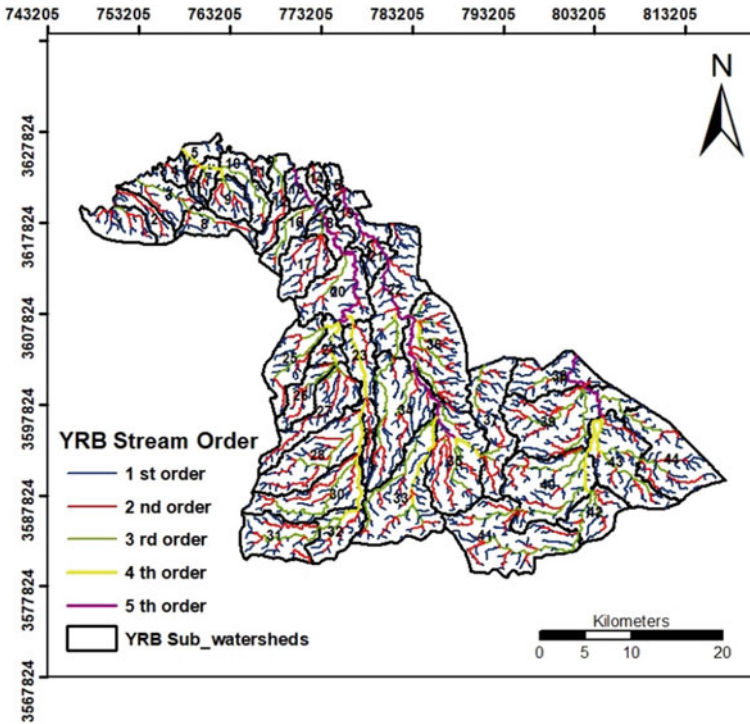
Fig. 20.4 Stream order and drainage pattern of YRB

a direct relationship with erodibility. Thus, the highest value of the linear or relief parameter was rated as rank 1, the second highest value as rank 2, and so on (Farhan and Anaba 2016; Javed et al. 2009). By contrast, the shape parameters have an inverse relation with erodibility (Farhan and Anaba 2016; Javed et al. 2009), which means that the lowest value of the shape parameter was rated as rank 1 and second lowest as rank 2 and so on. Parameters having the same values were assigned similar rankings.

The parameters which have a direct relationship with erodibility are: mean bifurcation ratio (R_{bm}), drainage density (D_d), length of overland flow (L_o), drainage texture (D_t), stream frequency (F_s), relief ratio (R_r), basin slope (S_w), and ruggedness number (R_n) (Farhan and Anaba 2016; Ameri et al. 2018). The parameters which have an inverse relationship with erodibility are: elongation ratio (R_e), circularity ratio (R_c), shape factor (B_s), and compactness coefficient (C_c) (Farhan and Anaba 2016; Ameri et al. 2018). After ranking sub-watersheds, the ranking values for all parameters of each sub-watershed were added up and then divided by the number of all parameters to calculate the compound factor (C_f). From the group of sub-watersheds, the highest prioritized rank was assigned to sub-watersheds which had the lowest compound factor and vice versa (Patel et al. 2012). The values of the compound factor were normalized from 0 for the lowest rank value and 1 for

Table 20.1 Morphometric parameters applied for soil erosion assessment

	Par. No.	Morphometric parameter
Direct relationship	1.	Mean bifurcation ratio (R_{bm})
	2.	Drainage density (D_d)
	3.	Length of overland flow (L_o)
	4.	Drainage texture (D_t)
	5.	Stream frequency (F_s)
	6.	Relief ratio (R_r)
	7.	Basin slope (S_w)
	8.	Ruggedness number (R_n)
Inverse relationship	9.	Elongation ratio (R_e)
	10.	Circularity ratio (R_c)
	11.	Shape factor (B_s)
	12.	Compactness coefficient (C_c)

Table 20.2 Classes of soil erosion prioritization based on C_f normalization

Normalization	Priority
0.0–0.2	Very high priority
0.2–0.4	High priority
0.4–0.6	Moderate priority
0.6–0.8	Low priority
0.8–1.0	Very low priority

the highest rank value to obtain a uniform scale, which was then grouped into five priority categories (very high, high, moderate, low, and very low) (Table 20.2).

20.3.2 Prioritization by Land Use/Land Cover (LULC)

Jawarneh and Biradar (2017) developed a Land Cover Database for Jordan at 30 m resolution. Based on this study, sub-watersheds of YRB were prioritized for soil erosion. Eight classes of LULC were considered for prioritization of the sub-watersheds: barren land, agriculture, rangeland, orchards, forest, rocky outcrops, built-up area and water body. The area and the proportion of each LULC class where calculated in each sub-watershed, and then each class rated for soil erosion priority (from 1 to 8). The highest priority (rate = 1) was assigned to barren land, and lowest priority (rate = 8) was given to water bodies according to local experts and literature. The weight of each class was calculated by multiplying the area by its rating. The weighted values were summed to calculate the compound factor (C_f) value for each sub-watershed. In the final step, all sub-watersheds were then grouped into

five priority categories (very high, high, moderate, low, and very low) based on the compound factor (C_f) values as follows:

$$C_f = \sum_{i=1}^{n} \frac{A}{100} 100\% \times R$$

where: C_f: compound factor, A: LULC type area in each sub-watershed, R: LULC rating value, n: number of sub-watersheds.

20.4 Results and Discussion

20.4.1 Prioritization Based on Morphometric Analysis

The results of the morphometric analysis of the whole basin are presented in Appendix 2, and those for the sub-watersheds are shown in Appendix 3. The dominating drainage pattern is dendritic (Fig. 20.4), which develops on a land surface that is homogeneous, non-porous, steeply sloped, with no structural control, and the underlying rock is of uniform resistance to erosion (Kabite and Gessesse 2018; Soni 2017). YRB is a fifth-order basin with a total area of 1393 km², a length of 76.94 km, and a perimeter of 247.70 km. The total number of streams (N_u) is 2109, where first-order streams formed 51.78% of the total streams. The mean bifurcation ratio (R_{bm}) is 2.05 indicating a low disturbed watershed by geologic structures (Strahler 1952).

20.4.1.1 Morphometric Parameters

1. **Basic Parameters**

The drainage area (A) indicates the volume of water that can be generated from precipitation and the number of streams that may increase runoff (Farhan and Anaba 2016). The drainage area of sub-watersheds in YRB ranges from 5.31 km² (SW6) to 74.34 km² (SW41). The smallest areas were found in sub-watersheds: 6, 14, 4, and 15, respectively. The largest areas were found in sub-watersheds: 41, 39, 33, and 34, respectively. The study showed that the maximum value of **perimeter (P)** is 52.60 km in SW39, and the minimum is 12.85 km in SW14. **Basin length (L_b)** constitutes a basic input parameter to calculate many other morphometric parameters specially shape parameters. It is important in hydrological calculations and increases as the drainage increases (Patel et al. 2012). Basin length for the 44 sub-watersheds in YRB varies between 3.83 km for SW4 to 16.34 km for SW33. **The stream order (U)** describes the drainage network in quantitative terms. In this study, the stream order is derived based on the Strahler method (1952). The highest stream order in

the YRB sub-watershed is 4. **The number of streams (N_u)** of various orders for each sub-watershed was counted in YRB. SW41 has the greatest total number of streams (122 streams) and SW6 has the lowest total number of streams (5 streams). The numbers of first-order streams (N_1) vary from one sub-watershed to another. It ranges from 3 in SW6 to 64 in SW41. Among the 44 sub-watersheds, SW39 has the greatest total length of streams (101.09 km), whereas SW15 has the lowest total length of streams (4.98 km).

2. **Linear Parameters**

Bifurcation Ratio (R_b) and Mean Bifurcation Ratio (R_{bm})

The bifurcation ratio is an indicator of relief and dissection (Farhan and Anaba 2016). In general, bifurcation ratio values vary between 2 for flat or rolling drainage basins, and 6 for watersheds where the geological structure has distorted the drainage pattern (Strahler 1964). Watersheds with low structure disturbance or without any distortion of drainage pattern have low values of R_b (Strahler 1964). The bifurcation ratio has a direct relationship with erosion. YRB showed a variation in R_{bm} from 1.14 for SW13 indicating the lowest sensitivity to erosion to 11.07 for SW17. The highest values of R_{bm} were found in SWs 17, 23, 40, and 20, respectively. Whereas the lowest values of R_{bm} were found in SWs 13, 37, 2, and 21, respectively.

Drainage Density (D_d)

Drainage density depends on climatic conditions, vegetation, landscape properties (e.g., soil and rock), and relief (Kelson and Wells 1989; Moglen et al. 1998; Oguchi 1997). It is a measure of runoff potential (Chorley 1969), which yields sediment transportation and erosion susceptibility (Bates and Campbell 2001; Ozdemir and Bird 2009). Subsoil material that is highly permeable, and under dense vegetation, low relief, and low runoff develop low drainage density, whereas landscapes characterized by impermeable subsoil materials, sparse vegetation, higher runoff, and mountainous relief develop high drainage density (Macka 2001; Chow 1964).

The values of D_d for the 44 sub-watersheds in YRB are relatively low. The lowest value of D_d (0.66) was found for SW5, which is considered a well-drained basin because of its high infiltration capacity. SW35 has the highest value (1.61) and is considered a poorly drained basin because of its low infiltration capacity which implies the presence of highly dissected topography, steep slopes, and impermeable subsurface materials. Therefore, sub-watershed 35 has the highest susceptibility to erosion. The highest values of D_d were identified in SWs 35, 36, 30, and 34, respectively. The lowest values of D_d were found in SWs 5, 15, 11, and 14, respectively.

Length of Overland Flow (L_o)

Length of overland flow (L_o) refers to the length of the flow of water over the ground before it becomes concentrated into indefinite stream channels (Horton 1945). It has a significant impact on the amount of water needed to exceed a particular erosion threshold. It is dependent on the kind of rock, permeability, climatic conditions,

vegetation cover, relief, and the length of erosion (Schumm 1956). The length of overland flow (L_o) has a direct relation with erosion. L_o varies from 0.31 for SW35 to 0.76 for SW5. The lower value of L_o indicates quicker surface runoff and a well-developed drainage network, a higher slope, lowest susceptibility to erosion. The highest values of L_o were found in SWs 5, 15, 11, and 14, respectively. The lowest values of L_o were found in SWs 35, 36, 30, and 34, respectively.

Drainage Texture (D_t)

Drainage texture is determined by the underlying lithology, infiltration capacity, and relief aspect of the landscape (Farhan and Anaba 2016). The value of the drainage texture ranges between 0.34 (SW6) and 2.9 (SW36). These values imply very coarse to coarse texture. The highest values of D_t were found in SWs 36, 35, 41, and 40, respectively, indicating the highest sensitivity to erosion The lowest values of D_t were found in SWs 6, 15, 11, and 2, respectively.

Stream Frequency (F_s)

Stream frequency refers to the number of streams per unit of area (Horton 1945). This parameter has a direct correlation with erosion (Carlston 1963). The value of stream frequency (F_s) in YRB ranges from 0.94 (SW6) to 2.46 (SW7). The highest values of F_s were found for SWs 7, 24, 36, and 42, respectively. The lowest values of F_s were found for SWs 6, 2, 30, and 25, respectively. Hence, SW7 with the highest F_s has the highest susceptibility to erosion.

3. **Shape Parameters**

Elongation Ratio (R_e)

The values of R_e varies from 0 (highly elongated shape) to 1.0 (perfectly circular shape). Strahler (1964), classified drainage basins into five categories based on R_e: circular (0.9–1.0), oval (0.8–0.9), less elongated (0.7–0.8), elongated (0.5–0.7), and more elongated (< 0.5). YRB is an elongated basin with R_e value of 0.55. R_e has an inverse correlation with erosion. A circular basin leads to more discharge of runoff than an elongated basin (Singh and Singh 1997). SW9 has the highest R_e value (0.81) which indicates the least sensitivity to erosion, whereas SW29 has the lowest R_e (0.39) and indicates more susceptibility to erosion (Table 20.3).

Circularity Ratio (R_c)

The length and frequency of streams, geological structures, climate, roughness, and slope determine the Circularity Ratio (R_c) (Ameri et al. 2018). The circular shape of the watershed, high roughness, and permeability of the surface is represented by high values of R_c (Ameri et al. 2018). In a circular catchment, runoff often travels a similar distance and is therefore likely to arrive at the outflow at the same time (Abuzied et al. 2016). The outflow is located at one end of the primary axis in the elongated catchments, though, and as a result, the runoff is likely to disperse over

Table 20.3 Drainage basins categories of elongation ratio in YRB

Shape	Sub-watersheds
(0.9–1.0) Circular	None
(0.8–0.9) Oval	9
(0.7–0.8) Less elongated	4, 13, 17, 18, 20, 35, 40
(0.5–0.7) Elongated	1, 3, 5, 6, 7, 8, 10, 11, 14, 15, 19, 21, 22, 23, 24, 25, 26, 28, 30, 31, 32, 33, 34, 36, 37, 38, 39, 41, 42, 43, 44
(> 0.5) More elongated	2, 12, 16, 27, 29

time and produce a smaller flood peak (Schumm 1956). R_c and soil erosion are inversely correlated (Aher et al. 2014; Ameri et al. 2018). R_c value varies from 0, for a perfectly elongated shape, to 1 for perfect circular shape (Bisht et al. 2018). YRB has R_c value of 0.29, where it varies from 0.19 for SW29, indicating low permeability and high susceptibility to erosion, to 0.60 for SW9, indicating high permeability and low susceptibility to erosion. The lowest values of R_c were found in SWs 29, 12, 27, and 16, respectively, whereas, the highest values of R_c were found in SWs 9, 32, 1, and 4, respectively.

Shape Factor (B_s)

The shape factor is largely affected by the rate of sediment, water volume, and the length and roughness of the drainage network (Ameri et al. 2018). The shape factor has an inverse relationship with erosion (Farhan and Anaba 2016; Ameri et al. 2018). Strong relief and steep ground slopes yield low B_s values which indicate high potential runoff hazards. B_s values in YRB sub-watersheds vary between 1.92 for SW9 and 8.39 for SW29. Accordingly, SW29 has the least susceptibility to erosion. The lowest values of B_s were found in SWs 9, 4, 13, and 40, respectively, whereas the highest values of B_s were found in SWs 29, 27, 12, and 16, respectively.

Compactness Coefficient (C_c)

The Compactness Coefficient (C_c) has a direct relationship with the watershed penetration capacity and has an inverse relationship with soil erosion potentiality (Ameri et al. 2018). The lowest C_c in YRB sub-watersheds was found for SW9 with a value of 1.29, indicating that this sub-watershed has the lowest infiltration capacity and is highly susceptible to erosion. SW29 has the highest C_c with a value of 2.27, indicating that this sub-watershed has the highest infiltration capacity and thus the lowest sensitivity to erosion. The lowest values of C_c were found in SWs 9, 32, 1, and 4, respectively, whereas, the highest values of C_c were found in SWs 29, 12, 27, and 16, respectively.

4. **Relief Parameters**

Basin Relief (H)

The total slope of the drainage basin and the severity of erosion processes that operate on the slopes of a watershed are indicated by the Basin relief (H) (Ameri et al. 2018). Basin relief has a direct correlation with erosion (Ameri et al. 2018). It is found that the total basin relief of the YRB is 1400 m, while it varies from a minimum of 90 m (SW42) to a maximum of 645 m (SW1).

Relief Ratio (R_r)

Usually, runoff flow (R_r) in watersheds has a direct relationship with the relief ratio, the slope of the earth's surface, and the slope of the streams and consequently, the erosion of the watershed (Ameri et al. 2018; Abuzied et al. 2016). The highest value of R_r in YRB sub-watersheds was found for SW4 (0.13) and the lowest value was found for SWs 22 and 43 (0.008). SW4 has the highest susceptibility to erosion compared to other sub-watersheds. The highest values of R_r were found in SWs 4, 11, 14, and 5, respectively. The lowest values of R_r were found in SWs 43, 22, 44, and 42, respectively.

Basin Slope (S_w)

The slope refers to the angular inclination of terrain between hilltops and valley bottoms. The slope steepness influences the formation of drainage networks. The slope is controlled by the climatomorphogenic processes and rock resistance (Gouri Sankar Bhunia 2013; Magesh and Chandrasekar 2014). The slope of a basin affects the amount and the timing of runoff, where a higher slope degree causes rapid runoff and increased erosion rate (potential soil loss) with less groundwater recharge potential (Meraj et al. 2013). The maximum slope of 7.90° was found for SW4, indicating high sensitivity of this sub-watershed to erosion, whereas the lowest slope was found for SW43 with a value of 0.48°, indicating that this sub-watershed is less prone to erosion. The highest values of S_w were found in SWs 4, 11, 14, and 5, respectively. The lowest values of S_w were found in SWs 43, 22, 44, and 42, respectively.

Ruggedness Number (R_n)

According to Aher et al. (2014), areas of low relief but high drainage density are described as ruggedly textured, whereas areas of high relief have less dissection. R_n has a direct correlation with erodibility (Ameri et al. 2018). The highest value of R_n in YRB sub-watersheds was observed in SW30 (0.78), where both total relief and drainage density values are high, i.e., in this sub-watershed slope is very steep associated with its slope length, indicating that SW30 (0.78) has the highest sensitivity to erosion, SW21 (0.10) has the lowest sensitivity to erosion. The highest values of R_n were found in SWs 30, 27, 2, and 1, respectively, and the lowest values of R_n were found in SWs 21, 42, 23, and 43, respectively.

Based on the computed morphometric parameters, the compound factor (C_f) was calculated for each sub-watershed and then normalized in order to classify the sub-watersheds into five categories of soil erosion susceptibility. The lowest C_f (12.25) was found in SW1 and thus the highest degree of soil erosion risk. SWs 3 and 35 have the same C_f value (17.08) with a very high priority of soil erosion, and SW7 with C_f (17.50) also has a very high priority of soil erosion. SWs 17, 27, 33, 4, 20, 10, 36, 28, 40, 30, 14, 32, 9, and 11 have a high priority compared with other sub-watersheds. The highest C_f (27.67) was found for SW21 with the least degree of susceptibility to soil erosion.

Results revealed that eighteen sub-watersheds (41% of the total) are classified as a very high and high priority. This means less than half of the YRB is expected to suffer from very high and high soil erosion susceptibility. Sub-watersheds with very high and high priority are found in the central, southwestern, and northwestern parts of the basin (Fig. 20.5). The main morphometric parameters affecting the spatial distribution of the susceptibility to soil erosion in the YRB are stream frequency (F_s), ruggedness number (R_n), relief ratio (R_r), mean bifurcation ratio (R_{bm}), drainage density (D_d), drainage texture (D_t), and compactness coefficient (C_c).

20.4.2   *Prioritization Based on Land Use/Land Cover (LULC)*

Prioritization of sub-watersheds by LULC is given in Table 20.4. It revealed that thirty-nine sub-watersheds (88.6% of the total area) are classified as a very high and high priority. SWs 1, 2, 3, 4, 5, 11, 13, 14, 15, 19, 23, 27, 28, 29, 30, 31, 32, 33, 34, 35, 36, 37, 38, and 44 are expected to suffer from very high soil erosion susceptibility. SWs 6, 7, 8, 9, 10, 12, 18, 20, 21, 22, 24, 39, 40, 41, and 43 are expected to suffer from high soil erosion susceptibility (Fig. 20.6).

The results obtained from the morphometric analysis suggest that 18 sub-watersheds with 613.29 km^2 (44% of YRB area) have the highest susceptibility to soil erosion. According to LULC analysis, there are 39 sub-watersheds with 1262.27 km^2 (90.60% of YRB area) that are expected to suffer from high soil erosion susceptibility. A combination of both methods suggests that 1, 3, 4, 7, 9, 10, 11, 14, 20, 27, 28, 30, 32, 33, 35, 36, and 40 are the most sensitive sub-watersheds to get influenced by soil erosion. The matching in the classification of the sub-watersheds potential for soil erosion using morphometric analysis and LULC methods was 61.36% (Fig. 20.6).
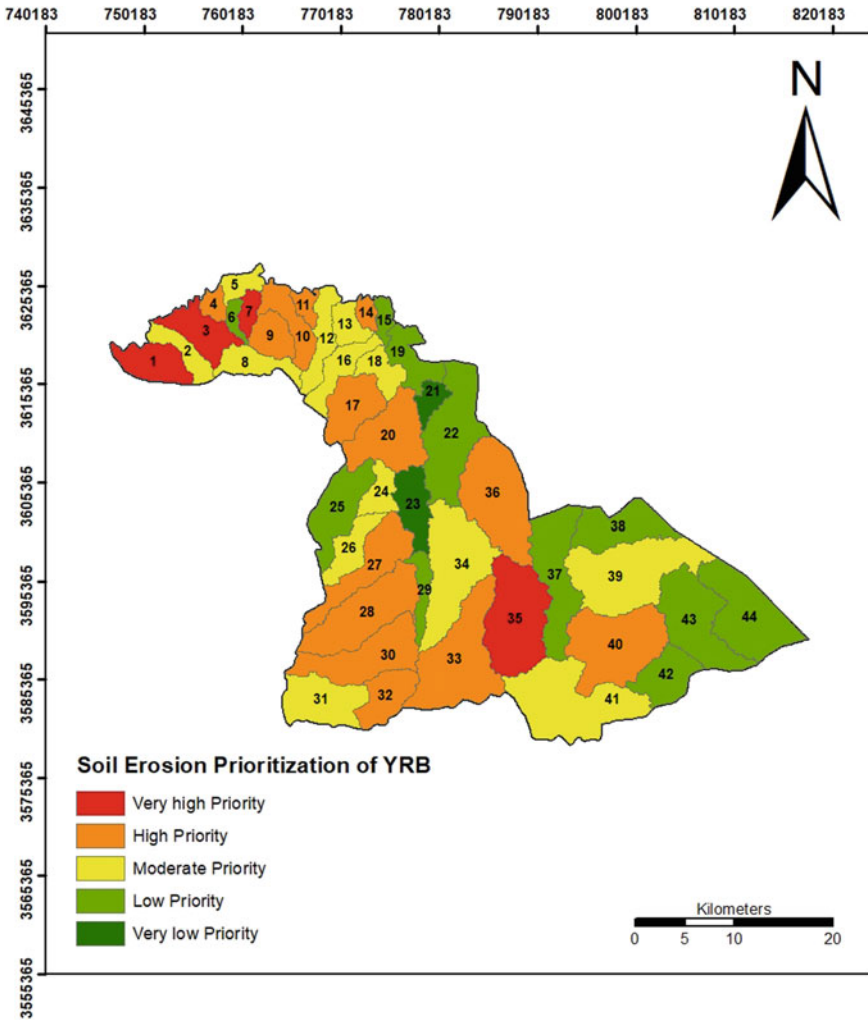
Fig. 20.5 Soil erosion susceptibility map for YRB sub-watersheds based on morphometric analysis

Table 20.4 Soil erosion susceptibility prioritization for YRB sub-watersheds based on LULC analysis

SW	Priority	SW	Priority	SW	Priority	SW	Priority
1	Very high	12	High	23	Very high	34	Very high
2	Very high	13	Very high	24	High	35	Very high
3	Very high	14	Very high	25	Very low	36	Very high
4	Very high	15	Very high	26	Very low	37	Very high
5	Very high	16	Moderate	27	Very high	38	Very high
6	High	17	Moderate	28	Very high	39	High
7	High	18	High	29	Very high	40	High
8	High	19	Very high	30	Very high	41	High
9	High	20	High	31	Very high	42	Moderate
10	High	21	High	32	Very high	43	High
11	Very high	22	High	33	Very high	44	Very high
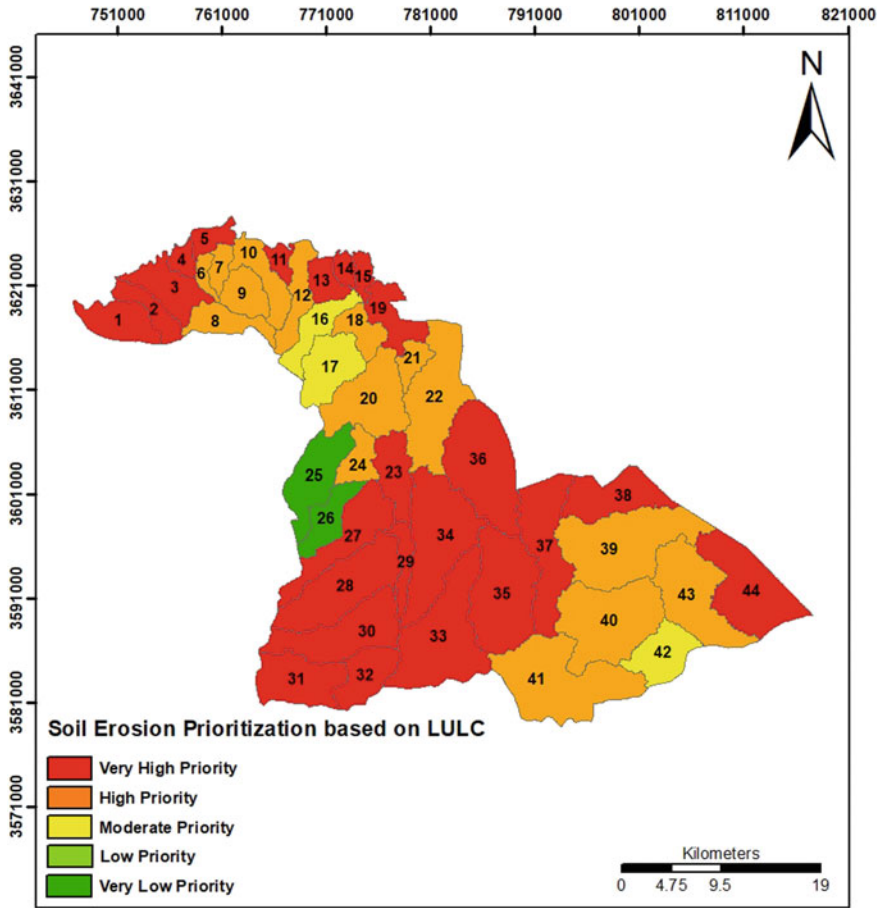
Fig. 20.6 Soil erosion susceptibility map for YRB sub-watersheds based on LULC analysis

20.5 Conclusions

Prioritization of sub-watersheds can be carried out by any one method, but in that case, the dependability of the result is low. Hence in this study, we adopted all two methods of prioritization so that the integration of these methods can provide more accurate and reliable results. The sub-watersheds with high susceptibility to erosion indicate that YRB is considerably affected by geologic structures (e.g., Sirhan Fault), which distorted the drainage pattern. The morphometric analysis points to many geometric distinctive features of the sub-watersheds of high soil erosion potential such as high drainage density, low permeability, sparse natural vegetation, and high relief. The elongated nature of the whole basin and its high stream frequency and density also contributed to the increased susceptibility to erosion. The multi-approach of sub-watershed prioritization decreases the uncertainty of results and hence makes

decisions of treatment simpler. Suitable erosion control measures are recommended strongly after field observations to preserve the land from further erosion.

Appendix 1: Methodology Adopted for Computation of Morphometric Parameters

Par. No.		Morphometric parameter	Formula/definition	References
Basic	1.	Basin area (A)	Plan area of the watershed (km^2)	Horton (1945)
	2.	Basin perimeter (P)	Perimeter of the watershed (km)	Horton (1945)
	3.	Basin length (L_b)	Length of the basin (km)	Horton (1945)
	4.	Stream order (U)	Hierarchical rank	Strahler (1952, 1964)
	5.	Total number of streams (N_u)	Total no. of streams of all orders	Strahler (1957)
	6.	Stream length (L_u)	Length of the stream (km)	Horton (1945)
	7.	Mean stream length (L_{sm})	$L_{sm} = L_u/N_u$ (km) where L_u = total stream length of all orders N_u = total no. of stream segments of order "u"	Horton (1945)
	8.	Stream length ratio (R_L)	$R_L = L_u/L_{u-1}$, where L_{u-1} = the total stream length of its next lower order	Horton (1945)
Linear	9.	Bifurcation ratio (R_b)	$R_b = N_u/N_{u+1}$, where N_{u+1} = no. of segments of the next higher order	Schumm (1956)
	10.	Mean bifurcation ratio (R_{bm})	R_{bm} = average of the bifurcation ratio of all orders	Strahler (1957)
	11.	Drainage density (D_d)	$D_d = L_u/A$, where L_u = total stream length of all orders (km) A = area of the watershed (km^2)	Horton (1945)
	12.	Length of overland flow (L_o)	$L_o = 1/(2 * D_d)$, where D_d = drainage density	Horton (1945)

(continued)

Par. No.		Morphometric parameter	Formula/definition	References
	13.	Drainage texture (D_t)	$D_t = N_u/P$, where N_u = total no. of stream segments of order "u" P = perimeter of the watershed (km)	Horton (1945)
	14.	Stream frequency (F_s)	$F_s = N_u/A$, where N_u = total no. of streams of all orders A = area of the basin (km^2)	Horton (1945)
Shape	15.	Elongation ratio (R_e)	$R_e = 1.128 * (A^{0.5})/L_b$, where A = area of the basin (km^2) L_b = basin length (km)	Schumm (1956)
	16.	Circularity ratio (R_c)	$R_c = 4 \times \pi \times A/P^2$, where $\pi = 3.14$ A = area of the basin (km^2) P = perimeter (km)	Miller (1953)
	17.	Shape factor (B_s)	$B_s = L_b^2/A$, where L_b = basin length (km) A = area of the basin (km^2)	Nooka Ratnam et al. (2005)
	18.	Compactness coefficient (C_c)	$C_c = 0.2812 * P/A^{0.5}$, where P = perimeter of the basin (km) A = area of the basin (km^2)	Horton (1945)
Relief	19.	Basin relief (H)	$H = h - h_1$, where h = maximum height (m) h_1 = minimum height (m)	Horton (1945)
	20.	Relief ratio (R_r)	$R_r = H/L_b$, where H = total relief (km) L_b = basin length (km)	Schumm (1956)
	21.	Relative relief ratio (R_v)	H/P, where H = total relief (km) P = perimeter of the basin (km)	Melton (1957)
	22.	Basin slope (S_w)	$H/L_b * 60$, where H = total relief (km) L_b = basin length (km)	Farhan and Anaba (2016)

(continued)

(continued)

Par. No.		Morphometric parameter	Formula/definition	References
	23.	Ruggedness number (R_n)	$R_n = D_d * H$, where H = basin relief (km) D_d = drainage density	Schumm (1956)
Hypsometric	24.	Hypsometric integral (HI)	$HI = (E_{mean} - E_{min})/(E_{max} - E_{min})$, where E_{mean} = the weighted mean elevation E_{max} = maximum elevation E_{min} = minimum elevation	Strahler (1952)

Appendix 2: Morphometric Parameters of YRB

Par. No.		Morphometric parameter					
Basic	1.	Basin area (A) (km^2)	1393.22				
	2.	Basin perimeter (P) (km)	247.70				
	3.	Basin length (L_b) (km)	76.94				
	4.	Stream order (U)	5	I	II	III	IV	V
	5.	Total number of streams (N_u)	2109	1092	519	307	85	106
	6.	Stream length (L_u) (km)	1854	890	493	315	78	79
	7.	Mean stream length (L_{sm}) (km)	0.88	0.82	0.95	1.03	0.91	0.74
	8.	Stream length ratio (R_L)			II/I	III/II	IV/III	V/IV
					0.55	0.64	0.25	1.02
Linear	9.	Bifurcation ratio (R_b)			I/II	II/III	III/IV	IV/V
					2.10	1.69	3.61	0.80
	10.	Mean bifurcation ratio (R_{bm})	2.052					
	11.	Drainage density (D_d) (km/km^2)	1.331					
	12.	Length of overland flow (L_o) (km)	0.376					

(continued)

Par. No.		Morphometric parameter							
	13.	Drainage texture (D_t)	8.514						
	14.	Stream frequency (F_s)	1.514						
Shape	15.	Elongation ratio (R_e)	0.547						
	16.	Circularity ratio (R_c)	0.285						
	17.	Shape factor (B_s)	4.249						
	18.	Compactness coefficient (C_c)	1.866						
Relief	19.	Basin relief (H) (m)	1400						
	20.	Relief ratio (R_r)	18.195						
	21.	Relative relief ratio (R_v)	0.006						
	22.	Basin slope (S_w)	1.092						
	23.	Ruggedness number (R_n)	1.863						
Hypsometric	24.	Hypsometric integral (HI)	0.5858						

Appendix 3: The Morphometric Parameters of Sub-watersheds in YRB

SW	A	P	L_b	U	N_u	L_u	L_{sm}	R_{bm}	D_d	L_o	D_t	F_s	R_e	R_c	B_s	C_c	H	R_r	S_w	R_n	R_v	HI
1	23.77	23.45	9.27	3	38	27.13	0.71	4.14	1.14	0.44	1.62	1.62	0.59	0.54	3.61	1.35	645	0.070	4.18	0.74	0.57	0.028
2	14.58	23.22	8.76	2	14	17.02	1.22	1.33	1.17	0.43	0.60	0.96	0.49	0.34	5.26	1.71	636	0.073	4.36	0.74	0.61	0.027
3	25.25	31.44	9.93	3	44	29.10	0.66	1.70	1.15	0.43	1.40	1.74	0.57	0.32	3.90	1.76	620	0.062	3.75	0.71	0.58	0.020
4	6.85	13.04	3.83	2	9	7.89	0.88	2.00	1.15	0.43	0.69	1.31	0.77	0.51	2.14	1.40	504	0.132	7.90	0.58	0.68	0.039
5	9.47	17.30	5.55	2	11	6.23	0.57	2.67	0.66	0.76	0.64	1.16	0.63	0.40	3.25	1.58	452.2	0.082	4.89	0.30	0.58	0.026
6	5.31	14.87	5.06	2	5	5.3	1.07	1.50	1.01	0.50	0.34	0.94	0.51	0.30	4.82	1.81	401	0.079	4.75	0.40	0.73	0.027
7	7.72	15.93	5.31	3	19	7.75	0.41	1.83	1.00	0.50	1.19	2.46	0.59	0.38	3.65	1.61	391	0.074	4.42	0.39	0.67	0.025
8	17.86	27.53	9.21	3	25	19.10	0.76	1.63	1.07	0.47	0.91	1.40	0.52	0.30	4.75	1.83	378	0.041	2.46	0.40	0.63	0.014
9	17.16	18.96	5.74	3	24	22.51	0.94	1.68	1.31	0.38	1.27	1.40	0.81	0.60	1.92	1.29	336	0.058	3.51	0.44	0.64	0.018
10	20.80	31.44	10.08	3	28	21.18	0.76	4.10	1.02	0.49	0.89	1.35	0.51	0.26	4.88	1.94	587	0.058	3.49	0.60	0.70	0.019
11	6.96	16.32	4.57	2	9	5.84	0.65	2.00	0.84	0.60	0.55	1.29	0.65	0.33	3.00	1.74	484	0.106	6.35	0.41	0.68	0.030
12	19.94	32.47	11.34	3	23	22.05	0.96	1.83	1.11	0.45	0.71	1.15	0.44	0.24	6.44	2.05	544	0.048	2.88	0.60	0.69	0.017
13	12.37	18.66	5.16	2	15	13.02	0.87	1.14	1.05	0.48	0.80	1.21	0.77	0.45	2.15	1.49	397	0.077	4.62	0.42	0.64	0.021
14	6.00	12.85	4.02	2	10	5.27	0.53	1.50	0.88	0.57	0.78	1.67	0.69	0.46	2.70	1.47	349	0.087	5.20	0.31	0.82	0.027
15	6.92	16.24	5.22	2	8	4.98	0.62	3.00	0.72	0.69	0.49	1.16	0.57	0.33	3.94	1.74	313	0.060	3.60	0.23	0.83	0.019
16	19.68	31.47	10.18	3	29	22.12	0.76	1.63	1.12	0.45	0.92	1.47	0.49	0.25	5.27	2.00	414	0.041	2.44	0.47	0.73	0.013
17	30.10	27.47	8.56	3	46	37.55	0.82	11.07	1.25	0.40	1.68	1.53	0.72	0.50	2.43	1.41	308	0.036	2.16	0.38	0.68	0.011
18	14.81	22.17	5.85	3	21	16.35	0.78	1.60	1.10	0.45	0.95	1.42	0.74	0.38	2.31	1.62	326	0.056	3.35	0.36	0.66	0.015

(continued)

(continued)

SW	A	P	L_b	U	N_u	L_u	L_{sm}	R_{bm}	D_d	L_o	D_t	F_s	R_e	R_c	B_s	C_c	H	R_r	S_w	R_n	R_v	HI
19	21.19	32.25	7.83	3	25	22.44	0.90	2.94	1.06	0.47	0.78	1.18	0.66	0.26	2.90	1.97	227	0.029	1.74	0.24	0.77	0.007
20	45.00	38.35	10.74	4	69	54.06	0.78	5.43	1.20	0.42	1.80	1.53	0.70	0.38	2.57	1.61	292	0.027	1.63	0.35	0.72	0.008
21	9.66	17.98	5.30	2	12	10.43	0.87	1.40	1.08	0.46	0.67	1.24	0.66	0.38	2.90	1.63	94	0.018	1.07	0.10	0.30	0.005
22	57.84	48.78	15.05	3	82	71.60	0.87	1.75	1.24	0.40	1.68	1.42	0.57	0.31	3.92	1.80	122	0.008	0.49	0.15	0.55	0.003
23	23.17	30.62	9.31	3	27	26.14	0.97	6.18	1.13	0.44	0.88	1.17	0.58	0.31	3.74	1.79	124	0.013	0.80	0.14	0.48	0.004
24	14.09	21.97	6.40	3	31	19.31	0.62	1.67	1.37	0.37	1.41	2.20	0.66	0.37	2.90	1.65	136	0.021	1.28	0.19	0.43	0.006
25	35.27	36.20	12.86	3	40	42.65	1.07	1.64	1.21	0.41	1.11	1.13	0.52	0.34	4.69	1.71	393	0.031	1.83	0.48	0.31	0.011
26	19.45	27.60	9.85	3	24	24.25	1.01	1.80	1.25	0.40	0.87	1.23	0.51	0.32	4.99	1.76	364	0.037	2.22	0.45	0.37	0.013
27	37.68	44.33	15.76	4	57	52.16	0.92	4.07	1.38	0.36	1.29	1.51	0.44	0.24	6.60	2.03	546	0.035	2.08	0.76	0.29	0.012
28	55.25	44.14	14.92	3	79	71.25	0.90	1.69	1.29	0.39	1.79	1.43	0.56	0.36	4.03	1.67	547	0.037	2.20	0.71	0.35	0.012
29	11.65	27.60	9.88	3	17	14.46	0.85	4.14	1.24	0.40	0.62	1.46	0.39	0.19	8.39	2.27	220	0.022	1.34	0.27	0.30	0.008
30	46.93	41.53	14.21	4	51	67.90	1.33	4.46	1.45	0.35	1.23	1.09	0.54	0.34	4.30	1.71	539	0.038	2.28	0.78	0.41	0.013
31	35.49	29.94	9.65	3	42	42.90	1.02	1.67	1.21	0.41	1.40	1.18	0.70	0.50	2.62	1.41	343	0.036	2.13	0.42	0.58	0.011
32	23.82	23.41	8.08	3	32	29.34	0.92	2.15	1.23	0.41	1.37	1.34	0.68	0.55	2.74	1.35	337	0.042	2.50	0.42	0.46	0.014
33	69.01	48.87	16.34	4	104	95.13	0.92	2.08	1.38	0.36	2.13	1.51	0.57	0.36	3.87	1.65	438	0.027	1.61	0.60	0.47	0.009
34	65.23	50.96	15.92	3	84	91.49	1.09	1.79	1.40	0.36	1.65	1.29	0.57	0.32	3.89	1.77	280	0.018	1.06	0.39	0.27	0.005
35	62.31	41.28	12.64	4	106	100.32	0.95	2.27	1.61	0.31	2.57	1.70	0.71	0.46	2.56	1.47	367	0.029	1.74	0.59	0.34	0.009
36	63.59	40.75	14.13	4	118	100.05	0.85	2.24	1.57	0.32	2.90	1.86	0.64	0.48	3.14	1.44	238	0.017	1.01	0.37	0.24	0.006
37	49.50	49.73	15.81	3	75	63.25	0.84	1.25	1.28	0.39	1.518	1.52	0.50	0.25	5.05	1.99	191	0.012	0.73	0.24	0.42	0.004
38	33.84	33.93	11.50	3	49	43.69	0.89	1.86	1.29	0.39	1.44	1.45	0.57	0.37	3.91	1.64	168	0.015	0.88	0.22	0.29	0.005

(continued)

(continued)

SW	A	P	L_b	U	N_u	L_u	L_{sm}	R_{bm}	D_d	L_o	D_t	F_s	R_e	R_c	B_s	C_c	H	R_r	S_w	R_n	R_v	HI
39	73.59	52.61	15.61	4	110	101.09	0.92	4.61	1.37	0.36	2.09	1.50	0.62	0.33	3.31	1.72	182	0.012	0.70	0.25	0.29	0.003
40	65.08	44.11	12.11	4	103	89.38	0.87	5.98	1.37	0.36	2.34	1.58	0.75	0.42	2.26	1.54	208	0.017	1.03	0.29	0.40	0.005
41	74.34	50.12	15.72	3	122	93.22	0.76	1.65	1.25	0.40	2.43	1.64	0.62	0.37	3.33	1.64	247	0.016	0.94	0.31	0.44	0.005
42	26.45	27.69	8.31	3	47	34.19	0.73	1.67	1.29	0.39	1.70	1.78	0.70	0.43	2.61	1.51	90	0.011	0.65	0.12	0.28	0.003
43	52.30	46.68	13.24	3	75	71.62	0.96	1.76	1.37	0.37	1.61	1.43	0.62	0.30	3.35	1.82	106	0.008	0.48	0.15	0.52	0.002
44	55.94	41.47	13.49	3	80	71.39	0.89	1.82	1.28	0.39	1.93	1.43	0.63	0.41	3.25	1.56	122	0.009	0.54	0.16	0.48	0.003

References

Abuzied S, Yuan M, Ibrahim S, Kaiser M, Saleem T (2016) Geospatial risk assessment of flash floods in Nuweiba area, Egypt. J Arid Environ 133:54–72. https://doi.org/10.1016/j.jaridenv.2016.06.004

Aher PD, Adinarayana J, Gorantiwar SD (2014) Quantification of morphometric characterization and prioritization for management planning in semi-arid tropics of India: a remote sensing and GIS approach. J Hydrol 511:850–860. https://doi.org/10.1016/j.jhydrol.2014.02.028

Ameri AA, Pourghasemi HR, Cerda A (2018) Erodibility prioritization of sub-watersheds using morphometric parameters analysis and its mapping: a comparison among TOPSIS, VIKOR, SAW, and CF multi-criteria decision making models. Sci Total Environ 613–614:1385–1400. https://doi.org/10.1016/j.scitotenv.2017.09.210

Awawdeh M, Bani Domi M (2009) Prediction of the soil erosion in the jordanian part of the yarmouk river basin using a gis-based revised universal soil loss equation. Abhath Al- Yarmouk Humanit Soc Sci Ser 25(2):443–452

Awawdeh MM, Jaradat RA (2010) Evaluation of aquifers vulnerability to contamination in the Yarmouk River basin, Jordan, based on DRASTIC method. Arab J Geosci 3(3):273–282. https://doi.org/10.1007/s12517-009-0074-9

Bates BC, Campbell EP (2001) A Markov Chain Monte Carlo Scheme for parameter estimation and inference in conceptual rainfall-runoff modeling. Water Resour Res 37(4):937–947. https://doi.org/10.1029/2000WR900363

Bhatt S, Ahmed SA (2014) Morphometric analysis to determine floods in the Upper Krishna basin using Cartosat DEM. Geocarto Int 29(8):878–894. https://doi.org/10.1080/10106049.2013.868042

Bisht S, Chaudhry S, Sharma S, Soni S (2018) Assessment of flash flood vulnerability zonation through Geospatial technique in high altitude Himalayan watershed, Himachal Pradesh India. Remote Sens Appl Soc Environ 12:35–47

Bisht DS, Mohite AR, Jena PP, Khatun A, Chatterjee C, Raghuwanshi NS, Singh R, Sahoo B (2020) Impact of climate change on streamflow regime of a large Indian river basin using a novel monthly hybrid bias correction technique and a conceptual modeling framework. J Hydrol 590:125448. https://doi.org/10.1016/j.jhydrol.2020.125448

Biswas S, Sudhakar S, Desai VR (1999) Prioritisation of subwatersheds based on morphometric analysis of drainage basin: a remote sensing and GIS approach. J Indian Soc Remote Sens 27(3):155–166. https://doi.org/10.1007/BF02991569

Carlston CW (1963) Drainage density and streamflow. U.S. geological survey professional paper

Chatterjee S, Krishna AP, Sharma AP (2014) Geospatial assessment of soil erosion vulnerability at watershed level in some sections of the Upper Subarnarekha river basin, Jharkhand, India. Environ Earth Sci. https://doi.org/10.1007/s12665-013-2439-3

Chorley R (1969) Introduction to fluvial processes. Methuen & Co Ltd., Bungay, UK

Chow VT (1964) Handbook of applied hydrology: a compendium of water-resources technology. McGraw-Hill, New York

Clark J (1966) Morphometry from maps. In: Dury GH (ed) Essays in geomorphology. Heinemann, London, pp 235–274

Farhan Y, Anaba O (2016) A remote sensing and GIS approach for prioritization of Wadi Shueib mini-watersheds (Central Jordan) based on morphometric and soil erosion susceptibility analysis. J Geogr Inf Syst 08:1–19. https://doi.org/10.4236/jgis.2016.81001

Frissell CA, Liss WJ, Warren CE, Hurley MD (1986) A hierarchical framework for stream habitat classification: viewing streams in a watershed context. Environ Manage 10(2):199–214. https://doi.org/10.1007/BF01867358

Gouri Sankar Bhunia SG (2013) Morphometric analysis of Kangshabati-Darkeswar interfluves area in West Bengal, India using ASTER DEM and GIS techniques. J Geol Geosci 02(04). https://doi.org/10.4172/2329-6755.1000133

Horton R (1945) Erosional development of streams and their drainage density: hydrophysical approach to quantitative geomorphology. Geol Soc Am Bull 56:275–370

Javed A, Khanday M, Ahmad R (2009) Prioritization of sub-watersheds based on morphometric and land use analysis using remote sensing and GIS techniques. J Indian Soc Remote Sens 37:261–274. https://doi.org/10.1007/s12524-009-0016-8

Jawarneh RN, Biradar CM (2017) Decadal national land cover database for Jordan at 30 m resolution. Arab J Geosci 10(22):483. https://doi.org/10.1007/s12517-017-3266-8

Kabite G, Gessesse B (2018) Hydro-geomorphological characterization of Dhidhessa River Basin, Ethiopia. Int Soil Water Conserv Res 6(2):175–183. https://doi.org/10.1016/j.iswcr.2018.02.003

Kanth TA (2012) Morphometric analysis and prioritization of watersheds for soil and water resource management in Wular catchment using geo-spatial tools. Int J Geol 2:12

Kelson KI, Wells SG (1989) Geologic influences on fluvial hydrology and bedload transport in small mountainous watersheds, Northern New Mexico, U.S.A. Earth Surf Process Landforms 14(8):671–690. https://doi.org/10.1002/esp.3290140803

Lal R (2004) Soil carbon sequestration impacts on global climate change and food security. Science 304(5677):1623–1627. https://doi.org/10.1126/science.1097396

Macka Z (2001) Determination of texture of topography from large scale contour maps. Geogr Vestn 73(2):53–62

Magesh NS, Chandrasekar N (2014) GIS model-based morphometric evaluation of Tamiraparani subbasin, Tirunelveli district, Tamil Nadu, India. Arab J Geosci 7(1):131–141. https://doi.org/10.1007/s12517-012-0742-z

Makhlouf I, Abu-Azzam H, Al-Hiayri A (1996) Surface and subsurface lithostratigraphic relationships of the Cretaceous Ajlun Group in Jordan. Natural Resources Authority, Subsurface Geology Division, Bulletin 8

Malik MI, Bhat MS, Kuchay NA (2011) Watershed based drainage morphometric analysis of Lidder catchment in Kashmir Valley using geographical information system. Recent Res Sci Technol. https://updatepublishing.com/journal/index.php/rrst/article/view/672

Melton M (1957) An analysis of the relations among elements of climate, surface properties and geomorphology. Department of Geology, Columbia University, Technical Report, 11, Project NR 389-042.Office of Navy Research, New York

Meraj G, Yousuf AR, Romshoo SA (2013) Impacts of the geo-environmental setting on the flood vulnerability at watershed scale in the Jhelum basin. M.Phil. dissertation, University of Kashmir, India. http://dspaces.uok.edu.in/jspui/handle/1/1362

Mesa LM (2006) Morphometric analysis of a subtropical Andean basin (Tucumán, Argentina). Environ Geol 50(8):1235–1242. https://doi.org/10.1007/s00254-006-0297-y

Miller V (1953) A quantitative geomorphic study of drainage basin characteristics in the Clinch Mountain Area, Virginia and Tennessee. Project NR 389 402, Technical Report 3, Columbia University, Department of Geology, ONR, New York

Moglen GE, Eltahir EAB, Bras RL (1998) On the sensitivity of drainage density to climate change. Water Resour Res 34(4):855–862. https://doi.org/10.1029/97WR02709

Moh'd B (2000) The geology of Irbid and Ash Shuna Ash Shamaliyya (Waqqas). Map sheet No. 3154-II and 3154-III. Natural Resources Authority, Geological Mapping Division, Bulletin 46

Nooka Ratnam K, Srivastava YK, Venkateswara Rao V, Amminedu E, Murthy KSR (2005) Check dam positioning by prioritization of micro-watersheds using SYI model and morphometric analysis—remote sensing and GIS perspective. J Indian Soc Remote Sens 33(1):25–38. https://doi.org/10.1007/BF02989988

Obeidat MM (1993) Petrographical, mineralogical, geochemical investigations of Wadi Sir carbonates, North Jordan. Unpubl. M.sc. thesis, Yarmouk University, Jordan

Oguchi T (1997) Drainage density and relative relief in humid steep mountains with frequent slope failure. Earth Surf Process Landforms 22(2):107–120. https://doi.org/10.1002/(SICI)1096-9837(199702)22:2%3c107::AID-ESP680%3e3.0.CO;2-U

Okumura M, Araujo AGM (2014) Long-term cultural stability in hunter–gatherers: a case study using traditional and geometric morphometric analysis of lithic stemmed bifacial points from Southern Brazil. J Archaeol Sci 45:59–71. https://doi.org/10.1016/j.jas.2014.02.009

Ozdemir H, Bird D (2009) Evaluation of morphometric parameters of drainage networks derived from topographic maps and DEM in point of floods. Environ Geol 56(7):1405–1415. https://doi.org/10.1007/s00254-008-1235-y

Pandey A, Mathur A, Mishra S, Mal B (2009) Soil erosion modeling of a Himalayan watershed using RS and GIS. Environ Earth Sci 59:399–410. https://doi.org/10.1007/s12665-009-0038-0

Parker D (1970) The hydrogeology of the Mesozoic-Cenozoic aquifers of the western highlands and plateau of east Jordan. Investigation of the sandstone aquifers of east Jordan, Technical Report No. 2: UNDP/FAO Project 212

Patel DP, Dholakia MB, Naresh N, Srivastava PK (2012) Water harvesting structure positioning by using geo-visualization concept and prioritization of mini-watersheds through morphometric analysis in the Lower Tapi Basin. J Indian Soc Remote Sens 40(2):299–312. https://doi.org/10.1007/s12524-011-0147-6

Pimentel D (2006) Soil erosion: a food and environmental threat. Environ Dev Sustain 8(1):119–137. https://doi.org/10.1007/s10668-005-1262-8

Pisal PA, Yadav AS, Chavan AB (2013) Morphometric analysis of Bhogavati River Basin, Kolhapur district, Maharashtra, India, p 8

Rothwell JJ, Robinson SG, Evans MG, Yang J, Allott TEH (2005) Heavy metal release by peat erosion in the Peak district, southern Pennines, UK. Hydrol Process 19(15):2973–2989. https://doi.org/10.1002/hyp.5811

Rudraiah M, Govindaiah S, Vittala SS (2008) Morphometry using remote sensing and GIS techniques in the sub-basins of Kagna river basin, Gulburga district, Karnataka, India. J Indian Soc Remote Sens 36(4):Article 4

Schumm S (1956) Evolution of drainage systems and slopes in badlands at Perth Amboy, New Jersey. Geol Soc Am Bull 67:597–646

Sebastian M, Jayaraman V, Chandrasekhar MG (1995) Space technology applications for sustainable development of watersheds. Technical report. Indian Space Research Organisation, Bangalore

Shivhare N, Rahul AK, Omar PJ, Chauhan MS, Gaur S, Dikshit PKS, Dwivedi SB (2018) Identification of critical soil erosion prone areas and prioritization of micro-watersheds using geoinformatics techniques. Ecol Eng 121:26–34. https://doi.org/10.1016/j.ecoleng.2017.09.004

Singh S, Singh MC (1997) Morphometric analysis of Kanhar River Basin. Nat Geograp J India 43:31–43

Singer MJ, Warkentin BP (1996) Soils in an environmental context: an American perspective. CATENA 27(3):179–189. https://doi.org/10.1016/0341-8162(96)00016-1

Singh O, Sarangi A, Sharma MC (2008) Hypsometric integral estimation methods and its relevance on erosion status of north-western lesser Himalayan watersheds. Water Resour Manag 22(11):1545–1560. https://doi.org/10.1007/s11269-008-9242-z

Singh SK, Jain SK, Bárdossy A (2014) Training of artificial neural networks using information-rich data. Hydrology 1(1):40–62. https://doi.org/10.3390/hydrology1010040

Soni S (2017) Assessment of morphometric characteristics of Chakrar watershed in Madhya Pradesh India using geospatial technique. Appl Water Sci 7(5):2089–2102. https://doi.org/10.1007/s13201-016-0395-2

Strahler AN (1952) Dynamic basis of geomorphology. GSA Bull 63(9):923–938. https://doi.org/10.1130/0016-7606(1952)63[923:DBOG]2.0.CO;2

Strahler A (1957) Quantitative analysis of watershed geomorphology. Trans, Am Geophys Union 38:913–920

Strahler A (1964) Quantitative geomorphology of drainage basins and channel networks. In: Chow V (ed) Handbook of applied hydrology. McGraw Hill, New York, pp 439–476

Sun W, Shao Q, Liu J (2013) Soil erosion and its response to the changes of precipitation and vegetation cover on the Loess Plateau. J Geogr Sci 23(6):1091–1106. https://doi.org/10.1007/s11442-013-1065-z

Yang D, Kanae S, Oki T, Koike T, Musiake K (2003) Global potential soil erosion with reference to land use and climate changes. Hydrol Process 17(14):2913–2928. https://doi.org/10.1002/hyp.1441

Chapter 21
Effects of Leachate from Osisioma Open Dumpsite in Aba, Abia State, Nigeria on Surrounding Borehole Water Quality

Eberechi Cecilia Osuagwu, Adanma Monica Uwaga, and Harry Prince Inemeawaji

21.1 Introduction

Water is one of the determinants of the human earth system and as a precious resource, water needs to be valued and conserved (Anju et al. 2015). However, in several parts of the world, humans do not have any access to safe drinking water, because the water is contaminated. Access to safe drinking water remains an urgent necessity, as most of the urban and rural population still depends completely on the untreated surface or groundwater resources (Ashwani and Abhay 2014).

Groundwater occurs in many different geological formations. Nearly all rocks in the upper part of the Earth's crust, whatever their type, origin, or age, possess openings called pores or voids. The volume of water contained in the rock depends on the percentage of these openings or pores in a given volume of the rock, which is termed the porosity of the rock. More pore spaces result in higher porosity and more stored water (Mohammad et al. 2014). The contribution from groundwater is vital; perhaps as many people depend directly upon aquifers for drinking water, and a large amount of the world's food is produced by irrigated agriculture that relies largely on groundwater. In the future, aquifer development will continue to be fundamental to economic development and reliable water supplies will be needed for domestic, industrial, and irrigation purposes (Mohammad et al. 2014). Groundwater is an important source of water as it constitutes about 95% of the freshwater on our planet (discounting that, locked in the polar ice caps), making it fundamental to human life and economic development, but is being mostly polluted due to the presence of open dumping sites, especially in Nigeria where open dumping of solid waste is practiced.

E. C. Osuagwu (✉) · A. M. Uwaga · H. P. Inemeawaji
Michael Okpara University of Agriculture, Umudike, Abia State, Nigeria
e-mail: osuagwu.eberechi@mouau.edu.ng

The leachate accumulates at the bottom of the landfill and percolates through the soil (Mor et al. 2006). This leachate drains from the dump, chiefly organic carbon largely in the form of fulvic acids, migrates downward and contaminate the groundwater (Ugwu and Nwosu 2009). The major environmental problem at landfills is the loss of leachate from the site and the subsequent contamination of groundwater (Jagloo 2002).

Dumpsites have been identified as one of the major threats to groundwater resources receiving a mixture of municipal, commercial and mixed industrial wastes. The depressions into which solid wastes are often dumped include valleys and excavations. Studies on the effects of unlined waste dumps on the host soil and underlying shallow aquifers have shown that soil and groundwater systems can be polluted due to poorly designated waste disposal facilities (Amadi et al. 2012). Some of these sites are indiscriminately located at streams, valleys, open fields, wetlands, and in abandoned borrow pits. Studies by Aluko (2001), and Akinbiyi (1992) have shown that there is an unconditional water rest aquifer underlying most areas of Aba and its environs of which Osisioma is one of them upon which all depend for their various needs including drinking water. So many waste dumpsites are located in various parts of Osisioma and its environs, apparently based on reasons of convenience.

The dumpsite that was assessed contains both biodegradable and non-biodegradable materials of all sorts which may contain different physical, chemical, and microbiological properties. The accumulation of waste in Aba mostly in Osisioma reduces the aesthetic value of the place and increases the rate of diseases among the individuals occupying these areas. It also increases the breeding conditions of some disease vectors and pathogens which invariably increases morbidity (Malaria, dysentery, and diarrhea) and mortality (Civeria and Lavado 2008) as well as the cost of medical expenditure among the local residents (Ejeona and Umah 2000).

Water-borne diseases may spring up through water pollution, especially groundwater contamination, and rapidly spread beyond human expectation because of its flow mechanism (Afolayan et al. 2012). The present study focused on examining the effect of leachate on surrounding borehole water quality within Osisioma open dumpsite in Aba, Abia State, Nigeria.

21.1.1   Description of the Study Area

Osisioma solid waste dumpsite lies within longitude 5° 8′ 59″ N, and latitude 7° 19′ 49″ E. It has a total population of about 219,632 and a land area of 198 km^2 at the 2006 census. As a result of urbanization, the area is surrounded by residential houses, industries, a gasoline station, a motor park, a popular ariaria market, and an automobile repair workshop. The area lacks a functional drainage system, and it is always flooded each time it rains heavily. Due to the poor disposal of solid wastes, the area is faced with the problem of indiscriminate dumping of wastes on streets and roads. The vegetation is, however, affected by activities like agriculture, construction, and urbanization.

21.2 Methods

21.2.1 Sample and Sampling Techniques

Cardinal point model was used via a systematic sampling technique to select the boreholes from which water samples were collected. BH 1, 2, 3, and 4 were assigned to the four borehole used. The distances of the boreholes were 80 m, 251 m, 348 m and 455 m respectively from the dumpsite which was at the center with respect to the cardinal point model that was used. The geographic coordinates of all sampling points were identified through the use of a hand-held Global Positioning System (GPS Channel 76CSx Garmin Model). A digital camera (Samsung WB150F, 14.2 megapixels, 18× optical zoom) was employed at the vantage point to take the aerial view of the dumpsite. Table 21.1 illustrates the location of the four (4) sampled boreholes with respect to their distance in meters to the dump site. Also, the geographical location and elevation of the study area and sampled boreholes ranged from 55 to 60 m above sea level (Fig. 21.1).

Table 21.1 Parameter concentration with distance from the dumpsite

Code	Elevation (m)	Distance (m)	High variable
BH 1	59	80	Colour (40PCU), nitrate (343.0 mg/L), nitrate-nitrogen (73.8 mg/L), chlorine (0.90 mg/L), iron (0.40 mg/L), arsenic (0.031 mg/L), lead (0.125 mg/L), total bacterial count (80 cfu/100 mL), total coliform count (33 cfu/100 mL), *E. coli* (7 cfu/100 mL)
BH 2	58	251	Colour (18PCU), nitrate (257.0 mg/L), nitrate-nitrogen (57.0 mg/L), chlorine (0.63 mg/L), total bacterial count (58 cfu/100 mL), total coliform count (17 cfu/100 mL), *E. coli* (4 cfu/100 mL)
BH 3	60	348	Nitrate (322.0 mg/L), nitrate-nitrogen (71.4 mg/L), chlorine (0.35 mg/L), total bacterial count (49 cfu/100 mL), total coliform count (21 cfu/100 mL), *E. coli* (4 cfu/100 mL)
BH 4	56	455	Colour (23PCU), nitrate (243.2 mg/L), nitrate-nitrogen (54.1 mg/L), chlorine (1.71 mg/L), total bacterial count (61 cfu/100 mL), total coliform count (24 cfu/100 mL), *E. coli* (11 cfu/100 mL), iron (0.42 mg/L), arsenic (0.041 mg/L)

BH borehole
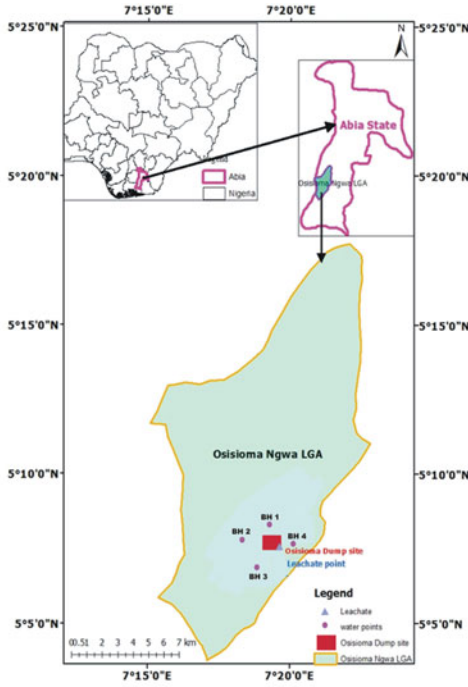
Fig. 21.1 Map of the study site: Osisioma dumpsite in Abia State, Nigeria

21.2.2 Groundwater and Leachate Sample Collection and Analysis

All samples were analyzed for selected physical, chemical (including heavy metals) and microbiological parameters, namely; temperature (°C), pH, Nitrate (NO_3^-), Chromium (Cr^{3+}), Dissolved Oxygen (DO), Conductivity, Alkalinity, Free Chlorine, Biological Oxygen Demand (BOD), Chemical Oxygen Demand (COD), Total

Bacteria count, Total Coliform count, *E. coli*, Lead (Pb), Zinc (Zn), Iron (Fe) etc. The criteria behind the selection of these parameters are based on the fact that the parameters are the common pollutant elements in groundwater. The methods adopted for analysis of all parameters in water and leachate were in accordance with APHA (1995, 2005) standard recommendation.

21.2.3 Statistical Analysis

The obtained data were subjected to descriptive statistical analysis such as mean, standard deviation, coefficient of variation, table and range. The mean and coefficient of variance were used to show the degree of variations in the examined variables. Results were also compared with World Health Organization (WHO 2010).

21.3 Results and Discussion

21.3.1 Physiochemical and Microbiological Parameters Concentration with Distance from the Dumpsite

From Table 21.1, it was observed that distance from the dumpsite played a role in concentrations of the different parameters that were analyzed. In BH 1 at 80 m away from the dumpsite: Colour—40PCU, Nitrate—343.0 mg/L, Nitrate-Nitrogen—73.8 mg/L, Chlorine—0.90 mg/L, Iron—0.40 mg/L, Arsenic—0.031 mg/L, Lead—0.125 mg/L, Total bacterial count—80 cfu/100 mL, Total coliform count—33 cfu/100 mL, *E. coli*—7 cfu/100 mL varied when compared with the values of parameters that persisted in BH 4 (Colour—23PCU, Nitrate—243.2 mg/L, Nitrate-Nitrogen—54.1 mg/L, Chlorine—1.71 mg/L, Total bacterial count—61 cfu/100 mL, Total coliform count—24 cfu/100 mL, *E. coli*—11 cfu/100 mL, Iron—0.42 mg/L, Arsenic—0.041 mg/L) at a distance of 455 m. It was assumed that the concentration of parameters in BH 4 was as a result of elevation (56 m) of the borehole, which was higher than that of BH 1 (59 m) and this made BH 4 at 56 m above sea level susceptible to contamination by percolated leachate even at a distance of 455 m from the dump site.

21.3.2 Concentration Variation in Physiochemical Parameters of Sampled Boreholes and Leachate

From Table 21.2 and Figs. 21.2 and 21.3, it was observed that variation occurred in the concentration of physiochemical parameters among sampled boreholes and leachate. The concentration of temperature (28.8 °C), pH (7.1) and BOD (4.8) were

Table 21.2 Concentration variation in physiochemical variables in sampled boreholes and leachate

Physiochemical	Leachate	BH 1	BH 2	BH 3	BH 4	BH mean	STD	C.V. %	Range	WHO limit
Temperature (°C)	28.8	29.7	29.5	27.2	26.7	28.28	± 1.546	5.47	3.00	20–30
Colour (PCU)	13,850	40	18	13	23	23.50	± 11.73	48.91	27.00	15
TDS (mg/L)	2847	57.2	35.1	57.9	26.0	44.05	± 16.02	36.39	31.90	250
pH	7.1	5.9	6.1	6.3	5.2	5.88	± 0.48	8.16	1.10	6.5–8.5
Conductivity (μs/cm)	4380	88	54	89	40	67.75	± 24.64	36.37	49.00	100
DO (mg/L)	25.2	8.4	7.5	6.2	8.0	7.53	± 1.66	22.05	2.20	> 4.0
Alkalinity (mg/L)	1900	60	10	5	50	31.25	± 27.80	88.96	55.00	200
NO_3^- (mg/L)	699.2	343.0	257.0	322.0	243.3	291.30	± 48.67	4.18	99.80	40
Nitrate-nitrogen (mg/L)	1580	73.8	57.0	71.4	54.1	64.08	± 9.96	15.54	19.70	15
BOD (mg/L)	4.8	2.6	1.4	1.3	1.9	1.80	± 0.59	32.78	1.30	30
COD (mg/L)	7.68	4.16	2.24	2.08	3.04	2.88	± 0.95	32.99	2.08	–

BH borehole; *STD* standard deviation; *C.V.* co-efficient of variance
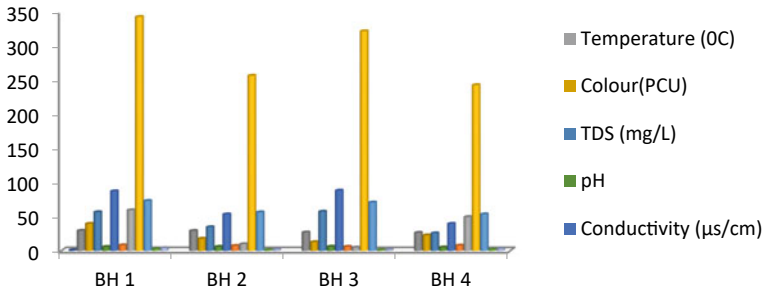
Fig. 21.2   Study area showing a section of the dumpsite
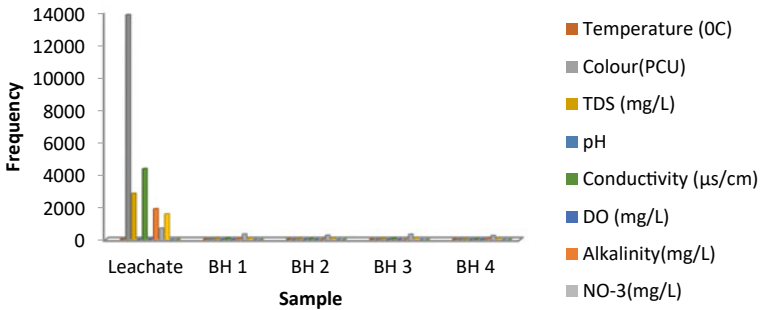
Fig. 21.3   Concentration variation in physicochemical variables in sampled boreholes and leachate

within the permissible limit provided by W.H.O. standard. The variation in BH 1, BH 2, BH 3 and BH 4, in the concentration of pH, Conductivity, Colour, Nitrate, BOD and COD ranged from 5.2 in BH 4 to 6.3 in BH 3, 40 in BH 4 to 89 in BH 3, 13 in BH 3 to 40 in BH 1, 243.2 in BH 4 to 343.0 in BH 1, 1.3 in BH 3 to 2.6 in BH 1, and 2.08 in BH 3 to 4.16 in BH 1 respectively. This variation in the values of parameters in sampled boreholes indicates the presence of contaminants.

Concentrations in alkalinity in water samples were below the W.H.O. standard limit, but that of the wastewater (leachate—1900 mg/L) was found above the permissible limit of W.H.O. standard. Alkalinity refers to the capability of water to neutralize acid and its importance is underscored by its ability to control pH changes. High alkalinity, while not detrimental to humans may cause drinking water to have a flat, unpleasant taste (Adams 2001).

Nitrate concentrations in all samples were found to exceed W.H.O. standard limit. Ingestion of nitrates in drinking water has been known to cause methemoglobinamia in infants less than six months (Johnson et al. 1987). Nitrate is a major component in crop production. After rainfall, varying quantities of nitrate are washed from farmland into nearby surface water and also into the groundwater table through infiltration, percolation, and seepage. It also gets into groundwater through manure from animal waste, leachate from landfills and dump site etc.

The Dissolved oxygen in all samples exceeded the WHO standard limit. Dissolved Oxygen is essential to the survival of aquatic life. If dissolved oxygen is high forming a lather with soap for domestic users will be a major challenge.

21.3.3 Concentration Variation in Chemical (Heavy Metals) Variables in Sampled Boreholes and Leachate

Observations from Table 21.3 and Fig. 21.4 showed that the number of heavy metals and other chemical parameters analyzed was more in BH 1 at a distance of 80 m from the dump site. This may be a result of its proximity to the dump site. The values of the parameters analyzed in BH 1 (Fe with 0.40 mg/L and As with 0.031 mg/L) were lower when compared to the values obtained in BH 4 at an elevation of 56 m and distance of 455 m (Fe with 0.42 mg/L and As with 0.041 mg/L). The variation in concentration of parameters in BH 4 irrespective of its distance from the dumpsite might be from the elevation or as a result of industrial activities being carried out around the BH 4 area.

The mean of boreholes parameters chromium (0.024), Arsenic (0.02), Lead (0.04), Copper (0.045) and Zinc (0.15) when compared to the leachate values for same parameters (Chromium—0.0000, Arsenic—0.0000, Lead—0.0000, Copper—4.0 and Zinc—0.2437) indicates that the pollution of sampled boreholes might not necessarily be from the dumpsite alone, but might have also resulted from industrial and agricultural activities going on in the area.

Copper concentration in all borehole water samples were within the stated W.H.O. limits except the Leachate sample. High intake of Copper can cause liver and kidney damage which may eventually result to death of the organism. It also causes stomach ache, dizziness, vomiting and diarrhea.

Iron concentrations in BH 1, BH 4 and leachate samples were found to exceed W.H.O. standards. Iron concentrations however do not pose a potential health risk as they fall well within the recommended daily dietary allowance (7–18 mg). Water with high iron concentrations may be discolored and may cause stain in clothes during washing (Adams 2001).

Lead (0.125 mg/L) was observed to be above standard limits in BH 1. Lead has many toxic effects on human health with children being the most vulnerable population (Payne 2008). Excessive exposure to Lead is associated with various neuro-developmental problems and a 4:1-fold increased risk of attention-deficit hyperactivity disorder in children (Brodkin et al. 2007; Sanborn et al. 2002).

Table 21.3 Concentration variation in chemical (heavy metals) variables in sampled boreholes and leachate

Chemical (heavy metals)	Leachate	BH 1	BH 2	BH 3	BH 4	BH mean	STD	C.V. %	Range	WHO limit
Copper (mg/L)	**4.0**	0.05	0.05	0.00	0.08	0.045	± 0.033	73.33	0.03	1.0
Iron (mg/L)	**41.5**	**0.40**	0.31	0.19	**0.42**	0.33	± 0.105	31.82	0.23	0.3
Chlorine (mg/L)	**122.5**	**0.90**	**0.63**	**0.35**	**1.71**	0.898	± 0.59	65.70	1.36	0.2–0.25
Chromium (mg/L)	0.0000	0.024	0.037	0.014	0.020	0.024	± 0.0082	34.17	0.023	0.05
Arsenic (mg/L)	0.0000	**0.031**	0.000	0.010	**0.041**	0.02	± 0.02	100	0.031	0.01
Lead (mg/L)	0.0000	**0.125**	0.023	0.001	0.012	0.04	± 0.057	142.5	0.124	0.05
Zinc (mg/L)	0.2437	0.11	0.14	0.09	0.25	0.15	± 0.06	40	0.16	5.0

BH borehole; *STD* standard deviation; *C.V.* co-efficient of variance
Bold signifies parameters with higher values that exceeds World Health Organisation (WHO) permissible limit
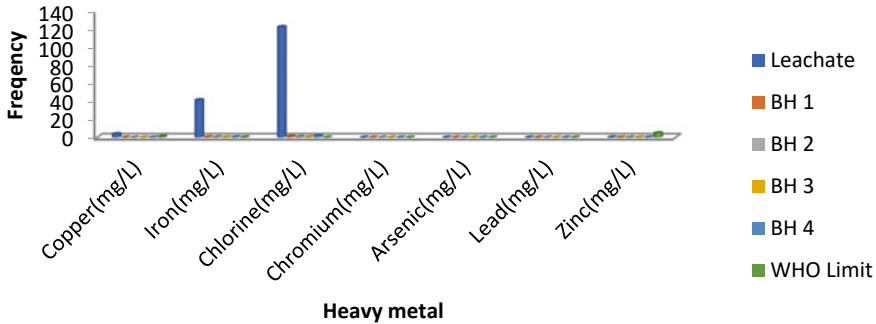
Fig. 21.4 Concentration variation in chemical (heavy metals) variables in sampled boreholes and leachate

21.3.4 Concentration Variation in Microbiological Variables in Sampled Boreholes and Leachate

From Table 21.4 and Figs. 21.5 and 21.6, the bacteriological parameters were higher than the permissible limit given by World health organization in all sampled boreholes and leachate. The mean value of the concentration of microbiological parameters when compared with the leachate values indicated that the sampled boreholes were polluted by not only the leachate from the dumpsite but also the presence of decayed or animal droppings, which might have percolated through the soil to the groundwater tables.

21.3.5 Relationship Between Sampled Borehole Water and W.H.O. Water Quality Standard

The physical parameters of the sampled borehole points (temperature, pH, conductivity and total dissolved solid) complied with W.H.O. standards. Colour was indicated to be higher than the W.H.O. standard limit in platinum cobalt unit (PCU) in BH 1 (40), BH 2 (18) and BH 4 (23), but BH 3 (13) complied with the standard (15PCU) (Table 21.5; Fig. 21.7).

Chemical parameters such as; Alkalinity, BOD, COD, Copper, Chromium and Zinc were in compliance with the World Health Organization standard limit in all sampling borehole points. While Dissolved Oxygen, Nitrate, Nitrate-Nitrogen, Chlorine were not in compliance with the W.H.O. standard limit. Arsenic and Iron were above the limit in BH 1 (0.031 and 0.40 mg/L) and BH 4 (0.020 and 0.42 mg/L), and Lead was found to be greater than the permissible limit of W.H.O. in BH 1 (0.125 mg/L).

Table 21.4 Concentration variation in microbiological variables in sampled boreholes and leachate

Microbiological (cfu/100 mL)	Leachate	BH 1	BH 2	BH 3	BH 4	BH mean	STD	C.V. %	Range	WHO limit
TBC	**2815**	**80**	**58**	**49**	**61**	62.00	± 13.04	21.03	31.00	5–10
TCC	**378**	**33**	**17**	**21**	**24**	23.75	± 6.80	28.63	16.00	10
E. coli	**286**	**7**	**4**		**11**	6.50	± 3.32	51.08	7.00	0

BH borehole; *TBC* total bacterial count; *TCC* total coliform count; *STD* standard deviation; *C.V.* co-efficient of variance
Bold signifies parameters with higher values that exceeds World Health Organisation (WHO) permissible limit

Fig. 21.5 Concentration variation in microbiological variables in sampled boreholes
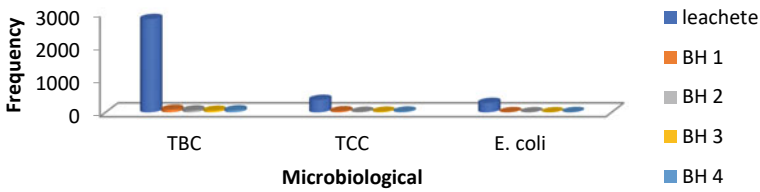
Fig. 21.6 Concentration variation in microbiological variables in sampled boreholes and leachate

Table 21.5 Relationship between sampled borehole water and W.H.O. standard limit

Parameters	W.H.O. STD	BH 1	BH 2	BH 3	BH 4
Dissolved oxygen (mg/L)	> 4.0	**8.4**	**7.5**	**6.2**	**8.0**
Colour (PCU)	15	**40**	**18**	13	**23**
Nitrate (mg/L)	40	**343.0**	**257.0**	**322.0**	**243.2**
Nitrate-nitrogen (mg/L)	15	**73.8**	**57.0**	**71.4**	**54.1**
Iron (mg/L)	0.3	**0.40**	0.31	0.19	**0.42**
Chlorine (mg/L)	0.2–0.25	**0.90**	**0.63**	**0.35**	**1.71**
Arsenic (mg/L)	0.01	**0.031**	0.000	0.010	**0.020**
Lead (mg/L)	0.05	**0.125**	0.023	0.001	0.012
Total bacterial count (cfu/100 mL)	5–10	**80**	**58**	**49**	**61**
Total coliform count (cfu/100 mL)	10	**33**	**17**	**21**	**24**
E. coli (cfu/100 mL)	0	**7**	**4**	**4**	**11**

BH borehole
Bold signifies parameters with higher values that exceeds World Health Organisation (WHO) permissible limit

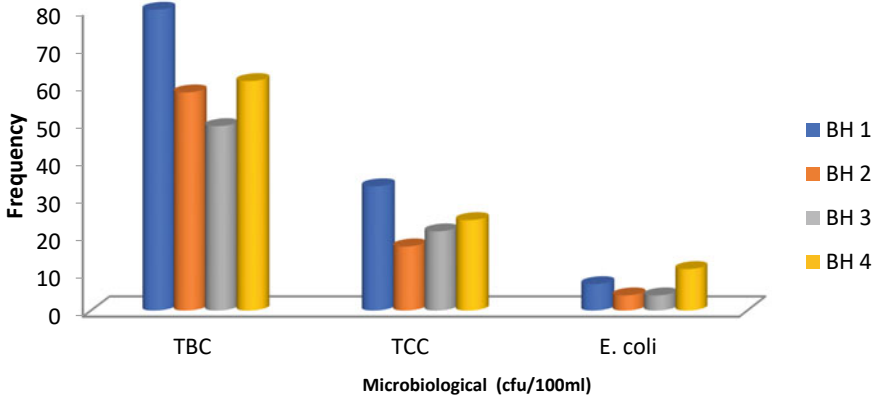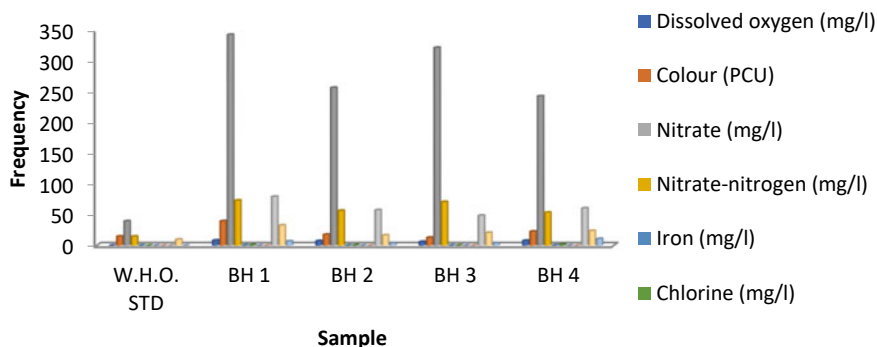**Fig. 21.7** Relationship between sampled borehole water and W.H.O. standard limit

The bacteriological parameters were above the limit of the world health organization standard in all the sampling borehole points. The sampled boreholes were therefore deemed unfit for domestic use from the water quality standard recommended by World Health Organization (2010).

21.4   Conclusion

Groundwater is a vital resource for human existence. Civilization, industrialization and commercialization have greatly influenced the quality and availability of groundwater resources. The study observes indiscernible migration of leachate into groundwater resource from the base of the open dumpsite to be the point source of groundwater pollution. It is obvious that the time, role of waste management strategy, soil stratigraphy, groundwater flow direction, open dump lifespan, distance from the leachate, season, and underlying geology, all play vital roles in groundwater quality around dumpsites in relation to waste decomposition, leachate formation and migration as well as groundwater contamination. These limit the use of groundwater for domestic, industrial and agricultural activities. Human health issues and other environmental issues could also be attributed to the pollution of groundwater.

Therefore, major water treatment (Chlorination, Sedimentation, and Filtration) needs to be conducted on the borehole water before it is deemed fit for human consumption. Dumping of fresh refuse on the study area should be discouraged with the use of sanctions and fines on defaulters. Government should adopt eco-friendly solid waste disposal management system such as sorting before disposal, incineration, landfill, waste conversion to biogas and compost as well as provision of potable water. Strong policies that will require permission before digging of the borehole to reduce indiscriminate borehole construction to preserve soil structure. Environmental organisations should continue sensitization programs to create awareness to the public on the menace that can be cause by groundwater pollution and its health

implications to the affected people not only within this study area but to the country at large which will encourage the Government to reconsider our waste management practices as well as discourage residents to stop disposing their waste within their neighborhood and ensure that they treat their water before consumption.

References

Adams D (2001) Lesson 2—interpreting a mineral analysis information sheet. http://animalrangee xtension.montana.edu/LoL/Module3b/3-Mineral2.htm. Accessed 20 June 2016

Afolayan OS, Ogundele FO, Omotayo A (2012) Comparative analysis of the effect of closed and operational landfills in groundwater quality in Solous, Lagos, Nigeria. J Appl Technol Environ Sanit 2(1):67–76

Akinbiyi R (1992) Improving the urban environment. Afr Health 15(1):26–28

Aluko OO (2001) Characterization and treatment of leachate from a municipal solid waste landfill site in Ibadan. MPH dissertation, University of Ibadan, Ibadan, Nigeria, pp 83–85

Amadi AN, Olasehinde PI, Yisa J, Okosun EA, Nwankwoala HO, Alkali YB (2012) Geostatistical assessment of groundwater quality from coastal aquifers of eastern Niger delta, Nigeria. Geosciences 2(3):51–59

Anju A, Dipu S, Salom Gnana Thanga V (2015) Effect of municipal solid waste leachate on ground water quality of Thiruvananthapuram district, Kerala, India. Appl Ecol Environ Sci 3(5):151–157. http://pubs.sciepub.com/aees/3/5/5

APHA (1995) Standard methods for the examination of water and wastewater, 19th edn. American Public Health Association Inc., Washington, DC, New York

APHA (2005) Standard methods for the examination of water and wastewater, 21st edn. American Public Health Association/American Water Works Association/Water Environment Federation, Washington, DC, New York

Ashwani KT, Abhay KS (2014) Hydro geochemical investigation and groundwater quality assessment of Pratapgarh district, Uttar Pradesh. J Geol Soc India 83:329–343

Brodkin E, Copes R, Mattman A, Kennedy J, Kling, R, Yassi A (2007) Lead and mercury exposures: interpretation and action. Can Med Assoc J 176(1):59–63

Civeria AC, Lavado MO (2008) Foreign materials and top soils; test of soil toxicity on boreholes, detrimental effects: physical properties, structural stability and water retention. Am J Chem 1(1):37–43

Ejeona UU, Umah NO (2000) Investigation on environmental hazard in Onitsha physio-chemical properties of soil: soil contamination density, caused by dumpsites. Sci Total Environ 345(1):10–14

Jagloo K (2002) Groundwater risk analysis in the vicinity of a landfill, a case study in Mauritius. M.Sc. thesis, Royal Institute of Technology, Stockholm

Johnson CJ, Bonrud PJ, Dosch TL, Kilness AW, Senger KA, Busch DC, Meyer MR (1987) Fatal outcome of methemoglobinamia in an infant. J Am Med Assoc 257:279–2797

Mohammad IN, Sahil S, Saqib F, Mohammad AD, Jayalakshmi R (2014) The effect of dumping site leachate on groundwater quality. A case study of Srinagar city, India. Int J Civ Struct Environ Infrastruct Eng Res Dev 4(1):1–8. ISSN (P): 2249-6866; ISSN (E): 2249-7978

Mor S, Ravindra K, Dahiya RP, Chandra A (2006) Leachate characterization and assessment of groundwater pollution near municipal solid waste landfill site. Environ Monit Assess 118:435–456

Payne M (2008) Lead in drinking water. Can Med Assoc J 179:253–254. https://doi.org/10.1503/cmaj.071483

Sanborn MD, Abelsohn A, Campbell M, Weir E (2002) Identifying and managing adverse environmental health effects: 3. Lead exposure. Can Med Assoc J 166:1287–1292

Ugwu SA, Nwosu JI (2009) Effect of waste dumps on groundwater in Choba using geophysical method. J Appl Sci Environ Manag 13(1):85–89

World Health Organization (2010) Water for health. In: World Health Organization standard guidelines for drinking water quality

Chapter 22
Groundwater Quality Assessment Using Principal Component and Cluster Analysis

Ahmed Garba, Ahmed Muhd Idris, and Jibrin Gambo

22.1 Introduction

The quality of groundwater is a very serious concern today, either naturally occurring processes or human actions may have a significant influence on the water quality of aquifer that may confine its usage. Understanding the groundwater characteristics is essential for groundwater management. Groundwater quality is shaped by natural and human activities such as climate, geology of the surrounding and agricultural practices. A poor quality of water threatens human health and as a result affects economic development and social prosperity (American Public Health Association [APHA] 2005).

Groundwater usually contains very low levels of trace metals depending upon the composition and the dissolution of the rock which is in interaction with the aquifer (American Society for Testing and Material 2004). The use of groundwater contaminated with trace metals may present environmental and public health risk in the city, depending on the contamination status (Bartram and Balance 1996).

The application of statistical techniques for the study of groundwater data provides an authentic understanding of aquifer and ecological condition and leads to the recognition of the potential sources that determine the groundwater system. This of course will serve as a tool for authentic and good management of water resources and speedy results on pollution problems (Belkhiri et al. 2011).

A. Garba (✉) · A. M. Idris
Department of Science Laboratory Technology, Binyaminu Usman Polytechnic, Hadejia, Nigeria
e-mail: gaahmed@bupoly.edu.ng

J. Gambo
School of General Studies, Binyaminu Usman Polytechnic, Hadejia, Nigeria

22.2 Principal Component Analysis (PCA)

Large datasets are increasingly widespread in many disciplines. In order to interpret such datasets, methods are required to drastically reduce their dimensionality in an interpretable way, such that most of the information in the data is preserved. Many techniques have been developed for this purpose, but principal component analysis (PCA) is one of the oldest and most widely used. Its idea is simple—reduces the dimensionality of a dataset, while preserving as much 'variability' (i.e. statistical information) as possible. Although it is used, and has sometimes been reinvented, in many different disciplines it is, at heart, a statistical technique and hence much of its development has been by statisticians.

This means that 'preserving as much variability as possible' translates into finding new variables that are linear functions of those in the original dataset, that successively maximize variance and that are uncorrelated with each other. Finding such new variables, the principal components (PCs), reduces to solving an eigenvalue/eigenvector problem. The earliest literature on PCA dates from Pearson and Hotelling, but it was not until electronic computers became widely available decades later that it was computationally feasible to use it on datasets that were not trivially small. Since then its use has burgeoned and a large number of variants have been developed in many different disciplines. Substantial books have been written on the subject and there are even whole books on variants of PCA for special types of data. In the formal definition of PCA will be given, in a standard context, together with a derivation showing that it can be obtained as the solution to an eigen problem or, alternatively, from the singular value decomposition (SVD) of the (centred) data matrix. PCA can be based on either the covariance matrix or the correlation matrix. The choice between these analyses will be discussed. In either case, the new variables (the PCs) depend on the dataset, rather than being pre-defined basis functions, and so are adaptive in the broad sense. The main uses of PCA are descriptive, rather than inferential; an example will illustrate this.

PCA stands for Principal Component Analysis. It is one of the popular and unsupervised algorithms that has been used across several applications like data analysis, data compression, de-noising, reducing the dimension of data and a lot more. PCA analysis helps you reduce or eliminate similar data in the line of comparison that does not even contribute a bit to decision making. You have to be clear that PCA analysis reduces dimensionality without any data loss. Principal component analysis, or PCA, is a statistical procedure that allows you to summarize the information content in large data tables by means of a smaller set of "summary indices" that can be more easily visualized and analyzed.

Principal component analysis today is one of the most popular multivariate statistical techniques. It has been widely used in the areas of pattern recognition and signals processing and is a statistical method under the broad title of factor analysis.

PCA forms the basis of multivariate data analysis based on projection methods. The most important use of PCA is to represent a multivariate data table as smaller set of variables (summary indices) in order to observe trends, jumps, clusters and

outliers. This overview may uncover the relationships between observations and variables, and among the variables. PCA is a very flexible tool and allows analysis of datasets that may contain, for example, multicollinearity, missing values, categorical data, and imprecise measurements. The goal is to extract the important information from the data and to express this information as a set of summary indices called principal components.

Principal Component Analysis helps you find out the most common dimensions of your project and makes result analysis easier. Consider a scenario where you deal with a project with significant variables and dimensions. Not all these variables will be critical. Some may be the primary key variables, whereas others are not. So, the Principal Component Method of factor analysis gives you a calculative way of eliminating a few extra less important variables, thereby maintaining the transparency of all information. Is this possible? Yes, this is possible. Principal Component Analysis is thus called a dimensionality-reduction method. With reduced data and dimensions, you can easily explore and visualize the algorithms without wasting your valuable time. Therefore, PCA statistics is the science of analyzing all the dimensions and reducing them as much as possible while preserving the exact information.

The PCA method permits the connection between the variables to be discovered, whereby the dimensionality of the data sets can be reduced. It is a strong method for approaching pattern recognition. PCA illustrated virtually the significant parameters, which depict the whole data set rendering data reduction with minimum loss of original information. In PCA Eigen values are normally used to determine the number of components (PCs) that are retained for further analysis. Number of components is equal to the number of variables in PCA.

22.2.1 Properties of Principal Component

Technically, a principal component can be defined as a linear combination of optimally weighted observed variables. The output of PCA are these principal components, the number of which is less than or equal to the number of original variables. Less, in case when we wish to discard or reduce the dimensions in our dataset. PCs possess some useful properties which are listed below.

PCs are essentially the linear combinations of the original variables, the weights vector in this combination is actually the eigenvector found which in turn satisfies the principle of least squares.

The PCs are orthogonal, as already discussed.

The variation present in the PCs decreases as we move from the 1st PC to the last one, hence the importance.

22.2.2   Guidelines When to Use the Principal Component Method of Factor Analysis?

Sometimes, you may be clueless about when to employ the techniques of PCA analysis. If this is your case, the following guidelines will help you.

You'd like to reduce the number of dimensions in your factor analysis. Yet you can't decide upon the variable. Don't worry. The principal component method of factor analysis will help you.

If you want to categorize the dependent and independent variables in your data, this algorithm will be your choice of consideration.

Also, if you want to eliminate the noise components in your dimension analysis, PCA is the best computation method.

22.2.3   Application of Principal Component Analysis

You can find a few of PCA applications listed below.

PCA techniques aid data cleaning and data preprocessing techniques.

You can monitor multi-dimensional data (can visualize in 2D or 3D dimensions) over any platform using the Principal Component Method of factor analysis.

PCA helps you compress the information and transmit the same using effective PCA analysis techniques. All these information processing techniques are without any loss in quality.

This statistic is the science of analyzing different dimensions and can also be applied in several platforms like face recognition, image identification, pattern identification, and a lot more.

PCA in machine learning technique helps in simplifying complex business algorithms.

Since Principal Component Analysis minimizes the more significant variance of dimensions, you can easily denoise the information and completely omit the noise and external factors.

22.2.4   PCA Applicability to Groundwater Geochemistry Data

PCA is a multivariate statistical procedure designed to classify variables based on their correlations with each other. The goal of PCA and other factor analysis procedures is to consolidate a large number of observed variables into a smaller number of factors that can be more readily interpreted. In the case of groundwater, concentrations of different constituents may be correlated based on underlying physical and chemical processes such as dissociation, ionic substitution or carbonate equilibrium

Table 22.1 Principal component analysis result

	VR1	VR2	VR3	VR4	VR5
pH	− 0.103	− 0.266	− 0.153	− 0.037	− 0.58
Temp	0.066	− 0.057	0.005	0.877	0.181
EC	− 0.292	− 0.729	0.112	0.046	− 0.176
T/H	0.871	− 0.187	− 0.180	− 0.234	0.153
TDS	0.869	0.169	0.341	0.237	0.034
Ca	0.362	0.201	− 0.661	0.069	0.395
Mg	− 0.015	0.497	0.665	0.005	0.288
Cl^-	0.549	− 0.048	0.621	0.305	0.204
NO_3	0.891	0.244	− 0.003	0.063	− 0.179
Fe	− 0.242	0.607	0.109	− 0.483	− 0.178
Cu	0.811	0.285	0.317	0.203	− 0.045
Zn	− 0.144	− 0.027	− 0.08	− 0.043	0.906
Mn	0.346	0.037	0.780	0.050	0.001
Cr	− 0.154	− 0.859	− 0.093	0.116	− 0.127
Pb	− 0.03	0.168	− 0.128	− 0.782	0.289
Eigen values	4.54	2.615	1.974	1.624	1.051
% of variance	30.267	17.431	13.161	10.826	7.006
Cumulative %	30.267	47.698	60.858	71.684	78.690

reactions. PCA helps to classify correlated variables into groups more easily interpreted as these underlying processes. The number of factors for a particular dataset is based on the amount of non-random variation that explains the underlying processes. The more factors extracted, the greater is the cumulative amount of variation in the original data (Table 22.1).

The results indicated that a total five factors were extracted and rotated using the varimax which accounts for about 78% of the total variance, which can be considered used to identify the principal source of variation in the hydrochemistry. The factor loading was grouped according to the criteria of Liu et al. (2003) by which strong, moderate and weak loadings corresponds to absolute loading values of > 0.75, 0.75–0.50, and 0.50–0.30 respectively (Muhaya et al. 2021).

The first component loading accounted for 30.27% of the total variance showed higher loading for TH, TDS, NO_3^-, Cu and Cl^-, with significant contribution from Ca and Mn. It is reasonable to observe a strong positive loading of TH, TDS, NO_3^-, with Cl^-, which possibly results due to leachate from domestic waste release in some part of the area. The higher Cl^- and TDS is an indication that there is a possibility that the groundwater is polluted by sewage, or waste from refuge dumping site. This factor can be labeled as the hardness and anthropogenic.

Second factor (VR2) described 17.43% of total variance, constituting higher loadings for Fe, and higher negative loading for Cr and EC, with significant contribution from Mg. These parameters may be considered to results from the ionic dissolution during groundwater migration. This factor can be labeled as a natural process leading to heavy metal pollution. VR3 accounted for about 13.16% of total variance and constitute loading on Mn, Mg, Cl, and moderate negative loading on Ca with significance contribution from TDS and Cu. The major variables constituting this factor is related to the hydro chemical variables might be from minerals in the groundwater.

Fourth Factor loading (VR4) for dry season accounted for 10.83% of the total variance and represents a higher a loading for temperature and negative higher loading for Pb with significance contribution from Cl^-.

Fifth Factor loading (VR5) for the dry season accounted for 7.01% of the total variance which represent higher loading for Zn with significance contribution from Ca.

22.3 Cluster Analysis

The assumptions of cluster analysis techniques include homoscedasticity (equal variance) and normal distribution of the variables. However, an equal weighing of all the variables requires long transformation and standardization (z-scores) of the data. Comparisons based on multiple parameters from different samples are made and the samples are grouped according to their 'similarity' to each other. The classification of samples according to their parameters is termed Q-mode classification. This approach is commonly applied to water-chemistry investigations in order to define groups of samples that have similar chemical and physical characteristics. This is because rarely is a single parameter sufficient to distinguish between different water types. Individual samples are compared with the specified similarity/dissimilarity and linkage methods are then grouped into clusters. The linkage rule used here is Ward's method. Linkage rules iteratively link nearby points (samples) by using the similarity matrix. The initial cluster is formed by linkage of the two samples with the greatest similarity. Ward's method is distinct from all the other methods because it uses an analysis of variance (ANOVA) approach to evaluate the distances between clusters. Ward's method is used to calculate the error sum of squares, which is the sum of the distances from each individual to the center of its parent group. These form smaller distinct clusters than those formed by other methods.

Cluster analysis has been carried out to substitute the geo-interpretation of hydrogeochemical data. Cluster analysis has been useful in studying the similar pair of groups of chemical constituents of water. The similarity/dissimilarity measurements and linkage methods used for clustering greatly affect the outcome of the Hierarchical Cluster Analysis (HCA) results.

After a careful examination of the available combination of 197 similarity/dissimilarity measurements, it was found that using Euclidean distance

(straight line distance between two points in c-dimensional space defined by c variables) as similarity measurement, together with Ward's method for linkage, produced the most distinctive groups. In these groups each member within the group is more similar to its fellow members than to any other member from outside the group. The HCA technique does not provide a statistical test of group differences; however, there are tests that can be applied externally for this purpose. It is also possible in HCA results that one single sample that does not belong to any of the groups is placed in a group by itself. This unusual sample is considered as residue. The values of chemical constituents were subjected to hierarchical cluster analysis. Based on the indices of correlation coefficients, similar pairs groups of chemical constituents have been linked. Then the next most similar pairs of groups and so on, until all the chemical constituents have been clustered in a dendrogram by an averaging method.

Cluster analysis (CA) is a statistical tool to sort the rightful groups of data according to their similarities to each other. It include broad suite of techniques designed to find groups of similar items within a data set. Hierarchical methods usually give rise to a graphical output called a dendrogram or tree that demonstrates this hierarchical clustering pattern. It categorizes the objects into the stratum on the basis of similarities within a class and dissimilarities between different classes. The result of CA helps in translating the data and suggest pattern.

22.3.1 Requirements of Clustering in Data Mining

The following points throw light on why clustering is required in data mining:

Scalability—We need highly scalable clustering algorithms to deal with large databases.

Ability to deal with different kinds of attributes—Algorithms should be capable to be applied on any kind of data such as interval-based (numerical) data, categorical, and binary data.

Discovery of clusters with attribute shape—The clustering algorithm should be capable of detecting clusters of arbitrary shape. They should not be bounded to only distance measures that tend to find spherical cluster of small sizes.

High dimensionality—The clustering algorithm should not only be able to handle low-dimensional data but also the high dimensional space.

Ability to deal with noisy data—Databases contain noisy, missing or erroneous data. Some algorithms are sensitive to such data and may lead to poor quality clusters.

Interpretability—The clustering results should be interpretable, comprehensible, and usable.

22.3.1.1 Clustering Methods

Clustering methods can be classified into the following categories:

- Partitioning Method
- Hierarchical Method
- Density-Based Method
- Grid-Based Method
- Model-Based Method
- Constraint-Based Method.

22.3.1.2 Applications of Cluster Analysis

Clustering analysis is broadly used in many applications such as market research, pattern recognition, data analysis, and image processing.

Clustering can also help marketers discover distinct groups in their customer base. And they can characterize their customer groups based on the purchasing patterns.

In the field of biology, it can be used to derive plant and animal taxonomies, categorize genes with similar functionalities and gain insight into structures inherent to populations.

Clustering also helps in identification of areas of similar land use in an earth observation database. It also helps in the identification of groups of houses in a city according to house type, value, and geographic location.

Clustering also helps in classifying documents on the web for information discovery.

Clustering is also used in outlier detection applications such as detection of credit card fraud.

As a data mining function, cluster analysis serves as a tool to gain insight into the distribution of data to observe characteristics of each cluster.

22.3.1.3 Points to Remember

- A cluster of data objects can be treated as one group.
- While doing cluster analysis, we first partition the set of data into groups based on data similarity and then assign the labels to the groups.
- The main advantage of clustering over classification is that, it is adaptable to changes and helps single out useful features that distinguish different groups.

22.3.1.4 Clustering Groundwater Geochemistry Parameters

Classification of wells according to their water quality can provide useful information for the users. Complex processes control the distribution of water quality parameters in groundwater, which typically has a large range of chemical composition. The

ground water quality depends not only on natural factors such as the lithology of the aquifer, the quality of recharge water and the type of interaction between water and aquifer, but also on human activities, which can alter these groundwater systems either by polluting them or by changing the hydrological cycle. Sophisticated data analysis techniques are required to interpret groundwater quality effectively Cluster is a group of objects that belongs to the same class. In other words, similar objects are grouped in one cluster and dissimilar objects are grouped in another cluster.

Cluster analysis is used to discover the correlation among the different sampling points. Cluster analysis yields either cluster or groups on the basis of similarity or dissimalarity of variables. Therefore, the cluster analysis is to discover a system of organized observations where a number of groups/variables share properties in common. From the dendrogram (Fig. 22.1), the outcome of cluster analysis lead to the grouping of the boreholes into four (4) distinct groups or clusters based on their similarities (Table 22.2).
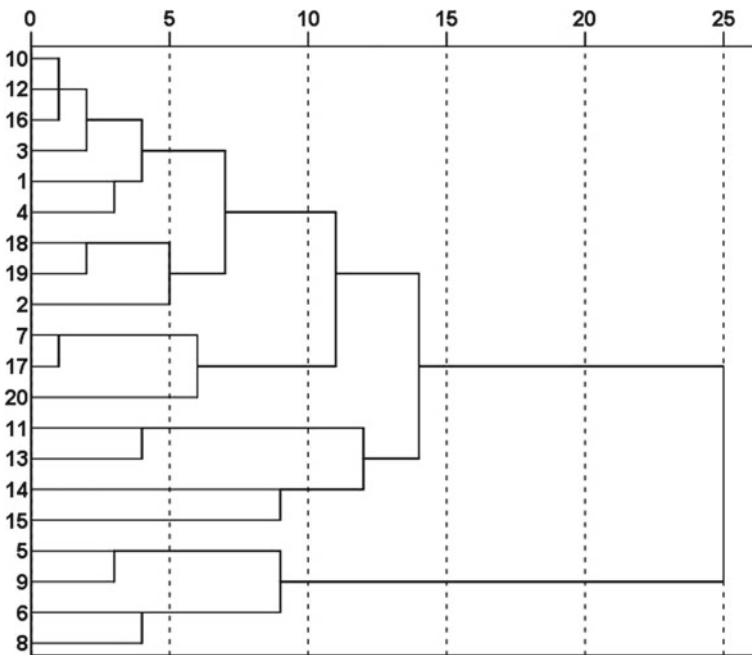

Fig. 22.1 Dendrogram of water sampling sites

Table 22.2 Mean values of geochemistry data

Cluster	pH	Temp	EC µS/cm	TH mg/L	TDS mg/L	Ca mg/L	Mg mg/L	Cl⁻ mg/L	NO₃⁻ mg/L	Fe mg/L	Cu mg/L	Zn mg/L	Mn mg/L	Cr mg/L	Pb mg/L
1 (n = 9)	6.53	27.8	235	154	207	53.8	30.4	1.98	7.35	0.49	0.48	0.34	0.75	0.11	1.57
2 (n = 3)	6.25	27.9	597	151	210	28	28	4.57	1.25	0.53	0.20	0.87	0.98	0.17	1.70
3 (n = 4)	6.38	27.8	286	301	588	44.8	32.5	6.79	29.7	0.29	3.53	0.05	5.56	0.08	1.39
4 (n = 4)	6.76	27.8	1116	145	91	19.7	20.1	0.28	2.78	0.26	0.01	0.03	0.93	0.18	0.99

The underlined values indicated "the value is the lowest among all the clusters"

Samples from cluster 1 is composed of nine (9) boreholes 1, 2, 3, 4, 10, 12, 16, 18 and 19, and constitute 45% of the water samples, and are characterized by high concentration of Ca, and low concentration of Mn and EC in all clusters. Sample from cluster 2 is composed of three (3) boreholes 7, 17 and 20 and constitute 15% of the water samples, and are characterized by high concentration of Fe, Zn and Pb and low concentration of NO_3^- in all clusters. Samples from cluster 3 is composed of four (4) boreholes 11, 13, 14 and 15 and constituted 20% of the water samples, and are characterized by high concentration of T/H, TDS, Mg, Cl^-, NO_3^-, Cu, Mn, and low concentration of Cr in all clusters. The higher values of EC, Total Hardness in some boreholes is obvious because of the solvent action as the water comes in contact with soil and rock is capable of dissolving Ca, Mg and other ions that promote EC and hardnessConductivity or specific conductance is a measure of the ability of water to conduct an electric current. It is sensitive to variations in dissolved solids, mostly mineral salts. The degree to which these dissociate into ions, the amount of electrical charge on each ion, ion mobility and the temperature of the solution all have influence on conductivity.

Samples from cluster 4 is composed of four (4) boreholes 5, 6, 8 and 9 and constituted of 20% of the water samples and are characterized by high values of EC and high concentration Cr and low values of T/H, TDS and low concentration Ca, Mg, Cl^-, Fe, Cu, Zn and Pb in all clusters.

22.4   Conclusion

This study demonstrated the usefulness of the PCA and CA in the interpretation of groundwater quality data by providing useful information on the possible sources that influence the water system and gives guide on effective management of the water resource. PCA was employed to look into the source of each water quality parameters and generated five factors/components with 78.69% total variance, indicating the major variations are related to human action and natural processes. Cluster analysis results sorted the 20 boreholes into four statistically significant clusters based on their similarities. The concentrations of Mn, Cr, and Pb determined were above the maximum permissible limit (Nigerian Standard for Drinking Water Quality (NSDWQ) 2007; Orisakwe 2013). Numerous researchers have reported on adverse effects on human health due to exposure to some of these trace elements in drinking water, for Cr (Ramadan and Haruna 2019; Shrestha and Kazama 2007), Pb (Shrestha and Kazama 2007; Vetrimurugan et al. 2017).

References

American Public Health Association [APHA] (2005) Standard methods for the examination of water and waste water, 20th edn. Washington, DC, pp 65–68

American Society for Testing and Material (2004) Annual book of ASTM standards, water and environmental technology. 11.01, Water (i). ASTM International, West Conshohocken, PA, pp 79–170

Bartram J, Balance R (1996) Water quality monitoring: a practical guide to the design of fresh water quality and monitoring programmes. Chapman and Hall, London, pp 34–39

Belkhiri L, Boudoukha A, Mouni L (2011) A multivariate statistical analysis of groundwater chemistry data. Int J Environ Res 5(2):537–544

Liu CW, Lin K, Kuo YM (2003) Application of factor analysis in the assignment of groundwater quality in blackfoot disease area in Taiwan. Sci Total Environ 313(1–3):77–89

Muhaya BB, Mulongo SC, Kunyonga CZ, Mpomanga WA, Kalonda ME (2021) Assessment of trace metal levels of groundwater in Lubumbashi, Kampemba and Kamalondo communes of Lubumbashi city, Democratic Republic of Congo. J Environ Sci Eng A 10(1):9–25. https://doi.org/10.17265/2162-5298/2021.01.002

Nigerian Standard for Drinking Water Quality (NSDWQ) (2007) Nigerian industrial standard. NIS 554:2007 ICs 13.060.20

Orisakwe KU (2013) Challenge detection analysis of land uses in Hadejia town, Nigeria. Int J Appl Sci Technol 3(3):60–168

Ramadan JA, Haruna AI (2019) Health risk assessment from exposure to heavy metals in surface and groundwater resources with Barkin Ladi, North Central Nigeria. J Geosci Environ Prot 7(2):1–21. https://doi.org/10.4236/gep.2019.72001

Shrestha S, Kazama F (2007) Assessment of surface water quality using multivariate statistical techniques: a case study of the Fuji river basin, Japan. Environ Model Softw 22:464–475

Vetrimurugan E, Brindha K, Elango L, Ndwandwe OM (2017) Human exposure risk to heavy metals through groundwater used for drinking water in an intensively irrigated river delta. Appl Water Sci 7:3267–3280. https://doi.org/10.1007/s13201-016-0472-6

Chapter 23
Sediment Assessment of Medjerda High Valley Dams (Tunisia) Using PISA Model

Sahar Abidi, Nasr Souid, Abderrezak Kamel Toubal, Mohamed Achite, and Lamia Lajili-Ghezal

23.1 Introduction

The total potential of surface water in Tunisia is estimated at 2700 Mm^3, representing an interannual average calculated over a period of about 50 years. The mobilizable resources are estimated at 2170 Mm^3, of which 85% come from flood contributions and 15% from basic contributions. Of this potential, 1800 Mm^3 are already mobilized, a rate of 83% (DGBGTH 2019). The main works of mobilization of surface water (large dams, hill dams and hill lakes) have been built on the rivers of the basins located in the north of the country. These basins are characterized by young reliefs dominated by marl soils and soils vulnerable to erosion, on the one hand, and by a forest cover limited to the most watered parts and a seasonal vegetation cover, on the other hand. In addition to these natural conditions, the torrential nature of the rainfall at the end of the dry season is responsible for erosion and the high solid load of flood waters (Mammou and Louati 2007).

Siltation or siltation is a direct consequence of the degradation of watersheds. In fact, it is currently a concern for water resource planners and [operators] in Tunisia since the national demand for water is still growing. It is therefore essential to address this problem seriously and scientifically in order to implement all its means to ensure the sustainability of existing water reserves.

S. Abidi (✉) · L. Lajili-Ghezal
Silvo-Pastoral Institute of Tabarka, University of Jendouba, Tabarka, Tunisia
e-mail: sahar.abidi@ISPTB.u-jendouba.tn

L. Lajili-Ghezal
e-mail: lamia.ghezal@esamg.u-carthage.tn

A. K. Toubal · M. Achite
Faculty of Nature and Life Science, Hassiba Benbouali University of Chlef, Chlef, Algeria

N. Souid · L. Lajili-Ghezal
Agriculture Higher School of Mogran, University of Carthage, Zaghouan, Tunisia

Based on this observation, our study has as main objective the quantification and evaluation of siltation of the Sidi Salem Dam with the (PISA) model (Previsioni Interimento Serbatoi Artificiali).

Bazzoffi and Van Rompaey (2004) applied PISA model for assessing sediment yield at 44 watersheds, as a volume of humid sediment per watershed area unit. They conclude that the estimated quantity by P.I.S.A. can be considered more consistent than USLE (Universal Soil Loss Equation) or the Ranking index to the quantity measured by OFSF (Off-Farm sediment flow) state indicator, which is detected from direct survey of reservoir sediment or from values of river sediment load, as indicated by OECD (Organisation for Economic Co-operation and Development 2001).

For the first time in Tunisia, Ouechtati and Baldassarre (2011) evaluated the siltation of the Siliana and Lakhmess dams located in the northwest of the country by the PISA model. Based on bathymetry measurements in 2003, the average annual specific erosion of the Siliana dam was 2619 t/km^2/year compared to a value estimated by P.I.S.A. of 3037.6 t/km^2/year; the difference is small. Concerning the Lakhmess dam, the bathymetric measurements carried out in 1991 give an annual specific erosion (pas sure, je n'ai pas bien compris ce que tu voulais dire) average of 800 t/km^2/year compared to the estimated value of 2035 t/km^2/year. PISA has overestimated the erosion in the Lakhmess BV.

For the first time in Algeria, Benkadja et al. (2012) applied the PISA. model for the estimation of the erosion rate in the watershed of oued K'sob (North-East Algeria). The authors concluded that the PISA model is appropriate for estimating soil loss and siltation in the K'sob, as the difference between the estimated value (2915 t/km^2/year) and the one measured by bathymetry (2780 t/km^2/year) is small.

A second application of the PISA model was carried out by Toubal and Achite (2014) on the Mina Watershed located in the North-West of Algeria. Given the importance of the surface of the watershed, the authors applied the model to the sub-watersheds. By summing the siltation indices of each sub-catchment, they obtained a difference between the estimated value and the one measured by bathymetry of 68.02%. By adding the volumes of sediments removed by the draining organs during the operation of the dam between 1978 and 2003 to the rate of siltation measured on the ground, this difference decreases to 6.3%. Thus, Toubal and Achite (2014) found that the P.I.S.A. model is adequate for estimating erosion in the Mina watershed.

23.2 Study Area

Medjerda river is the main Tunisian river. It originates in the semi-arid Atlas Mountains of eastern Algeria. The river then flows east, through the tectonic depression of the Ghardimaou basin (North-West Tunisia), characterized by an 8–10 m thick Holocene floodplain sediments. The Medjerda catchment covers approximately 24,000 km^2, of which 16,100 km^2 located in Tunisia and extends for 460 km including 350 in Tunisia (Faust and Zielhofer 2002). The studied watershed covers the high
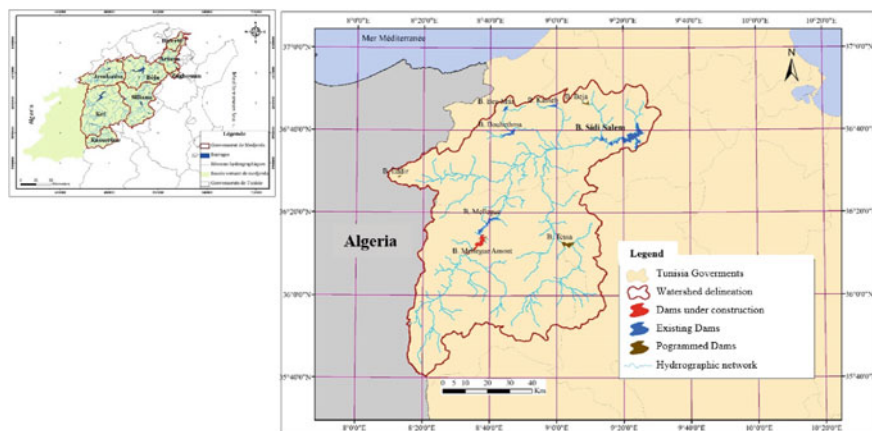
Fig. 23.1 Watershed localization map

plain of Medjerda basin (Fig. 23.1). It represents Sidi Salem dam basin, the most (ou an important) important dam in Mejerda.

With an area of 8649 km^2 and a perimeter of 590 km, the watershed has an elongated shape with a Gravelius coefficient of 1.79 and a relatively long time of concentration of water at the outlet; estimated 37 h (using Giandotti formula, 1934).

The study area is located in an altitude range from 49 to 1299 m. According to the classification of the O.R.S.T.O.M. (now IRD, Institute of Research for Development), the watershed is classified as strong relief with a specific difference in height of 274.5 m. The study of climatic data from four synoptic stations (Beja, Jendouba, Kef and Siliana) over 10 years (2010–2019) shows that the study area is located in a semi-arid climate zone.

23.3 Methodology

PISA model was developed to assess reservoir sedimentation (Bazzoffi 1987; Bazzoffi and Baldassarre 1996; Bazzoffi et al. 1998).

The conceptual basis of PISA model comes from the studies conducted on a wide range of environments since 1950s that demonstrated the dependence of sediment yield from measurable variables of the stream watershed as relief, geological characteristics (Jansen and Painter 1974; Judson and Ritter 1964; Ahnert 1970) drainage area (Walling 1983) rainfall and soil use that appears to be much more weighty than natural factors in sediment yield process (Renwick 1996).

The most recent version of PISA derives from the analysis of 44 watershed-reservoir systems spread all over the Italian Territory (Paolo and Anton 2004).

The model of prediction of siltation in artificial reservoirs (PISA) (in Italian: Previsionni Intermento Serbatoi Artificiali) is a parametric statistical model of

multiple linear regression, designed for the evaluation of sedimentation in reservoirs. It has been formulated to be easily and quickly applicable without the need for data collected directly in the field, but from input variables obtained from traditional mapping and time series analysis of hydrological variables (Ouechtati and Baldassarre 2011).

According to Bazzoffi (2000), the prediction of the solid supply in a BV with PISA, allows to reduce the arrivals of sediments at the level of the dam and the resulting negative impacts on the environment.

PISA model is based on climatic, morphological and physical parameters of the watershed, which can provide a prediction of the average annual sedimentation rate in artificial reservoirs expressed in m^3/km^2. It then allows an indirect estimation of soil erosion upstream of the dam (Bazzoffi and Van Rompaey 2004; Benkadja et al. 2012):

$$Y = 425.9334 - 1.3898A + 102.9576(S_{ER})^{0.5} - 9.84435S_l - 0.31\overline{p} + 116.718D \tag{23.1}$$

With:

Y: Sedimentation index expressed as the annual volume of wet sediment poured into the dam per unit area of the watershed (m^3/km^2);

A: Watershed area (km^2);

S_{ER}: Erodible surface (km^2); $S_{ER} = S_c + \left(\frac{1}{16}\right)S_{nc}$;

S_c: Cultivable surface, it concerns the agricultural lands (km^2);

S_{nc}: Non-cultivated agroforestry surface (km^2);

S_l: Average slope of basin (%); $S_l = \frac{d.L}{A}$;

d: Equidistance between two contour lines (m);

L: Total length of the contour lines (km);

$\overline{p}$: Average annual precipitation (mm) using Thiessen method for interpolation;

D: Density of drainage; $D = \frac{\sum_{i=1}^{n} L_i}{A}$;

Li: Length of the rivers (km).

To determine the different parameter of the model, we must elaborate Digital Elevation Model, Cover Soil, Slope, Hydrographic Network, Hypsometric (contour) and Average Precipitation maps.

We use the Shuttle Radar Topography Mission (SRTM) image (30 m resolution), to extract Digital Elevation Model, Hydrographic Network, Contours and slope maps.

The Erodible surface is extracted from the cover soil map which is established based on FAO data published in 2001 using the Land Capability Classification.

To determine the average annual precipitation, we collect data from 16 stations covering the basin (Fig. 23.2) for the period 1980–2015. The filling of missing data is done by using the data of the most correlated stations to those that have gaps according to Mus method (Wampler and McEacharn 2005). The average precipitation is determined using spatial interpolation by Thiessen polygon method.
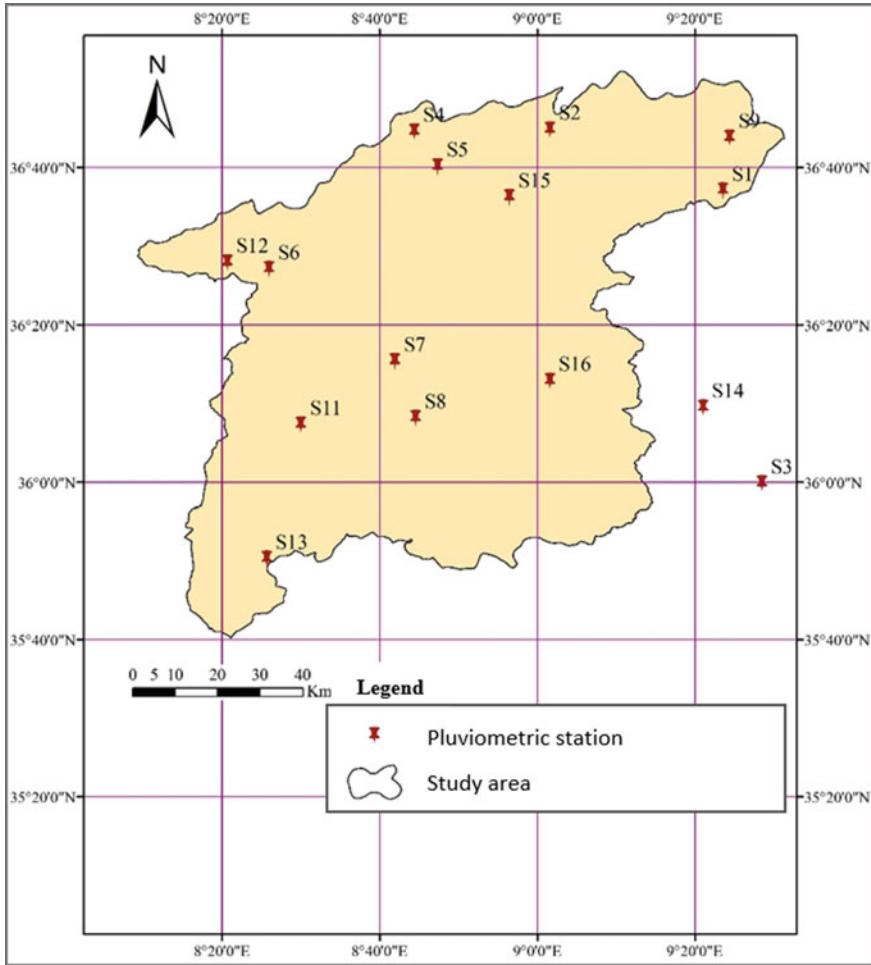
Fig. 23.2 Rainfall gauging stations localization

23.4 Results

A clear presentation of experimental results obtained, highlighting any trends or points of interest. Please use the decimal system of headings with no more than four levels.

23.4.1 Inputs Preparation

Using ArcGis software, we dressed the different maps. The Digital Elevation Model map shows the variation of the elevation in the basin (Fig. 23.3a); from 299 to 1299 m. From the SRTM 30 m (Shuttle Radar Topography Mission), we extract the hydrographic network (Fig. 23.3b), and we use Strahler method to classify the rivers, the main river (order 7) has a length of 151 km. The slope (Fig. 23.3c) varies between 0 and 65°: the minimum slope (0–3°) covers 26% of the basin area, an average slope (5–10°) covers 32% of the basin area and the rest of the basin has a high slope. The cover soil map (Fig. 23.3d) shows 16 cover classes illustrated in Table 23.1. 30% of the basin is covered by vegetation of cultivated land, and 30% are covered by Mosaic Vegetation, and 26% by non-irrigated cultivated land.

As we mentioned, the average rainfall is determined based on the spatial interpolation using Thiessen polygon method (Fig. 23.4); the value is 477 mm.

23.4.2 Model Application

With an Erodible surface of 7629, an average Slope of 15.5 Grade, an average annual precipitation of 477 mm and a Density of drainage 1.58 (km/km^2), we applied the P.I.S.A. model for the evaluation of the siltation of the Sidi Salem Dam, we found a value of -2718 m^3/km^2/year. Which is an aberrant value, we then proceed to the sensitivity study of the model to find the error reason. We analyzed the influence of each parameter on the value of the sedimentation index Y (Fig. 23.5).

We note that, the erodible surface seems to have a significant influence on the sedimentation rate compared to the other parameters i.e., the larger the erodible surface, the higher the sediment production and they have almost the same rate of variation.

Since the erodible surface depends on the surface of the watershed and referring to the methodology adopted by Toubal and Achite (2014) on the Mina basin (Algeria), we will subdivide the study area into sub-basins to reduce the surface (then the erodible surface) in order to improve the application results of P.I.S.A.

The watershed of Sidi Salem dam has been divided into 7 sub-basins (Fig. 23.6), based on the surfaces drained by the existing dams and the important tributaries. For each sub-basin, the parameters of the model are calculated (Table 23.2), and the sedimentation index are determinate (Table 23.3). So, the sedimentary index of the basin is the sum of the sub-basins' index. The events chosen for the study, are 6 bathymetric companions (1987, 1989, 1991, 1998, 2002 and 2006) of Sidi Salem dam.
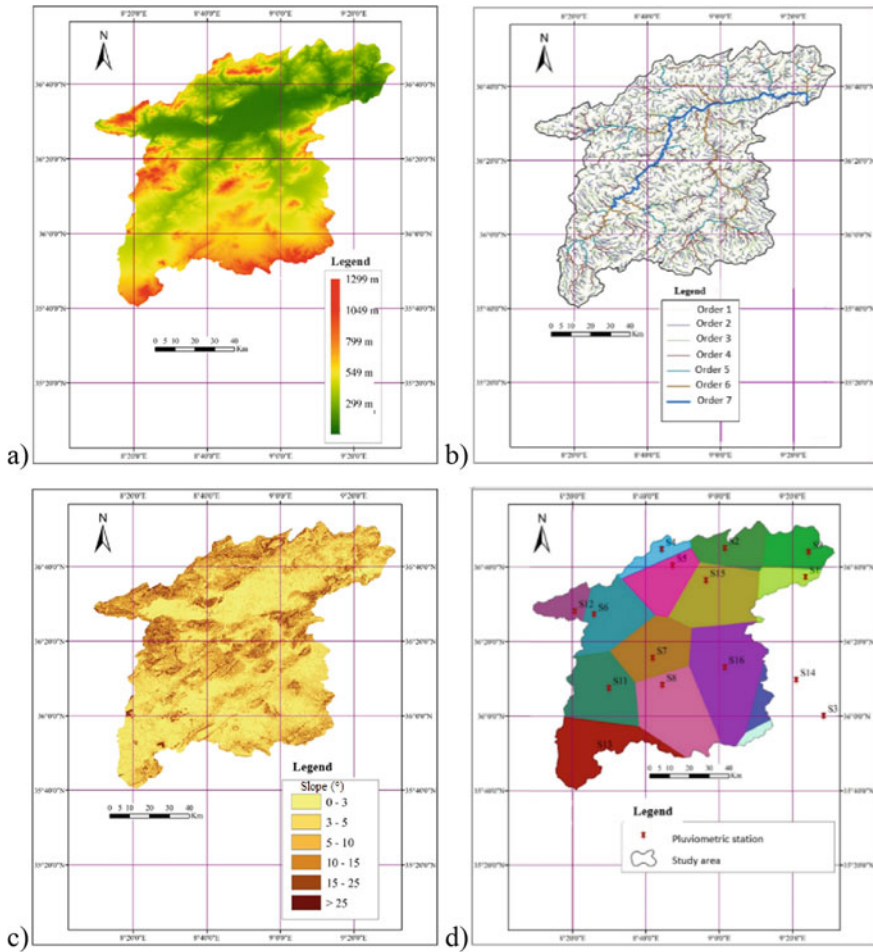
Fig. 23.3 **a** Digital elevation method, **b** hydrographic network map, **c** slope map, **d** Thiessen polygon map

23.5 Discussion

The sub-basin 1 holds the highest quantities of sediment production in all the years of bathymetry, with a maximum value of 2225.3 m^3/km^2/year in 1989, while the minimum quantities for all the companies were found in the sub-basin 6 with a maximum value of 1742 m^3/km^2/year in 1989.

The variability of the interannual sedimentation rates of the sub-basins is physically explained by:

The importance of erodible surface vulnerable to water erosion,

The spatial and temporal variability of precipitation,

The detachability and washout of particles.

Table 23.1 Soil occupation classes

Object	CLC code	% of area contributing to erodible area parameter	Soil use
C1	313	6.25	Forest and semi natural areas—mixed forest
C2	311	6.25	Forest and semi natural areas—broad-leaved forest
C3	312	6.25	Forest and semi natural areas—coniferous
C4	244	6.25	Agro-forestry areas
C5	241	100	Annual crops associated with permanent crops
C6	242	100	Complex cultivation patterns
C7	512	0	Water bodies
C8	243	100	Land occupied by agriculture, with significant areas of natural vegetation
C9	321	6.25	Scrub and/or herbaceous vegetation association—natural grasslands
C10	322	6.25	Scrub and/or herbaceous vegetation association—moors and heathland
C11	333	6.25	Opens spaces with little or no vegetation—sparsely vegetated areas
C12	211	100	Arable land—non-irrigated arable land
C13	333	6.25	Opens spaces with little or no vegetation—sparsely vegetated areas
C14	324	6.25	Scrub and/or herbaceous vegetation association—transitional woodland scrub
C15	323	6.25	Scrub and/or herbaceous vegetation association—sclerophyllous vegetation
C16	332	6.25	Open spaces with little or no vegetation—bare rocks

The quantification of sediments conveyed to the outlet of Sidi Salem basin consists in the sum of sediment produced by each sub-basin. Figure 23.7 represents the evolution of the volume of sediments over time.

It is noted that in a period of 19 years between 1987 and 2006 the volume of silt has multiplied 4 times which is explained in this case by the variability of climatic factors related mainly to rainfall.

The validation of the results of P.I.S.A. model, was carried out from the comparison with the bathymetric measurements from DGBGTH (2006). The difference between
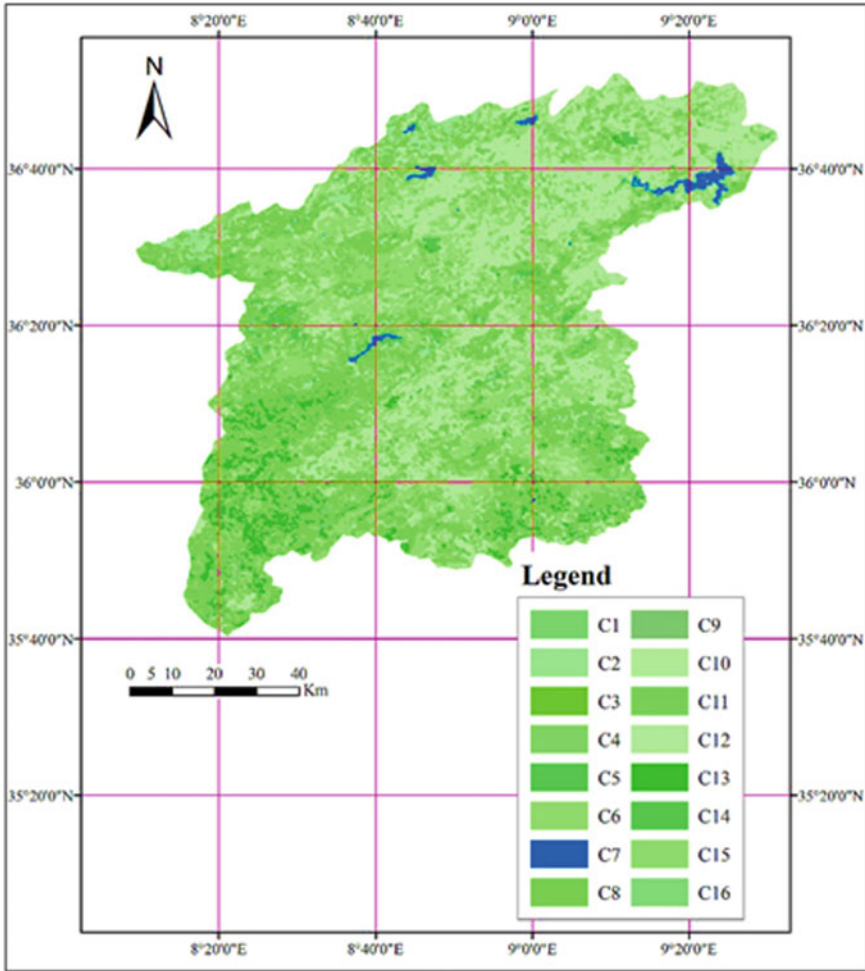
Fig. 23.4 Cover soil map

the values of cumulative siltation estimated by P.I.S.A. model and the cumulative siltation measured at Sidi Salem Dam from 1987 to 2006 is calculated by the formula:

$$\Delta' = \frac{Y - Y'}{Y'} \tag{23.2}$$

with:

Δ': Siltation deviation between the P.I.S.A. model and the bathymetric survey,
Y: Siltation of the SS dam estimated with the P.I.S.A. model (Mm^3),
Y': SS dam silting measured by bathymetric survey (Mm^3).
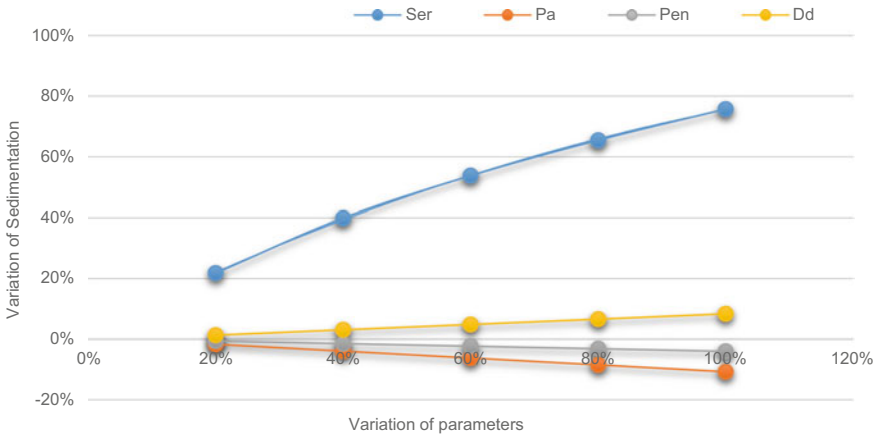
Fig. 23.5 Sensitivity analysis of P.I.S.A. Ser: erodible surface, Pa: average precipitation, Pen: average slope and Dd: drainage density

The application of P.I.S.A. model in the watershed of Sidi Salem dam (Table 23.4) tends to overestimate the value of siltation in comparison with the bathymetric survey for the years from 1987 to 1998, and underestimate for 2002 and 2006.

The application of this model in Tunisia for the first time by Ouechtati and Baldassarre (2011) reveals an overestimation of sediment rate double the measured value of Siliana dam and 4 times of Lakhmess dam. For the first time in Algeria, P.I.S.A. model was applied by Benkadja et al. (2012), the results found are almost similar to those found by Ouechtati and Baldassarre (2011), as the assessment of siltation of K'sob dam was 3 times higher than the values obtained by bathymetric measurements.

For our case the results are acceptable with deviation varied from 1.14 to 1.19%. for the years 2002 and 2006, the difference between estimated and measured is very low about 20 and 54 Mm^3. So, the model gave satisfactory results for siltation estimation. Even tis results, we need to ameliorate more the estimation by analyzing deeper the erodible surface since it's the sensitive parameter of P.I.S.A. model and the coefficients fixed by Benkadja et al. (2012).
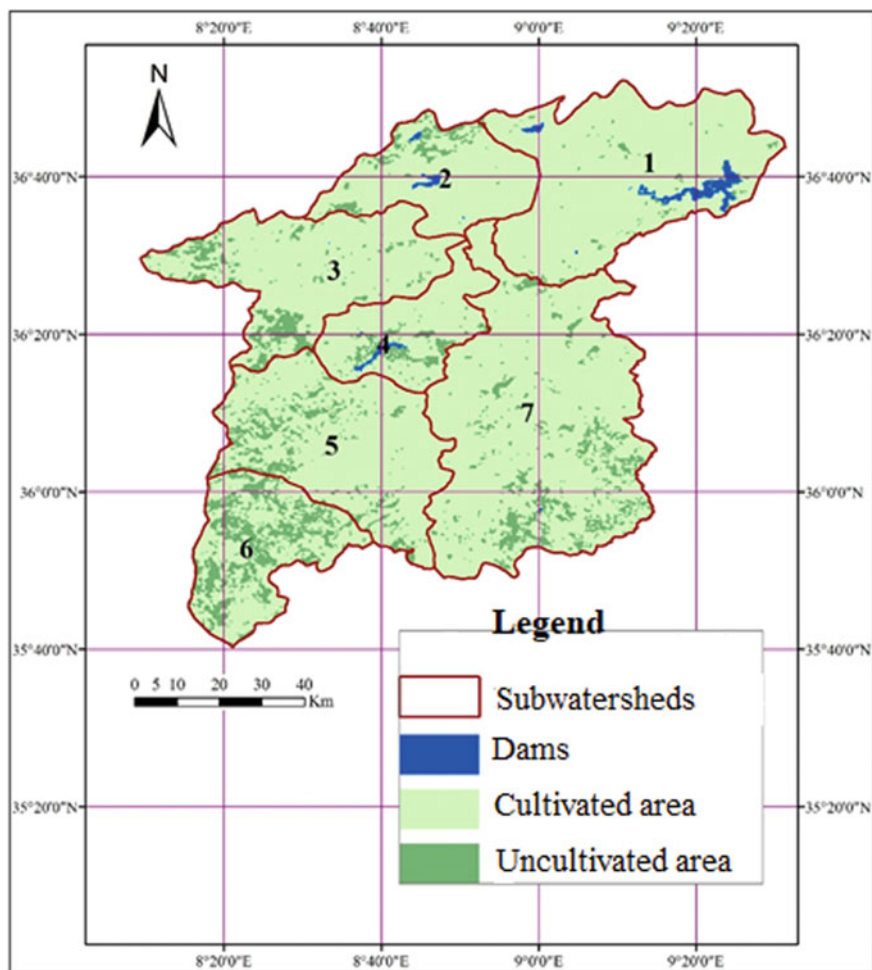
Fig. 23.6 Sub-basins of the study area

Table 23.2 Model parameters in each sub-basin

Sbw	A (km^2)	Erodible surface (km^2)	S$_l$ (grade)	D$_d$ (km/km^2)
1	1597.58	1557.33	9.19	1.58
2	737.92	671.04	10.41	1.48
3	1164.51	1023.79	11.93	1.52
4	599.85	514.69	10.45	1.60
5	1323.07	1149.48	9.10	1.61
6	820.22	553.18	7.68	1.65
7	2405.75	2159.58	9.10	1.65

Table 23.3 Sedimentation index of the sub-basins ($m^3/km^2/year$)

Year	1987	1989	1991	1998	2002	2006
SB 1	2187.4	2225.3	2205.8	2203.1	2204.0	2144.5
SB 2	1894.3	1935.0	1922.6	1915.9	1921.1	1828.8
SB 3	2006.0	2042.3	2016.0	2013.7	2002.6	1954.8
SB 4	1901.5	1931.4	1901.8	1902.8	1894.8	1850.2
SB 5	2068.1	2084.4	2060.4	2073.6	2071.0	2038.8
SB 6	1722.7	1742.1	1699.1	1732.9	1728.0	1701.3
SB 7	1854.2	1866.8	1843.2	1850.6	1842.5	1802.2
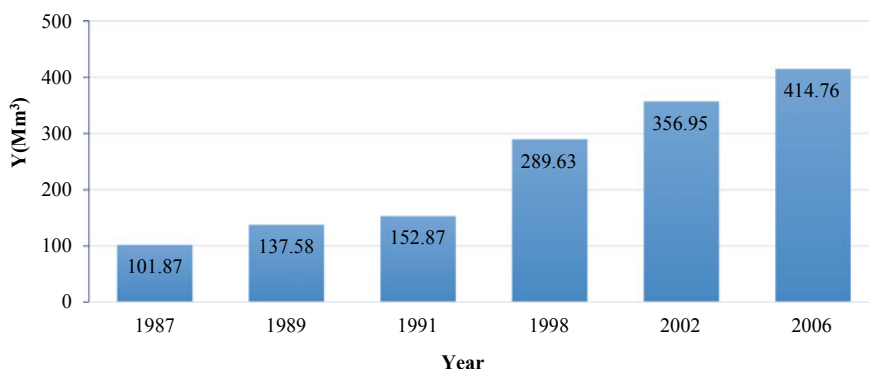
Fig. 23.7 Evolution of sediments' volume in Sidi Salem basin (1987–2006) (Mm^3)

Table 23.4 Difference between the P.I.S.A. model and the bathymetric survey

Year	Y estimé (Mm^3)	Y'mesuré (Mm^3)	Δ' (%)
1987	118	31	1.17
1989	120	47	1.19
1991	118	52	1.17
1998	118	87	1.17
2002	119	139	1.18
2006	115	169	1.14

23.6   Conclusions

This paper aimed to quantify and evaluate the siltation in the Sidi Salem Dam with the (PISA) model (Previsioni Interimento Serbatoi Artificiali). The evolution of silt in Sidi Salem basin is conditioned by climatic, morphological and physical factors of the watershed which are taken into consideration by the PISA model which shows that the siltation of the basin is a non-linear phenomenon over time. The application of the

PISA model gives a negative value then after a sensitivity study of the sedimentation index Y and referring to the methodology adopted by Toubal and Achite (2014) on the Mina BV (Algeria), we subdivided the BV into sub-BV to reduce the surface (then the erodible surface) in order to improve the results of application of PISA The results were satisfactory with a variable distribution of sediment production between 1.14 and 1.19%. Adding the siltation indices of each sub-basin, we obtain a sedimentation rate of 115 Mm^3 in 2006. This result is underestimated comparing to the bathymetric survey evaluated at 169 Mm^3; a difference of 1.14%. PISA model gave acceptable estimation of siltation especially for the years 2002 and 2006. We need to analyze deeper the parameters and calibrate the coefficients to get ameliorated results.

References

Ahnert F (1970) Functional relationship between denudation, relief and uplift in large mid-latitude drainage basins. Am J Sci 268:243–263

Bazzoffi P (1987) Previsione dell'interrimento nei serbatoi artificiali italiani, modello P.I.S.A. Idrotecnica 1:15–18

Bazzoffi P (2000) Methodology for the survey of a tillage erosion indicator based on precision aerophotogrammetry. In: Bini C (ed) Atti Conv. Naz. Scienza del Suolo, pp 239–249

Bazzoffi P, Baldassarre G (1996) Validation of PISA2 model for automatic assessment of reservoir sedimentation. In: Albertson M (ed) Proceedings of the international conference on reservoir sedimentation. Colorado State University

Bazzoffi P, Van Rompaey A (2004) PISA model to assess off-farm sediment flow indicator at watershed scale in Italy. In: Agricultural impacts on soil erosion and soil biodiversity: developing indicators for policy analysis. OECD, Paris, France. www.oecd.org/tad/env/indicateurs

Bazzoffi P, Pellegrini S, Rocchini A, Morandi M, Grasselli O (1998) The effects of urban refuse compost and different tractors tyres on soil physical properties, soil erosion and maize yield. Soil Till Res 48:275–286

Benkadja R, Hattab A, Mahdaoui N, Zehar C (2012) Assessment of soil losses and siltation of the K'sob hydrological system (semiarid area—East Algeria). Arab J Geosci. https://doi.org/10.1007/s12517-012-0653-z

DGBGTH (2006 & 2019) Situation of Medjerda dams

Faust D, Zielhofer C (2002) Reconstruction of the Holocene water level amplitude of Oued Medjerda as an indicator for changes of the environmental conditions in Northern Tunisia. Z Geomorphol Suppl 128:161–175

Giandotti M (1934) Previsione delle piene e delle magre dei corsi d'acqua. Ist Poligr Stato 8:107–117

Jansen JM, Painter RB (1974) Predicting sediment yield from climate and topography. J Hydrol 21:371–380

Judson S, Ritter DF (1964) Rates of regional denudation in the United States. J Geophys Res 69:3395–3401

Mammou A, Louati M (2007) Évolution temporelle de l'envasement des retenues de barrages de Tunisie. Rev Sci L'eau/J Water Sci 20(2):201–210

OECD (Organisation for Economic Co-operation and Development) (2001) Environmental indicators for agriculture. In: OECD (ed) Methods and results, vol 3, 409 pp

Ouechtati S, Baldassarre G (2011) Evaluation du transport solide et de l'envasement dans le bassin versant de Siliana (Tunisie): cas des barrages Siliana et Lakhmess. Bull Eng Geol Environ 70(4):709–722

Paolo B, Anton VR (2004) PISA model to assess off-farm sediment flow indicator at watershed scale in Italy. In: Francaviglia R (ed) Agriculture impacts on soil erosion and soil biodiversity: developing indicators for policy analysis. Proceedings from an OECD expert meeting, Rome, Italy, Mar 2003, pp 1–10

Renwick WH (1996) Continent-scale reservoir sedimentation patterns in the United States. IAHS Publ 236:513–522

Toubal AK, Achite M (2014) Evolution de l'envasement du barrage Sidi M'hamed Ben aouda dans le bassin versant de la Mina par l'application du modèle PISA. In: 3ème Séminaire nationale sur l'eau et l'environnement (SEE'2014)

Walling DE (1983) The sediment delivery problem. J Hydrol 65:209–237

Wampler B, McEacharn M (2005) Monetary-unit sampling using Microsoft Excel. CPA J 75(5): 36–40

Chapter 24
Impact Assessment of Inland Desalination Units on Groundwater Quality and Levels in Kuwait

Harish Bhandary

24.1 Introduction

Kuwait has three main agricultural areas, namely, Abdally in the north, Wafra in the south, and Sulaibiya in the central part. Agricultural activities in arid regions, like Kuwait, require great amount of water supply for irrigation. Saline groundwater quality, shortage in the treated wastewater supply and expensive freshwater have caused farmers to use on-site brackish groundwater reverse osmosis (RO) units to treat the saline groundwater. There are plenty of agricultural farms in Kuwait using RO units to treat the brackish groundwater to get the freshwater supply for agricultural activities. The continuous and uncontrolled extraction of groundwater has resulted in the increase of salinity and decline in the water table of groundwater (Akber et al. 1999; Fadlelmawla and Al-Otaibi 2005). The limitation of these RO units is the large volume (30–40% of feed water) of concentrated brine (reject water) they produce and their disposal mechanism (Mohamed et al. 2005). Yet, there have been no proper policy and regulations implemented by the authorities to handle this reject water from the RO units. Most of the time, brine reject water is disposed over open land surface or unlined pits. These reject brine water contains concentrated organic salts, small amount of anti-scalants, washing solutions, backwash slurries, and other chemicals used for the maintenance of RO units (Mohamed et al. 2005). This brine water with contaminants can reach groundwater table. Moreover, rapid increase in the number of agricultural farms and uncontrolled pumping of groundwater would drop the groundwater level drastically. Therefore, sustainable management of water resources is important in order to manage water systems to fully contribute to the needs of society at all times, while preserving their environmental, ecological, and hydrological integrity (Loucks 1997). Kuwait has established three agricultural areas to ensure partial food security since the early 70s (Fig. 24.1). There has been a steep

H. Bhandary (✉)
Water Research Center, Kuwait Institute for Scientific Research, P.O. Box 24885, Safat, Kuwait
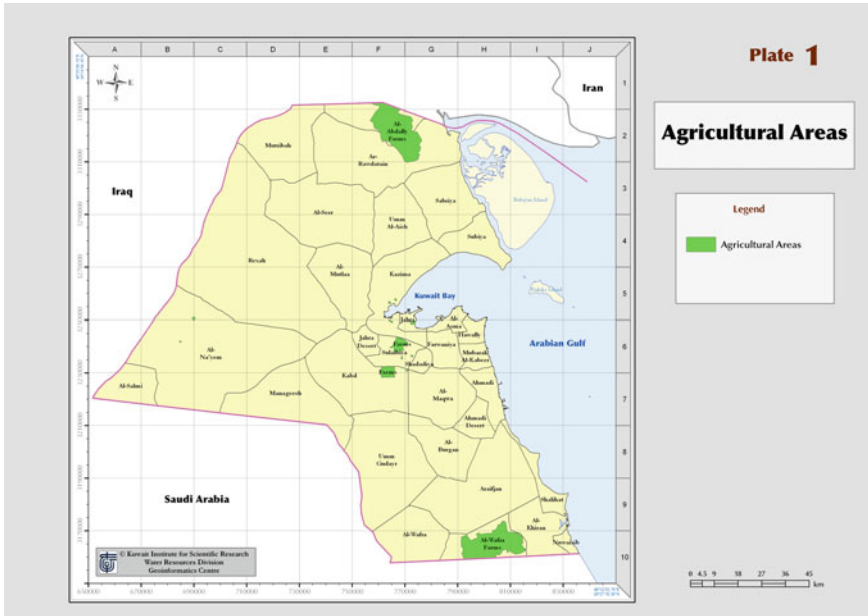e-mail: hkaup@kisr.edu.kw

Fig. 24.1 Agricultural areas of Kuwait (Fadlelmawla et al. 2009)

increase in the number of farms and wells in these areas that is, an area of 1125 ha with 127 farms and 100 wells in 1976 increased to over 37,500 ha with 1673 farms and 2119 wells in 2008 (Al-Murad et al. 2010).

Irrigated agriculture is practiced in Wafra, abstracts groundwater from the two main aquifers, the unconfined Kuwait Group (KG), and the confined Dammam aquifer. The crops grown in the Wafra farms are perennial. The commonly grown crops are seasonal vegetables and fruits with substantial area under alfalfa cultivation (Al-Murad et al. 2016). Crop production in Kuwait provides some 56% of the gross value of agricultural production with animal production providing 38% and fish and bees, the remaining. Self-sufficiency is about 93% in dates and almost 50% in vegetables; however, for fodders, the available information run counter with other sources (the most reported percent is 60%). Based on the 2011/2012 data, there were more than 12 fruity vegetable crops and more than 20 leafy vegetables, including herbs, that are produced in Kuwait. The most valuable crops among the vegetables are potato, cucumber, tomato, coriander, parsley, and peppers (hot and sweet) in descending order as to their value (FAO 2013).

The study area, Al-Abdally is located north of Kuwait (Fig. 24.1), is one of the agricultural areas where the shallow groundwater bodies in the Kuwait Group Aquifer have been subjected to excessive extraction for agriculture and related purposes. The aquifer is recharged by the lateral flow of brackish water and by direct percolation of precipitation during the rainy season. The ground elevation of the study area (Fig. 24.2) ranged from 5 to 60 m. The depressions formed due to these uneven
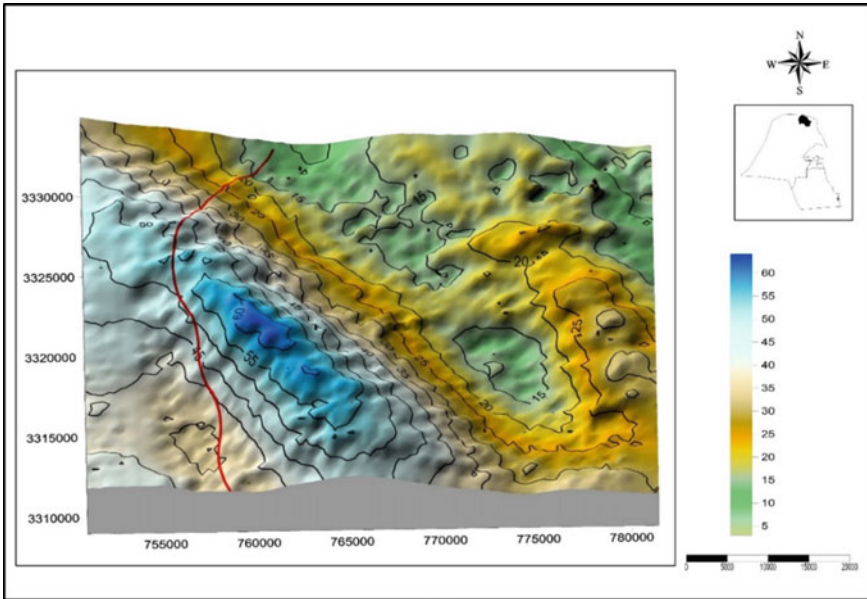
Fig. 24.2 Ground elevation at the study area

elevations forms temporary water lakes during rain events. The eastern part is elevated and gradually reduces towards Arabian Gulf. The salinity levels in the upper horizon are influenced mostly by rainfall infiltration, and to a lesser extent, by the freshwater flow from the neighboring Raudhatain depression. The groundwater quality in the lower horizon is of brackish quality and becomes more saline with depth (Senay 1985). Farming activities in Al-Abdally were started in the early 1960s. Since then, the farming areas have been increasing in size and number. The number of farms increased from 260 farms in 1989 (Al-Sulaimi et al. 1994) to 1012 farms in 2009 covering an area of over 180 km^2 (PAAFR 2009). The expansion of the farm area is associated with an increase in groundwater consumption for irrigation and other purposes. The groundwater is being extracted very heavily through more than 1436 pumping wells and 79 hand-dug wells (PAAFR 2009). Groundwater level contour for the year 2010 in presented in Fig. 24.3.

24.2   Methodology

Groundwater levels and salinity were measured in 20 monitoring wells of the study area. The water samples were collected from groundwater wells (RO feed water), product water, and brine water (RO reject). Collected water samples were analyzed for Na, K, Ca, Mg, Cl, SO$_4$, F, Br using ion chromatograph (method no. 4110),
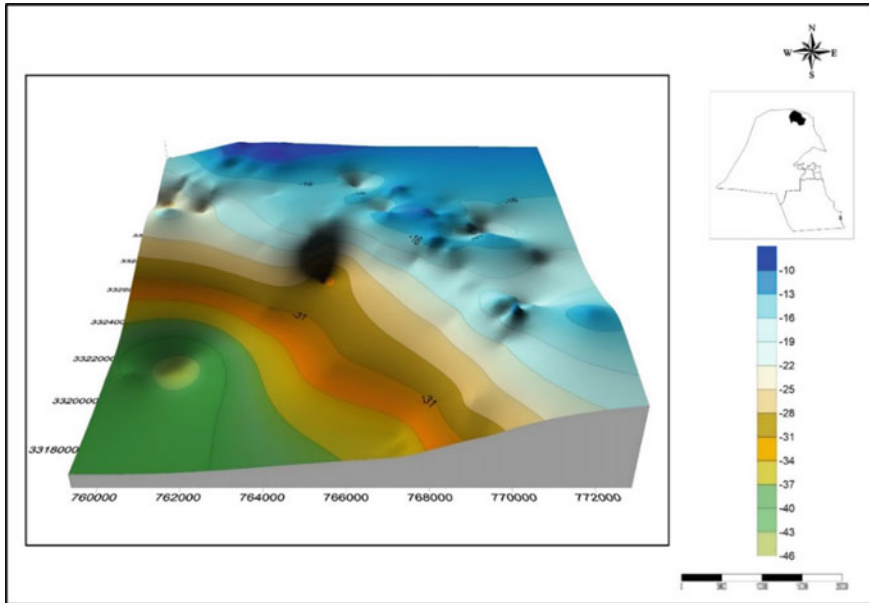
Fig. 24.3 Ground level at the study area during the year 2010

NO_3, NH_3, PO_4, and silicate (SiO_3) using discrete analyzer (method no. 4130), trace metals (Fe, Mn, V, Li, Sr, B, Al, Cu, Zn, Cd) were analyzed using ICP-OES (method no. 3120) in Water Research Center Laboratory at Kuwait Institute for Scientific Research. The standard methods have been adopted to analyze the water quality parameters in the laboratory as explained in the standard methods for the examination of water and wastewater (APHA 2015). This study will be concluded after conducting pumping test, geochemical modelling, and numerical modelling.

24.3 Results and Discussion

Groundwater levels and salinity were measured in 20 monitoring wells of the study area (Fig. 24.4). Two monitoring wells at the same location tapping upper and lower aquifers having screens at two different depths. The data was then compared with the water level and salinity data of the year 2010 (Table 24.1). The measured groundwater level ranged from 19.6 to 52.8 m with an average groundwater table of 29 m. Comparison of current groundwater level to the year 2010 showed decline in the groundwater table from 3.3 to 8 m, with the average decline of 4.6 m in a single decade (Fig. 24.5). Accordingly, the salinity comparison also showed maximum increase in salinity up to 4000 mg/L with an average increase of 2000 mg/L in a decade time (Fig. 24.6).
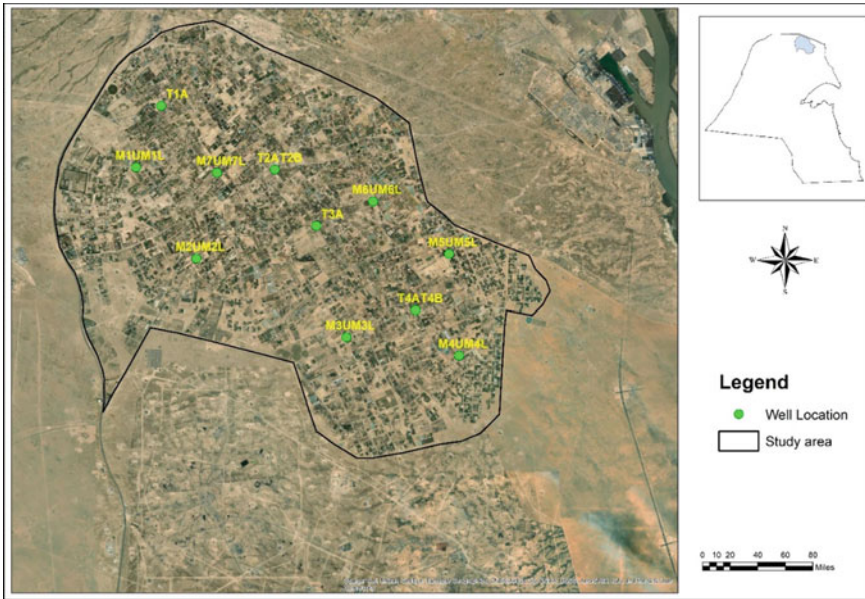
Fig. 24.4 Location of groundwater monitoring wells in the study area

Water samples were collected from 20 farms using brackish RO units (Fig. 24.7). The minimum, maximum and average of water quality parameters are presented in Table 24.2. Groundwater in the study area is dominated with Na–Cl water type followed by Na–SO$_4$ type (Fig. 24.8). Groundwater salinity ranged from 6885 to 15,128 mg/L with an average of 10,592 mg/L. The dominance of major ions is as follows; Cl > SO$_4$ > Na > Ca > Mg > NO$_3$ > HCO$_3$ > K. High sulphate concentration in the groundwater is due to the presence of gypsum in the aquifer materials and high nitrate concentration is attributed to the usage of fertilizers in the study area. Trace elements are found in very low concentrations. The salinity of produced water from the insitu desalination units ranged from 24 to 862 mg/L with an average of 372 mg/L and no significant concentration of trace elements detected. Brine reject water from the insitu desalination units had average salinity of 15,642 mg/L, which ranged from 9300 to 24,400 mg/L. Trace metals concentration in brine reject water are found to be higher for Al, Zn and Fe.

24.3.1 Brine Disposal

Brine water produced from the desalination plants is disposed to the environment using various methods (Mickley 2018). Different methods of brine water disposal from RO treatment units are given by Khordagui (1997). These methods are the following:

Table 24.1 Comparison of groundwater level and groundwater salinity

Well No.	Location		Screen interval [a](mbgs)	TDS (mg/L)		Groundwater level [a](mbgs)	
	East	North		2010	2021	2010	2021
M1U	759,583	3,324,095	44.3–49.5	9027	12,610	37.75	42.53
M1L	759,583	3,324,095	68.0–73.0	12,510	15,600	37.50	41.10
M2U	762,518	3,319,641	51.0–56.7	3891	4946	45.20	49.85
M2L	762,518	3,319,641	80.0–85.0	5117	6610	44.84	52.80
M3U	769,810	3,315,830	31.0–36.0	5924	6818	29.34	33.70
M3L	769,810	3,315,830	42.8–48.0	5820	6435	29.22	33.80
M4U	775,284	3,314,937	28.0–33.0	7380	7644	17.75	24.26
M4L	775,284	3,314,937	62.0–67.0	25,400	23,730	17.76	24.42
M5U	774,801	3,319,875	18.0–23.0	5296	7624	15.73	20.50
M5L	774,796	3,319,872	42.0–47.0	6912	10,809	15.73	20.67
M6U	771,099	3,322,432	18.0–23.0	6487	10,625	16.60	20.37
M6L	771,099	3,322,432	52.0–57.0	6090	7377	16.52	20.43
M7U	763,510	3,323,838	33.7–38.7	5468	6883	26.66	30.20
M7L	763,515	3,323,834	57.4–62.4	8020	9204	26.73	30.40
T1A	760,804	3,327,098	28.0–58.0	3207	5219	23.70	27.00
T2A	766,338	3,323,980	11.5–35.5	5327	7286	19.05	22.68
T2B	766,328	3,323,988	41.5–59.5	4628	4712	18.80	22.55
T3A	768,342	3,321,245	11.0–34.0	7852	10,777	21.55	25.32
T4A	773,165	3,317,137	39.8–57.0	3545	6409	14.38	19.71
T4B	773,165	3,317,137	32.0–44.0	5758	8000	14.38	19.64

[a]*mbgs* meters below ground surface

Discharged into well-engineered solar evaporation pond
Disposal to wastewater system
Land application (includes spray irrigation and percolation ponds)
Injection into deep saline aquifers (nondrinking water aquifers)
Disposal into land surface
Disposal into the sea through a pipeline.

As per the survey conducted by studies (Ahmed et al. 2001, 2000) on the brine disposal techniques of 23 RO units in UAE, Oman, and the Jordan, disposal to the evaporation ponds dominated, followed by utilization of brine water in irrigation after dilution, disposal of brines in deep boreholes, shoreline, wadi beds, and the ocean in the order of their use. Table 24.3 summarizes the different methods for brine disposal in the USA. The special brine disposal technique could make the RO system very costly.
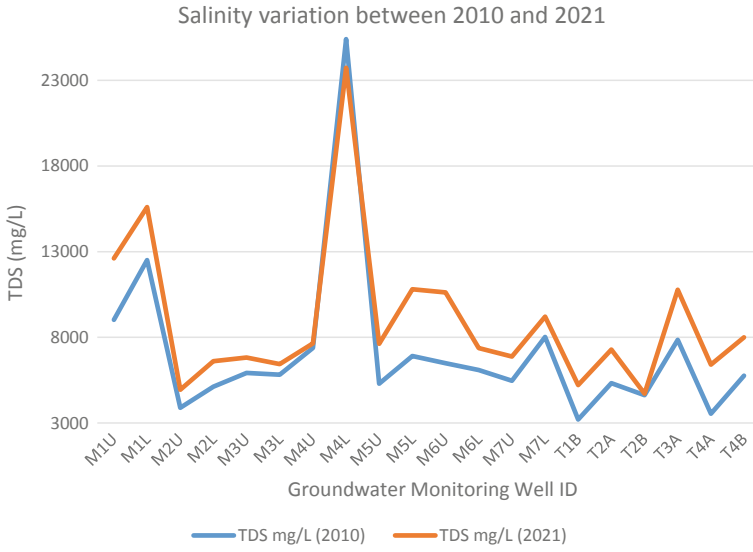
Fig. 24.5 Salinity variation between 2010 and 2021 in the study area
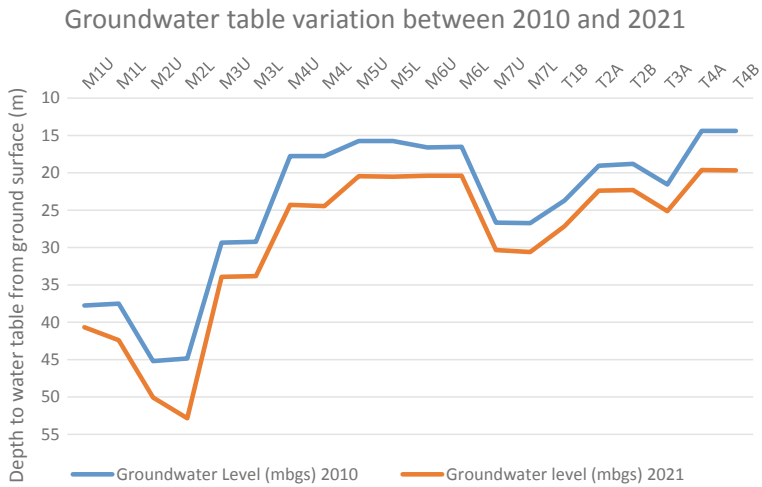
Fig. 24.6 Groundwater level variation between 2010 and 2021 in the study area
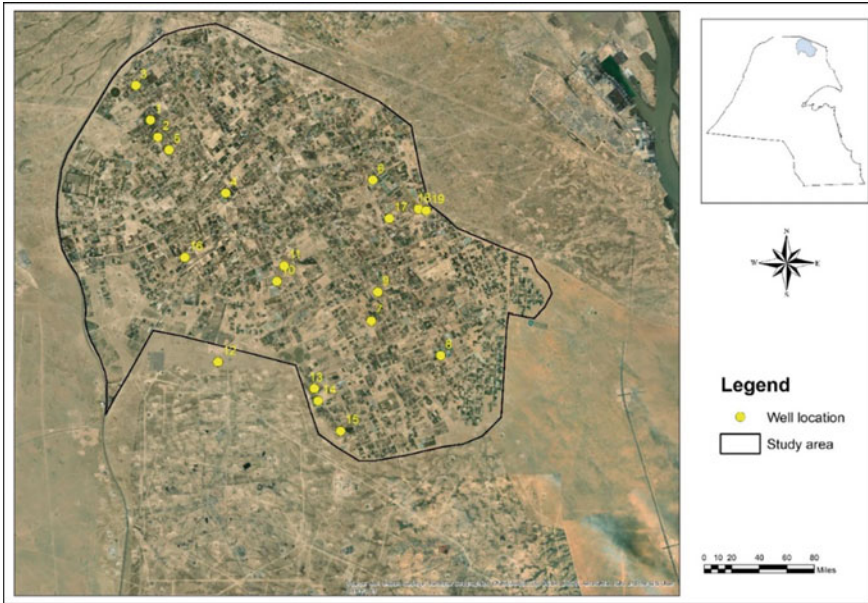
Fig. 24.7 Water sampling locations in Al-Abdally farms

A report published by United Nations Economic and Social Commission for Western Asia (UN ESCWA 2001), outlined that the cost plays an important role in selecting a method of reject brine disposal. The cost could range from 5 to 33% of the total cost of desalination (Khordagui 1997). The dual-purpose desalination and salt production plant is a promising technique to reduce the overall cost of pure water production and brine reject handling (Ariono et al. 2016; Suwaileh et al. 2020). Disposal to evaporation ponds is the most appropriate method for relatively warm dry climates with high evaporation rates, such as that of Kuwait. However, there would always be a potential risk of groundwater contamination with all types of land disposal procedures.

Table 24.2   Water quality in the study area

Parameter	Units	Groundwater (n = 22)			Product water (n = 22)			Reject water (n = 22)		
		Min	Max	Average	Min	Max	Average	Min	Max	Average
pH		6.4	8.53	7.91	6.83	9.36	8.07	7.29	8.53	7.95
EC	μs/cm	9180	20,170	13,993	35	1348	573	12,600	29,700	19,791
TDS	mg/L	6885	15,128	10,592	24	862	372	9300	24,400	15,642
CO_3^{2-}	mg/L	< 0.1	< 0.1	< 0.1	< 0.1	< 0.1	< 0.1	< 0.1	< 0.1	< 0.1
HCO_3^-	mg/L	79	177	124	4.6	54	15.60	102	316.2	180.7
F^-	mg/L	0.89	1.97	1.34	0.014	0.215	0.06	1.361	3.081	2.00
Cl^-	mg/L	1880	5607	3604	4.671	334	137	3010	9121	5513
Br^-	mg/L	2.05	6.83	4.13	0.033	0.481	0.2	3.507	11.33	6.44
NO_3^-	mg/L	75	214	152	0.89	31.85	17.13	103	336	220
SO_4^{2-}	mg/L	1658	3865	2883	3.88	160.7	48.19	2346	6646	4394
Li	mg/L	0.008	0.374	0.23	0.008	0.277	0.08	0.217	0.573	0.37
Na^+	mg/L	1674	3647	2649	6.31	226.2	90.20	1.06	6521	3809
NH_4^+	mg/L	0.358	4.191	0.90	0.034	0.489	0.09	0.73	1.88	1.11
K^+	mg/L	11.01	26.14	16.07	0.056	1.47	0.70	17.3	33	24.3
Ca^{2+}	mg/L	419	1059	660	1.125	40.03	10.46	597	1507	992
Mg^{2+}	mg/L	99	244	166	0.118	10.76	3.03	58	394	248
PO_4^{3-}	mg/L	0.02	2.48	0.15	0.02	0.08	0.02	0.02	1.13	0.11
SiO_3^-	mg/L	0.14	30.49	18.21	0.04	2.6	0.8	1.91	36.86	26.45
TOC	mg/L	0.277	3.5	1.28	0.324	2.28	1.00	0.46	3.5	1.50
Sr	mg/L	8.86	21.53	14.27	0.02	1.32	0.31	16	34.63	22.79
B	mg/L	1.41	6.17	3.78	0.89	3.31	1.90	0.01	7.71	4.08
Cr	μg/L	1.39	46.78	22.12	0.43	5.32	3.19	2.73	68.15	32.64
Ni	μg/L	1.11	12.57	4.96	1.04	7.39	4.33	1.6	13.93	6.66
Al	μg/L	83.62	281.5	196.5	13.94	142.0	58.17	106	345.7	223.9
Ba	μg/L	7.9	34.67	19.58	3.55	10.59	7.99	10.32	36.86	23.70
Pb	μg/L	0.92	10.6	5.65	2.86	9.87	4.90	2.39	9.97	6.84
Se	μg/L	7.41	31.87	18.14	3.95	10.09	6.78	11.82	41.26	26.80
Zn	μg/L	3.05	87.1	27.06	4.73	39.94	18.93	5.84	97.64	31.41
Fe	μg/L	6.85	178.8	65.93	3.57	128.1	56.75	4.28	194.73	69.23
V	μg/L	0.27	37.6	21.11	0.53	6.19	2.41	15.09	45.84	30.55
Cd	μg/L	0.22	2.76	1.89	0.15	1.81	1.4	0.24	3.84	2.88
Cu	μg/L	14.11	173.03	38.21	3.31	71.5	23.41	16.61	181.85	45.8
Mn	μg/L	0.09	15.42	2.83	0.19	5.9	2.04	0.06	32.35	4.78

Piper Diagram

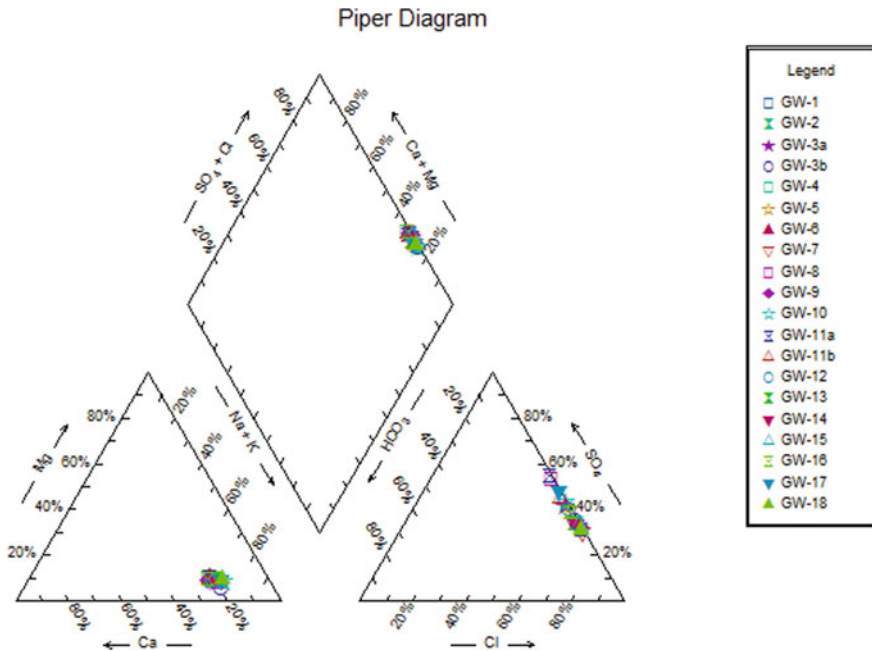**Fig. 24.8** Piper diagram showing groundwater quality in the study area

Table 24.3 Methods of concentrate disposal in USA

Method of disposal	%
Surface water	48
Discharged to wastewater treatment plants	23
Land application	13
Deep well injection	10
Evaporation ponds	6

Source Mohamed et al. (2005)

24.4 Conclusions

Water scarce arid regions like Kuwait needs alternative freshwater resources for agricultural activities in the country for food security. Inland brackish water desalination is one of the promising alternatives, however care should be taken so that it will not have adverse effect on groundwater, soil, and environment. Educating the farmers on the judicial use of water will be important as larger portion of the water go waste in agricultural activities due over irrigation or unscientific methods of irrigation. Considerable decline in the ground water level was observed in a decade, with an average decline of 4.6 m between the year 2010 and 2021. The groundwater salinity also deteriorated with an average salinity increase of 2000 mg/L in a decade time.

Therefore, over extraction of groundwater should be controlled. The groundwater quality in the study area is not suitable to use directly for crop irrigation, whereas the RO units product water is of freshwater quality and good for crop irrigation purposes. However, brine reject from these RO units should be disposed or reused in environment friendly manner. Prior to study conclusion, the remaining tasks of pumping test, geochemical modelling and numerical modelling will be carried out after the well drilling activities and collection of second round of samples.

References

Ahmed M, Shayya WH, Hoey D, Mahendran A, Morris R, Al-Handaly J (2000) Use of evaporation ponds for brine disposal in desalination plants. Desalination 130(2):155–168

Ahmed M, Arakel A, Hoey D, Coleman M (2001) Integrated power, water and salt generation: a discussion paper. Desalination 134(1–3):37–45

Akber A, Sherif M, Ghoneim H, Al-Senafy MN (1999) Evaluation of the groundwater conditions in Al-Wafra and Al-Abdally farm areas. Report no. KISR5582. Kuwait Institute for Scientific Research, Kuwait

Al-Murad M, Uddin S, Rashid T, Naseeb H, Al-Qallaf H, Bushehri A, Al-Salman B, Marzouk F, Jomaa M (2010) Causes and effects of water table rise in the Al-Wafra agricultural area

Al-Murad M, Saeed T, Al-Qallaf H, Rashid T, Al-Kandari J (2016) Assessment of the potential impacts of oil production produced water on the groundwater and the agricultural crops in Al-Wafra area, vol 1

Al-Sulaimi J, Viswanathan MN, Szekely F, Naji M, Naseeb H, Abdullah H, Siwek Z, Al-Awadi E, Joudeh O, Rabaa S, Barrak K, Otaibi M (1994) Geohydrological studies of Al-Wafra and Al-Abdally farm areas

APHA (2015) Standard method for the examination of water and wastewater. American Public Health Association

Ariono D, Purwasasmita M, Wenten IG (2016) Brine effluents: characteristics, environmental impacts, and their handling. J Eng Technol Sci 48(4):367–387. https://doi.org/10.5614/j.eng.technol.sci.2016.48.4.1

Fadlelmawla A, Al-Otaibi M (2005) Analysis of the water resources status in Kuwait. Water Resour Manag 19:555–570

Fadlelmawla A, Mukhopadhyay A, El-Gamily H, Rashid T (2009) Development of decision support maps for groundwater protection in Kuwait

FAO (2013) Good agricultural practices for greenhouse vegetable crops. Principles for Mediterranean climate areas. FAO plant production and protection paper 217

Khordagui H (1997) Environmental aspects of brine reject from desalination industry in the ESCWA region. ESCWA, Beirut, Lebanon

Loucks DP (1997) Quantifying trends in system sustainability. Hydrol Sci J 2(4):513–530

Mickley M (2018) Updated and extended survey of U.S. municipal desalination plants. Bureau of Reclamation

Mohamed A, Maraqa M, Handhaly JA (2005) Impact of land disposal of reject brine from desalination plants on soil and groundwater. Desalination 182(1–3):411–433

PAAFR (2009) Official letter from public authority for agricultural affairs and fish resources

Senay Y (1985) Brackish groundwater condition at northwestern Kuwait. Ministry of Electricity and Water Kuwait

Suwaileh W, Johnson D, Hilal N (2020) Membrane desalination and water re-use for agriculture: state of the art and future outlook. Desalination 491:114559. https://doi.org/10.1016/j.desal.2020.114559

UN ESCWA (2001) The role of desalinated water in augmentation of the water supply in selected ESCWA member countries. E/ESCWA/ENR/2001/19

Part VI
Water Resources Management

Chapter 25
Model for Optimal Regional Wastewater Systems Planning with Uncertain Wastewater Treatment Capacity

Faisal M. Alfaisal

Notations

I	Set of wastewater sources nodes on Iso-nodal line i.
J	Set of the possible location of collection nodes on Iso-nodal line j.
K	Set of possible location WWTP nodes on Iso-nodal line k.
QR_i	Amount of wastewater produced at sources node on Iso-nodal line i.
$QS_{i,j}$	Flow carried from sources nodes on Iso-nodal line i to collection nodes on Iso-nodal line j.
$QC_{j,k}$	Flow carried from intermediate nodes on Iso-nodal line j to WWTP nodes on Iso-nodal line k.
QT_k	Amount of treated wastewater at WWTP node on Iso-nodal line k.
$x_{i,j}$	Binary variable that will take value 1 if there is existence of a particular pathway that linking nodes on Iso-nodal line i to nodes on Iso-nodal line j and 0 otherwise.
$y_{j,k}$	Binary variable that will take value 1 if there is existence of a particular pathway that linking nodes on Iso-nodal line j to nodes on Iso-nodal line k and 0 otherwise.
$Qmin_{i,j}$ and $Qmin_{j,k}$	Minimum amount of wastewater from source nodes on Iso-nodal line i through collection nodes on Iso-nodal line j to WWTP nodes on Iso-nodal line k.

F. M. Alfaisal (✉)
Department of Civil Engineering, College of Engineering, King Saud University, P.O. Box 800, Riyadh 11421, Saudi Arabia
e-mail: falfaisal@ksu.edu.sa

$Qmax_{i,j}$ and $Qmax_{j,k}$	Maximum amount of wastewater from source nodes on Iso-nodal line i through collection nodes on Iso-nodal line j to WWTP nodes on Iso-nodal line k.
$\mu_{MaxQ_{wwtp}}$	The mean of maximum wastewater plant capacity $(MaxQ_{wwtp})$.
$\sigma_{MaxQ_{wwtp}}$	The standard deviation of maximum wastewater plant capacity $(MaxQ_{wwtp})$.
$Z_{B_{i,\alpha_i}}$	The quantal function for the normal distribution, or the cumulative distribution function, interpolated from the normal distribution tables for specific values of αi.

25.1 Introduction

The chapter's main objective is to use a chance-constrained method by taking the capacity uncertainty of wastewater treatment plants into account. The model is to reduce overall costs while taking uncertainty into account, with a given degree of reliability, ensuring that the amount of flow to be treated does not exceed the treatment capacity with reliability percentage. As known sanitary systems are most likely to storm sewer systems that considered to be a collection type network. So, the concept of Isonodal lines (INL) to identify sewer layout and pipe design in storm sewer systems for minimum costs is used herein. The various optimization methods used for the optimal pipe design and the optimal layout are discussed in more detail in Steele, et al. (2016) and Alfaisal and Mays (2021) and therefore are not reviewed herein. Alfaisal and Mays (2022) developed a deterministic approach for minimum total costs of sewer layout and WWTP locations for regional wastewater systems. The model developed here is an expansion of deterministic approach to include the uncertainty level by considering a percentage of reliability of WWTP capacity. The ability of the system to collect wastewater at treatment plant nodes at minimal cost is the actual issue with regional wastewater systems' reliability (Zeferino et al. 2014).

Chance constrained method have been used to solve many of water resources problems under uncertainty. Khatavkar and Mays (2017) and Stuhlmacher and Mathieu (2020) developed an optimization model using pump operations for uncertain demand pattens. Ackooij et al. (2014) used chance constrained approach in hydro reservoir management. Li et al. (2014) used chance constrained method for sustainable water quality management. Grosso et al. (2014) used the method to predative control of drinking water systems. Xu et al. (2017) used chance-constrained approach for water resource management in the Heshui River Basin, Jiangxi Province, China. Liu et al. (2017) used chance-constrained model in energy-water nexus for planning electric power systems. Zhang et al. (2017) developed chance-constrained method for optimal agricultural cultivation scale in an arid area. Wang and Zhu (2021) developed chance-constrained programming for booster optimization in water distribution system.

   The objectives of this chapter are as follows; (1) to explain the development of using a chance-constrained method in planning regional wastewater systems, (2) to present a mathematical formulation of regional wastewater systems under uncertain wastewater treatment capacity.

25.2 Optimization Model

Mays and Tung (2002) provide some detailed information of using chance constrained method in optimization problems. In order to ensure that the total amount of flow to be treated does not exceed the treatment capacity with reliability percentage, the model is formulated as chance-constrained. The optimization model contains of objective function subject to constraints. The objective function is to minimize the total costs of sewer links and WWTP. The costs are function of unit discharge of sewers. The objective function to minimize costs, Eq. (25.1) below, is expressed as follows

$$\text{Minimize } Z = \sum_i \sum_j C_{\text{Sewer}(i,j)} QS_{i,j} x_{i,j} + \sum_j \sum_k C_{\text{Sewer}(j,k)} QC_{(j,k)} y_{j,k}$$
$$+ \sum_k C_{\text{WWTP},k}(QT_k) y_{j,k} \tag{25.1}$$

where $C_{\text{Sewer}(i,j)}$ is total costs that associated with installing, operation and maintenance of sewer system per unit flow (\$/gpm) that connect source nodes on Iso-nodal line i to collection nodes on Iso-nodal line j; $C_{\text{Sewer}(j,k)}$ is total costs that associated with installing, operation and maintenance of sewer system per unit flow (\$/gpm) that connect collection nodes on Iso-nodal line j to WWTP nodes on Iso-nodal line k; $C_{\text{WWTP},k}$ is total costs that associated with a new plant construction, operation and maintenance of WWTP nodes k per unit flow (\$/gpm); $QS_{i,j}$ is wastewater carried from sources nodes on Iso-nodal line i to collection nodes on Iso-nodal line j; $QC_{j,k}$ is wastewater carried from collection nodes on Iso-nodal line j to WWTP nodes on Iso-nodal line k; $Q_{i,j}$ and $Q_{j,k}$ are the wastewater flows in the sewer system and QT_k is the treated wastewater that is leaving the treatment facility; $x_{i,j}$ is binary variable that will take value 1 if there is existence of a particular pathway that linking nodes on Iso-nodal line i to nodes on Iso-nodal line j and 0 otherwise; $y_{j,k}$ is binary variable that will take value 1 if there is existence of a particular pathway that linking nodes on Iso-nodal line j to nodes on Iso-nodal line k and 0 otherwise.

   The objective function is subject to continuity constraints, connectivity constraints, lower and upper constraints, and WWTP capacity constraints. Continuity constraints (25.2–25.5) for flows in the system states that all the system must be in equilibrium, so that the flow produced at source nodes on i must be sent to WWTP nodes on k. so the wastewater that generated in source nodes should be treated at waste water facility.

Where QR_i is amount of wastewater produced at sources node on Iso-nodal line i; $QS_{i,j}$, $QC_{j,k}$ and QT_k are described above.

$$\sum_j QS_{i,j} x_{i,j} = QR_i \quad \forall i \tag{25.2}$$

$$\sum_i QS_{i,j} x_{i,j} - \sum_k QC_{j,k} y_{j,k} = 0 \quad \forall j \tag{25.3}$$

$$\sum_J QC_{j,k} y_{j,k} = QT_k \quad \forall k \tag{25.4}$$

$$\sum_i QR_i = \sum_k QT_k \tag{25.5}$$

Connectivity constraints (25.6–25.7) are expressed as the flow from each source node i must flow through one collection node j, which can be satisfied as follows by using 0/1 binary variable $x_{i,j}$. The flow from each collection node j must flow through one WWTP node on INL k, which can be satisfied as follows using 0/1 binary variable $y_{j,k}$.

$$\sum_i x_{i,j} = 1 \quad \forall j \tag{25.6}$$

$$\sum_k y_{j,k} = \begin{cases} 1 & \text{If } \sum_k QC_{j,k} > 0 \\ 0 & \text{If } \sum_k QC_{j,k} = 0 \end{cases} \quad \forall j \tag{25.7}$$

Lower and upper constraints (25.8–25.9) for the flows should be identified into model. Qmin and Qmax are the minimum and the maximum amount of wastewater through the system; $Qmin_{i,j}$ and $Qmin_{j,k}$ are the minimum amount of wastewater generated by source nodes on Iso-nodal line i through collection nodes on Iso-nodal line j to WWTP nodes on Iso-nodal line k; $Qmax_{i,j}$ and $Qmax_{j,k}$ are the maximum amount of wastewater generated by source nodes on Iso-nodal line i through collection nodes on Iso-nodal line j to WWTP nodes on Iso-nodal line k

$$Qmin_{i,j} x_{i,j} \leq QS_{i,j} \leq Qmax_{i,j} x_{i,j} \quad \forall (i, j) \tag{25.8}$$

$$Qmin_{j,k} y_{j,k} \leq QC_{j,k} \leq Qmax_{j,k} y_{j,k} \quad \forall (j, k) \tag{25.9}$$

Chance Constrained method is applied in WWTP capacity constraint (25.10). $\mu_{MaxQ_{wwtp}}$ is the mean of maximum wastewater plant capacity $\left(MaxQ_{wwtp}\right)$. $Z_{B_{k,(1-\alpha_k)}}$ is the quantal function for the normal distribution, or the cumulative distribution function, interpolated from the normal distribution tables for specific values of αi. $\sigma_{MaxQ_{wwtp}}$ is the standard deviation of maximum wastewater plant capacity $\left(MaxQ_{wwtp}\right)$. $QC_{j,k}$ and $y_{j,k}$ are described above.

$$\mu_{\mathrm{MaxQ_{wwtp}}} + Z_{B_{k,(1-\alpha_k)}} \sigma_{\mathrm{MaxQ_{wwtp}}} \geq \sum_{j} QC_{j,k} y_{j,k} \qquad \forall k \qquad (25.10)$$

25.3 Solution Method

The model is presented here, one for a case of known wastewater treatment plant capacity (Eqs. 25.1–25.9) as a deterministic model, while the other one (25.10) is for uncertainty system which is for uncertainty model. Both models are mixed-integer linear programming (MILP) problems solved with GAMS system using BARON solver. BARON solver proved in GAMS can solve MILP problems which is much faster than local solver or "any solver" in GAMS. Also, Baron solver is guaranteed a global solution under fairly general assumptions (GAMS 2022).

25.3.1 Model Application

The model was applied to a hypothetical example of regional wastewater system. Figure 25.1 shows possible layout of the sewer system for the study area. The costs that applied are a realistic hypothetical for installing, operation, and maintenance of sewer system and WWTP. The unit cost of sewer system assumed to be $1 ~ $12 per unit flow rate ($QR_i$) and the unit cost of WWTP assumed to be $3.2 per unit treated discharge (QT_k). . In this example application, it assumed the cheapest possible connection from sources, collection to WWTP is showing in red dash line ($1 per unit flow rate). The average wastewater produced was 18 million gallons per day (mgd), 46 mgd, and 74 mgd, respectively, which reflect the maximum flow that occurs in that source node. The sources nodes can describe as large, medium, and small cities or certain zones in large cities.

As described above, formulated chance constraint model in such that the waste to be treated should not exceed reliability percentage of treatment capacity. The system has been run for different reliability percentage 60%–95% respectively. The mean and standard deviation for wastewater treatment plant capacity has been taken to be 150 mgd and 15 mgd, respectively.

Table 25.1 shows the assumption of total costs of installing, operation and maintenance that associated with sewer network connected source nodes to collection nodes. The total costs are assumed to connect collection node (n6) as minimum value which is $1/gpm from all source nodes (n1, n2, and n3) while it assumed to connect collection node (n5) as maximum value from source node n2.

In Table 25.2, it assumed that the total costs of sewer system connecting candidate collection nodes to candidate WWTP nodes are including installing, operation and maintenance per unite flow. The cheapest total costs are assumed to connect WWTP node (n8) as $1/gpm from all collection nodes (n4, n5, and n6).
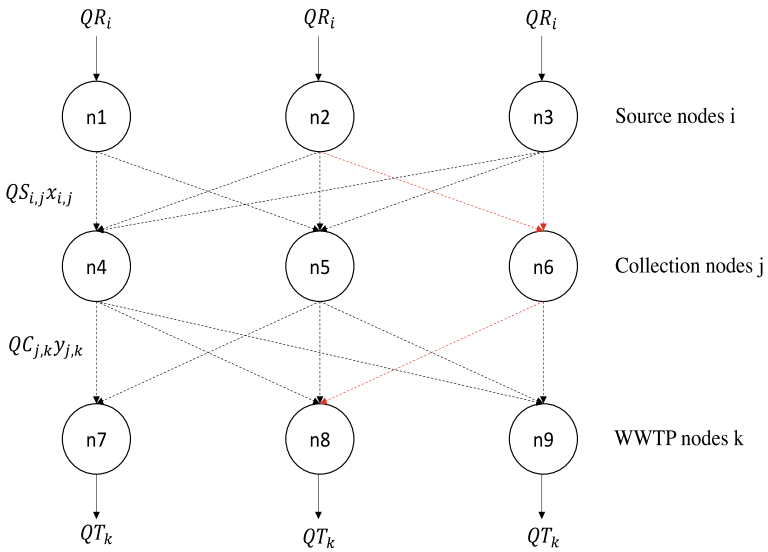
Fig. 25.1 Input data for example application

Table 25.1 The assumption of total costs, $\left(C_{\text{Sewer}(i,j)}\right)$, of installing, operation and maintenance from sources nodes i to collection nodes j per unit flow ($/gpm)

	n4 ($)	n5 ($)	n6 ($)
n1	1.2	1.2	1
n2	1.2	1.5	1
n3	1.2	12	1

Table 25.2 The assumption of total costs, $\left(C_{\text{Sewer}(j,k)}\right)$, of installing, operation and maintenance from collection nodes j to WWTP nodes k per unit flow ($/gpm)

	n7 ($)	n8 ($)	n9 ($)
n4	1.2	1	1.2
n5	10	1	1.2
n6	1	1	12

Table 25.3 shows the total costs of WWTP that includes new plant construction, operation and maintenance. It assumed total costs are same which is $3.2/gpm for all WWTP nodes (n7, n8, and n9). These value can be adjusted for any case.

A clear presentation of experimental results obtained, highlighting any trends or points of interest. Please use the decimal system of headings with no more than four levels.

Table 25.3 The assumption of total Costs, $\left(C_{WWTP,k}\right)$, of new plant construction, operation and maintenance of WWTP nodes k per unit flow ($/gpm)

	WWTP ($)
n7	3.2
n8	3.2
n9	3.2

25.4 Results

The regional wastewater systems are representing a dendritic type network as shown in Fig. 25.2 for the sewer layout and WWTP locations. At uncertainty level 5%, the optimized planning systems shows that source node 3 (biggest city) can have one WWTP at node 9 while sources nodes 1 and 2 are connected to WWTP at node 7 and total costs are 732.4 $Million. If the uncertainty level above 25%, the total costs of the system is reduced by 2% which is around 14.8 $ Millions and planning regional system would keep only one facility. The results are reasonable because from 60 to 75% reliability, the costs are the same, but once this value of reliability is over 80% the layout of the system and costs would be changed to be higher. Figure 2a shows the optimal sewer layout for uncertainty in WWTP capacity within reliability 95% while Fig. 2b shows the optimal sewer layout for uncertainty in WWTP capacity within reliability 75%. The optimum sewer layout for all different cases is same and that regarding minimum costs associated with a possible connection. The total costs of the system are increasing when reliability percentage increases (After 75% reliability). Interesting point, if we considered wastewater variation 5%, the total costs are 732.4 $ Millions. However, the total costs are decreasing when the wastewater variation is 20% and more. This means the best planning for regional wastewater system to consider only one WWTP instead of two WWTP with uncertainty 20%.
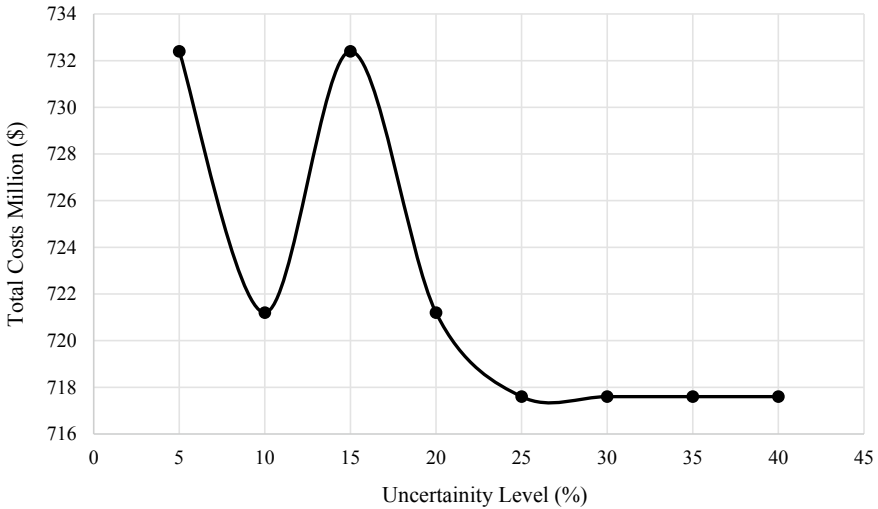
Table 25.4 shows the results for the total costs for different percent reliability along with the values of a mean (μ), and standard deviation (σ) for WWTP capacity and the cumulative distribution function (z) used for computation of the total costs. As noticed, the percent reliability increased the total costs increased while the mean value (μ) is 150 gpm and standard deviation value (σ) is 15 gpm in each case. It is another important factor when these values (the mean and standard deviation) are variables in the system. Figure 25.3 indicates that for treatment capacity satisfaction variations up to about 25%, there is a steady decline in the total costs of planning regional wastewater systems.
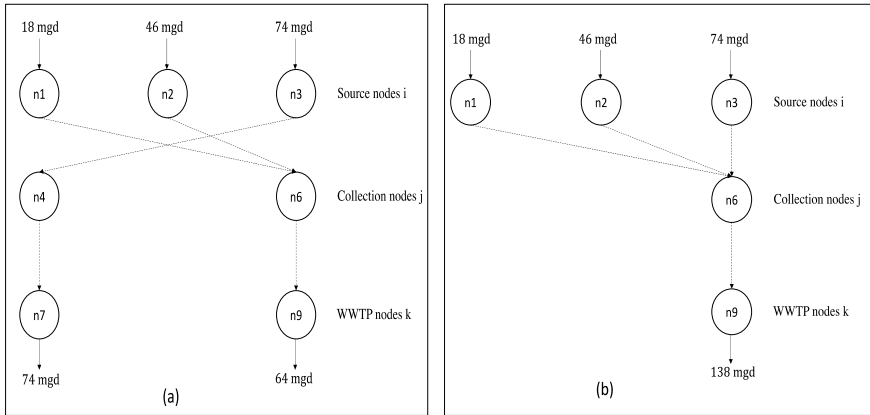
Fig. 25.2 Results of the optimal sewer layout and WWTP locations; **a** 95% reliability, and **b** 75% reliability

Table 25.4 The results of running the model for different reliability %

Reliability (%) (α)	Wastewater variation (%) ($1 - \alpha$)	Quantile function values (z)	WWTP capacity		Total costs $ million
			Mean (μ) (mgd)	Standard deviation (σ) (mgd)	
95	5	-1.645	150	15	732.4
90	10	-1.282	150	15	721.2
85	15	-1.036	150	15	732.4
80	20	-0.842	150	15	721.2
75	25	-0.6744	150	15	717.6
70	30	-0.5244	150	15	717.6
65	35	-0.38532	150	15	717.6
60	40	-0.2533	150	15	717.6

Fig. 25.3 Total cost ($) tends for different wastewater variation

25.5 Conclusions

A methodology for generating optimized sewer layout and WWTP locations for uncertain treatment capacity has been developed. This model can be used to reduce the total costs associated with planning regional wastewater systems. The optimized layout and WWTP locations show that wastewater variations up to 75% can reduce the total costs by 2% about 14.8 $Millions. Number of source, collection and WWTP nodes can be modified based on case study area and the planning should consider that all flows have to be in one direction which represents the topography contour lines. Also, the input petameter that applied into hypothetical example can be modified. In addition, this model can be applied for planning new medium to large-scale wastewater systems.

Further steps can improve the model, such as considering hydraulic constraints by introducing sewer pipe design. One significant addition to the solution method is considering an expansion of existing sewer pipes and facilities.

References

Alfaisal FM, Mays LW (2022) Testing of an optimization model for optimal sewer layout and wastewater treatment locations. Desal Water Treat 263(2022):152–159. https://doi.org/10.5004/dwt.2022.28220

Alfaisal FM, Mays LW (2021) Optimization models for layout and pipe design for storm sewer systems. Water Resour Manag 35:4841–4854. https://doi.org/10.1007/s11269-021-02958-5

GAMS (2022) Available solver. GAMS Development Corporation. Retrieved from https://www.gams.com/mccarlGuide/available_solvers.html

Grosso JM, Ocampo-Martinez C, Puig V, Joseph B (2014) Chance-constrained model predictive control for drinking water networks. J Process Control 24(5):504–516. https://doi.org/10.1016/j.jprocont.2014.01.010

Khatavkar P, Mays LW (2017) Model for optimal operation of water distribution pumps with uncertain demand patterns. Water Resour Manage 31:3867–3880. https://doi.org/10.1007/s11269-017-1712-8

Li T, Li P, Chen B, Hu M, Zhang X (2014) Simulation-based inexact two- stage chance- constraint quadratic programming for sustainable water quality management under dual uncertainties. J Water Resour Plan Manag 140(3):298–312. https://doi.org/10.1061/(ASCE)WR.1943-5452.0000328

Liu J, Li Y, Huang G, Suo C, Yin S (2017) An interval fuzzy-stochastic chance-constrained programming based energy-water nexus model for planning electric power systems. Energies 10:11. https://doi.org/10.3390/en10111914

Mays LW, Tung YK (2002) Hydrosystems engineering and management. Water Resources Publication

Steele JC, Mahoney K, Karovic O, Mays LW (2016) Heuristic optimization model for the optimal layout and pipe design of sewer systems. Water Resour Manag 30:1605–1620. https://doi.org/10.1007/s11269-015-1191-8

Stuhlmacher A, Mathieu JL (2020) Chance-constrained water pumping to manage water and power demand uncertainty in distribution networks. Proc IEEE 108(9):1640–1655

van Ackooij W, Henrion R, Moeller A, Zorgati R (2014) Joint chance constrained programming for hydro reservoir management. Optim Eng 15(2):509–531. https://doi.org/10.1007/s11081-013-9236-4

Wang Y, Zhu G (2021) Inexact left-hand side two-stage chance-constrained programming for booster optimization in water distribution system. J Environ Manag 298:113372

Xu J, Huang G, Li Z, Chen J (2017) A two-stage fuzzy chance constrained water management model. Environ Sci Pollut Res 24(13)

Zeferino JA, Antunes AP, Cunha MC (2014) Regional wastewater system planning under population dynamics uncertainty. J Water Resour Plan Manag 140(3):322–331

Zhang C, Li M, Guo P (2017) Two-stage stochastic chance-constrained fractional programming model for optimal agricultural cultivation scale in an arid area. J Irrig Drain Eng 143:9. https://doi.org/10.1061/(ASCE)IR.1943-4774.0001216

Chapter 26
Cyber-Physical System for Improving Building Water Use Efficiency

Bivin Pradeep and Parag Kulkarni

26.1 Introduction

Water is a fundamental necessity of mankind. Whilst the world population continues to climb, the availability of water resources to cater to this ever-increasing population isn't growing in proportion. UN estimates indicate that the water resources available to meet the needs of an extra two billion people expected on the planet over the next 30 years are not likely to change in comparison to what they are today. This calls for careful management of this scarce resource and is all the more important for arid regions in the world.

Buildings are known to have heavy water and energy consumption and a consequential environmental footprint. Given the rapid increase in urbanization, it is therefore vital to tackle the water and energy conservation problem in buildings. A public water efficiency benchmark report (Singapore Government 2020) from the Government of Singapore indicates that cooling, toilets and pantries account for 90% of water use in buildings with almost 54% of water being used in toilets and pantries. The focus of our work in this paper is on the reduction of water use in buildings through a reduction in cleaning cycles resulting in water conservation, cost savings and the corresponding reduction in the environmental impact.

Typically, washrooms in buildings have to be cleaned regularly for maintaining hygiene in that location. To ensure this, the housekeeping teams clean these premises

B. Pradeep · P. Kulkarni (✉)
Computer and Network Engineering Department, College of Information Technology, United Arab Emirates University, P.O. Box 15551, Al Ain, UAE
e-mail: parag@uaeu.ac.ae

B. Pradeep
e-mail: bivinz2013@uaeu.ac.ae

P. Kulkarni
National Water and Energy Center, United Arab Emirates University, P.O. Box 15551, Al Ain, UAE

periodically irrespective of the occupancy at the location. In light of the recent shift to remote working, occupancy in offices has dropped significantly. Therefore, periodic cleaning of these locations may not be necessary and instead, an occupancy-driven cleaning approach could greatly help to improve efficiencies in the process, i.e., reduce water consumption, improve savings by reducing costs and also reduce the overall carbon footprint of the organization.

A document (Seed Engineer 2021) published by a consultancy firm highlights typical water use breakdown in buildings and touches upon different aspects associated with improving water efficiency. Whilst this document outlines various opportunities such as usage-based pricing, detecting and fixing leaks, using technologies such as dual-mode flush systems, waterless urinals, use of greywater in flushing and retrofits to control water flow from faucets, taps, wash basins etc., it does not address the issue of reducing water use through the reduction in cleaning requirements.

A prototype for people counting using a live video feed information is presented in Herviana et al. (2020). The approach comprises capturing a video feed using a camera and analyzing this using the open-source OpenCV software. A virtual line was drawn inside the location which when crossed by the detected person would be counted as an entry. This approach purely focuses on person detection and was tested in a mall in Indonesia. Moreover, since it uses a camera, it doesn't protect a person's privacy. Another approach for people counting is proposed in Ghosh et al. (2021). Two virtual lines were used to accurately determine people entering and leaving a location. This system prioritized accuracy over privacy and was deployed in a museum setting. Yet another people counting technique using image recognition is proposed by Myint and Sein (2021). Images captured from a camera are fed to a classifier model to determine the presence or absence of a person. Whilst the above systems attempt to count people, the use of a camera compromises the people's privacy unlike in our proposed approach wherein one of the key objectives is to preserve the privacy of the people while ensuring accuracy.

The work presented in Kashima et al. (2013) explores the use of an ultra-wideband radio to detect motion in bathtubs targeted especially for the elderly in Japan who are prone to suffer from problems such as heat strokes, heart strokes, fainting as highlighted in their paper. Whilst the objective here is motion detection for health and safety, the purpose is not counting unlike in our proposed approach. Also, this solution is targeted to a very different problem, unlike our proposed solution which focuses on enhancing water use efficiency. Another solution for motion detection described in Instalator (2021) uses two sensors to control the lights in a bathroom-switch ON when people are detected and switch OFF otherwise. The approach uses two infrared sensors to determine entry and exit from the premises. Lights are switched on upon entry and switched off upon exit. Whilst this is a people detection solution, they do not keep track of real-time occupancy information and also, the focus is not on enhancing water use efficiency. Additionally, this solution uses multiple sensors for motion detection unlike our approach which uses a single sensor. In summary, whilst there exist various studies focusing on motion/occupancy detection in general, most of these approaches are intrusive (require use of a camera). Unlike this, the focus

of our work is to realize privacy-preserving occupancy detection and leverage such information for enhancing water use efficiency in buildings.

The work by Jayasinghe et al. (2018) argues that cleanliness is a subjective term and therefore, has proposed a system that classifies the cleanliness in restrooms into three categories clean, average and dirty. The approach uses images gathered from cameras placed in restrooms. Images labeled by the facilities managers as clean, average and dirty are used to train a classifier. The captured images are then fed to the classifier which classifies the state of the restroom. This approach primarily deals with the cleanliness of the facilities and does not address the issue of enhancing water use efficiency. Moreover, it assumes the availability of cameras inside restrooms which is not practical. Our approach does not rely on using any cameras and is, therefore, able to protect the visitor's privacy. Another approach for predicting the cleanliness of airport restrooms is presented in Ros et al. (2019). This involves soliciting visitor feedback through a dedicated device (smiley box) fitted in the restroom. The visitor presses on one of the smiley icons to give feedback. This feedback is then passed on to the cleaning team to improve the cleanliness of the facility. This work however does not gather any cleaning data (when and how often is cleaning carried out) and is also agnostic of the occupancy levels. We believe that such data can be useful to optimize cleaning decisions and this is in fact, one of the main contributions of our work.

26.2   Methods

In this section, we elaborate on the design of Dew, our experimental prototype. Dew was built using open off-the-shelf hardware components including the Raspberry Pi Zero platform (Raspberry Pi 2021), Passive Infrared (PIR) sensor (PIR 2021), general purpose RGB Light Emitting Diodes (RGB, LED 2021) and a tactile switch (Switch 2021). Figure 26.1 shows the Dew hardware prototype. The casing for the prototype was designed and 3D printed in-house. The Raspberry Pi Zero platform was chosen over the traditional Raspberry Pi 3 or 4 because of its small form factor and low power consumption. It also has an onboard WiFi radio module which was used to transport the sensor data to the backend system. This choice was motivated by the widespread availability of the University WiFi network. The backend system comprised a server running Linux Ubuntu operating system hosting a mongoDB database (MongoDB 2021) and Parse platform (Parse 2021). Data coming from the remote sensors was stored in the mongoDB database. mongoDB was chosen because of its ability to scale and to handle large amounts of data having dynamic schemas. This gave us the confidence of designing the prototype to send data in a much fine-grained manner. The Parse platform provided the Application Programming Interface (API) for interfacing the hardware prototype with the backend system. Parse server is widely known for it being an open source Backend-as-a-Service (BaaS) framework. It enables you to setup a backend system without having the need for any backend code or requiring to create your own custom API calls.

Fig. 26.1 Dew hardware prototype

26.2.1 Operation of the Prototype and Stakeholder Engagement

The prototype was designed to track the number of people that visit the facilities through the use of a PIR sensor which utilizes passive infrared rays to detect motion. A key element of this design is that such tracking is achieved anonymously, i.e., no personally identifiable information is gathered. To preserve the anonymity of the visitor while ensuring accuracy, we considered counting two instances of motion detection as a single visit, i.e., the entry and exit from the facility as a single count. The Dew box not only stores the count locally but also pushes this information to the server in real time so that this can be made available to the facilities management team. The reason to store the count locally as well was to ensure that data will not be lost and the device can continue to work even if the network signal goes down.

Figure 26.2 shows the Dew prototype components and the different operational states. The tactile switch on the Dew box was used to signal the beginning and end of a cleaning cycle. To maintain simplicity and easily identify the status of the box, we added a RGB LED that could indicate the status to the cleaning crew. To begin with, the LED on the Dew box would be Green starting with a count of zero, a state we refer to as "Active". The count would increment with each visitor visiting the facility. Before initiating a cleaning operation, the cleaning crew would press the tactile switch on the Dew box which would freeze the motion detection and count, a state we refer to as "Cleaning". This was essential as we did not want the
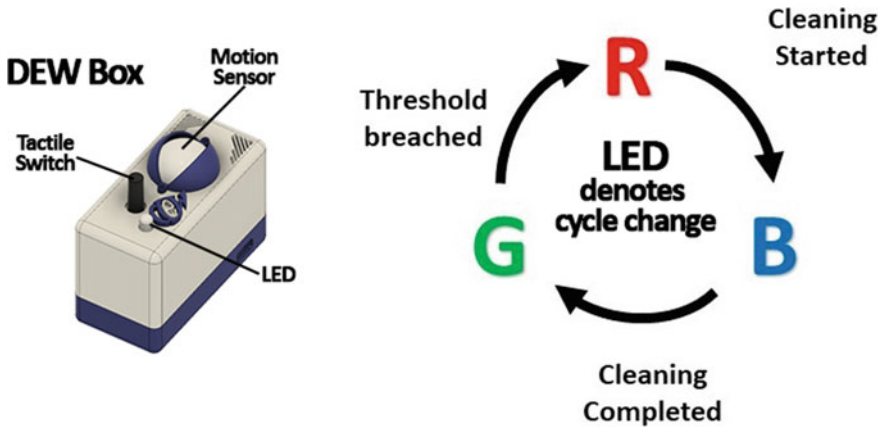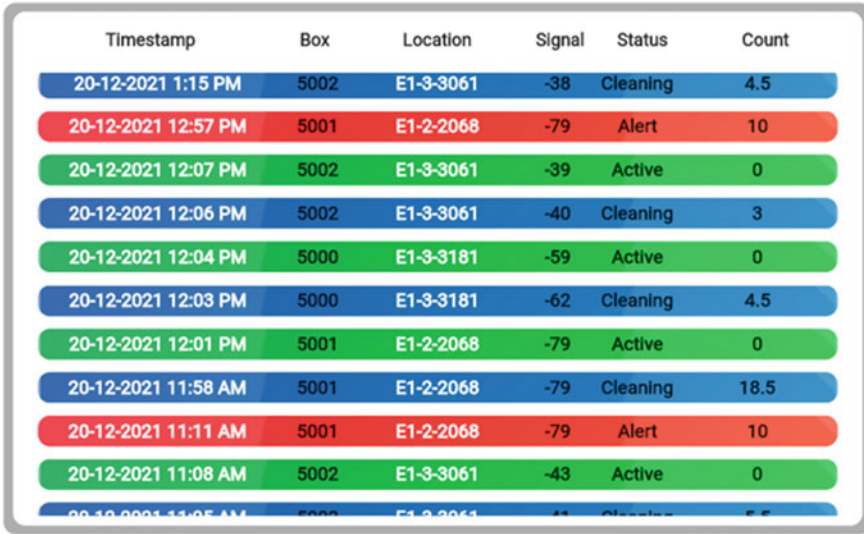
Fig. 26.2 Dew prototype and operational states

motion detector to count the movement of the cleaning crew. Once the cleaning was completed, the cleaning crew would press the tactile switch again which would turn the LED on the box to Green and start with a count of zero again (back to "Active" state). This way, the use of the tactile switch and the LED would not only provide a visual indicator of the operational state of the box but would also ensure that the Dew system would count only when cleaning is not in progress.

Whenever the tactile switch is pressed or a motion is detected by the sensor (see left hand side of Fig. 26.2), the corresponding state information (timestamp, box ID, location of the box, radio signal strength, box status and count) would be pushed to the server and captured in the dashboard as shown in Fig. 26.3. This way, one can keep track of when cleaning was initiated, when it was completed thereby providing insights into how often cleaning was carried out and how long it took for each cleaning operation. In addition to the above functionality, when the count crossed a certain threshold (dynamically configurable by the facilities management team), the LED would transition to show a constant RED, a state we refer to as "Alert". This would indicate the need to initiate cleaning of this facility. The right hand side of Fig. 26.2 depicts the transitions between the different operational states.

To field trial the proposed solution, it was vital to engage the campus facilities management team. They were keen to trial this solution and cooperated with us during the trial providing support as necessary. They were themselves keen to identify ways in which they could enhance operational efficiency, sustainability and reduce operating costs. The facilities cleaning crew were provided training on how to use the box and were advised to incorporate this as a part of their regular cleaning routine. The trial was planned in a way so as not to disrupt their regular operational procedure. Therefore, the facilities cleaning crew, as per their existing operating procedure, would continue to tick a paper sheet at the end of their cleaning operation mentioning the job completion time on this sheet in addition to pressing the tactile switch on the Dew box before and after completion of cleaning as described above.

Timestamp	Box	Location	Signal	Status	Count
20-12-2021 1:15 PM	5002	E1-3-3061	-38	Cleaning	4.5
20-12-2021 12:57 PM	5001	E1-2-2068	-79	Alert	10
20-12-2021 12:07 PM	5002	E1-3-3061	-39	Active	0
20-12-2021 12:06 PM	5002	E1-3-3061	-40	Cleaning	3
20-12-2021 12:04 PM	5000	E1-3-3181	-59	Active	0
20-12-2021 12:03 PM	5000	E1-3-3181	-62	Cleaning	4.5
20-12-2021 12:01 PM	5001	E1-2-2068	-79	Active	0
20-12-2021 11:58 AM	5001	E1-2-2068	-79	Cleaning	18.5
20-12-2021 11:11 AM	5001	E1-2-2068	-79	Alert	10
20-12-2021 11:08 AM	5002	E1-3-3061	-43	Active	0

Fig. 26.3 Dew dashboard

Additionally, we also created a dashboard for the facilities management team to enable them to view operational insights in real time in addition to tracking assets. The dashboard was developed using open-source Flutter software development kit (SDK) which is mainly used for creating cross platform applications using a single codebase. Currently the developed dashboard works on web and android devices. Figure 26.3 depicts a snapshot of the Dew dashboard which shows the operational state of the different Dew boxes over a day.

26.2.2 Deployment and Data Collection

To evaluate the proposed solution, the facilities managers provided us access to three locations in one of the buildings on the UAE University campus where the prototype was deployed. These locations were selected based on the varying type of traffic that would be seen at these facilities. Prior to deployment, we ran tests to assess connectivity at the deployment locations. We had to also ensure that the deployment location would not lead to unnecessary false positives, i.e., make sure not to deploy this in a location facing a corridor as that would lead to significant false positives. To overcome this, the box was not only deployed inside the main entrance door but a casing was 3D printed to cover part of the sensor so as to narrow the angle of detection (eye shaped blue object covering the sensor in Fig. 26.1). A few variations of the eye were also made in order to block unnecessary detection of movement outside the facilities area. Subsequently the box was placed such that even if people

moved around in its vicinity beyond the zone of detection, these would not affect the count. In terms of the deployment itself, the box was designed so as to minimize deployment time. To ease maintenance, the Dew box was programmed to support over-the-air (OTA) updates and remote management. Since we wanted to build the prototype in such a way that it could be scaled up and deployed easily, we added the option to track the deployed devices by linking the box to the particular location. This way a mapping is established between the location and the box (see Fig. 26.3). Finally, with respect to data collection, as highlighted earlier, the Dew box reported timestamp, box ID, location of the box, radio signal strength, box status and count when each visitor is detected as well each time there was a change in state of the box (when the tactile switch on the box was pressed by the cleaning crew). Each of the data points helped to determine the health of the deployed box, e.g., when was the last reported data point, what is the signal quality like from the device which is reporting data and other insights which we will elaborate in the ensuing section.

26.3 Results and Discussion

In this section we highlight the findings from a pilot trial conducted on our University campus.

Figure 26.4 shows average occupancy over a twelve-hour period starting from 8 am to 8 pm over the trial duration. As seen from the figure, we observe different occupancy levels attributed to their location and time of the day with the peaks occurring in the daytime and tailing off towards the end of the day. Location 1 and 2 are medium-sized facilities on different floors with four cubicles each located in a large corridor. Location 3 is a small facility with a single cubicle located in the faculty wing with relatively limited footfalls in comparison to the other locations. Each bar represents the average value over the trial duration for a particular hour, e.g., the bar corresponding to 9 am is the average visitor count between 9 am and 9.59 am over the entire trial duration. The gap seen at 6 pm could be attributed to the change in shift of the cleaning team.

During discussions with the facilities management team, we were informed that they have a Service Level Agreement to clean the facilities every three hours. However, they adopt a more aggressive approach and resort to cleaning almost once every hour and there isn't any data driven scientific basis for the same. The exact time of cleaning varies and so does the gap between cleaning cycles. It may not necessarily be exactly every hour as evident from the timestamps that are seen in Fig. 26.3. Looking at the average visitor count in Fig. 26.4, it is evident that cleaning may not be required on an hourly basis at each location and that there exist potential optimization opportunities in terms of a reduction in the number of cleaning cycles. For example, although the occupancy at location 1 is almost half that of location 2 on most occasions (see Fig. 26.4), the number of cleaning cycles are similar. This suggests that location 1 could do with lesser cleaning than location 2. Similarly, for
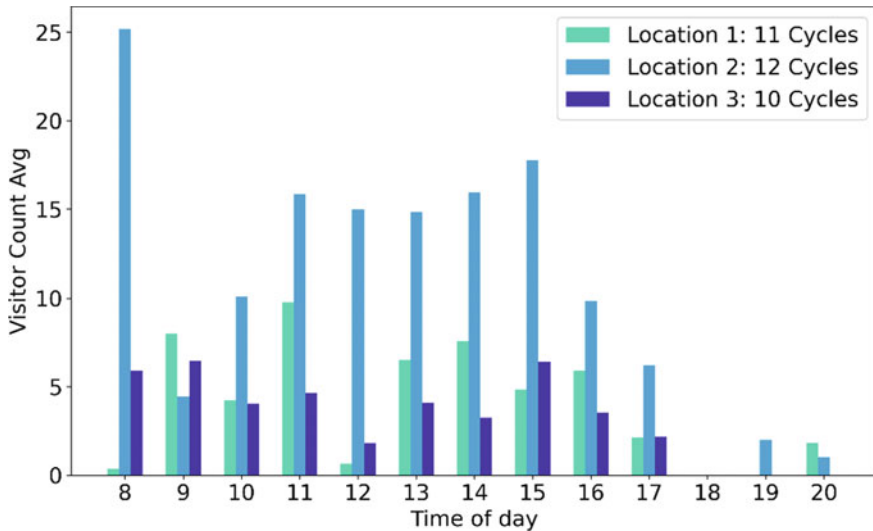
Fig. 26.4 Average visitor count at each of the three trial locations

location 3 which has a relatively lower occupancy than the other two, this could also do with fewer cleaning cycles.

If a thresholding-based approach were to be used for initiating cleaning, this would result in significantly reduced cycles. Figure 26.5 shows the cleaning cycles that would be required for a visitor threshold of ten for the same dataset used in Fig. 26.4. Observe that whilst you typically require eleven to twelve cleaning cycles in the traditional case (Fig. 26.4), this significantly reduces to five and four cycles respectively for locations 1 and 3 (a reduction of more than 50%, see Fig. 26.5). On the other hand, two extra cycles are required at location 2 to cater to the relatively higher occupancy levels. The number of cycles required would vary with a change in the threshold value which can be adjusted by the facilities management team depending on various parameters such as anticipated occupancy patterns during regular days, event days when high occupancy is expected, weekends and holidays when little/no occupancy is expected and other relevant parameters.

We now compare the water use and CO_2 emissions resulting from use of the traditional approach and the proposed approach (see Fig. 26.6) for a day. In general, cleaning requires the use of water and cleaning products both of which have a financial cost associated with them and a corresponding environmental footprint. Through optimization of the cleaning frequency, there are opportunities to reduce both water use and the use of cleaning products thereby resulting in a corresponding reduction in costs and the environmental footprint. During discussions with the facilities management team we were informed that cleaning of a cubicle within a facility consumes around 10 l of water (5 l per flush once before and once after the cleaning resulting in 10-l consumption) and another 3–5 l for cleaning the wash basin thereby resulting in an overall footprint of roughly 15 l. In light of the data presented in Figs. 26.4 and
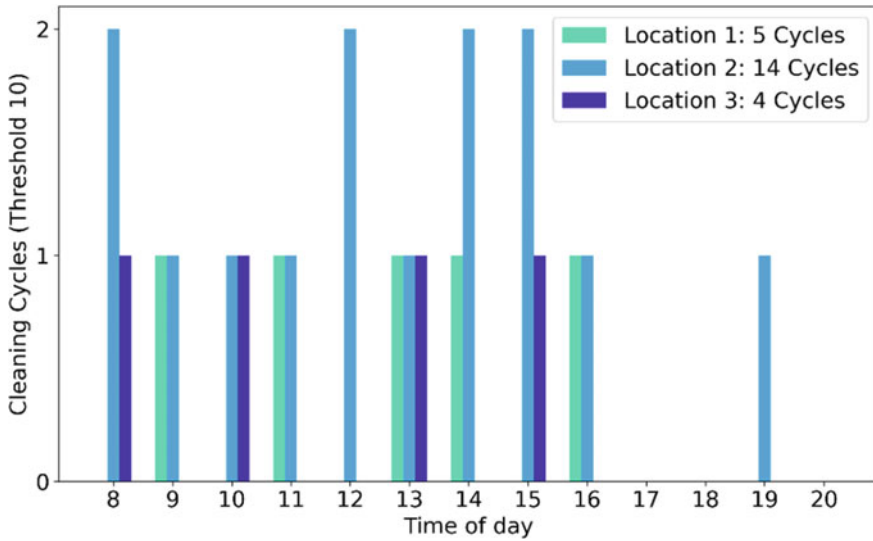
Fig. 26.5 Optimised cleaning cycles for the three trial locations

26.5, this translates to a water use of 495 l for the traditional approach (33 cycles in total * 15 l/cycle) and 345 l for the proposed approach respectively (23 cycles in total * 15 l/cycle). Given the cost of water is approximately 10 AED per cubic meter in the UAE, this translates to a cost of 4.95 and 3.45 AED respectively for a day. Whilst this may seem like a miniscule reduction, we elaborate on the cumulative effect in the next sub-section which discusses the massive potential of a scaled-up deployment over a prolonged period assuming a similar savings percentage as that in the current scenario. Finally, it is also worth understanding the CO_2 footprint of the traditional and proposed approaches. As per estimates provided in (The Sustainabilist 2020), desalination of 1 million liters of water results in 6.7 tonnes of carbon emissions which leads to a footprint of 6.7 gm CO_2 equivalent per liter of water. In the above case, this translates to 3.31 kg CO_2 equivalent and 2.31 kg CO_2 equivalent per day for the traditional and proposed approaches respectively.

26.3.1 Potential Savings in a Scaled-Up Deployment

In a large University campus such as the one in our case with a large number of buildings and several facilities with a different number of cubicles per facility, this results in a high consumption footprint. As an example, in our building, there are several facilities on different floors each with different capacities with a total of more than 50 cubicles in the building. As mentioned above, a 15-l consumption per cleaning cycle would result in 750 l of consumption for one cleaning cycle for each of these.
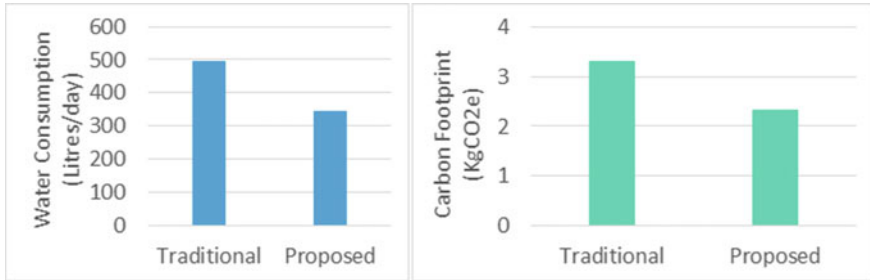
Fig. 26.6 Water use and carbon footprint over a day for the traditional and proposed approach for the current deployment

For roughly ten cycles per day, this translates to 7500 l of water and assuming 22 working days in a month, this figure is 165,000 l. If we are to assume a consumption over 10 months in a year (discounting two months of low occupancy during the different break times) this translates to the use of 1,650,000 l (1.65 million liters) of water per year for cleaning alone for one building. The cost of water in the UAE being approximately 10 AED per cubic meter results in a net cost of roughly 16,500 AED per year. Assuming a similar level of savings as that in the previous scenario, an estimated half a million liters of water could potentially be saved (Fig. 26.7). Whilst this might not seem like a large number in light of the operational budget, the impact of the cumulative effect of the savings taking into account the dozens of buildings on campus and student accommodation cannot be ignored.

Whilst the discussion above focuses purely on the water consumption and associated cost savings, there are other opportunities for cost savings too, e.g., a reduction in cleaning cycle implies reduced need for cleaning products which will result in a subsequent reduction in associated financial costs and also the environmental footprint. Additionally, the proposed solution also helps eliminate the traditional paper-based job completion sheets which can also help to reduce associated costs and enhance productivity through analysis of data which would now be available in an electronic format.

Finally, in light of the CO_2 footprint figures mentioned in the above section and the consumption figures for the scaled-up setting mentioned above, this translates to 11.05 tonnes of CO_2 equivalent (1.65 million liters * 6.7 tonnes/million liters) for the traditional case while a potential saving of 3.315 tonnes CO_2 equivalents
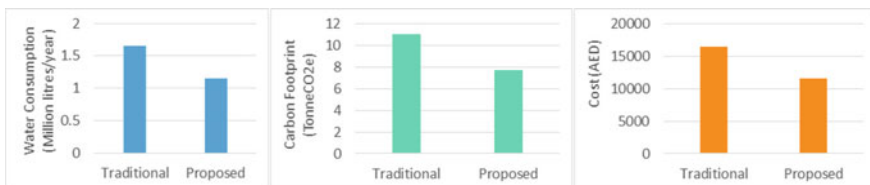
Fig. 26.7 Potential savings in a scaled-up deployment for our building with 50 cubicles

with the proposed approach. In summary, taking into account the cumulative effect, a widespread deployment across the building footprint in a city/country has the potential to deliver a significant impact both in terms of water conservation, cost savings and a corresponding reduction in the environmental impact.

26.4 Conclusions

In this paper, we presented a cyber-physical system for reducing water use in buildings. We highlighted the shortcomings of the traditional approach which involves periodic cleaning of facilities and showcased how a thresholding-based approach can help to optimize the number of cleaning cycles. Towards the same, we developed a proof-of-concept prototype called Dew which tracks the number of visitors using the facilities in a privacy-preserving manner and uses this information to determine the optimal number of cleaning cycles for the location. The proposed system was designed with ease of use in mind and a dashboard was also developed for the facilities management team to enable them to act on the insights offered by Dew. Findings from a pilot trial conducted in one of our campus buildings involving three locations have shown that the proposed solution can offer opportunities for significantly reducing water use, costs and the resulting environmental impact. Savings as high as 50% in two out of the three locations and on average 30% across all locations are realizable as shown in this study. This is a promising finding as this presents a tremendous potential for a scaled-up deployment comprising a large number of buildings over a prolonged period. This makes a strong case for the deployment of Dew.

Future work could look into a tighter integration of Dew with existing operational procedures, in particular, automatic notifications for the cleaning team through SMS/custom app notifications depending on the alerts generated by Dew. Avenues also exist to solicit visitor feedback through an app/kiosk deployment at the facilities and integrate this information with the one gathered by Dew.

References

Ghosh S, Kumar A, Saha S (2021) highly accurate real time human counter with minimum computation cost. In: 2021 International conference on advances in electrical, computing, communication and sustainable technologies (ICAECT), pp 1–7

Herviana A, Sudiharto DW, Yulianto FA (2020) The prototype of in-store visitor and people passing counters using single shot detector performed by OpenCV. In: 2020 1st International conference

on information technology, advanced mechanical and electrical engineering (ICITAMEE), pp 169–174

Instalator (2021) Bathroom lighting control based on visitor counter. https://discourse.world/h/2016/01/30/Bathroom-lighting-control-based-on-visitor-counter

Jayasinghe L, Wijerathne N, Yuen C (2018) A deep learning approach for classification of cleanliness in restrooms. In: 2018 International conference on intelligent and advanced system (ICIAS), pp 1–6

Kashima K, Nakamura R, Kajiwara A (2013) Bathroom movements monitoring UWB sensor with feature extraction algorithm. In: 2013 IEEE sensors applications symposium proceedings, pp 118–122

MongoDB (2021) Application data platform. https://www.mongodb.com/

Myint EP, Sein MM (2021) people detecting and counting system. In: 2021 IEEE 3rd global conference on life sciences and technologies (LifeTech), pp 289–290

P.I.R. (2021) Passive infrared sensor. https://learn.adafruit.com/pir-passive-infrared-proximity-motion-sensor/overview

Parse (2021) Backend-as-a-service platform. https://parseplatform.org/

Platform RP (2021) https://www.raspberrypi.com/products/raspberry-pi-zero/

RGB, LED (2021) 5mm RGB LED—Clear common cathode. https://shop.edwinrobotics.com/products/1411-5mm-rgb-led-clear-common-cathode-pack-of-5.html

Ros K, Mocanu E, Seifert C (2019) Airport restroom cleanliness prediction using real time user feedback data. In: 2019 IEEE 5th International conference on collaboration and internet computing (CIC), pp 1–10

Seed Engineer (2021) Water use efficiency in buildings. http://seedengr.com/Water%20use%20efficiency%20in%20buildings.pdf

Singapore Government. (2020) Water efficiency benchmark report. https://www.pub.gov.sg/Documents/WaterEfficiencyBenchmark_Office.pdf

Sustainabilist T (2020) Carbon footprint of water consumption. https://thesustainabilist.ae/carbon-footprint-of-water-consumption/

Switch (2021) Momentary push button switch 7mm. https://shop.edwinrobotics.com/products/427-momentary-push-button-switch-7mm-pack-of-5.html

Chapter 27
Measures Against Climatic Changes for Ghana's Volta River Basin

Check for updates

Eihab Fathelrahman, Timothy Green, and Kenneth Strzepek

27.1 Introduction

Climate change and variability are one of the most significant challenges this century and into the next. Developing countries in Sub-Saharan Africa (SSA) are particularly at risk in areas where temperatures will rise the fastest. They are also more vulnerable because they depend on agriculture, the most climate-sensitive sector. Despite uncertainty about the precision of climate science, there is now close agreement amongst climate scientists on several issues. Firstly, it has been firmly established that the earth is undergoing rapid changes due to significant greenhouse gas increases (GHGs) increases. For example, global GHG emissions have roughly doubled since the early 1970s and, on current policies, could rise by over 70% from 2008 to 2050. Atmospheric concentrations of carbon dioxide (CO_2) have increased by nearly 100 ppm (parts per million) compared to pre-industrial levels, reaching 379 ppm in 2005, and the Earth has warmed by 0.7 °C since 1900 (IPCC 2007; Brohan et al. 2006). Secondly, human activities, notably the burning of fossil fuels and deforestation, have been identified as prime causes of the changes observed in the 20th century and

E. Fathelrahman (✉)
Department of Integrative Agriculture, College of Agriculture and Veterinary Medicine, United Arab Emirates University, P.O. Box 15551, Al Ain, UAE
e-mail: eihab.fathelrahman@uaeu.ac.ae

T. Green
Water Management and Systems Research Unit, 2150-D Centre Ave. Suite 320, Fort Collins, CO 80526, USA
e-mail: tim.green@usda.gov

K. Strzepek
Environmental, and Architectural Engineering, University of Colorado, Boulder, CO, USA
e-mail: strzepek@mit.edu

are likely to contribute to further changes in the 21st century (IPCC 2001). These atmospheric changes will likely alter temperatures, rainfall patterns, and sea levels. Furthermore, it increases the frequency of extreme weather events and climate-related aspects.

Even though Ghana has considerable surface and groundwater resources, climate change will negatively affect usable water resource availability. Due to changing climate, lower precipitation, expanded evaporation, and frequent droughts will decrease water availability in the Volta River Basin (VRBN). Furthermore, the Akosombo dam, which provides about 70% of the country's energy needs, produces only 30%t during dry low water levels. Such energy reduction affects industrialization and private-sector development. Since farmers rely on rain-fed agriculture, these factors also contribute to significant variations in agricultural productivity (Kabo-Bah et al. 2016).

Agricultural development in Ghana is highly dependent on water availability across the Volta River Basin (VRBN). Ghana is more vulnerable because agriculture is the most climate-sensitive sector. The contribution of the farming industry in Ghana was estimated to be 42% of the country's Gross Domestic Product (GDP)—Fig. 27.1. The predicted climatic changes will adversely affect human well-being and activities, food insecurity, reduce water availability within the Volta River basin, and primarily reduce the agricultural sector's contribution to the country's income. The variability of the growth in the agriculture sectors is illustrated in Fig. 27.2. In response to these climate changes, people will migrate, searching for better land and water resources. The migration and relocation of the population from rural to urban areas cause pressure and higher demand on municipal services (e.g., water supply and sanitation, public health, energy, transportation, and housing services), which necessitate better management of the water flow at the basin in response to climate changes.

Dembélé et al. (2022) showed that disparities are observed in the spatial patterns of hydroclimatic variables across climatic zones, with higher warming in the Sahelian zone at the Volta River Basin (VRB). Authors showed that climate change would have severe implications for future water availability with concerns for rain-fed agriculture, weakening the water–energy–food security nexus and amplifying the local population's vulnerability. The variability between climate models identifies the uncertainties in the projections and indicates a need to represent complex climate features in regional models better. These findings could serve as a guideline for the scientific community to improve climate change projections and for decision-makers to elaborate adaptation and mitigation strategies to cope with the consequences of climate change and strengthen regional socio-economic development. Similarly, this study's main objective is to study the climate change impacts and adaptations for the agricultural sector in Ghana's Volta River Basin.
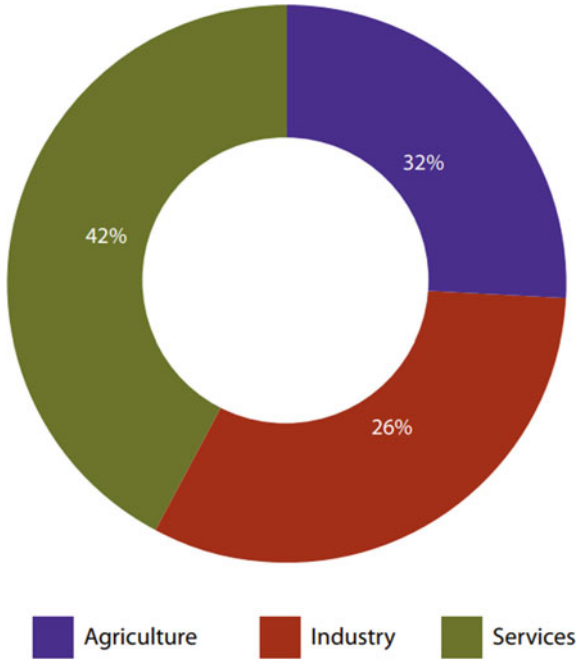
Fig. 27.1   Ghana's gross domestic product (GDP) contribution by sector
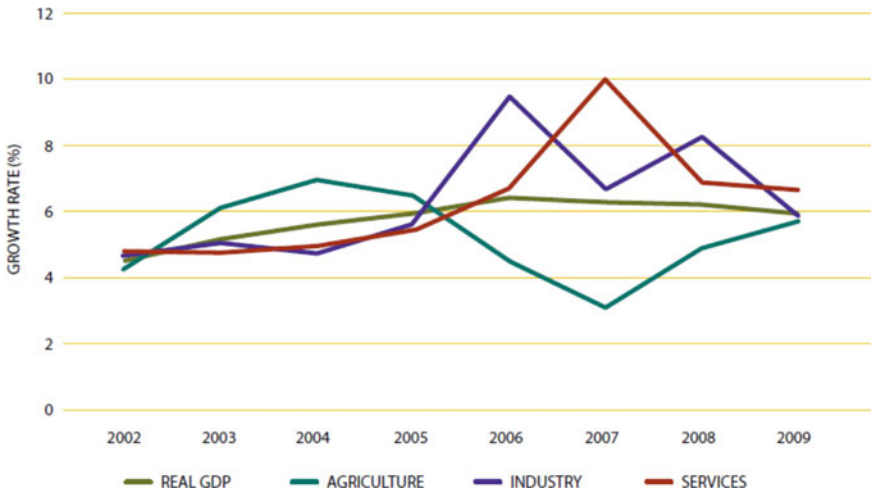

Fig. 27.2   Historical output growth trend (%)-agricultural sector contribution against the other sectors

27.2   Objectives

The two objectives of this study are:

Identifying proper River basin modeling of hydrology and Volta River basin to assess the hydrology and cropping systems vulnerability using CLI-Run (model for climate change simulations), Cli-Crop (model for crop yield impacts) and IMPEND (model for watershed optimization).

Investigate climate change (that include dry and wet climate change scenarios), economic impacts on the water and agricultural sectors in Ghana, and identify adaptation strategies that optimize resource use in the Vola River Basin (VRBN) by using if, then scenarios.

27.3   Methodology

To study the impact of climate changes on the agricultural sector and the Volta River Basin in Ghana, Volta River Basin, using the scenarios represented in Table 27.1. This study used the CLICROP Model. CLICROP is a crop model used to calculate the effect of changing daily precipitation patterns caused by increased CO_2 on crop yields and irrigation water demand—Eq. (27.1). The model was developed in response to the available crop models that use monthly average rainfall and temperature to produce crop yields. Model results serve as inputs to the Climate, Hydro, and Cost minimization models to produce the modeling outcomes/results—Figs. 27.3 and 27.4.

The following is the CLICROP yield equation.

$$\text{equation:} \left[1 \frac{Y_a}{Y_m} = K_y^d \cdot \left[1 - \frac{ETC^d}{ETA^d} \right] \right] \tag{27.1}$$

where

Y_a = predicted actual yield
Y_m = maximum yield
K_y^d = yield coefficient, different for development stage d
ETC^d = sum of daily ET crop demand for development stage d

Table 27.1 General circulation models scenarios for global and country's specific study

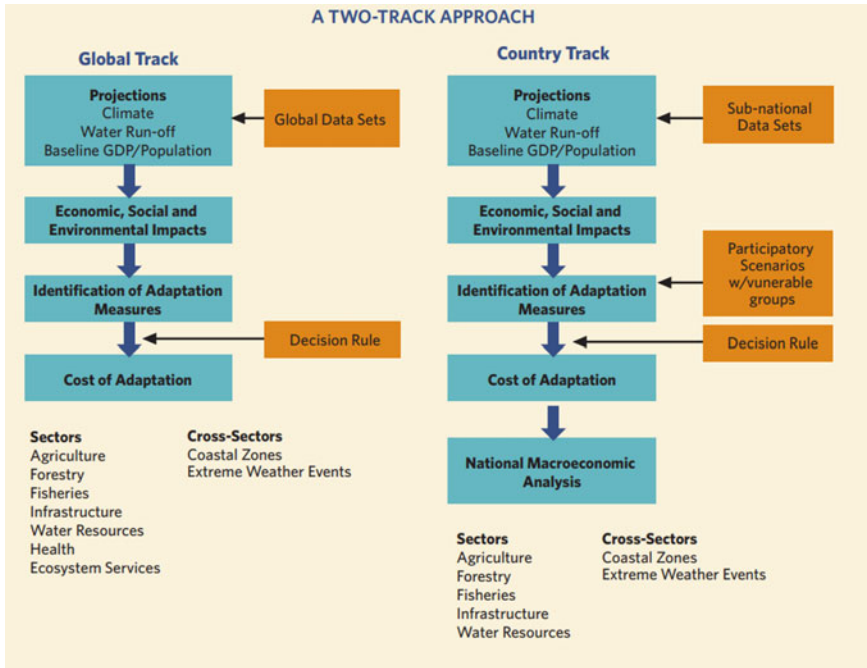| Scenario	General circulation model (GCM)	SERIES	Climate moisture index (CMI) deviation (%)
Global wet	ncar_ccsm3_0	A2	− 17
Global dry	csiro_mk3_0	A2	9
Ghana wet	ncar_pcm1	A1b	49
Ghana dry	ipsl_cm4	B1	− 66

**Fig. 27.3** Climate change scenarios applying the global and the country-specific tracks

ETA^d = sum of daily actual ET for development stage d

%Yield^d = ratio of actual yield over maximum yield, the value reported by CLICROP.

27.4 Results

The Volta River Basin (VRBN) is an essential transboundary basin in West Africa that covers more than 410 thousand square kilometers across six countries in western Africa. These countries include Benin, Burkina Faso, Côte d'Ivoire, Ghana, Mali, and Togo. The basin's natural resources sustain its population's living and contribute to economic development in Ghana and neighboring countries, Williams et al. (2019). Figure 27.5 compares the temperature range in the two and agroecological between the base scenario temperature range and the climate change scenario's range. The figure indicates a typical pattern of temperature changes across the various agroecological zones in Ghana. The Ghana Wet and Dry scenarios show higher temperature variability relative to the base scenario than the Global Wet and Global Dry scenarios.

The precipitation forecast reveals a cyclical pattern over 2010–2050 for all regions in Ghana, with high rainfall levels followed by a drought every decade. The wettest
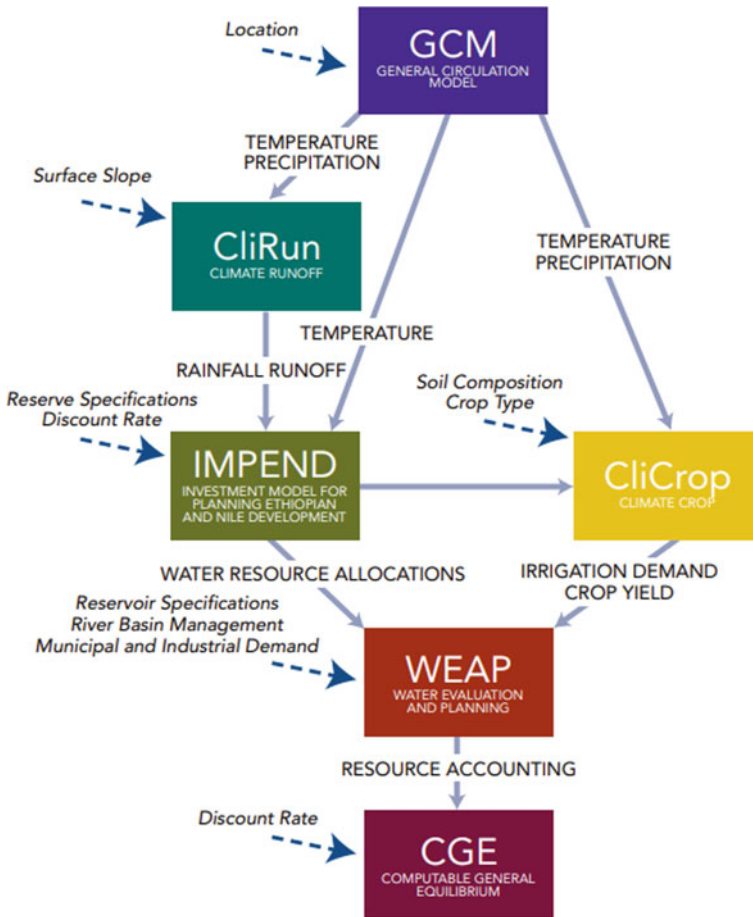
Fig. 27.4 Flowchart of the modules used to simulate climate change impacts and adaptation scenarios for the agricultural sector in Ghana's Volta River Basin (VRBN)

parts of the country are expected to be the Forest and Coastal agroecological zone. The Northern and Southern Savannah regions are expected to be relatively dry—Fig. 27.6.

As illustrated in Table 27.2, climate change economic in present value impacts (costs) in billion dollars result from global and Ghana-specific scenarios. The highest economic cost appears in the Ghana Global Dry scenario of 13.1 billion dollars or 31.5 dollars per capita per year. Meanwhile, the lowest costs are the outcome of the Ghana Dry country-specific scenario. The total economic costs are estimated to be 2.7 billion dollars and 9.7 dollars for the present value of lost welfare and the per capita annual income.
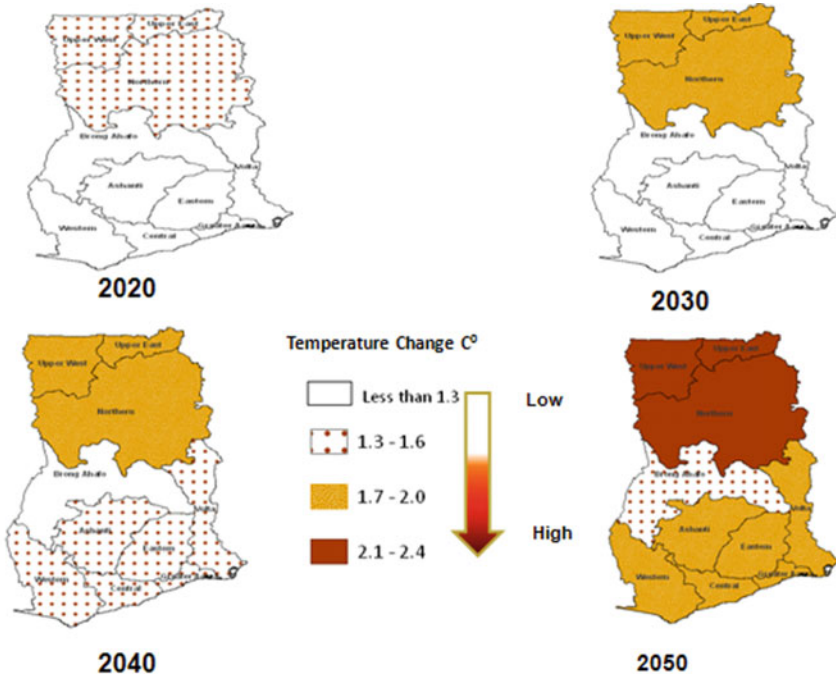
Fig. 27.5 Climate changes and temperature wet versus dry scenarios compared for every decade forecast from 2020 to 2050
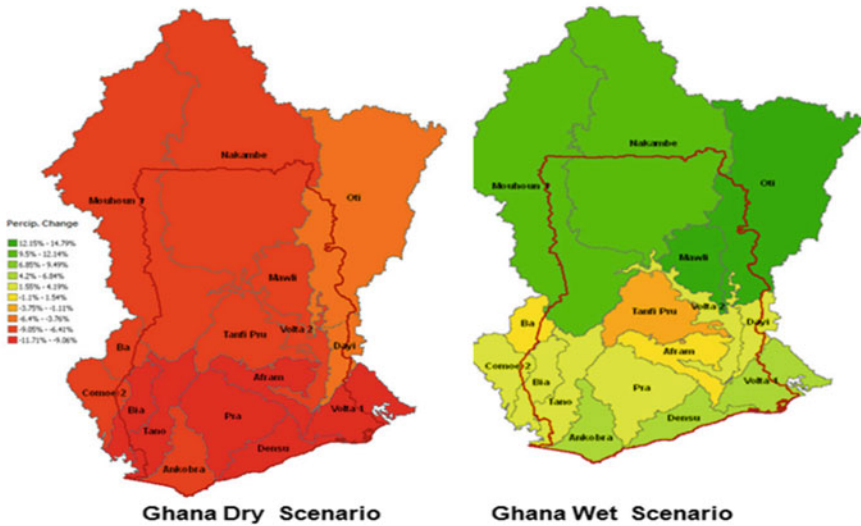

Fig. 27.6 Ghana's dry scenario and wet scenario precipitation changes compared to the base scenario, an average of 2010–2050

Table 27.2 Climate change results from global and Ghana-specific track scenarios

| Scenario	Present value of lost welfare ($ billion)	Equivalent annual value ($ billion)	The annual equivalent per capita ($)
Global dry	13.118	764.5	31.46
Global wet	10.095	558.3	24.21
Ghana dry	2.709	157.9	6.5
Ghana wet	5.05	236	9.71

Source World Bank (2010). Economics of adaptation to climate change: country case studies, Ghana report

Table 27.3 and Fig. 27.5 and below show the climate change scenarios' adaptation costs at selected sectoral levels (traditional non-irrigated rain-fed Agriculture, Hydro/Agriculture, and education sectors). The cost with no climate change is expected to be between 13.1 billion dollars in the Global Dry scenario and 2.7 billion dollars at the national level. At the sectoral level of road design, adaptation costs can be as high as 10.3 billion dollars. Traditional agriculture and irrigated agriculture climate change adaptation costs are expected to be moderate compared to the infrastructural sectors (Fig. 27.7).

Table 27.3 Climate change scenarios' results at the national and sectoral levels (present value in $ billion)

Scenario	No adaptation	Road design	Traditional rain-fed agriculture	Hydro/agriculture	Education
Global dry	− 13.118	− 10.308	− 0.121	− 0.941	− 2.09
Global wet	− 10.095	− 5.854	− 2.973	2.116	0.584
Ghana dry	− 2.709	− 3.009	− 1.193	− 1.782	− 1.308
Ghana wet	− 4.05	− 0.766	1.936	1.358	1.795

Source World Bank (2010). Economics of adaptation to climate change: country case studies, Ghana report
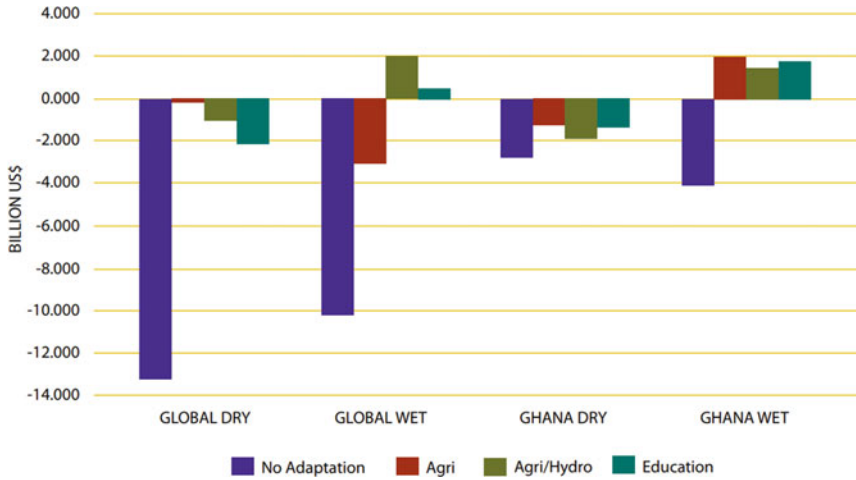
Fig. 27.7 Climate change costs of the scenarios on the traditional rain-fed agriculture, hydro-irrigated agriculture, roads sector, and education sector

27.5 Conclusion and Recommendations

The agricultural and hydro sectors' climate change adaptation measures in this study include investment in agricultural research and extension services, including transfer research and development findings (e.g., more drought-tolerant crop varieties and animal species) to the end-users (farmers and their inputs providers). Successful agricultural climate change adaptation measures must consider crops and livestock production and marketing activities from the farmers to the consumers' level (i.e., throughout the food supply chain). Climate change adaptation strategies also provide storage and better marketing capabilities for cash and non-cash crop producers. Agricultural climate change adaptation strategies should target both rain-fed as well irrigated lands. Climate change adaptation strategies may include programs and projects to enhance irrigation project efficiency in irrigated land. Analysis of agricultural sector climate change adaptation strategies will consider agroecological zones' production and crop compositions (cash crops versus food crops) and the possible economic implications of such classification.

Under the scenarios included in this study, part of the available resource envelope is spent on additional investments in hydropower relative to the baseline that eliminates negative climate change impacts on power generation. The remaining part of the resource envelope is spent on agricultural productivity improvements. An increase in agricultural productivity due to investment in infrastructure, R&D, and agricultural extension services has been widely reported in previous studies. For instance, Alston et al. (2000) showed that typically the return to investment in agricultural R&D generates 40–60% returns annually for each dollar invested. These returns include an increase in the productivity of crops and livestock products.

To be better prepared for floods and or droughts, there is a need for enhanced irrigation project efficiency. A higher level of irrigation efficiency significantly decreases water consumption and saves water for other sectors (Municipal and Industrial M&I). Climate change adaptation strategies may also provide the agricultural sector's stakeholders with modern climate forecasting capabilities. These forecasting capabilities may consist of climate monitoring stations and early warning systems. Low-income communities and households in Ghana are highly vulnerable and at risk of climate change. The agriculture climate change adaptation strategies work successfully in the presence of high-level coordination with the country's poverty reduction programs to optimize the outcome for the poor communities.

Climate change adaptations relevant to the agricultural and hydro sectors at the Volta River Basin (VB) include the need to improve water storage capacity to utilize excess water in wet years during dry years. It is recommended to improve agricultural and livestock extension services and marketing networks and construct small to mid-size irrigation facilities. Improve entrepreneurial skills to generate off-farm income. As well it was founded, improving access to loans and microcredit is essential. Other necessary measures include increasing water transfer from the Volta basin to meet the needs of a growing urban population. Finally, the study found that it is essential to construct efficient infrastructure and reduce the blocking of dry-stream channels to harvest rainwater to recharge the groundwater system, which serves as an alternative water supply during dry years and develop a program for afforestation initiatives to improve land-use practices, protection of river courses, and de-sedimentation of reservoirs.

References

Alston JM, Chan-Kang C, Marra MC, Pardey PG, Wyatt TJ (2000) A meta-analysis of rates of return to agricultural R&D: ex pede herculem? International Food Policy Research Institute. Research report 113

Brohan P, Kennedy JJ, Harris I (2006) Uncertainty estimates in regional and global observed temperature changes: a new data set from 1850'. J Geophys Res 111:D12106. https://doi.org/10.1029/2005JD006548

Dembélé M, Vrac M, Ceperley N, Zwart SJ, Larsen J, Dadson SJ, Schaefli B (2022) Contrasting changes in hydrological processes of the Volta River basin under global warming. Hydrol Earth Syst Sci 26(5):1481–1506

International Panel on Climate Change (IPCC) (2001) Climate change 2001: summary for policymakers. In: Watson RT (ed) A contribution of working groups I, II and III to the third assessment report of the intergovernmental panel on climate change. Cambridge University Press

International Panel on Climate Change (IPCC) (2007) Summary for policymakers. In: Parry ML, Canziani OF, Palutikof JP, Linden PJ, Hanson CE (eds) Climate change 2007: impacts, adaptation, and vulnerability. Contribution of working group II to the fourth assessment report of the intergovernmental panel on climate change. Cambridge University Press

Kabo-Bah AT, Diji CJ, Nokoe K, Mulugetta Y, Obeng-Ofori D, Akpoti K (2016) Multiyear rainfall and temperature trends in the Volta River basin and their potential impact on hydropower generation in Ghana. Climate 4(4):49

Williams PA, Crespo O, Abu M (2019) Adapting to changing climate through improving adaptive capacity at the local level–the case of smallholder horticultural producers in Ghana. Clim Risk Manag 23:124–135

World Bank (2010) Economics of adaptation to climate change: country case studies, Ghana Report. https://documents.worldbank.org/en/publication/documents-reports/documentd etail/278431468337213682/main-report

Chapter 28
Contribution to Implementing a Fair Water and Energy Exchange Between Israel and Jordan

Daniel Janowitz, Marco Margheri, Hamzeh Yakhoul, Jacob Bensabat, Bernd Rusteberg, and Süleyman Yüce

28.1 Introduction

Jordan is heading towards a serious water crisis, being one of the most water-scarce countries in the world. In this respect, recent water budget studies indicate that Jordan is facing a freshwater deficit of about 712 million m^3 per year by 2050 (Bourgoing et al., 2020a). Due to depleting groundwater sources, the freshwater deficit can only be met by developing new freshwater sources. Therefore, deploying seawater desalination (SWD) and water transfers to the Jordanian demand centres in the North is essential. Reverse osmosis (RO) is the prevailing technology for large-scale seawater desalination due to technical maturity, scalability and cost-effectiveness. Process innovations led to a major decrease in energy demand from 20 to 2.5–4 kWh/m^3 (Fritzmann et al. 2007). Furthermore, in contrast to thermal desalination plants that

D. Janowitz (✉) · S. Yüce
STEP Consulting GmbH, Eupener Str. 30, 52066 Aachen, Germany
e-mail: daniel.janowitz@rwth-aachen.de; janowitz@stepconsulting.de

S. Yüce
e-mail: yuece@stepconsulting.de

M. Margheri · H. Yakhoul
Dorsch International Consultants GmbH, Landsberger Str. 368, 80687 München, Germany
e-mail: Marco.Margheri@team.dorsch.de

J. Bensabat
EWRE Ltd, Shaar Halevanon Street 3, 3445402 Haifa, Israel
e-mail: jbensabat@ewre.com

B. Rusteberg
Rusteberg Water Consulting, RWC UG, Himmelsbreite 49, 37085 Göttingen, Germany
e-mail: brusteberg@rustebergwaterconsulting.com

S. Yüce
Chemical Process Engineering, RWTH Aachen University, Forckenbeckstr. 51, 52074 Aachen, Germany

were predominant in the past, RO only needs electrical energy for pumping, so combining renewable energies is much easier. In this respect, Israel has been investing in large-scale seawater desalination since the late 90 s producing around 600 million cubic meters per year (Mio. m^3/a) of freshwater today. In contrast, the geographical situation in Jordan makes national seawater desalination plants at the Red Sea and transporting the freshwater to the demand centre Amman in the North expensive. The significantly shorter distances for water transfer from the Israeli coastline to Jordanian demand centres seem to be far more economically advantageous than solutions based on seawater desalination at Aqaba (Rusteberg et al. 2022b). Therefore, transboundary water production and transfer (WPT) strategies are required to face Jordan's rapidly increasing freshwater deficits.

Worldwide efforts to reduce carbon dioxide emissions and to mitigate the impacts of climate change have been intensified. As a result, governments tightened their carbon dioxide reduction targets. In this respect, Israel intends to impose a carbon tax soon (MFI 2021) and recently tightened its carbon reduction targets by being carbon neutral by 2050 (MEI 2021a). In addition, Jordan intends to increase its renewable energy share in the electricity mix to 50% by 2050 (JNA 2021). Therefore, substantial efforts are expected to develop renewable energies in both countries. Harvesting the vast solar potential is the best option for deploying the needed large-scale electricity generation infrastructure. Photovoltaics or concentrated solar power systems are mature technologies that enable large-scale deployment. However, solar energy alone cannot represent a viable solution because it depends on weather conditions, seasons, and sun hours, reducing its reliability. Therefore, solar energy needs to be coupled with energy storage to produce electricity when solar energy cannot be harvested. This would require the allocation of large land areas for this purpose. But land availability for large-scale renewable energy generation deployment is a limiting factor in Israel and a challenging task (Tal 2018; Katz and Shafran 2019). In contrast, Jordan has large amounts of available land that could be used for solar energy generation and higher solar irradiation, which makes solar plants in Jordan even more economical.

The above-mentioned regional challenges are the basis for developing promising water-energy-exchange concepts between Israel and Jordan. This difference in national interests creates a potential synergy for cooperation between the two countries leading to mutual benefits. In this respect, Israel could deploy large-scale seawater desalination plants at its coastline for Jordan's freshwater production. In contrast, Jordan has large amounts of land available for solar energy generation for Israel in exchange for freshwater. Therefore, Israel and Jordan have recently signed a declaration of intent (DoI) which forms the basis for developing the exchange idea of exchanging Blue Water for Green Energy (MEI 2021b). The DoI aims to intensify the cooperation between the two countries by supplying 200 MCM/y freshwater from Israel to Jordan in exchange for 600 MW of electricity based on renewables to be produced in Jordan and supplied to Israel. The regional challenges and benefits that impact the exchange concept design and implementation are shown in Fig. 28.1.
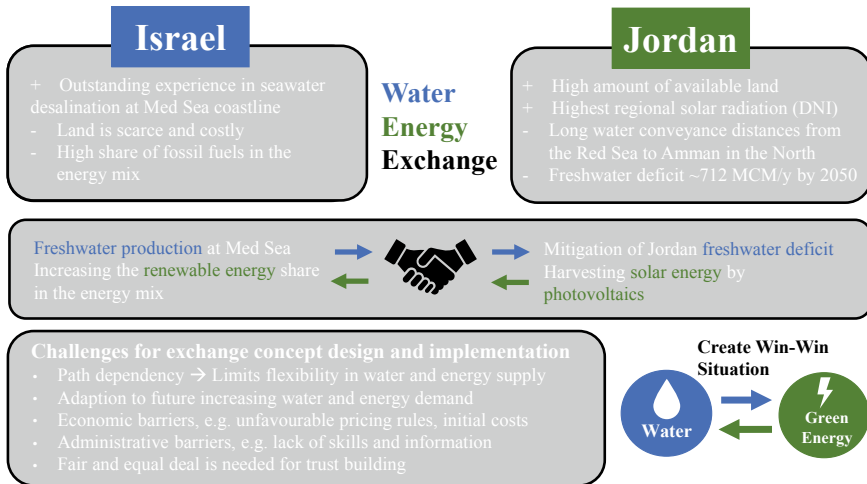
Fig. 28.1 Regional challenges and benefits influencing the fruitful design and implementation of a fair water energy exchange deal

The main objective of designing a water-energy-exchange concept is to create a win-win situation for both parties. In this respect, the above-mentioned regional challenges and benefits are only the basis since the concept implementation has some risks that must be tackled. For example, a rigid and unchangeable water-energy-exchange concept would lead to path dependency that limits future water policy flexibility (Katz and Shafran 2020). However, designing the implementation in a modular approach could reduce path dependency by enabling easy and flexible adaptation in the case of changing freshwater and energy demand. In addition, economic barriers such as unfordable pricing rules or administrative barriers such as lack of skills in plant operations also need to be considered (Katz and Shafran 2019). These barriers are particularly relevant concerning the availability difference in water production and renewable energy generation. For example, high plant availability in water production is essential to minimize water production costs in desalination plants. In contrast, the electricity output of solar energy generation plants depends on the solar hours and potential cloudiness. Therefore, the water-energy-exchange concept needs to be designed in a way that considers the availability differences. In summary, the challenges in such an ambitious project can only be overcome if the risks are calculable and a leap of faith is made based on mutual benefits. Furthermore, trust building in the cooperation can only happen through the project's successful implementation and cooperation on an equal footing. In this respect, trustful cooperation strengthens the water-energy exchange and can be the basis for further regional cooperation. However, working out the concepts of being fair and equal is imperative.

This article further takes the DoI agreement as a basis and concretizes the exchange concept on the results of the SALAM initiative. The work and results presented in

this article show the final results of the 2nd project phase of the SALAM initiative (SALAM 2022). The SALAM initiative is a joint research and development project involving 20 partner institutions from Palestine, Jordan, Israel and Germany, funded by the German Federal Ministry for Research and Development (BMBF). The main objective of this article is to present the potential realization of water-energy-exchange based on current market data and discuss the viability of a SWAP concept based on a bartering approach.

28.2 Methods

Considerations and concept discussions are available on the pre-feasibility level (Katz and Shafran 2020; Katz and Shafran 2019; ECO PEACE 2020). Furthermore, the scientific exchange with regional partners and stakeholders within the SALAM initiative enabled the concretization of water-energy-exchange concepts in line with the current market situation. Therefore, we assessed the feasibility and economic viability of a water-energy-exchange between Israel and Jordan by taking the following steps (Janowitz et al. 2022b):

(1) Identification of seawater desalination (SWD) production sites at the Med Sea coast in Israel, including onshore and offshore desalination possibilities
(2) Identification of optimal routes for freshwater conveyance between the SWD-plants and demand centres in Jordan
(3) Selection of promising strategies for water production and transfer
(4) Choice of options for renewable energy production by photovoltaics in Jordan
(5) Analysis of energy transfer to Israel.

28.2.1 Water Production, Including Offshore Desalination at the Israeli Coastline

As the most promising and predominant desalination technology, reverse osmosis was selected for producing the required freshwater from seawater. We determined the potential desalination sites by choosing the most appropriate feed points into the transport network and the proximity to the essential demand centres in Northern Jordan. The intake and brine discharge of onshore desalination plants can negatively impact the marine environment, particularly for large-scale plants. Higher salinity and temperature, as well as process chemicals in seawater brine, can negatively impact marine ecosystems and water and sediment quality (Janowitz et al. 2022a). In addition, public discussions and protests concerning appropriate land use led to a significant delay in realizing an additional onshore desalination plant at the Israeli cost already today. Therefore, we also considered offshore desalination

concepts on artificial islands to give an alternative to land scarcity having economic and environmental benefits compared to onshore solutions (Janowitz et al. 2022a). The preliminary design of the offshore structures included analyzing historical wind data from NCEP (National Centers for Environmental Prediction) and calculating the expected wave heights at the study locations (Janowitz et al. 2022a). Based on the water depths, the construction costs for the artificial islands were estimated by adopting conservative assumptions.

28.2.2   Water Transport and Regional Strategies

The SALAM initiative developed 12 water strategies based on seawater desalination at the Red Sea and Med Sea and water conveyance via pipelines to regional demand centres in both Jordan and Palestine (Rusteberg et al., 2022b). The resulting water production and transfer strategies are feasible and cost-effective to meet the projected freshwater deficits by 2050. Figure 28.2 shows the regional water distribution network as an overlay of the most technically and economically advantageous options (Rusteberg et al. 2022b). The potential sites for seawater desalination and water transport routes may be evaluated in a more detailed feasibility study to consolidate the suggested water-energy-exchange concept. The strategy development also considered offshore solutions for seawater desalination (Janowitz et al. 2022a). In particular, the water-energy-exchange concept presented in this article is based on the Jordanian strategy No. 3e, which is a bilateral solution in cooperation with Israel (Rusteberg et al., 2022b). The primary focus of the selected water production and transfer strategy is on meeting Jordan's freshwater deficit alone of ~ 700 million cubic meters per year (MCM/y) in 2050 by SWD at the Med Sea and the Red Sea. A Jordanian desalination plant at Aqaba would cover 300 MCM/y of the projected freshwater deficit. The remaining ~ 400 MCM/y could be covered by a large-scale seawater desalination plant north of Haifa Bay and fed into the Sea of Galilee via a tunnel. The freshwater would then be transferred via pipelines and pumping stations to central and northern Jordan demand centres. This route enables the exploitation of the topographic elevation difference between the Med Sea and lake Galilee of about 220 m for hydropower generation, which would reduce the energy demand of water production and transfer. Furthermore, if the short distance from Haifa to the water demand centers in Northern and Central Jordan into account, water production and transfer from the Med Sea, it is understandable that the transboundary solution is much more cost-effective compared to the Red Sea solution. If around 400 MCM/y of the Jordanian freshwater deficit, projected for 2050, would be covered by seawater desalination and water conveyance from Haifa, the specific water costs would be reduced to 1.72 \$/m^3 compared to ~ 2.06 \$/m^3 by covering the total expected Jordanian freshwater deficit from Aqaba, only (Schär and Geldermann 2022). If the share of Haifa regarding SWD and transfer would be increased to about 560 MCM/y, the specific water cost could be even decreased to 1.63 \$/m^3 (Bensabat et al. 2022; Rusteberg et al. 2022a).
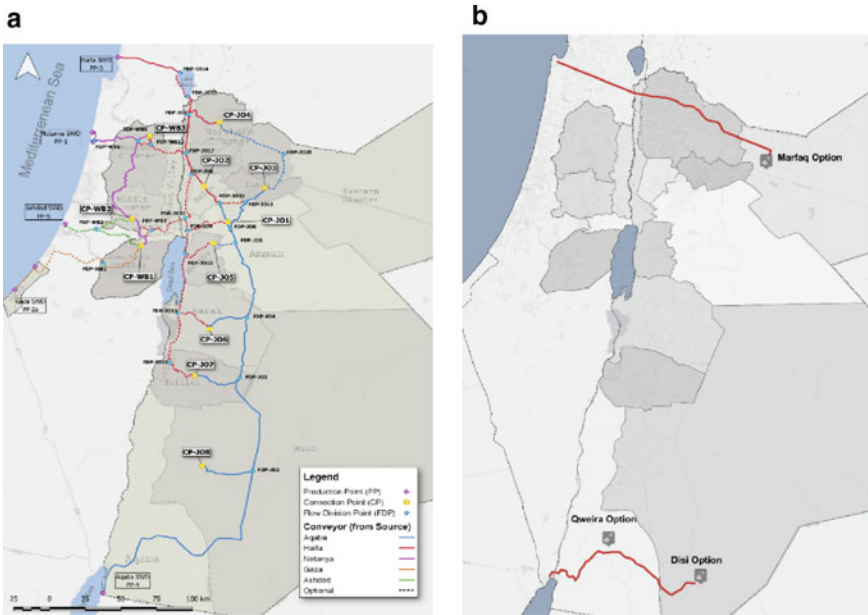
Fig. 28.2 **a** Relevant water productions and transport options, **b** potential sites for the production of electric power in Jordan for transport to Israel

28.2.3 Renewable Energy Production by Photovoltaics (PV) in Jordan

Recent cost reductions in photovoltaic systems make large-scale implementation cost-effective and attractive compared to other available technologies for renewable energy generation in solar-rich countries. Therefore, only electricity generated by PV as a counterpart within the water-energy exchange was considered. Potential locations for large-scale PV plant deployment in Jordan were identified for cost-effective and feasible implementation. The proximity to Israel's major load centres is essential to reduce power transmission costs. In addition, the solar radiation level within Jordan differs, leading to changing electricity output by choosing the same solar modules. After the preliminary assessment of possible locations for large-scale PV deployment, a short list of three alternatives was created for further evaluation. Considering a favourable short distance to Israel's major load centres, the area in the North-West of Jordan in the Mafraq Governorate is beneficial. However, the solar radiation is much higher at two feasible locations in the South of Jordan within the Aqaba and Ma'an Governorate. We assumed that a new transmission line would be constructed to connect a large city on the Israeli side (Haifa for the northern and Eilat for the southern alternatives). In addition, we must assume that the Israeli power network could consume the generated power.

Table 28.1 LCOET key assumption

Parameter	Value	Unit
PV cost	630	USD/kWp
HV substations	200	USD/kWp
HV transmission line	1,000,000	USD/km.GWp
PV O&M	10	USD/kWp/year
HV TL O&M	2000	USD/km.GWp/year
O&M increase	3	%/year
PV degradation	0.6	%/year
Transmission losses	7	%/1000 km
Financing + developer profit	5	USD/MWh

Considering the assumptions above, we conducted energy simulations using the PVsyst software to assess the proposed alternatives' generation potential (PVsyst 2022). A 1MWac PV plant with a 1.22 DC to AC ratio, using a single-axis tracking system with bifacial PV modules was simulated at the three locations, and the following results were obtained:

- Mafraq Governorate (close to Mafraq city):2,165 kWh/kWp, 180 km Transmission Line length)
- Aqaba Governorate (Qweira): 2,360 kWh/kWp, 70 km TL length)
- Ma'an Governorate (Disi): 2,402 kWh/kWp, 140 km TL length,

We determined the levelized costs of electricity generation and transmission by using the assumptions in Table 28.1.

28.2.4 Calculation of Water and Energy Amounts for Fair Swapping

The water-energy-exchange implementation concept could be partly based on monetary compensation or a direct exchange of water for energy. Bartering water for energy could be beneficial in creating a fair and interdependent deal for both parties. This article presents a method to calculate the bartering exchange amounts assuming a deal without monetary compensation. In this respect, the water flow rates and the amounts of transmitted power are measurable values that build the exchange basis. For creating a fair deal, equalizing the Israeli water production and transport costs to Jordan's energy generation and transport costs is assumed. The amount of electrical power P_{Swap} for the water-energy-exchange from Jordan to Israel was calculated according to Eq. (28.1) (Janowitz et al. 2022b):

$$P_{Swap}\left[\frac{MWh}{y}\right] = \frac{WPTC\left[\frac{\$}{m^3}\right] * C_{Desal}\left[\frac{m^3}{y}\right]}{LCOET_{PV}\left[\frac{\$}{MWh}\right]} \qquad (28.1)$$

P_{Swap} significantly depends on the water production and transfer costs ($WPTC$) bringing desalinated water from the Israeli coast to the demand centers in Northern and Central Jordan. The $WPTC$ were calculated using the levelized costs of electricity generation and transfer ($LCOET_{PV}$) bringing the electricity from photovoltaic from Jordan to Israel. In addition, the desalination capacity C_{Desal} and the $LCOET_{PV}$ itself must be considered.

28.3 Results and Discussion

Freshwater production at the Med Sea enables favourable freshwater conveyance to the demand centers in Northern and Central Jordan due to significantly reduced infrastructure investments and energy costs. In particular, the economic advantage of cooperating with Israel under a water-energy-exchange agreement is the significantly lower energy demand of Med Sea production options and water conveyance compared to only Jordanian desalination in Aqaba. Seawater desalination north of Haifa with water transfer via the Sea of Galilee is an exciting project alternative from an economic point of view, which could cover the projected large freshwater deficits in North and Central Jordan. The construction of a large-scale SWD plant with a production capacity of 400 MCM/a would cover almost the entire freshwater deficit by 2050 that could not be covered by the planned 300 MCM/a plant near Aqaba.

The analysis of potential sites for solar energy production in Jordan indicates that the Disi Option (see Fig. 28.2: (B)–Disi Option) is economically attractive, resulting in an LCOET of 30 USD/MWh. In addition, Disi has a large area availability and the best energy yield, which means the highest energy supply reliability and viability. Therefore, the Disi option was selected for the generation of renewable energy for a potential water-energy swap.

Figure 28.3 illustrates the potential water-energy swap concept between Israel and Jordan, including key values.

The amount of energy equivalent to the cost of producing and transmitting 400 MCM/y of freshwater from Israel and Jordan would be 12.8 TWh pa* of energy (* yearly average of the 25 years lifetime of the PV plant where the first year has the highest production due to PV system degradation). That energy production can be achieved by installing a 5.8 GWp PV plant with an area of ~ 72.9 km^2 in Disi. The renewable energy received will allow Israel to increase its renewable energy share in the energy mix significantly. Based on 2019 reports, the contribution of renewables in the energy mix was 2326 MW out of 19,366 MW (12%) in terms of power capacity
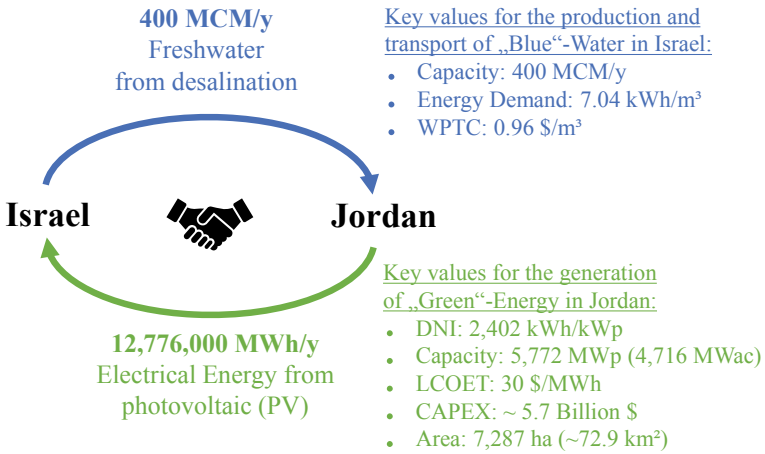
Fig. 28.3 Potential water-energy exchange between Israel and Jordan from the SALAM Initiative SALAM (2022)

and 3300 GWh out of 72,500 GWh (5%) in terms of energy. Including the power and energy needed by water desalination and conveyance, the Israeli renewable energy penetration would reach up to 36% in power capacity and 21% in terms of energy based on 2019 figures.

28.4 Conclusions and Next Steps Towards Implementation

Water- Energy-SWAP between Israel and Jordan based on a fair exchange between the two countries is a feasible concept, covering Jordanian future freshwater needs as well as providing an important contribution to meeting the Israeli demand for renewable energy, resulting in a win-win situation. Within the SALAM Initiative, water production and transfer strategies from Israel to Jordan were investigated, relying on economic, technical, and environmental decision criteria. In addition, potential options for renewable energy generation from PV were developed and resulting electrical energy costs were determined. A promising bartering strategy without any monetary compensation consists of the water production and transfer of 400 MCM/y freshwater from large-scale SWD North of Haifa Bay in exchange for megawatt-hours in renewable energies produced in Jordan. The results show that the exchange capacity agreed upon in the recent DoI signed by Israel and Jordan will have to be doubled. However, doubling the freshwater capacity refers to the planning horizon of 2050 and should consider the Jordanian freshwater deficit's development.

The implementation of the water-energy-SWAP should take this into account and, therefore, be planned and implemented in a modular way, taking place in expansion stages, starting with an initial stage of 200 MCM/y. Particularly in water infrastructure construction, costs can be saved if these are designed directly for future higher capacity. Furthermore, a modular approach allows flexible adaptation to the increasing need for water and renewable energy in Jordan and Israel, reducing costs and path dependencies.

We recommend carrying out technical/economic pre-feasibility studies for the selected water and energy production and transfer options, according to the achievements of the SALAM Initiative. The selection of the most suitable water-energy-exchange concept with the highest mutual benefits and political acceptance level should be based on a multi-criteria option comparison, considering economic, political, environmental, technical, and social aspects. Several research tasks need to be addressed before implementation. In particular, cost-efficient strategies are required which enable the production and transmission of renewable electrical energy from Jordan to Israel. Furthermore, it needs to be investigated whether the Israeli grid can handle the additional electricity loads and how it could be expanded. In addition, land ownership and its availability need to be clarified, including the social acceptance of such big projects. Concerning the realization of large-scale SWD plants, building artificial islands offshore the Israeli coastline is a promising alternative that requires more investigation, especially concerning local environmental impacts. Therefore, sustainable implementation of such a water-energy-exchange concept requires further research and close cooperation between both countries' water, energy and environmental authorities.

References

Bensabat J, Rusteberg B, Bourgoing P, Schär S (2022) Regional macro-model for transboundary water resources planning. In: de Bourgoing P, Nußbaum P, Rusteberg B, Sauter M (eds) The Salam initiative: transboundary strategies for the resolution of the water deficit problem in the Middle East, key products-policy briefs. ISBN (pp 978-3-943647-10-15)

de Bourgoing P, Al-Karablieh E, Sadah M-A, Rusteberg B (2022a) Future freshwater deficits in Palestine and Jordan. In: de Bourgoing P, Nussbaum P, Rusteberg B, Sauter M (eds) The Salam initiative: transboundary strategies for the resolution of the water deficit problem in the Middle East, key products-policy briefs. ISBN (pp 978-3-943647-10-15)

Fritzmann C, Löwenberg J, Wintgens T, Melin T (2007) State-of-the-art of reverse osmosis desalination. Desalination 216:1–76

Janowitz D, Groche S, Yüce S, Melin T, Wintgens T (2022a) Can large-scale offshore membrane desalination cost-effectively and ecologically address water scarcity in the Middle East? Membranes 12:323. https://doi.org/10.3390/membranes12030323

Janowitz D, Yüce S, Margheri M, Yakhoul H, Bensabat J, Rusteberg B, Sauter M (2022b) Innovative water-energy SWAP concept between Israel and Jordan. In: de Bourgoing P, Nussbaum P, Rusteberg B, Sauter M (eds) The Salam initiative: transboundary strategies for the resolution of the water deficit problem in the Middle East, key products-policy briefs. ISBN (pp 978-3-943647-10-15)

Jordan News Agency (2021) Jordan's electricity generated by renewable energy to reach 50% by 2030. Available online: https://petra.gov.jo/Include/InnerPage.jsp?ID=38950&lang=ar&name=en_news

Katz D, Shafran A (2019) Transboundary exchanges of renewable energy and desalinated water in the Middle East. Energies 12:1455. https://doi.org/10.3390/en12081455

Katz D, Shafran A (2020) Energizing Mid-East water diplomacy: the potential for regional water–energy exchanges. Water Int 45(4):292–310

Ministry of Finance Israel (2021) Israel to introduce carbon pricing for the first time. Available online: https://www.gov.il/en/departments/news/press_02082021_b

Ministry of Energy Israel (2021a) Promotion of renewable energy in the Israeli energy sector. Available online: https://www.gov.il/en/departments/general/renewable_energy

Ministry of Energy Israel (2021b) UAE, Jordan and Israel collaborate to mitigate climate change with sustainability project. Available online: https://www.gov.il/en/departments/news/press_221121

PEACE, ECO (2020) A green blue deal for the Middle East. https://ecopeaceme.org/wp-content/uploads/2021/03/A-Green-Blue-Deal-for-the-Middle-East-EcoPeace.pdf

PVsyst (2022) Software for PV system design. https://www.pvsyst.com/

Rusteberg B, Bensabat J, Bourgoing P, Sauter M (2022a) Assessment of freshwater strategies and recommendations for implementation. In: de Bourgoing P, Nussbaum P, Rusteberg B, Sauter M (eds) The Salam initiative: transboundary strategies for the resolution of the water deficit problem in the Middle East, key products-policy briefs. ISBN (pp 978-3-943647-10-15)

Rusteberg B, de Bourgoing P, Bensabat J (2022b) Water production and transfer strategies. In: de Bourgoing P, Nussbaum P, Rusteberg B, Sauter M (eds) The Salam initiative: transboundary strategies for the resolution of the water deficit problem in the Middle East, key products-policy briefs. ISBN (pp 978-3-943647-10-15)

SALAM (2022) Transboundary strategies for the resolution of the water deficit problem in the Middle East. https://salam2.uni-goettingen.de/

Schär S, Geldermann J (2022) Techno-economic assessment of water infrastructure projects. In: de Bourgoing P, Nussbaum P, Rusteberg B, Sauter M (eds) The Salam initiative: transboundary strategies for the resolution of the water deficit problem in the Middle East, key products-policy briefs. ISBN (pp 978-3-943647-10-15)

Tal A (2018) Addressing desalination's carbon footprint: the Israeli experience. MDPI. https://www.mdpi.com/2073-4441/10/2/197

Chapter 29
Hydroeconomic Groundwater Model for Managing Multi-salinity Aquifers in Arid Regions

Hamed Assaf

29.1 Introduction

Whether recharged via intermittent precipitation or recharged millennia ago during wetter periods, groundwater resources in arid regions are the primary source of water supply for domestic, industrial, and agricultural users. It is therefore of paramount importance to manage these scarce resources sustainably based on sound principles that optimize their socio-economic and environmental values. Several challenges face the sustainable management of groundwater resources. In many arid regions, fossil groundwater resources were exhausted to satisfy unsustainable agriculture schemes that required substantial amounts of irrigation water due to high evapotranspiration rates (Odhiambo 2017). Groundwater extraction requires substantial amounts of energy for pumping, treatment and transfer, making energy cost an important factor in managing groundwater resources. An issue of consideration is the impact of subsidies on groundwater depletion. In some regions, fresh groundwater resources are close to saline and brackish groundwater resources, which expose fresh groundwater resources to the risk of salinization that can render these resources unusable without costly desalination. An often-neglected issue in groundwater management is the opportunity cost of water which relates to the forfeited benefits from more optimal use of water. Also, climatic changes are projected to drive the desiccation of many semi-arid regions and to consequently exacerbate the water deficit in these regions.

H. Assaf (✉)

Department of Civil and Infrastructure Engineering, School of Engineering, American University of Ras Al Khaimah, Ras Al Khaimah 10021, UAE
e-mail: hamed.assaf@aurak.ac.ae

These intertwined and complex challenges point to the need of developing reliable and intuitive tools to manage water resources in arid regions (Alamanos et al. 2020; Harou et al. 2009). In addressing this need, the author developed the Hydroeconomic Groundwater Model for Arid Regions (HGMAR). The model utilizes equations and information introduced in an optimization study commissioned by the Environment Agency—Abu Dhabi and carried out by RTI International to assess the economic value of groundwater resources in Abu Dhabi (RTI International 2015). In contrast to the optimization approach of the RTI study, HGMAR offers groundwater managers an interactive and user-friendly environment to formulate and run simulations of alternative groundwater management policies. The following sections provide a description of HGMAR's Architecture and interface, and the application of the model to manage groundwater resources in the Emirate of Abu Dhabi, UAE.

29.2   Methods

29.2.1   *Theoretical Framework*

29.2.1.1   Model Main Approach and Aquifer Representation

HGMAR was developed using the Stella software based on the integration of hydrological and economic principles to determine the impact of extractions on groundwater levels and assess the economic value of these extractions. Stella is a system dynamics environment that simulates systems of differential equations (Cellier and Greifeneder 1991). It is widely used in developing policy and decision-support tools (Assaf 2009, Phan et al. 2021). HGMAR divides the area under consideration into several zones, each representing specific aquifer characteristics and user categories. In each zone, the aquifer is modeled as a stack of three aquifer layers each with a different level of salinity (fresh, brackish, and saline) as shown in Fig. 29.1. The freshwater layer sits on top of the brackish water layer, which in turn sits on top of the saline water layer. Although this representation is simplistic, it is deemed acceptable in capturing large-scale behavior of groundwater systems, particularly those of the Emirates of Abu Dhabi which tend to be less dynamic given the minimal recharge in most of the year. Changes to water levels are mostly driven by pumping. This concept of the salinity-stacked aquifer has been utilized in the development of the strategic Liwa's Aquifer Storage and Recovery (ASR), which relies on storing fresh water on top of saline and brackish groundwater layers with minimal mixing (Stuyfzand et al. 2017).
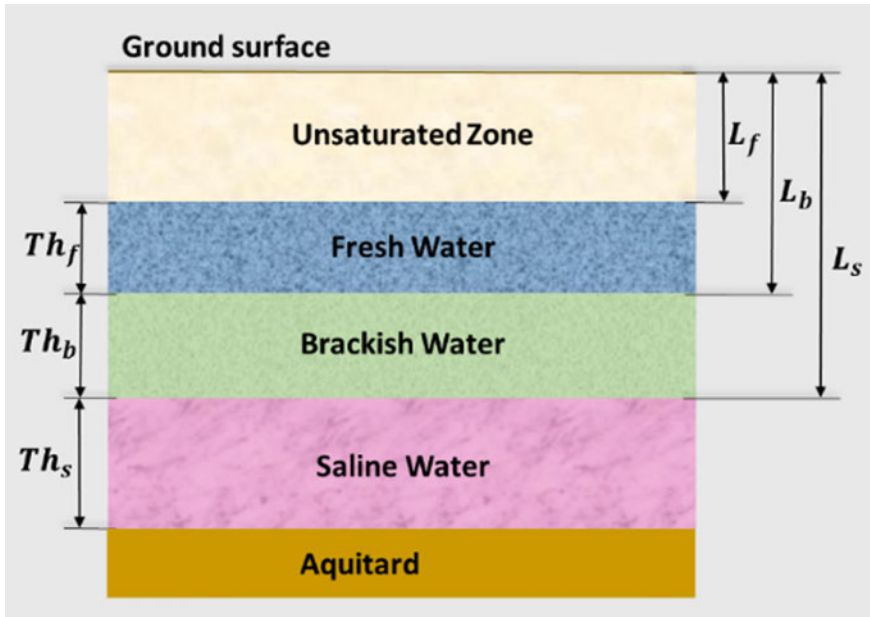
Fig. 29.1 Representation of aquifers in the model

29.2.1.2 Aquifer Water Balance

The state of the stock (S) and water level are determined by the balance between recharge (R) and withdrawal (W) by users as described in Eqs. (29.1) and (29.2).

$$\frac{dS}{dt} = R - W \tag{29.1}$$

$$\frac{dTh}{dt} = \frac{1}{A \times SY} \times \frac{dS}{dt} \tag{29.2}$$

where, Th is the aquifer thickness, SY is the specific yield of the aquifer, and A is the surface Area.

Equation (29.1) is represented graphically in Stella as shown in Fig. 29.2, where the square box, represents the stock, S, of water in the aquifer. Recharge to the aquifer, R, is represented as an arrow with a tap pointing towards the stock. Withdrawals, W, from the aquifer is represented by an arrow with a tap leaving the stock.

The lifts for the freshwater, brackish water and saline water layers, L_f, L_b, L_s, respectively are determined as shown in Eq. (29.3). The lifts are used to calculate pumping costs as indicated later.

$$L_f(t) = L_b(t) - Th_f(t); \; L_b(t) = L_s(t) - Th_b(t) \tag{29.3}$$
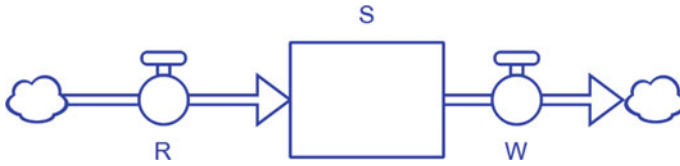
Fig. 29.2 Representation of the aquifer water balance in stella

29.2.1.3 Estimation of Groundwater Net Present Value

The Net Present Value (NPV) of extracted water is calculated as a time-discounted difference between Benefit (B) and Cost (C) as shown in Eq. (29.4).

$$NPV = \sum_{t=0}^{T} \frac{(B(t) - C(t))}{(1 + r)^t} \tag{29.4}$$

where, T is the planning horizon, and r is the discount rate.

The cost consists of four components: the cost of energy to pump water, water treatment cost, transportation cost, and the opportunity cost. The latter is defined as the forfeited benefits of extracted water for not using it in the next most economically optimal use (McKinney and Savitsky 2006). In this study, the opportunity cost is defined as the strategic value of keeping water in the aquifer for use during periods of low water availability. In Abu Dhabi, this is estimated equal to the cost of storing water in the Liwa Aquifer Storage and Recovery (ASR) system developed to provide multi-month storage of desalinated water (RTI International 2015). To highlight the strategic value of the Liwa ASR, most Gulf Corporation Council (GCC) countries have desalinated water storage capacity of only two to five days, making these countries vulnerable to interruptions in seawater desalination (Missimer et al. 2012). The opportunity cost of extracted water is calculated by first calculating the yearly cost of storing one unit of water—referred to as Strategic Water Reserve Value (SWRV)-in the Liwa ASR, and multiplying it by the volume of extracted water. The SWRV is calculated as the sum of the capital cost amortized over the lifetime (LT) of the project, operation and maintenance ($O\&M$), monitoring and transportation costs divided by the volume of the Liwa ASR as shown in Eqs. (29.5) and (29.6) (RTI International 2015).

$$SWRV_{Total} = r \frac{(C_{Capital})}{(1 - (1 + r)^{-LT})} + C_{O\&M} + C_{Monit} + C_{Transp} \tag{29.5}$$

$$SWRV = \frac{SWRV_{Total}}{Volume\ of\ ASR} \approx 3.1\ {^{AED}/_{m^3}}\ per\ year\ for\ r = 3\% \tag{29.6}$$

The pumping cost is calculated as the product of energy price, EP, in AED per kWh, and the energy required to lift water, $ER(kWh)$, as shown in Eqs. (29.7) and (29.8). The cost of pumping can be substantially skewed by energy subsidies.

$$C_{Pumping} = ER \times EP \tag{29.7}$$

$$ER = \frac{1}{\eta_{pump}} 3.6 \times 10^{-6} \times W \times L \times g \times \rho_{water} \tag{29.8}$$

where, W is the withdrawal from the aquifer in m^3, L is the groundwater lift in meters, and η_{pump} is the pump efficiency.

The benefits are attributed to those made by the water users. In the case of Abu Dhabi, four components of benefits are identified including agricultural, irrigated forests, landscaping and strategic reserve benefits. The agricultural benefits are estimated from marginal benefit curves obtained from the optimization study carried out by RTI International. The agricultural marginal benefit curves are approximated as linear functions as described in Eq. (29.9).

$$AMV = a \times AW + b \tag{29.9}$$

where, AMV is the agricultural marginal value in AED/m^3, AW is agricultural withdrawal in $m^3/year$, a is the slope of the marginal benefit curve in $AED/m^3/m^3$, b is the intercept of the marginal benefit curve in AED/m^3.

The model considers benefits from irrigated forests, which are a unique feature in the UAE, and have been planted in fulfilment of the Late Sheikh Zayed's vision to green the vast desert areas in the UAE (Al Yamani 2019). Benefits from these forests can be perceived as ecosystem services including carbon sequestration, provision of habitat for wildlife, contribution to cultural heritage, and protection of road infrastructure from encroachment by sand dunes. The value of a given forest ecosystem service is assumed to be linearly proportional to the amount of irrigation applied to the forests, with the maximum value achieved when the forests receive the amount required for optimal growth. In the model, the user specifies the forests optimal irrigation requirements, and the values of their ecosystem services under these conditions. During simulation, the model calculates the value of a given forest ecosystem service equal to the product of the value of the ecosystem service under optimal irrigation conditions and the ratio of available irrigation amount to the amount of irrigation required for the optimal growth of forests. Consequently, the forests' carbon sequestration benefits are determined as follows in Eq. (29.10):

$$B_{SC} = SVSC \times \frac{IRG_{Allocated}}{IRG_{Optimal}} \times SC_{Optimal} \tag{29.10}$$

where, B_{SC} is the value of sequestered carbon in AED, SVSC is the social value of sequestered carbon in AED per metric ton of carbon, defined as the avoided

climate change damage had this carbon been released as greenhouse gas to the atmosphere (Brainard et al. 2009), $IRG_{Allocated}$ is the groundwater allocated for forest irrigation, $IRG_{Optimal}$ is the amount of irrigation required for optimal growth of forests, and $SC_{Optimal}$ is amount of sequestered carbon under optimal irrigation conditions. $SC_{Optimal}$ can be obtained through surveying existing species of forest trees, their numbers and average stem size. The sequestered carbon is estimated by multiplying the number of trees by the amount of carbon stored per tree based on their species and stem size (RTI International 2015).

Similarly, the three other forest benefits, wildlife habitat provision, B_{WL}, contribution to cultural heritage, B_{CH}, and protection of road infrastructure, B_{RI} are calculated as follows:

$$B_{WL} = \frac{IRG_{Allocated}}{IRG_{Optimal}} \times B_{WL\_Optimal} \tag{29.11}$$

$$B_{CH} = \frac{IRG_{Allocated}}{IRG_{Optimal}} \times B_{CH\_Optimal} \tag{29.12}$$

$$B_{RI} = \frac{IRG_{Allocated}}{IRG_{Optimal}} \times B_{RI\_Optimal} \tag{29.13}$$

where, $B_{WL\_Optimal}$, $B_{CH\_Optimal}$ and $B_{RI\_Optimal}$ are the corresponding benefits under optimal irrigation conditions. $B_{WL\_Optimal}$ and $B_{CH\_Optimal}$ can be determined based on assessing willingness to pay (WTP) by residents to protect wildlife and maintain forests as cultural heritage. $B_{RI\_Optimal}$ can be estimated equal to avoided damages to road infrastructure from sand dunes and the cost of road service (RTI International 2015).

Benefits from landscaping can be assessed as the resident willingness to pay for irrigation water. Naturally stored water in aquifers offer a strategic reserve benefit given the limited capacity of storing desalinated water. The strategic reserve benefit is the value of maintaining water in the aquifer and is estimated as follows:

$$B_{SWR} = SWRV \times S \tag{29.14}$$

29.2.1.4 Policy Formulation

The model offers several parameters to formulate groundwater extraction and water allocation policies. For example, total groundwater withdrawal can be assigned as a fraction of available water stock according to Eq. (29.15).

$$TW(t) = \propto S(t); 0 \ll \propto \ll 1 \tag{29.15}$$

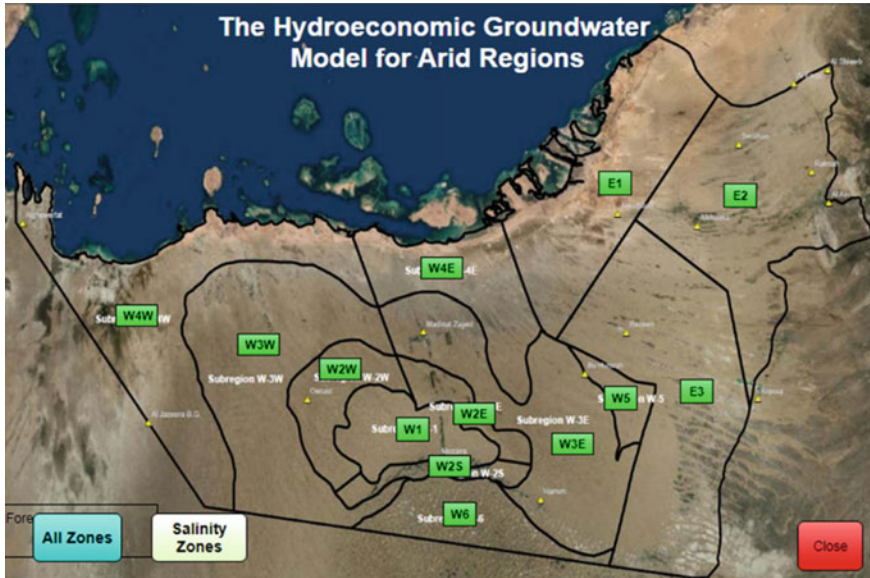where, $\propto$ is the ratio of withdrawn groundwater stock.

Fig. 29.3 The hydroeconomic model interface

29.2.1.5 Model Interface

The HGMAR was set up to represent groundwater resources in Abu Dhabi. The model users are first presented with a map of Abu Dhabi showing ground zone divisions (Fig. 29.3), where they can click on a button representing a specific zone or click on the "All Zones" button. This leads to a control panel (Fig. 29.4), where users can access and modify several economic parameters including discount rate, desalination cost, energy cost, and pump efficiency. Users can also specify aquifer characteristics including specific yield and initial groundwater levels, and set parameters for water withdrawal and allocation policies. A unique feature of the model is the ability to modify parameters during a simulation which facilitates assessing on-the-fly the impact of changing given parameters on the model results. For example, the user can pause the model simulation, modify the discount rate and resume the simulation run.

29.3 Results and Discussion

The model was calibrated by adjusting the groundwater withdrawal parameter $\propto$ to produce the best overall fit with measured groundwater levels in three locations in Abu Dhabi (Remah, Liwa Crescent and Madinat Zayed). The measurements were shifted to start at the same levels as the initial groundwater measurements reported by RTI (2015). This facility assesses how well the calculated values capture the trend
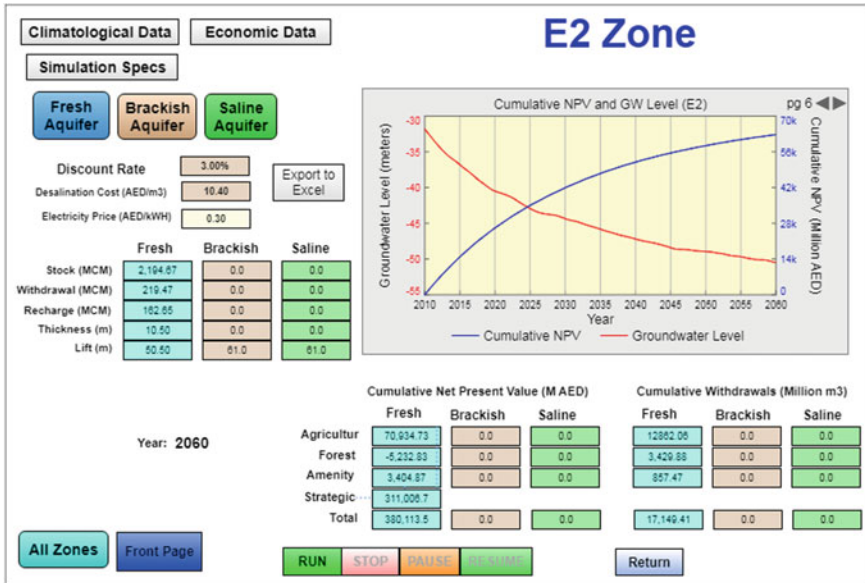
Fig. 29.4 Control and results display panel

in measurements. Calibration results indicate that $\propto$ equal to 0.1 produces the best overall fit in the three locations as shown in Figs. 29.5, 29.6, and 29.7. This indicates that the overall trend in groundwater withdrawals in Abu Dhabi from 2010 to 2017 can be approximated by a withdrawal policy of 10% of the groundwater stock each year on average.

The model was used to assess alternative groundwater extraction schemes. For example, Fig. 29.8 shows the impact of changing the withdrawal policy from $\alpha = 0.1$ to $\alpha = 0.05$ on the 50-year projections of groundwater levels and the cumulative
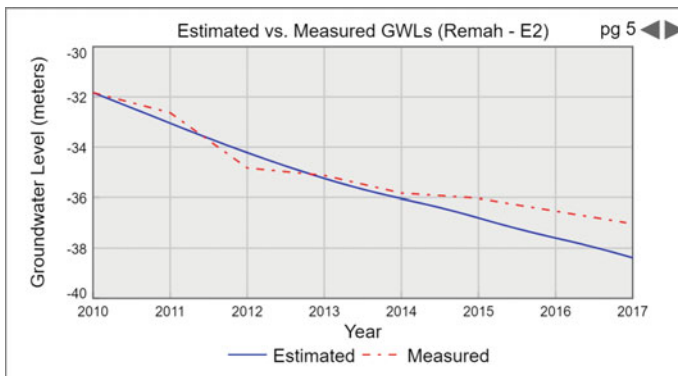

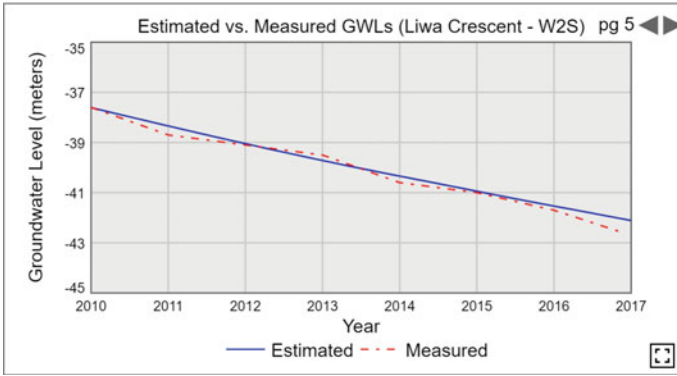**Fig. 29.5** Measured versus estimated groundwater levels in remah (zone E2)

Fig. 29.6 Measured versus estimated groundwater levels in liwa crescent (zone W2S)
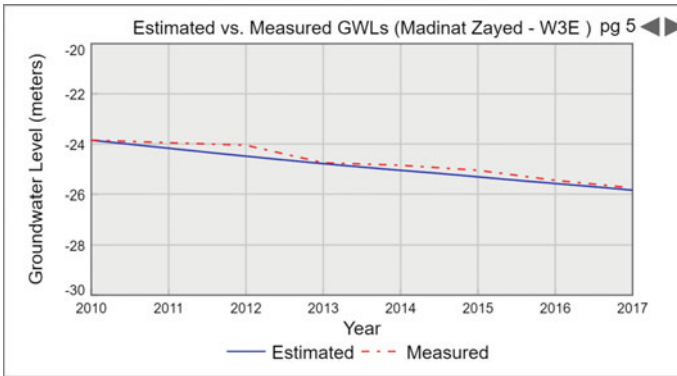

Fig. 29.7 Measured versus estimated groundwater levels in madinat zayed (zone W3E)
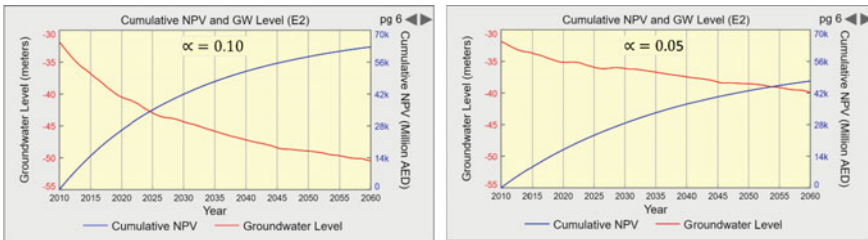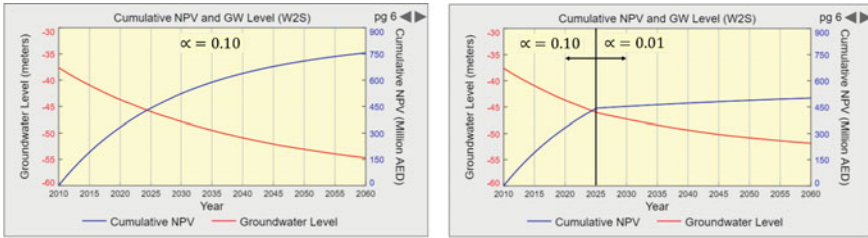

Fig. 29.8 The Impact of withdrawal policy on 50-year projections of groundwater and cumulative NPVs for zone E2

NPV in UAE Dirhams (AED). Reducing groundwater withdrawals would attenuate the decline in groundwater level. This would however reduce the NPV of groundwater as less water is available to users.

Fig. 29.9 The Impact of withdrawal policy on 50-year projections of groundwater and cumulative NPVs for zone W2S

One of the powerful features of the HGMAR is the ability to pause simulation to adjust given parameters and resume simulation. This emulates real management of water resources, where policy makers are interested in exploring measures to deal with urgent issues such as a major decline in groundwater level. For example, in the left plot of Fig. 29.9, the user kept the groundwater policy parameter α constant at 0.1. In the right plot, the user paused the model at year 2025, reduced α to 0.01 and then resumed the simulation. The impact of this change is significant reflected in the reduction in the rate of groundwater decline.

29.4   Conclusions

The paper presents the Hydroeconomic Groundwater Model for Arid Regions (HGMAR) developed by the author to manage multi-salinity aquifers in arid regions. The model was set up to manage groundwater resources in the Emirate of Abu Dhabi, which are allocated among three sectors: agriculture, landscaping and irrigation of afforested areas. Given the very low groundwater recharge levels in Abu Dhabi and the subsequent decline in groundwater levels, there is an urgent need to reduce groundwater extraction and optimize groundwater allocation. Several issues are being considered including agricultural economic return, and the impact of curtailing irrigated forests on their ecosystem services (social values, carbon sequestration, ecological role and infrastructure protection).

The HGMAR provides the user with an interactive interface to set up several hydrological and economic parameters including aquifer characteristics, discount rate, withdrawal policy, and energy price. The model offers users with the flexibility of adjusting parameters during simulation. The model was calibrated against groundwater level measurements in Abu Dhabi. Model simulations show that the general trend in the decline of groundwater levels over the period from 2010 to 2017 can be represented by an average withdrawal equal to 10% of groundwater stock each year on average.

References

Al Yamani W (2019) Maintaining the hyper-arid forests of Abu Dhabi by sustainable irrigation using treated sewage effluent in conjunction with groundwater. Ph.D. Thesis, School of Agriculture and Environment, Massey University. https://mro.massey.ac.nz/handle/10179/15308

Alamanos A, Latinopoulos D, Loukas A, Mylopoulos N (2020) Comparing two hydro-economic approaches for multi-objective agricultural water resources planning. Water Resour Manag 34:4511–4526. https://doi.org/10.1007/s11269-020-02690-6

Assaf H (2009) A hydro-economic model for managing groundwater resources in semi-arid regions. Water Resour Manag V 85–96. https://doi.org/10.2495/wrm090091

Brainard JS, Bateman IJ, Lovett AA (2009) The social value of carbon sequestered in Great Britain's woodlands. Ecol Econ 68(4):1257–1267

Cellier FE, Greifeneder J (1991) Continuous system modeling. Springer Science and Business Media

Harou JJ, Pulido-Velazquez M, Rosenberg DE, Medellín-Azuara J, Lund JR, Howitt RE (2009) Hydro-economic models: concepts, design, applications, and future prospects. J Hydrol 375(3–4):627–643. https://doi.org/10.1016/j.jhydrol.2009.06.037

International, R. T. I. (2015) Economic valuation of groundwater in the Abu Dhabi Emirate. Environment Agency, Abu Dhabi

McKinney DC, Savitsky AG (2006) Basic optimization models for water and energy management. University of Texas

Missimer TM, Sinha S, Ghaffour N (2012) Strategic aquifer storage and recovery of desalinated water to achieve water security in the GCC/MENA region. Int J Environ Sustain 1:87–99

Odhiambo GO (2017) Water scarcity in the Arabian Peninsula and socio-economic implications. Appl Water Sci 7:2479–2492. https://doi.org/10.1007/s13201-016-0440-1

Phan TD, Bertone E, Stewart R (2021) Critical review of system dynamics modelling applications for water resources planning and management. Cleaner Environ Syst 2(100031). https://doi.org/10.1016/j.cesys.2021.100031.

Stuyfzand PJ, Smidt E, Zuurbier KG, Hartog N, Dawoud MA (2017) Observations and prediction of recovered quality of desalinated seawater in the strategic ASR project in Liwa, Abu Dhabi. Water 9(3):177. https://doi.org/10.3390/w9030177

Chapter 30
A Review of the Applications of Nanomaterials to Augment Solar Still Productivity

Mahmoud Elgendi, Maryam AlMallahi, Abdel-Hamid I. Mourad, Hamdan Al Surihi, Sultan Saad, Ahmed Al Baeek, Mansour Al Dhaheri, and Nizamudeen Cherupurakal

30.1 Introduction

Clean alternative energy, such as wind energy (Abdelkhalig et al. 2022; Cheng et al. 2021) and solar energy, is sustainable, clean source of energy for sustainable cities and communities (AlMallahi et al. 2022; Elgendi et al. 2022b; Obaideen et al. 2021). Solar energy has multiple uses involving photovoltaics, thermal energy, solar heating, and other typical solar energy-harvesting methods. Solar still technology is a convenient and simple method for acquiring potable water from saline water (Elgendi and Selim 2022). Saline water can be fed manually or automatically (Elgendi et al. 2022a). Water evaporates naturally from the salty water surface and flows to the solar still top cover (El-Gendi 2018a, b; El-Gendi and Aly 2017). Although solar still is an affordable and convenient method, its major drawbacks include low efficiency. Several techniques are applied to enhance the solar still performance and increase its efficiency, such as the wick materials (Khalifa 2011), external reflector (Khalifa and Ibrahim 2010), and solar collector (Sampathkumar and Senthilkumar 2012). A major objective in

M. Elgendi (✉) · M. AlMallahi · A.-H. I. Mourad · H. Al Surihi · S. Saad · A. Al Baeek · M. Al Dhaheri · N. Cherupurakal
Mechanical and Aerospace Engineering Department, College of Engineering, United Arab Emirates University, P.O. Box 15551, Al Ain, UAE
e-mail: mahgendi@uaeu.ac.ae

M. Elgendi · A.-H. I. Mourad
National Water and Energy Center, United Arab Emirates University, P.O. Box 15551, Al Ain, UAE

M. Elgendi
Department of Mechanical Power Engineering and Energy, Faculty of Engineering, Minia University, Minia, Egypt

A.-H. I. Mourad
Faculty of Engineering, Helwan University, Cairo, Egypt

solar still fields is to enhance the distillate production of drinkable water. Solar still
distillate yield is dependent on the availability of solar radiation, which is intermittent.
The applicability of a solar still system is determined by meteorological parameters
such as solar radiation, wind velocity, and ambient temperature. In addition, using
nanomaterials in solar still significantly increases its productivity (Elgendi et al.
2021a). Nanomaterials can be mixed with saline water to form a nanofluid or coat
the absorber or the cover (Chamsa-ard et al. 2020). Also, it can be doped in phase
change materials to improve its thermal characteristics.

30.2   Bibliometric Analysis

With the growing attention on the solar stills field, a substantial volume of research
literature has evolved. Bibliometric approaches are helpful for statistically analyzing
large-scale research publications and determining a field's development state and
research performance. The bibliometric analysis has been widely utilized to reveal
the state of research in numerous study sectors. For instance, (Kandeal et al. 2022)
reviewed recent water harvesting technologies with the help of bibliometric anal-
ysis. Similarly, (Ding et al. 2021) discussed the research status and development in
the hybrid thermal energy storage systems field. This section presents a comprehen-
sive bibliometric analysis of solar stills and PCM/nanomaterials. The data in this
study were obtained from the Web of Science and Scopus databases. The docu-
ment type and search language were not restricted, the period span is all years from
(2010 to 2022) and data analysis was performed on 24 October 2022. A total of
262 were collected and exported for bibliometric analysis as demonstrated in Table
30.1. Figure 30.1 displays the publication trend of solar stills research from 2010 to
2022.

Table 30.1   Main information about the data obtained

| Description	Results
Timespan	2010:2022
Documents	262
Annual growth rate %	42.31
Average citations per document	29.82
References	10,672
Research article	182
Book chapter	5
Conference paper	39
Conference review	5
Review paper	31
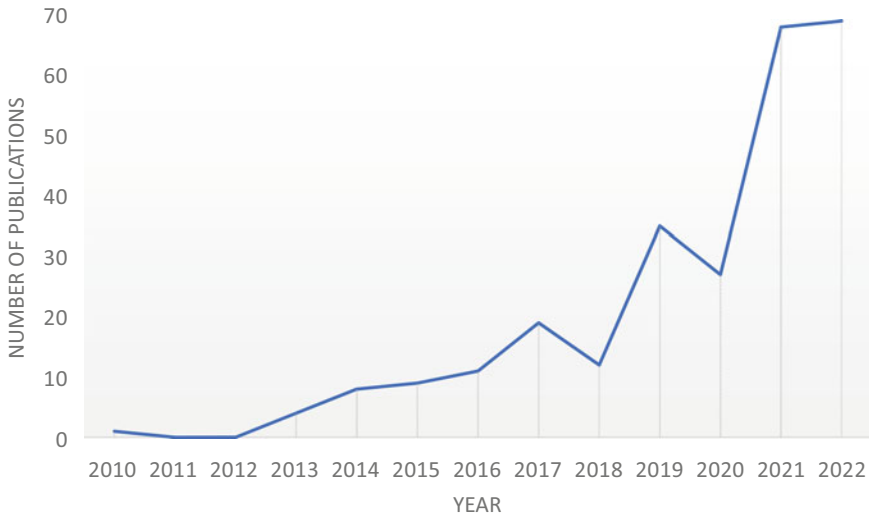
Fig. 30.1 Number of studies on solar stills and PCM/nanomaterials that have been published based on web of science and scopus databases

Figure 30.2 portrays the primary authors' collaborative network. The size of the circle symbolizes the author's number of publications; the connection between the authors reflects the strength of the collaboration. By examining the collaboration network of high-yield authors, we can rapidly grasp the primary research team in the field of solar stills cooperation and identify the research frontier.

Fig. 30.2 Collaboration networks of the most productive authors in this field
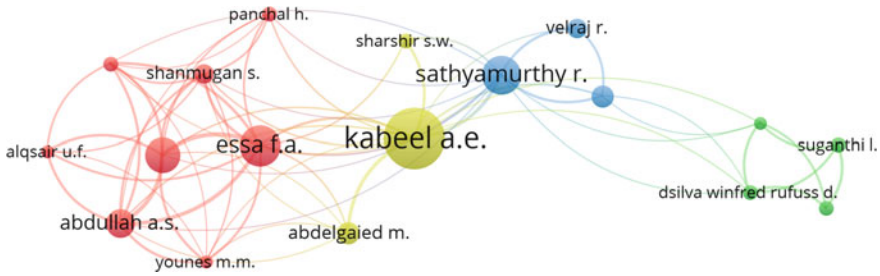
Fig. 30.3 Country collaboration network

The collaboration network among countries and the number of publications are demonstrated in Fig. 30.3. It can be shown that significant levels of collaboration occur between countries located in the same geographical area, such as India, Egypt, and neighboring countries.

The number of citations usually represents the academic significance of the article. Highly cited publications demonstrate that this paper's research material has been acknowledged by other researchers on the same subject and has a high reference value. Table 30.2 lists the top ten most referenced papers on the topic of solar stills and nanomaterials/PCM. The article with the most total citations (222) was Khanafer and Vafai (2018). Correspondingly, Table 30.3 shows the top 8 most repeated words in the search string set. Because many studies' end goals are applications, it is normal for researchers to be concerned about productivity. Scholars also appear to be concerned about paraffin wax and nanoparticles in this field.

The three most relevant global affiliations related to publications on solar stills and PCM/nanomaterials are Tanta University (Egypt), Kafrelshiekh University (Egypt), and Anna University (India). This implies that the majority of relevant research

Table 30.2 Top 10 most cited papers in the search string (2010–2022)

Sr.	Paper	Total citations
1	Khanafer 2018, Renew Energy (Khanafer and Vafai 2018)	222
2	Al-Harahsheh 2018, Appl Therm Eng (Al-harahsheh et al. 2018)	195
3	Omara 2015, Energy Convers Manag (Omara et al. 2015)	188
4	Sharshir 2017, Appl Energy (Sharshir et al. 2017)	179
5	Kabeel 2014, Energy Convers Manag (Kabeel et al. 2014)	177
6	Kabeel 2016, Desalination (Kabeel and Abdelgaied 2016)	172
7	Faegh 2017, Desalination (Faegh and Shafii 2017)	162
8	Sharshir 2016, Appl Therm Eng (Sharshir et al. 2016)	162
9	Arunkumar 2013, Desalination (Arunkumar et al. 2013)	159
10	Shalaby 2016, Desalination (Shalaby et al. 2016)	150

Table 30.3 Word repetition frequency

Sr.	Terms	Frequency
1	Solar still	131
2	Phase change material(s) OR PCM	130
3	Desalination	46
4	Productivity	26
5	Solar desalination	26
6	Solar energy	25
7	Paraffin wax	18
8	Nanoparticles	16

Table 30.4 Most relevant affiliations and countries

| Sr.	Country	Affiliation	Articles
1	Egypt	Tanta University	58
2	Egypt	Kafrelsheikh University	31
3	India	Anna University	25
4	Saudi Arabia	Prince Sattam Bin Abdulaziz University	16
5	Iran	Islamic Azad University	15
6	Egypt	Delta University for Science and Technology	13
7	India	Hindustan Institute of Technology and SciencE	13

on solar stills comes from Middle East and South Asia countries. Table 30.4 demonstrates the most relevant affiliations and countries in this search string.

Cluster analysis showed that the terms naturally clustered into six clusters, as shown in Fig. 30.4a. Keywords from the same cluster are frequently found in the same body of literature. Each cluster might identify several research hotspots. On the other hand, word clouds are useful for providing an overview of the literature on any topic during a certain time. The magnitude of the term indicates how frequently authors used it in their publications. Figure 30.4b shows a word cloud of the most frequently used keywords selected by authors. Solar stills, heat storage, productivity, nanoparticles, energy efficiencies, and other words were identified.

The three-field plot in Fig. 30.5 demonstrates the best-performing country, source (journal), and finally research focus. The thicker rectangle is, the greater frequency is. The connecting nodes, inflows, and outflows show more connections and thicker nodes.
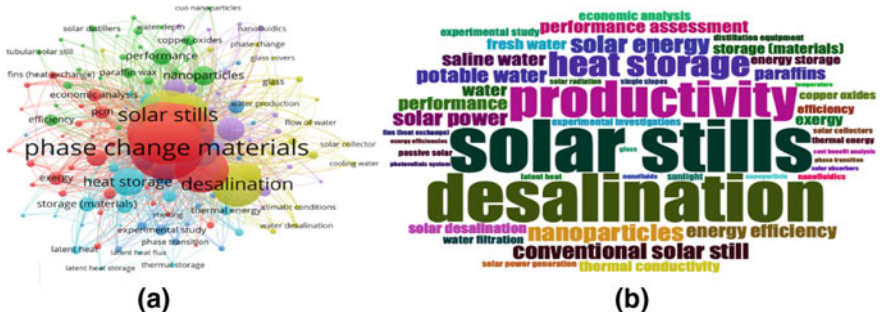
Fig. 30.4 **a** Network visualization of most used keywords, **b** word cloud on publications related to "solar stills" AND "phase change materials" OR "nanomaterials"
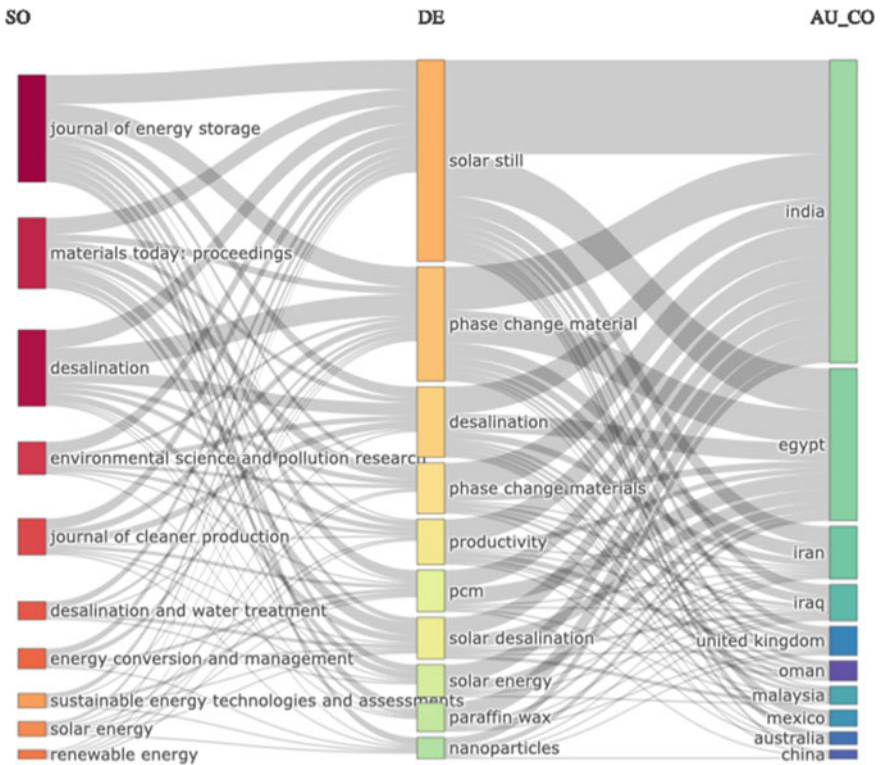
Fig. 30.5 Three-field plot of literature in the field of solar stills, PCM and nanomaterials, source (SO), keywords (DE), authors' countries (AU_CO)
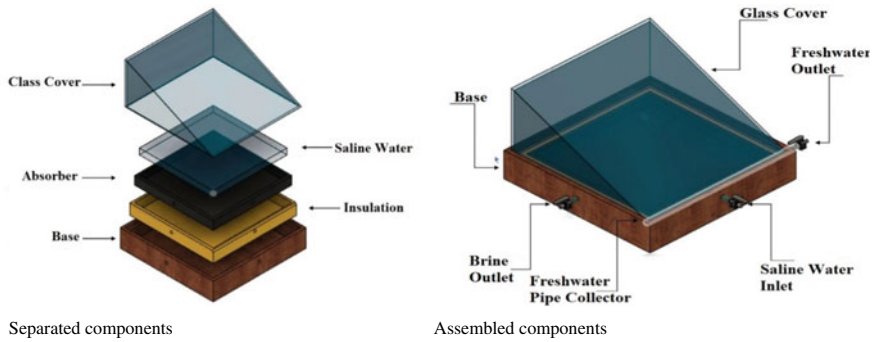
Fig. 30.6 Solar still components: (1) cover, (2) saline water, (3) absorber, (4) insulation, and (5) box

30.3   The Main Components of the Solar Still

The solar still has a simple design (Elgendi et al. 2021b). Figure 30.6 shows the primary features of the solar still:

A transparent cover, usually made from glass, allows the transmission of solar radiation. Also, the distilled water condenses on its inner surface. Nanomaterials can be applied to its inner surface to improve the wettability properties.

Saline water absorbs solar energy to evaporate. Nanomaterials can be added to saline water to improve its thermal characteristics. Therefore, the mixture will be a nanofluid.

Absorbers are usually coated with black paint and made from non-corrosive materials to hold the saline water and absorb solar energy. In addition, nanomaterials can cover the absorber to increase the absorbed energy.

Insulation hinders the dissipation of thermal energy. Phase change materials (PCM), thermal storage materials, can be added between the absorber and insulation. Nanomaterials can dope the PCM to improve its thermal characteristics.

Box or base usually made from wood includes solar still components.

30.4   Techniques to Enhance the Solar Still Performance

The productivity of the solar still can be affected by meteorological parameters, operational parameters, and design and fabrication parameters. As illustrated in Fig. 30.7, numerous factors impact solar still performance.

Several studies have been carried out in the literature to improve solar still performance. For example, a single-slope solar basin with a movable aluminum-suspended absorbent plate is proposed (El-Sebaii et al. 2000). The baffle-suspended absorber boosts the productivity of the solar still by 20% because the preheating time for water evaporation is reduced.
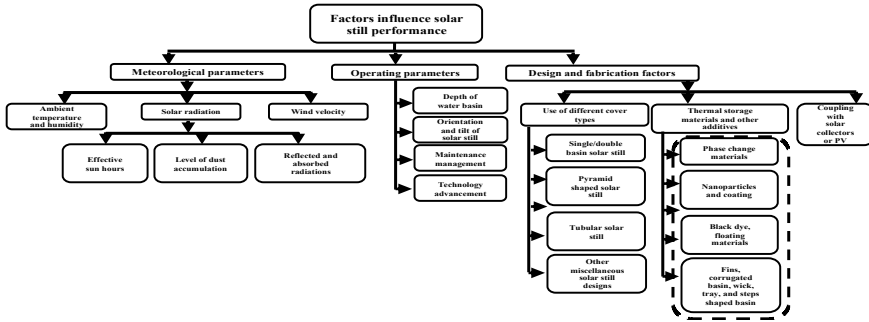
Fig. 30.7 Factors influence solar still performance

Naim and Abd El Kawi (Naim and Abd El Kawi 2003) proposed a solar still system that utilizes charcoal particles as the absorber medium. The effect of charcoal particle range, saline water flow rate, and glass cover inclination on productivity is examined. As a strong absorber medium, the charcoal particles increase solar still productivity by 15%. Correspondingly, a packed sheet mounted at the bottom of the solar still basin optimizes the performance of the solar still (Addel-Rehim and Lasheen 2005). The compressed layer's substance has superior thermal properties. The packed coating of glass balls aids in heating saline water during the day and night and raises freshwater productivity to 7.5%.

Heat can be stored in the phase change materials as latent heat. For example, heat is applied to a substance to change its phase from solid-state to liquid by preserving the heat as latent heat of fusion or from liquid to vapor by storing the heat as latent heat of vaporization. Energy storage materials (ESM) improve the efficiency of a solar still (Addel-Rehim and Lasheen 2005). The ESM is inserted in the solar still tray during the still assembly process. The combination of paraffin wax, paraffin oil, and water is an energy storage medium.

Jute fabric has a porous surface that improves its absorption property. Furthermore, jute thread is very solid and one of the least expensive natural fibers available (Sakthivel et al. 2010). It also has high insulating characteristics, low heat conductivity, and a limited capacity to recover moisture. In the regenerative solar still, the air-vapor mixture temperature is lowered and becomes lower than that in the traditional still. The latent heat generated by the glass cover is used to evaporate water from the jute cloth. It was discovered that yield potential was increased by 20%, and performance was increased by 8% compared to the traditional solar still.

Moreover, the influence of coated and uncoated metallic wiry sponges, as well as volcanic pebbles, on solar still production was explored. Compared to the traditional solar still, The yield of coated metallic wiry sponges, uncoated metallic wiry sponges, and volcanic rocks is improved by 28%, 43%, and 60%, respectively (Abdallah et al. 2009).

The glass cover inclination parameter mainly influences the efficiency of the solar still. In winter, increasing the inclination raises the yield, and vice versa in the summer (Khalifa 2011). On the other hand, increasing the inclination decreases the evaporation rate in the summer and winter. Moreover, an increased tilt angle increases heat losses from the cover while decreasing yield by increasing reflected radiation from the absorber.

Water quickly evaporates at much lower temperatures by creating a vacuum within the solar still, using less energy than traditional techniques. The productivity of a solar desalination device depends on the solar still pressure (Nassar et al. 2007). The experimental model is an elliptical, metallic container positioned in the focus of the concave reflector. The saline water is subjected to an absolute vacuum pressure of 25 kPa, and in a condenser, the distilled water is collected. Applying vacuum pressure improves the efficiency by 303% and the output ratio by 900% (Nassar et al. 2007). Table 30.5 presents a summary of the papers reviewed and their objectives.

30.5 Applications of Nanomaterials in Solar Still

Nanomaterials coat the absorber to increase the thermal conductivity and, thus, the hourly productivity of coated absorber using nano-Fe_2O_3 particles (Balachandran et al. 2020). The basin water temperature peak is 66 °C for nano-Fe_2O_3 coated solar still, which is 3 and 5 °C higher than those of micro-coated and conventional solar stills, respectively. The maximum efficiency of nano-Fe2O3 solar still was 68% and 55% for water depths equal to 5 mm and 10 mm, respectively (Balachandran et al. 2020).

Graphene oxide (GO) decreases the melting temperature of paraffin as phase-change materials (PCMs) (Safaei et al. 2019). Paraffin is an organic material and is considered the most futuristic PCMs because of its ideal characteristics, such as remarkable latent heat. Graphene oxide nanomaterial is applied to improve the thermal efficiency of PCM. The absorbed heat transfers to the paraffin/graphene oxide during the daytime. At a temperature of 45 °C, graphene oxide is dispersed into melted paraffin to maximize the solar still's yeild. Furthermore, the stored heat in the PCM as latent heat boosts solar efficiency at night. The solar still performance with GO/paraffin solar still has higher productivity by 25% than solar performance with PCM only. The daily yield of solar still was 5 kg/m^2 and 6.25 kg/m^2 for GO/PCM and PCM solar still, respectively (Safaei et al. 2019).

Because of the outstanding durability and inexpensive cost of oxide nanoparticles, oxide nanofluids are the most often utilized nanofluid in solar still (Elango et al. 2015). Al_2O_3 is a useful oxide nanoparticle among many others in passive solar stills. Al_2O_3, SnO_2, and ZnO nanofluids had thermal conductivities of 0.63556 W/(m^2+K), 0.6215 W/(m^2+K), and 0.6105 W/(m^2+K), respectively. The performance of the solar still is enhanced by 29.5%, 18.63%, and 12.67%, by Al_2O_3, SnO_2, and ZnO nanofluids, respectively.

Table 30.5 Objectives of the papers reviewed in brief

Reference	Main objectives and findings
Katekar and Deshmukh (2020a)	A review on PCMs and nanoparticles for solar stills. The authors found that CuO nanoparticles are the most suitable nanoparticles for mixing with paraffin wax
Singh et al. (2020)	A comparison study on solar stills and the impact of nanofluids on their performance are carried out. Adding nanoparticles to passive solar still with a double slope top cover boosted productivity
Singh et al. (2021)	Different types of nanofluid integrated with various types of solar collectors were studied. The carbon black-Ethelene glycol nanofluid improves total thermal conversion efficiency by 27.90% when applied to direct absorption solar collector
Katekar and Deshmukh (2020b)	The paper is categorized based on the design, slope, basin, passive, active, and other modifications. Nanoparticle coating was applied and studied for solar stills. The authors stated that the single basin cascade solar still is the most suitable for domestic uses, and tubular solar still with a wick is the optimum design for industrial uses
Arunkumar et al. (2021)	Capillary flow driven for water evaporation and nanoparticles were investigated. The highest evaporation rate found was achieved by Ti_2O_3-nanoparticles/polyvinyl alcohol absorber
Kaviti et al. (2021)	Solar desalination is generally studied, and it explicitly investigates solar still. Moreover, it focuses on nanomaterials applications in solar stills. Solar vapor generation materials outperform other efficient materials, with more than 96% absorption broadband wavelength
Sharshir et al. (2019)	The authors discussed the methods utilized to enhance tubular solar stills. One of these techniques include nanomaterials. The usage of ZnO nano-rod shape enhanced the production by 30%
Chauhan et al. 2021)	The paper discussed direct solar desalination, and the integration of PCM with nanocrystal can substantially increase the yield. This enhancement is due to the boost of overall thermal conductivity of the basin water
Naveenkumar et al. 2020)	The authors segregated the paper based on effect and impact of nanomaterial such as CuO, TiO_2, Al_2O_3, and ZnO. This survey provides a good information basis for researchers to use in selecting optimal nanomaterials to boost solar still production rates
Iqbal et al. (2021)	A review of nanofluid assisted solar still was performed, and several aspects of economic and environmental benefits were investigated. The researchers showed that using NF-based SSs was a highly efficient system with considerable economic and environmental benefits

Table 30.5 (continued)

Reference	Main objectives and findings
Mevada et al. (2020)	The effect of fin configuration was investigated through a review. Fins are known to enhance the surface area, thus rate of heat transfer and the heat dissipation of the bottom of solar still is reduced
Arunkumar et al. (2018)	The thermal conductivities of Al_2O_3, CuO, Cu_2O, ZnO, SnO_2, TiO_2, SiO_2, Cu, Fe_2O_3, SiC, and multiwalled carbon nanotubes distributed in water with varying volume fractions are examined
Patel and Modi (2020)	The use of nanoparticles serves as a sensible energy storage material, accumulating energy throughout the day and releasing it at night. To increase performance, the authors analyzed different solar stills slopes and covers
Yang et al. (2020)	The paper showcases different studies that examine PCM and nano-PCM where nano-PCM outperformed PCMs by 8–11 times. Also, literature confirmed that the presence of nanoparticles could lower melting temperatures while increasing freezing temperatures

Black paint blended with titanium oxide nanoparticles is applied to the absorber of a solar still, a 0.25 m^2 mild steel basin formed into an equilateral triangle (Kabeel et al. 2019). To stop escaping heat to the outside environment, insulation was added on the bottom and sidewalls of the solar still. Black paint called TiO_2 nanoparticles raises water temperature by 1.5 °C compared to an absorber without them. As a result, TiO_2 nanoparticles enhance the solar still's production by 12% at the maximum water depth. For the absorber plate with and without a TiO_2 nanoparticle coating, the cumulative yield from the solar still is 6.6 and 6.2 kg/m^2, respectively (Kabeel et al. 2019).

The standard solar still was modified using flake graphite nanoparticles (FGN), phase change material (PCM), and film cooling (Sharshir et al. 2017). The still's productivity is 50.28%, 65%, 56.15%, and 73.8%, with FGN (modification A), FGN and PCM (modification B), FGN and film cooling (modification C), and FGN, PCM, and film cooling (modification D), respectively. As the water depth grows, the solar still performance of modificatoins A and B declines (Sharshir et al. 2017).

30.6 Conclusions

In this chapter, the main elements of the solar still are illustrated and the most common solar still systems are summarized and compared. The importance of utilizing nanotechnology to improve solar still efficiency using different techniques is discussed. Nanomaterials and saline water can be combined to create nanofluids. Some techniques include coating the absorber, coating the cover, or dispersing PCM.

The suggestions for future work can be summarized as follows:

- Combine two or three nanomaterials
- Combine new PCM with nanomaterials
- Coat the glass cover to decrease the temperature (previous research affects the wettability)
- Combine a nanomaterial and a sensible storage material (previous with PCM)
- Investigate the effect of nanomaterial morphology
- Coat both the absorber and glass.

References

Abdallah S, Abu-Khader MM, Badran O (2009) Effect of various absorbing materials on the thermal performance of solar stills. Desalination 242(1–3):128–137

Abdelkhalig A, Elgendi M, Selim MY (2022) Review on validation techniques of blade element momentum method implemented in wind turbines. IOP Conf Ser: Earth Environ Sci

Addel-Rehim ZS, Lasheen A (2005) Improving the performance of solar desalination system. Renew Energy 30:1955–1971

Al-harahsheh M, Abu-Arabi M, Mousa H, Alzghoul Z (2018) Solar desalination using solar still enhanced by external solar collector and PCM. Appl Therm Eng 128:1030–1040

AlMallahi MN, El Haj Assad M, AlShihabi S, Alayi R (2022) Multi-criteria decision-making approach for the selection of cleaning method of solar PV panels in United Arab Emirates based on sustainability perspective. Int J Low Carbon Technol 17:380–393

Arunkumar T, Denkenberger D, Ahsan A, Jayaprakash R (2013) The augmentation of distillate yield by using concentrator coupled solar still with phase change material. Desalination 314:189–192

Arunkumar T, Raj K, Denkenberger D, Velraj R (2018) Heat carrier nanofluids in solar still—a review. Desalin Water Treat 130:1–16

Arunkumar T, Wang J, Denkenberger D (2021) Capillary flow-driven efficient nanomaterials for seawater desalination: Review of classifications, challenges, and future perspectives. Renew Sustain Energy Rev 138:110547

Balachandran GB, David PW, Mariappan RK, Kabeel AE, Athikesavan MM, Sathyamurthy R (2020) Improvising the efficiency of single-sloped solar still using thermally conductive nano-ferric oxide. Environ Sci Pollut Res 27(26):32191–32204

Chamsa-ard W, Fawcett D, Fung CC, Poinern G (2020) Solar thermal energy stills for desalination: a review of designs, operational parameters and material advances. J Energy Power Technol 2(4)

Chauhan VK, Shukla SK, Tirkey JV, Rathore PKS (2021) A comprehensive review of direct solar desalination techniques and its advancements. J Clean Prod 284:124719

Cheng S, Elgendi M, Lu F, Chamorro LP (2021) On the wind turbine wake and forest terrain interaction. Energies 14(21):7204

Ding Z, Wu W, Leung M (2021) Advanced/hybrid thermal energy storage technology: material, cycle, system and perspective. Renew Sustain Energy Rev 145:111088. https://doi.org/10.1016/j.rser.2021.111088

Elango T, Kannan A, Murugavel KK (2015) Performance study on single basin single slope solar still with different water nanofluids. Desalination 360:45–51

El-Gendi M (2018a) Transient turbulent simulation of natural convection flows induced by a room heater. Int J Therm Sci 125:369–380

El-Gendi MM (2018b) Numerical simulation of unsteady natural convection flow inside a pattern of connected open square cavities. Int J Therm Sci 127:373–383

Elgendi M, Selim MY (2022) Determination of the effect of water depth on the yield of a solar still using an automatic feedwater system. Environ Sci Pollut Res 29(10):14595–14603

Elgendi M, Selim MY, Aldhaheri A, Alshehhi W, Almarshoodi H, Alhefeiti A (2022a) Design procedures for a passive pyramid solar still with an automatic feed water system. Alex Eng J 61(8):6419–6431

El-Gendi MM, Aly AM (2017) Numerical simulation of natural convection using unsteady compressible navier-stokes equations. Int J Numer Methods Heat Fluid Flow

Elgendi M, Al Dhaheri M, Al Baeek A, Saad S, Al Surihi H (2021a) Nanotechnology in solar still: conceptual design. In: 2021a 6th International conference on renewable energy: generation and applications (ICREGA)

Elgendi M, AlHefeiti A, Almarshoodi H, Aldhaheri A, Alshehhi W, Selim M (2021b) Embodiment design and detailed design of a pyramid solar still with an automatic feedwater system. IN: 2021b 6th International conference on renewable energy: generation and applications (ICREGA)

Elgendi M, Tamimi JA, Alfalahi A, Alkhoori D, Alshanqiti M, Aladawi A (2022b) Wall panels using thermoelectric generators for sustainable cities and communities: a mini-review. IOP Conf Ser: Earth Environ Sci

El-Sebaii A, Aboul-Enein S, El-Bialy E (2000) Single basin solar still with baffle suspended absorber. Energy Convers Manag 41(7):661–675

Faegh M, Shafii MB (2017) Experimental investigation of a solar still equipped with an external heat storage system using phase change materials and heat pipes. Desalination 409:128–135

Iqbal A, Mahmoud MS, Sayed ET, Elsaid K, Abdelkareem MA, Alawadhi H, Olabi A (2021) Evaluation of the nanofluid-assisted desalination through solar stills in the last decade. J Environ Manag 277:111415

Kabeel A, Abdelgaied M (2016) Improving the performance of solar still by using PCM as a thermal storage medium under Egyptian conditions. Desalination 383:22–28

Kabeel A, Omara Z, Essa F (2014) Improving the performance of solar still by using nanofluids and providing vacuum. Energy Convers Manag 86:268–274

Kabeel AE, Sathyamurthy R, Sharshir SW, Muthumanokar A, Panchal H, Prakash N, Prasad C, Nandakumar S, El Kady M (2019) Effect of water depth on a novel absorber plate of pyramid solar still coated with TiO2 nano black paint. J Clean Prod 213:185–191

Kandeal AW, Joseph A, Elsharkawy M, Elkadeem MR, Hamada MA, Khalil A, Eid Moustapha M, Sharshir SW (2022) Research progress on recent technologies of water harvesting from atmospheric air: a detailed review. Sustain Energy Technol Assess 52:102000. https://doi.org/10.1016/j.seta.2022.102000

Katekar VP, Deshmukh SS (2020a) A review of the use of phase change materials on performance of solar stills. J Energy Storage 30:101398

Katekar VP, Deshmukh SS (2020b) A review on research trends in solar still designs for domestic and industrial applications. J Clean Prod 257:120544

Kaviti AK, Ram AS, Kumari AA, Hussain S (2021) A brief review on high-performance nano materials in solar desalination. Mater Today: Proc 44:282–288

Khalifa AJN (2011) On the effect of cover tilt angle of the simple solar still on its productivity in different seasons and latitudes. Energy Convers Manag 52(1):431–436

Khalifa AJN, Ibrahim HA (2010) Effect of inclination of the external reflector of simple solar still in winter: an experimental investigation for different cover angles. Desalination 264(1–2):129–133

Khanafer K, Vafai K (2018) A review on the applications of nanofluids in solar energy field. Renew Energy 123:398–406. https://doi.org/10.1016/j.renene.2018.01.097

Mevada D, Panchal H, kumar Sadasivuni K, Israr M, Suresh M, Dharaskar S, Thakkar H (2020) Effect of fin configuration parameters on performance of solar still: a review. Groundwater Sustain Dev 10:100289

Naim MM, Abd El Kawi MA (2003) Non-conventional solar stills part 1. Non-conventional solar stills with charcoal particles as absorber medium. Desalination 153(1–3):55–64

Nassar YF, Yousif SA, Salem AA (2007) The second generation of the solar desalination systems. Desalination 209(1–3):177–181

Naveenkumar R, Gurumoorthy G, Kunjithapatham G, Bharath A, Ravichandran M (2020) Impact of adding various nano materials in the efficiency of single slope solar still: a review. Mater Today: Proc 33:3942–3946

Obaideen K, AlMallahi MN, Alami AH, Ramadan M, Abdelkareem MA, Shehata N, Olabi A (2021) On the contribution of solar energy to sustainable developments goals: case study on Mohammed bin Rashid Al Maktoum Solar Park. Int J Thermofluids 12:100123

Omara Z, Kabeel A, Essa F (2015) Effect of using nanofluids and providing vacuum on the yield of corrugated wick solar still. Energy Convers Manag 103:965–972

Patel SK, Modi KV (2020) Techniques to improve the performance of enhanced condensation area solar still: a critical review. J Clean Prod 268:122260

Safaei MR, Goshayeshi HR, Chaer I (2019) Solar still efficiency enhancement by using graphene oxide/paraffin nano-PCM. Energies 12(10):2002

Sakthivel M, Shanmugasundaram S, Alwarsamy T (2010) An experimental study on a regenerative solar still with energy storage medium—Jute cloth. Desalination 264(1–2):24–31

Sampathkumar K, Senthilkumar P (2012) Utilization of solar water heater in a single basin solar still—an experimental study. Desalination 297:8–19

Shalaby S, El-Bialy E, El-Sebaii A (2016) An experimental investigation of a v-corrugated absorber single-basin solar still using PCM. Desalination 398:247–255

Sharshir S, Yang N, Peng G, Kabeel AE (2016) Factors affecting solar stills productivity and improvement techniques: a detailed review. Appl Therm Eng 100:267–284

Sharshir S, Peng G, Wu L, Essa F, Kabeel A, Yang N (2017) The effects of flake graphite nanoparticles, phase change material, and film cooling on the solar still performance. Appl Energy 191:358–366

Sharshir SW, Ellakany YM, Algazzar AM, Elsheikh AH, Elkadeem M, Edreis EM, Waly AS, Sathyamurthy R, Panchal H, Elashry MS (2019) A mini review of techniques used to improve the tubular solar still performance for solar water desalination. Process Saf Environ Prot 124:204–212

Singh AK, Singh D, Dwivedi V, Tiwari G, Gupta A (2020) Water purification using solar still with/without nano-fluid: a review. Mater Today: Proc 21:1700–1706

Singh G, Singh DB, Kumar S, Bharti K, Chhabra S (2021) A review of inclusion of nanofluids on the attainment of different types of solar collectors. Mater Today: Proc 38:153–159

Yang L, Huang J-N, Zhou F (2020) Thermophysical properties and applications of nano-enhanced PCMs: an update review. Energy Convers Manag 214:112876